JOURNAL OF THE
MYANMAR ACADEMY OF
ARTS AND SCIENCE

Physics

Vol. XVIII, No. 2C, July, 2020

Myanmar Academy of Arts and Science

Journal of the Myanmar Academy of Arts and Science

Vol. XVIII, No.2C

Contents

Physics

Edition

2020, July, 1000 Copies

Published by

Dr Aung Min (00322) Chairman, Journal Publication Committee,
Myanmar Academy of Arts and Science

ISSN 2520-0186
LCCN 2003-323143

Printed by

U Win Aung (00171), Manager,
Universities Press, Yangon, Myanmar

J. Myanmar Acad. Arts Sci. 2020 **Vol. XVIII.No.2C**

ELEMENTAL ANALYSIS OF LAYERS OF ONION

Thu Thu Thaw Myint[1], Win Sin[2]

Abstract

The individual layers of an onion have been analysed using EDX-7000 to study the elements contained in each layer and the change in concentrations of elements according to layer positions. The major elements found in each layer are potassium, sulphur and copper.

Keywords: Onion, EDXRF, Elemental Analysis

Introduction

Minerals are important for our body to stay healthy. Our body uses minerals for many different jobs, including keeping our bones, muscles, heart, and brain working properly. Minerals are also important for making enzymes and hormones.

There are two kinds of minerals: macrominerals and trace minerals. We need larger amounts of macrominerals. They include calcium, phosphorus, magnesium, sodium, potassium, chloride and sulfur. We only need small amounts of trace minerals. They include iron, manganese, copper, iodine, zinc, cobalt, fluoride and selenium. Most people get the amount of minerals they need by eating a wide variety of foods.

Onions are cultivated and consumed across the world. They are usually served cooked. They can also be eaten raw and are used in pickles and chutneys. The onion has a strong taste and a sharp, pungent flavor. Though it is a temperate crop, it can be grown under a wide range of climatic conditions.

Onions are super-healthy. They are excellent sources of vitamin C, sulphuric compounds, flavonoids and phytochemicals. They contain sulfur**,** potassium**,** protein**,** vitamin A, vitamin C, calcium and iron**.** Onions' sulfurs may be effective anti-inflammatory agents. Onions encourage a healthy heart in many ways, including lowering blood pressure and lowering heart attack risk.

We have tried to embody the concentrations of elements in various layers of onion and how the value changes from outer layer to inner layer. Interestingly it is found that onion contains precious macrominerals and the concentration changes from layer to layer.

Theoretical Background

X-ray Fluorescence Analysis

X-ray fluorescence (XRF) analysis is a powerful analytical tool for the elemental analysis of almost all the elements present in a sample. XRF radiation is induced when photons of sufficiently high energy, emitted from an x-ray source, impinge on a material. These primary x-rays undergo interaction processes with the analyte atoms. High-energy photons induce ionization of inner shell electrons by the photoelectric effect and thus electron vacancies in inner shells (K, L, M,…) are created.

---

[1] Dr, Assistant Lecturer, Department of Physics, University of Yangon

[2] Dr, Associate Professor, Department of Physics, West Yangon University

The creation of a vacancy in a particular shell results in a cascade of electron transitions, all correlated with the emission of photons with a well-defined energy corresponding to the difference in energy between the atomic shells involved. The family of characteristic x-rays from each element including all transitions allows the identification of the element.

The working principle of XRF analysis is the measurement of wavelength or energy and intensity of the characteristic x-ray photons emitted from the sample. This allows the identification of the elements present in the sample and the determination of their mass or concentration. All the information for the analysis is stored in the measured spectrum. In energy dispersive x-ray fluorescence analysis (EDXRF), the result is an x-ray energy vs intensity spectrum [Jekins RE 1999].

X-Ray Fluorescence (XRF) Instrumentation

The incident x-ray beam is typically produced from a Rh target. Various types of detectors are used to measure the intensity of the emitted beam. The flow counter is commonly utilized for measuring long wavelength (> 0.15 nm) x-rays that are typical of K spectra from elements lighter than Zn. The scintillation detector is commonly used to analyze shorter wavelengths in the x-ray spectrum (K spectra of element from Nb to I; L spectra of Th and U). X-rays of intermediate wavelength (K spectra produced from Zn to Zr and L spectra from Ba and the rare earth elements) are generally measured by using both detectors.

The x-ray tube consists of a vacuum enclosure containing an electron source and target anode. A thin window is mounted in the vacuum wall to allow the x-rays to exit the tube enclosure. Commercial tubes are typically manufactured from glass, although metal tubes with glass or ceramic electrical insulators are common. The exit window is typically a thin beryllium (Be) foil. The electron beam is generated using a thermionic cathode and is accelerated toward the anode by an electrostatic potential of typically 30-100 keV. In most applications the acceleration voltage is achieved with the anode assemble at ground potential and with the insulated cathode assembly at the appropriate negative high voltage.

EDXRF is relatively simple and inexpensive compared to other techniques. It requires and x-ray source, (50-60) kV, (50-300) W x-ray tube. The second major component is the detector, which must be designed to produce electrical pulses that vary with the energy of the incident x-rays. Most laboratory EDXRF instruments use liquid nitrogen or Si(Li) detectors [Rene E, Van Grieken, Andrzej 1993.].

Main Specifications of Shimadzu EDX-7000 Spectrometer

Measurement principle	X-ray fluorescence spectrometer
Measurement method	Energy dispersive
Target samples	Solids, liquids, powders
Measuring range	11 Na to 92 U

X-ray Generator (EDX-7000)

X-ray tube	Rhodium (Rh) target
Voltage	4 kV to 50 kV
Current	1μA to 1000 μA

Cooling method	air cooling (with a fan)
Irradiated area	10 mm diameter (standard)
Primary filters	Automatic selection from among 5 types of filter

Detector

Type	Silicon drift detector (SDD)

Sample Chamber

Measurement Atmosphere	Air, vacuum, helium
Sample replacement	12- sample turret
Sample observations	Semiconductor camera

Sample Collection and Preparation

Red onions, cultivated in Myit-Thar region, were bought from local market. Onion layers were cut into small round pieces of 1 cm diameter. The bottom of the cell is covered with film, and the samples were put into the cell, and covered with film again. The cells were put into chamber and analysed.

Results and Discussions

The elemental concentrations of various layers of onion are shown in Table 1 and the respective graph is shown in Figure 1. Major elements found are potassium, sulfur and calcium. The minor element found is copper.

The comparison of potassium contained in individual layers of onion is shown in in Figure 2. Potassium concentration becomes larger from outer layer to inner layer. The highest concentration of potassium is found in second innermost layer.

The comparison of calcium contained in individual layers of onion is shown in Figure 3. Calcium concentration becomes smaller from outer layer to inner layer. Calcium is not detected in the two innermost layers.

The comparison of sulfur contained in individual layers of onion is shown in Figure 4. Sulfur concentration becomes larger from outer layer to inner layer. The highest concentration of sulfur is found in second innermost layer.

The comparison of copper contained in individual layers of onion is shown in Figure 5. Copper concentration is the same in all layers. The concentration is greatest in third layer.

Conclusion

Potassium lowers blood pressure, protects against loss of muscle mass, preserves bone mineral density, and reduces the formation of kidney stones.

Our body needs calcium to build and maintain strong bones. Our heart, muscles and nerves also need calcium to function properly.

Sulfur makes up vital amino acids used to create protein for cells, tissues, hormones, enzymes, and antibodies. Sulfur is needed for insulin production.

Copper is essential for infant growth, bone strength, red and white blood cell maturation, iron transport, cholesterol and glucose metabolism, heart muscle contraction and brain development.

From our study, onion is found to contain essential macrominerals. Minerals concentration changes from layer to layer. Doing more research on this may develop a relation between the layer position and mineral concentration.

Acknowledgements

We would like to express our profound thanks Dr khin Khin Win, Professor and Head, Department of Physics, University of Yangon for her kind permission to carry out this research.

Our sincere thanks also all of Professors, Department of Physics, University of Yangon for their kind encouragement to carry out this research.

We also thanks all members of the staff of Physics department, Yangon University, for their constant encouragement and help during this research work.

References

Cesareo R (2000) "X-Ray Physics: Interaction with Matter, Production, Detection" (Bologna: La Rivista del Nuovo Cimento)

Chevallier, A. (1996). The encyclopedia of medicinal plants. London: Dorling Kindersely Limited.

Donal E Leydon (1999) "Fundamentals of X-Ray Spectrometry as Applied to Energy Dispersive Techniques", Spectrace Instruments Technical Paper

Jekins RE (1999) "X-Ray Fluorescence Spectrometry" (New York: Wiley- Interscience)

Peter N. Brouwer, (2003) Theory of XRF 1st ed PANalytical B.V The Netherlands.

Rene E, Van Grieken, Andrzej (1993) " Handbook of X ray Spectrometry Methods and Techniques" (New York : Marcle Dekker)

Tertain R & Classie F (1982) "Principles of Quantitative X ray Fluorescence Analysis " (London: Heyden)

Table 1 Elemental Concentration (W%) of Onion layers

Element	Layer 1	Layer 2	Layer 3	Layer 4	Layer 5
K	0.042	0.058	0.088	0.113	0.069
Ca	0.018	0.017	0.015	0.000	0.000
S	0.046	0.046	0.049	0.053	0.050
Cu	0.001	0.001	0.002	0.001	0.001

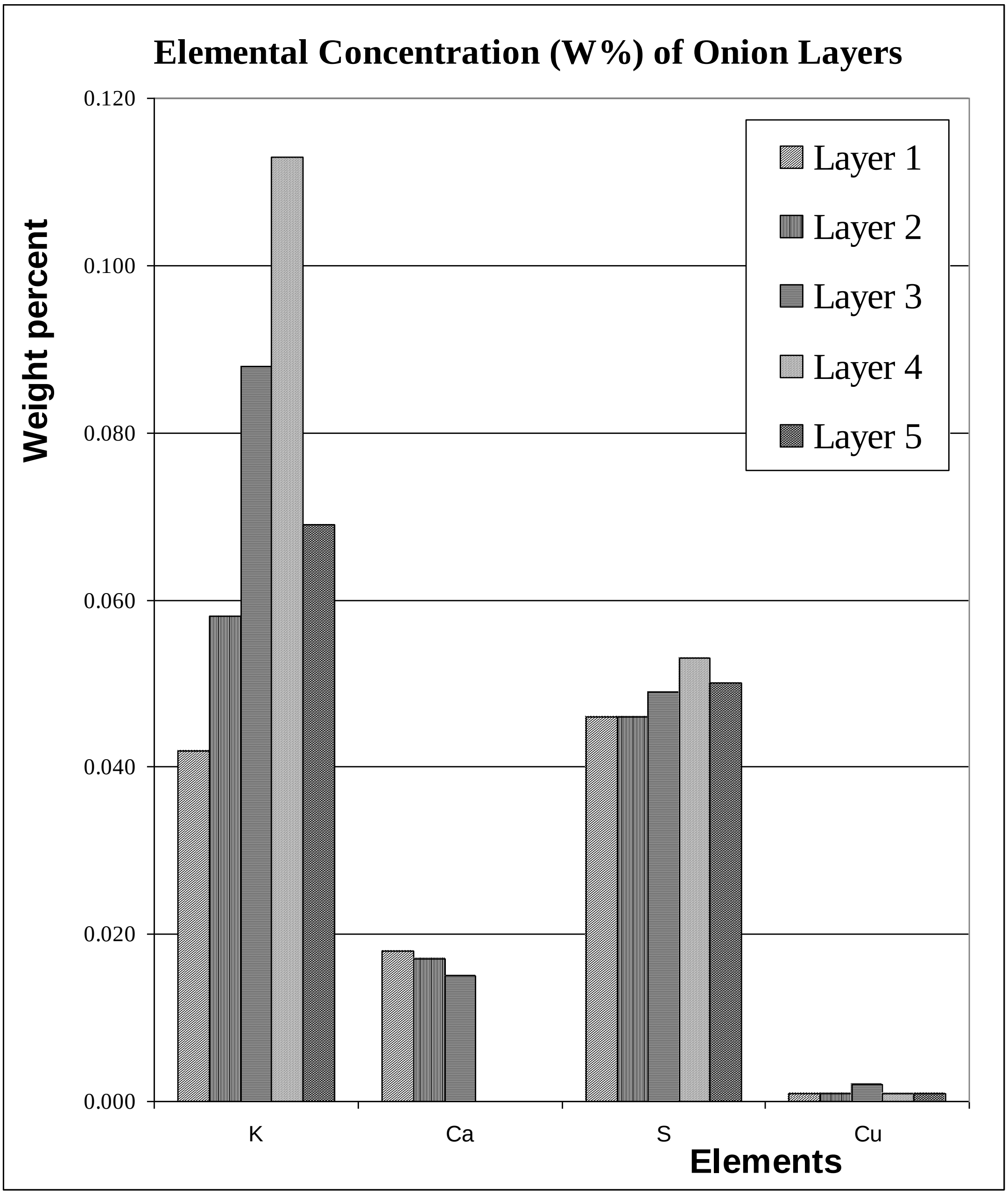

Figure 1 Elemental Concentration (W%) of Onion layers

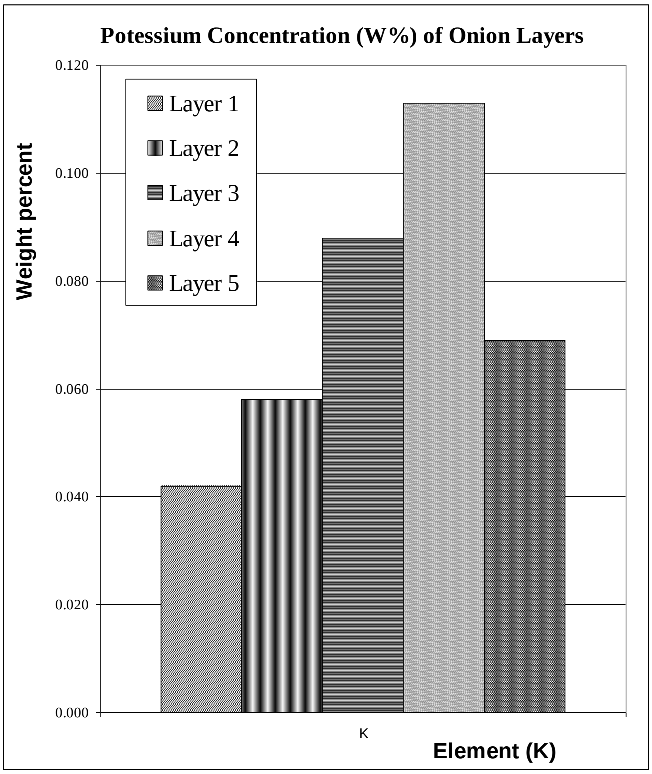

Figure 2 Potassium Concentration (W%) of Onion layers

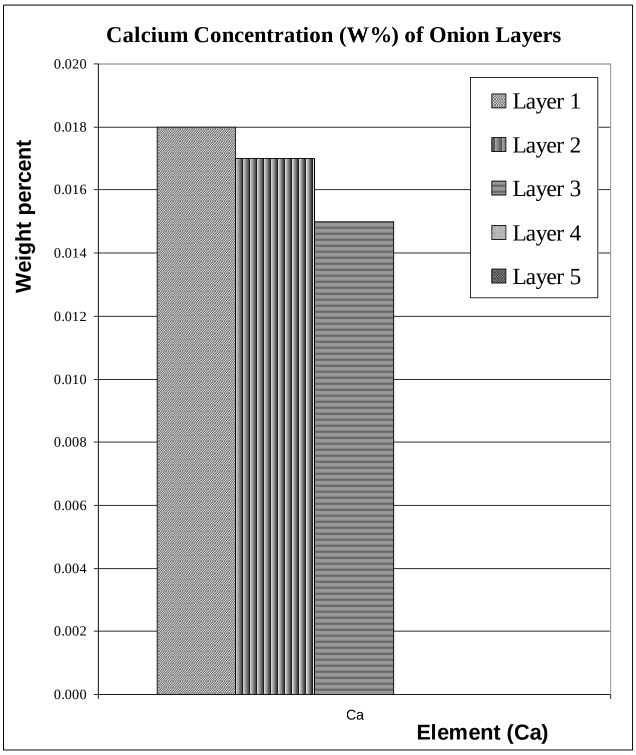

Figure 3 Calcium Concentration (W%) of Onion layers

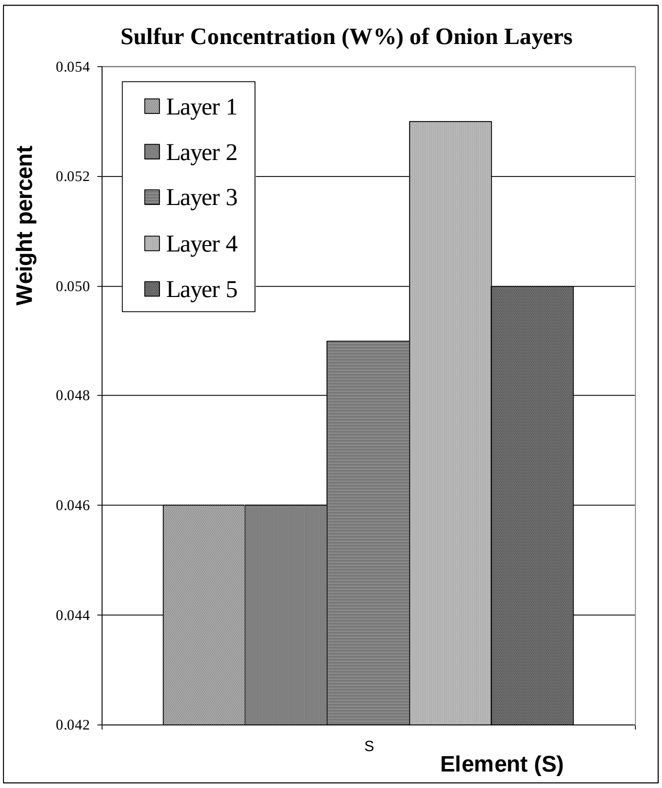

Figure 4 Sulfur Concentration (W%) of Onion layers

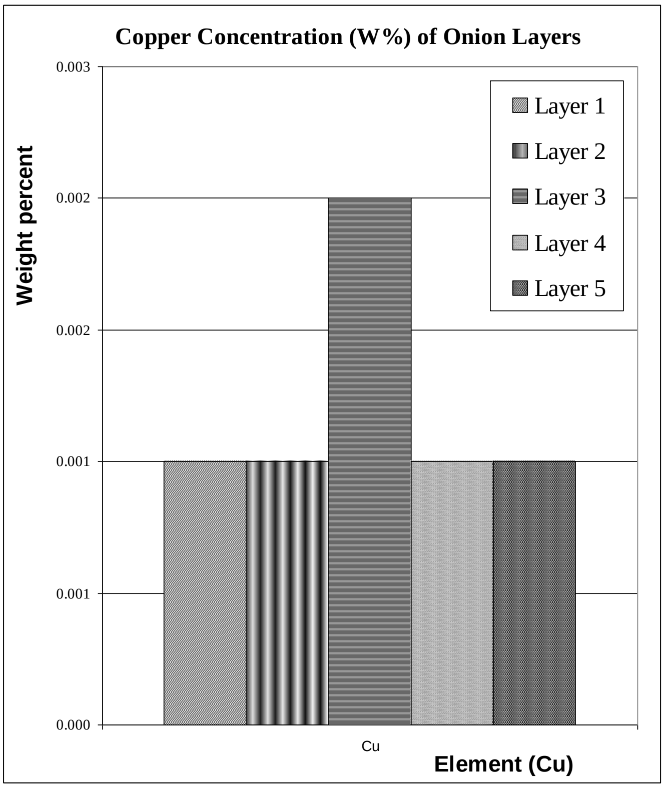

Figure 5 Copper Concentration (W%) of Onion layers

```
Sample   : Onion Shell-1
Operator: DRWLO
Comment : with mylar film
Group    : FP Balance_5mm
Date     : 2019-01-10 12:55:46

Measurement Condition
---------------------------------------------------------------------------------
Instrument: EDX-7000    Atmosphere: Air    Collimator:  5(mm)      Sample Cup:Mylar
---------------------------------------------------------------------------------
Analyte               TG kV   uA      FI    Acq.(keV) Anal.(keV)  Time(sec)    DT(%)
---------------------------------------------------------------------------------
Al-U                  Rh 50  137-Auto ----   0 - 40   0.00-40.00  Live- 100     29
```

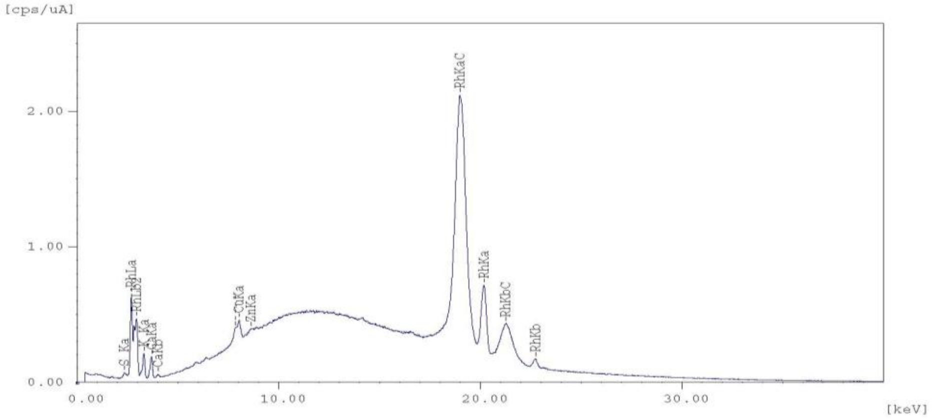

```
Qualitative Result
---------------------------------------------------------------------------------
Element: S , Rh, K , Ca, Cu, Zn

Quantitative Result
---------------------------------------------------------------------------------
Analyte                 Result           [3-sigma] Proc.-Calc. Line   Int.(cps/uA)
---------------------------------------------------------------------------------
S                        0.046 %          [ 0.004] Quan-FP     S Ka       0.2669
K                        0.042 %          [ 0.001] Quan-FP     K Ka       1.0781
Ca                       0.018 %          [ 0.000] Quan-FP     CaKa       0.9367
Cu                       0.001 %          [ 0.000] Quan-FP     CuKa       1.5772
Zn                       0.000 %          [ 0.000] Quan-FP     ZnKa       0.3821
CH                      99.892 %          [------] Balance     -------- --------
```

```
Sample   : Onion Shell-2
Operator: DRWLO
Comment : with mylar film
Group    : FP Balance_5mm
Date     : 2019-01-10 12:58:25

Measurement Condition
---------------------------------------------------------------------------------
Instrument: EDX-7000    Atmosphere: Air    Collimator:  5(mm)      Sample Cup:Mylar
---------------------------------------------------------------------------------
Analyte               TG kV   uA      FI    Acq.(keV) Anal.(keV)  Time(sec)    DT(%)
---------------------------------------------------------------------------------
Al-U                  Rh 50  118-Auto ----   0 - 40   0.00-40.00  Live- 100     29
```

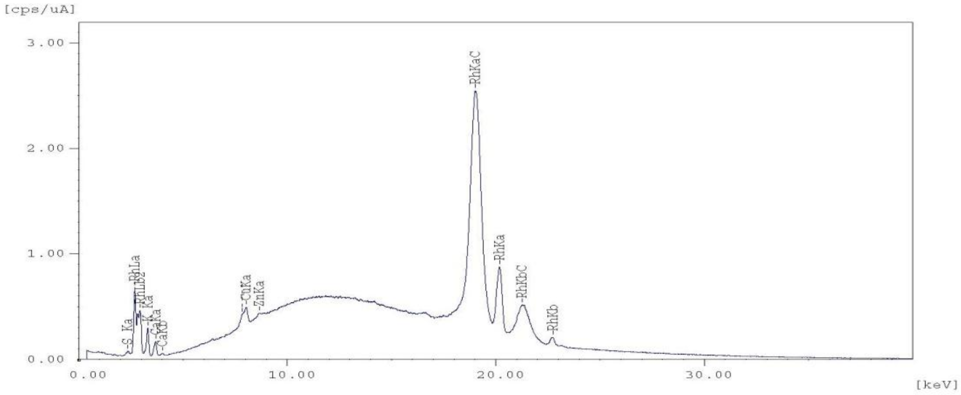

```
Qualitative Result
---------------------------------------------------------------------------------
Element: S , Rh, K , Ca, Cu, Zn

Quantitative Result
---------------------------------------------------------------------------------
Analyte                 Result           [3-sigma] Proc.-Calc. Line   Int.(cps/uA)
---------------------------------------------------------------------------------
K                        0.058 %          [ 0.001] Quan-FP     K Ka       1.4955
S                        0.046 %          [ 0.004] Quan-FP     S Ka       0.2670
Ca                       0.017 %          [ 0.001] Quan-FP     CaKa       0.8426
Cu                       0.001 %          [ 0.000] Quan-FP     CuKa       1.7414
Zn                       0.000 %          [ 0.000] Quan-FP     ZnKa       0.4861
CH                      99.877 %          [------] Balance     -------- --------
```

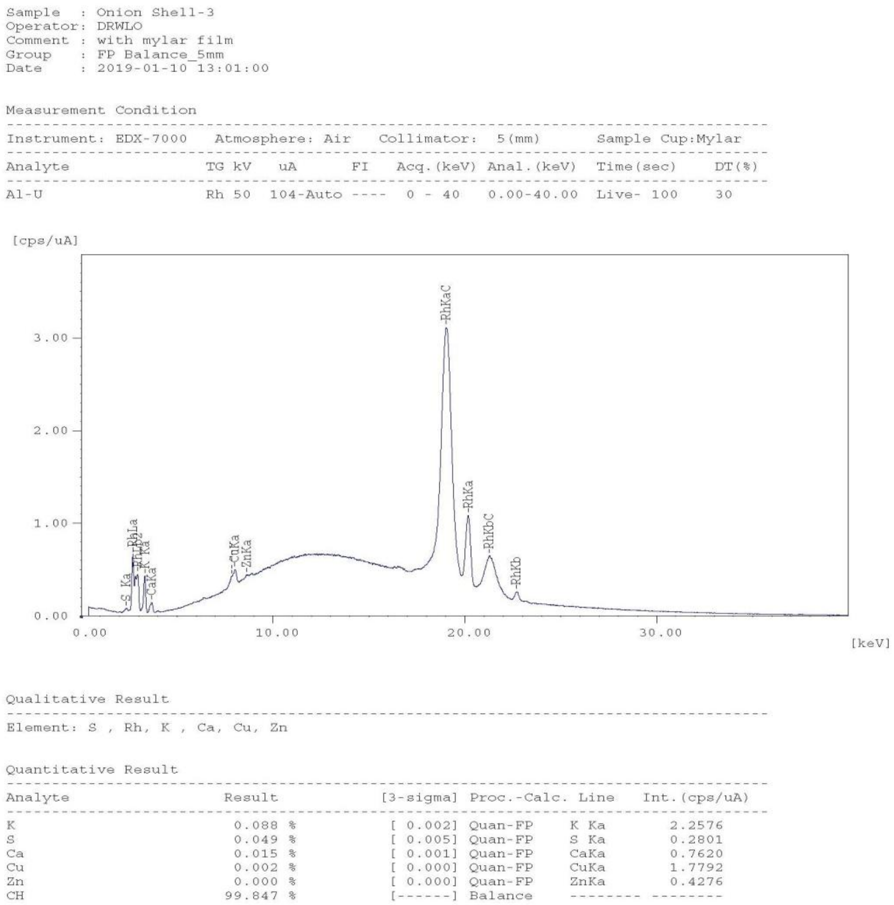

```
Sample  : Onion Shell-3
Operator: DRWLO
Comment : with mylar film
Group   : FP Balance_5mm
Date    : 2019-01-10 13:01:00

Measurement Condition
-------------------------------------------------------------------------------
Instrument: EDX-7000   Atmosphere: Air   Collimator:  5(mm)      Sample Cup:Mylar
-------------------------------------------------------------------------------
Analyte              TG kV   uA      FI   Acq.(keV) Anal.(keV)  Time(sec)    DT(%)
-------------------------------------------------------------------------------
Al-U                 Rh 50  104-Auto ----   0 - 40   0.00-40.00  Live- 100    30
```

```
Qualitative Result
-------------------------------------------------------------------------------
Element: S , Rh, K , Ca, Cu, Zn

Quantitative Result
-------------------------------------------------------------------------------
Analyte                  Result            [3-sigma] Proc.-Calc. Line   Int.(cps/uA)
-------------------------------------------------------------------------------
K                         0.088 %          [ 0.002] Quan-FP     K Ka       2.2576
S                         0.049 %          [ 0.005] Quan-FP     S Ka       0.2801
Ca                        0.015 %          [ 0.001] Quan-FP     CaKa       0.7620
Cu                        0.002 %          [ 0.000] Quan-FP     CuKa       1.7792
Zn                        0.000 %          [ 0.000] Quan-FP     ZnKa       0.4276
CH                       99.847 %          [------] Balance     -------- --------
```

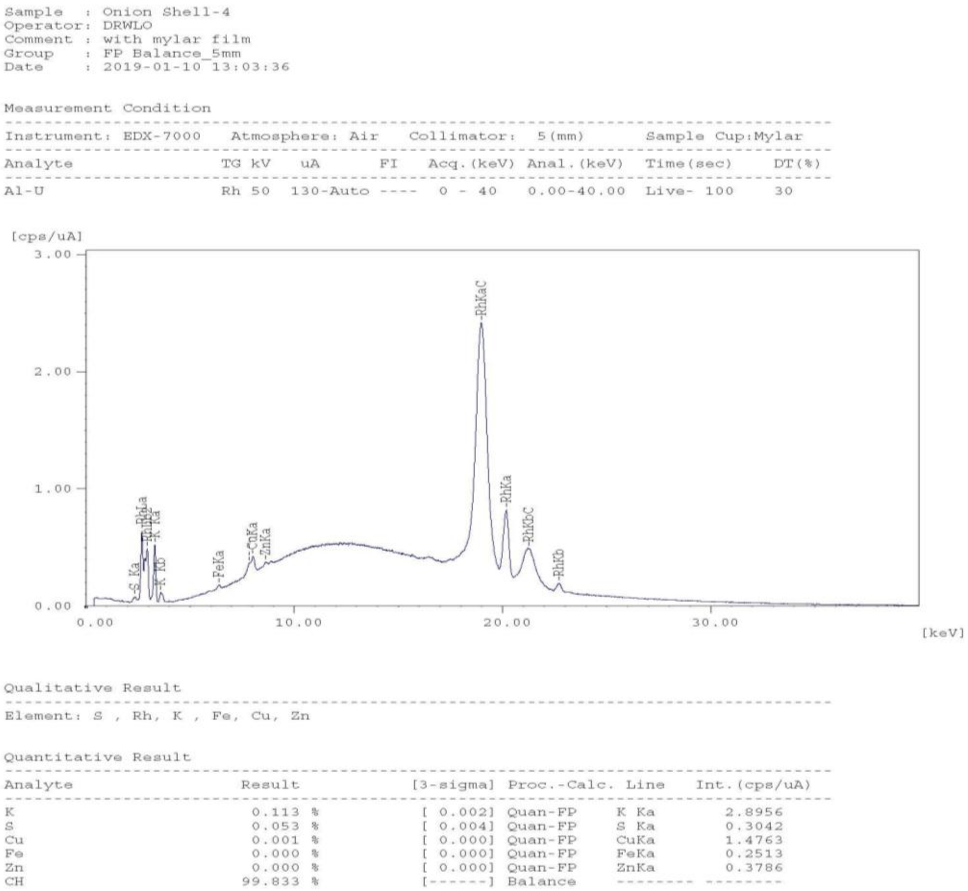

```
Sample  : Onion Shell-4
Operator: DRWLO
Comment : with mylar film
Group   : FP Balance_5mm
Date    : 2019-01-10 13:03:36

Measurement Condition
-------------------------------------------------------------------------------
Instrument: EDX-7000   Atmosphere: Air   Collimator:  5(mm)      Sample Cup:Mylar
-------------------------------------------------------------------------------
Analyte              TG kV   uA      FI   Acq.(keV) Anal.(keV)  Time(sec)    DT(%)
-------------------------------------------------------------------------------
Al-U                 Rh 50  130-Auto ----   0 - 40   0.00-40.00  Live- 100    30
```

```
Qualitative Result
-------------------------------------------------------------------------------
Element: S , Rh, K , Fe, Cu, Zn

Quantitative Result
-------------------------------------------------------------------------------
Analyte                  Result            [3-sigma] Proc.-Calc. Line   Int.(cps/uA)
-------------------------------------------------------------------------------
K                         0.113 %          [ 0.002] Quan-FP     K Ka       2.8956
S                         0.053 %          [ 0.004] Quan-FP     S Ka       0.3042
Cu                        0.001 %          [ 0.000] Quan-FP     CuKa       1.4763
Fe                        0.000 %          [ 0.000] Quan-FP     FeKa       0.2513
Zn                        0.000 %          [ 0.000] Quan-FP     ZnKa       0.3786
CH                       99.833 %          [------] Balance     -------- --------
```

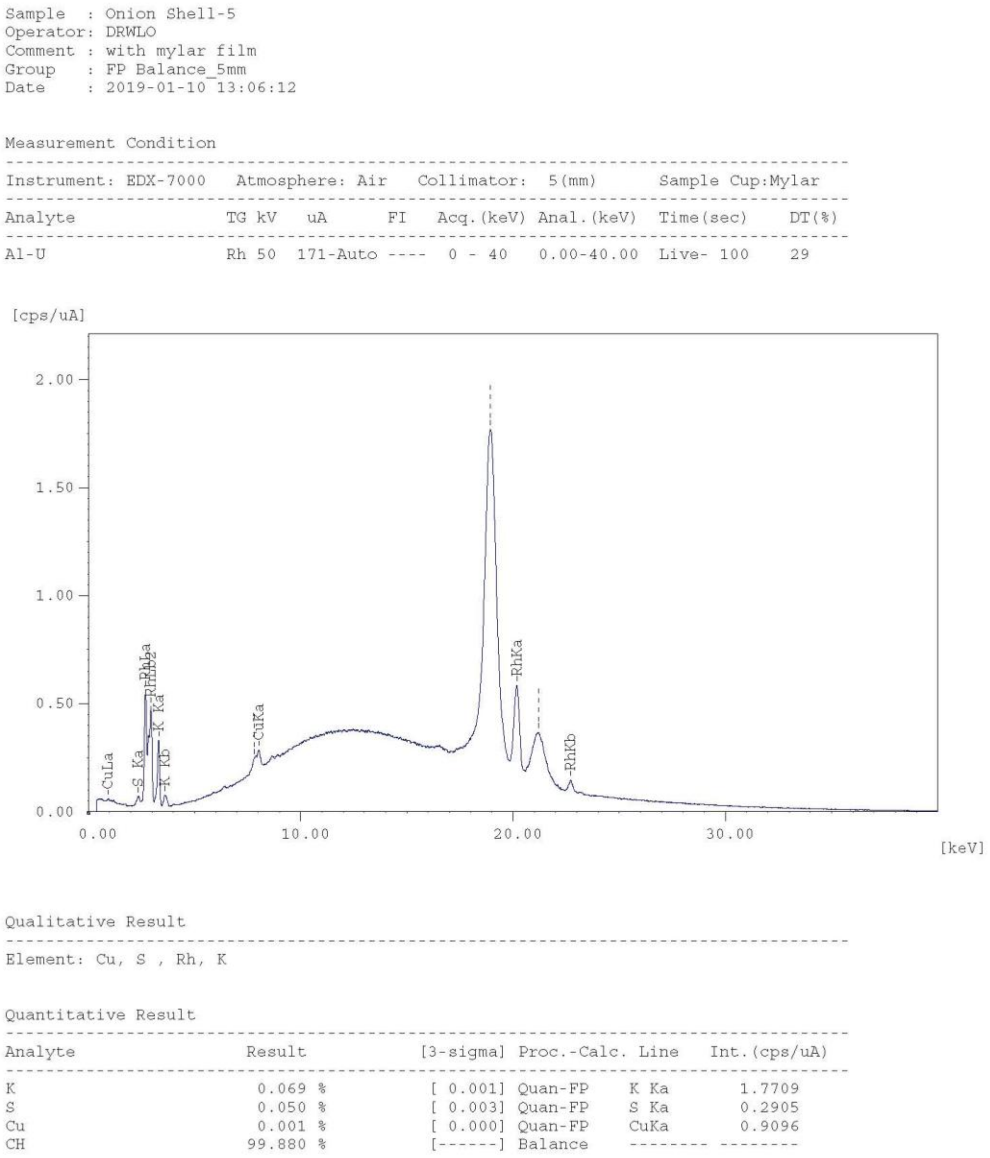

```
Sample   : Onion Shell-5
Operator: DRWLO
Comment  : with mylar film
Group    : FP Balance_5mm
Date     : 2019-01-10 13:06:12

Measurement Condition
------------------------------------------------------------------------------------
Instrument: EDX-7000   Atmosphere: Air   Collimator:  5(mm)      Sample Cup:Mylar
------------------------------------------------------------------------------------
Analyte              TG kV   uA      FI   Acq.(keV) Anal.(keV)  Time(sec)     DT(%)
------------------------------------------------------------------------------------
Al-U                 Rh 50  171-Auto ----   0 - 40   0.00-40.00  Live- 100     29
```

```
Qualitative Result
------------------------------------------------------------------------------------
Element: Cu, S , Rh, K

Quantitative Result
------------------------------------------------------------------------------------
Analyte                  Result          [3-sigma] Proc.-Calc. Line   Int.(cps/uA)
------------------------------------------------------------------------------------
K                         0.069 %         [ 0.001] Quan-FP    K Ka       1.7709
S                         0.050 %         [ 0.003] Quan-FP    S Ka       0.2905
Cu                        0.001 %         [ 0.000] Quan-FP    CuKa       0.9096
CH                       99.880 %         [------] Balance    -------- --------
```

J. Myanmar Acad. Arts Sci. 2020 **Vol. XVIII.No.2C**

STUDY ON THE ANTIMICROBIAL PROPERTIES OF TiO_2 NANOPARTICLESBY POUR PLATE CULTURE METHOD FOR APPLICATION IN WATER TREATMENT

Su Su Hlaing[1], Khin Lay Thwe[2], May Thu Aung[3]

Abstract

TiO_2 nanoparticles were synthesized by the sol-gel combustion hybrid method using acetylene black as a fuel. The starting materials were: titanium isopropoxide, isopropanol and acetylene black which was obtained by the decomposition of acetylene and ammonium hydroxide. The obtained TiO_2nanopowderswere examined by X-ray Diffraction (XRD). The sizes of the particles were estimated by using Scherrer's equation. The as-prepared TiO_2nanoparticles synthesized at 500°C were applied to study the antimicrobial behaviour. The activity of TiO_2 nanoparticle against Escherichia coli (E.coli) using a serial dilution and pour plate culture method were investigated for application in water treatment.

Keywords: Antimicrobial behaviour, E.coli, Pour plate culture method, Sol-gel combustion hybrid method, TiO_2nanoparticles.

Introduction

The unique, unusual and interesting physical, chemical and biological properties of nanometer-sized materials have recently attracted a great deal of interest in the scientific community(Choi. S.Y.et al, 2004). There is a need to develop a simple and efficient method to obtain TiO_2 nanoparticles with a narrow size distribution and high crystallinity (Rana. N.et al, 2016).Sol-gel combustion is a novel method that uses a unique combination of the chemical sol-gel process and combustion. The sol-gel combustion method is based on the gelling and subsequent combustion of an aqueous solution containing salts of the desired metals and an inorganic fuel such as acetylene black and it yields a voluminous and fluffy product with alarge surface area (Yun. H. S. et al, 2013). This process has the advantages of inexpensive precursors, a simple preparation method and the ability to yield nanosized powders.

E.coli is a microscopic organism that indicates fecal contamination of drinking water. Most of the drinking water originates from rivers and lakes near where people live. Depending on where it is, the water may pick up bacteria and other microorganisms as well as pollutants from industry, agriculture, roadways, and other sources.

Some of water contaminants may cause acute illness, such as what might occur from bacteria or other microbes, like *E.coli*, which may cause illness and even death(Kormann. C. et al, 1988). It is important that waterpollution should be concerned and act upon it. Good thing that there are processes that can get rid of these microbes(Prado. A. G. S. et al, 2008).

In the present work, the TiO_2 nanoparticles were synthesized by sol-gel combustion hybrid method. The as-prepared TiO_2 nanoparticles were used to study the antimicrobial behaviour against Escherichia coli (*E.coli*) using a serial dilution and pour plate culture method(Han. C. H. et al, 2007)for application in water treatment.

---

[1] Dr, Assistant Lecturer, Department of Physics, University of Yangon, Myanmar

[2] Dr, Lecturer, Environment and Water Studies Department, University of Yangon, Myanmar

[3] Dr, Department of Physics, University of Yangon, Myanmar

Experimental procedures

(i) Synthesis of Nanocrystalline TiO_2 Powder

TiO_2 nanoparticles have been synthesized using various methods. Among the various methods, the sol-gel combustion hybrid method is found to have many advantages over others. This method uses a unique combination of chemical sol-gel process and combustion. It is based on the gelling and subsequent combustion of an aqueous solution containing salts of desired metals and an inorganic fuel such as acetylene black. With the sol-gel method, it is advantageous to yield nanopowders of high purity and good homogeneity at low processing temperature while with the combustion method, requirements of simple equipments, low energy and short operation time are advantages as this method uses a sustainable exothermic solid-solid reaction among the raw materials. Consequently, the sol-gel combustion hybrid method has the advantages such as needs of inexpensive precursors and simple method of preparation to yield nanosized powder with considerably short operation time. It may also yield a voluminous fluffy product with a large surface area. Figure1shows the flow scheme of the combustion processes used for the synthesis of nanocrystalline TiO_2 powder.

TiO_2 nanoparticles were synthesized by the sol-gel combustion hybrid method using acetylene black as a fuel. The starting materials are: titanium isopropoxide, isopropanol, acetylene black which was obtained by the decomposition of acetylene and ammonium hydroxide. First, 3.5mL of titanium isopropoxide was dissolved in 10mL of isopropanol and 0.2 g of acetylene black was added to the titanium solution followed by an aqueous NH_4OH solution dropwise under constant stirring until it was transformed into a sol at ambient conditions. The sol was heated at 100ºC to obtain a dry gel. The gel was ignited in air at 500ºC resulting in an auto-combustion process that yielded TiO_2 powders.

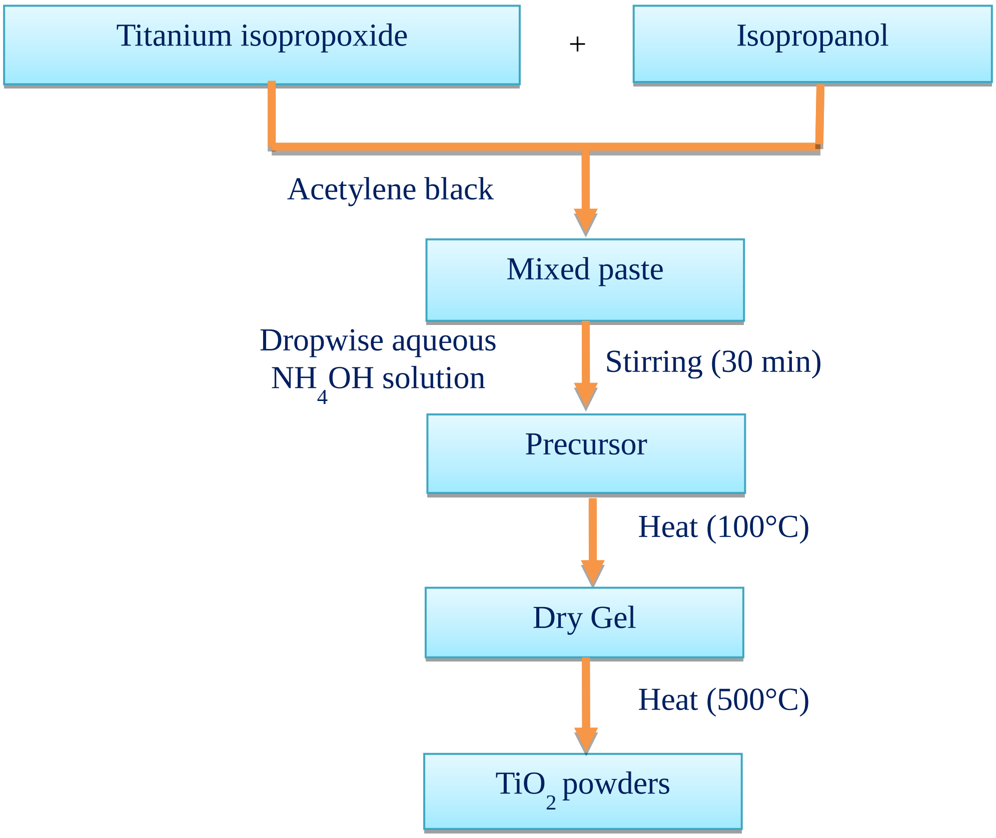

Figure 1 Flow scheme of the combustion process for the synthesis of NanocrystallineTiO_2 powders

The obtained TiO_2nanopowders were examined by powder X-ray diffraction (XRD: RIGAKU-RINT 2000 X-ray diffractometer).The crystallized sizes of these nanoparticles were estimated by using Scherrer's equation. The synthesis processes of TiO_2nanopowder were shown in Figure 2 (a), (b), (c), (d), (e) and (f).

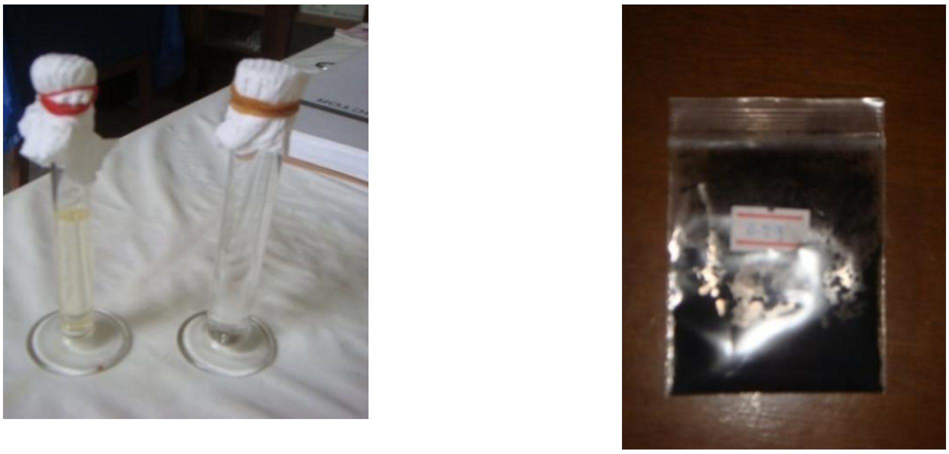

(a) Titanium isopropoxide and isopropanol (b) Acetylene black

(c) Dropwise aqueous NH_4OH solution (d) Heating the sol at 100ºC

(e) Home-made furnace and temperature sensor (f) Annealing the gel at 500ºC

Figure 2 The synthesis processes of TiO_2nanopowder

(ii) Antimicrobial Activity of TiO_2 Nanoparticlesby Pour Plate Culture Method

The as-prepared TiO_2 nanopowders synthesized at 500°C were applied to study the antimicrobial behavior. The activity of TiO_2 nanoparticle against Escherichia coli (E.coli) were investigated by using a serial dilution and pour plate culture method.

The nutrient broth (1g) and plate count agar (5g) were added to 50 ml of distilled water. This solution was added to the conical flask (each conical flask per 25 mL). The agar solution was heated on the hotplate until boil to well dissolve. These conical flasks were added to the autoclave at 121°C for 45 min. After 45 min, these conical flasks were cooled about 30 min. Then TiO_2 nanopowders (0.005, 0.01, 0.05, 0.1, 0.25, 0.3, 0.35, 0.4, 0.45 and 0.5g) were mixed to the liquefied agar, respectively. The initial dilution was made by transferring 1mL of E.coli sample to a 9 mL sterile saline with water (1:10 or 10^{-1} dilution). The 10^{-1} dilution was then shaken by grasping the tube between the palms of both hands and rotating quickly to create a vortex. This serves to distribute the bacteria and break up any clumps. Immediately after the 10^{-1} dilution has been shaken, uncap it and aseptically transfer 1 mL to a second 9 mL saline with water (1:100 or 10^{-2} dilution) through to 1:10000 or 10^{-5}. Since the third was a 10^{-3} dilution, the fifth represents a 10^{-5} dilution of the original sample. Then 1 mL of 10^{-3} dilute saline solution containing E.coli was placed into the ten sterilized petri dishes each 1 mL. After that, 50 mL of ager solution was poured into 10^{-3} petri dishes each 25 mL. The bacterial agar solution and sample were immediately mixed gently moving the plate. This process for the remaining ten plates of the 10^{-5} dilution was repeated. After the pour plates have cooled and the agar has hardened, they were moved into the incubator at 37°C for 24 hours. The process of antimicrobial test as shown in Figure 3(a), (b), (c), (d), (e), (f), (g) and (h).

At the end of the incubation period, all of the petri plates containing between 30 and 300 colonies were selected. Plates with more than 300 colonies cannot be counted and were designated too many to count (TMTC) and plates with fewer than 30 colonies were designated too few to count (TFTC). Then the colonies on each plate were counted. From the counted number of colonies numbers, numbers of bacteria per mL were calculated by the following formula.

$$\frac{number\ of\ colonies\ (CFUs)}{dilution\ \times amount\ of\ specimen\ added\ to\ liquified\ agar} = number\ of\ bacteria/mL$$

(a)Plate count agar

(b)Heating agar solution on the hotplate

(c)Placing in the autoclave

(d) Adding TiO_2nanoparticles

(e)*E. coli* dilution

(f)Adding *E. coli* dilution

(g) Pouring the agar solution

(h)Incubating at 37°C for 24 h

Figure 3 The processes of antimicrobial test

Results and Discussion

3.1 Analysis of TiO_2 Nanopowders by XRD

The TiO_2 nanopowders were examined by powder X-ray diffraction (XRD: RIGAKU-RINT 2000 X-ray diffractometer). The X-ray diffraction data were recorded by using CuKα radiation (λ= 0.154056 nm). The average grain size of the samples was estimated with the help of Scherrer's equation using the diffraction intensity of the peak.

$$\mathrm{D} = \frac{0.9\lambda}{B\cos\theta}$$

Where λ is the wavelength, B is the full width at half- maximum (FWHM) and $\theta$is the diffraction angle. The powders calcined at 500°C showed with particle size between 20-30 nm. The XRD patterns of TiO_2 nanopowder scalcined at 500° was shown in Figure 4.

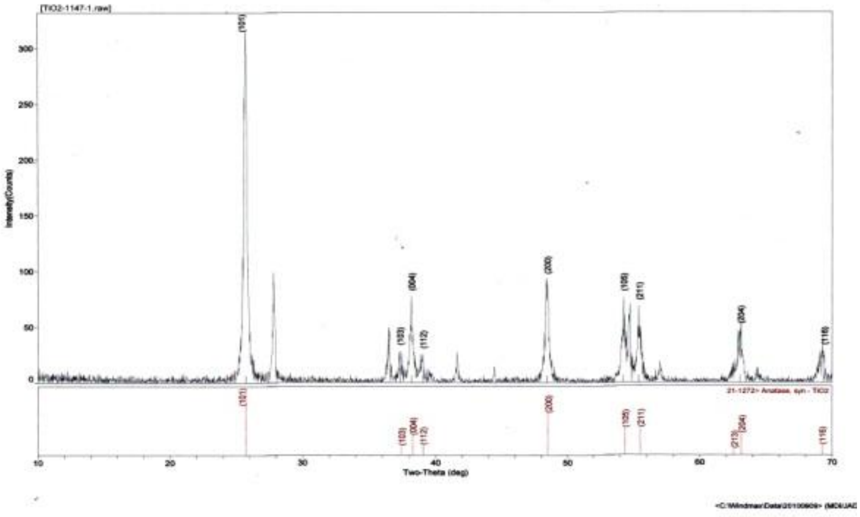

Figure 4 XRD pattern of TiO_2 nanopowders calcined at 500 °C

3.2 Investigation of Antimicrobial Properties

TiO_2 nanopowder synthesized at 500°C was applied to test the antimicrobial activity against Eschericia coli by using a serial dilution and pour plate culture method. E.coli inhibition was observed at 0.005g, 0.01g, 0.05g, 0.1g, 0.25g, 0.3g, 0.35g, 0.4g, 0.45g and 0.5g per 25 mL of bacteria agar solution after 24hours of incubation. After the incubation period, all of the petri plates were selected and counted containing between 30 and 300 colonies. Plates with more than 300 colonies cannot be counted and are designated too many to count (TMTC). For the ten samples with 10^{-3} dilution showed too many to count (TMTC) but the ten samples with 10^{-5} dilution, the numbers of colonies were found to be 207, 183, 169, 149, 106, 89, 76, 70, 50 and TFTC respectively. Figure 5 (a) and (b) showed Bacterial count for control 10^{-3} dilution and 10^{-5} dilution and Figure 6(a), (b), (c), (d), (e) and (f) showed bacterial count for 10^{-5} dilution.

The calculation revealed (4140 x 10^6, 1830 x 10^6, 338 x 10^6, 149 x 10^6, 42.4 x 10^6, 29.6 x 10^6, 21.7 x 10^6, 17.5 x 106, 11.1 x 10^6 and TFTC) bacteria per milliliter respectively shown in Table 1. It was found that count decreased as increased the amount of sample.

Figure 7 showed amount of TiO_2(g) Vs number of bacteria/mL in 10^{-5} dilution. This showed that TiO_2 nanoparticles have good antibacterial activity against E-coli.

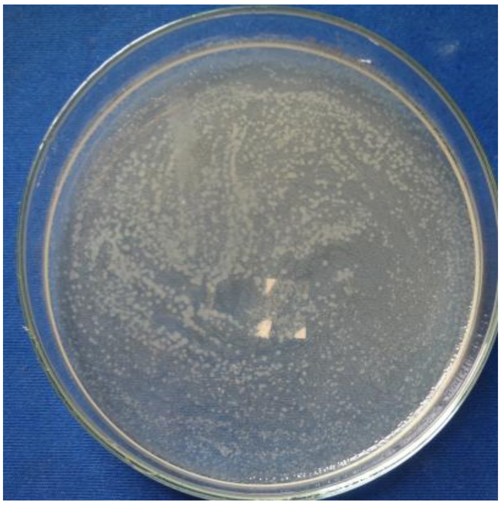

Figure 5(a) 10^{-3} dilution as control

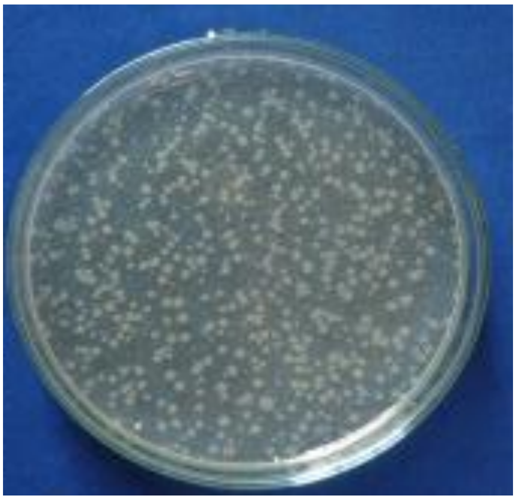

Figure 5(b) 10^{-5} dilution as control

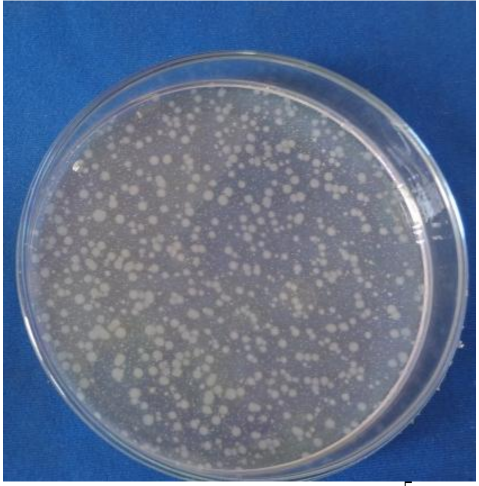

Figure 6(a) Bacterial count for 10^{-5} dilution with TiO_2-0.005g

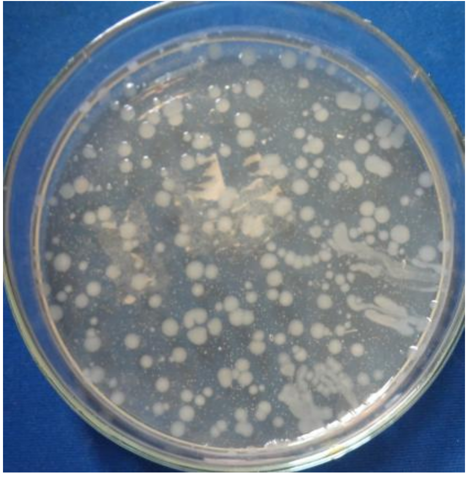

Figure 6(b) Bacterial count for 10^{-5} dilution with TiO_2- 0.01g

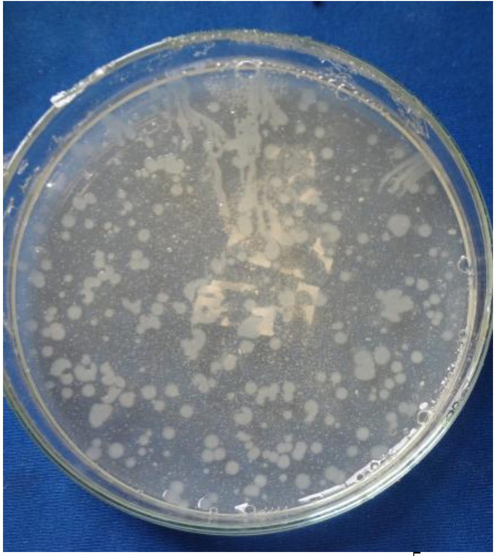

Figure 6(c) Bacterial count for 10^{-5} dilution with TiO_2-0.05g

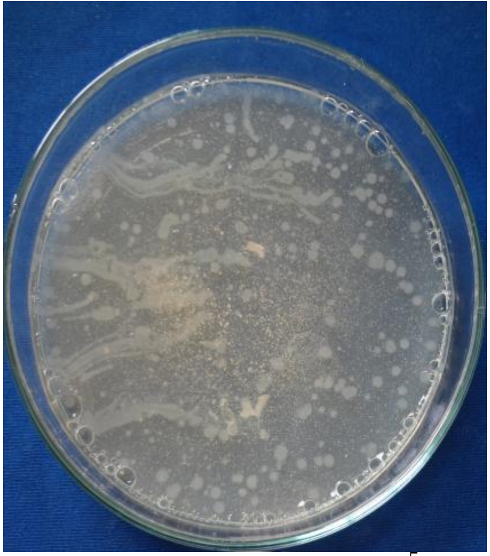

Figure 6(d) Bacterial count for 10^{-5} dilution with TiO_2- 0.25g

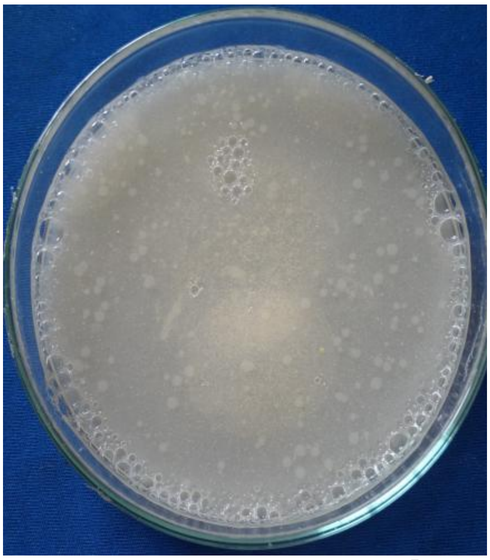

Figure 6(e) Bacterial count for 10^{-5} dilution with TiO_2- 0.35g

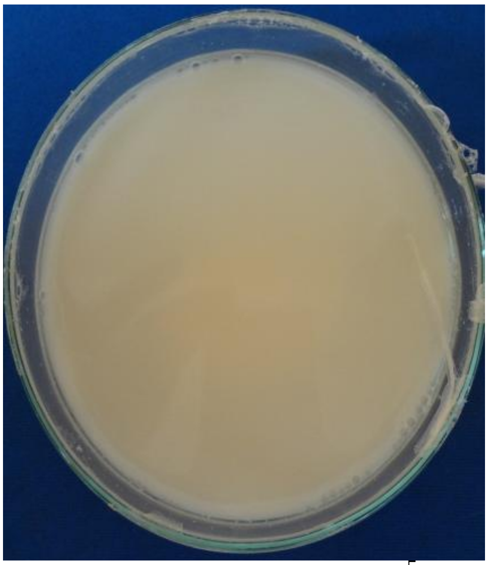

Figure 6(f) Bacterial count for 10^{-5} dilution with TiO_2- 0.5g

Table 1.1 Bacterial counts for 10^{-3} and 10^{-5} dilution

Amount of TiO_2 (g)	Number of colonies in 10^{-3} dilution	Number of colonies in 10^{-5} dilution	Number of bacteria/ml in 10^{-5} dilution
0.005	TMTC	207	4140×10^6
0.010	TMTC	183	1830×10^6
0.050	TMTC	169	338×10^6
0.100	TMTC	149	149×10^6
0.250	TMTC	106	42.4×10^6
0.300	TMTC	89	29.6×10^6
0.350	TMTC	76	21.7×10^6
0.400	TMTC	70	17.5×10^6
0.450	TMTC	50	11.1×10^6
0.500	TMTC	TFTC	TFTC
Control	**Number of colony in 10^{-3} dilution**	**Number of colony in 10^{-5} dilution**	
-	TMTC	224	

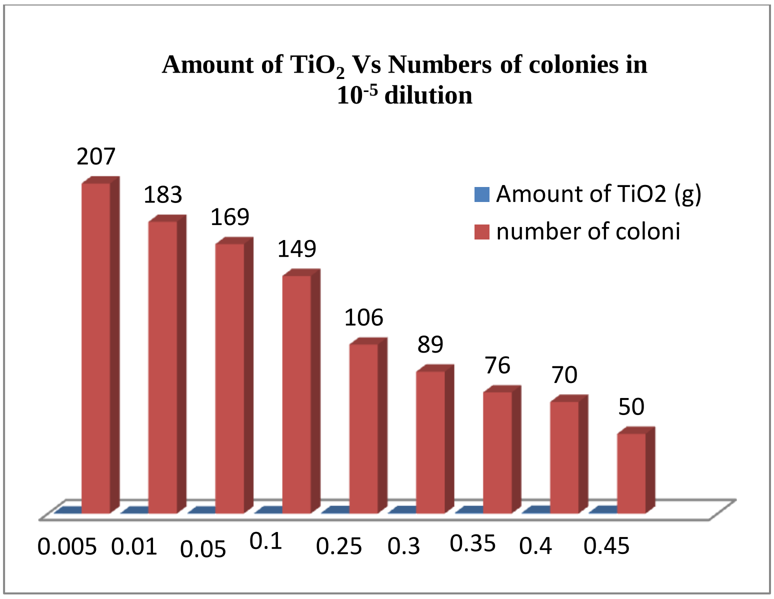

Figure 7 Amount of TiO_2 (g) Vs Numbers of colonies in 10^{-5} dilution

Conclusion

TiO_2 nanoparticles have been synthesized by using the sol-gel combustion hybrid method. Acetylene black was used as a fuel and to prevent increase in the size of the TiO_2 particles. It was found that the particle size of TiO_2 nanopowder scalcined at 500°C was between 20-30 nm. The sol-gel combustion hybrid method would also be useful for the large-scale production of nanosized ceramic materials. TiO_2 nanopowders synthesized at 500°C were applied to study the antimicrobial behavior by using serial dilution and pour plate culture method. For 10^{-3} dilution showed too many to count (TMTC) but the samples with 10^{-5} dilution showed that the amount of TiO_2 increases, the bacterial count decreases. It was found that TiO_2 nanoparticles have good antibacterial activity against E-coli. So TiO_2nanoparticles can be applied in water treatment.

Acknowledgements

We would like to express our special thanks to Prof. Dr Khin Khin Win, Professor and Head of Department of Physics, University of Yangon, for her encouragement to carry out this work.

I am deeply wished to express my gratitude to the Department of Zoology, University of Yangon, Myanmar.

References

Choi. S. Y.,Mamak. M., Coombs. N., Chopra.N. andOzin. G. A., (2004) ,“ Advance Function Materials,” vol.14, pp. 331- 335.

Han.C. H., Gwak.J., Han S. D. and Khatkar.S. P.,(2007), “*Material Letters”*, vol. 61, pp. 1695-1701.

Kormann.C., Bahnemann.D. W. and Hoffmann.M. R., (1988), “*Environ SciTechnol”*, vol. 22, pp.798.

Prado.A. G. S., Bolzon.L. B., Pedroso.C. P., Moura.A. O. and Costa.L. L.,(2008),“*ApplCatal B Environ”*,vol. 86, pp. 219.

Rana.N., Chand. S. andGathania. A. K., (2016), “*Int Nano Lett”*, vol. 6, pp. 91.

Yun.H. S., Miyazawa.K., Zhou.H. S., HonmaI. and Kuwabara. M., (2013),“Advance Matter,” vol. 13,pp. 1375-1377.

J. Myanmar Acad. Arts Sci. 2020 **Vol. XVIII.No.2C**

STUDY ON SHAZAUNG-LET-PAT (*Aloe vera* Linn.) HYDROGEL BY RADIATION AND THEIR PHYSICAL PROPERTIES

Ni Ni War[1], Kyi Thar Myint[2], & Khin Khin Win[3]

Abstract

The films forming composed of polyvinyl alcohol (PVA) and *Aloe vera*(AV) gel were prepared and characterized by different ratios of PVA/AV hydrogel films 1:1, 1:2 and 1:3 variations in the *Aloe vera* contentsby by using the solvent casting technique. The physical parameters like the effect of the actual dose rate, measured dose rate and specific heat capacity of the *Aloe vera* leaf, natural gel and hydrogel were analyzed and compared with geometrical 0modificationby gamma radiation of a ^{137}Cs source at room temperature. The specific heat capacity of *Aloevera* composite hydrogel was found to be 4.33 kJ/kgK, which was higher than that of liquid water4.20 kJ/kgK. The standard value of the total mass absorption coefficient (μ_m) with weighing factors of constituted elements in hydrogelby using Energy Dispersive X-Ray Fluorescence (EDXRF) analysis was calculated to be 0.069 cm^2/g. From the experimental results showed that the comparative analysis with the mass absorption coefficient (μ_m)value of film 3, used as absorber was obtained to be 0.065 cm^2/gby using Sodium Iodide Scintillation Detector [NaI(Tl)] STX-x64software ST 360 counter and approximately equal to the standard value.After studying the microstructure characterizations of all the composite films were performed by Scanning Electron Microscopy (SEM) analysis.

Keywords: *Aloe vera,* PVA, EDXRF, SEM,^{137}Cs source,NaI(Tl)STX - x64software ST 360 counter.

Introduction

Skin is the largest organ of the human body, acting as a protective barrier between the internal body and the external atmosphere. Concerning skin damage, the treatment of burns is complex and painful and requires the use of several drugs administered separately or combined (J.M. Marshall, 1990).Potential vectors for the controlled release of substances for the treatment of skin damage occurring in wounds and burns are polymeric films. Thin-film offers advantages over other pharmaceutical forms, such as liquid or semisolid drug delivery products, as it provides a large surface area of application, adhesion to the damaged tissue, and absorption of exudates(Katie, I, Katime, O y Katime, D, 2oo5). The use of natural polymers is supported by their many desirable properties, such as biocompatibility, low irritancy, and lack of toxicity, as in the case of polysaccharides. To reduce pain and accelerate the healing process, many natural substances have been traditionally used and more recently have been scientifically studied, such as Aloe. *Aloe vera* has been used in a host of curative purposes including treatment of skin disorders and healing of wounds. In relation to this, the objective of the present work has been to develop and characterize a polymer film containing *Aloe vera* and polyvinyl alcohol with the aim of providing an innovative system for radiation burn wound treatment. Polyvinyl alcohol was used as a film-forming agent and has been often used in combination with other polymers for wound healing applications. The solvent casting technique is regarded as one of the simplest and most economical techniques for preparing films of reasonably good quality. The properties of composite films depend on the preparation conditions. Several therapeutic properties have been assigned to the *Aloe vera* hydrogel films and synthesis of natural gel and leaf. This work also investigates the usefulness of the heat absorption test of radiation around the gamma-ray from a

---

[1] PhD Candidate, Lecturer, Department of Physics, University of Yangon

[2] Dr, Professor (Retd), Department of Physics, West Yangon University

[3] Dr, Professor & HOD, Department of Physics, University of Yangon

Cs-137 source at room temperature and also determine by mass absorption coefficient, which provides a standardized coefficient.

Materials and Methods

Preparation of *Aloe vera* Extracts

An *Aloe vera* leaf was obtained by surface sterilized with ethanol. The outer, green dermis of the leaf was peeled off using a sterile blade. Fillets were extensively washed with distilled water to remove the exudes from their surfaces. The fillets were homogenized in a blender and then the homogenized mass was filtered. After that, the flesh gel was weighed and 25 g of this was added 5 ml of distilled water to it. Then the mixture was boiled for 15 minutes at 90ºC. After cooling to room temperature, it was filtered to get the collection of gel as shown in Figure 1.

Preparation of films (Solvent casting technique)

Polyvinyl Alcohol (PVA)3 ml of the 3% solution and the *Aloe vera*(AV) gel extract were incorporated to the ratio of 1:1, 1:2, and 1:3 (v/v) respectively. PVA solutions were prepared to vary the concentration for 3% (v/v), dissolving PVA in distilled water under constant stirring for 2 hr at 70ºC. To prepare films, solutions of PVA and *Aloe vera* (AV) were mixed for each concentration of PVA with magnetic stirrer during 30 minutes at 100ºC and then the mixtures were isolated at room temperature for 6 or 7 days to remove bubbleduring the process. The same procedures were repeated in triplicate for each ratio of PVA/AV used. The PVA/AV films as shown in Figure 2 and the flow chart of the preparation for PVA/AV films as shown in Figure 3.

Figure1 Collection of gel

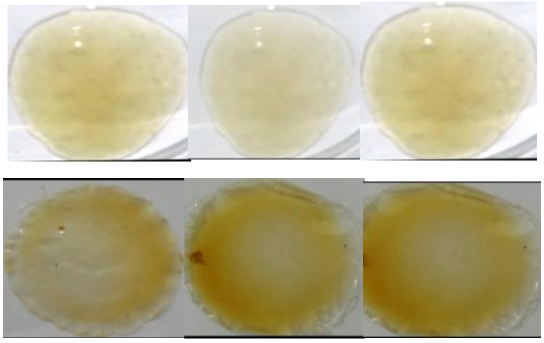

Figure 2 PVA/AV gel (1:1, 1:2 & 1:3) wet & dry films

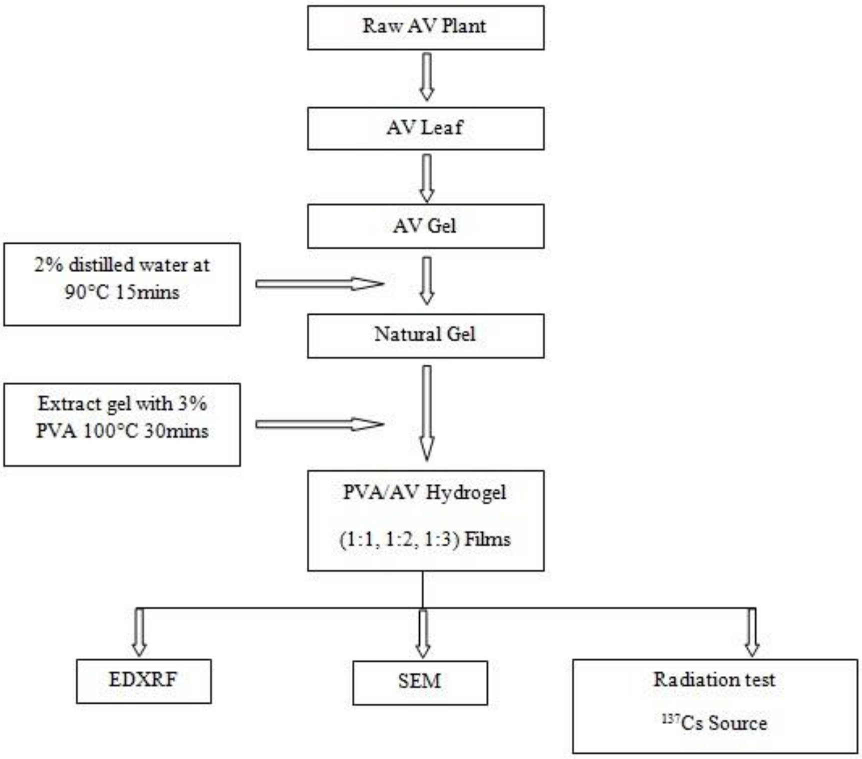

Figure 3 Flow chart of preparation for PVA/AV films

Activity and Dose rate of Caesium-137 Radioactive Source

The standard source^{137}Cs as the radiation source for field applications because of its longer half-life and the greater penetrating of its emitted photon. Gamma rays source^{137}Cs has one peak. It has a strength of 392.67 kBq and half-like of 30.174 years and the energy of the source is 0.662 MeV. The activity of a radioactive source is the number of disintegrations occurring within it per unit time. The rate of decay is referred to as the activity of a radioactive material expressedin the following equation (1) and (2).

$$dN/dt = A = - N\lambda \,. \tag{1}$$

$$\text{Similarly } A = A_o\, e^{-\lambda t} \tag{2}$$

Where A is the activity remaining at time t and A_o is the original activity equal to N_0(Loftus T P. 1970). Activity at installation(A_o) of the^{137}Cs source (at Radiation Toxicology Research Division, Department of Medical Research) is 90 µCi and between the date of experiment and date of installation is (1.12.2005 to 1.10.2018). The half-life of Cs^{137} is 30 years. The actual activity is 67.014 µSv/hr. The dose rate due to source strength was calculated by the equation (3) (Tsoulfanids N. 1995).

$$H_o = \frac{ESQ}{m} \tag{3}$$

Where H_o is dose rate due to source strength, S is the activity of source and m is the mass of the sample. In a dosimeter calibration description, the dose rate around the source (core) is 7 µSv/hr and 90 µSv/hr. Therefore, the average dose rate is 23.5 µSv/hr. The geometry of the source and target for the hydrogel, natural gel, and *Aloe vera* leaf can be illustrated as shown in Figure 4(a) and (b).

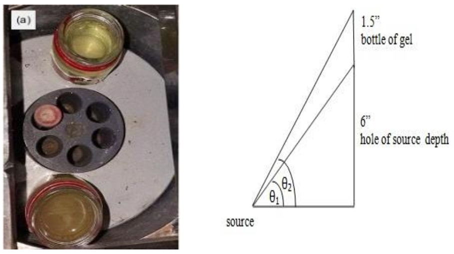

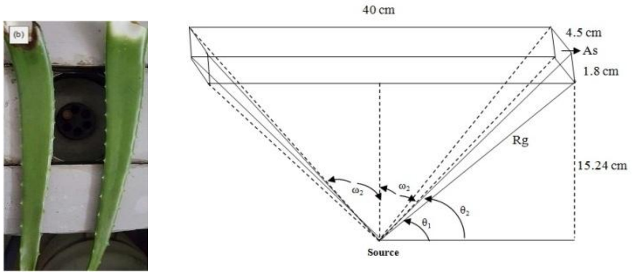

Figure 4 (a) natural gel and hydrogel **Figure 4** (b) *Aloevera*leaf

The solid angle of natural gel and hydrogel were calculated to be the geometry equation(4).

$$\Omega = \frac{1}{2}\{\sin\theta_2 - \sin\theta_1\} \tag{4}$$

The solid angle of the *Aloe vera* leaf was calculated to be the geometry equation (5).

$$\Omega = \frac{A_S}{4\pi R_S^2} \tag{5}$$

The actual dose rate of natural gel, hydrogel and *Aloe vera* leaf were calculated to be the geometry equation (6).

$$H_a = H_o F \Omega \tag{6}$$

The net rate of heat flow due to radiation and specific heat capacity of *Aloe vera* hydrogel, natural and leaf were calculated from equation (7) and (8).

$$H = e\boldsymbol{\sigma}A\,(T_f^4 - T_s^4) \tag{7}$$

$$Q = mC\Delta\theta \tag{8}$$

Where F is the correction factor = 1 ± 0.001, Ω is solid angle,T_s isuniform temperature (room temperature) = 23ºC, $\Delta\theta = T_f - T_i$and $\boldsymbol{\sigma}$ is (5.67×10^{-8}W/m^{2}K^4) (Tsoulfanids N. 1995).

The Absorption of Gamma-radiation

The basic property of the absorption of gamma-rays is the exponential decrease in the intensity of radiation as a homogeneous beam of gamma-rays passes through a thin slab of matter as following the absorption equation (10), (11) and (12).

$$I = I_o e^{-\mu d} \tag{10}$$

$$I = I_o e^{-\frac{\mu d}{\rho}\times\rho} \tag{11}$$

$$I = I_o e^{-\mu_m d_m} \tag{12}$$

Where μ is the linear absorption coefficient of the film absorbers, μ_m is the mass absorption coefficient of the film absorbers, d_m is the mass thickness of absorption material, I_o and I are origin Intensity and Intensity of gamma-ray transmitted(J.H.Hubbel, 1969).The incident beam intensity and the attenuated beam intensity were measured by calculating the mass absorption coefficient of these samples. The experimental measurement of counting rate of the absorber PVA/AV films was detected by using STX- x64 software ST 360 counter in Nuclear Research Laboratory of the Department of Physics, University of Yangon. The experimental setup and procedures were shown as follows in Figure 5.

The Experimental Setup

Applied operating voltage = 900V

The distance between source and absorber = 3 cm

The distance between detector and absorber = 9 cm

Detector - NaI(Tl) scintillation detector

Irradiation time = 10 min

Background counting rate in the beginning, b_1 = 2297 count/min

Background counting rate in the end, b_2 = 2095 count/min

Average background counting rate, $b = \frac{b_1 - b_2}{2} = 2196$ count/min.

Figure 5 NaI (Tl) STX- x64 software ST 360 counter

Results and Discussion

EDXRF measurement

From the results of EDXRF measurement, it was found that the mostly constituted Calcium (Ca) concentration in these samples was65.79%, which can be calculated by the mass absorption coefficient is 0.051 cm^2/g. Similarly the mass absorption coefficient of other elements were calculated corresponding to potassium (K) 15.58%,Sulfur (S) 4.42%, Iron (Fe) 1.260%, Manganese (Mn) 0.94%, Copper (Cu) 0.497%,Zinc (Zn) 0.297% respectively. It was obtained that the total mass absorption coefficient of the concentration of the element is 0.069cm^2/g. The EDXRF spectrum of *Aloe vera* hydrogel was shown in figure 6.

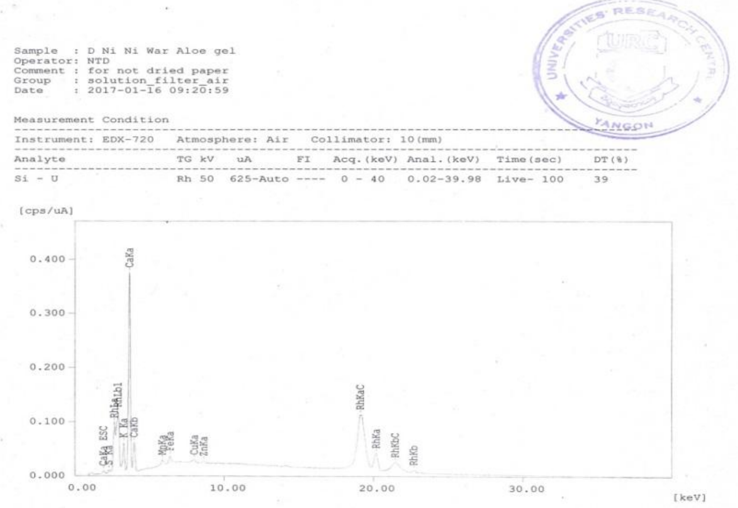

```
Sample   : D Ni Ni War Aloe gel
Operator: NTD
Comment  : for not dried paper
Group    : solution_filter_air
Date     : 2017-01-16 09:20:59

Measurement Condition
------------------------------------------------------------------------------
Instrument: EDX-720   Atmosphere: Air   Collimator: 10(mm)
------------------------------------------------------------------------------
Analyte                 TG kV   uA        FI   Acq.(keV) Anal.(keV)  Time(sec)    DT(%)
------------------------------------------------------------------------------
Si - U                  Rh 50  625-Auto ----  0 - 40    0.02-39.98  Live- 100    39
```

Figure 6 EDXRF Spectrum of *Aloe vera*hydrogel

Heat Absorption and Radiation Test

From geometrical results showed that the comparison of actual calculated(H_a)and measured dose rate (H_m) were shown in Table 1and Figure 7.The dose rate of *Aloe vera* leaf, natural gel and hydrogel were obtained to be 1.21 µSv/hr, 0.90 µSv/hr and 0.92 µSv/hr respectively.The specific heat capacity of the hydrogel is higher than natural gel and leaf were shown in Table 2. The measurement of the intensity count rate and mass absorption coefficient by the absorber PVA/AV films 1, film 2 and film 3 using STX- x64 software ST 360 counter as shown in Tables 3 and 4.

Table 1 Dose rate of the natural gel, hydrogel, and leaf

Sample	Mass(g)	H_0(µSv/hr)	H_a(µSv/hr)	H_m(µSv/hr)
Leaf	111.80	8.46	1.21	1.12
Natural gel	39.30	23.50	0.90	0.90
Hydrogel	39.30	24.06	0.92	0.91

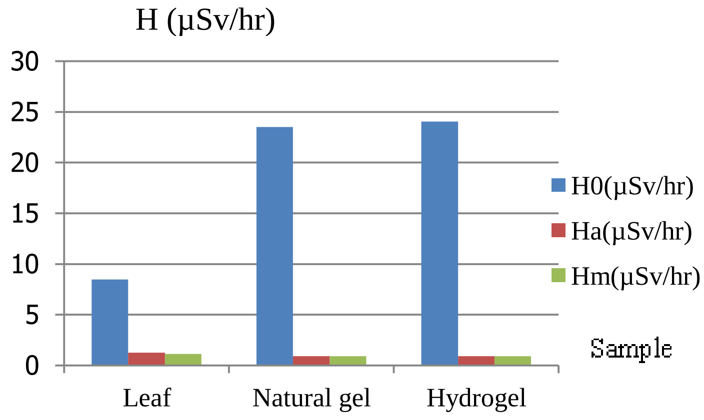

Figure 7 Actual dose rate and measure dose rate of a leaf, natural gel, and hydrogel

Table 2 The specific heat capacity of three samples

Sample	Mass (g)	T_i (°C)	T_f(°C)	C (kJ/kgK)
Leaf	111.80	26.08	28.12	3.91
Natural gel	39.30	26.99	28.80	4.02
Hydrogel	39.30	27.12	28.80	4.33

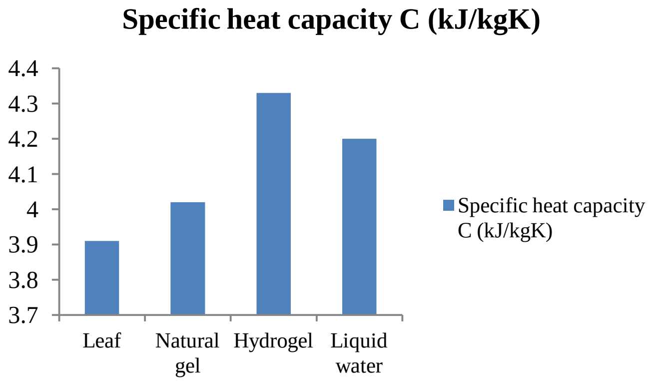

Figure 8 The specific heat capacity of three samples compare with liquid water

Table 3 Counting rate of the absorber AV films 1,2 and 3 using STX- x64 software ST 360 counter

Sr No	Source Io (count/min)	Absorber film 1 I (count/min)	Absorber film 2 I (count/min)	Absorber film 3 I (count/min)
1	98308	96870	95486	94497
2	98770	96858	95214	94069
3	97502	96265	94734	93783
Avg	98193	96664	95145	94116

Table 4 The mass absorption coefficient of absorbers film 1,film 2 and film 3.

Total mass absorption coefficient(EDXRl (cm^2/g)	The mass absorption coefficient of film 1 (cm^2/g)	The mass absorption coefficient of film 2 (cm^2/g)	The mass absorption coefficient of film 3(cm^2/g)
0.069	**0.037**	**0.053**	**0.065**

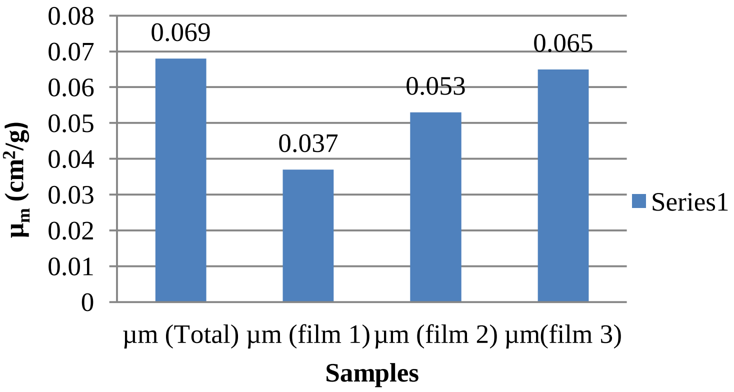

Figure 9 The mass absorption coefficient of absorbers film 1,film 2 and film 3.

Scanning Electronic Microscopy(SEM)Analyses

The SEM micrograph of the surface structure of *Aloevera* hydrogel film samples 1, 2 and 3 is shown in figure 10.The SEM analysis revealed a smooth and homogeneous surface without significant defect, which can be attributed to the excellent filming properties of polyvinyl alcohol. This image confirms that the material is forming micro-size and the surface structure of the hydrogel film images was taken at an operating voltage of 15 kV.

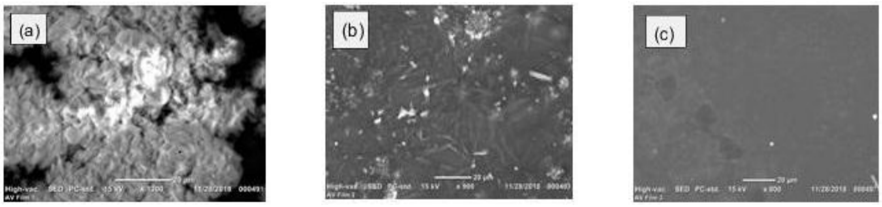

Figure 9 The SEM micrograph of the *Aloe vera* hydrogel

(a) (1:1) film, (b) (1:2) film and (c) (1:3) film

Conclusion

From the comparative study of the heat absorption test, the actual calculated and measured dose rates were found to be nearly the same values. The difference between the temperature decreased with increasing specific heat capacity. In this study, the specific heat capacity of *Aloe vera* hydrogel was calculated to be 4.33 kJ/kgK and is higher than that of liquid water 4.2 kJ/kgK. The mass absorption coefficient of *Aloe vera* hydrogel films were undertaken to be0.037cm^2/g, 0.053 cm^2/g and 0.065cm^2/g shown in Table 4 and Figure 9.It observed that the PVA/AV film 3,used as absorber nearly equal to those of standard value the total mass absorption in *Aloe vera* hydrogel is to be0.069cm^2/g by using EDXRF analysis.This study was indicated that the *Aloe vera* based hydrogel, and PVA/AV film suitable to use wound healing, treating various skin problems such as eczema, psoriasis, prevent progressive due to burns, electrical injury and reduces radiation-induced skin reaction. And so on it may be suitable for the treatment ofapplications used to protect for good absorber against radiation damage to the skin due to heat accompanying with together radiation.

Acknowledgments

I would like to express my sincere thanks to my Supervisor Professor Dr.Khin Khin Win, Head of Department of Physics, University of Yangon, for her kind permission to carry out this work, then for her supervision, helpful advice, and valuable suggestion. I am also grateful to my Co-Supervisor Dr. Kyi Thar Myint, Professor (Retd), Department of Physics, West Yangon University for her valuable guidance.

References

J.M.Marshall, (1990), “ Aloevera gel, The Pharmaceutical Journal, Vol 24,pp.360-362.

J.H.Hubbel, (1969),”Photon Cross Sections, Attenuation Coefficients, and Energy Absorption Coefficients “, pp 596-602.

Katime, I, Katime, OyKatime,D,(2005) “Material Inteligents Hydrogels macromoleculars, algunas application sbiomedicas. Anales de la Real Sociedad Espafiola de Qulmica” pp 35-50.

Loftus T P. (1970) Standardization of Cesium-137 Gamma-Ray Sources in terms of Exposure Unit Journal of Research of the International Bureau of standards A Physics and Chemistry.

Tsoulfanids N. (1995)“Measurement and Detection of Radiation”,2nd Edi Washington, Taylor& Francis,pp267-270.

J. Myanmar Acad. Arts Sci. 2020 **Vol. XVIII.No.2C**

DISCOVERY OF DOUBLE STRANGENESS NUCLEAR SYSTEM BY EMULSION COUNTER-HYBRID EXPERIMENT

Myint Kyaw Soe[*]and E07 collaboration

Abstract

E07 emulsion-counter hybrid experiment has been carried out at J-PARC to discover double strangeness nuclei. The scanning work is performed by establishing automatic track following system which has been successfully developed. More than 100 double hypernuclear events are expected from this experiment.

Keywords: emulsion counter hybrid, double strangeness nuclei, automatic track following

Introduction

E07 experiment was performed by Emulsion-counter hybrid method . Double strangeness nuclei are main available sources to study Λ−Λ ınteraction and Ξ−N interaction. Λ−Λ and Ξ−N interaction are important roles to build EOS of neutron star . They are also linking to add one component as strangeness (S) into 2D nuclear chart to become 3D nuclear chart with proton, neutron and strangeness. Although existences of many double hypernuclei are suggested theoretically, experimental information is so poor. There is only one uniquely identified double hypernuclear event over the world, namely “NAGARA event” which gives Λ−Λ interaction in 6He (helium) to be 0.67 ± 0.17 MeV. Experimental information of these interactions are very limited by number of double-hypernuclear events. Firstly, Danysz et al., had good fortune to detect a sample of double−Λhypernucleus among four candidate events of Ξ− hyperon stopping in nuclear emulsion experiment over five decadesago . In 1991, the existence of double strangeness system was confirmed by E176 experiment which is first generation of emulsion counter hybrid experiment. They found one double hypernucleus by observing nearly 80 Ξ− hyperon stopping evets and they also found two twin single hypernuclear events, gives the Ξ−N interaction. After 10 years later, E373 experiment was carried out to get a greater statistics number of hypernuclear events than that of E176. E373 experiment was second generation of E176but some experimental setups were different and they found NAGARA event among seven double−Λ hypernuclear envents. Therefore, NAGARA event becomes a rule of double lambda hypernuclear event and two twin single hypernuclear events were also observed in E373 experiment. To study systematically the interaction of Λ−Λ and Ξ−N with large number of double hyernuclear events E07 experiment has been carried out at J-PARC. In emulsion experiment, the scanning is heavy work to be able to detect events. Therefore, we have successfully developed new technique namely, “automatic track following system”.

Production of double strangeness nuclear events

As first the Ξ− hyperon is produced by the reaction of K− + “p” → Ξ− + K+. In this reaction, “p” is quasi free proton in Carbon as the diamond target and the incident K− beam is nearly 1.66 GeV/c. The emitted K+ will go to forward direction of incident beam and will carry large momentum and while Ξ− will remains as recoiled one and enters into the emulsion stack as demonstrated in Fig 2.1.

---

[*] Dr, Demonstrator, Department of Physics, Yadanabon University, email: npkyaw1@gmail.com

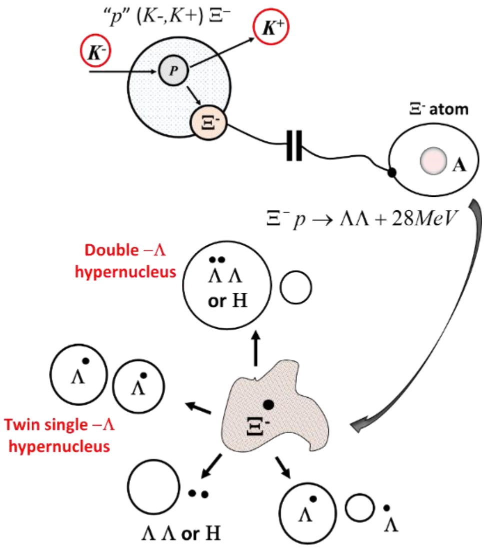

Figure 2.1 Production of double lambda hypernuclear events

When Ξ– hyperon enters into nuclear emulsion, its momentum will loss and it will be at rest due to ionization with atoms in emulsion. Finally, Ξ– hyperon will stop everywhere in emulsion sheet and it will be captured by one atom of emulsion and absorbed by nucleus into inner orbits. The excited Ξ– atom or nucleus will decay into four possible modes such as double Λ hypernucleus, Twin-single Λ hypernucleus, tow free Λ with one normal nucleus and one single Λ hypernucleus with one free lambda and normal nucleus. Among them, double Λ and twin single lambda hypernucleus are our subject.

Experimental setup of E07 Emulsion-counter hybrid experiment

Fig 3.1 is the experimental setups around emulsion stack. The incident K- is the secondary beam with momentum of 1.8GeV/c which is available to produce strangeness (S=2). After K- beam passed through the collimator, it hits the diamond target is mounted in front SSD which is silicon strip detector to record the tracks of X- hyperons emitted from target. SSD gives the estimated positions and angles of X-hyperon candidate tracks. The estimated position and angle of candidates are very important to be continue the following them in nuclear emulsion sheets. Since the position of K- beam is fixed, mover brings the emulsion stack mounted on it to change the irritated position and hence, it works to be able to expose the whole surface of emulsion sheets. The Hyperball-X is mounted at the upstream of diamond target and it has six GM counters which detect X-rays from the capture of X- hyperons to study the X-N interaction. At the downstream of emulsion stack, KURAMA magnet is placed to trace the K+ emitted from "p"(K-,K+)X reaction. At the end of experimental setup, TOF (time of flight) is located to measure the real time of K- and K+ particle and their momentum can be calculated.

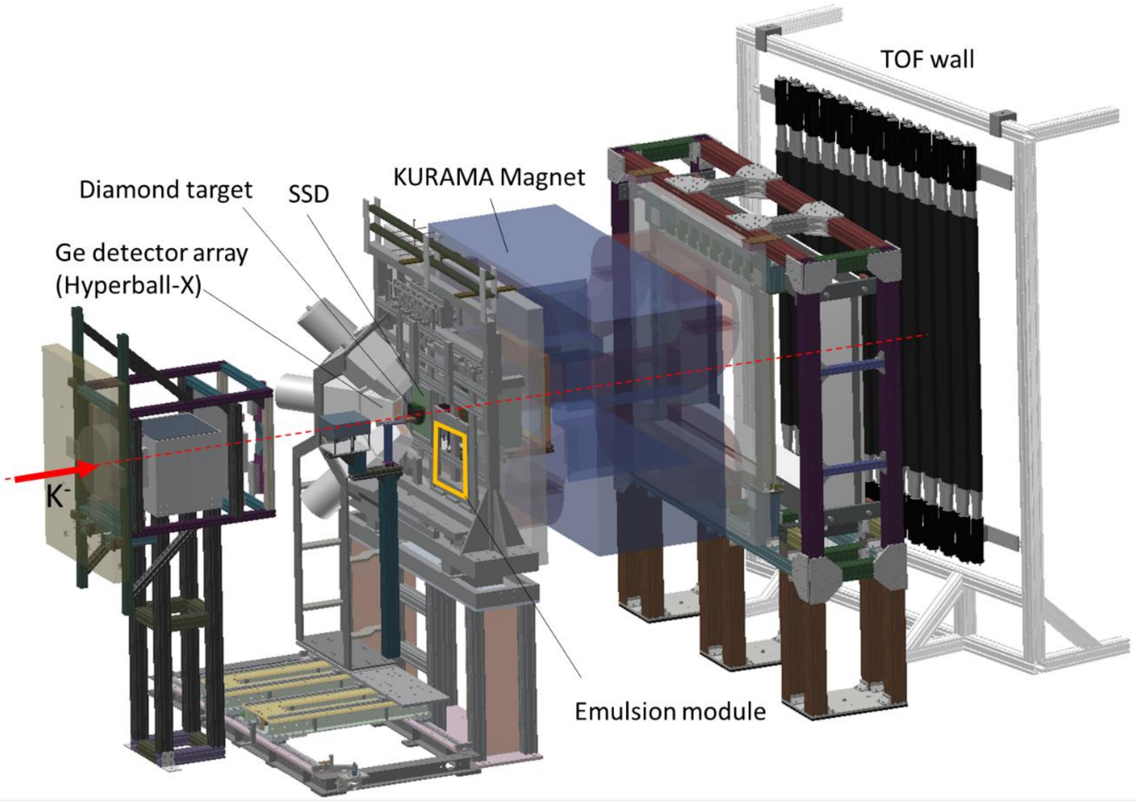

Figure 3.1 Experimental setup of E07 experiment

Nuclear emulsion

Nuclear emulsion is the best one of 3-dimentional detectors. The good ability of this detector is very effective one to detect the short-life particle such as Λ, Ξ, Σ and so on, and their life-time is in order of 10-10 s. Emulsion gel is composed of eight elements as expressed in Table 4.1. In table, it can be seen that nearly eighty percent of composition is Ag+Br- crystals. When charged particles enter in the emulsion, they ionize with Ag+Br- crystals as Ag+ + e– + Br → Ag and Ag+ + e– becomes the latent image. When the emulsion sheet is performed by photographic development, the latent image can be seen as dark grain under microscope. Therefore, the dark grains will appear along the travel of charged particles and the series of dark grains is the track of charged particles. The range of charged particle travelled in emulsion give their kinetic energy by aid of range-energy relation.

Table 4.1 Composition of Nuclear Emulsion

Material	Weight (%)	Mole ratio (%)
I	0.9	0.2
Ag	46.0	24.4
Br	33.2	21.7
S	0.2	0.2
O	6.5	12.2
N	2.9	6.0
C	8.8	19.9
H	1.4	15.4

Automatic track following system

In emulsion counter hybrid method, the estimated position and angles of Ξ− candidates are supplied by SSD detector. By using estimated data, the tracks of Ξ− candidates have to be followed in nuclear emulsion sheet until their stopping points as shown in Fig 5.1. The following of all Ξ− candidates was had work in E373 experiment because they used semi-automatic tracking system. Scanning time was for many years in E373 and besides, the human errors may exist when the track is followed sheet by sheet. We have to follow the Ξ− tracks from 1st sheet to the sheet where it stopped. Therefore, the automatic track following system has been established to reduce following time and to follow the tracks with high accuracy.

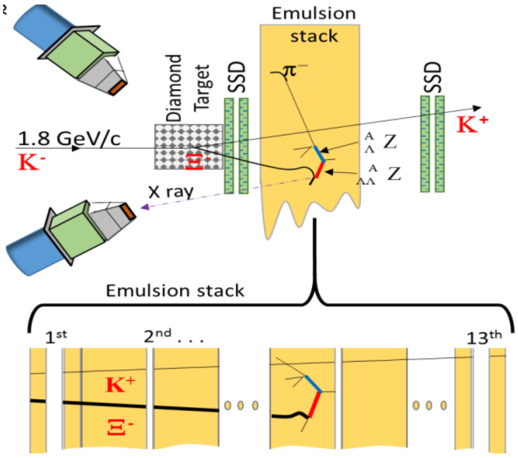

Figure 5.1 Experimental setup of emulsion stack

Automatic track following system was built by computer-aids microscopic system. Fig. 5.2 shows the stage of microscope system. The emulsion plates are set on X-Y stage and a 50-time oil-immersion objective lens with effective field of 110 μm × 130 μm is located in optical Z direction. One CCD camera which is mounted on the top of optic part is employed to seize image through the objective lens and its resolution is 552(H) × 440(W) pixels with 8 bits. The light luminance for optics is supplied from the LED below the X-Y stage. A vacuum pump is connected to X-Y stage to keep the emulsion plates flat on X-Y stage. The white rubber frame (Oil lake) protect the oil for objective lens does not spread outside and to be able to reuse the oil. The motor motion of X-Y stage and optic part in Z direction, the adjustment of light luminance from LED, image taking of CCD camera and data processing are worked together under automatic controlled system.

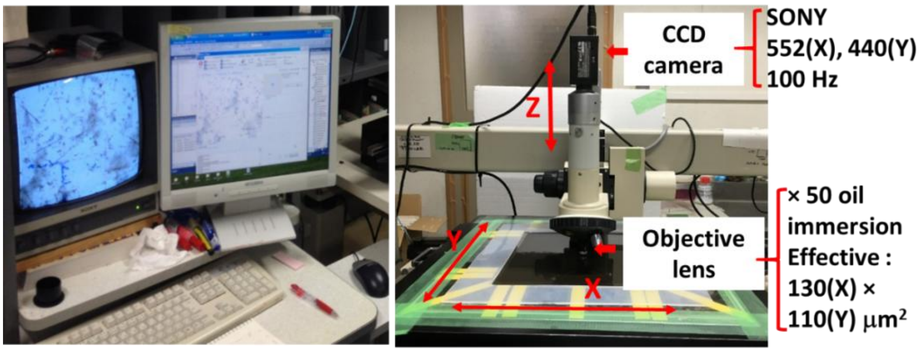

Figure 5.2 Computer aid microscopic system

There are three main parts such as (a) automatic emulsion surface detection, (b) sheet to sheet alignment with K- beam pattern and (c) track recognition and following.

Summary

E07 experiment has been carried by emulsion-counter hybrid method. The automatic track following system has been successfully established with high accuracy. The tracking work will be finished within a few year and we expect to detect more than 100 double hypernuclear events from E07 experiment in near future.

Acknowledgment

This work was supported by JSPS KAKENHI, Grant Numbers 23224006 and 16H02180, and MEXT KAKENHI Grant No. 24105002.

Reference

A. Ichikawa et al., Physics Letters B 500 (2001) 37–46

A. ohashi et al., Nuclear Physics A 835 (2010) 374–377

H. Takahashi, et al., Phys. Rev. Lett. 87 (2001) 212502.

J.K.Ahn, et al., Phys. Rev. C 88 (2013) 014003.

K.Imai, K.Nakazawa, H.Tamura, J-PARC E07 Proposal ⟨http://j-parc.jp/ researcher/Hadron/en/ pac_0606/pdf/p07-Nakazawa.pdf⟩, 2006.

K. Nakazawa, H. Takahashi, Prog. Theor. Phys. Suppl. 185 (2010) 335.

M. Danysz, et al., Nucl. Phys. 49 (1963) 121.

Myint Kyaw Soe et al., Nuclear Instruments and Methods in Physics Research A 848 (2017) 66–72

S. Aoki, et al., Prog. Theor. Phys. 85 (1991) 1287.

S. Aoki, et al., Nucl. Phys. A 828 (2009) 191.

J. Myanmar Acad. Arts Sci. 2020 **Vol. XVIII.No.2C**

STRUCTURE CALCULATION OF ${}^{16}_{\eta}\mathrm{O}$ NUCLEUS

Hla Hla Win[1], Khin Nilar Myo Thet[2], Theingi[3]

Abstract

The purpose of this research is to investigate the structure of η-mesic oxygen nucleus theoretically which is a bound system of η-meson and Oxygen core nucleus. Since original functional form of η-N interaction cannot be analytically solved, we have transformed the functional form into Gaussian form by applying the Gauss elimination method. The transformed η-N potentials are equivalent to that of original potential by using the optimum sets, $\mu_1 = 0.05\ \text{fm}, \mu_N = 20\ \text{fm}$ and N=20. The η-nucleus interaction is obtained by folding the η-N interaction with Oxygen nucleus nuclear density. By applying the η-nucleus folding potential we have computed the binding energy of ${}^{16}_{\eta}\mathrm{O}$ system which is 3.2814 MeV and its level width is 0.3704 MeV.

Keywords:, Gauss elimination method, folding potential, Power Inverse Iteration Method, resonance energy

Introduction

The existence of η-mesic nucleus was first predicted by Q. Haider and L.C. Liu in 1986. It is a consequence of the attractive interaction between the η meson and all the nucleons in the nucleus. The attractive nature of the interaction follows from the work of R.S. Bhalerao and L.C. Liu who found, from a detailed coupled-channel analysis of πN → πN, πN → ππN, and πN →ηN reactions, that near-threshold ηN interaction is attractive. The reaction mechanisms used for eta production are usually based on models similar to those used for other mesons such as the pions and kaons.

Since its discovery, extensive theoretical and experimental efforts have been devoted towards achieving a better understanding of the η-meson properties and its interaction with other particles. This was due to the special role played by the η-meson in particle physics. The latter can be attributed to quantum mixing of the quark states corresponding to the η and π^0 mesons.

Although the η-meson is four times heavier, it is in many respects similar to the π^0-meson. Both are neutral, spinless and have almost the same lifetime, ~10^{-18}s. The kindship between the two mesons manifests itself very clearly in their decay modes. They are the only mesons that have a high probability of pure radiative decay. The pion almost entirely (98.798%) decays into the radiative channel $\pi^0 \to \gamma + \gamma$. For the η the purely radiativedecay is also the most probable mode,

---

[1] Lecturer, Department of Physics, Taunggyi University

[2] Master of Research student, Department of Physics, University of Mandalay

[3] Associate Professor, Department of Physics, University of Distance Education

$$\eta \rightarrow \begin{cases} \gamma + \gamma & (38.8\%) \\ \pi^0 + \pi^0 + \pi^0 & (31.9\%) \\ \pi^+ + \pi^- + \pi^0 & (23.6\%) \\ \pi^+ + \pi^- + \gamma & (4.9\%) \\ \text{other decays} & (0.8\%). \end{cases}$$

Therefore, when π^0 and η are viewed as elementary particles, they look quite similar. However their interaction with nucleons is different. The experimental searches involve the production of η mesons and hence signals for the existence of eta-mesic states via their possible decay modes and final state interactions of eta mesons with nuclei.

Resonances

The first resonance in particle physics was discovered by H. Anderson, E. Fermi, E. A. Long, and D. E. Nagle, working at the Chicago Cyclotron in 1952. Resonance states are formed when quantum particles collide at certain (resonant) energies. Before moving apart, they stay together for a while. During the resonance lifetime, the particles move around each other and “forget” the direction from which they came. Therefore, when the resonance eventually decays, the particles “choose” the direction to move away at random.

A resonance can be viewed and approached from two different angles, as a delay connected with an enhanced phased shift in a scattering process or as a long-lived but decaying state of a compound system. The main observable characteristics of a resonance are position and the width. The real and imaginary parts of the energy give the position and width of the resonance, respectively.

A resonance energy is $E_{res} = E_r - i\frac{\Gamma}{2}$ has a negative imaginary part , which is called resonance width. The use of a complex energy allows a classification of the energy levels of a quantum system.

Two-Body Calculation

We use the Gaussian basis wave function as the total wave function of our two-body system which has the following form;

$$u(r) = r^{\ell+1} \sum_j c_j e^{-\left(\frac{r}{b_j}\right)^2} \tag{1}$$

where c_j’s expansion coefficient and b_j’s are range parameters.

The Schrödinger equation is written as

$$H\Psi = E\Psi \tag{2}$$

The two body Hamiltonian is

$$H = -\frac{\hbar^2}{2\mu}\frac{d^2}{dr^2} + \frac{\hbar^2}{2\mu}\frac{\ell(\ell+1)}{r^2} + V(r)$$

where reduce mass , $\mu = \dfrac{m_1 m_2}{m_1 + m_2}$

And then we can write as;

$$\sum_{i,j}[T_{ij} + V^{\ell}_{ij} + V_{ij}]c_j = E\sum_{i,j} N_{ij}\, c_j \qquad (3)$$

$$\sum_{j=1}^{N} H_{ij}c_j = E\sum_{j=1}^{N} N_{ij}c_j \qquad (4)$$

Eq.(4) can be written as

$$H_{11}C_1 + H_{12}C_2 + \dots\dots + H_{1N}C_N = E(N_{11}C_1 + N_{12}C_2 + \dots\dots + N_{1N}C_N)$$
$$H_{21}C_1 + H_{22}C_2 + \dots\dots + H_{2N}C_N = E(N_{21}C_1 + N_{22}C_2 + \dots\dots + N_{2N}C_N)$$
$$.$$
$$H_{N1}C_1 + H_{N2}C_2 + \dots\dots + H_{NN}C_N = E(N_{N1}C_1 + N_{N2}C_2 + \dots\dots + N_{NN}C_N)$$

The above N equations can be written as a matrix form as follows;

$$\begin{bmatrix} H_{11} & H_{12}\dots & H_{1N} \\ H_{21} & H_{22}\dots & H_{2N} \\ & & \\ H_{N1} & H_{N2}\dots & H_{NN} \end{bmatrix} \begin{bmatrix} C_1 \\ C_2 \\ \\ C_N \end{bmatrix} = E \begin{bmatrix} N_{11} & N_{12}\dots & N_{1N} \\ N_{21} & N_{22}\dots & N_{2N} \\ & & \\ N_{N1} & N_{N2}\dots & N_{NN} \end{bmatrix} \begin{bmatrix} C_1 \\ C_2 \\ \\ C_N \end{bmatrix} \qquad (5)$$

$$[H][C] = E\,[N][C] \qquad (6)$$

$$[N]^{-1}[H][C] = E\,[C] \qquad (7)$$

$$[A][C] = E\,[C] \qquad (8)$$

$N_{ij}, T_{ij},\ V^{\ell}{}_{ij}$ are analytically solved by using standard integral. We solved the two body Schrödinger equation to obtain the resonance energies. By diagonalization the Hamiltonian matrix elements, we obtained the complex energy eigenvalues.

Eta-Nucleon Interaction

In our calculation, we use the potential between η and nucleon which is the following functional form,

$$V_{\eta N}(r) = a_1\exp(-b_1(r_1 - r)^2) - a_2\exp(-b_2 r^2) - i\ a_3\exp(-b_3 r^2) \qquad (9)$$

with parameters a's, b's and r_1 from "MSc Thesis" (J.S. De Villiers, 2005). The value of their parameters are described in Table (1) and shown in Fig. (1) and Fig(2).

Table 1 Parameters of the η-N potential

Parameter	*Value*
r_1	1.95616478619031975fm
a_1	57.5826586837329657MeV
a_2	26.8157044304329091MeV
a_3	0.603932024464326478MeV
b_1	0.0715471865601824408fm^{-2}
b_2	0.0271505486074286040 fm^{-2}
b_3	0.0338015704618582769 fm^{-2}

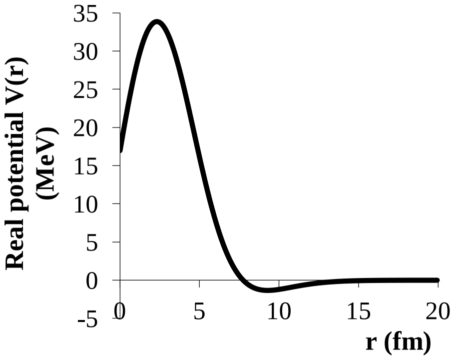

Figure 1 Real part of the Eta-Nucleon Potential

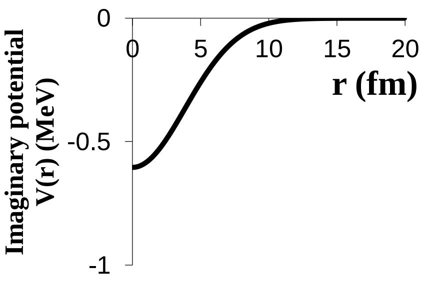

Figure 2 Imaginary part of the Eta-Nucleon Potential

Transformation of Functional form to Gaussian Form

Real part of Gaussian potential between η and nucleon has the following form,

$$V^{\mathrm{Real}}_{\eta\text{-N}}(r) = \sum_{k=1}^{N} V_k \, e^{-\left(\frac{r}{\mu_k}\right)^2} \qquad (10)$$

where, V_k and μ_k are the potential strengths and range parameters which are adjusted in the calculations with

$$\mu_N = c^{N-1}\mu_1 \, , \; c = \left(\frac{\mu_N}{\mu_1}\right)^{\frac{1}{N-1}} \qquad (11)$$

The transformation equation can be expressed as

$$V^{\mathrm{Real}}_{\eta\text{-N}}(r) \; = \; \sum_{k=1}^{N} V_k \, e^{-\left(\frac{r}{\mu_k}\right)^2} . \qquad (12)$$

Multiplying both sides of the equation by $e^{-\left(\frac{r}{\mu_\ell}\right)^2}$ from the right and integration through the equation, we obtain

$$\int_0^\infty V_{\eta\text{-N}}^{\text{Real}}(r)\ e^{-\left(\frac{r}{\mu_\ell}\right)^2} dr = \sum_{k=1}^{N} \int_0^\infty V_k \ e^{-\left(\frac{r}{\mu_k}\right)^2} e^{-\left(\frac{r}{\mu_\ell}\right)^2} dr. \qquad (13)$$

The left hand side of the equation (13) was numerically solved and the right hand side was solved by using standard integral form.

The above equation becomes

$$\int_0^\infty V_{\eta\text{-N}}^{\text{Real}}(r) e^{-\left(\frac{r}{\mu_\ell}\right)^2} dr = \frac{1}{2} \sum_{k=1}^{N} V_k \sqrt{\frac{\pi}{\frac{1}{\mu_k^2}+\frac{1}{\mu_\ell^2}}}\ . \qquad (14)$$

$$\text{Let}\, A_\ell = \int_0^\infty V_{\eta\text{-N}}^{\text{Real}}(r)\ e^{-\left(\frac{r}{\mu_\ell}\right)^2} dr \text{ and } B_{\ell k} = \frac{1}{2} \sqrt{\frac{\pi}{\frac{1}{\mu_k^2}+\frac{1}{\mu_\ell^2}}} \qquad (15)$$

The equation (14) is written as

$$A_\ell = \sum_{k=1}^{N} B_{\ell k}\ V_k$$

where ℓ goes from 1 to N

$$A_1 = B_{11} V_1 + B_{12}\ V_2 + B_{13} V_3 + \cdots + B_{1N} V_N$$

$$A_2 = B_{21} V_1 + B_{22}\ V_2 + B_{23} V_3 + \cdots + B_{2N} V_N$$

$$\vdots$$

$$A_N = B_{N1} V_1 + B_{N2}\ V_2 + B_{N3} V_3 + \cdots + B_{NN} V_N$$

These N linear equations are solved by using the Gauss elimination Method. The transformed Gaussian potential is found to be $\mu_1 = 0.05 \text{ fm}, \mu_N = 20 \text{ fm}$ and N=20 which are shown in Table (2).

Table 2 The range parameters and potential strengths of the transformed η-N Gaussian potential

Range parameter (fm)	***Potential strength(MeV)***
$\mu(1) = 0.10000$	$V(1) = -0.65741$
$\mu(2) = 0.13216$	$V(2) = 0.89916$
$\mu(3) = 0.17466$	$V(3) = -3.57331$
$\mu(4) = 0.23084$	$V(4) = 6.28714$
$\mu(5) = 0.30508$	$V(5) = -11.5881$
$\mu(6) = 0.40321$	$V(6) = 14.70480$
$\mu(7) = 0.53289$	$V(7) = -21.12319$
$\mu(8) = 0.70428$	$V(8) = 23.41650$
$\mu(9) = 0.93079$	$V(9) = -32.04554$
$\mu(10) = 1.23015$	$V(10) = 33.71635$
$\mu(11) = 1.62580$	$V(11) = -49.02017$
$\mu(12) = 2.14869$	$V(12) = 52.08892$
$\mu(13) = 2.83976$	$V(13) = -101.83089$
$\mu(14) = 3.75308$	$V(14) = 59.00174$
$\mu(15) = 4.96016$	$V(15) = 86.98296$
$\mu(16) = 6.55545$	$V(16) = -49.78051$
$\mu(17) = 8.66382$	$V(17) = 13.37485$
$\mu(18) = 11.45028$	$V(18) = -4.59364$
$\mu(20) = 20.00000$	$V(20) = -0.21711$

Eta-Nucleus Interaction

The interaction between η and the core nucleus ^{16}O is obtained by folding the $V_{\eta N}$ interaction with the density distribution of ^{16}O as

$$V_{\eta-\text{nucl}}(\vec{R}) = \int V_{\eta N}(\vec{R}-\vec{r})\,\rho_{\text{nucl}}(\vec{r})\,d\vec{r} \qquad (16)$$

where $\vec{R}$ is the distance betweenη particle and the center of the mass of the core nucleus and $\rho_{\text{nucl}}(\vec{r})$ is the nuclear density distribution of the core nucleus ^{16}O, $\vec{r}$ is the distance between nucleon and center of mass of the core nucleus as shown in Fig. (3). $V_{\eta-\text{nucl}}(\vec{R})$ is the folding potential of η and the core nucleus ^{16}O system. The density distribution of $\rho_{\text{nucl}}(\vec{r})$ in harmonic oscillator model is given as follows;

$$\rho_{\text{nucl}}(\vec{r}) = \rho_0\left\{1+\frac{\alpha}{a^2}r^2\right\}e^{-\left(\frac{r}{a}\right)^2} \qquad (17)$$

where,α=1.544, a=1.833fm from [8].

$$\rho_0 = \frac{A}{a^3\pi^{3/2}\,(1+1.5\alpha)}$$

where, A=mass number of the core nucleus.

For $^{16}_{8}O$ nucleus, the density of nuclear matter ρ_0=0.14067 fm^{-3}.

Then the folding potential for the phenomenological η-N interaction is

$$V_{\eta-\mathrm{nucl}}(\vec{R}) = \int \rho_{\mathrm{nucl}}(\vec{r})\, V_{\eta N}(\vec{R}-\vec{r})d\vec{r}$$

$$V_{\eta-\mathrm{nucl}}(\vec{R}) = \int \left\{\rho_0 + Y\, r^2\right\} e^{-\left(\frac{r}{a}\right)^2} \sum_{K=1}^{N} V_K e^{-\left(\frac{\vec{r}-\vec{R}}{\mu_K}\right)^2} d\vec{r} \qquad (18)$$

$$V_{\eta-\mathrm{nucl}}(\vec{R}) = \sum_{K=1}^{N} V_K \left(\frac{\pi}{A}\right)^{3/2} \left\{ P e^{-\left(\frac{\vec{R}}{D_K}\right)^2} + Q\; R^2 e^{-\left(\frac{\vec{R}}{D_K}\right)^2} \right\}$$

where, $P = \rho_0 + \frac{1.5}{B} Y$, $Q = \frac{Y}{B^2 \mu_K^4}$, $Y = \rho_0 \frac{\alpha}{a^2} = 0.0646$,

$$B = \frac{1}{a^2} + \frac{1}{\mu_K^2} \text{ and } \frac{1}{D_K^2} = \frac{1}{\mu_K^2} - \frac{1}{B\mu_K^4}.$$

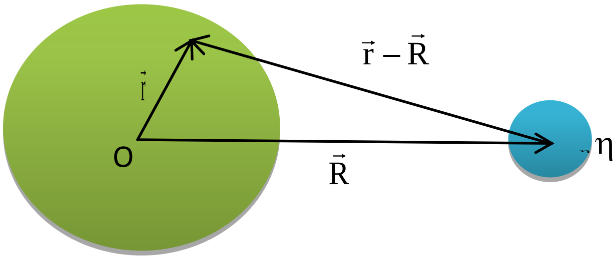

Figure 3 The core nucleus and η particle

Density of nuclear matter (ρ_0)

We find the existence of the value ρ_0, known as the 'density of nuclear matter'. The normalization of the charge distribution is

$$4\pi \int \rho(r) r^2 dr = Ze. \qquad (19)$$

The density is only approximate, since we have neglect the finite size of both proton and neutron and the effect of Coulomb forces, but it indicates that at the centre of a nucleus.

$$\int \rho_{\mathrm{nucl}}(\vec{r})\, d\vec{r} = A \qquad (20)$$

where A=mass number of the core nucleus

$$4\pi \int \rho(r) r^2 dr = A$$

The Harmonic Oscillator density distribution is Gaussian

$$\rho(r) = \rho_0\left[1+\alpha\left(\frac{r}{a}\right)^2\right]e^{-\left(\frac{r}{a}\right)^2} \quad .$$

Equation (19) becomes

$$4\pi\int \rho_0\left[1+\alpha\left(\frac{r}{a}\right)^2\right]e^{-\left(\frac{r}{a}\right)^2} r^2 dr = Ze \qquad (21)$$

By using the Standard Integral form $\int_0^\infty r^{2N}e^{-Ar^2}dr = \frac{(2N-1)!!}{2^{n+1}}\frac{1}{A^N}\sqrt{\frac{\pi}{A}}$ and

the result is $\rho_0\left[\frac{1!!}{2^2}\frac{1}{1/a^2}\sqrt{\frac{\pi}{1/a^2}} + \frac{\alpha}{a^2}\frac{3!!}{2^3}\frac{1}{1/a^4}\sqrt{\frac{\pi}{1/a^2}}\right] = \frac{Ze}{4\pi}$

$$\rho_0 = \frac{Ze}{4\pi}\frac{4}{a^3\sqrt{\pi}[1+3/2\alpha]}$$

For ${}^{16}_{8}O$ nucleus, Ze= 16.

Substituting the parameter a=1.833fm, $\alpha = 1.544$, π=3.142 and A=16 for ${}^{16}_{8}O$,we get ρ_0 is 0.14067fm^{-3}.

Results and Discussion

Binding Energy and Level Width of ${}^{16}_{\eta}O$ Nucleus

Our research is to investigate the structure of η-mesic Oxygen nucleus ${}^{16}_{\eta}O$ theoretically, considering as a bound system of η-meson and Oxygen core nucleus. It is found that although the η - N interaction is attractive, it is not strong enough to have a two-body bound state. Since Oxygen is the double magic nucleus, it is a very high stability nucleus. Therefore we expect to be a bound system of double magic oxygen nucleus and η - meson.

Before performing the studying of η-meson Oxygen system, we have transformed the functional form into Gaussian form which is nearly equivalent to original potential by applying the Gauss elimination method. The η-N interaction which is functional form cannot be analytically solved. The transformed Gaussian potential is obtained by applying the optimum parameter set, $\mu_1 = 0.05$ fm, $\mu_N = 20$ fm and N=20. These transformed potential compared with original potential is shown in Fig.(4).

To study the η-nucleus bound system, we have to know the interaction between η and oxygen core nucleus. By folding the η-N interaction with oxygen nucleus nuclear density, we obtained the η-nucleus interaction. And then we have computed the eigen value of ${}^{16}_{\eta}O$ system with the η-nucleus folding potential. Oxygen nucleus nuclear density for Harmonic Oscillator model is $\rho_0 = \frac{A}{a^3\pi^{3/2}\left[1+1.5\,\alpha\right]}$. By applying the parameter a=1.833fm, $\alpha = 1.544$,π=3.142 and A=16, our calculated nuclear density ρ_0 is 0.14067 fm^{-3}.

In order to calculate the structure of two-body quantum system we solved Schrödinger equation. To solve the Schrödinger radial equation we use the Gaussian basis wave function. We have calculated the eigenvalue E with corresponding eigenvectors C_j by using FORTRAN CODE. To solve the eigen value equation, we used the Power Inverse Iteration Method. Our calculated result is 3.2814 MeV and its level width is 0.3704 MeV.

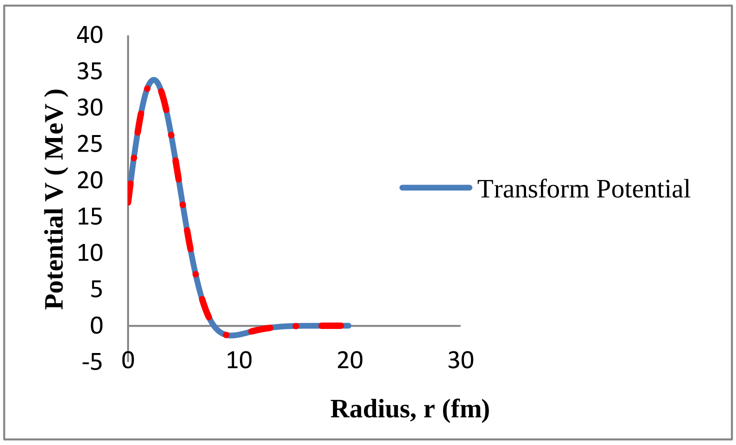

Figure 4 The real part of potentials between η and the nucleon, solid and dotted curve indicate the functional form and the transformed Gaussian potential, respectively.

Conclusion

Our thesis is to investigate the structure of η-mesic Oxygen nucleus $^{16}_{\eta}O$ theoretically, considering as a bound system of η-meson and Oxygen core nucleus. To study the η-Oxygen nucleus bound system, we have to know the interaction between η and Oxygen core nucleus $^{16}_{8}O$. The η-N interaction which is functional form cannot be analytically solved, so we transformed the functional form into Gaussian form by applying the Gauss elimination method. By folding η-N interaction with Oxygen core nucleus nuclear density we obtained the η-nucleus interaction. And then we compute the eigen value of $^{16}_{\eta}O$ system with the η-nucleus folding potential. Our calculated result is 3.2814 MeV with a level width is 0.3704 MeV.

Acknowledgement

The authors would like to express their sincere thanks to Professor Dr Khin Swe Myint , Rector (Rtd.), Emeritus Professor, Department of Physics, University of Mandalay for her valuable advice and helpful discussion in this research work. The authors would like to thank Dr Khin Khin Htoot, Professor, Head of Physics Department, Taunggyi University for her encouragement.

References

B.J. Roy et al; (2002) Phys. Lett. **B 550,** 47.

C. Wilkin, (1993) Phys. Rev. **C 47**, 398.

H.De Vries et al; (1987) "Atomic Data and Nuclear Data Tables", **36** 495-536.

J.S. De Villiers, (2005) "MSc Thesis", University of South Africa.

Khin Aye Win (2014) "PhD Thesis", University of Mandalay.

N G Kelkar et al; (2013) arXiv:nucl-th**V2,** 1306.

Q. Haider and L.C. Liu, (1986) Phys. Lett. **B172**, 257.

R.S. Bhalerao, L.C. Liu, (1985) Phys. Rev. Lett. **54**, 865.

J. Myanmar Acad. Arts Sci. 2020 **Vol. XVIII.No.2C**

ANALYSIS OF PHYSICAL AND CHEMICAL PROPERTIES FOR BIOCHAR FROM RICE HUSK BIOMASS

Thinzar Lwin[1], Thin Thin Kyu [2], Than Than Win[3], Yin Maung Maung[4]

Abstract

Biomass play significant roles in the production of eco-friendly biochar and as substitutes for renewable sources of energy. In this study, investigations were carried out on physical and chemical analysis of rice husk biochar (RHBs) from rice husk. The rice husk biomass was heated at 300˚C for 1h and sieved to the average particle size. The physical and chemical properties of RHBs were determined by direct measurements and calculations. Rice husk biochar (RHBs) were characterized for biochar yield, pH and Bulk Density. The biochar chemical analysis gave the following results; biochar yield of 73% for RHB-HT and 68% for RHB-PT, the pH values of 7.14% and 7.49%, Bulk density of 0.42% and 0.43% for RHBs. RHBs were characterized by analyzing the chemical composition mainly based on X-ray diffraction (XRD), Energy Dispersive X-ray Fluorescence (EDXRF), Fourier transform infrared spectroscopy (FTIR) and surface morphology from Field emission SEM (FE-SEM) and energy dispersive X-ray micro-analysis (EDXA). The XRD showed the carbon amorphous structure of rice husk biochar (RHBs), which consists of surface morphology from FE-SEM. The carbon (C), oxygen (O) and silica (Si) were observed by Energy Dispersive X-ray spectroscopy (EDX). Fourier transform infrared spectroscopy (FTIR) analysis showed the presence of a variety of functional groups for RHBs. The results of the physical and chemical properties of the rice husk biochar provide the prominent source of useful energy.

Keywords : Biomass, EDXRF, FE-SEM, FTIR, Rice Husk Biochar, XRD.

Introduction

Now a day, biomass is important one of a renewable energy resources. Biomass is a nonpolar and biodegradable organic material directly obtained from plants, animals or microorganisms [Demirbas, A.et.al (2009), Adilah Shariff et.al (2014)]. Biomass resources generally contained the various natural and artificial things such as woody and herbaceous species, wood wastes, sawdust, rice husk, bio solids, grass, waste from food processing, animal wastes, aquatic plants and algae [Adilah Shariff et.al (2014), Yaman, S. et.al (2004)]. Biomass can be transfer into liquid, solid and gaseous fuel via transformation of some physical, chemical and biological phenomenon. Rice husk is one of the biomass raw materials for thermochemical conversion. Although it can be widely used in pyrolysis and gratification, it is restricted for the application areas of biomass technology to measure some properties such as its high oxygen content, high moisture, low calorific value, large particle size, and grinding. Its advantages are observed to be the further development of biomass application technology [Van der Stele et.al (2014), Chen, D. Y. et.al (2012 a), Yin, R. Z. et.al (2012)].

Biochar is sustainably produced from biomass sources and it can be used in agricultural as non-oxidative application. Moreover, it can be also applied in the area of carbon sequestration [Lehman et.al (2015)]. Actually, biochar is almost the same with charcoal, the carbon chance into CO_2 by firing the biochar and may apply as fuel. In the past decade, potential attention increase

---

[1] Assistant Lecturer, Department of Physics, West Yangon Technological University, Myanmar

[2] Department of Physics, University of Yangon, Myanmar

[3] Department of Physics, Pang Long University, Myanmar

[4] Department of Physics, University of Yangon, Myanmar

the research concerned with biochar due to its novel application. The remarkable advantage outcome of the biochar is its used in carbon sequestration [S.P. Galinato et.al (2011), C.J. Barrow et.al (2012)]. Biochar can be employed in use for various for various applications and feedstock for many process according to its physicochemical characteristics [D.Ozcimen et.al (2010), X. Wang et.al (2009)]. In this research, rice husk collected from Ayewaddy Region in Myanmar conduct to carry out experiments as function of heating temperature and time. In the presence investigation, the main objective was to produce biochar from agricultural wastes namely rice husk biomass. The physicochemical characteristics of the resulting biochar was examined to evaluate biochar yield, pH and Bulk density. Crystal structucture and phase identification of biochar was characterized by X-ray diffraction (XRD). The rice husk biochar samples were also analyzed by Field Emission-Scanning Electron Microscope (FE-SEM) equipped with an energy dispersion X-ray Spectroscopy (EDX) and FRIR for identification of surface morphology and functional groups.

Materials And Methods

Biochar Preparation from Rice Husk

The rice husk used for the present work were obtained from Ayewaddy Region in Myanmar. Two different types of biochars derived from rice husk biomass were investigated. Biochar, rice husk from Hinthada, noted hereafter as RHB-HT and biochar, rice husk from Pathein, noted hereafter as RHB-PT.

Table 1 Sample label

Sir No.	Sample
1.	RHB-HT
2.	RHB-PT

20-g of rice husk were first washed with deionized (DI) water 1 L for 2 h at 90˚C. After successive washing, the wet rice husk was dried at room temperature for 48 h. Then rice husk was heated at 300˚C for 1 h. After heating, samples were sieved to the average particle size.

Biochar Chemical Analysis

Biochar Yield

The biochar yield was calculated as the propotion of the weight of biochar product to the original material. The percentage of biochar yield was calculated using the following equation. [Sadaka S et.al (2014), G.Stella Mary P.Sugumaran et.al (2016)]

$$\mathbf{Yield}_{\text{biochar}} = \frac{\textbf{Mass of biochar (g)}}{\textbf{initial Mass of biomass (g)}} \times 100\%$$

Where, Yield $_{\text{biochar}}$ = mass yield of biochar %

pH Measurement

For pH determination, 1 g of bio-char was dispersed in 100 mL of deionized water with stirring. The mixture is heated at 90˚C with stirring for 20 min and then cooled at room temperature. The insoluble solute is separated from the solution by filtration with filter paper. The filtered solute is taken. The pH value was measured with pH meter.

Bulk Density Measurement

Bulk density was determined for rice husk biochar. The biochars were crushed and sieved through a mesh with 250 µm openings. An empty 25 mL graduated measuring cylinder was dried in a drying oven and weighed out. It was then filled up to a volume of 10 mL with the biochars. Then the biochar dried in oven at 80 C for 5h. With the filling of every 2 mL, the cylinder was tapped for 1-2 min onto a padded surface to compact the char and the bulk density was calculated by following formula:

$$\text{Bulk density (\%)} = \frac{\text{weight of dry material (g)}}{\text{Volume of packed dry materials (ml)}} \text{x}100$$

Results and Discussion

Biochar Chemical Analysis

The biochar yield of RHBs at 300˚C are summarized in Table. 2. Several studies indicate that the yield of biochar is highly dependent on the pyrolysis conditions such as temperature, heating rate and heating time [Tsai WT, Lee MK et.al (2007)] and is also greatly influenced by chemical, physical and biological properties of the biomass [Knoepp JD et.al (2005), Lehmann J et.al (2007), Basta AH et.al (2011)]. Biochar yield was found that low temperature produced a higher biocher yield and enhance volatile matter composition than the high temperature. The pH of biochars may change and either decrease or increase depending on type of feedstock. The pH of biochar may also change post-production depending on the environmental conditions. The pH of 7.14 for RHB-HT and 7.49 for RHB-PT (Table 2). In this study, the pH of RHBs were recorded alkaline pH. Bulk density of biochar, differing according to the raw materials used, is that of the material comprising multiple particles and includes the macro porosity each particle and the antiparticle voids. In this study, Bulk density of 0.42 for RHB-HT and 0.43 for RHB-PT.

Table 2 Physical and chemical characteristics of the rice husk biochar at 300˚C

Physical and chemical characteristics of RHBs from rice husk					
Sir No.	**Samples**	**Temperature (˚C)**	**Biochar Yield (%)**	**pH (%)**	**Bulk Density (g/mL) (%)**
1.	**RHB-HT**	**300˚C**	73	7.14	0.42
2.	**RHB-PT**	**300˚C**	68	7.49	0.43

X-ray Diffraction (XRD) Analysis

X-ray Diffraction (XRD) Analysis XRD is the most useful method to see the particle size and crystalline and amorphous materials. Figure 1. shows the X-ray diffraction (XRD) pattern of the rice husk biochars RHB-HT and RHB-PT at 300˚C respectively. Appearance of broad diffraction peak and the absence of a sharp peak reveals a predominantly amorphous structure. All the samples showed the same diffraction patterns, where the broad peak was observed between 15˚ and 30˚, the ranges are corresponding to the presence of amorphous carbon. Also, the XRD patterns revealed the absence of any ordered crystalline structure. It is desire to have amorphous carbon as the carbon fuel, however, we are unable to tell the percentage of amorphous carbon in the biochars RHB-HT and RHB-PT.

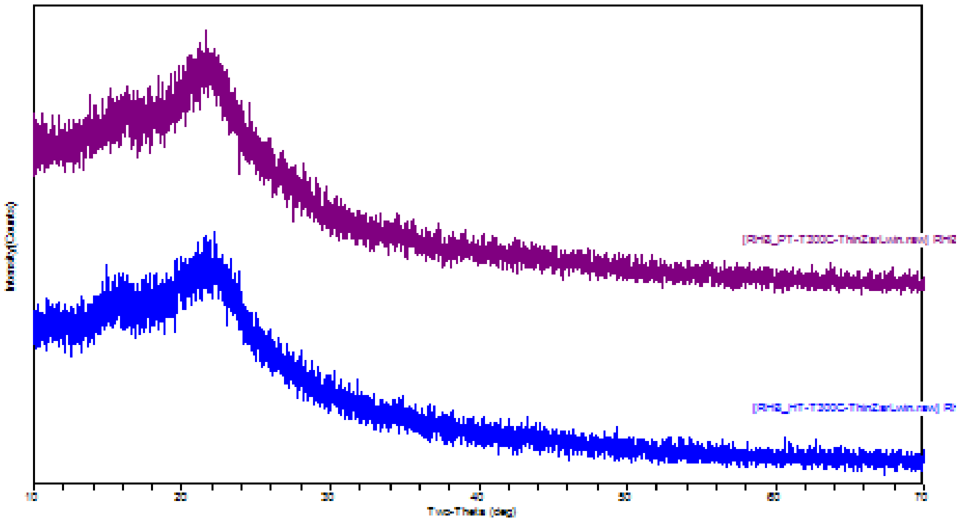

Figure 1 X-ray diffraction patterns of Rice Husk Biochar RHB-HT and RHB-PT at 300˚ C

Field Emission Scanning Electron Microscopy (FE-SEM) Analysis

Figures 2 (a-b). show the FE-SEM micrographs (100x) of the surface morphology of the RHB-HT and RHB-PT at 300˚C. The carbon is mainly localized in the tips of the domes, whereas a lower amount of carbon can be found in other regions of the RHBs (RHB-HT and RHB-PT). In addition, [Bidayatul Armynah et.al (2018)] have demonstrated from FE-SEM experiments, that the characteristic of surface morphology is dot may contain high carbon.

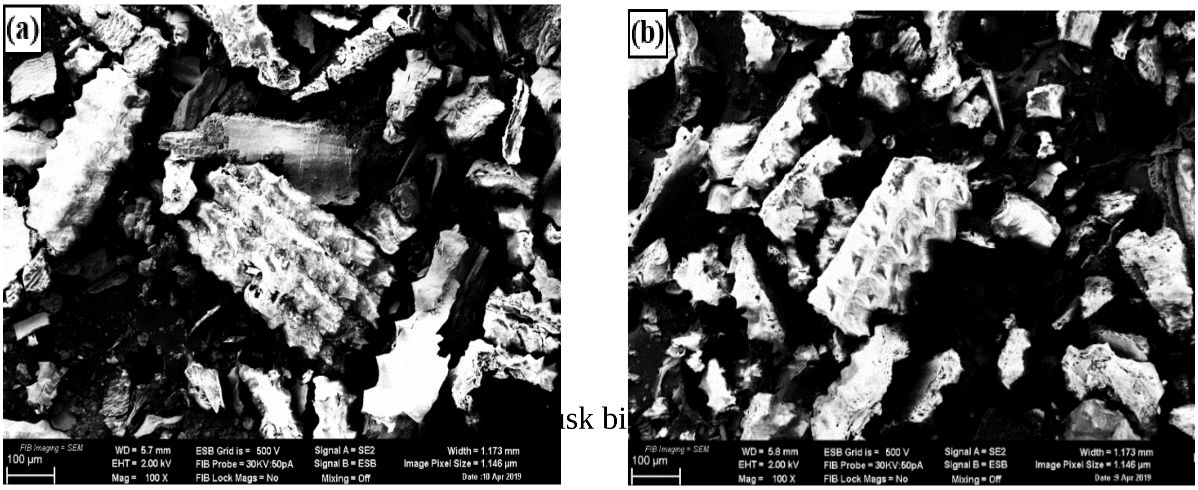

Figure 2 (a-b) FE-SEM micrograph of rice husk biochar RHB-HT and RHB-PT at 300˚C

Energy Dispersive X-ray (EDX) Analysis

The compositional analysis of the RHBs (RHB-HTT and RHB-PT) at 300˚C was analyzed by Energy Dispersive X-ray spectroscopy. The EDX results for RHBs samples obtained the elements of Carbon (C), Oxygen (O), Silicon (Si). Fig. 3(a-b) shows C, O and Si content in the RHBs at 300˚C and the corresponding weight percent of the elements present in the RHBs and result obtained further assures that no other impurity is present in the RHBs. Fig. 3(a) shows the EDX spectrum of RHB-HT at 300˚C. The strong peaks observed in the spectrum related to the Carbon and Oxygen. The elemental constitution of RHB-HT at 300˚C with one major peak and one minor peak were found to have weight percentage of 69.23 for Carbon and 30.77 for oxygen. The RHB-HT have atomic percentage of 70.22 for Carbon and 29.69 for Oxygen. Fig. 3(b) shows the EDX spectrum of RHB-PT at 300˚C. The elemental constitution of RHB-PT at 300˚C with two major peaks and one minor peak were found to have weight percentage of 65.42 for Carbon, 34.55 for oxygen and 0.03 for Silica. The RHB-PT have atomic percentage of 58.69 for Carbon, 41.29 for Oxygen and 0.01 for Silica (Fig. 3-b). From these result, the RHB-HT at 300˚C sample have 79.23% (wt %) and 70.22% (At %) of carbon elements which is the higher percentage than RHB-PT at 300˚C. It contains low fractions and absent of various elements such as S, Cl, K, Zn and Mg. This is important to study the influence of these impurities on the fuel source, high Carbon (C) content and low Sulphur content were required. Elemental and atomic content for RHBs-HT and RHB-PT at 300˚C expressed in percentage by EDX analysis are summarized in Table. 3.

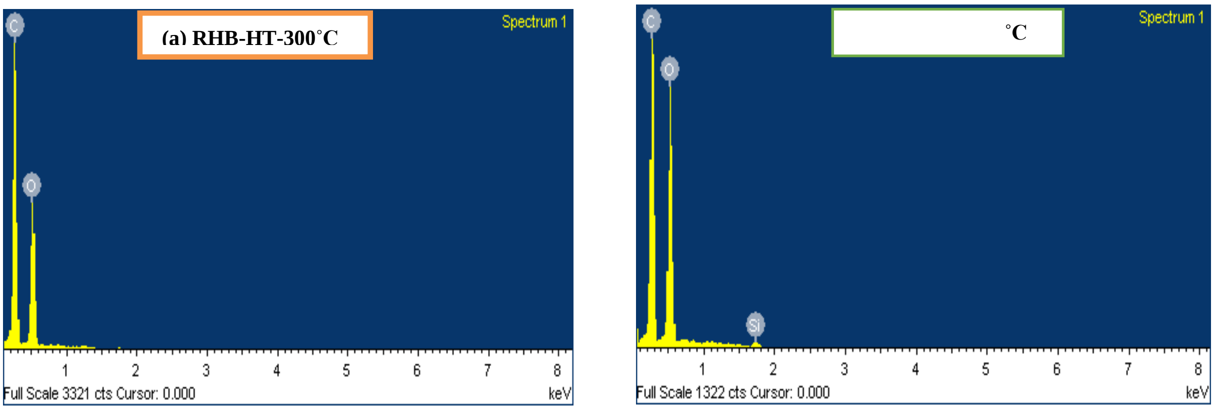

Figure 3 (a-b) EDX spectrum of RHB-HT and RHB-PT at 300˚C

Table 3 Element content for RHB-HT and RHB-PT at 300˚C

Component	**RHB-HT**		**RHB-PT**	
	300˚C		**300˚C**	
	Weight%	Atom%	Weight%	Atom%
Carbon	69.23	70.22	65.42	58.69
Oxygen	30.74	29.78	34.55	41.29
Silicon	0.03	0.01	0.03	0.01

Energy Dispersive X-ray Fluorescence (EDXRF) Analysis

Table 4 indicates that elemental concentration in RHB-HT and RHB-PT at 300˚C. Eleven elements namely C, K, Si, Ca, S, Fe, Cr, Cu, Mn, Ti and Ni were detected in the rice husk biochar sample by EDXRF technique. Carbon (C) was found to be present as the major element, whereas K, Si, Ca, S, Fe, Cr, Cu, Mn, Ti and Ni were present as minor element. Therefore, RHB-

HT and RHB-PT at 300˚C were quantified by EDXRF. From the result, RHB-HT contains 96.912 % of Carbon (C) which is higher than RHB-PT at 300˚C. This results are good agreed with FE-SEM result.

Table 4 Chemical composition for RHB-HT and RHB-PT were measured by using EDXRF

Elemental Analysis of RHBs												
Sir. No	**Sample**	**Content Weight%**										
		C	K	Si	Ca	S	Fe	Cr	Cu	Mn	Ti	Ni
1.	**RHB-HT**	96.912	2.019	1.025	0.004	0.001	0.002	0.020	0.035	0.004	0.051	0.000
2.	**RHB-PT**	95.902	3.004	0.035	0.000	0.003	0.001	0.010	0.018	0.002	0.025	0.010

Fourier Transform Infrared Spectroscopy (FTIR) Analysis

FTIR results of RHB-HTT and RHB-PT for 300˚C were shown in Fig. 4 (a-b). As it was explained in the introduction, the organic part of the rice husk mainly composed of cellulose, hemicellulose, lignin, and waxes, which most likely consist of alkene, esters, aromatics, ketones, and alcohols. At 300˚C, FTIR spectra contain four peaks at 3344.65 cm^{-1}, 2345.79 cm^{-1}, 1617 cm^{-1}, 1050.76 cm^{-1} and 788.36 cm^{-1} for RHB-HT and 3330.35 cm^{-1}, 2361.12 cm^{-1}, 1602.51 cm^{-1}, 1051.14 cm^{-1}, 793.02 cm^{-1} for RHB-PT.

i) O-H stretching

The peaks obtained for RHBs at 300˚C were 3344.65 cm^{-1} for RHB-HT and33330.35cm^{-1} for RHB-PT respectively. The peaks indicate O-H stretching (3650 to 3200 cm^{-1}) carboxylic group. [Demirbas, A. (2000), De Rosa, I. M. et.al (2010), Socrates, G. et.al (1994).]

ii) C-O stretching

The band visible at 2360 cm^{-1} – 2365 cm^{-1} corresponds to the stretching vibration of the C-O for carbon monoxide or carbon dioxide derivatives in RHB-HT and RHB-PT [H.P.S. Abdul Khalil et.al (2013)].

iii) C=C stretching

The peaks recoded for RHBs (300˚C) were at 1599.55 cm^{-1} for RHB-HT and 1602.51cm^{-1} for RHB-PT respectively. These were indicating C=C stretching vibration consists of aromatic groups in lignin [G. Stella Mary (2016)].

iv) C-O stretching

The presence of peaks 1050.76 cm^{-1} for RHB-HT and 1051.14cm^{-1} for RHB-PT at 300˚C were indicative of C-O secondary alcohol stretching for cellulose, hemicellulose, and lignin [Bidayatul Armynah et.al (2018)].

v) C-H bending

The RHBs at 300˚C showed four strong peaks; the peaks recoded at 788.36 cm^{-1} for RHB-HT and 793.02 cm^{-1} for RHB-PT respectively, which reveals alkynes with C-H bending is present [Bidayatul Armynah et.al (2018)].

The presence of functional groups such as the carboxylic group, alcohol aromatics and alkynes groups suggest that these RHBs could be affected in fuel source. The functional groups identified in FTIR analysis for RHBs are tabulated in Table 5.

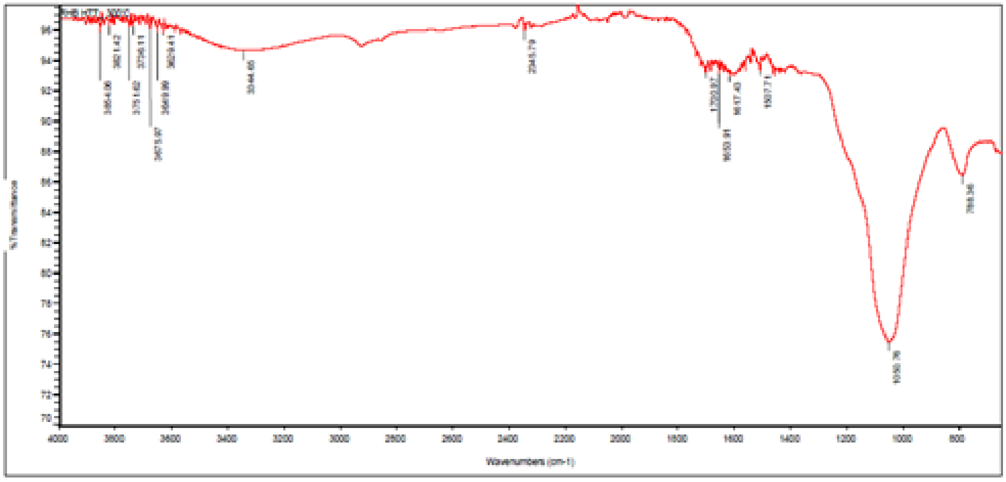

Figure 4(a) FTIR spectrum of RHB-HT at 300˚C

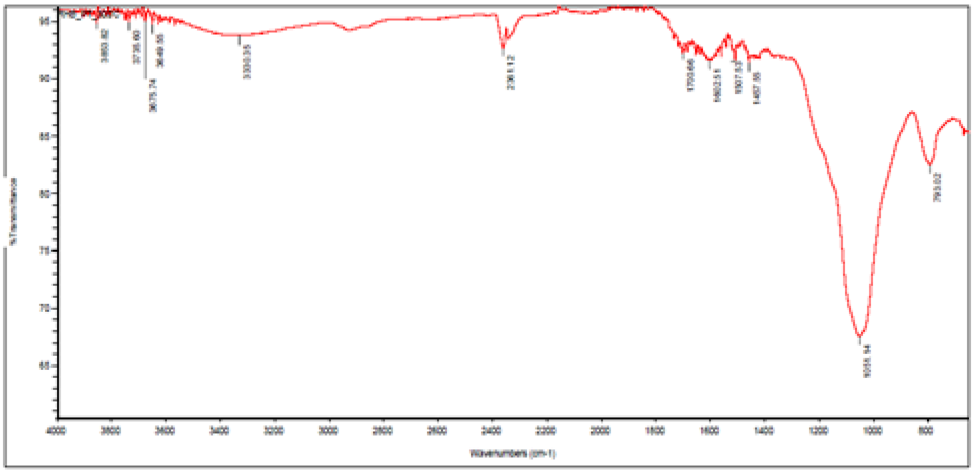

Figure 4(b) FTIR spectrum of RHB-PT at 300˚C

Table 5 Functional groups identified in FTIR analysis of RHBs at 300˚C

Sr No.	Chimical bond	RHB-HT	RHB-PT
		300˚C Peak position (cm^{-1})	300˚C Peak position (cm^{-1})
1.	O-H	3344.65	3330.35
2.	C-O	2345.79	2361.12
3.	C=C	1617.00	1602.51
4.	C-O	1050.76	1051.14
5.	C-H	788.36	793.02

Conclusion

RHBs were produced from rice husk biomass heating at low temperature. The properties of biochars have different chemical structures and carbon content depend on agricultural conditions and types of raw material. The XRD shows the same diffaration pattern and amorphous carbon structure. Surface morphology from FE-SEM indicated high carbon content. The RHBs were quantified by EDXRF spectrometer. Carbon (C) was found that the highest concentration in the RHBs (RHB-HT and RHB-PT). But RHB-HT is higher carbon content than RHB-PT. FTIR shows aromatic compound group corresponds to carbon atoms C=C at (1602-1617 cm^{-1}). These results of physical and chemical composition characteristic, structural properties, surface morphology and bonding formation of RHB-HT show that the prominent source of useful energy can replace as the fuel.

Acknowledgements

The authors would like to thank Department of Research and Innovation (DRI). Ministry of Education, Yangon, for opportunity to do this research and their support.

References

Adilah Shariff, Nur Syairah Mohamad Aziz and Nurhayati Abdullah, (2014). "Slow Pyrolysis of Oil Palm Empty Fruit Bunches for Biochar Production and Characterization", Journal of Physical Science, vol. 25, pp. 97-112.

Basta AH, Fierro V, El-Saied H, Celzard A (2011), "Effect odeashing rice straws on their derived activated carbons produced by phosphoric acid activation", Biomass Bioenergy, Doi: 10.1016/j.biombioe.2011.01.043, vol. 35, pp. 1954-1959.

Bidayatul Armynah, Atika, Zuryati Djafar, Wahyu H Piarah, Dahlang Tahir, (2018) "Analysis of Chemical and Physical Properties of Biochar from Rice Husk Biomass", doi:10.1088/1742-6596/979/1/012038, pp. 1-8.

Chen, D. Y., Li, K., and Zhu, X. F. (2012a). "Determination of effective moisture diffusivity and activation energy for drying of powdered peanut shell under isothermal conditions," Bio resources, vol. 7, pp. 3670-3678.

C. J. Barrow, (2012), "Biochar: Potential for countering land degradation and for improving agriculture," Appl. Geogr., vol. 34, pp. 21–28.

Demirbas, A. (2009). "Fuels from biomass. In Demirbas, A. (Ed.). Biohydrogen for future engine fuel demands",London: Springer, pp. 43-57.

D. Özçimen and A. Ersoy-Meriçboyu, (2010), "Characterization of biochar and bio-oil samples obtained from carbonization of various biomass materials," Renew. Energy, vol. 35, pp. 1319–1324.

Demirbas, A. (2000). "Mechanisms of liquefaction and pyrolysis reactions of biomass," Energy. Convers. Manage. Vol. 41, pp. 633-646.

De Rosa, I. M., Kenny, J.M., Puglia, D., Santulli, C., and Sarasini, F. (2010). "Morphological, thermal and mechanical characterization of okra (Abelmoschus esculentus) fibers as potential reinforcement in polymer composits," Compos. Sci. Technol, vol. 70, pp. 116-122.

G.Stella Mary P.Sugumaran , S. Niveditha , B. Ramalakshmi, P.Ravichandran, S.Seshadri, (2016), "Production, Characterization and Evaluation of biochar from pod (Pisum sativum), leaf (Brassica oleracea) and peel (Citrus sinensis) wastes", Int J Recycl Org Waste Agricult, doi: 10.1007/s40093-016-0116-8, vol. 5, pp. 43-53.

H.P.S. Abdul Khalil, M. Jawaid, P. Firoozian, Umer Rashid Aminual Islam, and Hazizan Md. Akil, (2013), "Activated Carbon from Various Agricultural Wastes by Chemical Activation with KOH": Preparation and Characterization, Journal of Biobased Materials and Bioenergy, vol. 7, pp. 1-7.

Knoepp JD, DeBano LF, Neary DG (2005), "Wildland fire in ecosystem; effect of fire on soils and water",General Technical Report RMRS-GTR 42-4, U.S. Department of Agriculture, Forest Service, Rocky Mountain Research Station, Ogden, UT, pp. 53-71.

Lehmann J, (2007) "A handful of Carbon. Nature", Doi:10.1038/447143a, vol. 477, pp. 143-144.

Lehmann, J.; Joseph, S., (2015) "Biochar for environmental management: An introduction In Biochar for Environmental Management", Science, Technology and Implementation; Lehmann, J., Joseph, S., Eds.; Routledge: Oxford, UK.

S. P. Galinato, J. K. Yoder, and D. Granatstein, (2011) "The economic value of biochar in crop production and carbon sequestration," Energy Policy, vol. 39, pp. 6344–6350.

Sadaka S, Sharara MA, Ashworth A, Keyser P, Allen F, Weight A (2014), "Characterization of biochar from switchgrass carbonization", Energies doi:10.3390/en7020548, vol. 7, pp. 548-567.

Socrates, G. (1994). "Infrared Characteristic Group Frequencies", John Wiley and Sons, New York.

Tsai WT, Lee MK, Chang YM (2007), "First pyrolysis of rice husk: product yields and composition", Biochar Technol vol. 98, pp. 22-28.

Van der Stele, M. J.C., Gerhauser, H., Kiel, J. H. A., and Ptasinski, K.J. (2011). ''Biomass upgrading by torrefaction for the production of biofuels: A review, "Biomass and Bioenergy" vol. 35, pp. 3748-3762.

X. Wang, H. Chen, X. Ding, H. Yang, S. Zhang, and Y. Shen, (2009) "Properties of gas and char from microwave pyrolysis of pine sawdust," BioResources, vol. 4, pp. 946–959.

Yaman, S. (2004), "Pyrolysis of biomass to produce fuels and chemical feedstocks", Energy Convers. Manage., vol. 5, pp. 651-671.

Yin, R. Z., Liu, R. H., Wu, J. K., Wu, X. W., Sun, C., and Wu, C. (2012). "Influence of particle size on performance of a pilot-scale fixed-bed gasification system," Biosource Technology, vol. 119, pp. 15-21.

J. Myanmar Acad. Arts Sci. 2020 **Vol. XVIII.No.2C**

DETERMINATION OF RADON CONCENTRATION IN SOME WATER SAMPLES COLLECTED FROM THREE VILLAGES IN SALINGYI TOWNSHIP WITH SSNTDs

Tin Tin Phyo Lwin*

Abstract

Water is the most abundant substance on earth, and it is the principal constituent of all living things. Radon dissolved in water can cause to significant health problems for humans through inhalation and ingestion. In the present work, a total of eleven water samples from the three villages near the Mine area in Salingyi Township were analyzed for dissolved radon by using solid state nuclear track detection technique. The principle of this technique/e is based on the production of track in the detector due to alpha particles emitted from radon and its progeny. To detect the alpha track, LR-115 plastic track detectors were used for an exposure time of 100 days. After exposure, the tracks are made visible by chemical etching and counted manually under the binocular microscope. The measurement track density is converted into radon concentration. The concentration of radon has been found to be varying from 0.36±0.02 $pCil^{-1}$ to 0.61±0.04 $pCil^{-1}$. The present results show that the radon concentrations in all water samples are below the allowed limit from International Commission on Radiological Protection agency which is 27 $pCil^{-1}$(ICRP 2009). In addition to the radon concentrations, the annual effective dose has been calculated.

Keywords: Track density, Radon concentration, Annual effective dose.

Introduction

Radon is a colorless, odorless, tasteless radioactive gas. It forms naturally from the decay of radioactive elements, such as uranium, which are found at different levels in soil and rock throughout the world. Radon gas in the soil and rock can move into the air and into ground water and surface water. Radon is present outdoors and indoors. It is normally found at very low levels in outdoor air and in drinking water from rivers and lakes. It can be found at higher levels in the air in houses and other buildings, as well as in water from underground sources, such as well water.

Radon breaks down into solid radioactive elements called radon progeny such as polonium- 218, polonium-214 and lead-214. Radon progeny can attach to dust and other particles and can be breathed into the lungs. As radon and radon progeny in the air break down, they give off alpha particles, a form of high energy radiation that can damage the DNA inside the body's cells.

In this research work, the LR-115 SSNTD film is used to measure the alpha track detection. Track detectors are successfully performed in ^{222}Rn (radon) concentration measurement. Solid state nuclear track detection technique was simple, easy and useful technique to measure the alpha detection because it was low cost and not concerned with the electronic detector assembly. This research is carried out in order to know whether it is dangerous or not for people who live near the Mine area, as a result of radon output in water samples from three villages near the Mine area in Salingyi Township, Sagaing Region.

---

* Dr, Assistant Lecturer, Department of Physics, University of Yangon

Method and Materials

Sample Collection

To measure the radon concentration, eleven kinds of water samples (eight water samples from wells, one water sample from tube-well, one water sample from Yama stream and one water sample from waste water) were collected from Kan Gon village, Done Daw village and Ywa Tha village, near the Mine area, in Salingyi Township, Sagaing Region. The list of collected places and locations are shown in the Table (1). The location map of three villages is also shown in Fig. (1).

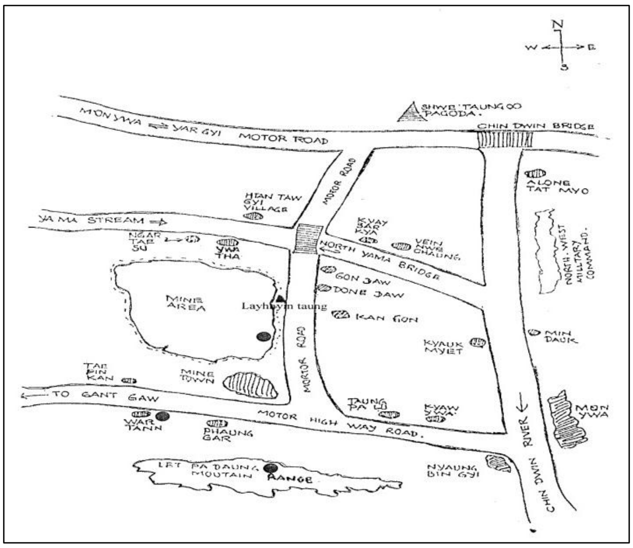

Figure 1 The location map of three villages

Table 1 List of collected places and location of water samples

Sr No	Name of Sample	Collected places	Kind of water	Depth of well (m)	North latitude	East Longitude	Elevation (m)
1	W1	Done Daw Village	well water	~ 12	22° 8.19′	95° 3.79′	71
2	W2	Kan Gon Village	well water	~ 15	22° 7.67′	95° 3.78′	81
3	W3	Kan Gon Village	well water	~ 14	22° 7.66′	95° 3.78′	81
4	W4	Kan Gon Village	well water	~ 15	22° 7.49′	95° 3.34′	103
5	W5	Kan Gon Village	tube-well water	~ 61	22° 7.50′	95° 3.35′	103
6	W6	Done Daw Village	well water	~ 14	22° 7.69′	95° 3.42′	75
7	W7	Ywa Tha Village	well water	~ 16	22° 8.83′	95° 2.55′	68
8	W8	Ywa Tha Village	well water	~ 14	22° 8.79′	95° 2.33′	82
9	W9	Ywa Tha Village	stream water	-	22° 8.78′	95° 2.32′	82
10	W10	Ywa Tha Village	waste water	-	22° 8.77′	95° 2.31′	82
11	W11	Done Daw Village	well water	~ 12	22° 7.96′	95° 3.24′	73

Experimental Details

In our research work, the LR-115 (cellulose nitrate) films, solid state nuclear track detector, are used. 100 mL of water sample was placed in a cylindrical plastic can of diameter 7 cm and height 5.5 cm. 1cm×1cm LR-115 film was fixed on the top of inner surface of the Can, in such a way, that its sensitive surface is facing the water sample. The Can is sealed air tight with adhesive tape and kept for exposure of about 100 days. The geometrical parameters of plastic can as illustrate in Fig. (2). During exposure period, the sensitive side of the detector faced the sample is exposed freely to the emergent radon form the sample in the Can, so that it can record alpha particle resulting from the decay of radon in the remaining volume of the Can. At the end of exposure time, these detectors were removed from the Cans and etched in 2.5N NaOH 100 mL at 60°C for 60 minutes.

To be 2.5N NaOH 100mL, 10g of NaOH was put into measuring cylinder and poured the distilled water 100 mL. Then the distilled water was stirred with glass rod to dissolve all NaOH. During etching, the temperature was kept constant with accuracy of ±1°C and without stirring. After etching these detectors, the solution in the beaker was poured into another beaker through small plastic sieve with handle. Then, the detectors were washed with water until the surfaces of the detectors become cleaned. Finally, the detectors were taken out and dried on the filter paper and tracks produced by alpha particles were observed under binocular microscope.

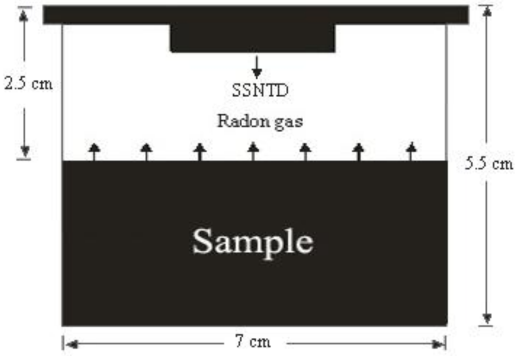

Figure 2 Experimental set-up for the measurement of radon concentration

Track Counting and Track Density Calculation

Track counting was performed by using binocular microscope (100X magnification). Only tracks that have completely perforated the sensitive layer had been counted. The number of tracks viewed on the camera was counted for different fifty views by changing the vertical and horizontal position of detector under the microscope.

The track density of each sample was calculated by using track density equation:

$$\begin{array}{c}\text{Track Density}\\ (\text{Track cm}^{-2}\ \text{day}^{-1})\end{array} = \frac{\text{Number of Net Track}}{\text{Microscopic View Area}} \times \frac{\text{Magnification}}{\text{Exposure Time}} \qquad (1)$$

Radon concentration was also calculated by following equation:

In the present work, because of some difficulties encountered in here, the calibration factor could not be found out ourselves. Thus, the calibration factor obtained from the others' work was used. The calibration factor used for radon concentration was,

0.05016 track $\text{cm}^{-2}\text{day}^{-1}$ = 1 Bqm^{-3} for LR-115 Type II (Muramatsu, 2002)

$$\text{Radon Concentration (Bqm}^{-3}\text{)} = \frac{\text{Track Density (track cm}^{-2}\text{day}^{-1}\text{)}}{0.05016\text{ track cm}^{-2}\text{day}^{-1}\text{/ Bqm}^{-3}} \qquad (2)$$

To convert becquerel per cubic meter to picocuries per liter; 37Bqm^{-3} = 1 pCil^{-1} was used. Then the annual effective dose was also calculated by following equation:

$$1\text{ pCil}^{-1} = 1.62\text{ mSv yr}^{-1}$$

$$\underset{\text{(mSv yr}^{-1}\text{)}}{\text{Annual Effective Dose}} = \underset{\text{(pCil}^{-1}\text{)}}{\text{Radon Concentration}} \times \underset{\text{(mSv yr}^{-1}\text{/pCil}^{-1}\text{)}}{1.62} \qquad (3)$$

In this research, the background of detector has been measured and its value was 0.12±0.03 track cm^{-2} day^{-1}.

Results

In this research, a total of eleven water samples from three villages in Salingyi Township were analyzed. The results of the alpha track densities, radon concentrations and annual effective doses in water are summarized in Table (2). The comparison graph of alpha track densities, radon concentrations and annual effective doses for these samples are presented from Fig. (3) to Fig. (5). Table (2) Alpha track density, radon concentration and annual effective dose for water samples

Sr No	**Water Samples**	**Alpha track density (track cm^{-2} day^{-1})**	**Radon Concentration (pCi l^{-1})**	**Annual effective dose (mSv yr^{-1})**
1	W1	0.73 ± 0.05	0.39 ± 0.03	0.64 ± 0.04
2	W2	0.86 ± 0.04	0.46 ± 0.02	0.75 ± 0.04
3	W3	0.81 ± 0.05	0.43 ± 0.02	0.69 ± 0.04
4	W4	0.94 ± 0.06	0.50 ± 0.03	0.82 ± 0.05
5	W5	1.13 ± 0.07	0.61 ± 0.04	0.99 ± 0.06
6	W6	0.77 ± 0.05	0.41 ± 0.03	0.67 ± 0.04
7	W7	0.96 ± 0.06	0.52 ± 0.03	0.84 ± 0.05
8	W8	0.78 ± 0.05	0.42 ± 0.03	0.68 ± 0.04
9	W9	0.67 ± 0.04	0.36 ± 0.02	0.59 ± 0.03
10	W10	0.75 ± 0.05	0.40 ± 0.03	0.66 ± 0.04
11	W11	0.67 ± 0.04	0.36 ± 0.02	0.59 ± 0.03

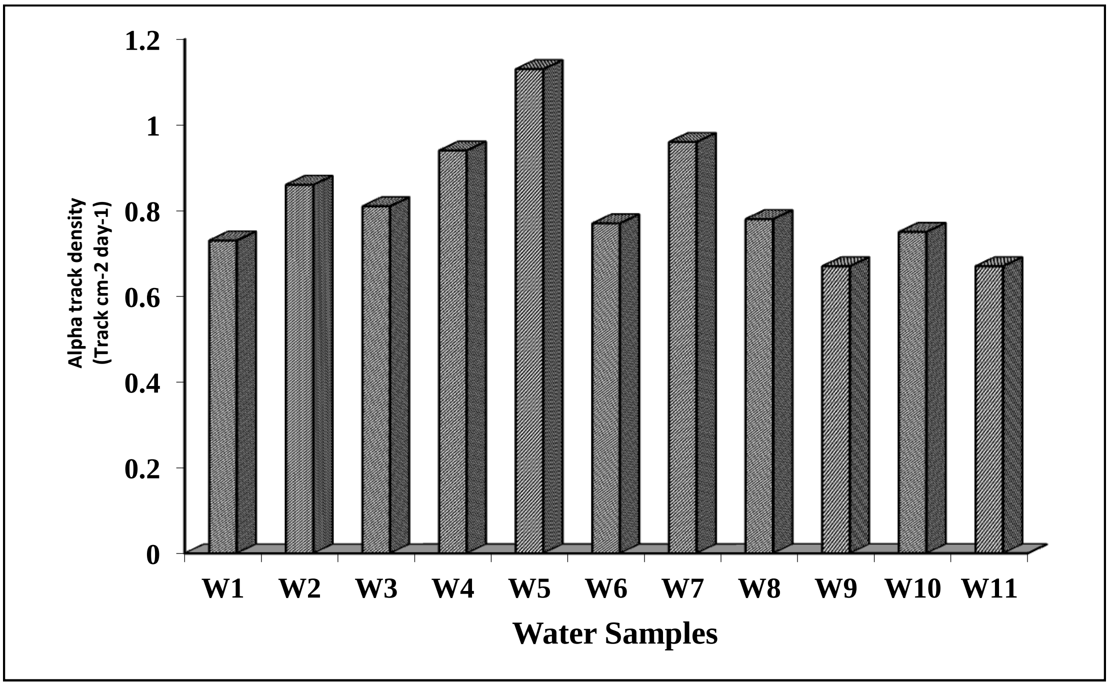

Figure 3 Comparison graph of the alpha track density for water samples

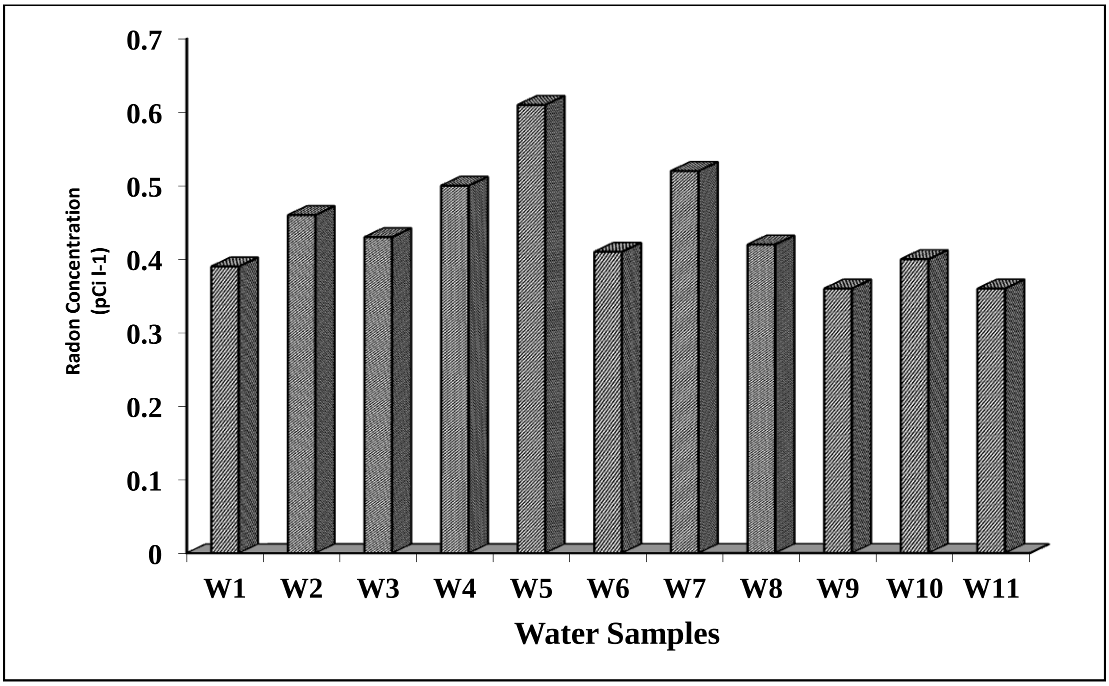

Figure 4 Comparison graph of the radon concentration for water samples

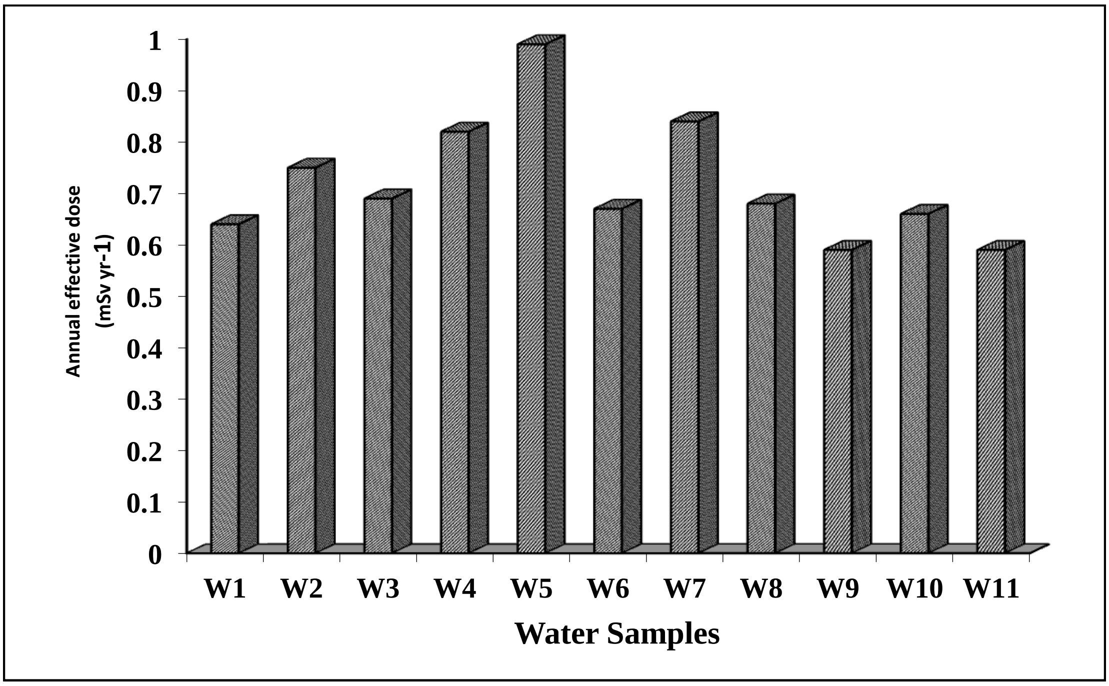

Figure 5 Comparison graph of the annual effective dose for water samples

Discussion

The concentration of radon in water samples varies from a minimum value of 0.36±0.02 pCil-1 to a maximum value of 0.61±0.04 pCil-1. The minimum value of annual effective dose is 0.59±0.03 mSvyr-1 and the maximum value is 0.99±0.06 mSvyr-1.

Radon concentration of sample W5 is the highest among eleven samples. This sample is collected from 61m depth tube-well in Kan Gon village. There is a lot of waste soil from Mine, copper purifying and near the acid factory at the Mine area.

The radon concentration of sample W7 and W4 are lower than the sample W5 and higher than the other samples. Sample W4 and W5 are the same in village but their depth of well are different. So, the values of radon concentrations are also different.

Sample W9 and W11 are the lowest radon concentrations in all samples. Sample W9 is collected from Yama stream near Ywa Tha village and sample W11 is collected from 12m depth well in Done Daw village. Sample W11 is the drinking water for Done Daw village and the other villages which are near the Done Daw .

Sample W1 and W10 are slightly different in their radon concentrations. Sample W1 is collected from 12m depth well in Done Daw village and W10 is collected from waste water of Mine area which flows into the Yama stream.

Sample W3, W6 and W8 are collected from the same depth of 14m well and different in villages, which are Kan Gon village, Done Daw village and Ywa Tha village respectively. Among in three water samples, sample W3 has the highest radon concentration. This is due to that the Kan Gon village have waste soil and copper purifying.

The present results show that the radon concentration in water is below the allowed limit from International Commission on Radiological Protection (ICRP) agency which is 27 $pCil^{-1}$ (2009). In addition to the radon concentrations, the annual effective dose in water is also below the permissible limit from ICRP agency which is 3 - 10 $mSvyr^{-1}$ (2009).

Conclusion

The result of this research was found that the radon concentration and the annual effective dose measured by sample W5 (collected from 61m depth tube well) is the largest and that of the sample W9 (collected from Yama stream) and W11 (collected from 12m depth well) are the smallest among the other samples. This is due to the samples are taken from different places; the materials contain radioactive elements in different proportions depending upon local geology and depth of the water source. And then, the radon is not concerned in water that comes from lakes, rivers and reservoirs (called surface water) because the radon will be released into the air before reaching water supplier or home. The result for all water samples are well within the prescribed safe limit. It can be concluded that the samples of water in this research are safe for radiation hazards to the villagers and visitors by using these water.

Acknowledgements

I would like to express my sincere thanks to Dr Khin Khin Win, Professor and Head, Department of Physics, University of Yangon for her kind encouragement and permission to carry out this research,

I would like to thank Dr Myo Lwin, Professor, Dr Ye Chan, Professor and Head, Universities' Research Center, Dr Aye Aye Thant, Professor, Department of Physics, Dr Yin Maung Maung, Professor, Department of Physics and Dr Than Zaw Oo, Professor, Universities' Research Center, University of Yangon, for their suggestion and comments for this research.

References

Muratmatsu .H, tashiro.Y et al (2002) "Seasonal variations of ^{222}Rn concentrations in the air of a tunnel located in Nagano city" Journal of Environmental Radioactivity 60 p 263-274 (Japan)

http://www.cancer.org/cancer/cancercauses/othercarcinogens/pollution/radon?

http://www.seered.co.uk/radon07.htm

http://www.icrp.org/ICRP Publication (2009)

J. Myanmar Acad. Arts Sci. 2020 **Vol. XVIII.No.2C**

CHARACTERIZATION OF ACTIVATED CARBONS FROM COCONUT AND PEANUT SHELLS BIOMASS

Zin Min Tun[1], Zin Min Myat[2], Than Than Win[3] and Yin Maung Maung[2]

Abstract

Biomass is organic material that comes from plants and animals, and it is a renewable source of energy. The coconut and peanut shells biochar were produced by heat decomposition of these biomasses. These biomasses were heated in a muffle furnace at 300 °C, 400 °C and 500 °C for 2 h respectively. The aim of this study was to use coconut and peanut shells in the preparation of activated carbon. The elemental compositions of these samples were analyzed by X-ray fluorescence (XRF). The surface morphology of these biomasses was determined by Scanning Electron Microscopy (SEM). Phase formation and structural properties of samples were characterized by X-ray Diffraction (XRD). Fourier Transform Infrared Spectroscopy (FTIR) was used to determine the chemical properties of the coconut and peanut shells biomass. In this research, the physicochemical characteristics of coconut and peanut shells biomass with activated carbons (ACs) were reported and discussed rapid deployment of renewable energy and energy efficiency and technological diversification of energy sources would result in significant energy security and economic benefits.

Keywords - EDXRF, FTIR, XRD, SEM, coconut and peanut shells

Introduction

Biochar is produced by thermal decomposition of biomass under oxygen-limited condition (pyrolysis), and it has received attention in soil remediation and waste disposal in recent years. Bio-char is a stable solid, rich in carbon and can endure in soil for thousands of years [Aysu et al 2013, Aigbodion V S et al 2010]. The characteristics of biochar are influenced mainly by the preparation temperature of biomass. Higher pyrolysis temperature often results in the increased surface area and carbonized fraction of bio-char leading to high absorption capability for pollutants [Anthony B V et al 2000, CANIARES, P. et al 2006]. Bio-chars derived from various source materials show different properties of surface, porosity and the amount of functional groups which are important concerning on the effect of bio-char. Bio-char has been proved to be effective in improving soil properties and increasing crop biomass. It has also been suggested that it can even enhance crop resistance to disease [Dural. M.U et al 2011, El-barbary MH, et al 2009]. Bio-char has recently been used to remediate soil with both heavy metal and organic pollutant. In addition to its potential for carbon sequestration and decrease greenhouse gas emission from agriculture, biochar is reported to have numerous benefits as a soil amendment, increased plant growth yield, improved water quality, reduced leaching of nutrients, reduced soil acidity, increased water retention and reduced irrigation and fertilizer requirements [Garg.V.K et al 2003, Karaosmanoglu et al 2005]. Bio-char carbon species vary in complexity from graphite like carbon to high molecular weight aromatic rings, which are known to persist in soil for thousands to millions of years. Biochar is a name for charcoal when it is used for particular purpose, especially as a soil amendment like all charcoal, biochar was created by pyrolysis of biomass [Lehmann. J and Joseph. S, 2009].

---

[1] Dr, Assistant Lecturer, Department of Physics, West Yangon University

[2] Assistant Lecturer, Department of Physics, University of Yangon

[3] Professor, Department of Physics, Panlong University

Materials and Method

The raw coconut and peanut shells were cleaned with distilled water to remove the dust and impurities. These shells were dried in sun for one day and then hand crushed to smaller pieces. Then, the smaller pieces of these shells were dried at room temperature about one week. The weight of coconut and peanut shells were measured with electronic digital balance. After that carbonization process using the furnace at three different temperatures, which were 300°C, 400°C and 500°C for 2 h respectively. After carbonization, coconut and peanut shell biochars were obtained. The weight of coconut and peanut shell biochars were also measured by balance. Finally, the prepared biochars were ground into powder by pestle. Biochar powders were obtained. The obtained coconut and peanut shell biochar powders were characterized by structural analysis of XRD (X-ray Diffraction) and elemental analysis of EDXRF (Energy Dispersive X-ray Fluorescence) method. The morphology and microporous structures of biochars were determined by Scanning Electron Microscopy (SEM) and the chemical properties of biochars were examined by Fourier Transform Infrared Spectroscopy (FTIR). The block diagram for experimental procedure of coconut and peanut shell biochars were shown in figure 2.2. Table 1 and 2 showed the weight loss and shrinkage of coconut and peanut shell biochars.

Table 1 Weight loss and shrinkage of coconut shell biochar

Temperature	Initial weight, W_1	Final weight, W_2	Weight loss, $W = W_1 - W_2$	Shrinkage
300 °C	5 g	2.10 g	2.90 g	58.00 %
400 °C	5 g	1.57 g	3.43 g	68.60%
500 °C	5 g	1.11 g	3.89 g	77.80 %

Table 2 Weight loss and shrinkage of peanut shell biochar

Temperature	Initial weight, W_1	Final weight, W_2	Weight loss, $W = W_1 - W_2$	Shrinkage
300 °C	5 g	2.67 g	2.33 g	46.60 %
400 °C	5 g	1.88 g	3.12 g	62.40 %
500 °C	5 g	1.35 g	3.65 g	73.00 %

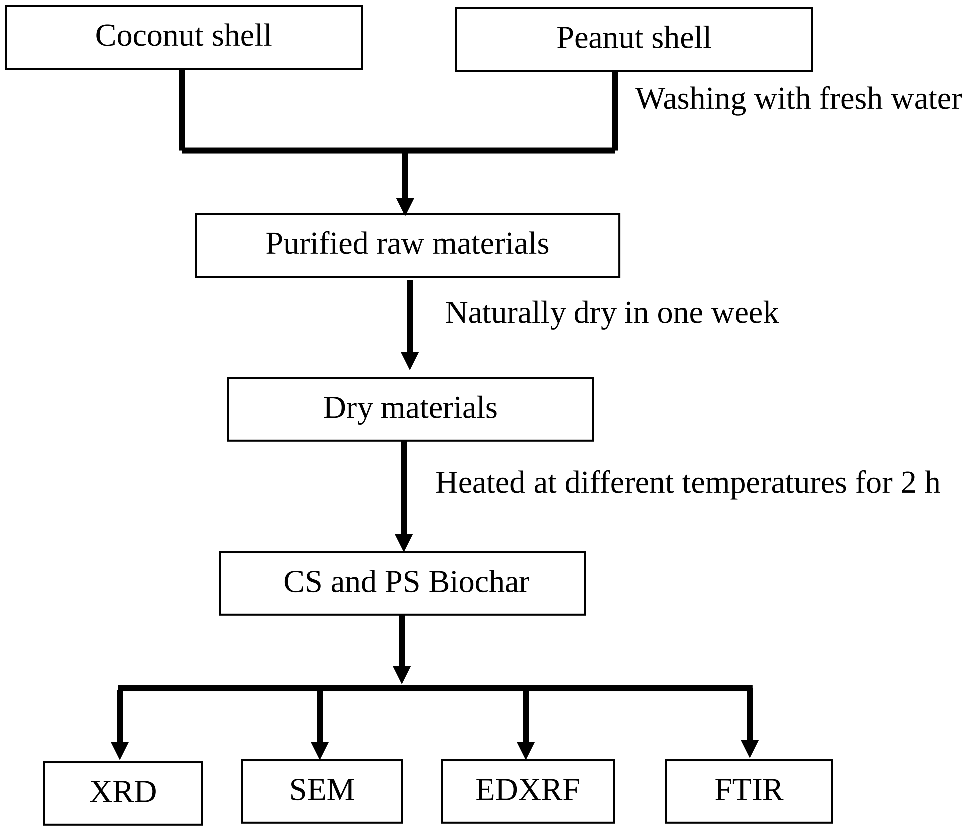

Figure 1 The block diagram for experimental procedure of coconut and peanut shell biochars

Results and discussion

X-ray diffraction analysis

X-ray diffraction is to determine the structure properties of coconut and peanut biochar using monochromatic CuKα radiation ($\lambda = 1.54056$ Å) operated at 40 kV (tube voltage) and 40 mA (tube current). Analysis of coconut and peanut shell biochar at different temperature values (300 ˚C, 400 ˚C and 500 ˚C) for 2 h were shown in figure 2.

From XRD results, these biochar exhibit the dominant diffraction peak located at around $2\theta = 20^\circ - 30^\circ$ that revealed the presence of amorphous structure which was disorderly stacked up by carbon rings. The XRD patterns of the coconut and peanut shell biochar showed the asymmetric (111) peak and (110) peaks maxima which were characteristic of graphite and carbon structures.

FTIR Analysis of Coconut and Peanut shell biochars

FTIR spectroscopy was applied to measure the chemical properties and absorption of energy from the range of 4000 cm^{-1} - 500 cm^{-1} by studied samples. Spectral registration was examined with use of solid-state samples which is made of a complex organic material. The FTIR analysis demonstrated the functional groups presented on two biochar types (coconut shell (CS) and peanut shell (PS)). The functional groups of two samples CS and PS have found to be O-H stretching vibration, C-H stretching vibration, C=O stretching vibration and C=C stretching vibration respectively. The spectrum of these samples showed some characteristic bands related to physical and chemical changes. As shown in figure 3(a-c) and figure 4 (a-c), the infra-red spectra of these biochar types are comparable but there are some changes in the functional groups. The water O-H stretch can occur in the CS about 3373.25 cm^{-1}, 3372.85 cm^{-1} and 3372.40 cm^{-1} at three different temperatures. The strong hydroxyl group can display in the PS for about 3334.54 cm^{-1}, 3338.65 cm^{-1} and 3335.82 cm^{-1} at three different temperatures respectively. The absorption bands, between 3000 cm^{-1}-3300 cm^{-1} indicated the presence of strong carboxylic acid O-H stretch. Comparing with other biochar types, CS and PS were associated with strong absorption bands at 3180.95 cm^{-1} and 3214.62 cm^{-1}, respectively. As a observed peak of CS, C ≡ C ring stretching is associated with peak value 2110.89 cm^{-1}. The presence of the band located at 824 cm^{-1}- 600 cm^{-1} showed a C-OH out-of-plane bending modes of aromatic compounds. According to FTIR analysis, all of the absorption bands are due to hydroxyl group in cellulose, carbonyl groups of acetyl ester in hemicellulose, and carbonyl aldehyde in lignin.

SEM Analysis of Sugarcane bagasse biochar

SEM is one of the most versatile instruments available for the examination and analysis of the microstructure characteristics of a solid. The most important reason for using SEM is high resolution that can be obtained when bulk sample are examined. SEM micrographs for external morphology of CS and PS biochar at temperatures 300 °C, 400 °C and 500 °C for 2 h were shown in figure 5 (a-c) and figure 6(a-c). According to figure 5 (a-c), the clear porous nature had observed the CS biochar at 300 °C, 400 °C and 500 °C. After increasing temperature, it was found that the CS biochar had more clearer porous nature and uniform with microporous structure. From SEM analysis as shown in figure 6 (a-c), it can be observed that the microstructure of PS biochar samples by varying the pore sizes with different temperatures. At 300 °C, the pores of PS biochar were non-uniform and not clear. At 400 °C, the pores looked like tube shape and the more uniformly microporous structure was found at 500 °C of PS biochar.

For CS biochar, the average pore sizes of the samples were found to be about 5.15 µm at 300 °C, 8.80 µm at 400 °C and 5.13 µm at 500 °C and for PS biochar, 3.42 µm at 300 °C, 3.54 µm at 400 °C and 2.52 µm at 500 °C respectively.

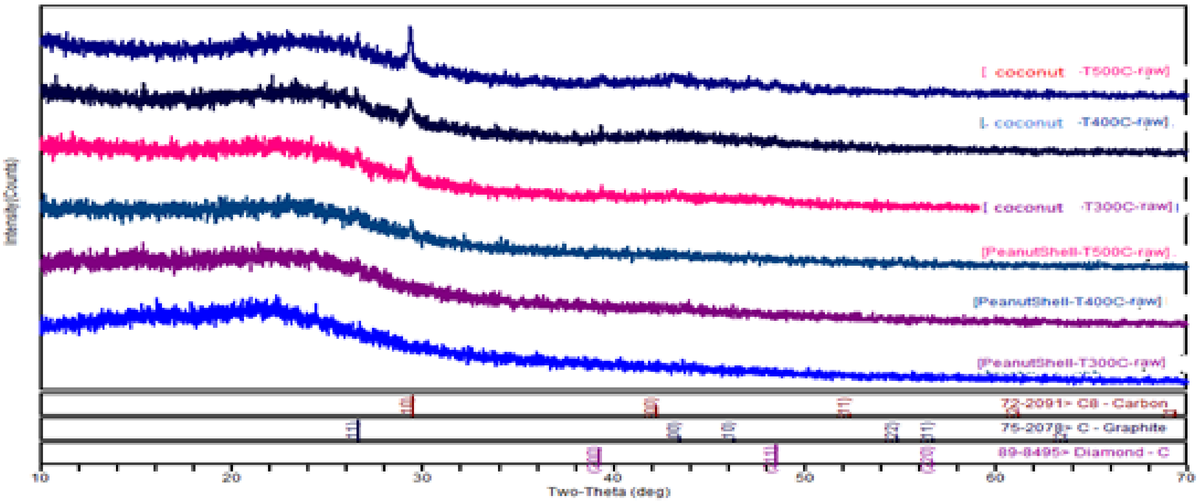

Figure 2 XRD patterns of Coconut and Peanut shell biochars at different temperatures

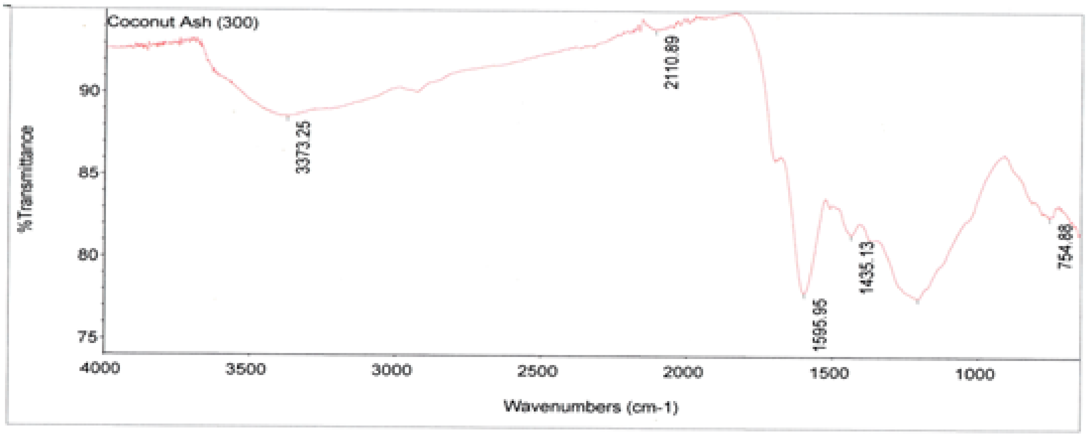

(a) FTIR spectrum for CS-300 ˚C

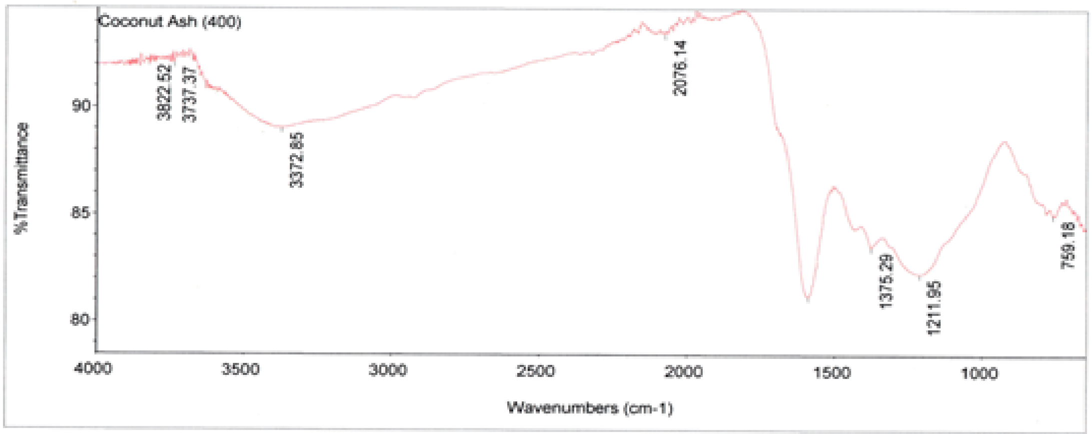

(b) FTIR spectrum for CS-400 ˚C

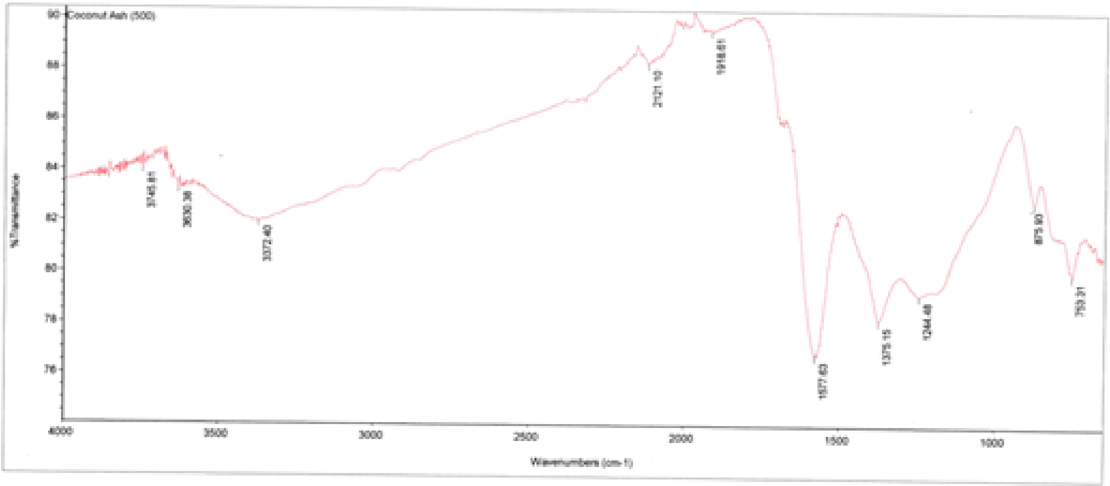

(c) FTIR spectrum for CS-500˚

Figure 3 (a-c) FTIR spectra of CS biochar

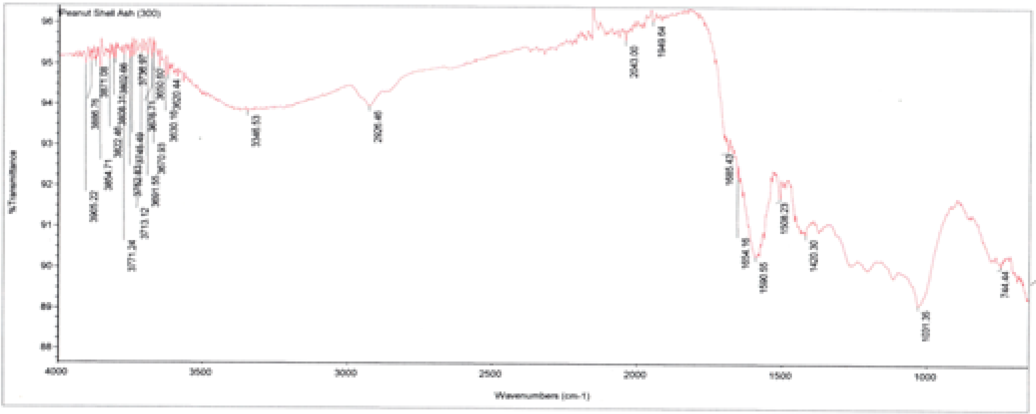

(a) FTIR spectrum for PS-300 ˚C

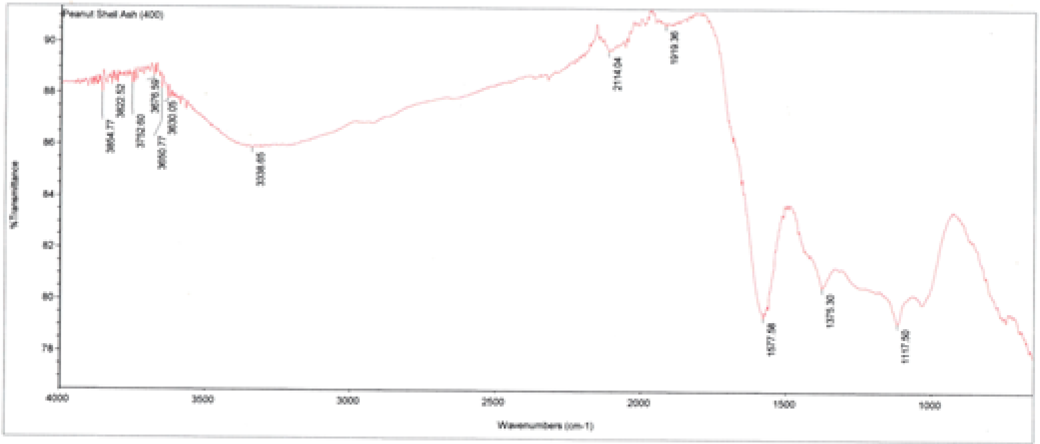

(b) FTIR spectrum for PS-400 ˚C

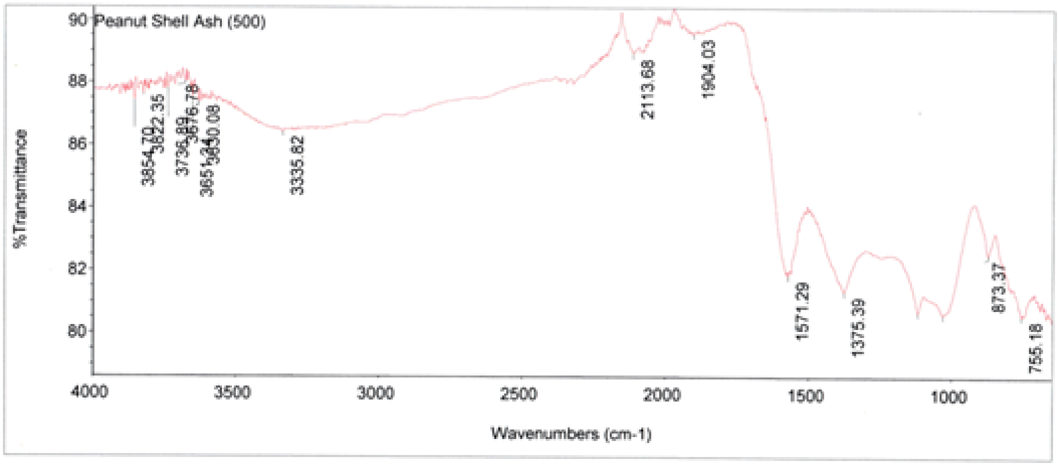

(c) FTIR spectrum for PS-500 ˚C

Figure 4 (a-c) FTIR spectra of PS biochar

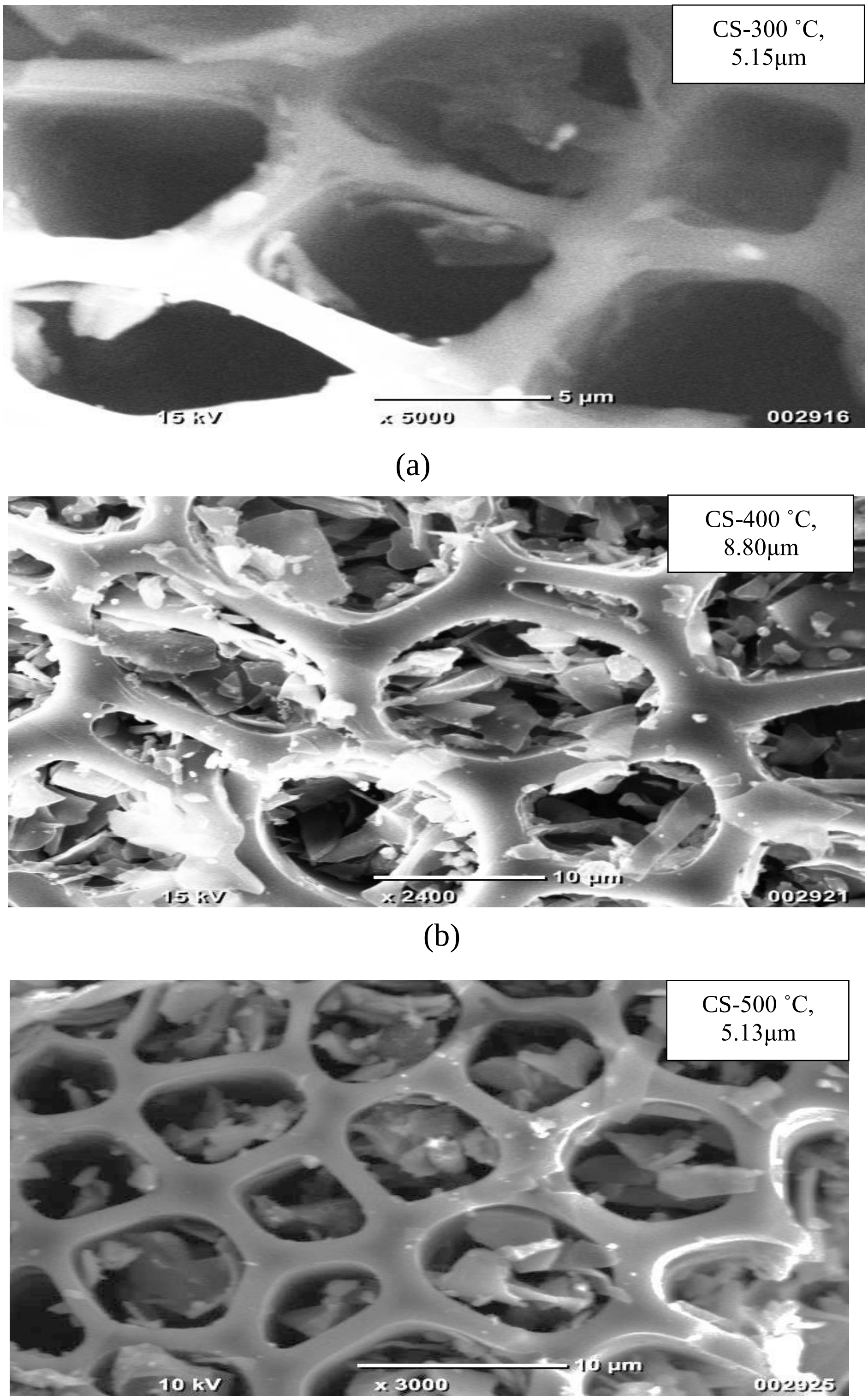

(a)

(b)

(c)

Figure 5 (a-c) SEM micrographs of CS biochar at different temperatures

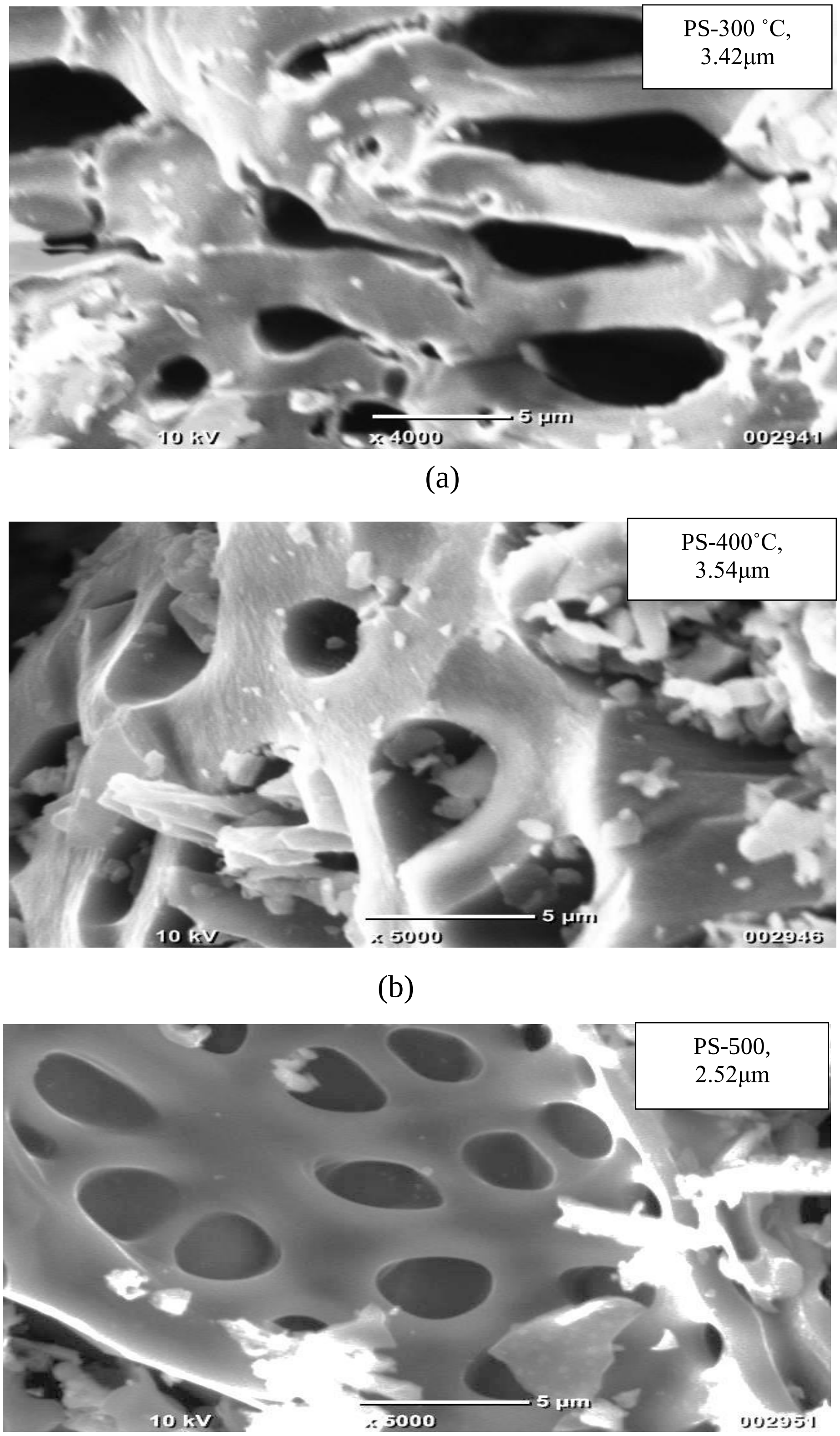

(a)

(b)

(c)

Figure 6 (a-c) SEM micrographs of PS biochar at different temperatures

EDXRF Analysis

In this research, two kinds of CS and PS biochar were analyzed by the EDXRF technique. The concentrations of elements contained in the samples were measured by using the SHIMADZU Energy Dispersive X-ray Fluorescence Spectrometer (EDX-7000). According to the result, it was found that the concentration of elements contained in CS and PS biochar at different temperatures were shown in Table 3 and Table 4.

Table 4.1 The concentration of elements contained in coconut shell biochar at different temperatures

Coconut Shell	Relative concentration of elements (% wt)		
Elements	**300 ˚C**	**400 ˚C**	**500 ˚C**
K	58.444	59.388	64.047
Cl	21.177	19.308	15.672
Ca	12.093	10.552	9.849
Si	6.604	7.728	5.473
P	-	0.937	0.687
S	0.691	0.733	0.767
Fe	0.525	0.785	0.394
Cu	0.153	0.125	0.128
Mn	-	0.082	-
Cr	-	0.067	-
Ti	0.132	0.194	2.655
Zn	0.077	0.031	0.087
Ag	0.042	-	-
Br	0.036	0.027	0.024
Rb	0.027	0.027	0.029
Sr	-	0.015	-

Table 4.2 The concentration of elements contained in peanut shell biochar at different temperatures

Peanut Shell	Relative concentration of elements (% wt)		
Elements	**300 ˚C**	**400 ˚C**	**500 ˚C**
K	51.391	49.318	53.623
Ca	22.433	20.303	20.821
Si	11.041	11.540	9.260
Fe	6.868	9.652	7.719
S	3.730	4.034	2.810
P	2.611	1.573	2.676
Ti	0.884	1.992	1.777
Mn	0.581	0.740	0.580
Cr	-	0.280	-
Cu	0.241	-	0.204
Zn	0.106	0.201	0.140
Ni	0.083	0.095	0.072
Sr	0.032	0.068	0.044

Conclusion

The present investigation shows that the activated carbon obtained from coconut and peanut shell biochar were prepared and characterized by studying physical, chemical and mechanical properties. In the physical properties measurements, the biochar weight loss and shrinkage increased with increasing the reaction temperatures. Coconut and peanut biomass provides the solution to use it and produce the low cost, energy efficient and clean energy in the form of briquetted biomass. According to FTIR analysis, low temperature, 300 °C both biochar types is more suitable for their absorption bands due to hydroxyl group in cellulose, carbonyl groups of acetyl ester in hemicellulose, and carbonyl aldehyde in lignin. According to XRD result, there are several diffracted peaks were observed. They were not perfectly identified. It could be say that the CS and PS samples were found to be amorphous structure with little crystalline. XRD patterns of CS and PS were quite acceptable. Almost all the reflections were found to be consistent with carbon. SEM investigation showed that the porous structure of both samples. Besides, in this study, the quantitative data calculated by the EDX-7000 spectrometer were based on the 100 percent of weightiness of just inorganic elements contained in the sample of interest and not considered on the organic compounds and dark matrix elements. It means that the data show the relative concentration of elements contained in the samples of analysis. From the EDXRF results obtained, the major element of each biochar samples were potassium (K), calcium (Ca), chlorine (Cl), silicon (Si), iron (Fe) and phosphorous (P). These elements (K, Ca, Cl, Si, Fe and P) concentrations in each sample were much more than other elements. So it was mostly effective for plants growth.

Acknowledgements

I would like to express my sincere gratitude to Professor Dr Khin Khin Win, Head of Department of Physics, University of Yangon, for her kind permission.

I would also like to mention my gratitude to Professor Dr Yin Maung Maung, University of Yangon for his encouragement on this research. This research was fully supported by the Department of Physics, University of Yangon, Myanmar (2018-2019).

References

Aysu et al 16th Dec 2013. Biomass pyrolysis in a fixed-bed reactor: Effects of Pyrolysis parameters on product yields and characterization of products. *Energy.* **64** (1): 1002-1025

Aigbodion V S et al 2010. Potential Utilization of Solid Waste (Bagasse Ash). *Journal of Minerals & Materials Characterization & Engineering*, 9 (1) 67-77

Anthony BV, Peacocke GVC, 2000 Mar. Fast pyrolysis processes for biomass. Renewable and Sustainable Energy Reviews; 4(1):1-73.

CANIARES, P. et al, feb./apr.2006. Adsorption equilibrium of phenol onto chemically modified activated carbon F400. Journal of Hazardous Materials, Amsterdam,v.131, n.1, p.243-248.

Dural. M.U, Cavas. L, Papageorgious, S.K, 2011, Methylene blue adsorption on activated carbon prepared from Posidonia oceanica (L) dead leaves: Kinetics and equilibrium studies, Chem. Eng. J. 168 77-85

El-barbary MH, Philip HS. 2009 May, Characterization of fast pyrolysis bio-oils produced from pretreated pine wood. Journal of Applied Biochemistry and Biotechnology.; 153(1-3):3-13.

Garg.V.K, Gupta.R, Yadav.A.B, Kumar.R, 2003, Dye removal from aqueous solution by adsorption on treated sawdust, Bioresour. Technol. 89 121-124.

Karaosmanoglu, Angin D, Sensoz S. 2005, Characterization of the bio-oil of rapeseed cake. Energy Sources; 27(13):12217-23.

Lehmann. J and Joseph. S, 2009, " Biochar for Enviromental management," Science and Technology, Earthscan: London, UK

J. Myanmar Acad. Arts Sci. 2020 **Vol. XVIII.No.2C**

EFFECT OF MOLAR RATIO IN FORMATION OF BIPHASIC HYDROXYAPATITE/α-TRICALCIUM PHOSPHATE BIOCERAMICS

Khin Khin Hlaing[1] and Aye Aye Thant[2]

Abstract

Biphasic Hydroxyapatite/α-Tricalcium Phosphate (HAP/α-TCP) with three Ca : P molar ratios of 1.60 : 1, 1.57 : 1 and 1.54 : 1 were prepared by precipitation method. The filtrated white paste samples were analysed by Thermogravimetric and Differential Thermal Analysis (TG / DTA)) to determine the weight loss %, and to enable the qualification of endothermic energy changes. After heat-treatment at 1200˚C for biphasic HAP /α-TCP, the powder samples were characterized by X-ray Diffraction (XRD) and the lattice parameters, volume of the unit cell, the crystallite sizes, and weight percent ratios were evaluated. The morphology of biphasic HAP/α-TCP powder was studied by using the Scanning Electron Microscopy (SEM).

Keywords: Hydroxyapatite, α-tricalcium phosphate, Ca: P molar ratios, precipitation.

Introduction

Hydroxyapatite (HAP), $Ca_{10}(PO_4)_6(OH)_2$, and other calcium phosphates such as α-TCP, $Ca_3(PO_4)_2$, have been utilised extensively as implant materials because of their compositional similarity to that of the mineral phase of hard tissue in human bones [Juliana, M.,2009]. The main difference between HAP and α-TCP is the resorption rate when they are implanted in the body. HAP resorbs very slowly and most stable, while α-TCP dissolves 10 times faster in the body than HAP [Klein, C.P., 1983]. To control their resorption rates, currently there is an increasing interest on the preparation of mixtures of two or more calcium phosphates. When they combine each other, the formed biphasic HAP/ α-TCP ceramic controls the resorbability of TCP and maintains the osteoconductive property of HAP [Klein, C.P., 1983]. Moreover, biphasic calcium phosphates have more reliable bioactivity on physical and chemical properties [Caroline, V., 2002].

Materials & Methods

Diammonium hydrogen phosphate, $(NH_4)_2HPO_4$ and calcium nitrate tetra hydrate, $Ca(NO_3)_2.4H_2O$ were dissolved individually in distilled water and stirred for 10 minutes at 37°C to obtain two clear solutions. Then, calcium nitrate solution was slowly added to phosphate solution and concentrated ammonium hydroxide solution was also added and stirred for 2 hours at 37°C. The reaction temperature was controlled by water bath. The milky solution was filtered and the precipitate was washed with distilled water and aged for 24 hours to get the white paste sample. Then the paste was dried at 60˚C for 24 hours and the dried solids were made into powder and calcined for 12 hours (soaking time) at 850˚C to get biphasic HAP/ β-TCP. Then, this biphasic HAP/ β-TCP sample was heated again at 1200 ˚C with the soaking time of 3.5 hours and the biphasic HAP/α-TCP was obtained.

Characterization

By using the DTG-60H, the thermal analysis for white paste samples was carried out. The powder x-ray diffraction (XRD) was performed for biphasic HAP/α-TCP powder by Cu-Kα

---

[1] PhD candidate, Demonstrator, Department of Physics, University of Medicine I

[2] Dr, Professor, Department of Physics, University of Yangon

radiation. The morphology and grain size of biphasic HAP/α-TCP powder samples were observed by employing the Scanning Electron Microscopy (SEM).

Results and Discussion

Thermal analysis of the white paste samples was carried out by using Simultaneous TG/DTA Analyser (Shimadzu DTG-60/60H). The enthalpy change (ΔH) was calculated by the following equation,

$$\Delta H = (k/m) \int_{t1}^{t2} \Delta T dt \qquad (1)$$

Where, ΔH is the enthalpy change, $\int_{t1}^{t2} \Delta T dt$ is the area enclosed by a curve, m is mass and k is thermal conductivity.

The area enclosed of endothermic curve was calculated by the trapezoid rule with the equation;

$$\text{Area of Trapezium} = [(b_1 + b_2)\, h] / 2 \qquad (2)$$

Where, b_1, b_2 are the bases of the trapezium and h is the height of the trapezium

Figure 1, 2 and 3 are the graphs of TG/DTA analysis of three white paste samples. In these graphs, each DTA curve contains one broad peak with endothermic nature and it indicates that the absorption of heat of the reacting substances during the phase change process.

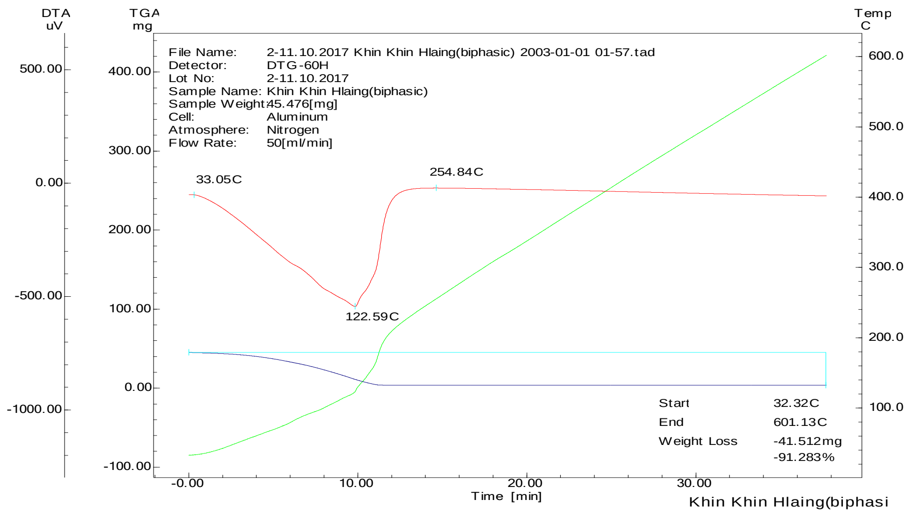

Figure 1 TG/DTA analysis of white paste sample S1

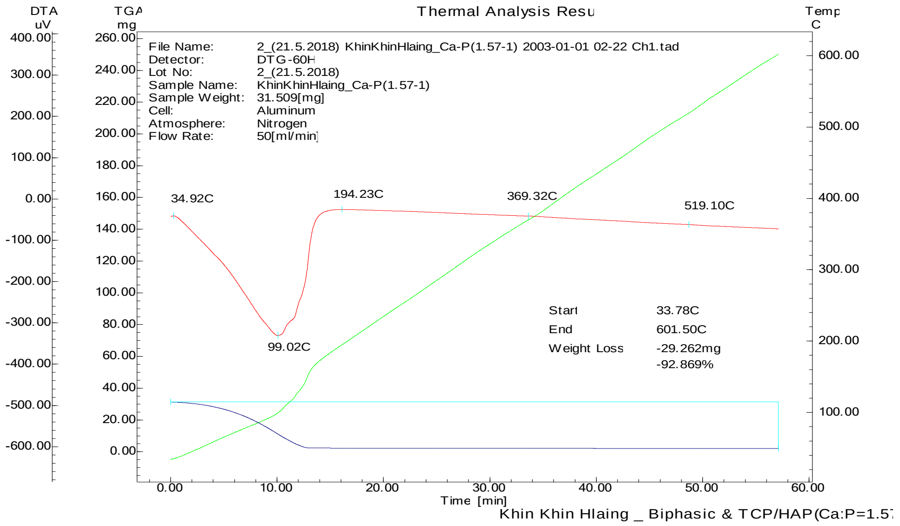

Figure 2 TG/DTA analysis of white paste sample S2

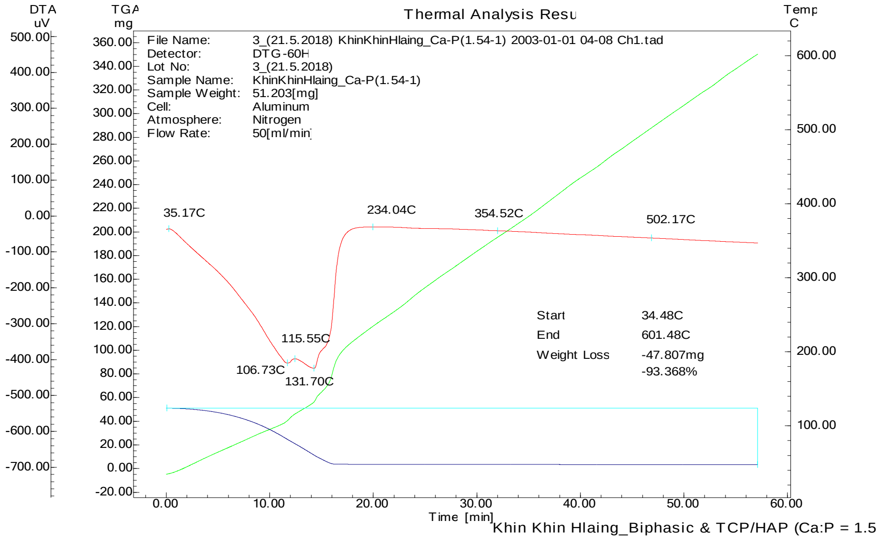

Figure 3 TG/DTA analysis of white paste sample S3

Table 1 shows the comparison of the decomposition temperatures of the reacting substances, $(NH_4)_2HPO_4$ and $Ca(NO_3)_2.4H_2O$ obtained from DTA analysis and their literature values. It is worth to note that the peak decomposition temperatures from the DTA analysis agree well with the literature values of the reactants.

Table 2 shows the values of the thermal parameters of each endothermic reaction from DTA analysis for three white paste samples. During the phase change process, the temperature range increase from sample S1 to S3 when their Ca: P molar ratios decrease.

Table (3) shows the area enclosed of endothermic peak and enthalpy values in DTA analysis of three white paste samples. The sample S2 exhibits the smallest area enclosed and enthalpy while the sample S3 possesses the greatest values and the sample S1 remain between them.

Table 4 shows the values of the weight loss % of three white paste samples calculated from TG analysis. It can be observed that the weight loss % of the samples increase when the Ca : P molar ratios decrease.

Table 1 Comparison of the decomposition temperatures of $(NH_4)_2HPO_4$ and $Ca(NO_3)_2.4H_2O$ from DTA analysis and their literature values

Sample	Ca: P	Reacting Substance	Decomposition Temperature (°C)	
			DTA Result	Literature Value
S1	1.60 : 1	$(NH_4)_2HPO_4$	158	155
		Ca $(NO_3)_2.4H_2O$	130	132
S2	1.57 : 1	$(NH_4)_2HPO_4$	150	155
		Ca $(NO_3)_2.4H_2O$	135	132
S3	1.54 : 1	$(NH_4)_2HPO_4$	150	155
		Ca $(NO_3)_2.4H_2O$	120	132

Table 2 Thermal parameters of endothermic reactions from DTA analysis of three white paste samples S1, S2 and S3

Sample	Ca : P Molar Ratio	Starting Temperature (°C)	Ending Temperature (°C)	Temperature Range (°C)
S1	1.60: 1	40	230	190
S2	1.57: 1	35	232	197
S3	1.54: 1	38	240	202

Table 3 Area of Endothermic Peak and Value of Enthalpy change calculated from DTA analysis of three white paste samples

Sample	Process	A (µV min)	A (V sec)	I (A)	W (J)	ΔH (cal)
S1	Endothermic	3901.33	0.2341	13.64	3.194	0.76
S2	Endothermic	2757.33	0.1654	13.64	2.256	0.54
S3	Endothermic	4406.80	0.2644	13.64	3.606	0.86

Table 4 Loss of weight % of three white paste samples from TG analysis

Sample	Ca : P	Initial weight (mg)	Final weight (mg)	Weight loss (%)
S1	1.60:1	45.476	4.0	91.283
S2	1.57:1	31.509	2.5	92.870
S3	1.54:1	51.203	3.0	94.140

XRD Analysis

Phase composition of biphasic HAP/α-TCP powder samples were examined by X-ray diffraction (XRD) by the Cu-Kα radiation. The mean crystallite size (L) was calculated from Scherrer equation,

$$L = \kappa \lambda / \beta \cos \theta \qquad (3)$$

Where, L is crystallite size, k is Scherrer's constant, λ is X-ray wavelength, β is line broadening at half the maximum intensity and θ = Diffraction angle.

Reference Intensity Ratio (RIR) value and weight % of the HAP and α-TCP were determined by using the following formulae.

$$RIR_{\alpha\text{-}TCP} = I_{\alpha\text{-}TCP} / (I_{\alpha\text{-}TCP} + I_{HAP}), \qquad (4)$$

$$RIR_{HAP} = I_{HAP} / (I_{\alpha\text{-}TCP} + I_{HAP}) \qquad (5)$$

$$\text{Weight \%} = (RIR \times 100)\ \% \qquad (6)$$

Where, $I_{\alpha\text{-}TCP}$ and I_{HAP} are maximum intensities of phase α-TCP and HAP.

Volume of unit cell of Hexagonal and Orthorhombic crystal systems were calculated by

$$V = a^2c \sin 60° \qquad (7)$$

$$V = a\ b\ c \qquad (8)$$

Where, a, b, c are the lattice parameters of a unit cell

Figures 4, 5 and 6 represent the XRD patterns of three powder samples heated at 1200℃. The patterns of HAP and α-TCP phases are matched with reference files from ICDD (PDF-2 Release 2015 RD). All diffraction peak positions of the samples agree well with the standard XRD patterns of HAP and α –TCP and revealed the formation of biphasic HAP/ α -TCP after heating at 1200℃.

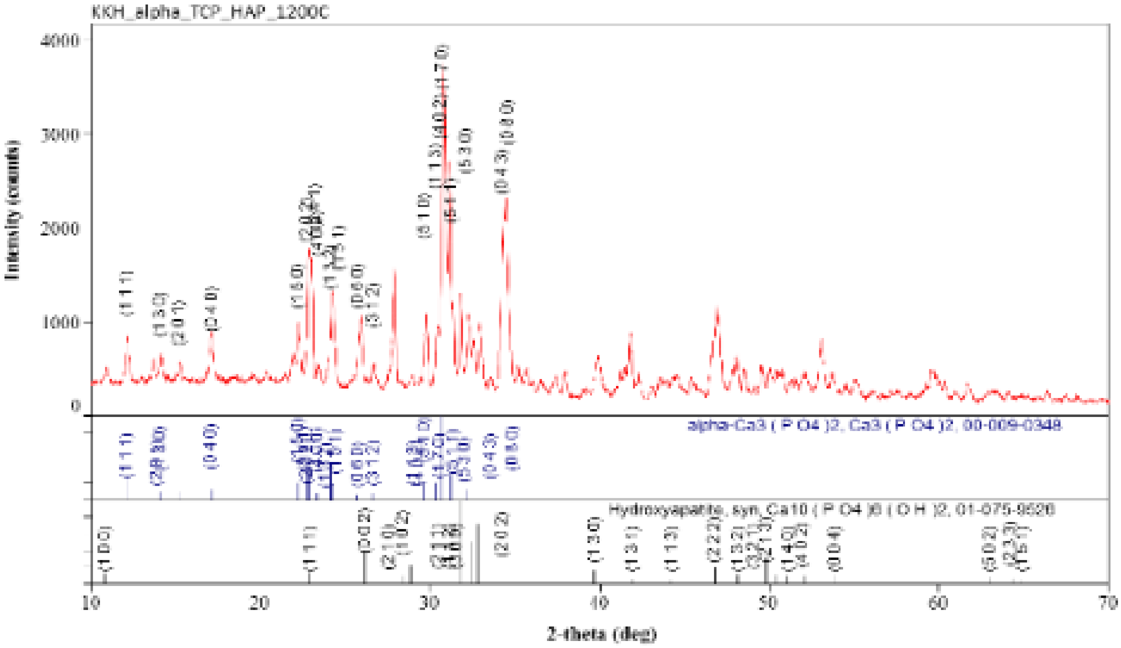

Figure 4 XRD pattern of biphasic HAP/α-TCP (Sample S1)

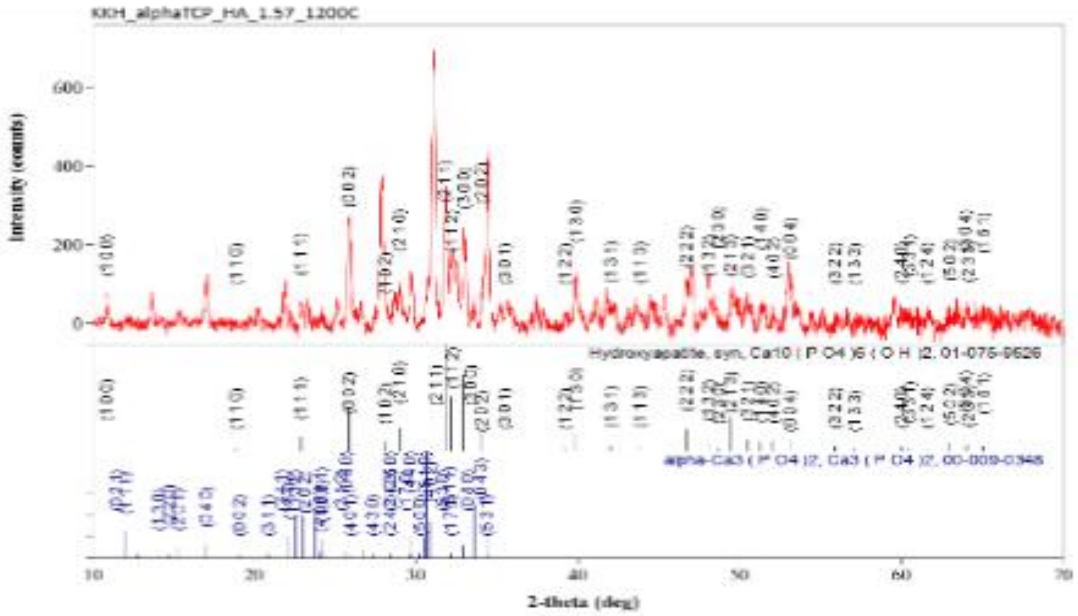

Figure 5 XRD pattern of biphasic HAP/α-TCP (Sample S2)

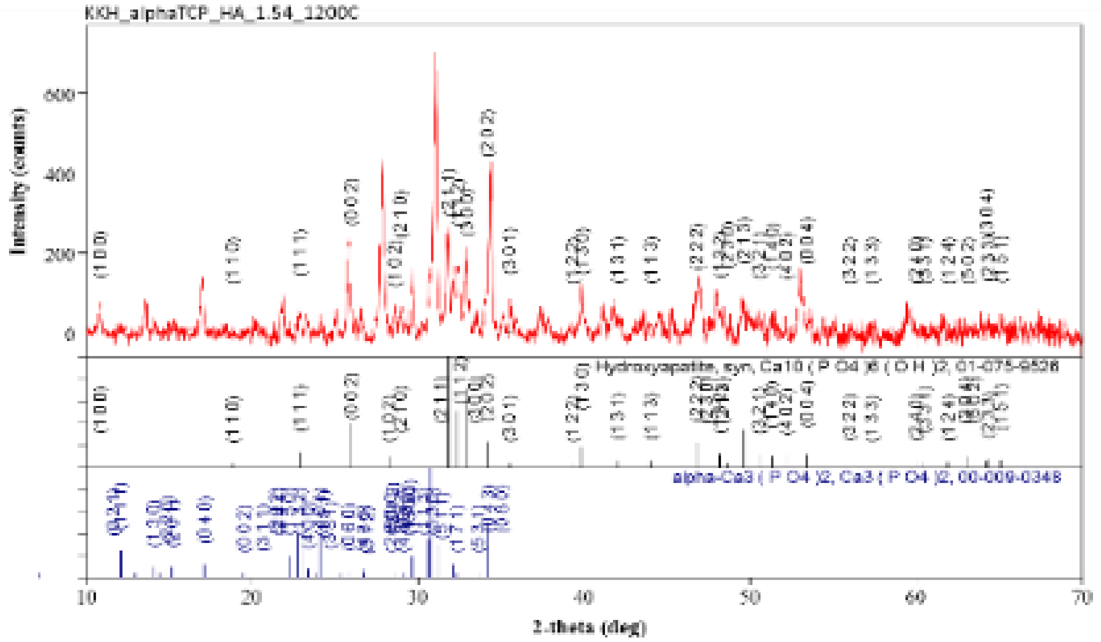

Figure 6 XRD pattern of biphasic HAP/α-TCP (Sample S3)

Table 5 shows the comparison of the values of the lattice parameters and volumes of unit cells of the HAP and α-TCP in three biphasic HAP/α-TCP samples. The values of the lattice parameters of HAP and α-TCP are agreed with their literature values. In both phases of HAP and α-TCP, the values of a, b and c increase with the decrease in Ca: P molar ratio (except the value of ‘a’ in sample S2 in α-TCP). It has been observed that with the increasing of the lattice parameter, the volumes of a unit cell also increase in both HAP and α-TCP. Moreover, the unit cell volume of α-TCP is always larger than that of HAP in every sample.

Table 6 shows the comparison of the Reference Intensity Ratio (RIR) and weight % of HAP and α-TCP in biphasic HAP/α-TCP. When the weight % of HAP and that of α–TCP are compared for each ratio, the weight % of α-TCP is nearly 5 times larger than that of HAP for Ca : P of 1.60 : 1 but 2 times for 1.57 : 1 and 3 times for 1.54 : 1.

Table 7 shows the comparison of the crystallite sizes of HAP and α-TCP in three biphasic HAP/α-TCP powder samples. The crystallite sizes of HAP and α-TCP increase when the Ca: P molar ratio of each sample decreases. And, the crystallite size of α-TCP is always larger than that of HAP in every sample.

Table 5 Comparison of the lattice parameters and unit cell volume of HAP and α-TCP in three biphasic HAP/α-TCP samples

Phase	Crystal system /Space group	Ca : P	Lattice parameter			Volume (Å)^3
			a (Å)	b(Å)	c(Å)	
HAP	Hexagonal / 176:P63/m	1.60 : 1	9.382	9.382	6.810	519.1
		1.57 : 1	9.396	9.396	6.856	524.2
		1.54 : 1	9.400	9.400	6.914	529.1
α-TCP	Orthorhombic / 47:Pmmm	1.60 : 1	15.171	20.700	9.071	2848.7
		1.57 : 1	14.760	20.800	9.311	2858.6
		1.54 : 1	15.222	20.830	9.316	2953.9

Table 6 Comparison of the RIR value and weight % of HAP and α-TCP in biphasic HAP/α-TCP sample

Ca : P	Relative Intensity		RIR value		Weight (%)	
	HAP	α-TCP	HAP	α-TCP	HAP	α-TCP
1.60:1	19.64	100	0.16	0.84	16	84
1.57:1	40.19	67.52	0.37	0.63	37	63
1.54:1	31.96	100	0.24	0.76	24	76

Table 7 Comparison of the average crystallite size of HAP and α-TCP

Sample	Ca : P	Crystallite size (nm)	
		HAP	α - TCP
S1	1.60 :1	36.23	38.13
S2	1.57 :1	37.42	40.72
S3	1.54 :1	39.65	53.14

SEM Analysis

The surface morphology of biphasic HAP/α-TCP power samples was observed by Scanning Electron Microscopy (SEM). Figures 7, 8 and 9 show the SEM images of surfaces of three biphasic HAP/α-TCP powder samples. The average particle sizes of HAP and α-TCP were calculated by Eq (9),

$$\text{Particle sizes} = \text{Total length of the particles} / \text{Number of particles} \qquad (9)$$

Table 8 shows the comparison of the average particle sizes of HAP and α-TCP calculated from SEM analysis for three biphasic HAP/α-TCP samples. The smaller the Ca: P molar ratio of the samples, the smaller the particle size of HAP and the larger the size of α-TCP Moreover, the particle size of α-TCP is always larger than that of HAP in each sample.

Table 8 Comparison of the average particle size of HAP and α-TCP from SEM analysis

Sample	Ca : P	Particle size (µm)	
		HAP	α - TCP
S1	1.60 :1	0.83	0.91
S2	1.57 :1	0.58	1.20
S3	1.54 :1	0.31	1.46

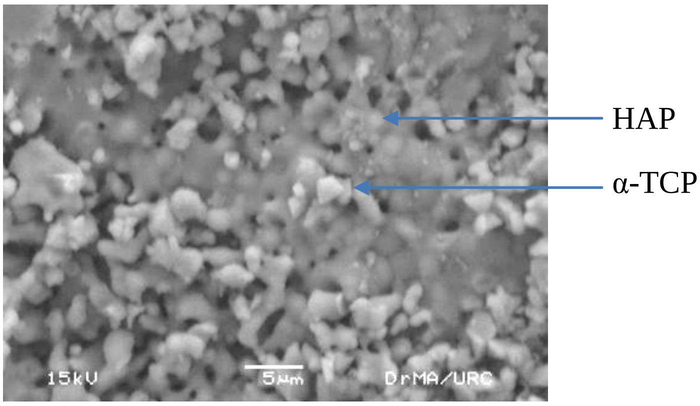

Figure 7 SEM image of biphasic HAP/α-TCP (S1)

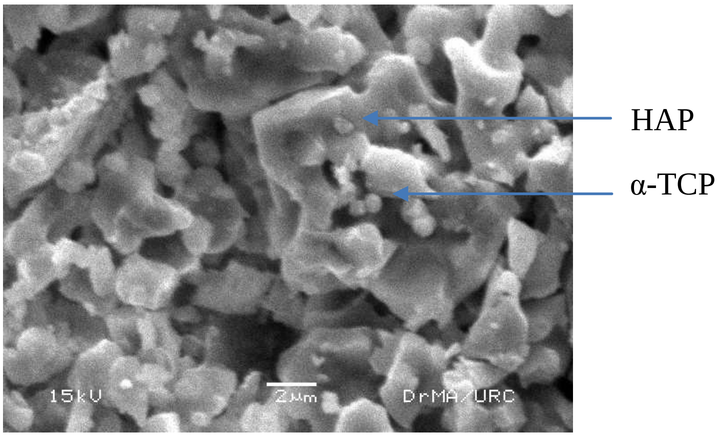

Figure 8 SEM image of biphasic HAP/α-TCP (S2)

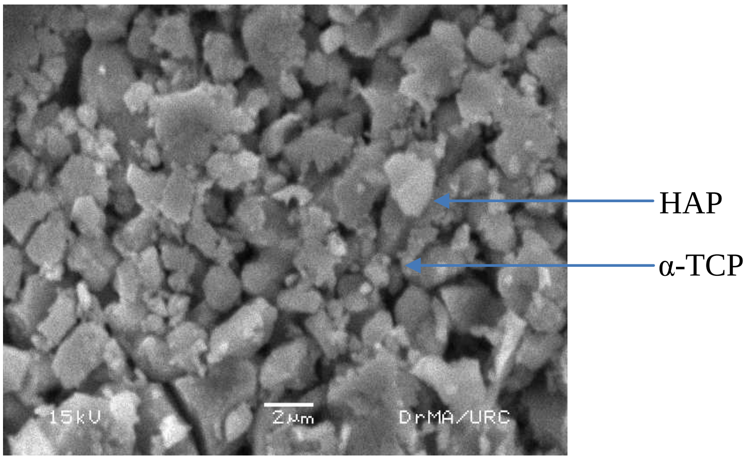

Figure 9 SEM image of biphasic HAP/α-TCP (S3)

Conclusion

The three biphasic HAP/α-TCP samples with Ca: P molar ratio of 1.60: 1, 1.57:1 and 1.54:1 were prepared via precipitation method by using Ca $(NO_3)_2.4H_2O$ and $(NH_4)_2HPO_4$ as precursors. The decomposition temperatures of the reacting molecules obtained from the DTA analysis well agree with the literature values. It has been proved that when the amount of Ca decreases in Ca: P molar ratio, the temperature range in which endothermic reaction occurred increases (DTA analysis), the value of % weight loss increases (TG analysis). Importantly, the values of lattice parameters (except 'a' in sample S2 in α-TCP phase), the volume and crystallite sizes in both HAP and α-TCP become larger with the decrease in the amount of Ca in Ca: P molar ratio. The SEM analysis prove that the particle size of α-TCP is always larger than that of HAP and it well agrees with the XRD results. Therefore, this research reveals that the molar ratio of Ca: P does effect the formation of biphasic hydroxyapatite/α-tricalcium phosphate bioceramics in structural and thermal behaviors.

Acknowledgements

The authors are grateful to the Department of Physics and Universities' Research Centre, University of Yangon, for the supports with research facilities.

References

Caroline,V., & F.D. Gnanam, (2002) "Synthesis and Characterization of biphasic Calcium Phosphate." *Journal of Functional Biomaterials*, vol.16 (1), pp.12-14.

Juliana, M, (2009) "Influence of Synthesis conditions on the Characteristics of Biphasic Calcium Phosphate Powders." *International Journal of Applied Ceramic Technology,* vol. 6(1), pp.60-71.

Klein, C.P., A.A. Driessen, K. Groot, and A. Hoof, (1983) "Biodegradation Behaviour of Various Calcium Phosphate Materials in Bone Tissue." *Journal of Biomedical Materials Research*, vol. 17(5), pp.769-84.

https://en.m.wikipedia.org>wiki

J. Myanmar Acad. Arts Sci. 2020 **Vol. XVIII.No.2C**

STUDY ON STRUCTURAL AND ELECTRICAL PROPERTIES OF MAGNESIUM FERRITE PREPARED BY CO-PRECIPITATION METHOD

Swe Swe Win[1] and Aye Aye Thant[2]

Abstract

Ferrite materials with tunable electrical and magnetic properties are potential candidates for modern technological applications. The magnesium ferrites; $MgFe_2O_4$ having excellent combination of magnetic and dielectric properties can particularly be used for high-frequency applications. The synthesis conditions such as sintering and composition can manage the properties of these materials. On this background, the magnesium ferrite has been prepared by employing the co-precipitation method. The X-ray diffraction (XRD) patterns of prepared samples confirm the formation of a single phase cubic spinel structure. The crystallite size and lattice parameters of the sample have been calculated from XRD data. The FTIR study has been confirmed the presence of the functional group of O-H band and Fe-O band. Scanning Electron Microscopy (SEM) has been employed to observe the morphological features of $MgFe_2O_4$. Response of capacitance has been studied and the dielectric constants show the variation at relatively low frequency and both become stable at relatively higher frequency ranges.

Keywords: $MgFe_2O_4$, co-precipitation, capacitance, XRD, SEM, FTIR

Introduction

Ferrites include a wide range of materials with various crystal structures, compositions and applications. They are ceramic materials, dark gray or black in appearance and very hard and brittle. Spinel ferrites have interesting magnetic and electrical properties. Nowadays, these materials are largely synthesized in nanometric scale for new and improved properties.

The magnetic and electrical properties of spinel ferrites can be tailored for specific device applications by choosing the cation type and cation distribution between tetrahedral (A) and octahedral (B) sites of the spinel lattice. Moreover, the preparation conditions, sintering temperature, sintering time and the method of preparation are other important parameters in the synthesis route. Magnesium ferrites are suitable materials for miniaturizing the size of antennas, along with enhanced properties. The variations of thermal treatment, type of precursors, molar ratio and synthesis route affect the properties of magnesium ferrite and its area of applications.

Experimental Procedure

Magnesium nitrate hexahydrate $Mg(NO_3)_2.6H_2O$, iron nitrate nonahydrate $Fe(NO_3)_3.9H_2O$ and sodium hydroxide NaOH are used as raw materials. Aqueous solutions of analytical graded $Mg(NO_3)_2.6H_2O$, $Fe(NO_3)_3.9H_2O$ have been mixed by magnetic stirring. To obtain smaller size, narrow size distribution and chemically homogeneous ferrite particles, the precipitating reagent (NaOH) has been mixed quickly into the metal solutions. The pH of the solution is maintained at 12.5. For the transformation of metal hydroxides into ferrites, the temperature of the solution has been maintained at 80°C for 40 minutes with constant stirring. Then the solution has been filtered with filter paper and repeatedly washed with distilled water. The washed powder was dried in an electric oven at 100°C for 3 hours to remove water content. The dried powder has been grinded with A-gate mortar and calcined at 900°C for 3 hours. After

---

[1] PhD candidate, lecturer, Department of Physics, University of Veterinary Science

[2] Dr, Professor, Department of Physics, University of Yangon

calcination, the phase identification has been conducted by the RIGAKU MULTIFLEX X-ray diffractometer.

Fourier Transform Infrared Spectroscopy (FTIR) spectra of $MgFe_2O_4$ have been recorded in the range 4000-400cm^{-1}. After the samples have been synthesized, the morphological features of the samples have been studied by Scanning Electron Microscope (SEM). The grain size, shape and homogeneity of the samples have been estimated from the SEM images. Again, the sample is made into pellets and final- sintered at 1200°C, 1250°C, 1300°C, 1350°C and 1400°C for 3 hours. After sintering, the phase identification has been conducted by the RIGAKU MULTIFLEX X-ray diffractometer and the morphological features of the samples have been studied by Scanning Electron Microscope (SEM). Dielectric measurements have been done by Fluke LCR meter-189 in the frequency range of 1 kHz to 1 MHz.

Results and Discussions

Structural Analysis of X-ray Diffraction (XRD)

The X-ray diffraction (XRD) spectra of the synthesized samples are taken by the RIGAKU MULTIFLEX X-ray diffractometer. The XRD spectra show that all samples of $MgFe_2O_4$ are formed spinel phase cubic structures. The data has been collected in a 2θ range from 10°C to 70°C. The lattice parameter of $MgFe_2O_4$ sample has been calculated from X-ray lines broadening of the reflections of the (220), (311), (222), (400), (422), (440) and (511) peaks. XRD spectrum of $MgFe_2O_4$ pre-sintered at 900ºC and final-sintered at 1200ºC, 1250ºC, 1300ºC, 1350ºC and 1400ºC are shown in Figure 1 to Figure 6. XRD data of $MgFe_2O_4$ pre-sintered at 900ºC is shown in Table 1 and variations of average lattice constant and average crystallite size with final-sintering temperature are shown in Table 2.

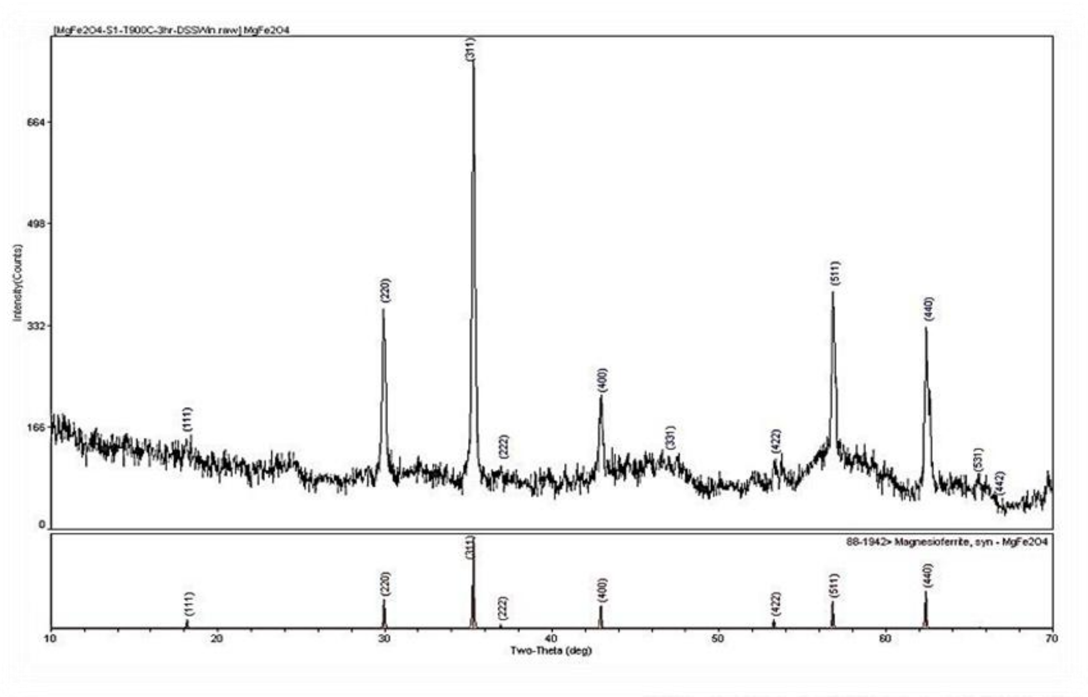

Figure 1 XRD spectrum of $MgFe_2O_4$ pre-sintered at 900ºC

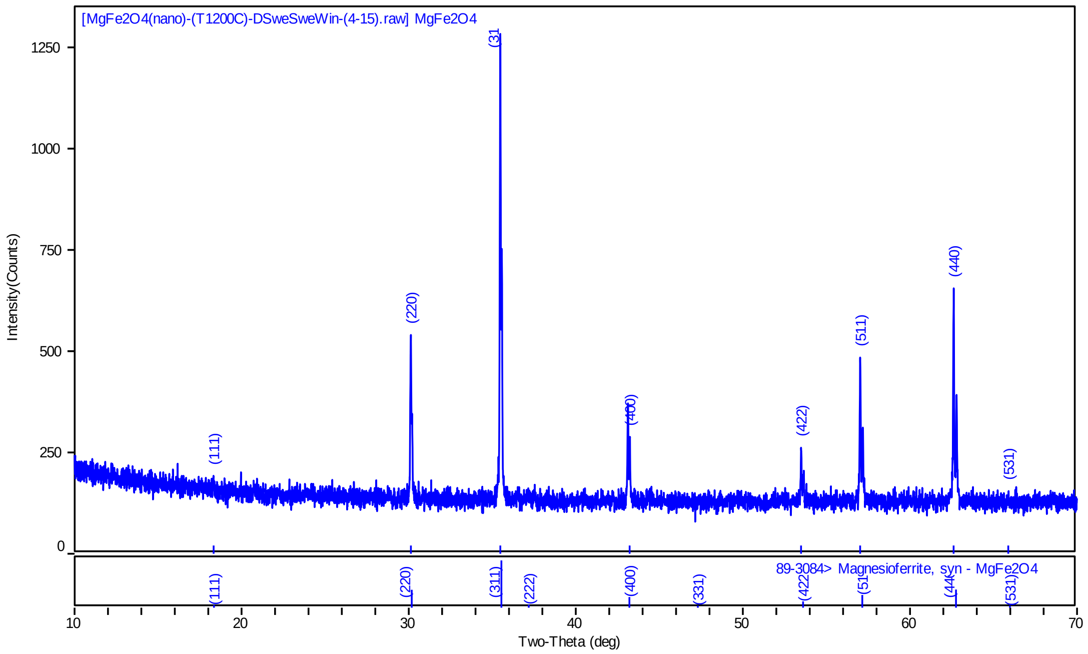

Figure 2 XRD spectrum of $MgFe_2O_4$ final-sintered at 1200ºC

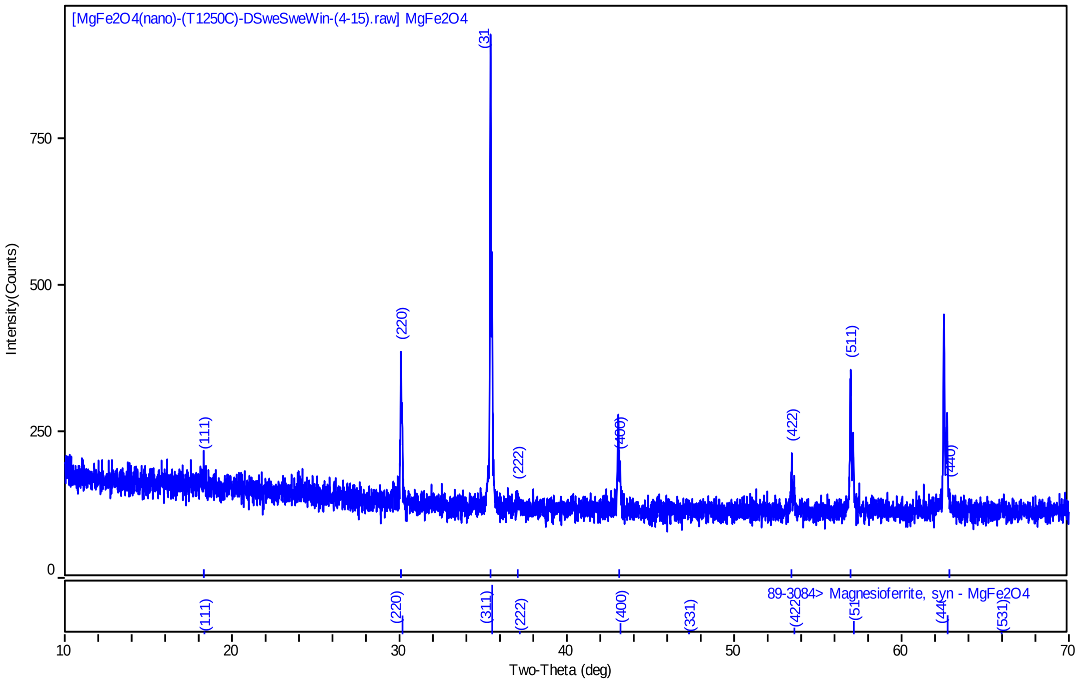

Figure 3 XRD spectrum of $MgFe_2O_4$ final-sintered at 1250ºC

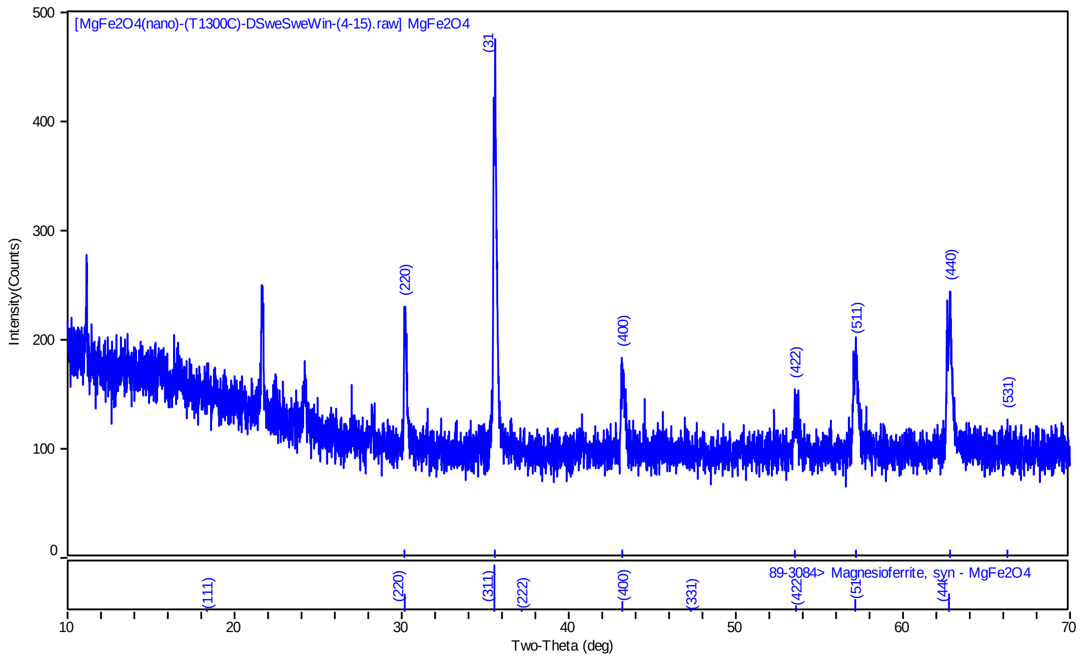

Figure 4 XRD spectrum of $MgFe_2O_4$ final-sintered at 1300°C

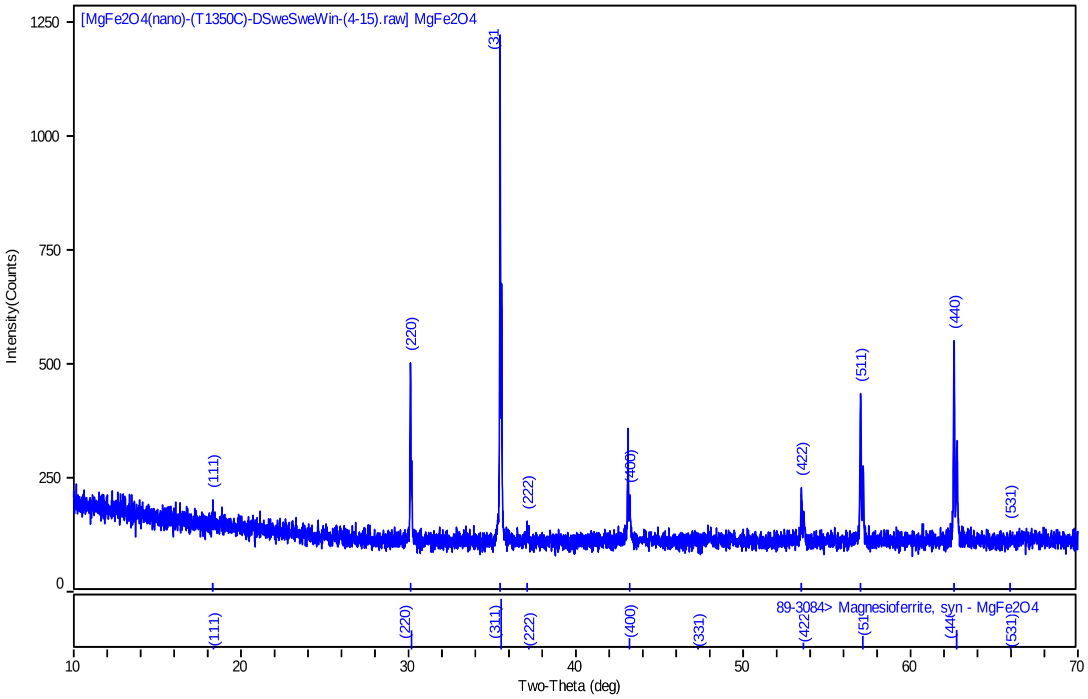

Figure 5 XRD spectrum of $MgFe_2O_4$ final-sintered at 1350°C

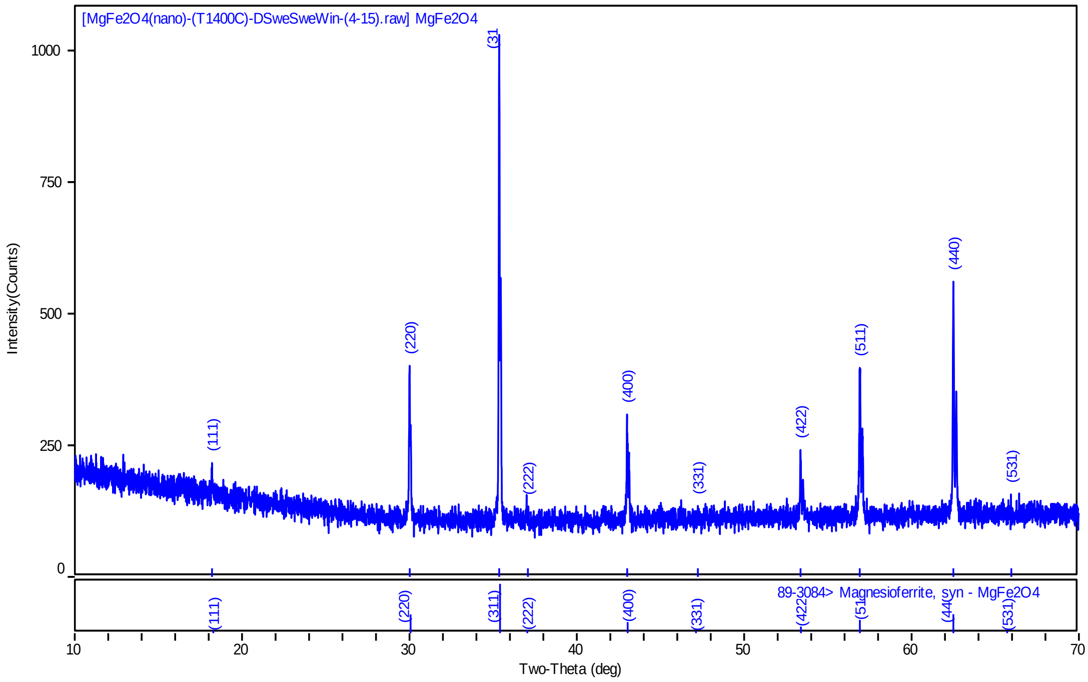

Figure 6 XRD spectrum of $MgFe_2O_4$ final-sintered at 1400ºC

Table 1 XRD data of $MgFe_2O_4$ pre-sintered at 900 ºC

No	2θ (deg)	Diffraction Peak (hkl)	FWHM (deg)	B (rad)	Lattice Constant a (Å)	Crystallite size (nm)
1	30.06	(220)	0.256	0.0045	8.4018	32.13
2	35.38	(311)	0.232	0.0041	8.4067	35.94
3	43.02	(400)	0.288	0.0050	8.4032	29.65
4	53.344	(422)	0.332	0.0058	8.4067	26.77
5	62.50	(440)	0.296	0.0052	8.3993	31.39
6	56.92	(511)	0.275	0.0048	8.3985	32.86
Average					8.4027	31.46

Table 2 Variation of average lattice constant and average crystallite size with final-sintering temperature

Final-sintering temperature (°C)	Average lattice constant (Å)	Average crystallite size (n m)
1200	8.3808	57.60
1250	8.3847	48.10
1300	8.3637	37.14
1350	8.3816	67.35
1400	8.4051	72.10

Study on Microstructure and Surface Morphology of $MgFe_2O_4$

The microstructure and morphology play the important roles in determining magnetic and electrical transport properties. These studies for the materials are essential in order to understand the relationship between their processing parameters as well as the behavior when they are used in practical applications. Microstructures of the sintered $MgFe_2O_4$ have been analyzed by a high resolution scanning electron microscope (SEM). The SEM images of $MgFe_2O_4$ final-sintered at different temperatures are given in Figure 6 (a), (b), (c), (d) and (e). The variation of average grain size with the sintering temperature is shown in Table 2.From SEM images, it is confirmed that the microstructure is composed of regular grains. Moreover, the surface morphology represents a homogeneous structure. There is no impurity in the surface of $MgFe_2O_4$. With the increasing temperature, the grains become bigger and the average grain size increases from 0.95 µm to 1.60 µm. The pores are rarely visible between the grain boundaries and within the grain.

Table 3 Variation of average grain size with sintering temperature

Final-sintering temperature (°C)	Average grain size (µ m)
1200	0.95
1250	1.03
1300	1.04
1350	1.38
1400	1.60

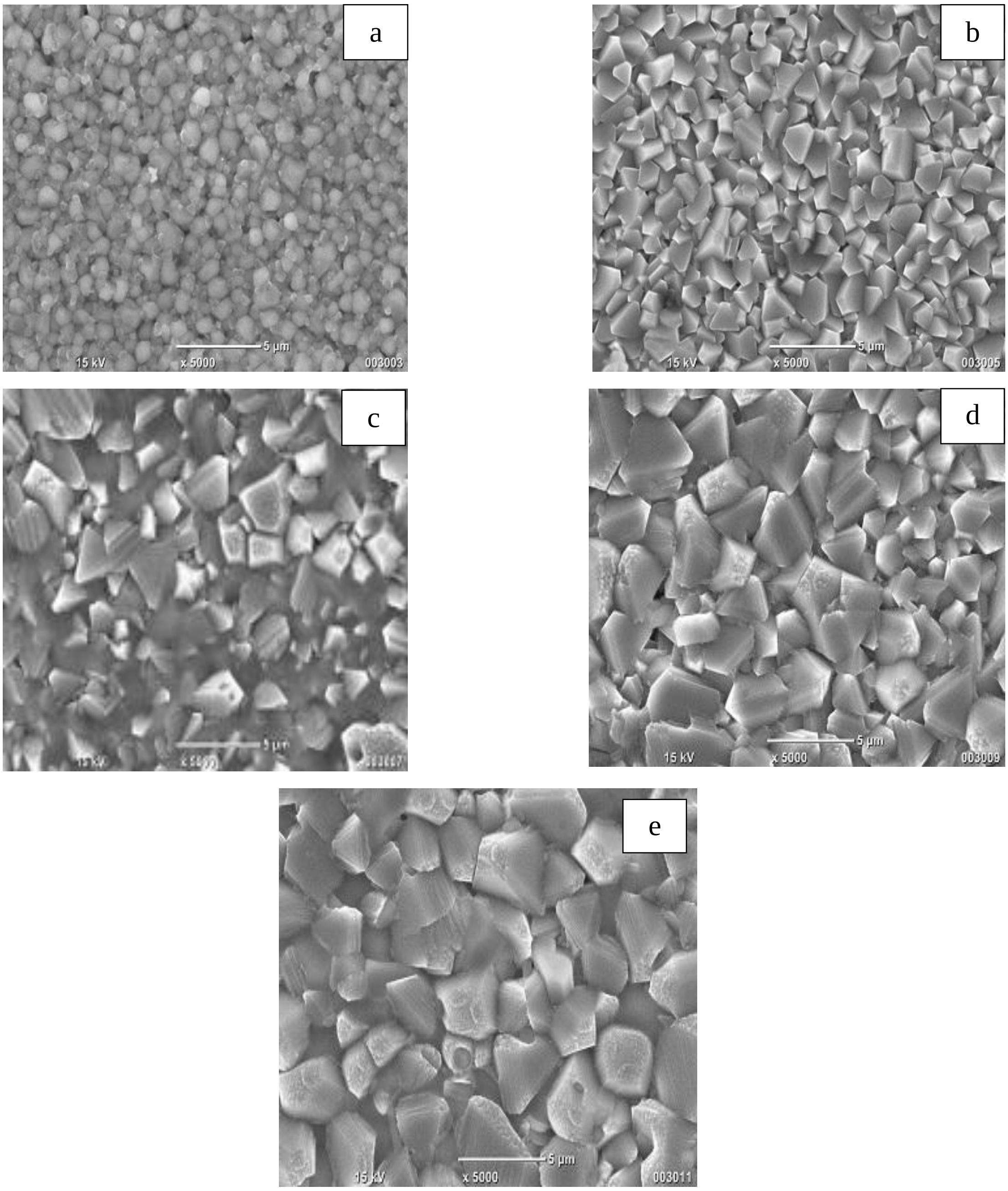

Figure 7 SEM micrographs of $MgFe_2O_4$ final-sintered at (a) 1200ºC (b) 1250ºC (c) 1300ºC (d) 1350ºC (e) 1400º**C**

Study on the Molecular vibration

The molecular vibrations have been examined by Fourier Transform Infrared Spectroscopy (FTIR). The strength of IR peak is roughly dependent on the change in dipole moment during vibration. The FTIR spectra of $MgFe_2O_4$ powder which is final sintered at 1200ºC, 1250ºC, 1300ºC, 1350ºC and 1400ºC are presented in Figure 8 to Figure12. The vibrational frequencies of the chemical bonds in the $MgFe_2O_4$ nanoparticles can be assigned from FTIR spectra which were recorded in the region 400 cm^{-1} to 4000 cm^{-1}. This vibration is an indicative of formation of spinel ferrite structure. Therefore, it can be said that FTIR analysis strongly supports the XRD result.

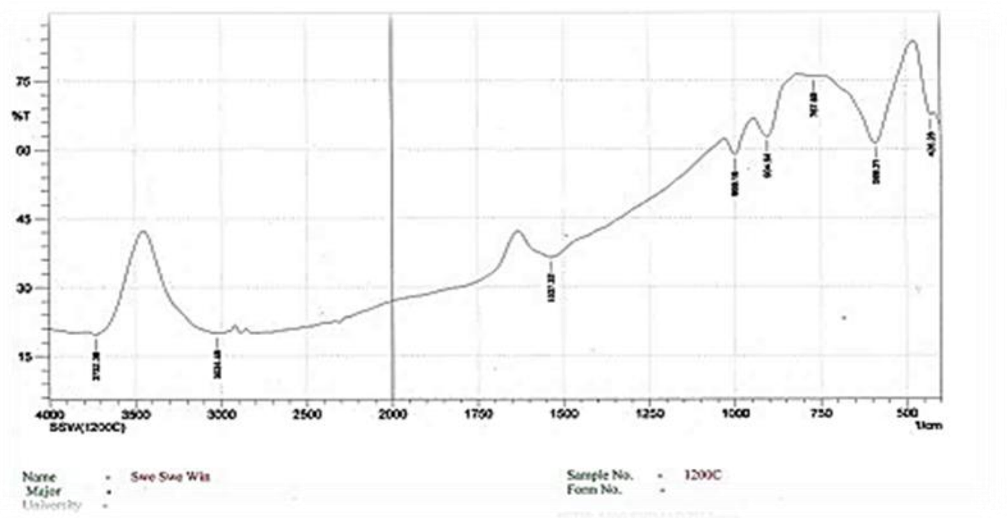

Figure 8 FTIR spectrum of $MgFe_2O_4$ final -sintered at 1200ºC

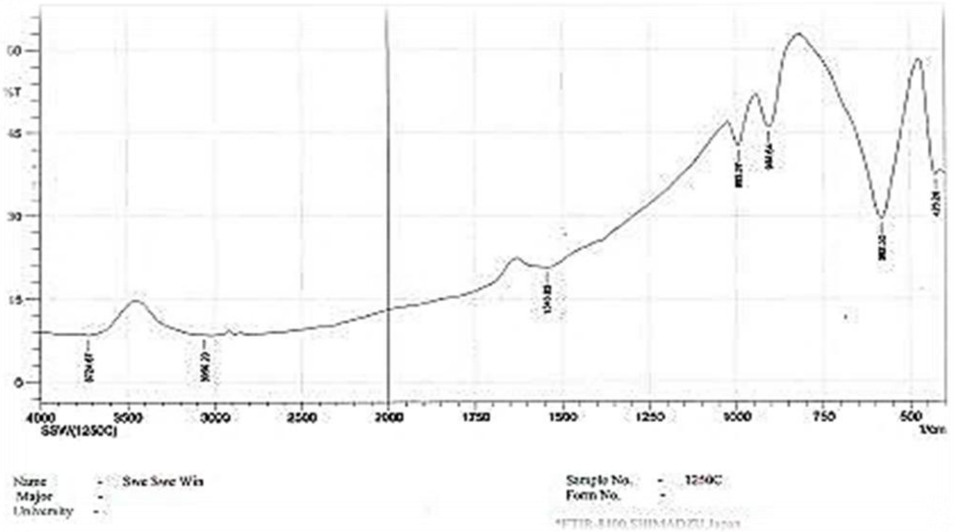

Figure 9 FTIR spectrum of $MgFe_2O_4$ final- sintered at 1250ºC

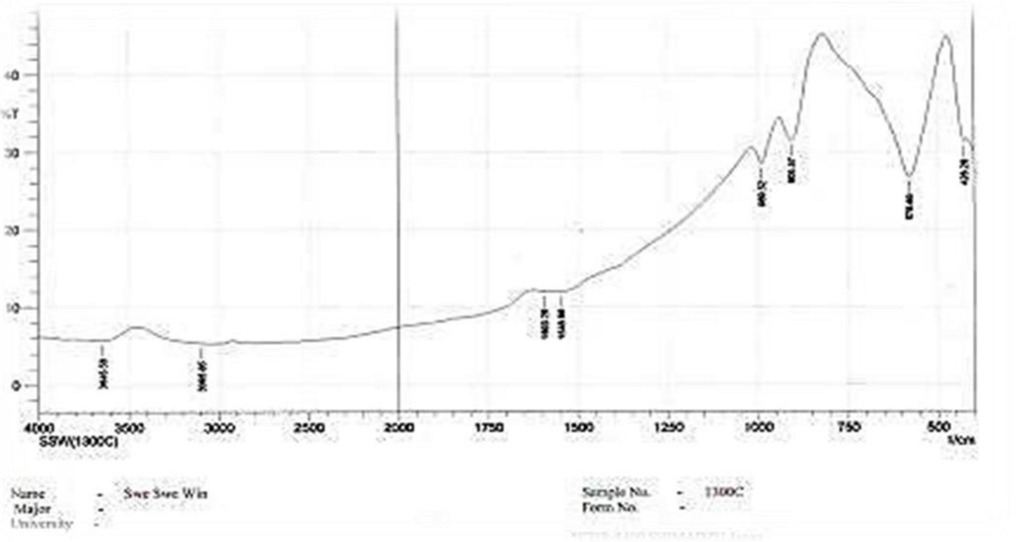

Figure 10 FTIR spectrum of $MgFe_2O_4$ final -sintered at 1300ºC

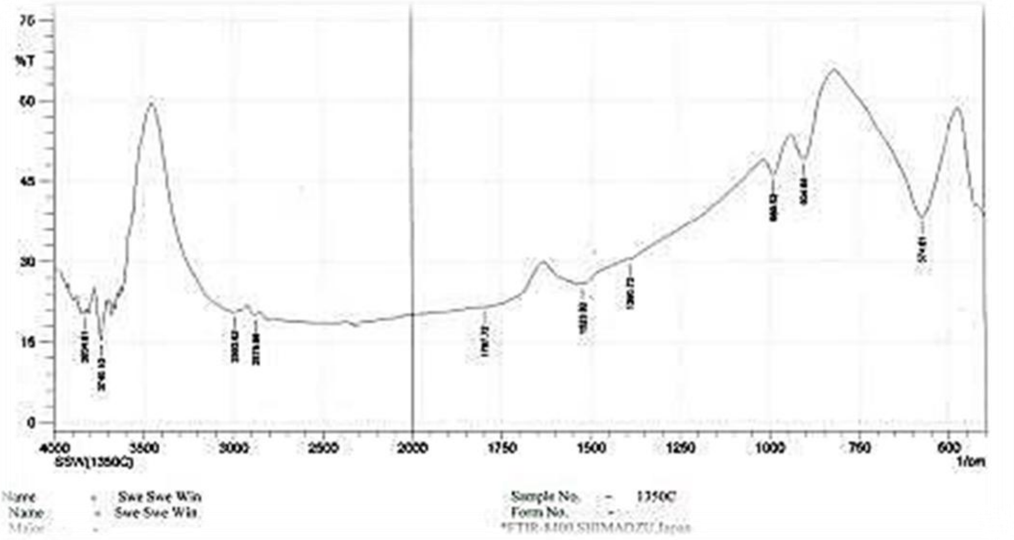

Figure 11 FTIR spectrum of $MgFe_2O_4$ final- sintered at 1350ºC

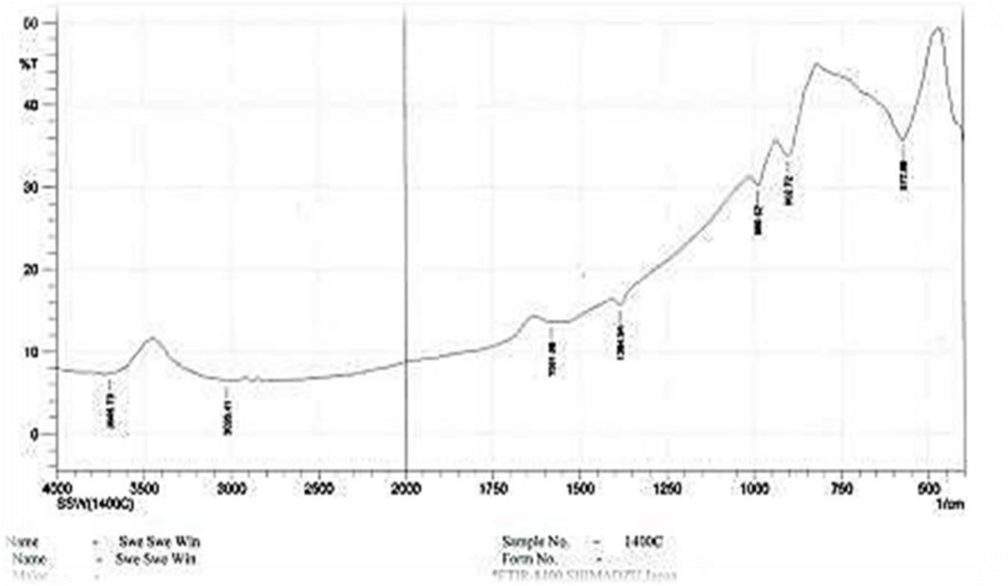

Figure 12 FTIR spectrum of $MgFe_2O_4$ final- sintered at 1400ºC

Study on Frequency Dependent Dielectric Constant

The electrical properties of samples have been measured using Fluke -189 LCR meter in the frequency range of 1kHz to 1 MHz. The dielectric constant (ε_r) was calculated by the relation

$$\varepsilon_r = \frac{Cd}{\varepsilon_0 A} \tag{1}$$

where, d is the thickness, C is the capacitance, ε_0 is the permittivity of free space and A is the cross-sectional area of the pellet. The dielectric constant of samples has been determined from experimentally obtained capacitance values. The dielectric properties of ferrites are dependent upon several factors such as method of preparation, chemical composition, grain structure and grain size.

The variations of dielectric constant with frequency are shown in Figure 13. From these graphs, the values of dielectric constant of the samples show a variation in lower frequency region. The variation of dielectric constant in lower frequency region is due to the grain boundary defects of ferrite and the dielectric constant becomes stable in higher frequency region. In the lower frequency region, the dipole polarization is hindered by the grain boundaries; however this effect can be overcome in the higher frequency region.

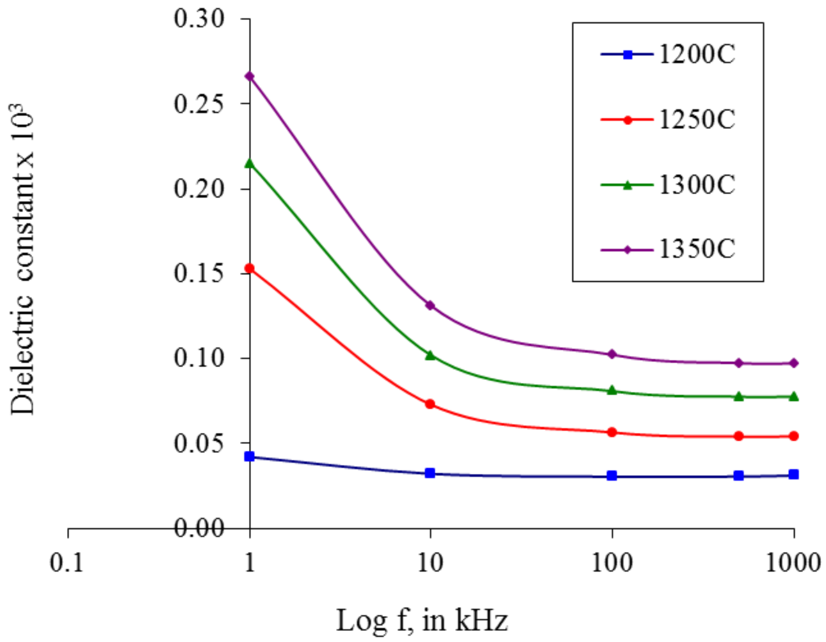

Figure 13 The variations of dielectric constant with frequency

Table 4 The variation of frequency dependent dielectric constant with temperature

Frequency (kHz)	**Dielectric constant x10^3**			
	1200℃	**1250℃**	**1300℃**	**1350℃**
1	0.0360	0.0600	0.1000	0.3900
10	0.0280	0.0130	0.0400	0.1600
100	0.0137	0.0070	0.0150	0.0450
500	0.0061	0.0010	0.0050	0.0160
1000	0.0140	0.0110	0.0120	0.0200

Conclusion

Magnesium ferrite, $MgFe_2O_4$, has been successfully prepared by co-precipitation method in this work. As the starting powder characteristics are strongly determined the product, the raw materials have been selected to ensure their purities. The XRD characterization of the sintered ferrite has been identified the formation of the typical cubic spinel structure. The lattice parameters and crystallite size have been calculated for further characterization. The sizes of crystallites in the sample have been evaluated by using the FWHM of the most intense peaks and the results confirm the formation of ferrite particles. The average crystallite size of $MgFe_2O_4$ decreased until nanometer range due to the synthesis by chemical co-precipitation technique. The average crystallite size is 31.6 nm when the sample is pre-sintered at 900 ℃ and becomes bigger at final-sintering temperatures. The typical lattice parameter values from 8.3637 Å to 8.4027 Å have confirmed the consistency of synthesis route in this work. Based on the SEM micrographs, when the samples have been sintered at higher temperature, subsequent grain growth has taken place. At the final-sintering temperatures, the average grain size increases from 0.95 μ m to 1.60 μ m. The values of dielectric constant of the samples show a variation at relatively lower frequency range due to the grain boundary defects of ferrite and the dielectric constant becomes stable at relatively higher frequency range.

Acknowledgement

The authors are greateful to the officials from Department of Physics and Universities' Research Center, University of Yangon for the supports with facilities.

References

Auzans, E.Zins, D., Blums, E and Massart, R.(1999).Synthesis and Properties of Ferrites .Journal of Materials Science,34(6),1253-1260. 1]

Auzans, E., Zins, D, E ., & Massart, R. (1999). Synthesis and Properties of Ferrite. Journal of Materials Science, 34(6), 1253-1260.

Bertotti G (1998)‘‘ Hysteresis in Magnetism’’ (New York: Academic Press)

Goldstein, etal (1981) “Scanning Electron Microscopy and X-Ray Microanalysis annuals”(Singapore: Plenum).

Khu Rmi R.S.(2005) “Material Science” S. Chand Company

J. Myanmar Acad. Arts Sci. 2020 **Vol. XVIII.No.2C**

ELEMENTAL ANALYSIS OF DIFFERENT ETHYLENE TREATMENTS ON MUSA

Aye Aye Myint[*]

Abstract

Ethylene is a naturally occurring plant growth substance that has numerous effects on the growth, development and storage life of many fruits, vegetables. Harvested fruits and vegetables may be intentionally or unintentionally expose to biologically active levels of ethylene and both *endogenous* and *exogenous* sources of ethylene contribute to its biological activity. In this paper the concentration of elements contained in the musa samples were analyzed by using EDXRF method and discussed the effects of different ethylene treatments on the musa.

Keywords: ethylene, biological activity, concentrations of elements, **e**thylene treatment

Introduction

Wonderfully sweet with firm and creamy flesh, bananas come prepackaged in their own yellow jackets and are available for harvest throughout the year. The banana plant grows l0 to 26 feet and belongs to the *Musaceae* family of plants along with *plantains.* The cluster of fruits contain anywhere from 50 to 150 bananas with individual fruits grouped in bunches, known as "hands", containing 10 to 25 bananas.

Bananas are thought to have originated in Malaysia around 4,000 years ago. From there, they spread throughout the Philippines and India. Since the development of refrigeration and rapid transport in the 20th century, bananas have become widely available. Today, bananas grow in most tropical and subtropical regions with the main commercial product including Irrawaddy Division.

Musa

Banana fruits contain high nutrition sources of carbohydrate, minerals and vitamins. A banana is an edible fruit produced by several kinds of large herbaceous flowering plants in the genus Musa. The fruit is variable in size, color and firmness, but is usually, elongated and curved, with soft flesh rich in starch covered with a rind which may be green, yellow, red, purple, or brown when ripe. The fruits grow in clusters hanging from the top of the plant. Almost all modern edible parthenocarpic (seedless) bananas come from two wild species-Musa acuminata and Musa balbisiana.

Scientific classification of banana

Scientific name : *Musa paradisiacal* L.
Genus : *Musa*
Species : *paradisiacal*
Family name : Musaceae
English name : Banana
Myanmar name : Phee-gyan-hnget-pyaw
Distribution : tropical and sub-tropical regions of the world
Part used : Pulp

---

[*] Dr, Lecturer, Department of Physics, Hinthada University

Banana, a wonderfully sweet fruit with firm creamy flesh that available for harvest throughout the year consists mainly of sugars and filers which make it a source of immediate and slightly prolonged energy. When consumed, reduces depression, anaemia, blood pressure, stroke risk, heartburns, ulcers, stress, constipation and diarrhea. It confers protection for eyesight, healthy bones, kidney malfunctions, morning stickness, itching and swelling.

Table 1 The nutrient of Banana.

Nutrient of Banana, fresh 1.00 medium (118.00 grams)	
Vitamin B6	25%
Manganese	16%
Vitamin C	14%
Potassium	12%
fiber	12%
Copper	10%
biotin	10%

Growth Habit

Bananas are today grown in every humid tropical region and constitutes the 4th largest fruit crop of the world. The plant needs 10- 15 months of frost-free conditions to produce a flower stalk. Bananas, especially dwarf varieties, the plant will also need period repotting as the old plant dies back and new plants develop. Eventually producing the terminal inflorescence which will later bear the fruit. Each stalk produces one huge flower cluster and then dies.

Fruit Harvest

Stalks of bananas are usually formed in the late summer and then winter over. Occasionally, a stalk will form in early summer and ripen before cold weather appears. The fruit can be harvested by cutting the stalk when the bananas are plump but green. For tree-ripened fruit, cut one hand at time as it ripens. Once harvested the stalk should be hung in a cool, shady place. Since ethylene helps initiate and stimulate ripening, and mature fruit gives off this gas in small amounts, ripening can be hastened by covering the bunch with a plastic bag.

Ethylene

Ethylene is a naturally occurring plant growth substance that has numerous effects on the growth, development and storage life of many fruits, vegetables. Harvested fruits and vegetables may be intentionally or unintentionally exposed to biologically active levels of ethylene and both endogenous and exogenous sources of ethylene contribute to its biological activity. Ethylene synthesis and sensitivity are changed during certain stages of plant development. Exposure may occur inadvertently in storage or transit from atmospheric pollution or from ethylene produced by adjacent crops. Intentional exposure primarily used to ripen harvested fruit. The detrimental effects of ethylene on quality center on altering or accelerating the natural processes of development, ripening and senescence, while the beneficial effects of ethylene on quantity center on roughly the same attributes as the detrimental effects. A number of techniques to control the effects of ethylene are discussed in relation to their application with commercially important fruits and vegetables.

Ethylene naturally occurring odourless and coluorless gas, which acts as a growth regulator in plants, and acts as in inhibitor of sprouting in long term storage of potatoes and onions, leaving no chemical residues on the surface of the produce after treatment. It is also used widely in ripening of bananas, citrus and other fruits.

There are two classes of fresh produce in terms of ethylene production. There are climateric products, mainly fruit that pruduce a burst of ethylene as they ripen, as well an increase in respiration and there are the non-climateric products that do not increase ethylene production when they ripen. The moreobvious way of establishing which class a product fits in to is whether or not the product ripens after harvest. Products that ripens after harvest are classed as climateric and they typically ripen by softening significantlv, by changing colour and become sweeter, examples are bananas. Non-climateric fruits do not change significantly after harvest. They will soften a little, lose green colour and develop rots as they become old but they do not change to improve their eating characteristics. Non-climateric crops include leafy vegetables, strawberries and grapes.

Table 2 Examples of climacteric and non-climateric and non-climateric product.

Climateric (Ethylene producting)	**Non-climateric (Non ethylene producing)**
Apples, pears, quince	Cherry, blackbemy, strau, berry
Apricot, nectarine, peach	Eggplant, cucumber, pepper
Mango, avocado, banana	Lemon, orange, mandarin
Tomato, sapodilla	Water melon, honey dew melon
Rock melon, passionfruit	Grape, lychee, loquat

General Information of Ethylene

1. Name (OECD) : Ethylene

2. Molecular formula : CH_2CH_2

3. Structure formula :

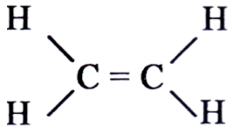

4. Use Pattern : Chemical industry; as raw material for synthesis of chemicals, petrochemicals and resins. Minor quantities used for fruit ripening and as an aesthetic gas.

5. Sources of explosure : Fuel, coal, and gas combustion. Leakage from chemical industry.

6. Environment :	Ethylene is, due to its physical and chemical properties released mainly into the atmospheric compartment. About three quarters of atmospheric ethylene originates from natural sources.
7. Human Health :	Relevant studies have indicated a low toxicity of ethylene and no risk to human health has been identified neither from occupational exposure of general public, either exposed directly or indirectly via the environment.

Experimental Procedure

Sample Collection

Banana hands were harvested at optimum stage of maturity from an orchard near the Hinthada Township. Irrawaddy Division. Mature-green banana samples were used for this experiment.

Ethylene treatment on Musa

There were six treatments of musa and ethylene concentration and post exposure storage temperature on the ripening process of musa. Thus the total number samples in the experiment were six banana hands. The treatments were carried out as follows.

Sample A. Non-treatment Control	(72 hr)
Sample B. Exposure to ethylene 2%	(48 hr)
Sample C. Exposure to ethylene 2.5%	(42 hr)
Sample D. Exposure to ethylene 3%	(36 hr)
Sample E. Exposure to ethylene 3.5%	(30 hr)
Sample F. Exposure to ethylene 4%	(24hr)

The first groups without ethylene treatment were used as controls.

Group II (sample B) were treated with 2% v/v ethylene solution for 5 min at 27˚C.

Group III (sample C) were treated with 2.5% v/v ethylene solution for 5 min at 27˚C.

Group IV (sample D) were treated with 3% v/v ethylene solution for 5 min at 27˚C.

Group V (sample D) were treated with 3.5% v/v ethylene solution for 5 min at 27˚C.

Group VI (sample D) were treated with 4% v/v ethylene solution for 5 min at 27˚C.

Table 3 Ripening conditions for Musa ethylene treatment.

Sample	Temperature (˚C)	% (v/v) of Ethylene	Treatment time (hr)
A	27˚C	control	72
B	27˚C	2%	48
C	27˚C	2.5%	42
D	27˚C	3%	36
E	27˚C	3.5%	30
F	27˚C	4%	24

Plate I Ethylene treatment was used as controls in 5 min at 27˚C

Plate II Ethylene treatment was used as controls in 36 hr at 27˚C

Plate III Ethylene treatment was used as controls in 72 hr at 27˚C

Plate IV Treated with 2% v/v ethylene solution for 5 min at 27˚C

Plate V Treated with 2% v/v ethylene solution for 36 hr at 27˚C

Plate VI Treated with 2% v/v ethylene solution for 72 hr at 27˚C

Plate VII Treated with 2.5% v/v ethylene solution for 5 min at 27˚C

Plate VIII Treated with 2.5% v/v ethylene solution for 36 hr at 27˚C

Plate IX Treated with 2.5% v/v ethylene solution for 72 hr at 27˚C

Plate X Treated with 3% v/v ethylene solution for 5 min at 27˚C

Plate XI Treated with 3% v/v ethylene solution for 36 hr at 27˚C

Plate XII Treated with 3% v/v ethylene solution for 72 hr at 27˚C

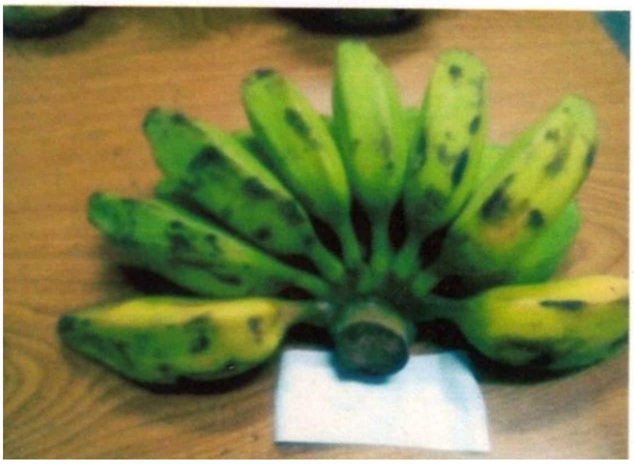

Plate XIII Treated with 3.5% v/v ethylene solution for 5 min at 27˚C

Plate XIV Treated with 3.5% v/v ethylene solution for 36 hr at 27˚C

Plate XV Treated with 3.5% v/v ethylene solution for 72 hr at 27˚C

Plate XVI Treated with 4% v/v ethylene solution for 5 min at 27˚C

Plate XVII Treated with 4% v/v ethylene solution for 36 hr at 27˚C

Plate XVIII Treated with 4% v/v ethylene solution for 72 hr at 27˚C

Result and Discussion

In this research work musa were collected from six different ethylene treatment, A=control, B=2% ethylene concentration. C=2.5% ethylene concentration, D=3% ethylene concentration, E=3.5% ethylene concentration, and F=4% ethylene concentration. These musa samples were dried and ground into fine power. These powders use made pallets using hydraulic pallet machine at Physics Department of Taungoo University.

Musa Samples

In powdered musa samples, Potassium (K). Calcium (Ca). Iron (Fe). Manganese (Mn), Rubidium (Rb), Copper (Cu), Zinc (Zn) and Strontium (Sr) elements were detected. All elements are determined as trance level. The elemental concentration for six kinds of Musa samples are shown in Table (4).

Figure (1) shows the comparison of potassium (K) concentration of element analyzed in this work. From this figure, potassium (K) was found in all samples. The amount of ethylene given in Musa increase, the concentration of elements (K) in musa gradually increase and was not much different or little changes in each sample.

Figure (2) shows the comparison of calcium (Ca) concentration of element analyzed in this work. From this figure, calcium (Ca) was found in all samples. The amount of ethylene given in musa increase, the concentration of elements (Ca) in musa gradually decrease and was not much different or little changes in each sample.

Figure (3) shows the comparison of elemental concentration of from (Fe), analyzed in this work. From this figure iron (Fe) was found in all samples. Among then, the concentration of (Fe) in samples (A) was highest and the other rest samples were in random. There was not much different in each sample.

Figure (4) shows the comparison of manganese (Mn) concentration of element analyzed in this work. From this figure, manganese (Mn) was found in all samples. The amount of ethylene given in musa increase, the concentration of elements (Mn) in musa gradually increase and was not much different or little changes in each sample.

Figure (5) shows the comparison of elemental concentration of rubidium (Rb), analyzed in this work. From this figure rubidium (Rb) was found in all samples. Among then, the concentration of (Rb) in samples (C), (E) were highest and the other rest samples were in random. There was not much different in each sample.

Figure (6) slows the comparison of elemental concentration of copper (Cu) analyzed in this work. From this figure copper (Cu) was found in all samples. Among then the concentration of copper (Cu) in sample (A) was lowest and the other rest samples were in random. There was not much different in each sample.

Figure (7) shows the comparison of zinc (Zn) concentration of element analyzed in this work. From this figure, zinc (Zn) was found in all samples. The amount of ethylene given in musa increase, the concentration of elements (Zn) in musa gradually decrease and was not much different or little changes in each sample.

Figure (8) shows the comparison of elemental concentration of strontium (Sr), analyzed in this work. From this figure strontium (Sr) was found in all samples. Among then, the concentration of (Sr) in sample (E) lowest and the other rest samples were in random. There was not much different in each sample.

Table 4 The elemental concentrations of musa control and ethylene treatment by BDXRF Method (Relative concentration %)

Element	Sample (A)	Sample (B)	Sample (C)	Sample (D)	Sample (E)	Sample (F)
K	61.678 %	65.617 %	68.389 %	70.133 %	71.994 %	75.391 %
Ca	31.678 %	27.597 %	24.470 %	22.740 %	20.165 %	16.619 %
Fe	2.449 %	1.849 %	1.706 %	1.259 %	1.427 %	0.987 %
Mn	1.569 %	1.818 %	1.865 %	2.677 %	3.136 %	3.290 %
Rb	1.077 %	1.353 %	1.855 %	1.514 %	1.658 %	2.015 %
Cu	0.607 %	0.809 %	0.792 %	0.852 %	0.945 %	1.070 %
Zn	0.712 %	0.703 %	0.680 %	0.593 %	0.518 %	0.444 %
Sr	0.260 %	0.254 %	0.243 %	0.232 %	0.157 %	0.184 %

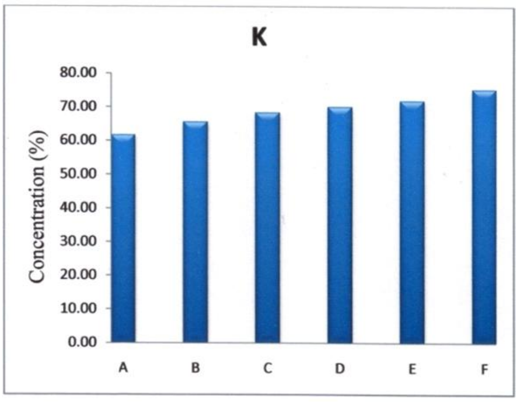

Figure 1 Potassium (K)

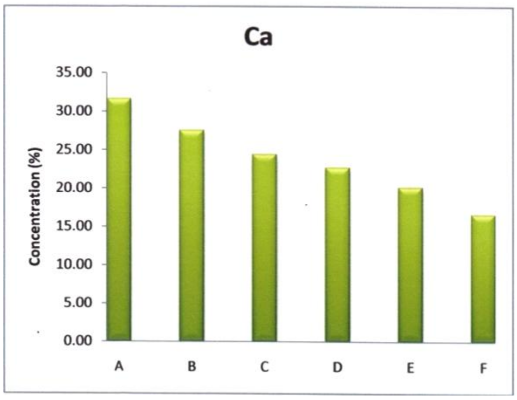

Figure 2 Calcium (Ca)

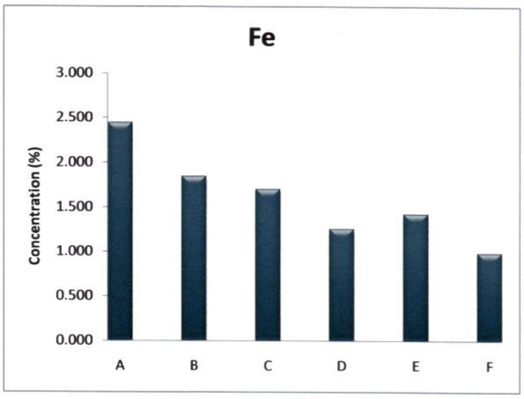

Figure 3 Iron (Fe)

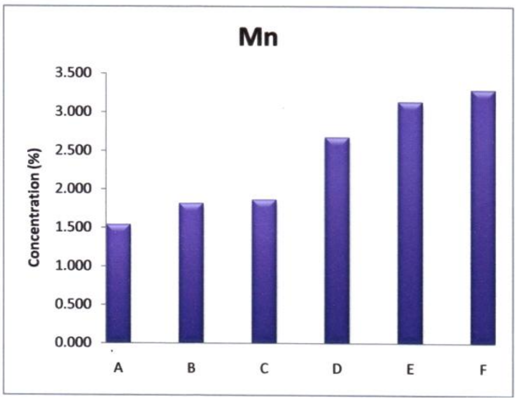

Figure 4 Manganese (Mn)

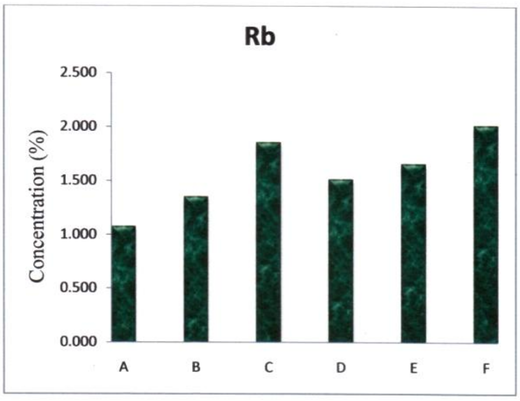

Figure 5 Rubidium (Rb)

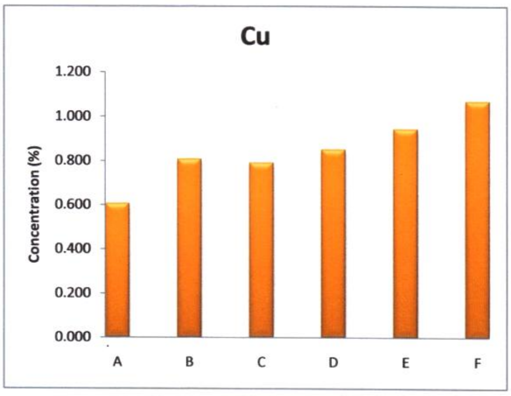

Figure 6 Copper (Cu)

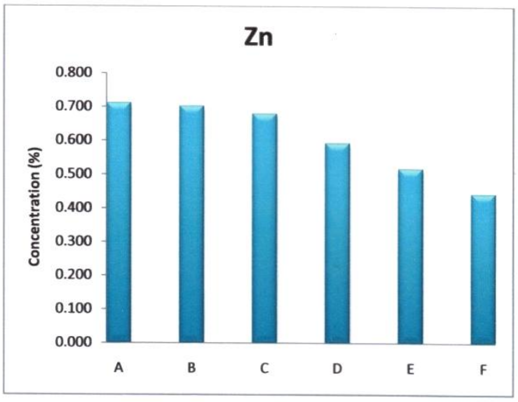

Figure 7 Zinc (Zn)

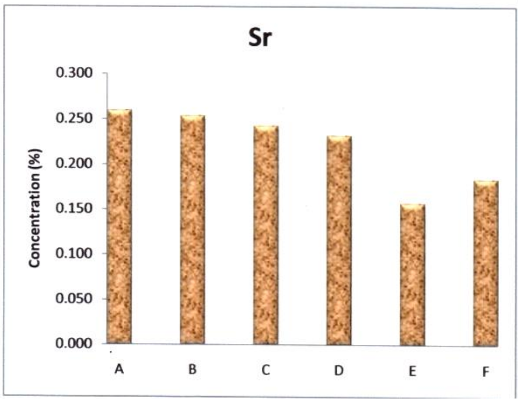

Figure 8 Strontium (Sr)

Figure (1 to 8) Comparison of concentration in six Musa samples (control and Ethylene treatments)

Conclusion

Fruits naturally ripen in trees. But generally 80% fruits are artificially ripened process. Ripe fruits are not suitable to carry and distributed. So unripe fruits and use certain methods to increase the ripening process.

Bananas are the developing world's fourth most important food up (after rice, wheat and maize) in terms of gross value of production. The crop is grown in more than 100 countries through the tropic and sub-tropics.

Banana is highly perishable fruit. It is often harvested in a mature but unripe condition, and is subsequently allowed to ripen further. In natural conditions, bananas ripen slowly, leading to high weight loss, desiccation, ripening is also uneven and fails to develop good colour and aroma. The marketable quality deteriorates.

Bananas are growing in a range of Irrawaddy Division and produce fruit throught the year and produce fruit through the year. However in the colder climatic condition the old type of smoke treatment is crude and ineffective of evolution carbon monoxide is hazardous to health. Improper smoke treatment leads to leads to uneven ripening and also poor external colour.

The present study was taken up to evaluate the effect of ethylene treatment. Commercially ethylene solution was used to ripen various fruits faster than the regular ripening rate of fruits.

The most commenly know use of ethylene is to trigger ripening is some crops, such as bananas and avocados. The concentration of ethylene required for the ripening of different products varies. In general, the concentration applied is within the range of 2% v/v and 3.5% v/v. The time and temperature also influences the rate of ripening with fruit being ripened at temperatures about 27˚C.

During transportation, the naturally ripened fruits may become over ripen and inedible. A part of naturally ripened fruits can also be damaged during difficult conditions of transportation. It is an economic loss for the fruit and marketing to minimize the loss, fruit. Therefore artificially have been ripen fruits before selling to the consumers.

The application of ethylene at a controlled rate means that these products can be presented to customer as 'ready to eat'. A number of techniques to control the effects of ethylene was discussed in relation to their application with commercially important fruits and vegetables.

Acknowledgement

I wish to express my sincere thanks to Professor Dr. Khin Khin Win, PhD (YU), Head of Department of Physics, University of Yangon, for this kind of permission to carry out this research.

I am greatly indebted to my Professor Dr. Win Win Thein, PhD (YU), Department of Physics, Hinthada University, for her valuable supervision and guidance.

References

Kumar, K. P. S., D. Bhowmik, S. Duraivel and M. Umadevi. (2012). “Traditional and Medicinal Uses of Banana”. *Journal of Pharmacognosy and Phytochemistry*, 1(3), 51-63

Molina, A. B. and R. V. Valmayor. (1999). *Banana Production System in South East Asia.* INIBAP, 423-436

Saltveit, M. E. (1999). “Effect of Ethylene on Quality of Fresh Fruits and Vegetables”. *Postharvest Biology and Technology,* **15**, 279-292

Sogo-Temi, C. M., O. A. Idowu and E. Idowu. (2014). “Effect of Biological and Chemical Ripening Agents on the Nutritional and Metal Composition of Banana (*Musa* spp)”. *J. Appl. Sci. Environ. Manage.,* **18**(2), 243-246

J. Myanmar Acad. Arts Sci. 2020 **Vol. XVIII.No.2C**

MEAN-MULTI THRESHOLDING BASED LIVER LESION DETECTION FROM CT SCAN IMAGES

Thida Pyone[1], Aye Aye Thant [2] and Khin Khin Win[3]

Abstract

The objective of this research is the liver lesion regions detection and extraction for diagnostics. It involves four stages in this work such as pre-processing, extraction of liver, detection of liver, segmentation of liver and estimation of lesion regions. The outputs of lesion regions are analyzed from segmented livers. Lesion regions detection stage is used with mean-multi thresholding method and implemented with Matlab Programming language. Hundred data sets of CT abnormal liver images (256 × 256 pixel, 2D liver slices) are tested and lesion regions are calculated from the criteria that the number of gray pixels which are greater than mean value of that block is greater than one-third time of total pixels. The comparative results in this research can be shown with mean value of lesion regions of benign liver CT images is in the range 149-167 and malignant liver CT images is in the range 125-135.

Keywords: CT-liver, lesion regions, detection, extraction.

Introduction

Image processing procedures are very useful appliance in medical diagnosis and surgical operation. Image processing is a quite time-consuming phase. There are various imaging modalities such as Computed tomography (CT) scan, Ultrasound, X-Ray, and Magnetic Resonance Imaging (MRI) can be used to diagnose. The liver is the biggest gland in the body as it can weigh up to 1.5kg in an adult human. It has a central role in the body's metabolism as it secretes bile, a secret that metabolizes many of the essential nutrients for survival (Stewart B, 2014). The novelty of this work is using difference of intensity and texture features between lesion and surrounding area from normal liver tissue to classify liver lesion into benign or malignant. The CT scan is often preferred for diagnosing liver diseases, especially as being considered of high accurate imaging and cheaper than MRI. They have greatly improved the possibility for the human body to examine without using invasive methods. Computed tomography (CT) is an imaging procedure that uses special x-rays equipment to create a series of detailed pictures, or scans, of areas inside the body. X-rays tomography is a technology that uses computer-processed X-rays to produce tomographic images of specific areas of a scanned object, allowing the users to see inside the object without cutting. Digital geometry processing is used to generate a three-dimensional image of the inside of the object from a large series of two-dimensional radiographic images taken around a single axis of rotation.

Related Work

Images of multiple phases are required to detect and diagnose the liver lesions but most publicly available CT datasets contain only the portal phase with pre-pixel segmentation labeling. Automatic liver lesion detection is a fundamental requirement in medical diagnosis. Liver lesion detections were presented in many research works which were tested with computed tomography (CT) images with different models. Kalpana M.K (2011) and his colleagues studied liver noise

---

[1] PhD Candidate, Lecturer, Department of Physics, University of Yangon

[2] Dr, Professor, Department of Physics, University of Yangon

[3] Dr, Professor & HOD, Department of Physics, University of Yangon

detection techniques to determine the upper limit of noise for detection of small low-contrast lesions in a liver phantom. Bi L (2018) and his colleagues presented Deep Residual Networks for Segmentation that liver lesions are segmented automatically. They solved the problem of the training degradation of training accuracy in very deep networks and used additional layers for learning more discriminative features. Lee S-G (2018) and his colleagues proposed the Single Multibox Detector (SSD) based real-world clinical lesion detection which is a deep learning-based object detection model. The strength of this model can leverage richer information of the multi-phase CT data. Their experimental results are tested CT dataset of 64 subjects by five-fold cross validation.

Material and Methods

Experimental procedure

The 100 datasets from 80 patients were acquired from No.2, 500 bedded Military Hospital in Yangon and these liver CT images are 256 by 256 pixel (2D liver slices). These results are obtained using MATLAB R 2018a. The proposed framework is emphasized to early stage detection of liver lesion regions which has four stages, pre-processing, detection of liver, segmentation of liver and detection of lesion regions.

Medical image Filtering

Median filtering is very widely used in digital image processing because under certain conditions, it preserves edges while removing noise. The morphological operators are based on set theoretic approach and are suitable for extracting shape information with the help of a structuring element. Morphological operations are dilation, erosion and opening. Erode and dilate are the fundamental operators of mathematical morphology, a theory for the analysis of spatial structure (Senthilraja. S, March- 2014). Opening operators are generally used as filters that remove dots characteristic of pepper noise and to smooth the surface of shapes in images. It can be generally applied in succession and the number of times they are depends on the structural element size and image structure (Kalpana M. K, 2011). Filling is used to fill the gaps, holes present in the binary image. One of the fundamental morphological operators erosion is a process used to shrink the area of an object in the image. Dilation, expand the images is the complementary process to erosion.

Segmentation of Liver Region

Segmentation is the essential process for detection of the image. This process is separated the liver and other abdominal organs such as stomach, spleen and pancreas etc. Generally, liver segmentation methods are divided into two main classes, semi-automatic and fully automatic methods, under each of these two categories, several methods, approaches, related issues and problems will be defined and explained (Alagdar M.A, 2015; Lagdar .M.A.A,2015). The aim of segmentation is to represent an image to be more meaningful and easier to analyze. And then, segmentation could be used to diagnose and study of anatomical structures or localization of pathologies such as cancer tumors but it is a still challenging problem in medical image. The detection of liver region is the most important for early diagnosis and treatment of liver diseases. Medical image detection can be used to estimate of the boundary of an object, classification of tissue abnormalities, shape analysis, contour detection (Nader H. Abdel-massieh, 2010).

Nevertheless, the model generation is time consuming and could not respond sensitively among different patients. The grayscale image and dilated binary image are masked out in this step.

Detection of Lesion Regions

The detection of liver Lesion regions is the essential step for early diagnosis and treatment of liver diseases. Segmented liver images are blocked 8X8 that mean value, maximum value and minimum value are calculated in each block. The block has no lesion if all pixels of each block is normally distributed of grayscale value. Otherwise most of intensity gray values are fluctuated in each block, that block may have lesion.

Results and Discussion

Pre-processing is the first step of our proposed framework which has grayscale conversion, binarilization, text noise removing and morphological opening processes. The better preprocessed images gives more precise liver from other organs. Input image is converted to grayscale image and then binarilized. The tested images are satisfied with threshold value 0.4256. The patient information of text are removed with filters and morphological opening processes. Morphological dilation processes and some filtering processes are help to process in the liver detection mask. Figure 1-5 are the output liver images of pre-processing step and detected liver region is shown in figure 6 .It is the second step of proposed framework.

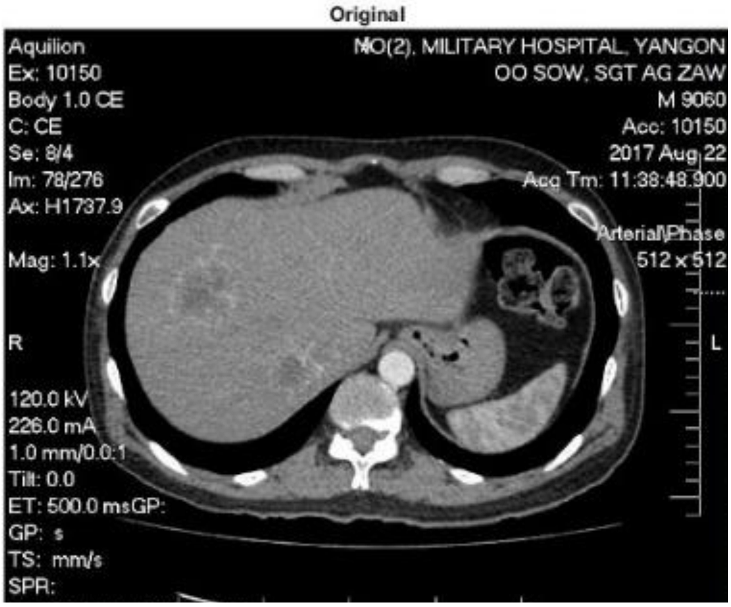

Figure 1 Original Liver Image

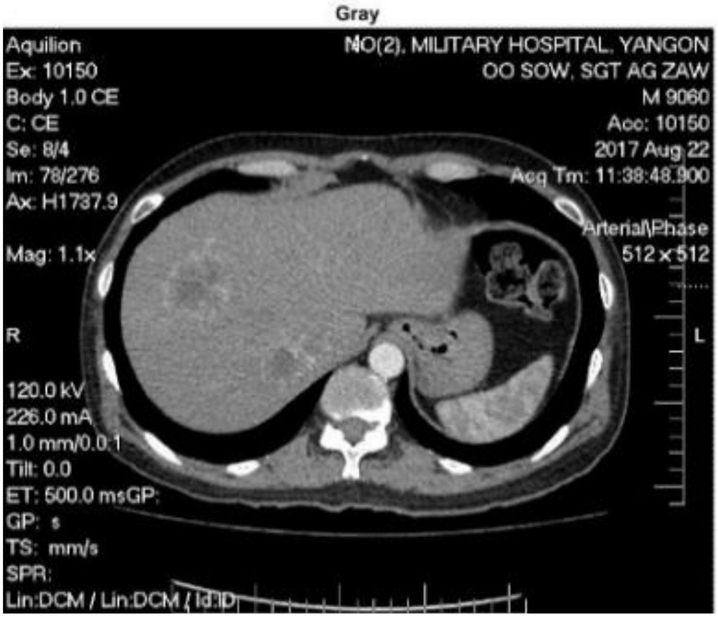

Figure 2 Grayscale Liver Image

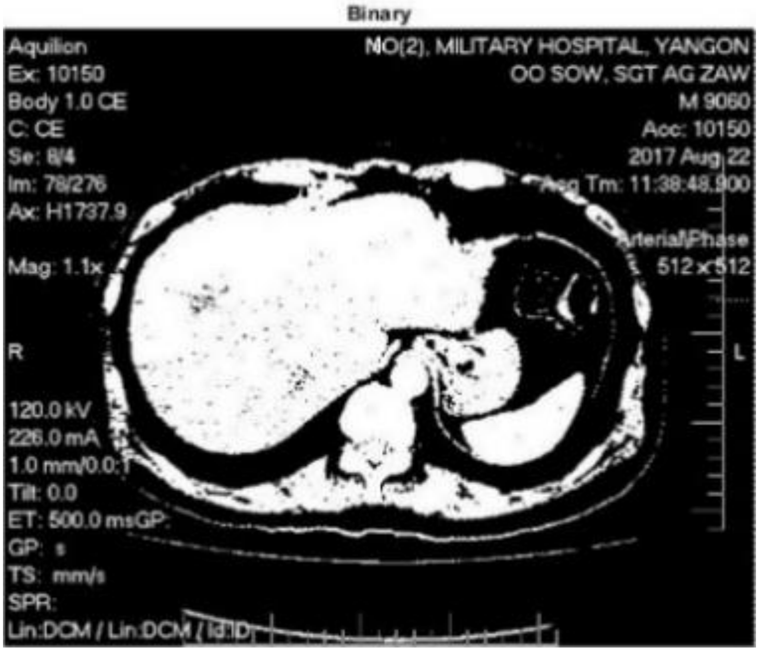

Figure 3 Binary Liver Image

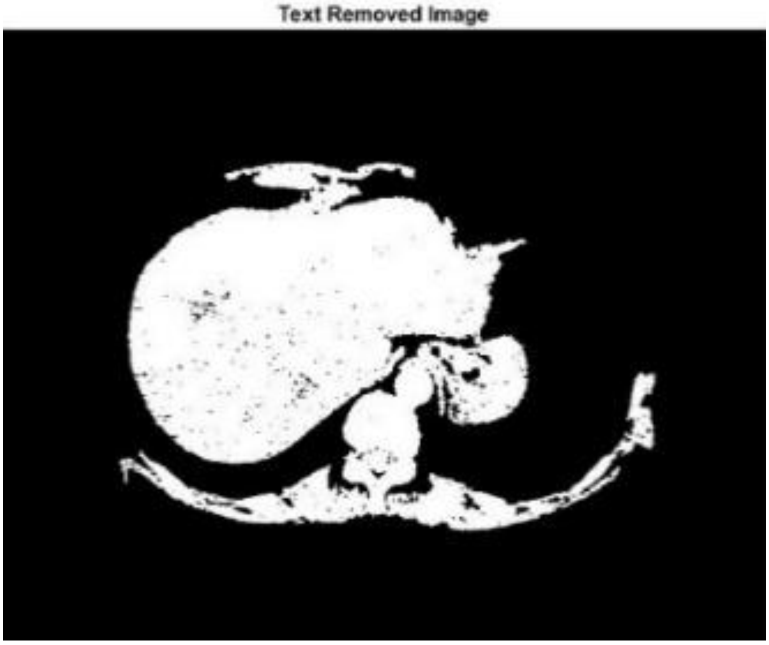

Figure 4 Text Noise Removed Liver Image

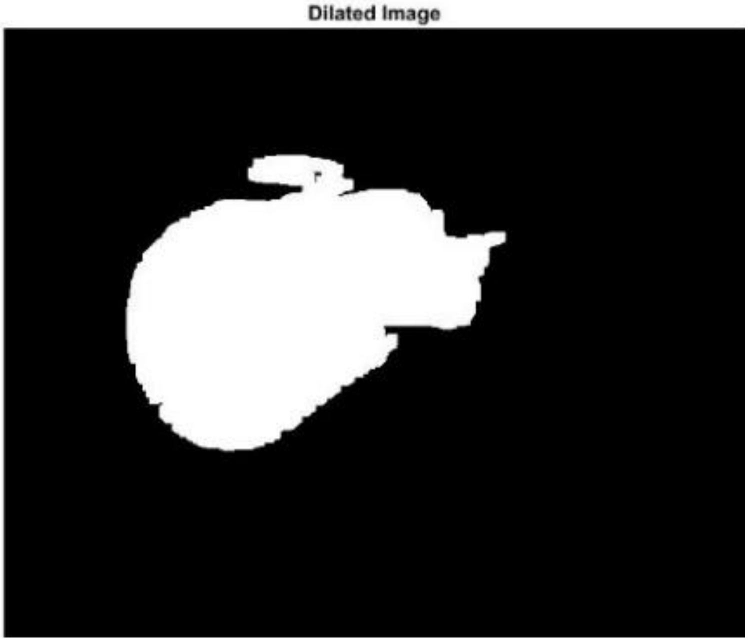

Figure 5 Dilated Liver Image

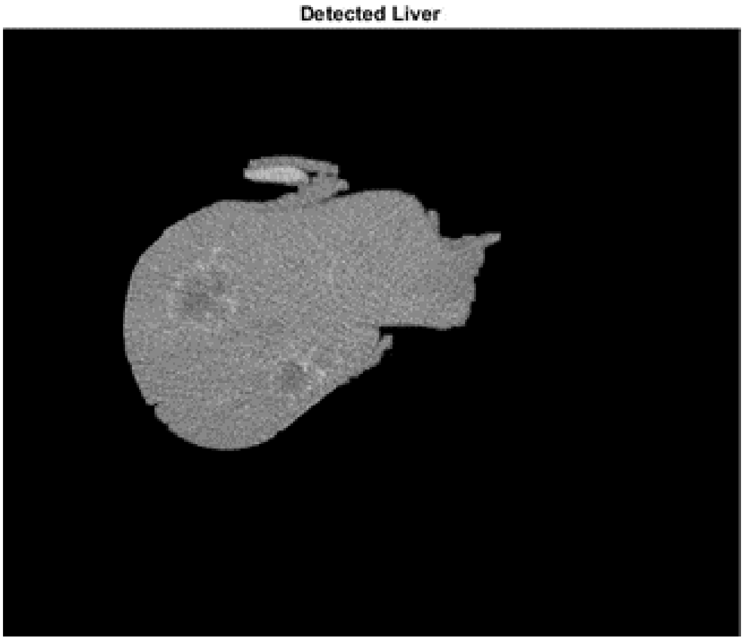

Figure 6 Detected Liver Image

The grayscale image and dilated binary image are masked out in this step. In the third step, the histogram value of detected liver image are calculated and finding the points A, B, C and D which points are the left top point of detected liver, right top point, left bottom point and right bottom point respectively shown in Figure 7. By using these points, the segmented liver are automatically as shown in figure 8.

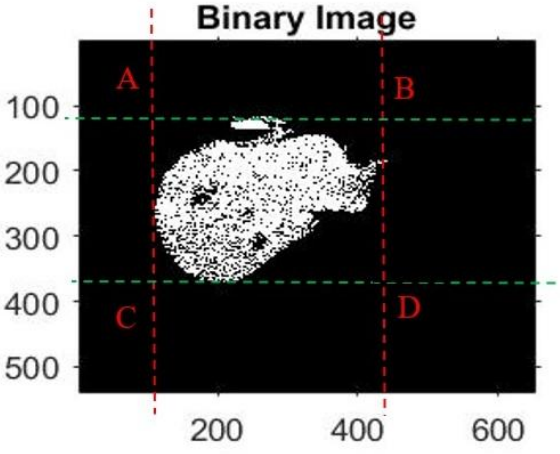

Figure 7 Finding liver edge D

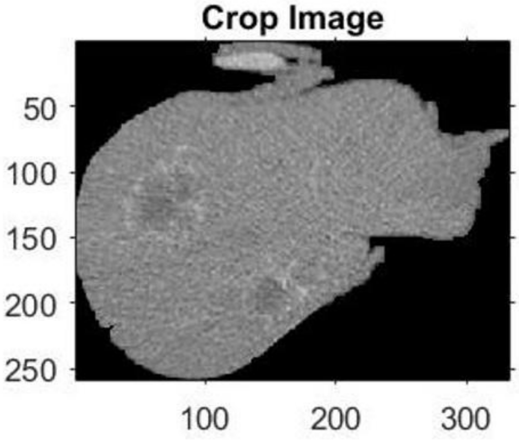

Figure 8 Segmented Liver Image

In this research work, detection constant φ *is* $\frac{1}{3}$. Samples of lesion regions by performing with grayscale intensity matrix are shown in Figure 9 and 10. Mean value can be calculated from equation (1) and (2) count the number of pixels which intensity value is greater than mean value of respective block. The CT scan images are tested and lesion regions are calculated from the criteria that the number of gray pixels which are greater than mean value of that block is greater than one-third time of total pixels.

$$\mu = \frac{\sum_{i=1}^{N} X_i}{N} \quad (1)$$

$$C(B_k) = \begin{cases} 1 & X_i > \mu \\ 0 & otherwise \end{cases} \quad (2)$$

Where μ= mean value of each block

N= Number of pixels of each block

C (B_k) = Count of pixels which are greater than mean value

If Lesion Region satisfies the following condition:

C (B_k) > M_k × φ then B_k is Lesion Region.

M_k = Number of pixels in B_k

φ = Detection Constant

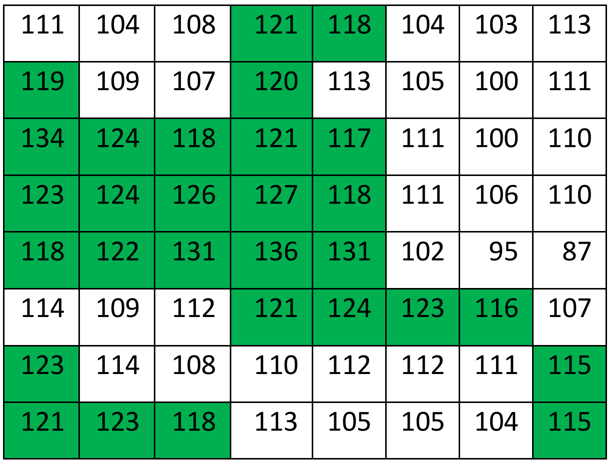

111	104	108	121	118	104	103	113
119	109	107	120	113	105	100	111
134	124	118	121	117	111	100	110
123	124	126	127	118	111	106	110
118	122	131	136	131	102	95	87
114	109	112	121	124	123	116	107
123	114	108	110	112	112	111	115
121	123	118	113	105	105	104	115

$\mu = 114.109, min = 87, max = 136,$
$C(B_k) = 29, M_k = 64, \varphi = \frac{1}{3}$

Figure 9 Sample of Liver Lesion Region

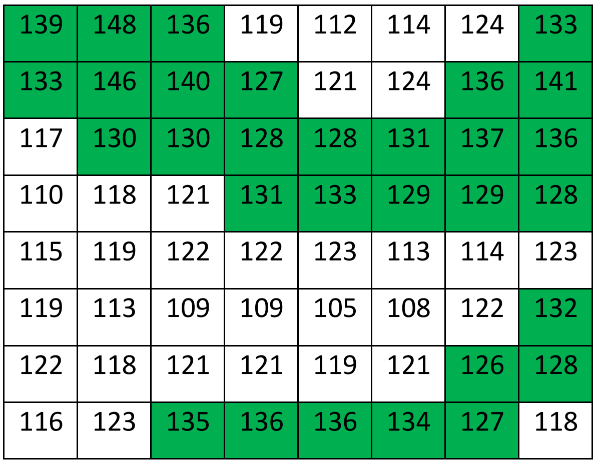

139	148	136	119	112	114	124	133
133	146	140	127	121	124	136	141
117	130	130	128	128	131	137	136
110	118	121	131	133	129	129	128
115	119	122	122	123	113	114	123
119	113	109	109	105	108	122	132
122	118	121	121	119	121	126	128
116	123	135	136	136	134	127	118

$\mu = 124.969, min = 105, max = 148,$
$C(B_k) = 30, M_k = 64, \varphi = \frac{1}{3}$

Figure 10 Sample of Liver Lesion Region

Morphological dilation is used to refine the segmentation results. Segmented liver images are blocked 8X8 that mean value, maximum value and minimum value are calculated in each block are shown in table 1 and 2. The block has no lesion if all pixels of each block is normally distributed of grayscale value. Mean value of lesion regions which benign liver CT images is in the range 149-167. Mean value of lesion regions which malignant liver CT images is in the range125-135.

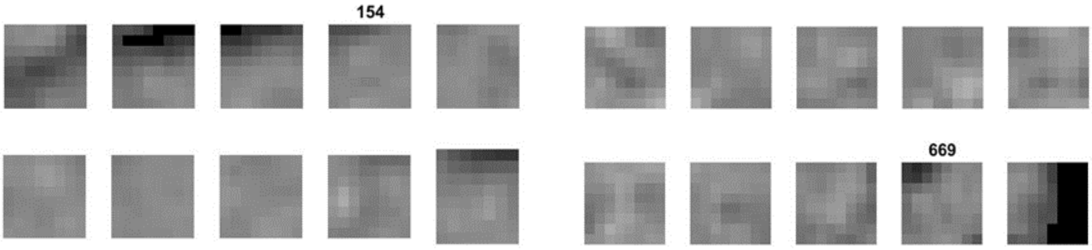

Figure 11 Block 154 and 669 are Lesion Regions

Table 1 Some Experimental results of benign liver region

Input CT image	Mean	Maximum	Minimum
B_1	167.0012	180.0033	162.0051
B_2	164.0002	166.0012	1640031
B_3	180.0000	181.0005	171.0011
B_4	163.0101	181.0001	158.0521
B_5	161.0112	150.1205	148.0001
B_6	156.1006	179.0044	170.0054
B_7	152.3621	150.8731	150.7764
B_8	138.9218	145.9425	142.0000
B_9	145.9924	144.0987	137.0041
B_10	149.8754	150.01115	149.7691
B_11	152.0019	145.1409	138.5241

Table 2 Some Experimental Results of malignant liver region

Input CT Image	Mean	Maximum	Minimum
M _1	135.2811	136.5659	134.0151
M _2	122.0147	121.9938	133.7781
M _3	126.4311	128.8140	126.4082
M _4	125.5576	122.6940	121.1616
M _5	128.3201	133.9364	133.6906
M _6	135.4928	140.1780	138.8933
M _7	115.7018	126.9384	128.1335
M _8	150.2997	148.1046	147.6892
M _9	128.0763	126.7986	123.5444
M _10	129.0208	129.6627	128.7222
M _11	157.6499	150.0308	160.8747

Conclusion

A grayscale image is a data matrix whose values represent intensities within some range. MATLAB stores a greyscale image as an individual matrix, with each element of the matrix corresponding to one image pixel. In this study, the step of the algorithm adaptive morphological operations are performed including largest connected component selection, hole filling and morphological opening. In order to check the accuracy of automated segmented from all liver region images is segmented manually by the radiologist and oncologist. After tested hundred segmented liver images and are obtained 70% of lesion regions are detected with detection constant one third in this experimental results. The block size in this research is 8×8 and therefore the comparison of mean value of the regions will be performed by using different block sizes and various detection constants. It is expected to identify liver tumor and liver diseases in our future work.

Acknowledgements

The author would like to express my gratitude to my Supervisor Professor Dr Khin Khin Win, Head of Department of Physics, and University of Yangon for her kind permission to carry out this work, then for her supervision, helpful advice and valuable suggestion.

I wish to show my sincere thanks to my Co-Supervisor Professor Dr Aye Aye Thant, Department of Physics, University of Yangon, for her discussion and suggestion in this work.

We would like to thank all the people who encourage and support me during the undertaking of this work.

References

Alagdar M.A., M.E. Morsy, M.M. Elzalabany "Segmentation of Liver CT Images". *Applied Science & Engineering Technology (IJRASET)*. 2015; 3(IX): 2321-9653.

Bi L, J Kim, A Kumar, D Feng. "Automatic liver lesion detection using cascaded deep residual Networks". *Compos Sci Technol.* 2018; 1704.00436v1

Gonzalez R. C, & R. E Woods and S. L Eddins, (2009), “Digital Image Processing using MATLAB*”*, 2ndEdition.

Kalpana M. K, H .Jonathan, Chung, J Wang, P Bhargava, R. Jennifer. Kohr, P William. Shuman, K. Brent Stewart. "Image Noise and Liver Lesion Detection with MDCT". *Medical Physics and Informatics*.2011.

Lagdar .M.A.A, & M.E Morsy and M.M Elzalabany (2015), "Segmentation of Liver CT Images",Monsoura University, Egypt.

Lee S-G, J Seok Bae , H Kim , J Hoon Kim , Yoon. Liver Lesion Detection from Weakly-labeled Multi-phase CT Volumes with a Grouped Single Shot MultiBox Detector. *Electrical and Computer Engineering* 2018; 1807.00436v1.

Nader H. Abdel-massieh, Mohiy M. Hadhoud, Kamel A. Moustafa (2010), "A Fully Automatic and Efficient Technique for Liver Segmentation from Abdominal CT Images", Menoufia University.

Senthilraja. S, Suresh .Dr.P, Suganthi.Dr.M. (March-2014) “, Noise Reduction in Computed Tomography”, International Journal of Scientific & Engineering Research, Vol-5, Issue 3.

Stewart B. Wild C. P, World cancer report 2014, *Medical Physics*. 2014.

J. Myanmar Acad. Arts Sci. 2020 **Vol. XVIII.No.2C**

STUDY ON THE VARIOUS ANNEALING PROCESSES OF CUO-MNO$_2$-ZNO ELECTROLYTE FOR LOW-TEMPERATURE SOLID OXIDE FUEL CELLS

Nang Htoo[1], Than Than Win[2], Yin Maung Maung[3]

Abstract

CuO-MnO$_2$-ZnO (CMZO) mixed oxide was prepared by solid state reaction for the purpose of low temperature solid oxide fuel cell (LTSOFC) applications. Solid-oxide fuel cells (SOFCs) promise high efficiencies in a range of fuels. CuO–MnO$_2$–ZnO mixed oxides with different Cu : Mn : Zn atomic ratios were obtained at 200°C, 300°C, 400°C and 500°C in 1 h. The change in the annealing temperature had a significant influence on the structural, surface morphology and optical properties. Powder X-ray diffraction and scanning electron microscopy with energy dispersive X-ray diffraction spectroscopy confirm the phase purity and the particle size of CMZO mixed oxide. Based on optical absorbance measurements, it was shown that CMZO with higher annealing temperature were characterized by a higher cut-off wavelength and lower optical band gap energy.

Keywords: mixed oxide; solid state reaction; X-ray diffraction; surface morphology, optical properties

Introduction

A composite material (also called a composition material or shortened to composite, which is the common name) is a material made up of two or more constituent materials with major different physical or chemical properties, that combines to produce a material with different features from the individual components. The individual component remain separate and distinct within the finished structure, differentiation composites from mixtures and solid solutions [McEvoy.M.A.et.al (2015)]. Due to its strangeness, lightness or less expensiveness, it is favoured to traditional materials [Science.et.al (2015)]. ZnO has got an agreement of attention in the application of electronics and optoelectronics such as battery active materials, solar cells, gas sensors and light-emitting diodes due to its good electrochemical activity, well-known surface conductivity, high electron mobility, wide bandgap and eco-friendly nature [S.Zaman.et.al (2012)]. ZnO, a wide band gap (3.37eV) n-type semiconductor, have a large excition binding energy (60meV) and piezoelectric properties [Y.P.Gao.et.al (2007)]. CuO is an important narrow band gap (1.3eV) p-type semiconductor with many applications in sensors, catalysis, batteries, high temperature superconductors, solar cells and field emitters [R.Saravanan.et.al (2013)]. Among the available metal oxides, MnO$_2$ receives much attention due to its prospective application in the field of catalytic and electrochemical applications. Due to the low cost and plenty of MnO$_2$, it can compare to other metal oxides [Fanhui Meng.et.al (2013)]. Composite nanostructures of these two wide and narrow band gap semiconductors may offer united functionalities and open the way for new enhanced applications, such as photocatalysts [T.Chang.et.al (2013)], gas sensors [A.Zainelabdin.et.al(2012)], humidity sensors [T.Soejima. et.al (2013)], biosensors [M.H.Habibi.et.al (2013)] and solar cell [Jianmin Shen.et.al (2012)].

---

[1] Assistant Lecturer, Physic Department, Dangon University

[2] Physics Department, Panglong University

[3] Department of Physics, University of Yangon

Materials and Methods

The raw materials of CuO, MnO_2 and ZnO were chosen as starting materials. The purity of materials was characrterized by X-ray diffraction (XRD). ZnO (60mol%), CuO(20mol%) and MnO_2 (20mol%) were mixed according to the stoichometric ratio by solid state reaction method to form composite. Physical grinding method is adopted in this experiment for the size reduction of CMZO material. The CuO-MnO_2-ZnO material was put in a ball milling machine which having high speed rotator. It was grinded for 3h then annealed at 200˚C, 300˚C, 400˚C and 500˚C. In the present work, the preparation and characterization of CMZO composite by using solid state reaction method. The resultant samples obtained by this method were be measured by XRD, SEM and UV-visible absorption spectrum to calculate the effect of different temperature at the same time on the formation of crystalline structure, morphological features and optical properties of the resultant composite.

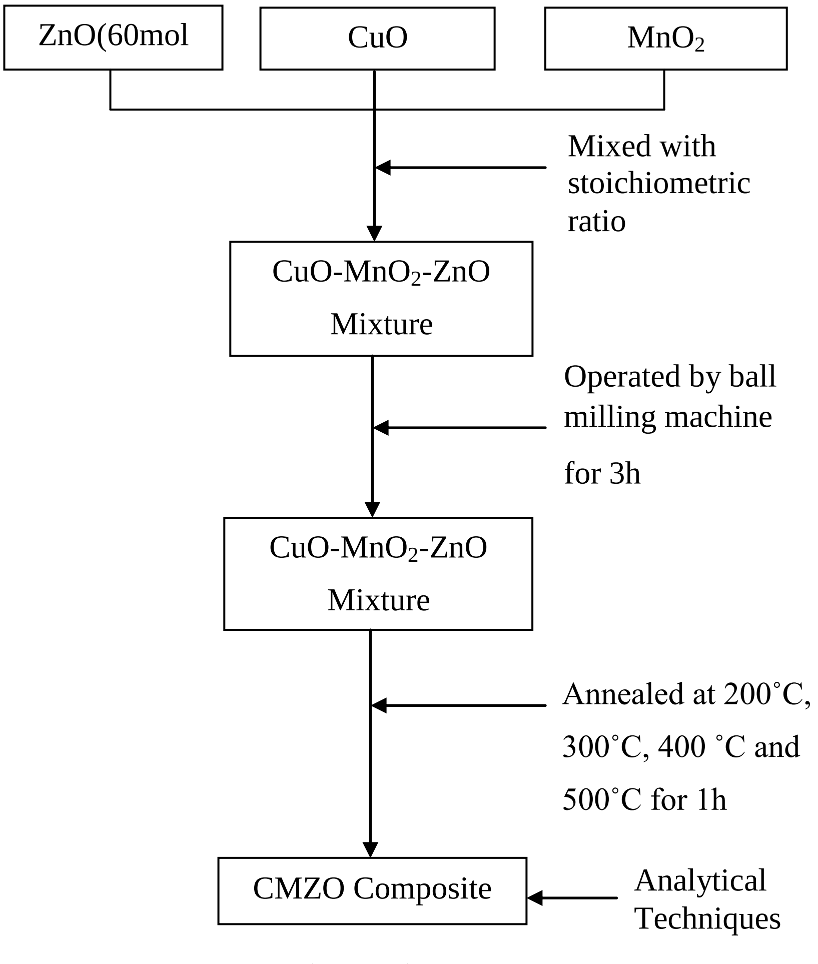

Figure 1 CuO-MnO_2-ZnO (CMZO) composite preparation sequence

Results and Discussion

The crystal structure was confirmed by XRD. The XRD diffraction patterns for CuO-MnO_2-ZnO(CMZO) nanoparticles after annealing at 200˚C, 300˚C, 400˚C and 500˚C was shown in figure 2(a-d). After annealing at given temperature, the composites was a mixture of the individual binary oxide phases co-existing in one material. Some reflection peaks were not matched with the standard peak. The intensity of XRD peaks of the sample reflects that the formed nanoparticles are crystalline and broad diffraction peaks indicate small size cryatallite. The CuO phase crystallized in the monoclinic crystal structure, MnO_2 in tetragonal and ZnO in hexagonal.

XRD technique is capable of gathering many useful information relating the crystal structure. In this research work, X-ray diffractrometer was used for the phase analysis of the films calcined at different temperatures using Cu-$K\alpha_1$ radiation (λ=1.54056Å) at an accelerating voltage of 40kVand a current of 50mA. The film samples were mounted on a flat XRD plate and scanned at room temperature in the range $10 \leq 2\theta \leq 70$. X-ray line broadening technique was used to determine crystallite size of the films calcined at different temperatures using Scherrer formula,

$$G = \frac{0.9 \times \lambda(\AA)}{B(rad) \times \cos\theta_B}$$

Where G is the crystallite size, B is the full width at half-maximum XRD peak in radians, λ is the wavelength of the X-ray radiation and θ_B is the Bragg angle in radians. XRD data of CMZO composite was shown in table 1(a-c).

Table 1(a) XRD data of CMZO material for CuO

Temp (˚C)	cosθ	FWHM (rad)	Crystallize Size (nm)
200	0.94	0.005	34.76
300	0.95	0.005	42.93
400	0.94	0.004	41.10
500	0.95	0.006	29.72

Table 1(b) XRD data of CMZO material for ZnO

Temp (˚C)	cosθ	FWHM (rad)	Crystallize Size (nm)
200	0.93	0.002	78.96
300	0.92	0.002	65.92
400	0.92	0.004	42.83
500	0.93	0.004	57.09

Table 1(c) XRD data of CMZO material for MnO_2

Temp (˚C)	cosθ	FWHM (rad)	Crystallize Size (nm)
200	0.92	0.004	48.32
300	0.93	0.004	53.30
400	0.93	0.005	35.08
500	0.89	0.006	53.89

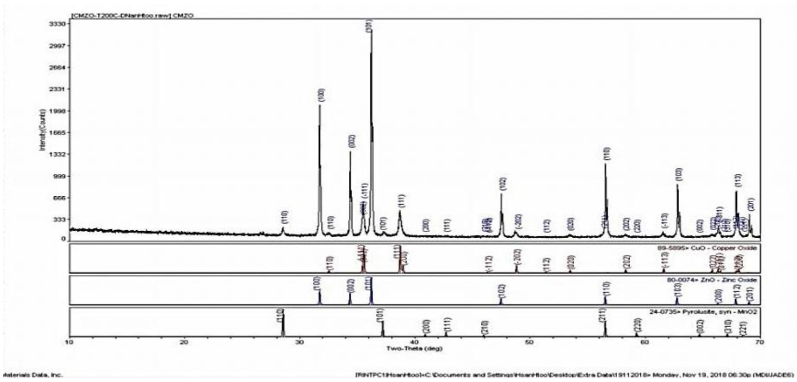

Figure 2(a) XRD pattern of CMZO material at annealing 200˚C

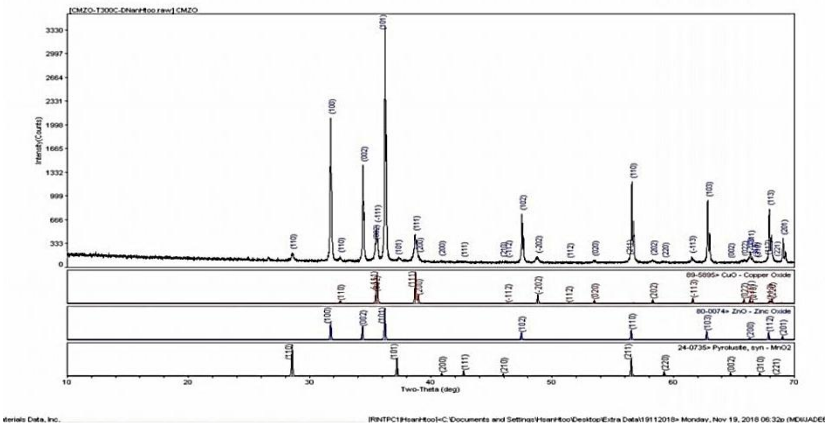

Figure 2(b) XRD pattern of CMZO material at annealing 300˚C

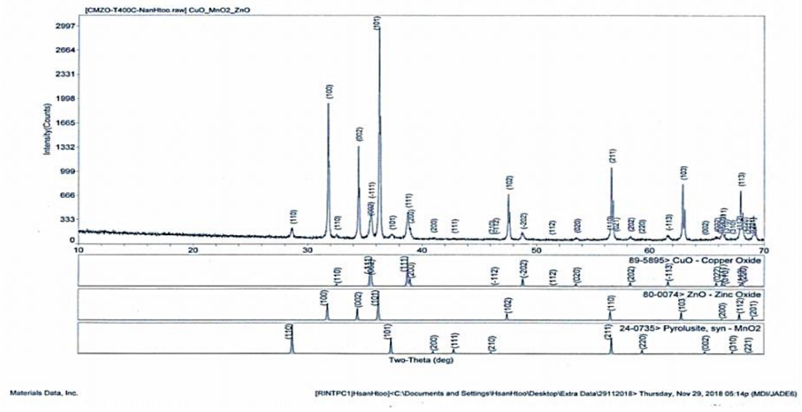

Figure 2(c) XRD pattern of CMZO material at annealing 400˚C

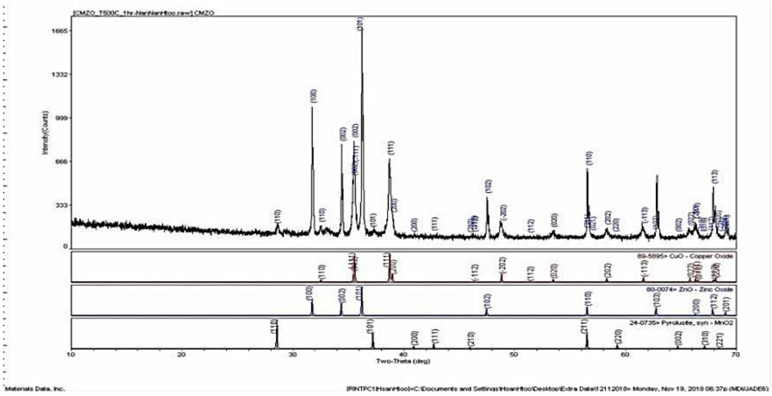

Figure 2(d) XRD pattern of CMZO material at annealing 500˚C

A Scanning Electron Microscope was used to chatacterize the morphological feature of the CMZO composite after calcination at 200˚C - 500˚C for 1h and showed in figure 3(a-d). To determine the elemental composition, EDX mapping as well as point analysis were used as a selected area. CMZO composite were composed of non-homogeneous mixed clusters with different elements. Table 2(a-d) showed elemental composition of CMZO composite

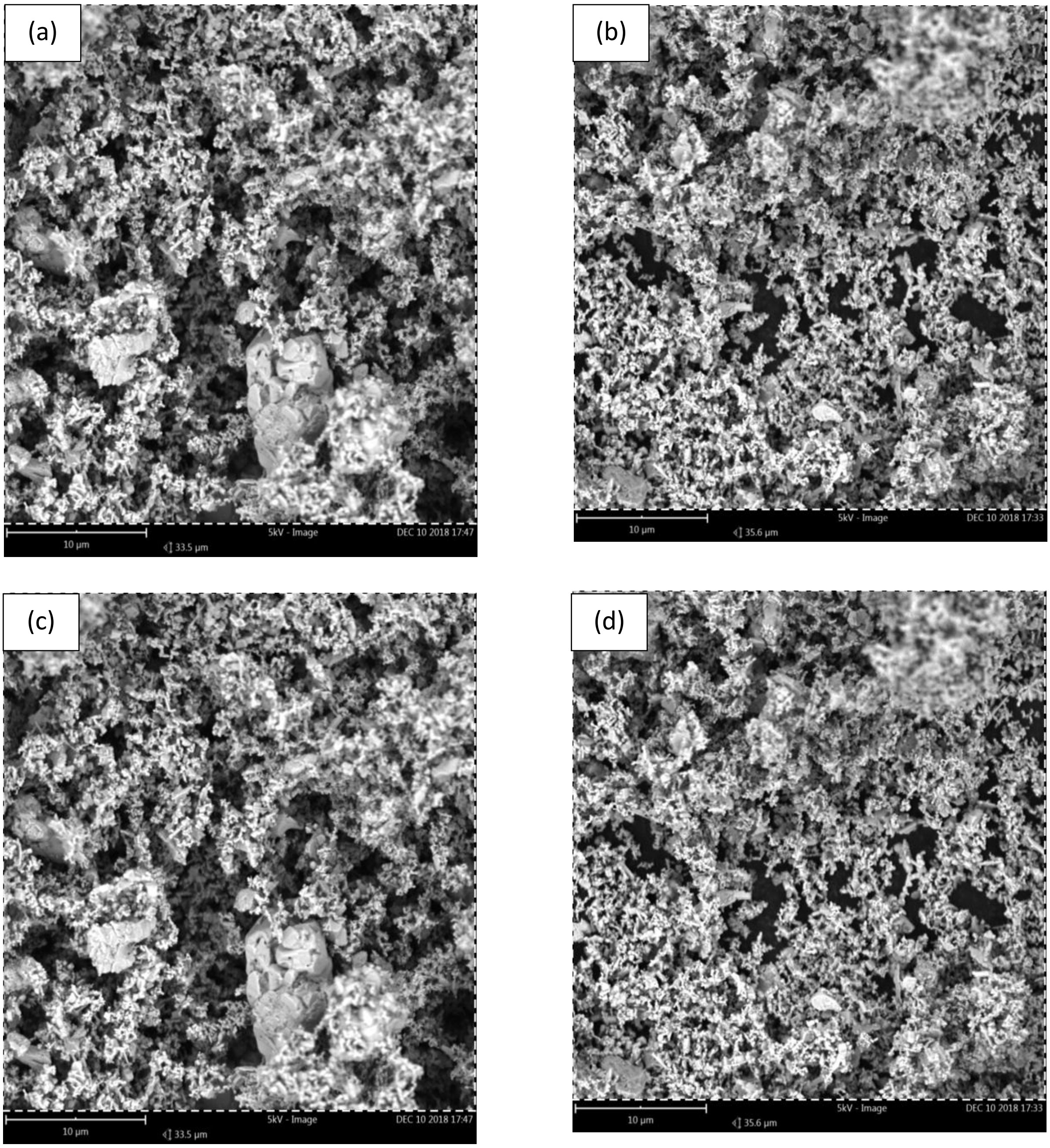

Figure 3 SEM image of CMZO composite (a) at 200ºC/1h (b) at 300ºC/1h (c) at 400ºC/1h (d) at 500ºC/1h

Table 2 Elemental composition CuO-MnO_2-ZnO (CMZO) mixed oxide composite determined by EDX at various point

(a) at 200ºC/1h

Elements	Position 1 (%)	Position 2 (%)
O	46.83	75.26
Cu	2.59	0
Mn	0	18.06
Zn	50.40	6.61

(b) at 300ºC/1h

Elements	Position 1 (%)	Position 2 (%)	Position 3 (%)	Position 4 (%)
O	41.81	27.95	32.64	17.00
Cu	2.30	34.56	0	0
Mn	0	0	0	0
Zn	55.70	37.50	47.55	79.33

(c) at 400ºC/1h

Elements	Position 1 (%)	Position 2 (%)
O	14.00	13.32
Cu	8.30	11.14
Mn	0	0
Zn	73.33	59.64

(d) at 500ºC/1h

Elements	Position 1 (%)	Position 2 (%)	Position 3 (%)
O	46.02	43.70	41.74
Cu	11.25	32.41	8.05
Mn	0	0	0
Zn	42.66	23.81	44.55

UV-vis absorption spectroscopy is widely used tool for checking the optical properties of nanosized particles. Figure 4(a-d) showed the absorption spectrum of CMZO composite at different annealing temperature (200˚C, 300˚C, 400˚C and 500˚C). The absorption coefficient can be calculated by using this equation,

$$\alpha = \frac{2.303\,A}{t}$$

Where, α is the absorption coefficient, A is absorbance and t is sample holder thickness. From the spectrums, the absorbance and relation wavelengths of CMZO composite at different temperatures were described in table 3(a-d). Figure 5(a-d) showed the values of $(\alpha h\upsilon)^2$ plotted against hυ. The energy band gap of the composite E_g was determined by extrapolating the linear of the plot to the hυ axis. The resultant value of E_g for CMZO composite were found to be about 3.27eV, 3.7eV, 3.1eV and 3.25eV at different temperature.

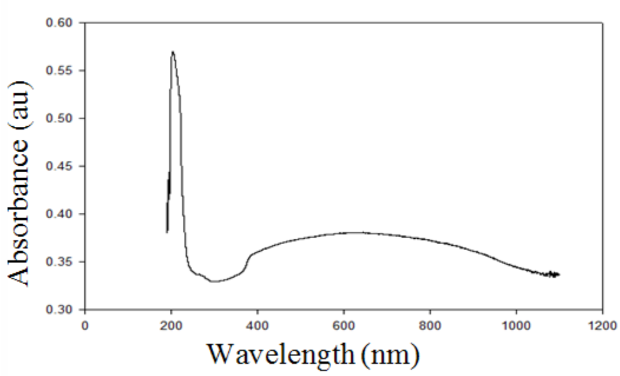

Figure 4(a) Absorbance spectrum of CMZO composite at 200˚C

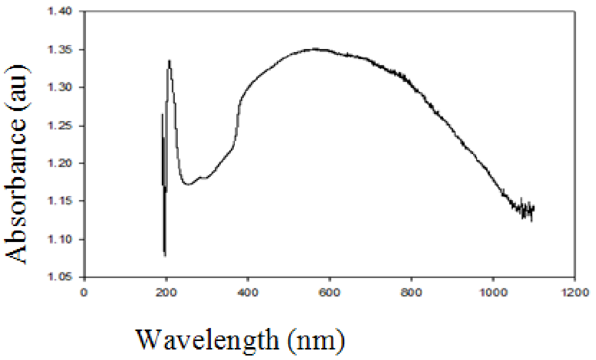

Figure 4(b) Absorbance spectrum of CMZO composite at 300˚C

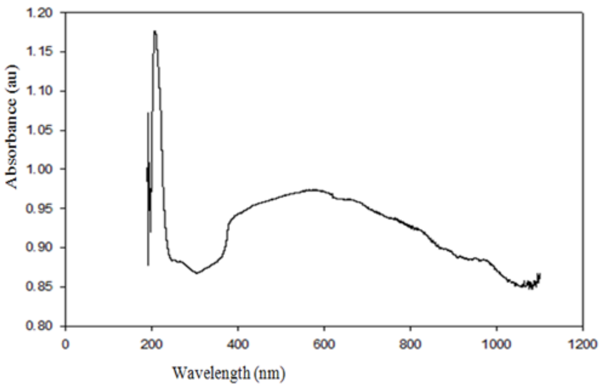

Figure 4(c) Absorbance spectrum of CMZO composite at 400˚C

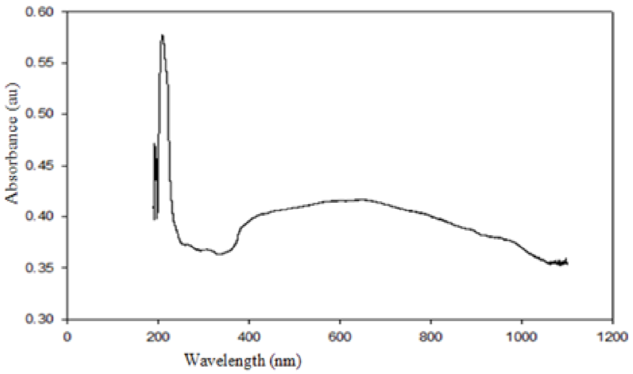

Figure 4(d) Absorbance spectrum of CMZO composite at 500˚C

Table 3 (a) Absorbance and wavelength of CMZO composite from absorption spectrum at 200˚C

No	Absorbance (au)	Wavelength (nm)
1	0.570	203.368
2	0.443	194.200
3	0.381	644.000

Table 3 (b) Absorbance and wavelength of CMZO composite from absorption spectrum at 300˚C

No	Absorbance (au)	Wavelength (nm)
1	1.351	570.011
2	1.336	207.655
3	1.324	750.955
4	1.320	772.977
5	1.316	782.377
6	1.280	845.912

Table 3 (c) Absorbance and wavelength of CMZO composite from absorption spectrum at 400˚C

No	Absorbance (au)	Wavelength (nm)
1	0.577	208.902
2	0.472	192.175
3	0.468	194.917
4	0.417	648.752

Table 3 (d) Absorbance and wavelength of CMZO composite from absorption spectrum at 500˚C

No	Absorbance (au)	Wavelength (nm)
1	1.177	207.426
2	1.074	192.198
3	1.011	193.764
4	0.976	195.855
5	0.974	578.983

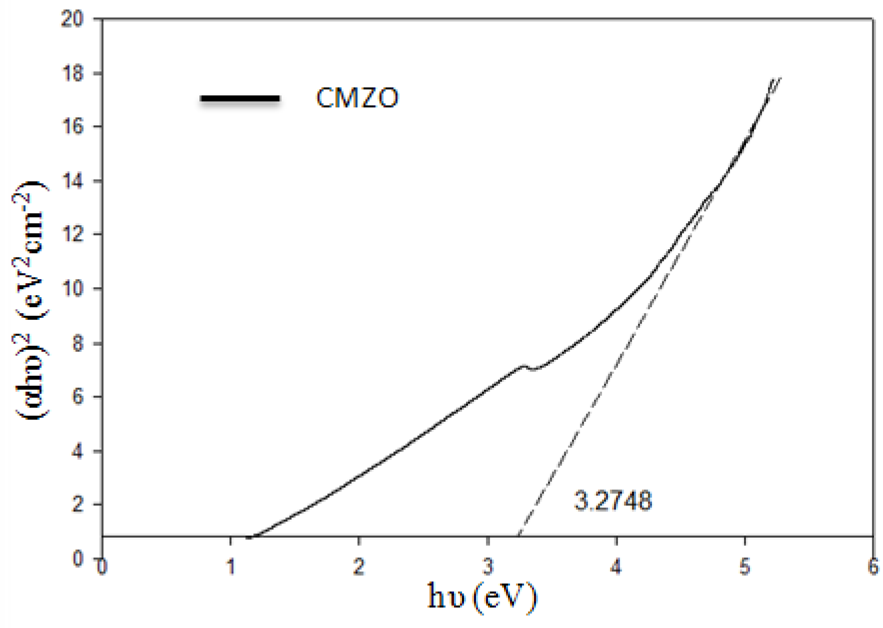

Figure 5(a) Plot of $(\alpha h\upsilon)^2$ versus photon energy (hυ) of CMZO composite at 200˚C

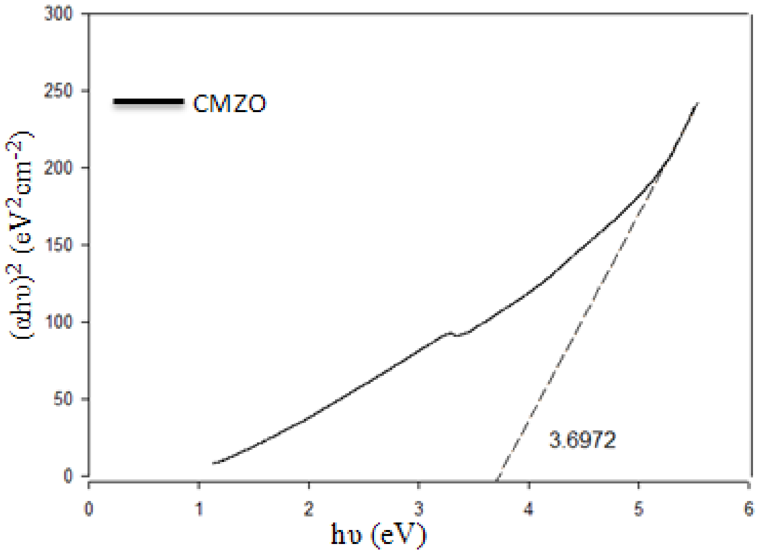

Figure 5(b) Plot of (αhυ)^2 verus photon energy (hυ) of CMZO composite at 400˚C

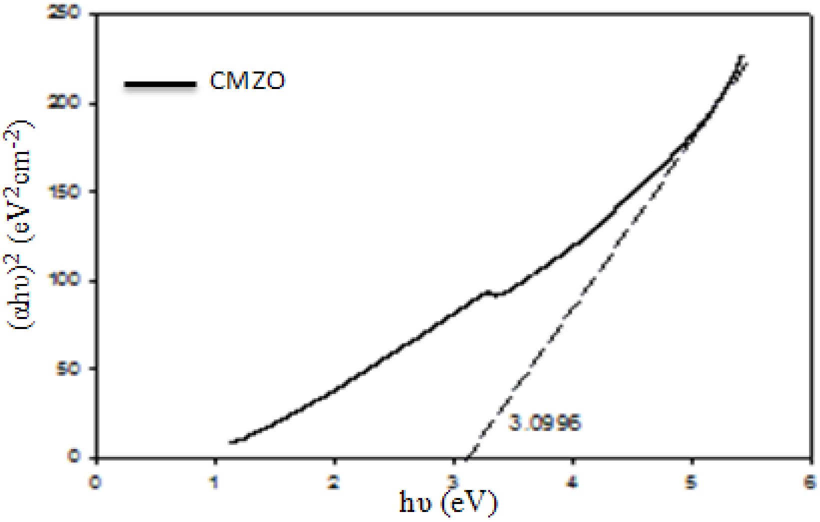

Figure 5(c) Plot of (αhυ)^2 versus photon energy (hυ) of CMZO composite at 400˚C

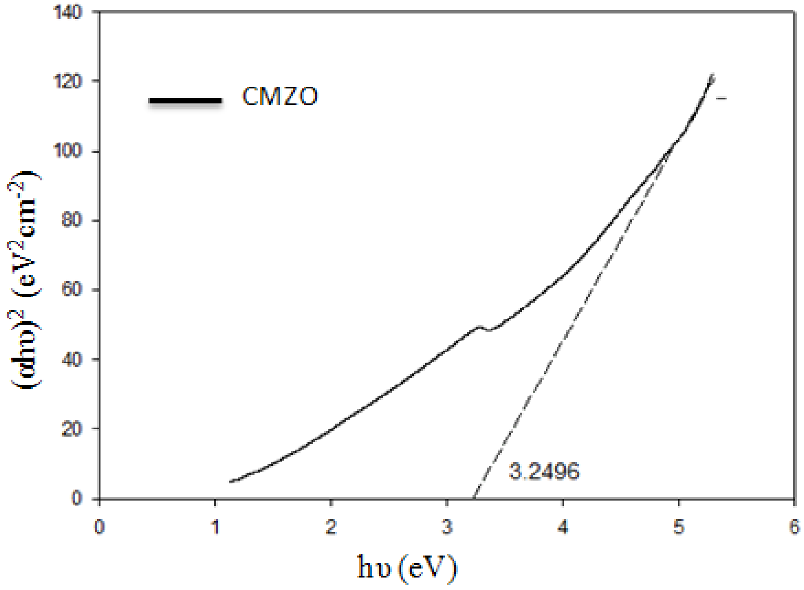

Figure 5(d) Plot of (αhυ)^2 versus photon energy (hυ) of CMZO composite at 500˚C

Conclusion

CuO-MnO_2-ZnO (CMZO) mixed oxide was prepared by solid state reaction method and annealed at 200˚C, 300˚C, 400˚C and 500˚C. CuO-MnO_2-ZnO (CMZO) phases were observed from the XRD measurements after annealing the sample at given temperatures. XRD studies showed distinct monoclinic for CuO, tetragonal for MnO_2 and hexagonal for ZnO. The crystallite sizes was found to be between 29 nm and 42 nm for CuO, 43-79 nm and for ZnO and 35-53 nm for MnO_2. The average crystallite sizes for the three oxide phases in the composite were found to be between 30 nm and 79 nm. These results introduce multiphase mixed oxide composite. SEM data showed that the distribution of Cu, Mn and Zn was not uniform across the selected area of the sample, which suggested that the oxides were not uniformly intermixed in the composite. The observed band gap of 3.27eV, 3.7eV, 3.1eV and 3.25eV lie between that of CuO, MnO_2 and ZnO. It is possible to use in anode or cathode of solid oxide fuel cell.

Acknowledgements

I would like to thank Professor Dr Khin Khin Win, Head of Department of Physics, University of Yangon for her kind permission to carry out this research work. I greatly indebted to my supervisor Dr Yin Maung Maung, Professor, Department of Physics, University of Yangon and Co-supervisor Dr Than Than Win, Professor, Department of Physics, University of Panglong for their kind and wise discussions.

References

A. Zainelabdin, G. Amin, S. Zaman et al., (2012) "CuO/ZnO Nanocorals synthesis via hydrothermal technique: growth mechanismand their application as Humidity Sensor,"Journal of Materials Chemistry, (22), (23), 11583–11590.

Fanhui Meng., Xiuling Yan., Ye Zhu., Pengchao Si., (2013) Nanoscale Res. Lett. (8), (179).

Jianmin Shen., Andong liu., Yu Tu, Hong Wang., Rongrong Jiang., Jie Ouyang., Yuan Chen., (2012), Electrochim.cta. (78), (122).

McEvoy, M. A.; Correll, N. (2015). " Materials that couple sensing, actuation, computation and communication".

M. H. Habibi, B. Karimi, M. Zendehdel, and M. Habibi, (2013) "Fabrication, characterization of two nano-composite CuO-ZnO working electrodes for dye-sensitized solar cell, "Spectrochimica Acta A: Molecular and Biomolecular Spectroscopy, (116), 374–380.

R. Saravanan, S. Karthikeyan, V. K. Gupta, G. Sekaran, V.Narayanan, and A. Stephen, (2013) "Enhanced photocatalytic activityof ZnO/CuO nanocomposite for the degradation of textile dyeon visible light illumination," Materials Science and Engineering C, (33), (1), 91–98,.

Science.Archived from the original on (2015-03-23) doi: 10.1126/science.1261689. (**347),** (6228).

S. Zaman, (2012) Synthesis of ZnO, CuO and their composite nanostructures for optoelectronics, sensing and catalytic applications [Ph.D.dissertation], Link¨ oping University, Norrk¨ oping, Sweden.

T. Chang, Z. Li, G. Yun, Y. Jia, and H. Yang, (2013) "Enhanced photocatalytic activity of ZnO/CuO nanocomposites synthesized by hydrothermal method," Nano-Micro Letters, (5), (3), 163–168.

T. Soejima, K. Takada, and S. Ito, (2013) "Alkaline vapor oxidation synthesis and electrocatalytic activity toward glucose oxidation of CuO/ZnO composite nanoarrays," Applied Surface Science, (277), 192–200.

Y. P. Gao, C. N. Sisk, and L. J. Hope-Weeks, (2007) "A sol-gel routeto synthesize monolithic zinc oxide aerogels," Chemistry of Materials, (19), (24), 6007–6011.s

J. Myanmar Acad. Arts Sci. 2020 **Vol. XVIII.No.2C**

ANALYSIS OF GROUND WATER SAMPLES AND THEIR POSSIBLE HEALTH EFFECTS IN MON STATE

Shwe Sin Oo[1], Nyein Thida[2], Aye Aye Mar[3], Shwe Nan Htet[4]

Abstract

Analysis of water sample is one of the major issues during water quality monitoring of either surface or ground water sources. The objective of this study was to determine elemental concentration, some properties of ground water of hand-dug wells in one village of Mawlamyine district and two villages of Thaton district at Mon State, Myanmar and also their possible effects on the health of the inhabitants. Apparently, ground water in most countries is contaminated by the large number of chemical fertilizer used in our daily life and disposal of massive industrial effluents and mining activities. These wastes have negative effects on human health. Different waste products have different affects depending on their locations and kinds. It is essential to examine the water quality to avoid its hazard on local people. In this paper, ground water samples were analyzed using atomic absorption spectroscopy (AAS) to determine the concentration of some dissolved elements. The metal analysis is done to detect (i) arsenic (ii) lead (iii) cadmium (iv) iron (v) magnesium (vi) copper (vii) zinc using AAS method and some water parameters such as (i) pH (ii) electrical conductivity, (iii) temperature. The results obtained are compared with guidelines for drinking water quality World Health Organization (WHO) (2011). All the observed values except Cd are within the safe limitations (WHO). The observation from this job revealed that the measured pH values were in the range of 7.1 to 7.5, the values of electrical conductivity were found 43 to 625 μS/cm. The achieved turbidity values of all ground water samples are less than 5.

Keywords: water quality, AAS method, health effects, concentration of elements.

Introduction

Water is not only an absolute necessity for life but also a carrier of many diseases. As water is referred to as a universal solvent, the composition and quality of ground water is dependent not only on natural factors such as geological, topographical, meteorological, hydrological and biological and climatic effects but also on human influences such as industrialization, human activities and vast population. Therefore, the deterioration of aquatic system is common in everyplace for the developing world. So, water quality analysis is urgently required to achieve the water quality standards determined by WHO (2011) and Myanmar Emission Guideline (2015). Water quality standards are needed to determine whether ground water of a certain quality is suitable for its intended use. Ground water is the water stored beneath Earth's surface in aquifers. Once ground water is contaminated, its quality cannot be restored back easily and to device ways and means to protect it.

The natural concentration of metals in raw water which has not been treated or purified varies from state to state and country to country. Most metal species in natural fresh water occur in organic compounds, organic complexes or colloids. From the point of health, elements can be divided into two categories:

---

[1] Dr, Assistant Lecturer, Department of Physics, Yangon University, Myanmar.

[2] Associate Professor, Department of Physics, University of Yangon.

[3] Assistant Lecturer, Department of Physics, University of Yangon.

[4] Lecturer, Department of Physics, University of Yangon.

(i) Elements with undesirable effect such as
    (a) Iron (Fe)
    (b) Magnesium (Mg)
    (c) Copper (Cu)
    (d) Zinc (Zn)
(ii) Elements with a potential toxic effect (inorganic chemicals) such as
    (a) Arsenic (As)
    (b) Lead (Pb)
    (c) Cadmium (Cd)

Arsenic is a great health problem worldwide and heavy metals such as lead and cadmium are toxic and can be large potential to cause carcinogenic. Therefore, the above elements are oriented to analyze in this work.

Materials and Methods

(i) Study Sites

Three sampling sites were selected in various villages of two districts, Mon State in Southern part of Myanmar. Mon state lies between Kayin State to the east, the Andaman Sea to the west, Bago Division to the north and Tanintharyi Division to the south. Traditional agriculture is the most important income source of the districts. Besides, there are industrial zones such as gold purification and production of minerals. Water samples were collected from each site to assess it for a period of May, 2019. All water samples were collected in the morning hour from 9:00 to 12:00 am using dry and clean plastic bottle. The study area (Mawlamyine) lies between latitude 16º 29' N and longitudes 97º 37' E. It is situated at elevation 52 meters above sea level. Thaton district is located between latitude 16º 56' N and longitudes 97º 22' E and is situated at elevation of 24 meters above sea level.(Figure 1)The depth of all three hand dug wells are round about 30 feet. The water of all wells is used for drinking, domestic usage and agriculture.

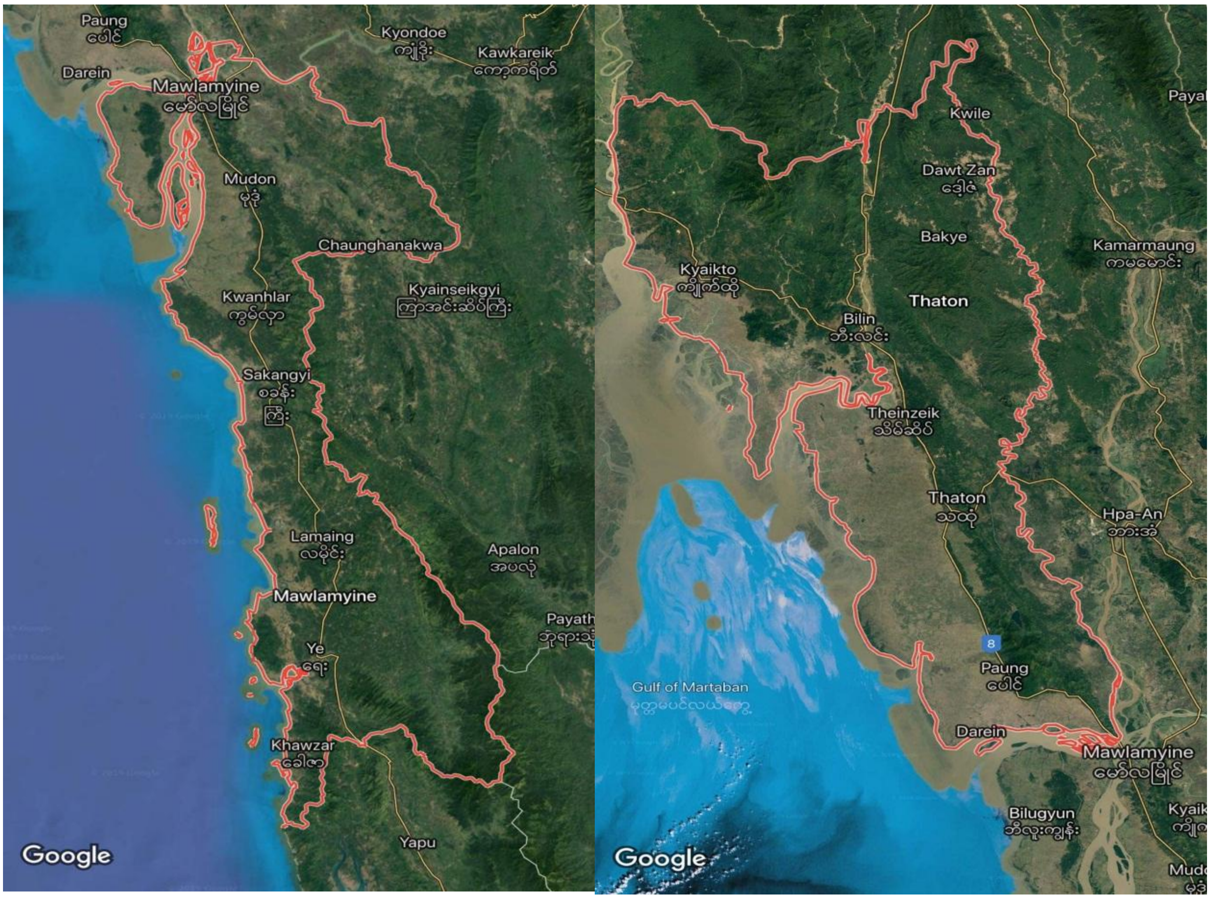

Figure 1 Map of study locations (Mawlamyine and Thaton districts).

(ii) Location of Study Area

Water samples were taken from three different sources:

Sample 1: ThwayThauk village near Mawlamyine university, Mawlamyine district. It has an old antimony mine but production of minerals was stopped since last 7 years.

Sample 2: Mae Wyne village in Hpa Pun township, Thaton district. There is a small gold mine in this village. Now, it is running annually.

Sample 3: Kwinkalay village in Bilin township, Thaton district. There is a gold mine which has production seasonally.

(iii) Climate of Study Area

Mawlamyine and Thaton districts in Mon State have covered a tropical climate. It has temperate weather as it is located in the low latitude zone and near the sea. During summer, the temperature shoots up to 47°C and in winter the temperature may fall to 2°C. Water temperature in summer was high due to low water level, high air temperature and clear atmosphere. This state has only slight changes in temperature. Annual rainfall in Mawlamyine is round about 190 inches (4.8 m).

(iv) Sample Collection

All water samples were collected from three different sources in two districts of Mon State. Samples were collected in clean and dry plastic bottles that were fitted with covers and then these bottles were put in a box that cannot be entered any effects including sunlight. After that all water samples were brought into laboratory for the measurement of various parameters but water temperature were recorded at the time of sample collection using thermometer. The recorded temperatures of all samples were displayed in table -1.

(v) Analysis of Water Sampling

Selection of appropriate sample container is also utmost important for the analysis of water. Normally, plastic or glass may be preferred for containing and storing of sample water. Before using, sampling plastic (polyethylene) should be washed and rinsed first with tap water and then these bottles were dried under room temperature. For some metal ion, sample containers were used plastic bottles but for mercury ion analysis but now the samples were stored in plastic bottles. Sample preparation is very important step in analytical job. Therefore, collecting ground water and analysis of water samples were prepared very carefully without any mistake or careless.

Parameters to be analyzed: For the analysis of ground water quality of the hand dug wells of selected regions in Mon State, the following water parameters are analyzed (i) pH (ii) electrical conductivity (iii) arsenic (iv) lead (v) cadmium (vi) iron (vii) magnesium (viii) copper and (ix) zinc. The chemical characteristics of water parameters analyzed and their health effects in this paper include:

(i) pH: pH of the solution is defined as negative logarithm of H^+ ions for many practical experiments. The value of pH varies zero to 14 and pH value 7 is neutral. The range of pH from zero to 7 is acidic solution and from 7 to 14 is alkaline. pH usually does not have direct impact on human but it is one of the most important operational water quality parameters. Besides, extreme pH values also increase solubility of elements and compounds making them toxic. Furthermore, temperature has an inverse relationship with pH that is, as temperature increases pH levels decrease and vice versa. In this job, pH of all samples was measured using HANNA HI 98129, 98130 water proof pH tester [Electrode method] in Ecological Laboratory. The measured pH values of ground water samples were described in table-1.

(ii) Electrical conductivity: Conductivity is the capacity of water to carry an electrical current. This conductivity depends on the total concentration of ionized constituents of water, mobility, types of ions and relative concentration and on the temperature of solution. Moreover, conductivity is directly related to salinity that is conductivity improves with high salinity. In this study, conductivity of water samples were also analyzed by HANNA HI 98129,98130 water proof EC tester [Electrode method] in Ecological Laboratory. The obtained results of water samples were shown in table-2.

(iii) Arsenic: Arsenic is highly toxic, contaminated water used for drinking, food preparation and irrigation of food crops poses the greatest threat to public health. In many studies, long term exposure to arsenic in drinking-water is causally related to increased risks of cancer in the skin, lungs, bladder and kidneys. Arsenic is one of WHO’s 10 chemicals of major public health concern.[2] In this work, As is analyzed by PinAAcle™ 900H atomic absorption spectrometer instrument in the laboratory of URC at University of Yangon.

(iv) Lead: Exposure to lead is very dangerous for young children compared to an adult because children's growing rate is much higher than that of an adult. Lead can damage brain, kidney, nerves and blood cells. For infants, large amount of lead can delay physical and mental development. Now, concentration of Pb is also measured by AAS method.

(v) Cadmium: Cd is one of the very heavy metal posing severe risks to human health. Cadmium is biopersistent and, once absorbed by an organism, remains resident for many years. Cadmium can be determined using a high performance atomic absorption spectrometer instrument in URC.

(vi) Copper: Even though copper is an essential element in human diet but the amount of copper eaten by human is nearly 1.0 μg per day. For copper ions is exceeded, the immediate health effects are vomiting, diarrhea, stomach cramps and nausea. Long term exposure of copper can cause serious problems in kidney and liver. Diarrhea are included in top ten leading cause of morbidity in Myanmar and according to Health in Myanmar 2014 published by Ministry of Health and Sports.

(vii) Zinc: Zinc is present approximately 0.05 g/kg in the earth crust. Symptoms of zinc toxicity in human include vomiting, dehydration, electrolyte imbalance, abdominal pain. Concentration of Zn was measured using both methods in this work.

(viii) Iron: Concentration of iron in ground water will usually be 0.5-1 mg/litre.Iron is an essential element in human nutrition. Estimates of the minimum daily requirement for iron depend on age, sex range from about 10 to 50 mg/day. Insufficient or excess levels of iron can have negative effect on body functions. Concentration of Fe is determined using AAS method in this paper.

(ix) Magnesium: Magnesium is the fourth most abundant cation in the body and the second most abundant intracellular cation. Magnesium plays important mineral in bone structure, muscle contraction and nerve impulse transmission, blood clotting. Experts in this field tell us that total magnesium intake must be at least 450–500 mg per day, and drinking water should contain a minimum of 25–50 ppm magnesium.

(x) Temperature: Water temperature depends on the season, geographic location, sampling time, temperature of surrounding air and weather condition. Temperature will impact on the acceptability of inorganic constituents and chemical contaminants. High ground water temperature enhances the growth of micro-organisms and may increase physical characteristics of water such as taste, odour, color and corrosion**.**

(vi) Atomic Absorption Spectrometry (AAS)

Atomic Absorption Spectrometry (AAS) is an analytical technique for measuring quantities of chemical elements present in environmental samples by measuring the absorbed radiation by the chemical element of interest. Atomic absorption method measures the amount of energy in the form of photons of light that are absorbed by the sample. Atomic absorption Spectrometer has many uses in different area of research in most of scientific fields. Now, high-performance PinAAcle™ 900H atomic absorption spectrometer is used in this study. It is a combined flame/furnace system with continuum source background correction. The PinAAcle 900H is controlled by the proven WinLab32™ for AA software – whoever the user and whatever the application, WinLab32 software makes it fast and easy to get from sample to results.

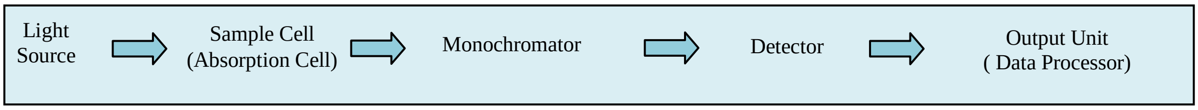

Figure 2 Schematic diagram of an atomic absorption spectrometer.[8]

Figure 3 High-performance PinAAcle™ 900H atomic absorption spectrometer instrument in the laboratory of URC at Yangon University.

(vii) Possible Health Effects of Contaminated Water

There is a greater relation between metal contaminated water and health problem. Some heavy metals are essential for health but in limited concentration, high concentration creates harmful effect on health. Higher concentrations of metal ions result into adverse environment and several types of human health problems. Health risk associated with polluted water includes different diseases such as respiratory disease, cancer, diarrheal disease, neurological disorder and cardiovascular disease. And also, poor quality water destroys the crop production and infects our food which is hazardous for aquatic life and human life. Heavy metals, especially iron affects the respiratory system of fish and aquatic animals. Metal contaminated water leads to hair loss, liver cirrhosis, renal failure and neutral disorder. Bacterial, viral and parasitic diseases are spreading through polluted water and affecting human health.

Results and Discussion

Table1 Physiochemical Properties of water samples from study area in Mon State, Myanmar.

No	Water Samples	pH			Turbidity (FAU)		Temperature (°C)
		Results	Standard Limits WHO (2011)	MEG (2015)	Results	Standard Limits	
1	Sample-1	7.5	6.5-8.5	6.5-9.0	< 5	≤ 10	28
2	Sample-2	7.3	6.5-8.5	6.5-9.0	< 5	≤ 10	25
3	Sample-3	7.1	6.5-8.5	6.5-9.0	< 5	≤ 10	26

MEG (2015) – Myanmar Emission Guideline (2015)

The maximum pH value is 7.5 for sample-1 and minimum value is 7.1 for sample-3. All measured pH values are within the WHO standards. The measured pH values, turbidity values and temperatures of water samples from each of study area are described in table-1 compared with standard limits (WHO). The pH values between 6.5 and 8.5 usually indicate good water quality and this range is typical of most drainage basins of the world. Therefore, the observed pH values for three sources have no deviation from the standard pH range limited by Myanmar Emission Guidelines (2015) and WHO drinking water quality (2011). Turbidity of all water samples are less than 5 and below the standards. Ground water temperature value in study area varies from 25 ºC to 28 ºC with an average value is 26.33 ºC. These results suggest that the ground water temperature is generally ambient and good for consumers in these areas.

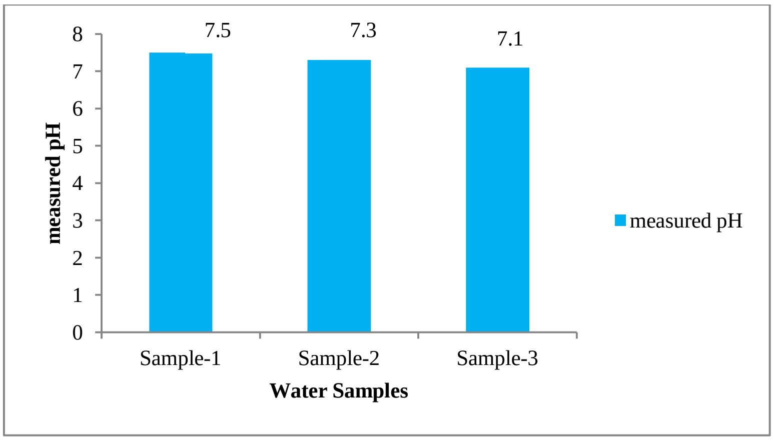

Figure 4 Statistical representation of physiochemical property (pH) of three water samples.

Table 2 Electrical Conductivity of water samples from study area in Mon State, Myanmar.

No	Water Samples	Electrical Conductivity (µS/cm)	
		Results	Standard Limits (WHO)
1	Sample-1	625	1500
2	Sample-2	206	1500
3	Sample-3	43	1500

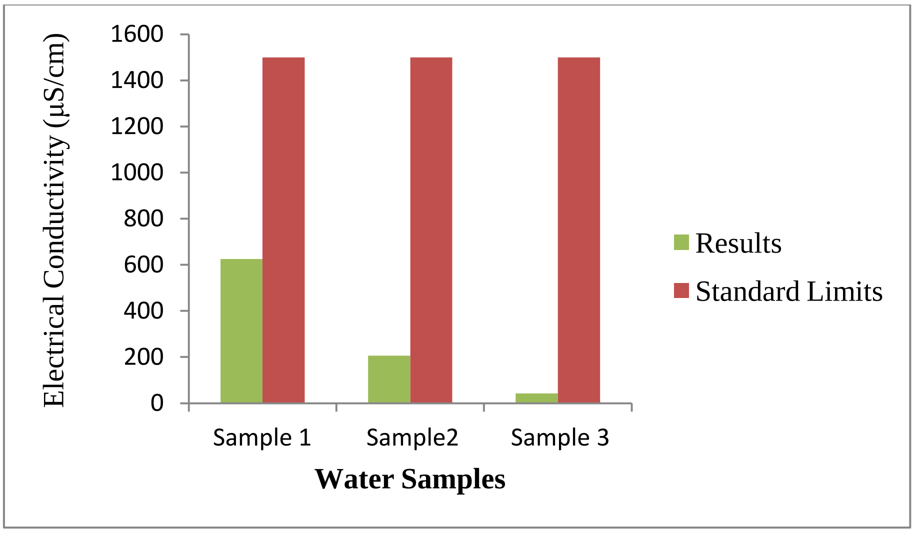

Figure 5 Comparison of results of electrical conductivity and WHO standard limits.

The results of electrical conductivity of three samples were listed in table-2 and displayed in figure (5) compared with WHO standards limits. The most electrical conductivity is 625 µS/cm for sample-1 and the least is 43 µS/cm for sample-3. Conductivity of the ground water for the entire study area stands at an average of 874 µS/cm. By studying this, electrical conductivities of water samples from study area in Mon State were good condition to use for domestic and agriculture.

Table 3 Comparison of some elemental concentration of all ground water samples using AAS method with WHO standards.

Elements	Measured Values (µg/L)			Standard Limit (WHO) (µg/L)
	Sample - 1	Sample - 2	Sample - 3	
As	1.608	1.035	0.735	10
Pb	ND	ND	ND	10
Cd	12	23	25	3
Fe	ND	ND	ND	300
Mg	4500	3170	8400	30000
Cu	ND	ND	ND	2000
Zn	ND	ND	ND	5000

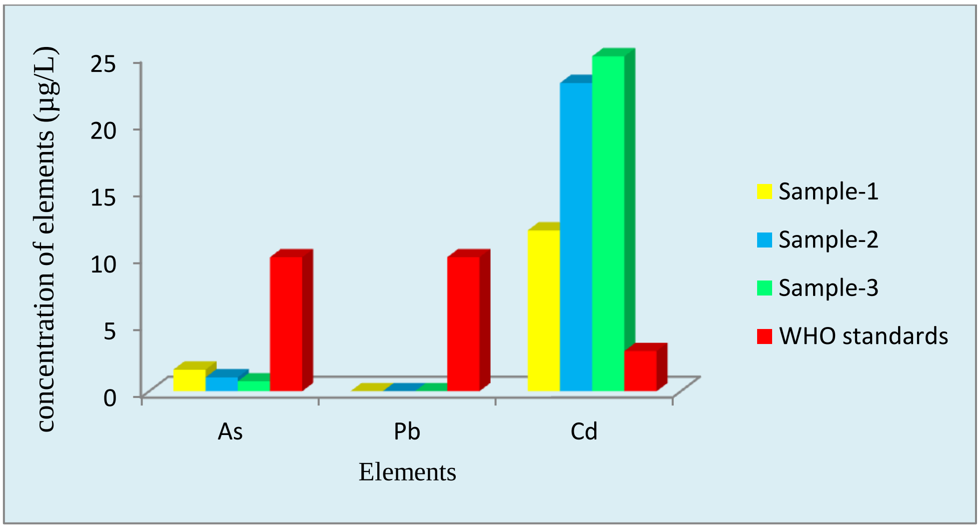

Figure 6 Concentrations of As, Pb and Cd for water samples from study area compared with WHO standards.

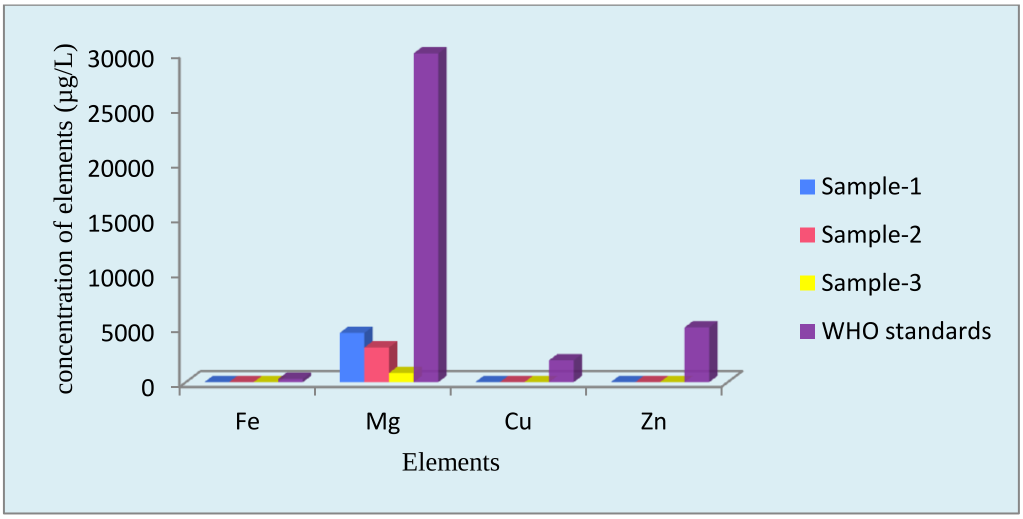

Figure 7 Concentrations of Fe, Mg, Cu and Zn for water samples from study area with reference to WHO standards.

Studying the elemental concentration of all water samples using AAS method, (6) kinds of metals' concentrations are well below the WHO standards except Cd. From this study, the concentrations of cadmium (Cd) for all ground water samples were higher than that of allowed value (WHO). The average daily intake of Cd for humans is estimated as 1µg from water but levels may vary widely. On account of the concentrations of the Cd (heavy metal) studied from this research paper , water samples are not suitable for drinking purposes. Concentrations of magnesium for three water samples were detectable but it is found within allowed limits. In this observation, lead (Pb), iron (Fe), copper (Cu) and zinc (Zn) could not be detected for all ground water samples. Based on the comparison of the achieved data using AAS method, we can conclude that there are no significant differences between the listed drinking water guidelines (WHO) (2011) and measured values in all of water samples in both of the discussed districts except cadmium (Cd). From this observation, results of magnesium content by AAS method were detectable in all samples but it was still within the safe limits.

Conclusion

Water quality is dependent on the type of the pollutant added and the nature of mineral found at particular zone of hand dug wells. From this analysis of water samples in the study area, there was no significant difference in the pH value compared with guidelines for drinking water quality (WHO) 2011 and also electrical conductivity and turbidity for all ground water samples are lower than WHO standards of water quality. The rest of observed values (elemental concentration) were within the WHO standards except Cd. By studying the measured values from AAS method, cadmium concentration is greater than that of highest standard level (WHO) in all samples. This may have a negative impact on human health. There was harmful contamination that causes health hazardous of habitants. Based on the achieved results, we can conclude that the health of the population in selected area has no safety for that ground water to drink and domestic usage. The outcome of this research could be beneficial to local as baseline information on ground water quality in terms of physio-chemical parameters some elemental concentration of ground water in Mawlamyine and Thaton districts. The results obtained from the present investigation shall be useful in future management of the ground water in Mon State, Myanmar.

Acknowledgements

First and foremost, praises and thanks to the Buddha, for his kind throughout my research work to complete the research successfully.

I am extremely grateful to my parents for their love, prayers, nurturing and sacrifices for my future. They are the ultimate role models for me.

I would like to express my gratitude to Professor Dr Khin Khin Win (Head), Department of Physics, Yangon University for her kind permission to give me the opportunity to do research.

I am also grateful to Dr Myo Lwin (Professor), Dr Aye Aye Thant (Professor) and Dr Yin Maung Maung (Professor), Department of Physics, Yangon University for their help and critical suggestions.

Special thanks are due to all my colleagues, friends and students from various fields who actively participated during the process.

References

Environmental Health in Myanmar, February 2018.

Guidelines for Drinking water Quality, Fourth Edition, WHO (2011), ISBN 978 924 154 81 51.

https://www.accuweather.com/en/mm/mawlamyine/244419/january.weather/244419

https://www.google.com/map/place/Mon state

https://apps.who.int/iris/bitstream/10665/43836/1/9789241563550_eng.pdf

https://www.hanninst.com

http://www.who.int/entity/water_sanitation_health/dwq/chemicals/iron and zinc.pdf

Journal of Laboratory Chemical Education (2013),1(3):54-58

WHO (1992) *Cadmium.* Geneva, World Health Organization (Environmental Health Criteria 134).

J. Myanmar Acad. Arts Sci. 2020 **Vol. XVIII.No.2C**

INVESTIGATION ON ATTENUATION CHARACTERISTICS OF Al-Zn METAL ALLOY FOR GAMMA RAY SHIELDING

Shwe Nan Htet[1], Aye Aye Mar[2], Shwe Sin Oo[3] and Nadar Hnin Yee[4]

Abstract

The main purpose of this study was to investigate gamma ray attenuation characteristics of Al-Zn metal alloy shielding material. The attenuation coefficients of Al-Zn metal alloy for various gamma sources were determined using gamma ray spectrometer systems. The gamma ray attenuation characteristics of Al-Zn metal alloy shielding material could be tested by calculating half value layer (HVL), tenth value layer (TVL) and mean free path (MFP).It was found that the photon intensity decreased as attenuator thickness increased. It was seen that linear and mass attenuation coefficients of Al-Zn metal alloy sample decreased while half value layer (HVL), tenth value layer (TVL) and mean free path (MFP) of that sample increased when the gamma energies increased. Therefore, Al-Zn metal alloy shielding materialwere applicable for low energy gamma ray.

Keywords: Al-Zn metal alloy, half value layer (HVL), tenth value layer (TVL),mean free path (MFP)

Introduction

The practice of absorber material blocking radiation consists in placing a barrier between the external radioactive source and the receptor. By doing this, some or all amount of the radiation emitted by the source will be scattered or absorbed by the constitutive atoms of the material. This process is called attenuation and is the fundamental physical principle upon which radiation shielding is based. With shielding, radiation dose can be lowered to a desired level. Furthermore; different types of radiation can be shielded by different types of materials. The attenuation capability of a given material is strongly dependent on the type of radiation and the range of energies associated with the radiation. (Anon, 2003)

For shield designs, gamma ray was one of the main types of nuclear radiation, which have to be considered; since any shield attenuates the gamma rays will be more effective for attenuating other radiations.

The ability of an absorber material to absorb gamma rays is expressed by the linear attenuation coefficient for that material

Therefore, design and construction of effective radiation shields require an in-depth knowledge of the types of interaction between radiation and the target material.(Anon, 2003)

Linear Attenuation Coefficient

The attenuation of gamma radiation can be described by the following equation.

$$I=I_0 .e^{-\mu x} \qquad (1)$$

where I is intensity after attenuation, I_o is incident intensity, μ is the linear attenuation coefficient (cm^{-1}), and physical thickness of absorber (cm).

---

[1] Dr, Lecturer, Department of Physics, University of Yangon

[2] Assistant Lecturer, Department of Physics, University of Yangon

[3] Assistant Lecturer, Department of Physics, University of Yangon

[4] MRes Student, Department of Physics, University of Yangon

Mass Attenuation Coefficient

The mass attenuation coefficient is defined as the ratio of the linear attenuation coefficient and absorber density (μ/ρ). The attenuation of gamma radiation can be then described by the following equation:

$$I=I_0 .e^{-(\mu/\rho).\rho x} \qquad (2)$$

whereρ is the material density, (μ/ρ) is the mass attenuation coefficient and ρ.x is the mass thickness. The measurement unit used for the mass attenuation coefficient cm^2/g.

Half Value Layer

The thickness of any given material where 50% of the incident energy has been attenuated is known as the half value layer (HVL). The HVL is inversely proportional to the attenuation coefficient and the two values are related by the following equation. Since μ is normally given in units of cm^{-1}, the HVL is commonly expressed in units of cm.

$$HVL= 0.693/\mu \qquad (3)$$

where, μ is linear attenuation coefficient (cm).

Tenth Value Layer

The tenth value layer (TVL) is the average amount of material needed to absorb 90% of all radiation, i.e., to reduce it to a tenth of the original intensity. TVL is greater than or equal to $\log_2$ (10) or approximately 3.32 HVLs, with equality achieved for a monoenergetic beam.

$$TVL= \ln 10/ \mu \qquad (4)$$

where, μ is linear attenuation coefficient (cm).

Mean Free Path

Mean free path (λ) is the average distance a gamma ray travels in the absorber before interacting and is given by formula

$$\lambda= \frac{1}{\mu} \qquad (5)$$

where μ is the linear attenuation coefficient of glass samples.

Experimental Procedure

Sample Preparation

To measure the attenuation coefficients of Al-Zn alloy sample, square shape of that sample (7 cm × 7 cm) was cut with increasing five different thickness ranging from 0.1025 to 0.9225cm.

Experimental Measurement

The measurement of gamma attenuation for Al-Zn metal alloy was carried out Nuclear Physics Laboratory, Department of Physics in University of Yangon. The experimental arrangement in the present attenuation measurement consists of NaI (Tl) detector (working high voltage, 650V) with photomultiplier tube connected to a high voltage supply and a multichannel analyzer, MCA controlled by a connected computer installed Phywe Systeme Gmbh Software 'measure' MCA Module Gamma Acquisition & Analysis software. The gain and offset of MCA measure software in present measurement were gain level 1 and offset 1.

In this study, each attenuator sample was placed between gamma ray detector and sources as the same experimental set-up. The distance between source and detector was 12 cm and the source to sample distance was 4 cm only. To get various thicknesses, the samples were stacked on one by one. The incident beam intensity I_0(without sample) and attenuated beam intensity I (with samples) for^{137}Cs,^{22}Na and ^{60}Cogamma ray sources were measured with accumulation time 900 s. Half value layer (HVL), tenth value layer (TVL) and mean free path (MFP) of Al-Zn metal alloy were tabulated for shield design. The arrangement of the experimental set up was shown in Figure 1.

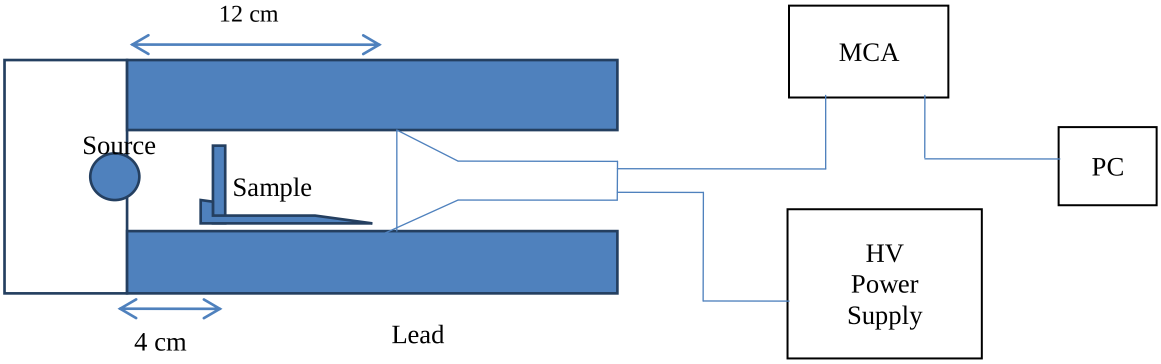

Figure 1 The arrangement of Experimental Setup

Results and Discussion

The behavior of the investigated alloys against γ radiation sources (Cs-137, Na-22 and Co-60) were studied experimentally. The transmission of γ rays were measured at four different γ energies. Tables 1 described the experimental attenuation coefficient results of alloy sample for each source. Figures 2, 3, 4, 5, 6, 7, 8 and 9show the attenuation graphs for material thickness and density thickness for samples. Due to the good geometry, the slopes of these graph lines gave the straight lines because of the less scattering effect. The slopes of attenuation graph for material thickness gave the experimental linear attenuation coefficient values, μ(cm^{-1}) and in this way, density thickness graph gave the experimental mass attenuation coefficient values, μ/ρ (cm^2/g). These experimental results as a function of γ energies were shown in Figure10 and Table 2. It also described that the attenuation coefficient values, half value layer (HVL), tenth value layer (TVL) and mean free path (MFP) of the sample were varied with different gamma energies. Thus, it is easier to attenuate low γ photons. As the γ energy increases, the coefficient of the samples decreases. It can be said that high energy photons are able more deeply compared to a lower energy photon.

Table 1 Gamma ray attenuation parameters of Al-Zn alloy sample with different thicknesses and density thicknesses by using gamma source

Thickness		lnI (Cs) (662 keV)	ln I(Co) 1173 keV	ln I(Na) 1275 keV	ln I(Co) 1332 keV
cm	gcm^{-2}				
0.1025	0.5535	9.1526	7.784	7.4261	7.5592
0.3075	1.6786	9.0832	7.7285	7.3883	7.521
0.5125	2.8051	9.0192	7.6779	7.3493	7.4764
0.7175	3.9449	8.9572	7.616	7.2862	7.4322
0.9225	4.999	8.8991	7.5575	7.2488	7.3875

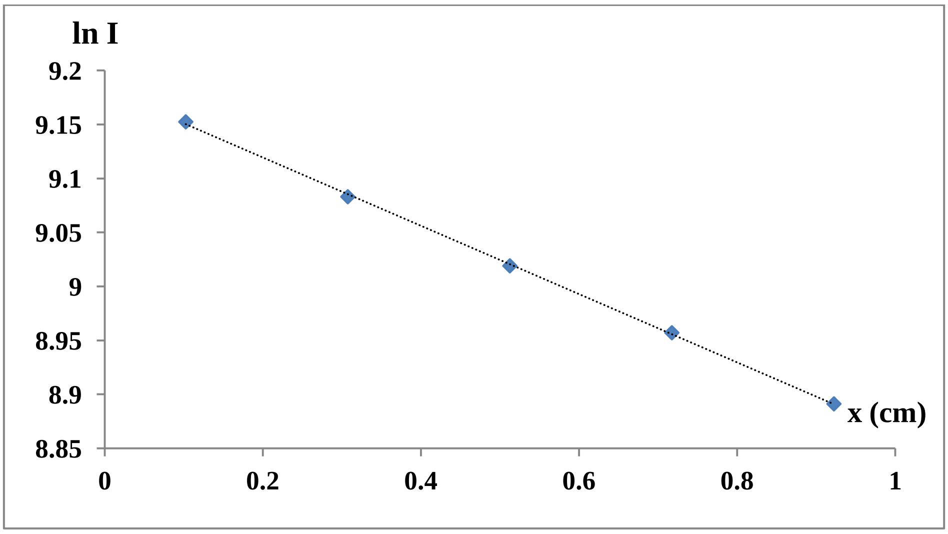

Figure 2 Attenuation graph for 5 different thickness of Al-Zn alloy against Cs-137 gamma source

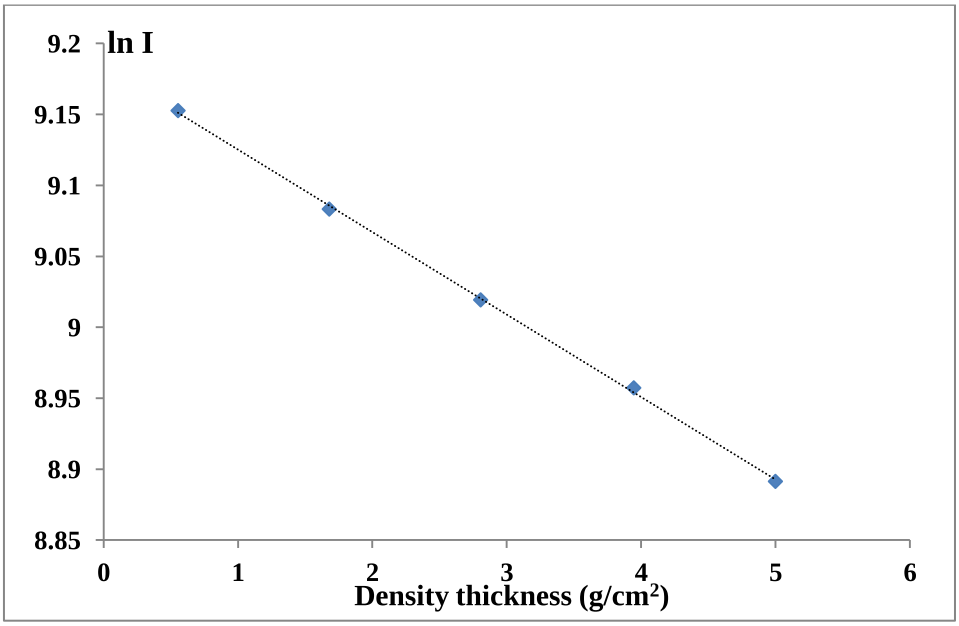

Figure 3 Attenuation graph for 5 different density thickness of Al-Zn alloy against Cs-137 gamma source

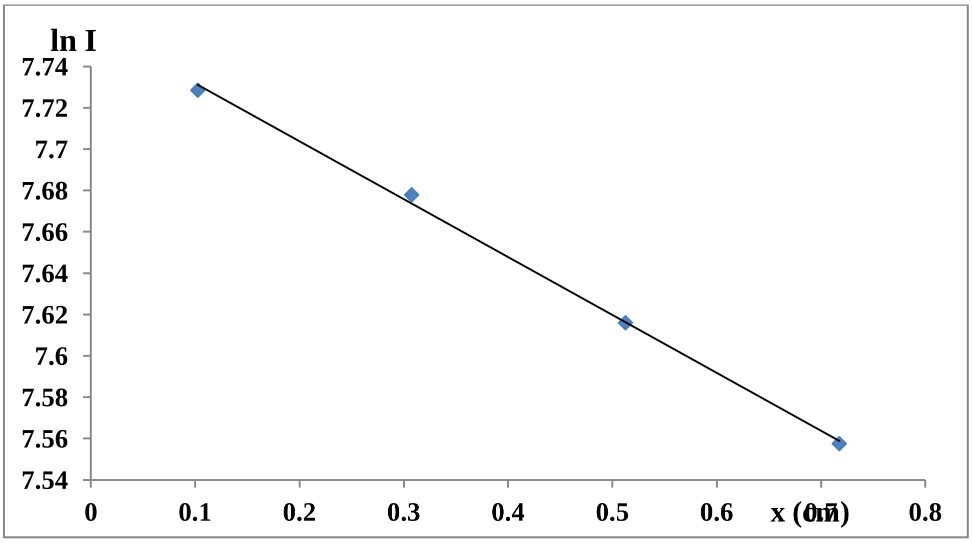

Figure 4 Attenuation graph for 5 different thickness of Al-Zn alloy against Co-60 gamma source at energy 1173 keV

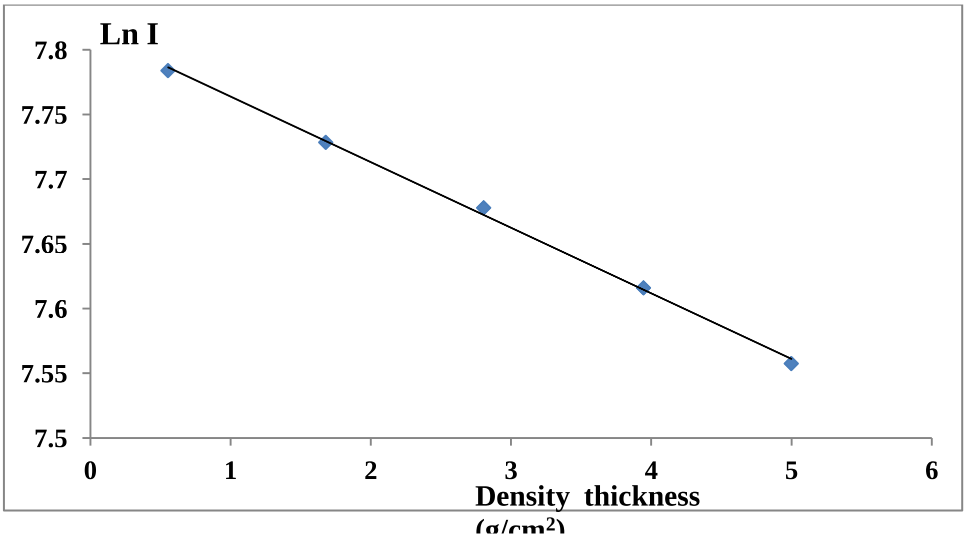

Figure 5 Attenuation graph for 5 different density thickness of Al-Zn alloy against Co -60 gamma source at energy 1173 keV

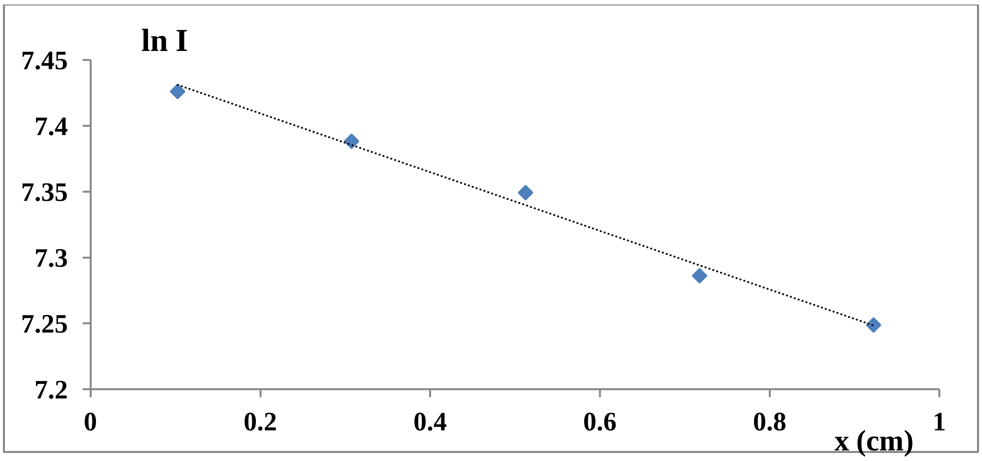

Figure 6 Attenuation graph for 5 different thickness of Al-Zn alloy against Na- 22 gamma source at energy 1275 keV

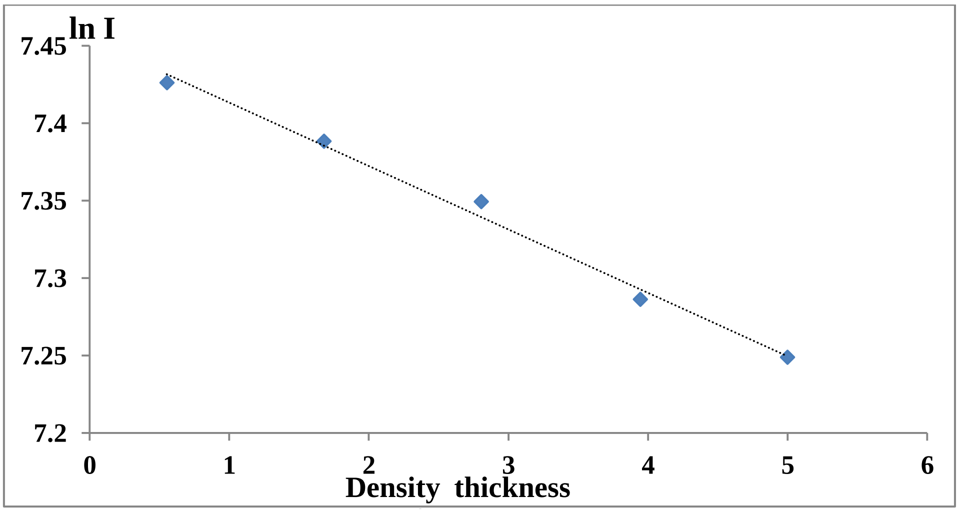

Figure 7 Attenuation graph for 5 different density thickness of Al-Zn alloy against Na- 22 gamma source at energy 1275 keV

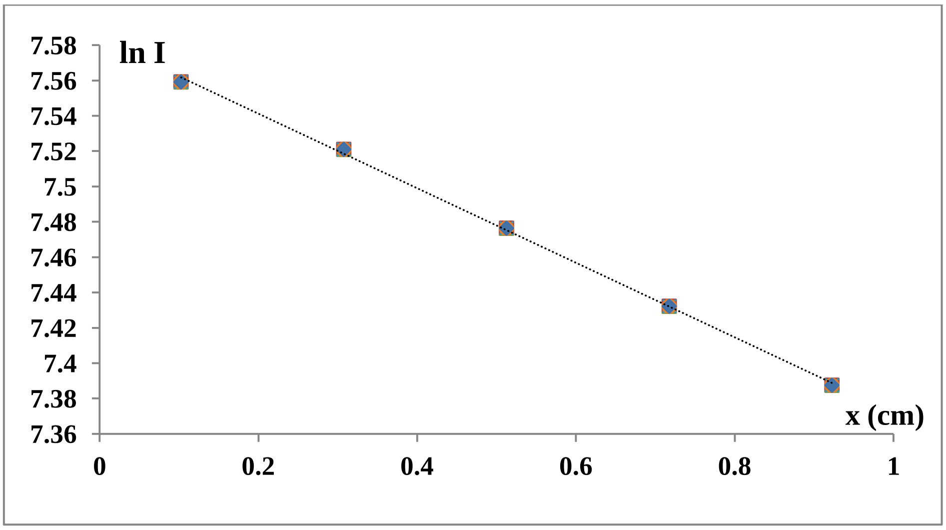

Figure 8 Attenuation graph for 5 different thickness of Al-Zn alloy against Co-60 gamma source at energy 1332 keV

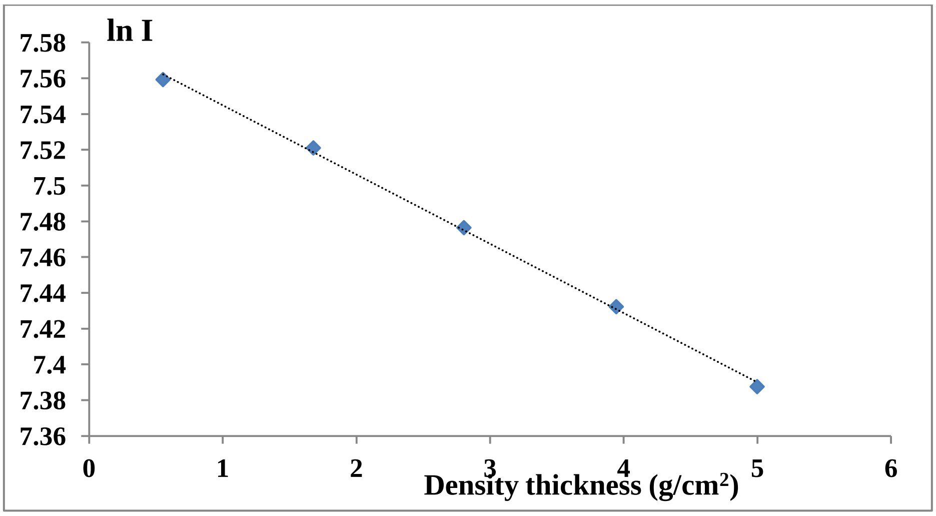

Figure 9 Attenuation graph for 5 different density thickness of Al-Zn alloy against Co-60 gamma source at energy 1332 keV

Table 2 Attenuation Coefficients, half value layer (HVL), tenth value layer (TVL) and mean free path (MFP) of Al-Zn alloy Samples with Various Gamma Energies

Sources	Energy (keV)	μ (cm^{-1})	μ/ρ(cm^2/g)	HVL (cm)	TVL (cm)	λ(cm)
^{137}Cs	662	0.3164	0.0581	2.1906	7.2775	3.1606
^{60}Co	1173	0.2804	0.0507	2.4718	8.2118	3.5663
^{22}Na	1275	0.2228	0.0409	3.1109	10.3348	4.4883
^{60}Co	1332	0.2108	0.0387	3.2880	10.9231	4.7438

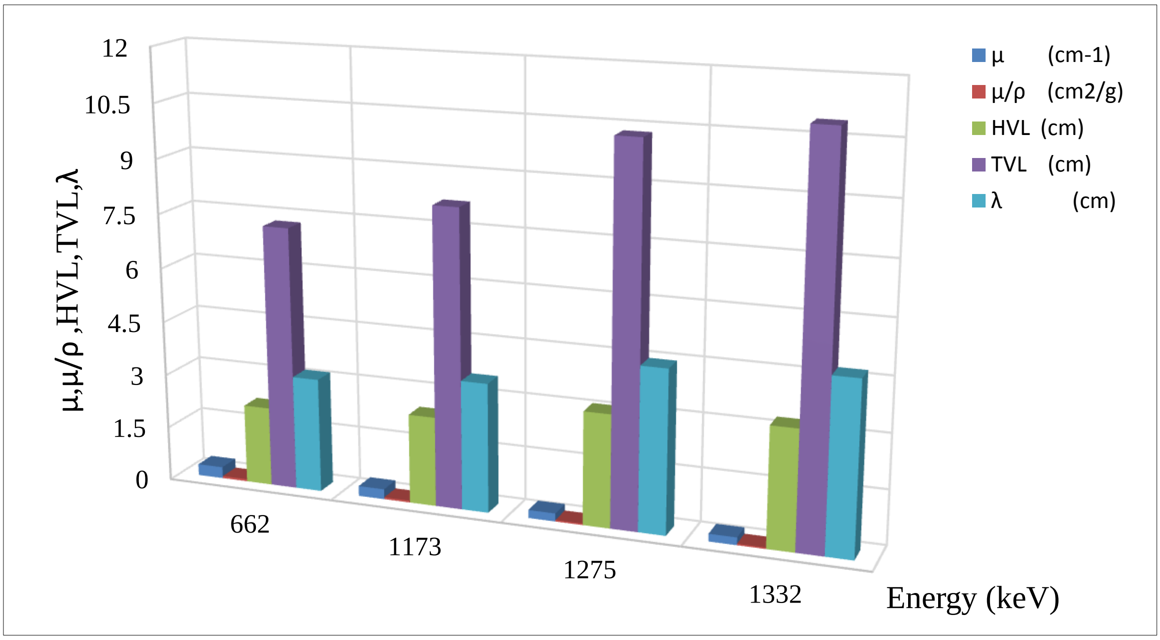

Figure1 Attenuation Coefficients, half value layer (HVL), tenth value layer (TVL) and mean free path (MFP) of Al-Zn alloy Sample with Various Gamma Energies

Conclusion

In view of this study, radiation shielding characteristics such as linear attenuation coefficient, mass attenuation coefficient, half- value layer, tenth value thickness and mean free path of Al-Zn metal alloy were measured using different gamma energies. The results of γ-ray attenuation values of Al-Zn metal showed that the linear and mass attenuation coefficients decreased but the half value layers (HVL) and tenth value layers (TVL) were increased with increase of gamma energy. It was observed that Attenuation coefficient depends on the energy of incident photons and the nature of the material and half value layers (HVL) and tenth value layers (TVL) are also photon energy dependent, like the attenuation coefficient. So, the shielding materials tend to attenuate double range energies source more than single energy. Thus, gamma irradiation is an efficient factor of Al-Zn metal alloys to be used as shielding materials.

Acknowledgements

I would like to thank Professor Dr Khin Khin Win, Head of Department of Physics, University of Yangon, for her kind permission and encouragement to carry out this work.

I would like to thank Professor Dr Aye Aye Thant, Professor Dr Myo Lwin and Professor Dr Yin Maung Maung, Department of Physics, University of Yangon for their encouragement.

References

American University in Bulgaria. Retrieved 27 March 2016 "Gamma Spectroscopy with a Scintillation Detector and Multichannel Analyzer" *(PDF).*

Anon, (2003), "Radiation Shielding Internet Information Radiation Protecting & Shielding".

G. Nelson, D. Reilly, (1991), "Gamma Ray Interactions with Matter", in Passive Nondestructive Analysis of Nuclear Materials (Los Alamos National Laboratory)

Gilmore G & Hemingway J D, (1995), "Practical Gamma Ray Spectroscopy" (Chichester: John Wiley)

Harvard University Radiation Protection Office, Providing radiation guidance to Harvard University and affiliated institutions.

Hubbell, J. H.; Seltzer, S. M. Retrieved September (2007)"Tables of X-Ray Mass Attenuation Coefficients and Mass Energy-Absorption Coefficients". National Institute of Standards and Technology (NIST).

N. Damla, U. Cevik, A.I. Kobya, A. Celik, N. Celik, I. Yildirum, "Assessment of natural radioactivity and mass attenuation coefficient of brick and roofing tile used in Turkey", Radiation Measurements, 46, 701-708, (2011).

J. Myanmar Acad. Arts Sci. 2020 **Vol. XVIII.No.2C**

CONSTRUCTION OF SMALL SCALE WATER FLOW TURBINE FOR RURAL AREA APPLICATION

Hla Toe[1], Khin Khin Kyaw[2] and Wynn Mar Aye[3]

ABSTRACT

The objective of this research is to construct of small scale pilot plan flow turbine for rural area application in Myanmar. In Myanmar, there are many water resources. Water flow turbines are considered, designed and constructed based on rural area electricity requirement. All parts are available in local market and were installed in laboratory. The constructed flow turbine performed their functions correctly. This turbine can be applied over a water flow area and head range 3 m to 10 m in test running condition. This turbine can be constructed simply by people from rural area in our country with local materials. The small scale cross-flow turbine produces maximum power 4.8 w of under a head length of 10 m. This type of turbines is sample design, easy to maintain and low cost to construct.

Keywords: Flow turbine, blades, rural area, output power

Introduction

Abundant of stream, river and long coastal regions have in Myanmar. Therefore, run off river installation do not have any adverse effect on the local environment as large hydro. Small hydro plants maybe standalone system in isolated areas but could also be grid connected. The connection to the grid has the advantage of the easier control of the electrical system frequency of the electricity, but the disadvantage of being tripped off the system due to problems outside of the plant operator control [Andy Karsner (2008- May).].

Instead, a fraction of the water's stream is diverted downhill through a pipe to a small turbine that sits alongside the stream. The design and applications of hydraulic turbines has evolved over time. Functionally, there are several different types of hydraulic turbines, each of which operates under a characteristic set of operating conditions [Andy Karsner (2008- May).]. The flow water pushes directly to blade of turbine. The blade directly drives to shaft and turn to generator and produced electricity, so gear is not used in this turbine. This type of turbine includes in RE, which have many advantages and disadvantages. The initial cost of installation of renewable energy technologies is higher than the cost of the devices that use conventional energy sources. This pilot plan turbine is constructed for use in Phalan Township, Chin state.

Construction of flow turbine

This turbine was constructed as pilot plan to use in Chin mountain area. Flow turbine was constructed after studying of different papers and design calculations. Different fabrication and design were also taken into consideration to study their angles of attack and flow rate of water. The construction of flow turbine based on the flow water was pushed to the concave surface of blades for the efficient performance and electricity output from the alternator.

[1, 2.] Dr, Associate Professor, Physics Department, University of Yangon

[3.] Dr, Associate Professor, Physics Department, Dagon University

Blade Construction

Different materials are brought in local for the setup of flow turbine. Iron sheet was cut and rolled for blades of flow turbine, it is cut into the size of 8 inches × 24 inches of area of 8 pieces of iron plane sheet. Its exact weight is 2.21 lb for each iron blade. Blades are arranged at the attach angle of 25 degrees. The space between the blades was 254 mm and total 8 blades were arranged. Size 2 cm diameter shaft with length 24 inches was taken and attached to both two alternators.

Frame Construction

Frame structure support rotor and alternator was fixed setup with shaft. Frame structure was important for definite place to provide the proper RPM of alternator. 2 inches width L shape iron bar was bought from the market for the frame of the whole setup. A channel of length 20 feet for 1 bar and 4 bars were used. The construction of frame is according to the dimension of 3ft×3ft×2.5 ft with 2 inches L shape iron bar. Frame after construction is bolted with to both ends with alternator was mounted on frame with arrangements.

Rotor Construction

Bicycle wheel was mainly used to attain maximum rotational speed by the drive of water flow and convert into the electrical energy, which was lighter than iron frame rotor and to minimize energy losses. The frictional force was reduced and increases the kinetic energy by using the mass and velocity of water to the blades surface for maximum output. Blades were put on the connecting bar between two bicycle wheels by the tight of screws. The pipe for two different diameters was used to control the proper movement and flow of water to the blades for the better RPM at the shaft. In this turbine have no transmission gear.

Generators

Alternator was used to convert from the mechanical energy into the electrical energy. The shaft output was carried which was direct drive to alternator with the turbine section. Shaft rotation provides the generation of electricity through the alternator. It was stand above from base 2 feet to the shaft height by the frame. Two alternators are connecting the ends of shaft and instantaneously rotate by drive of rotor. The electricity output and sent to storage battery.

All the manufacturing activities were carried out at science workshop except standard parts such as bolts and nuts etc., which were purchased from the market. The construction detail procedure photos are shown in Figures 2 to 9.

(a) Calculation of the water flow rate (Q)

The water flow rate was calculated by measuring river or stream flow velocity (V_F) and river cross-sectional area (A), $Q = V_F \times A$ (m^3/sec)

(b) Calculation of turbine power (Pt)

The electrical power of the turbine in Watt can be calculated as:

$P_t = Q \times Hn \times \rho \times g \times \eta_h$ (W)

Q - discharge [m^3/s] H_n - gross head [m] η_h - hydraulic efficiency [-]

ρ - water density [kg/m^3] g - gravitational acceleration [m/s^2]

(c) Number of blades:

The selection of optimum number of blades is very important in the design of Turbine Runner, fewer no of blades may cause incomplete utilization of water available to the turbine and excessive number of blades may cause the pulsating power and reducing the turbine efficiency. The following relation exists for the number of Blades in a Turbine runner: As circumference of rotor is $2\pi R = 2\times \pi \times 310 = 1946.8\ mm$

And blade spacing is $S_b =$ 240.35 mm

So, no of blades will be $\frac{1946.8}{240.35} = 8.099 \approx 8\ nos$

(d) Blade spacing: Proper blade spacing allows the water to strike, on the blades for maximum thrust production, the blade spacing depends upon the number of blades used in the turbine runner. Blade spacing can be calculated as:

$S = [\pi * D - n(t)]/n \quad S = [3.14 \times 620 \times 10^{-3} - 8 \times 3 \times 10^{-3}]/8$

S = 240.35 mm

(e) Calculation of turbine efficiency (η_t)

The maximum turbine efficiency can be calculated as:

$$\eta = \frac{1}{2} \times C^2 \times (1+ \psi) \times \cos^2(\propto)$$

ψ - blade roughness coefficient (0.98) C - the nozzle roughness coefficient (0.98).

η - the hydraulic efficiency of turbine. $\propto$ - the attack angle of 20° to the runner.

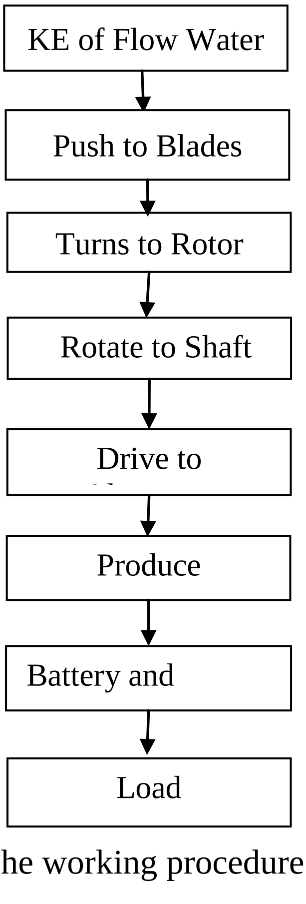

Figure 1 The working procedure of flow turbine

Photos for Construction of Flow Turbine

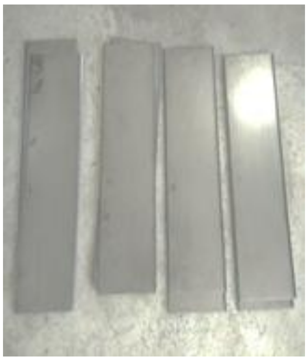

Figure 2 Iron sheet for lade

Figure 3 Mounted for frame

Figure 4 and 5 Setup of frame, rotor and iron bar

Figure 6 Installation of flow turbine and **Figure 7** Water flow turbine

The measurement and test of flow turbine

Figure 8 Test run of flow turbine by 2-inch pipe and 10 feet height.

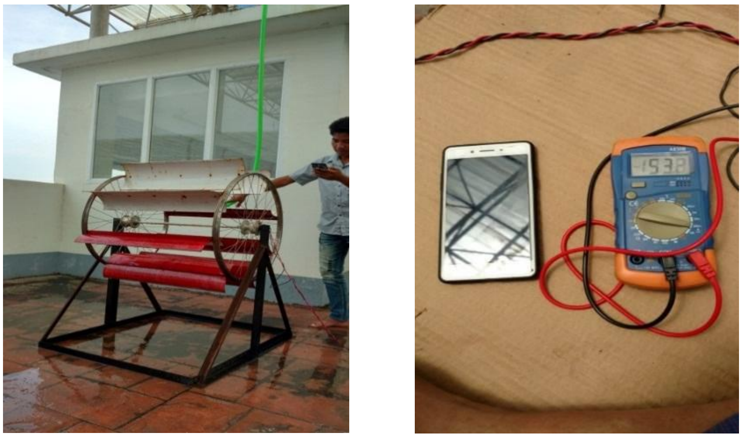

Figure 9 Test run of flow turbine by 1-inch pipe and 10 feet height

Results

The small scale flow turbine for rural area application was designed and constructed. It has (6) main categories; blades, dynamo, rotor, frame, shaft and charging controller. Blades, frame and charging controller was designed our self. The blade was carved by cutting and roller machine. Generator and rotor are bought from local market in Sawbwar Gyi kone, Mayangon Township. Other portions were made in science work shop Hlaing Township. The Results are shown in table and graph.

Table 1 Basic parameters of pilot plan flow turbine

Sr	Specifications		Measurements
1	**Blades**	Length	60 cm
		Thickness	0.4 cm
		Radius of curvature	12 cm
		Pitch angle	45°
		No. blade	8×24 inch
		Blade Attack Angle	25°
2	**Rotor**	Weight	8×7.68lb
		Diameter	65cm
		Inner	60 cm
		Outer	62 cm
		Weight	60 lb.
		Length	60cm
3	**Shaft**	Weight	2lb
		Length	60 cm
		Diameter	2 cm
4	**Flow rate**	Head length	3m to 10m
		RPM	150
		Volt	4.8 w

Table 2 Calculation of the water flow rate for 1 inch.

Sr	Diameter		Velocity of fluid (m/s)	flow rate (Q) ($\mu m^3/s$)
	inches	meter(m)		
1	1	0.0254	0.05	24.5312
2	1	0.0254	0.0833	40.8854
3	1	0.0254	0.1667	81.7708

Table 3 The input power of flow water for 1inch head and height of 3 m, 5 m, 10 m.

Sr	Diameter		Acceleration due to gravity (ms^{-2})	High (m)	flow rate (Q) ($\mu m^3/s$)	Density of fluid (kg/m^3)	input power of the turbine (watt)
	inches	meter (m)					
1	1	0.025	9.81	3	24.5312	1000	0.61
2	1	0.025	9.81	5	40.8854	1000	1.685
3	1	0.025	9.81	10	81.7708	1000	6.738

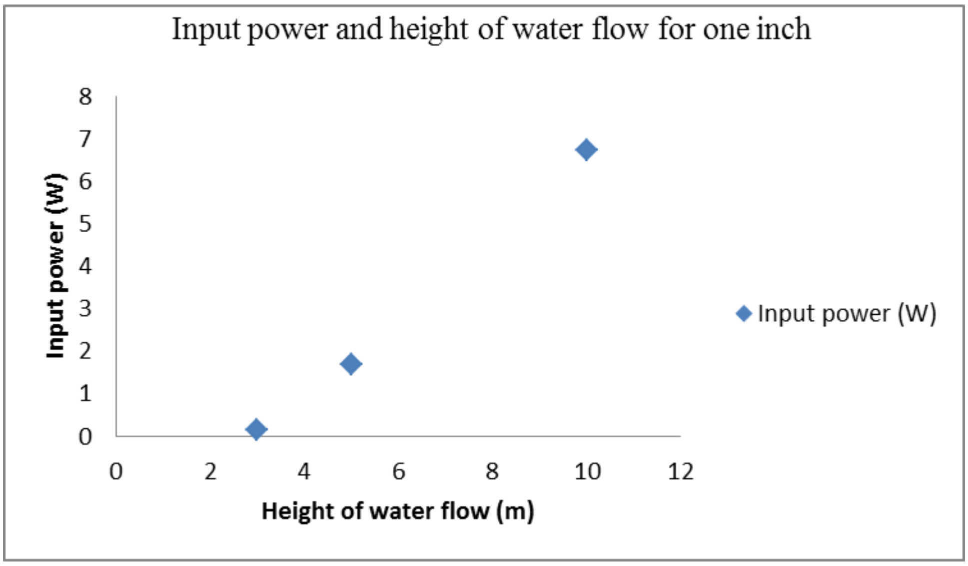

Figure 10 Input power depend on height of water flow with one-inch pipe

Table 4 Calculation of the water flow rate for 2 inch.

Sr	Diameter		Acceleration due to gravity (ms^{-2})	High (m)	flow rate (Q) ($\mu m^3/s$)	Density of fluid (kg/m^3)	input power of the turbine (watt)
	inches	meter (m)					
1	2	0.05	9.81	3	98.125	1000	2.426
2	2	0.05	9.81	5	163.5416	1000	6.738
3	2	0.05	9.81	10	327.0833	1000	26.953

Table 5 The input power of flow water for 2-inch head and height of 3m, 5m, 10m.

Sr	Diameter		Acceleration due to gravity (ms^{-2})	High (m)	flow rate (Q) ($\mu m^3/s$)	Density of fluid (kg/m^3)	input power of the turbine (watt)
	inches	meter (m)					
1	2	0.05	9.81	3	98.125	1000	2.426
2	2	0.05	9.81	5	163.5416	1000	6.738
3	2	0.05	9.81	10	327.0833	1000	26.953

Table 6 Experimental results for flow turbine for height of 3 m with 1 inch.

1	Volume	H (m)	Time (min)	Volt (V)	Current(I) (mA)	RPM	Power(P) (mW)
2	20 L	3	0.77	2.2 V	53	30	0.117
3	20 L	3	0.77	1.9 V	52	29	0.099
4	20 L	3	0.75	2.2 V	56	31	0.123
5	20 L	3	0.749	2.3 V	61	32	0.140
6	40 L	3	1:08	4.5 V	124	82	0.558
7	40 L	3	01:00	6 V	141	110	0.846

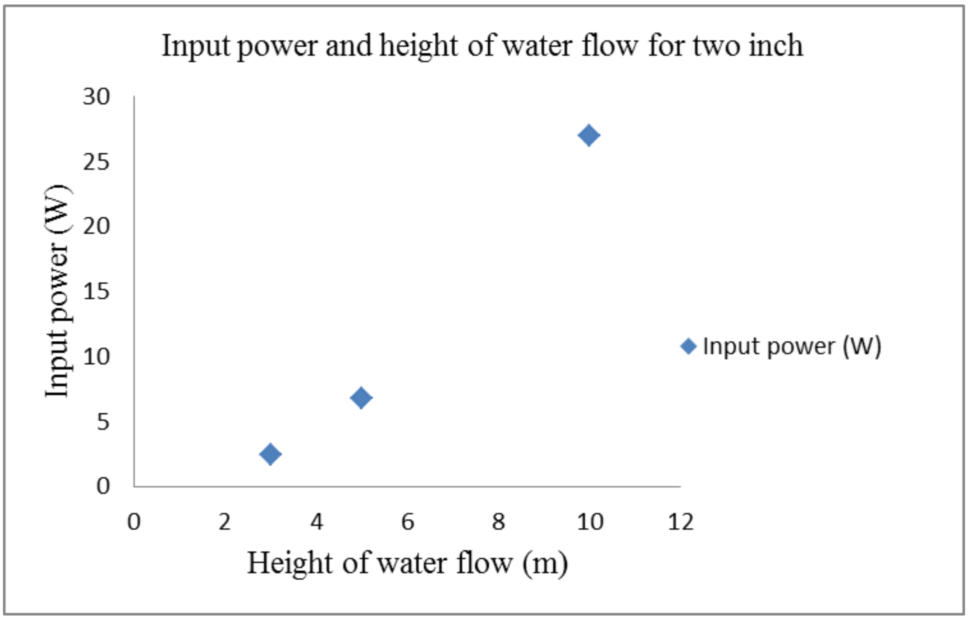

Figure 11 Input power depend on height of water flow with 2 inch pipe

Discussion

Design applied to the development of products, environments which has a user perspective and drives development based on your specific customer needs. Especially in mountainous areas where grid connection was connect to difficult and expensive. Other ways unreliable energy sources were required. Flow turbine was suitable device for this area. Flow turbines were few moving parts, compact systems and good efficiency. Flow turbines can operate continuously or on demand and be either grid connected or stand alone. Not like the big hydro plants that use dams and create giant lakes behind the dams, flown turbine plants only divert a fraction of the stream and they don’t need a water storage pool. In rare cases where the site is close to grid lines, part of the produced power can be sold back to the utility, and the grid serves as backup for future plane. The flow turbine plant requires low maintenance.

Flow turbine systems produce no pollution. Flow turbine is made easily by local materials. This turbine can make themselves live in rural area peoples. Main disadvantage is required always flow stream nearby setup area. During the summer there will be less flow and therefore less power output. Advanced planning and research will be needed to ensure adequate energy requirement.

Conclusion

The flow turbine efficiency was depend upon the water flow rate, head length and blades factors. It can modify to output power 1 kW with same structure. As the power demand increases the size of the plant can be easily expandable. During the summer, there will be less flow and therefore less power output. This flow turbine is capable of producing up to 4.8 W output power at the head length of 10 m and flow rate of the performance test at selected site location by changing the water flow rate. The power output of this turbine is 0.85 watt with 110 RPM for 3 m height and 1-inch head. Advanced planning and research will be needed to adequate energy requirements. Thus, this turbine is suitable for rural area in Myanmar.

Acknowledgements

The Authors would like to thanks Professor Dr Khin Khin Win, Head of Department of Physics, University of Yangon for her kind encouragement to complete this research paper. I would like to express my sincere thanks to Myanmar Academy of Arts and Science for their kind permission to reading of this research. I am also very grateful to all Professors and teachers of Department of Physics, University of Yangon, for their kind understanding.

References

Andy Karsner (2008- May). Electricity – Innovative Technologies towards Sustainable Development. Pg.1-21.

Abhishek Sharma, D. Buddhi (2016). Design and Development of a Cross Flow Micro Hydro Turbine., *International Journal of Science, Engineering and technology.* Volume 4 Issue (2), pg.351-358.

MRS. Urmila S. Zope (2017 – March). Design and Manufacturing Process of Small Scale Water Turbine by Using RPRT for Energy Harvesting. *International Journal of Research Publications in Engineering and Technology.* Volume3, ISSUE3, pg.44-52

Nippon Koei / IEEJ, Design of Generation Equipment. The Study on Introduction of Renewable Energies in Rural Areas in MYANMAR, Volume 4 Manuals Part 2. pg.54-73.

Hemant Sharma, Jasvir Singh, Run -off -River Plant: Status and Prospects, *International Journal of Innovative Technology and Exploring Engineering (IJITEE)*, Volume-3, Issue-2, July 2013, pg. no: 210-213.

J. Myanmar Acad. Arts Sci. 2020 **Vol. XVIII.No.2C**

ANNEALING EFFECTS ON TRACKS IN MAKROFOL DETECTORS (SSNTDs)

Khin Moe War[1], Win Min Than[2]

Abstract

A change of fission track density and track length in Makrofol with different annealing temperature and annealing time was investigated. Ten pieces of (1 cm x 1 cm) Makrofol detectors each was contacted with ^{252} Cf source for 1 hour. Among them, two pieces were unannealed. Four pieces of Makrofol with fission tracks were annealed at 60° C and the other four pieces were annealed at 100°C for 30 min, 60 min, 90 min and 120 min respectively. After that the annealed and unannealed detectors were etched in 6.25N NaOH at 60°C for 75 min. The fission fragment tracks were counted and the tracks length were measured with the aid of an optical microscope. The average tracks densities of detector were calculated at different temperature and various time. It was found that the tracks length and tack density decrease with the increasing of annealing time and annealing temperature.

Keywords : Makrofol, SSNTDs, unannealed, annealed

Introduction

Solid state nuclear track detectors (SSNTDs) have been used in different areas of science such as nuclear physics, particle physics, cosmic ray physics, environmental physics, and archaeology. Polycarbonate Track Detector is a commonly used Solid State Nuclear Track Detector (SSNTD) to identify the fission fragment. Makrofol, a polycarbonate material, is a particular group of thermoplastic polymers. It is available in three types which are Makrofol N, KG and Makrofol SKG blue. Makrofol N and KG are not available in suitable thickness below 20 µ m. Makrofol SKG blue is available in suitable thickness of 2.0 µm and 6.0 µm. Makrofol polycarbonates are prepared from diphenylol-alkanes, of which the commonest is 2,2- diphenylol - propane or Bisphenol A (BPA) with structural formula as shown in figure 1(a)and (b).

Makrofol-N (white in colour) is a bisphenol-A polycarbonate with a chemical composition of $C_{16}H_{14}O_3$ known as a good industrial material with high impact resistance and dimensional stability over a broad temperature range.

(a)

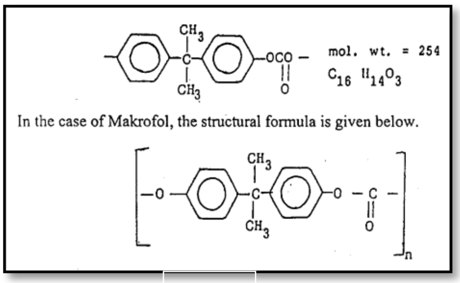

(b)

Figure 1 (a) Photograph of Makrofol-N detector (b) The structural diagram of Makrofol

---

[1] Dr, Assistant Lecturer, Department of Physics, University of Yangon

[2] Assistant Lecturer, Department of Physics, University of Yangon

When ionizing particles like alpha particles and fission fragments pass through a non-conducting material, like crystal, polycarbonate, etc., damaged sites known as latent tracks occur along their paths. Polymers composed of large molecules and the damages form as a result of breaking of the molecular bonds.

The annealing is supposed to start with recombination of ions and electrons to form atoms at interstices and later diffusion of atoms towards the damaged zone. The diffusion takes place under stress. One of the advantages of this process is to eliminate the pre-existing background track signal. And annealing temperature must be carefully applied since overheating causes some structural changes in the detector material and in extreme conditions may even disfigure it.

If an SSNTD is chemically etched after exposure to radon and fission products, tracks caused by the radiation will enlarge. These tracks can then be counted with an ordinary optical microscope.

The present paper deals with the study of thermal annealing with track density and track length of ^{252}Cf fission fragments using unannealed and annealed Makrofol-N detectors.

Experimental Procedure

Materials and methods

In the present work, Makrofol-N polycarbonate plastic was used as fission track detector. Dependence of fission track length and track density of Makrofol on annealing time and temperature was studied. The block diagram of experimental procedure of Makrofol is shown in figure (2).

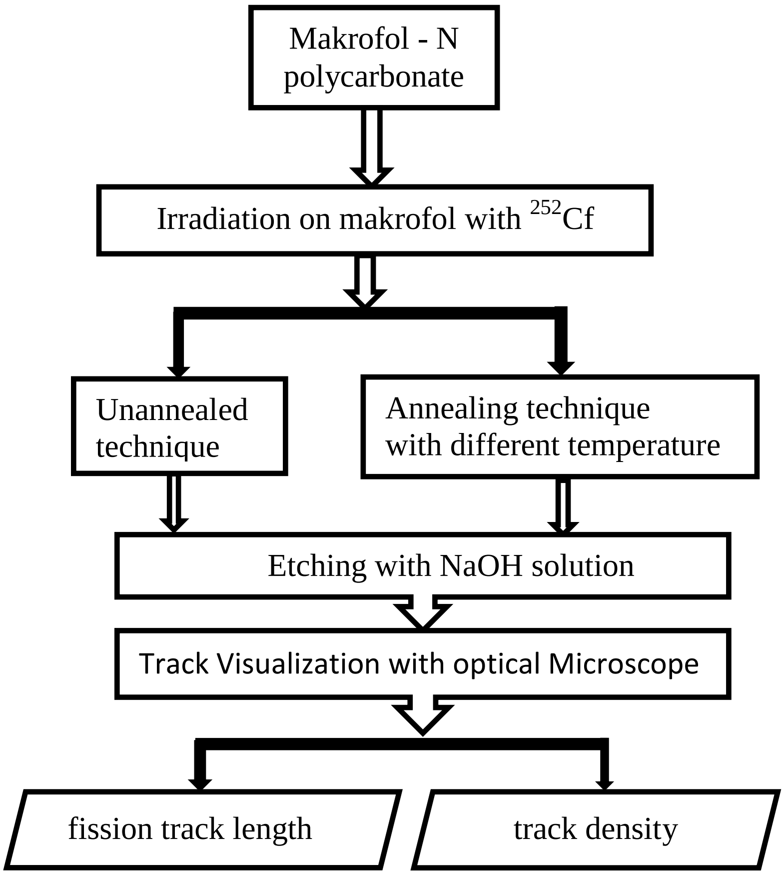

Figure 2 The block diagram of experimental procedure of Makrofol

Irradiation on Makrofol with ^{252}Cf

Californium ^{252}Cf fission source was used for irradiation of the makrofol detectors in the present work. Its diameter is 25 mm and its thickness is 0.5 mm. The active area is a diameter of 10 mm and the source activity is 1.02 µCi. The nuclide ^{252}Cf disintegrates with a probability of 3.09 % by spontaneous fission. The fission fragments have fission energies 80 MeV and 104 MeV. Its half-life is 2.64 years. The energy of emitted a particles are 6.1184 MeV, 6.076 MeV and 5.977 MeV. The fission rate is about10^3 fission per µCi with fission fragments energies ranging from 80 MeV to 104 MeV.

A sheet of Makrofol ($C_{16}H_{14}O_3$) detectors were cut into small pieces with dimension of 1 cm x 1 cm in each piece. Each piece of detector was irradiated for 1 hour with ^{252}Cf sources in contact under the atmosphere. The schematic diagram of detector irradiation was shown in figure (3).

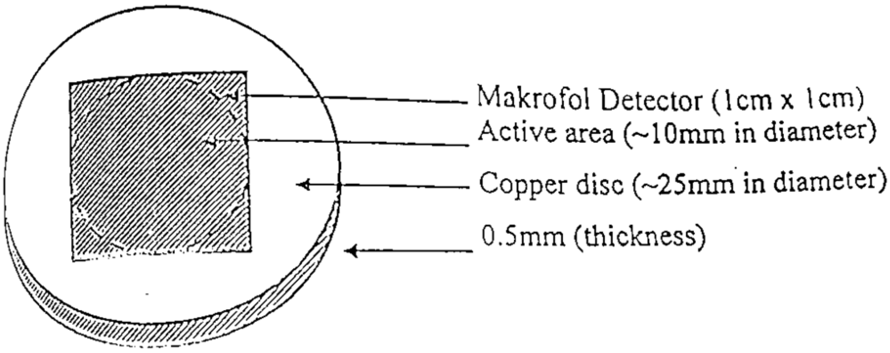

Figure 3 Detector irradiation with ^{252}Cf source

Annealing technique with different temperature

After irradiation, the tracks of fission fragments were formed in the pieces of Makrofol samples. Among them, four pieces each was heated in a muffle furnace at 60° C for 30 min, 60 min, 90 min and 120 min respectively. Then they were cooled under the atmosphere at the room temperature. Other four pieces of irradiated Makrofol detectors each individual was annealed at 100°C from 30 min to 120 min respectively. After annealing all the detectors were cooled down at the room temperature.

Preparation of the Etchant

6.25 N NaOH solution was prepared for etching all the annealed and unannealed detectors. To obtain 6.25 N NaOH solution, 25 g of NaOH pellets (99% purity) were put into 100 ml measuring cylinder. Then distilled water was poured on the NaOH pallets in the measuring cylinder and stirred with a glass rod, until all NaOH pellets were dissolved. The distilled water was added to get 100 ml solution. After that, the solution was poured into a 100 ml glass beaker. Figure (4)

25 g NaOH Distilled water 6.25 N NaOH solution

Figure 4 Preparation of 6.25 N NaOH

Etching of the detectors

The solution of NaOH (6.25 N) in the beaker was heated on a stove with temperature controller. The process of etching and microscopic observation are repeated till the optimum condition of tracks and the maximum track length became invariant with furture etching. When the temperature reached at 60°C, it has no invariant condition, the annealed and unannealed detectors of Makrofol were put into the beaker for 70 min. All samples were held at the same depth in the etchant solution. During etching, the temperature was kept 60°C with an accuracy of ±1°C. After etching, the etched detectors were collected with plastic sieve with handle. Then, the detectors were washed under the running water until the surfaces of detectors were cleaned from etchant. Finally the detectors were dried with filter paper. Figure (5).

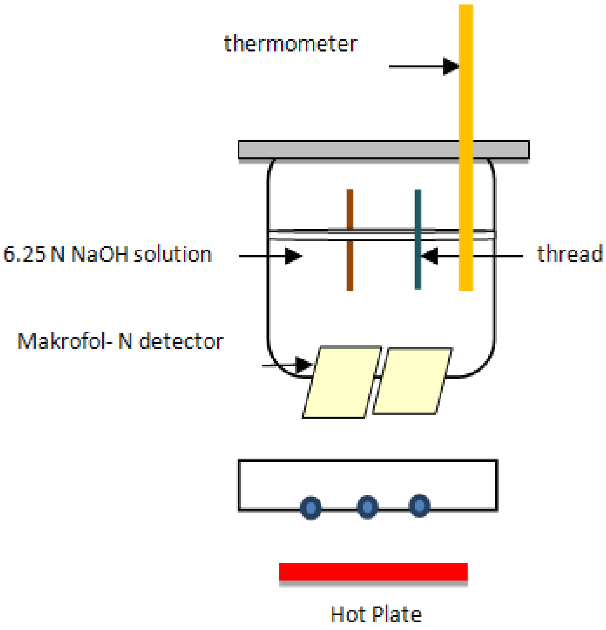

Figure 5 The schematic diagram of chemical etching

Track Visualization with optical Microscope

After doing the etching process, the tracks visualization, track photographing, track counting and measuring the length of tracks were done by using optical microscope (Nikon Eclipse 50 i) at a magnification of 40 x and 100 x to get the fission track length and number of fission tracks.(Figure 6)

The microscope was attached with DS camera and camera control unit to take microphotograph of detectors. The number of tracks on the detector was recorded view by view by changing the vertical and horizontal position of detector.

Figure 6 optical microscope (Nikon Eclipse 50 i) with DS -5M camera

The average track density on the detector was calculated from the following equation.

$$\text{Average Track density} = \frac{\text{no of truck}/_{\text{view}}}{\text{area}/_{\text{view}}}$$

After that,the standard deviation of track densities and track length were calculated from the following equation.

Standard Deviation's equation

$$SD = \sqrt{\frac{1}{N}\ \sum_{i=1}^{N}(x_i - \bar{x}\ )^2}$$

Where, N = no of views
x = no of tracks per area
$\bar{x}$ = average tracks per area
SD = standard deviation

Results and Discussions

After observing the variation of track lengths and track densities under optical microscope attached with digital camera, the following results for each annealing condition have been expressed.

The average track density due to different annealing temperature at 60ºC and 100ºC are shown in Table (1) and Table (2). The curves using data from Table (1) and (2) are shown in Figure (7) and (8).

The average track length due to different annealing temperature at 60°C and 100°C are shown in Table (3) and Table (4). The curves using data from Table (3) and (4) are shown in Figure (9) and (10).

Figure (11) and Figure (12) showed the comparison of average fission track densities and track length in makrofol detectors after annealing at 60°C and 100°C for different annealing time.

The photographs of Makrofol detector with fission track of annealing time for 30 min and 60 min at annealing temperature 60°C and 100°C were illustrated in Figure (13) to Figure (16).

For Makrofol detectors with fission track, it is found that the average track density and average track length decrease with increasing annealing temperature and annealing time. It may be due to the repairing of broken molecular chain in the Makrofol as annealing proceeds.

Table 1 Average fission track densities in Makrofol SSNTDs for after annealing at 60°C for different annealing time

Sr. No	Annealing temperature (°C)	Annealing time (min)	Average track densities (track/mm^2)
1.	-	0	115.92 ± 3.52
2.	60	30	110.20 ± 3.67
3.		60	107.75 ± 3.89
4.		90	99.18 ± 2.03
5.		120	91.43 ± 3.90

Table 2 Average fission track densities in Makrofol SSNTDs for after annealing at 100°C for different annealing time

Sr. No	**Annealing temperature (°C)**	**Annealing time (min)**	**Average track densities (track/mm^2)**
1.	-	0	82.44 ± 2.06
2.	100	30	78.36 ± 2.32
3.		60	71.83 ± 1.75
4.		90	65.30 ± 1.23
5.		120	60.41 ± 1.37

Table 3 Average fission track length in Makrofol SSNTDs after annealing at 60°C

Sr. No	**Annealing time (min)**	**Average track length (μm)**
1.	0	6.24 ± 1.47
2.	30	5.36 ± 1.67
3.	60	4.92 ± 1.44
4.	90	3.80 ± 1.23
5.	120	2.76 ± 1.65

Table 4 Average fission track length in Makrofol SSNTDs after annealing at 100ºC

Sr. No	Annealing time (min)	Average track length (μm)
1.	0	3.84 ± 0.83
2.	30	3.20 ± 1.52
3.	60	2.82 ± 0.89
4.	90	2.22 ± 1.00
5.	120	1.89 ± 0.81

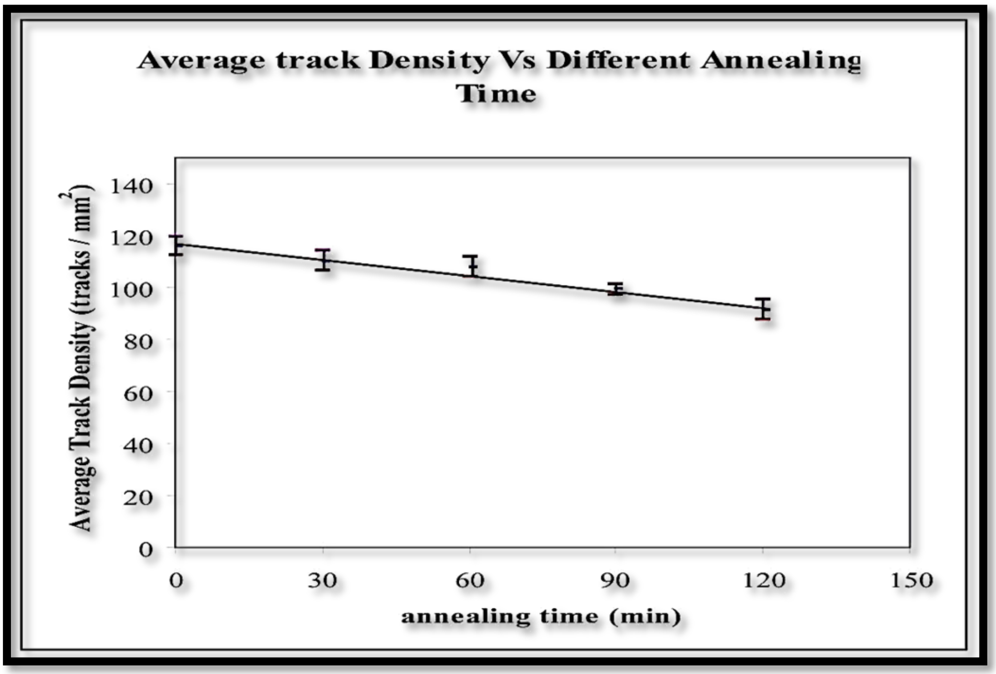

Figure 7 The variation of average track densities in Makrofol SSNTDs after annealing at 60ºC for different annealing time.

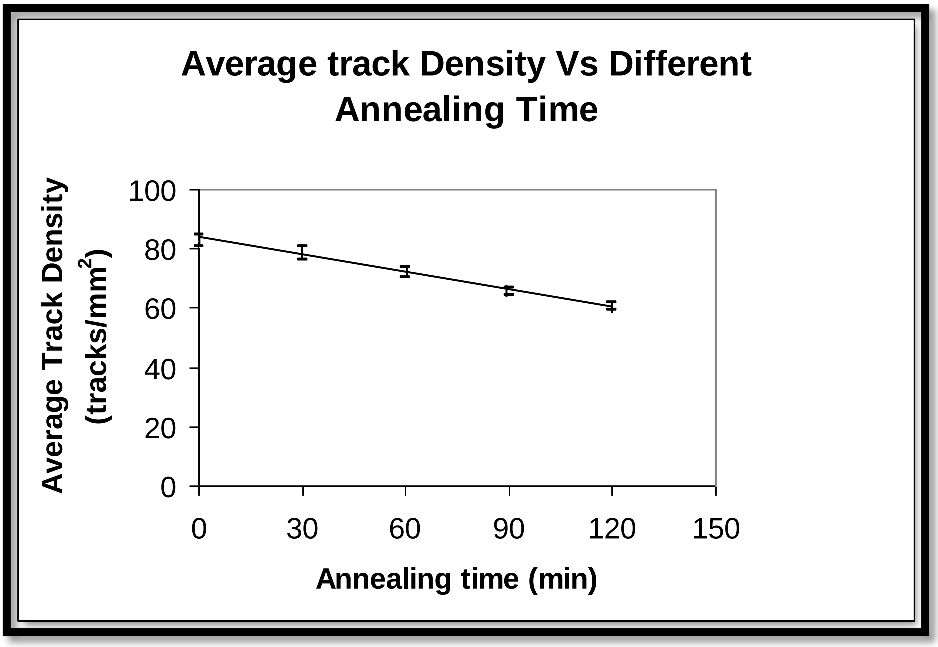

Figure 8 The variation of average track densities in Makrofol SSNTDs after annealing at 100ºC for different annealing time.

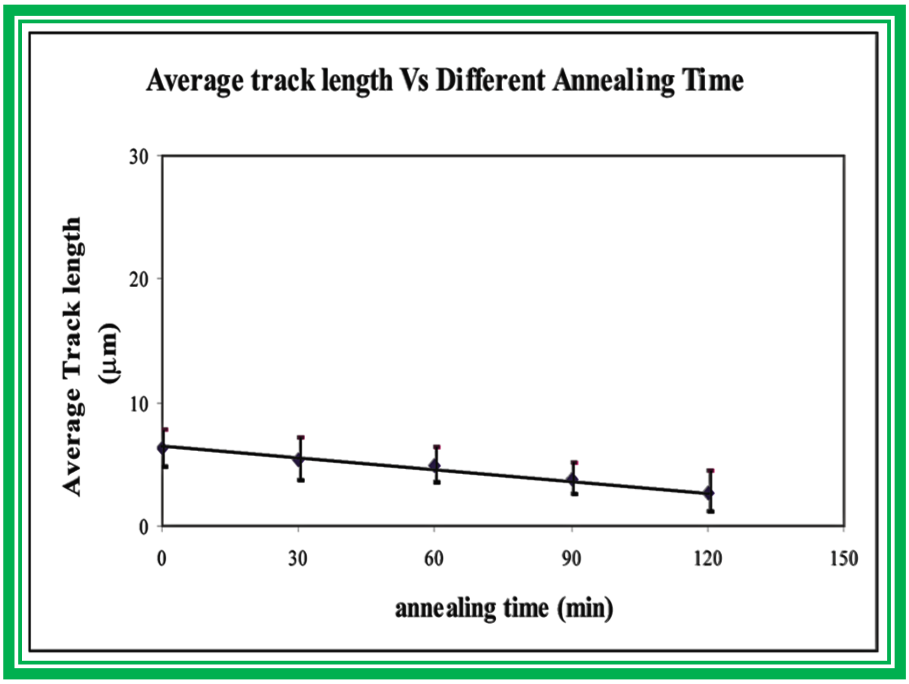

Figure 9 The comparison of average track lengths due to different annealing time for annealing temperature at 60ºC and 100ºC in makrofol (SSNTDs)

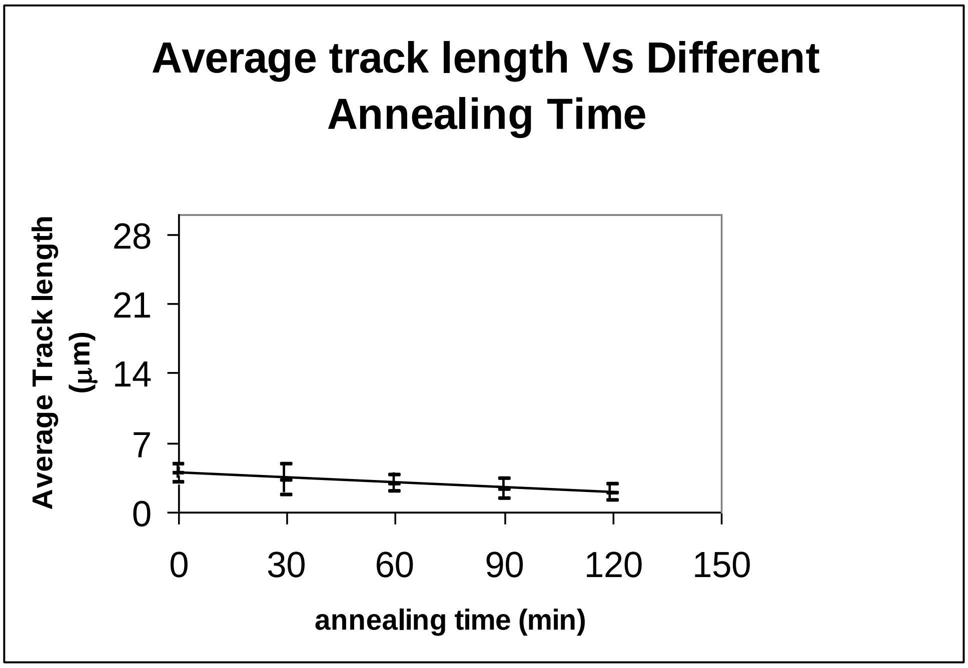

Figure 10 The variation of average track lengths with different annealing time at 100ºC in Makrofol (SSNTDs)

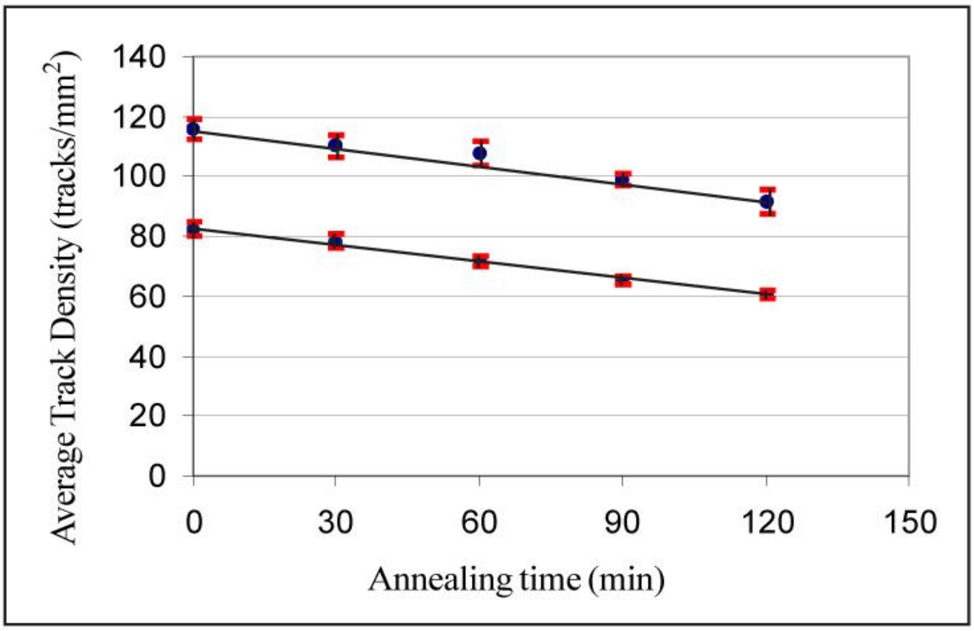

Figure 11 The comparison of average fission track densities in Makrofol SSNTDs after annealing at 60ºC and 100ºC for different annealing time.

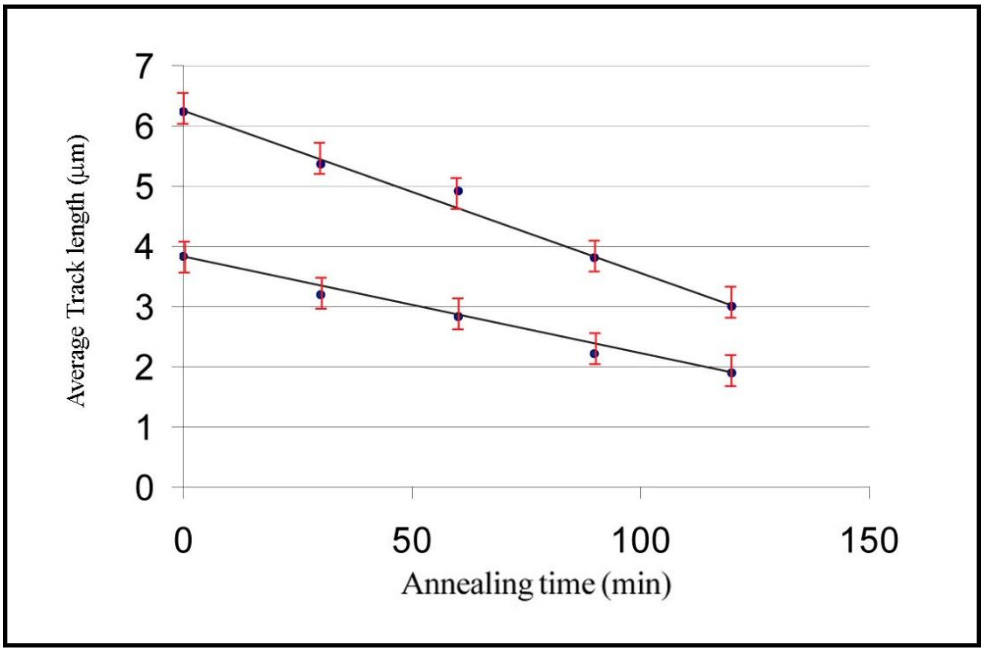

Figure 12 The comparison of average track lengths due to different annealing time for annealing temperature at 60ºC and 100ºC in Makrofol (SSNTDs)

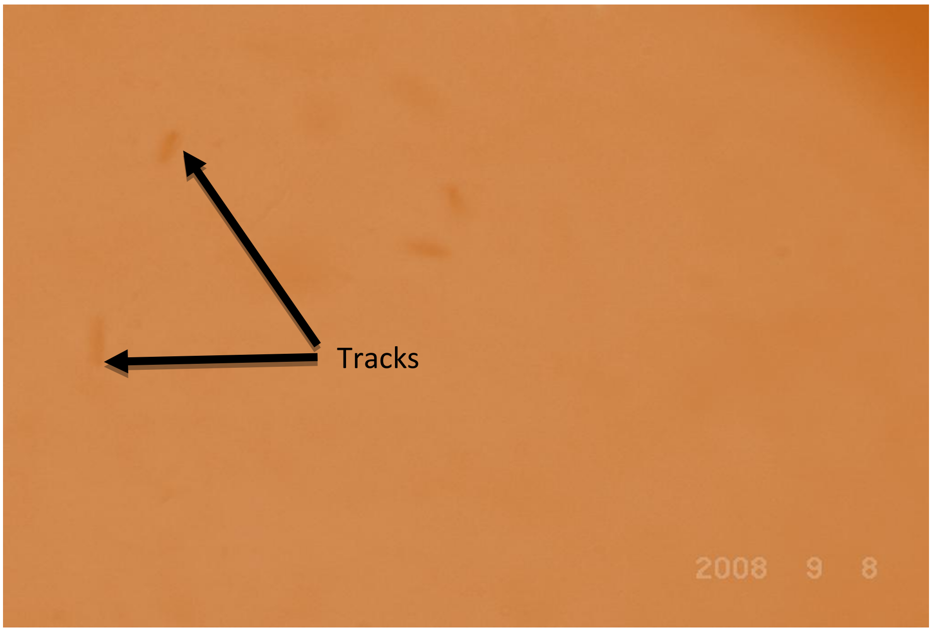

Figure 13 Photomicrograph of fission tracks in Makrofol detector after annealing at 60°C for 30 min

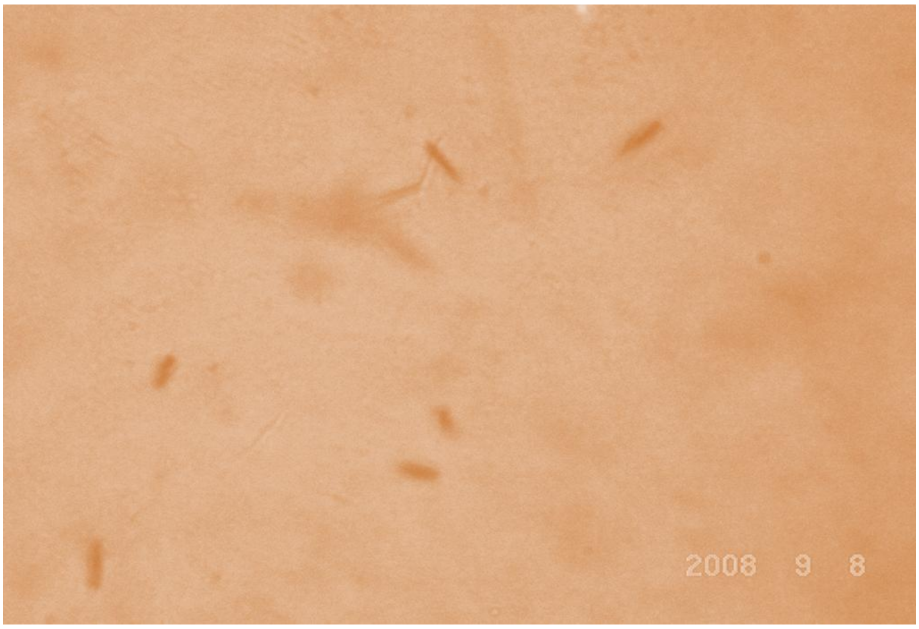

Figure 14 Photomicrograph of fission tracks in makrofol detector after annealing at 60ºC for 60 min

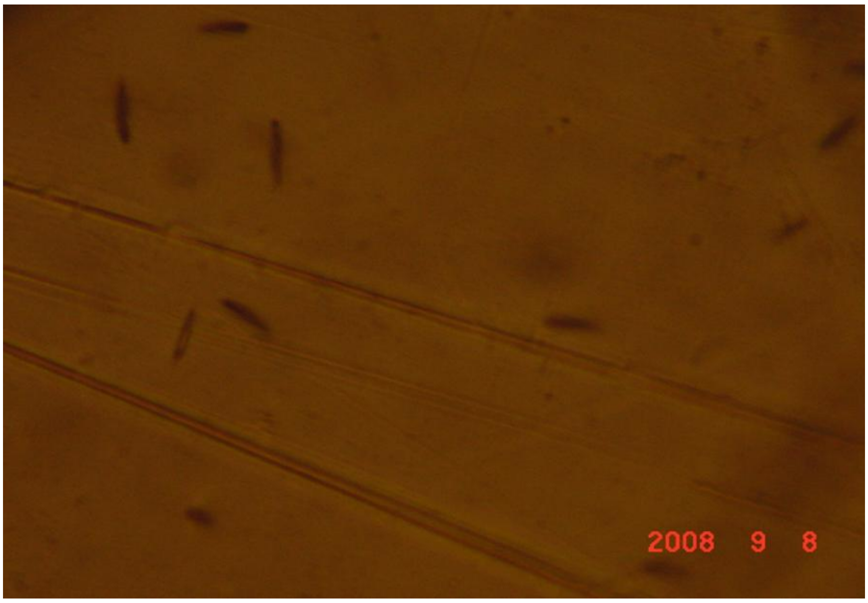

Figure 15 Photomicrograph of fission tracks in makrofol detector after annealing at 100ºC for 30 min

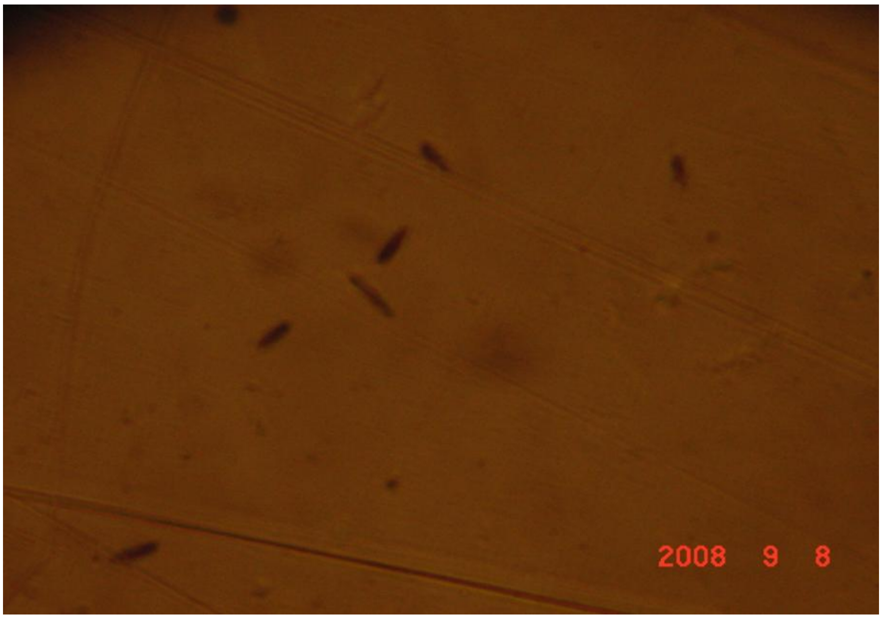

Figure 16 Photomicrograph of fission tracks in Makrofol Detector after annealing at 100ºC for 60 min

Conclusion

From the results, the average densities of unannealed Makrofol are 115.92 ± 3.52 track/ mm^2 and 82.44 ± 2.06 track/mm^2 . And the average track lengths are 6.24 ± 1.47 μm and 3.84 ± 0.83 μm. It was found that the average density and average track length of unannealed samples were more than that of annealed samples at different temperature and time by comparing data. There is an annealing effect on tracks in both Makrofol. The annealing of the damage trails at elevated temperature presumably occurs via the movement of molecular fragments with a Makrofol.

It was concluded that the tracks length and tack density decrease with the increasing of annealing time and annealing temperature.

Acknowledgements

I would like to thank Professor Dr Khin Khin Win, Head of Department of Physics, University of Yangon , for her kind permission to carry out this research.

I also would like to thank Dr Myo Lwin, Professor, Department of Physics, University of Yangon, for her allowing me to do this work.

I also would like to thank Dr Aye Aye Thant, Professor, Department of Physics, University of Yangon, for her allowing me to do this work.

I also would like to thank Dr Yin Maung Maung, Professor, Department of Physics, University of Yangon, for her allowing me to do this work.

References

Yi Yi Myint 2005 " A study of Alpha Tracks in LR-115 Type II Red Cellu Lose Nitrate Solid State Nuclear Track Detectors" , PhD Thesis, (University of Yangon: Myanmar)

P F Green and S A Durrani 1977 "Annealing Studies of Tracks in Crystals" Nuclear. Track. Detection 1,33-9.

Fleischer R L, Price P B, Walker R M 1975 " Nuclear Tracks in Solids Principles and Applications", (Berkeley: University of California)

Shwe Nan Htet 2007 "Annealing Effect on Tracks in CR 39 And Neutron Effect on CR 39, Makrofol SSNTD" PhD Thesis, (University of Yangon: Myanmar).

J. Myanmar Acad. Arts Sci. 2020 **Vol. XVIII.No.2C**

STUDY ON DIFFERENT PYROLYSIS TEMPERATURES OF DRACONTOMELON DAO (PACIFIC WALNUT) BIOCHAR

Nway Han Myat Thin[1], Toe Toe Wai[2], Shwe Sin Aung[3], Zin Min Myat[4]

Abstract

Biochar derived from biomass waste is accepted as multifunctional material for various applications according to its specific characteristics. It is therefore popular to investigate biochar properties under the improvement of research application. In this study, biochar derived from Dracontomelondao fruit shell (DD nut) (English: Pacific Walnut) from Moe Nyin Township, Kachin State was prepared by different pyrolysis temperatures (400, 500 and 600ºC) at one hour each. Structural properties of the resulted biochar were characterized by X-ray Diffraction (XRD) technique, infrared spectroscopy (FTIR), and Scanning Electron Microscopy (SEM) technique. Changes in properties of Dracontomelondao biochar with different temperatures were investigated.

Keywords*:* Dracontomelondao, biochar, pyrolysis temperature

Introduction

Dracontomelon-dao (Myanmar: ngapauk thee; Indonesian: dahu; Malay: sengkuang; Thai: ka-kho) also known as New Guinea walnut, Pacific walnut or Paldao, is a tropical canopy tree distinguished mostly by its height (reaching up to about 148 feet) for its grayish-brown trunk which is branchless up to about (66 ft) and for its narrow buttresses which can reach up its trunk up to (20ft) high. [Prasad.K *et al* 1993].Its lobes are divided into five lobes. In Myanmar, it is called ngapauk thee due to the fruit is divided into five lobes. Under the methodology, biochar may be produced from any biomass residues from forestry and agriculture, municipal solid waste and other biomass-based materials. In the present work, the DD nut fruit biochar is produced from sustainably managed forests from Moe Nyin Township, Kachin State (generally it is found abundantly in the Upper Myanmar). Biochar refers to the C-rich residues of incomplete combustion of biomass under oxygen limited conditions and at relatively low temperatures [Mosa*et.A.A et al* 2017]. Biochar is more benefit to attention as a functional material in environmental and agricultural application. It has been concerned with multiple benefits with the ability to improve soil fertility, generate carbon neutral energy and increase agricultural output [Harish.K.N *et al* 2013].

Experimental Procedure

The raw materials biomass collected from Moe Nyin Township, Kachin State, were shown in figure (1).The DD nut fruit shells were washed with fresh water to remove soil, dust and other impurities. After washing many times, these shells were dried under sunlight to remove the moisture content. To dry completely, these shells were taken under sunlight about one week. Then the dried and cleaned biomass was heated at 400ºC, 500ºC, 600ºC for one hour each in a muffle furnace. Finally the resulted solid biochar were obtained in figure (2). These biochars were grounded with the aid of agate motor for two hours each to obtain the fined powder biochar. The block diagram was shown in figure (4). These biochars were characterized by XRD, SEM and FTIR spectroscopy.

---

[1] Dr, Assistant Lecturer, Department of Physics, University of Yangon
[2] Dr, Assistant Lecturer, Department of Physics, University of Yangon
[3] Dr, Assistant Lecturer, Department of Physics, University of Yangon
[4] Dr, Assistant Lecturer, Department of Physics, University of Yangon

Figure 1 Photographs of Dracontomelon dao plant and fruit shell

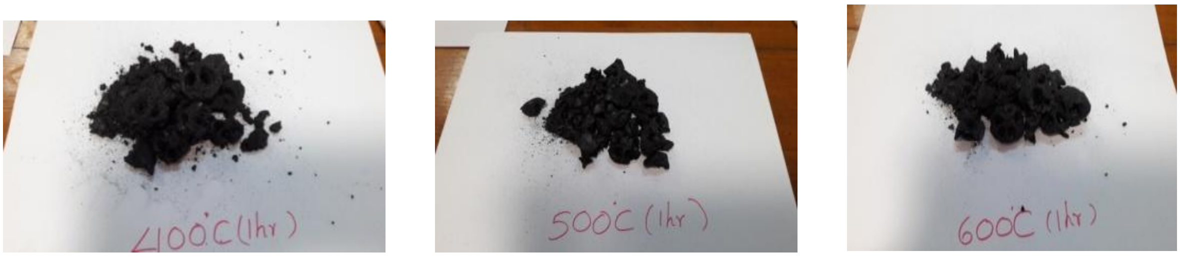

Figure 2 The photograph of solid Dracontomelon dao shell biochar after heating

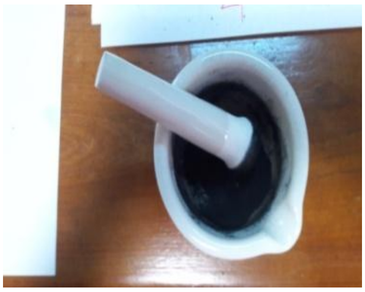

Figure 3 The photograph of powder Dracontomelondao shell biochar

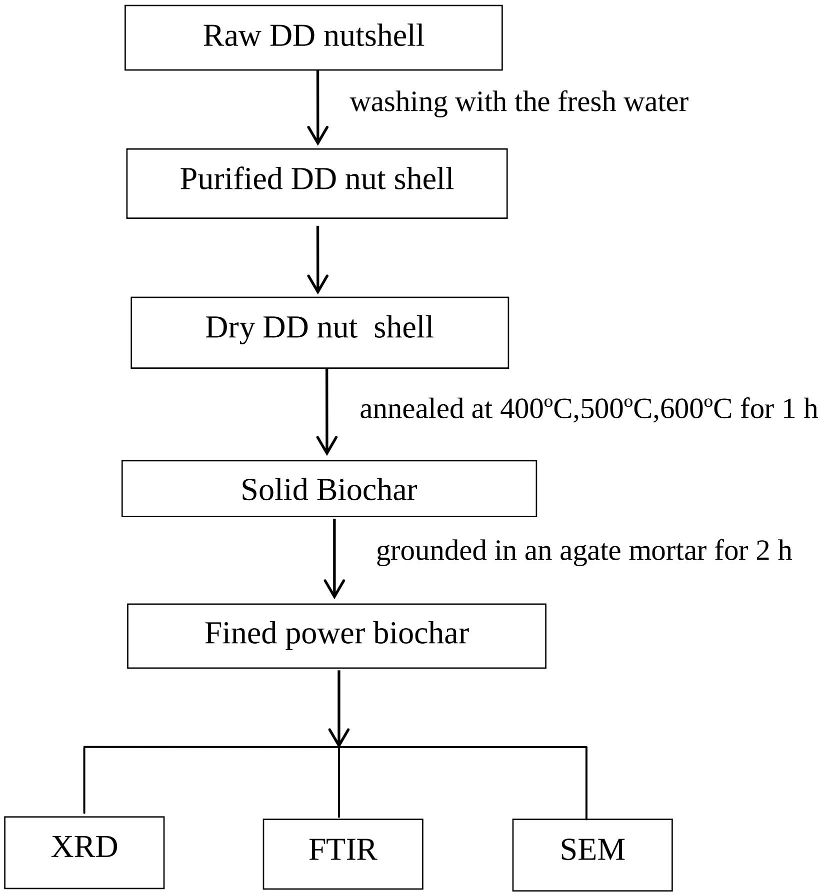

Figure 4 Block diagram for preparation of Dracontomelon dao shell biocher

Results and Discussion

The experimental results and discussion from XRD, SEM and FTIR measurement of Dracontomelon dao shell powders prepared at different temperatures 400°C, 500°C, and 600°C for 1*h* each**.**

XRD Analysis of Dracontomelon Dao Shell Biochar

X-ray diffraction technique (XRD) is a powder technique for dimension of crystal structure, interplanar spacing by using X-ray beam. XRD was used to detect crystalline phase and amorphous structure and any compound were included in this biochars. The XRD spectra on different pyrolysis temperatures (400˚C, 500˚C and 600˚C for 1*h)*were shown in figure 5(a-c). According to XRD result, there are some dominant peaks were observed and other were not perfectly identified. It count be said that the biochar of three different temperatures were found to be amorphous structure with little crystalline peaks. All of the results were found the same metals in the spectra as graphite, carbon, diamond and chaoite.

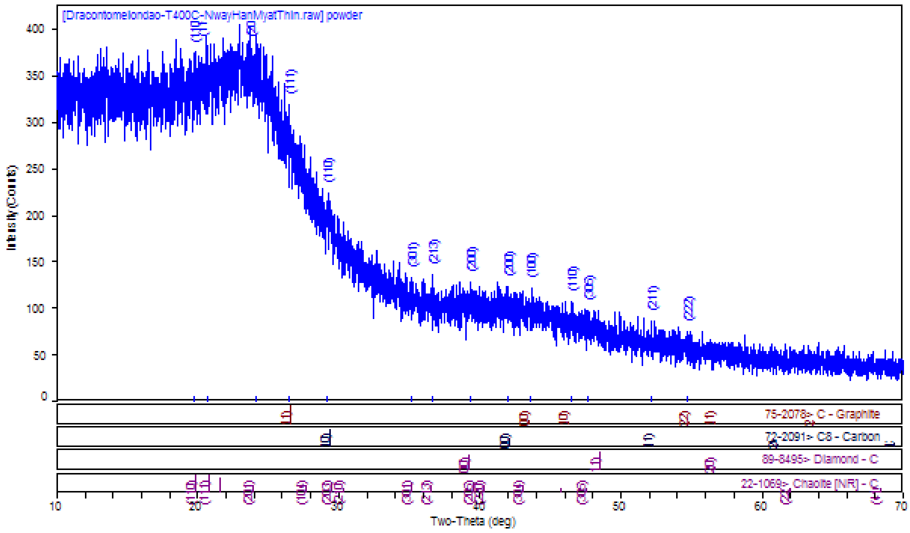

Figure 5 (a) XRD Pattern of Dracontomelon dao shell biocher prepared at 400℃

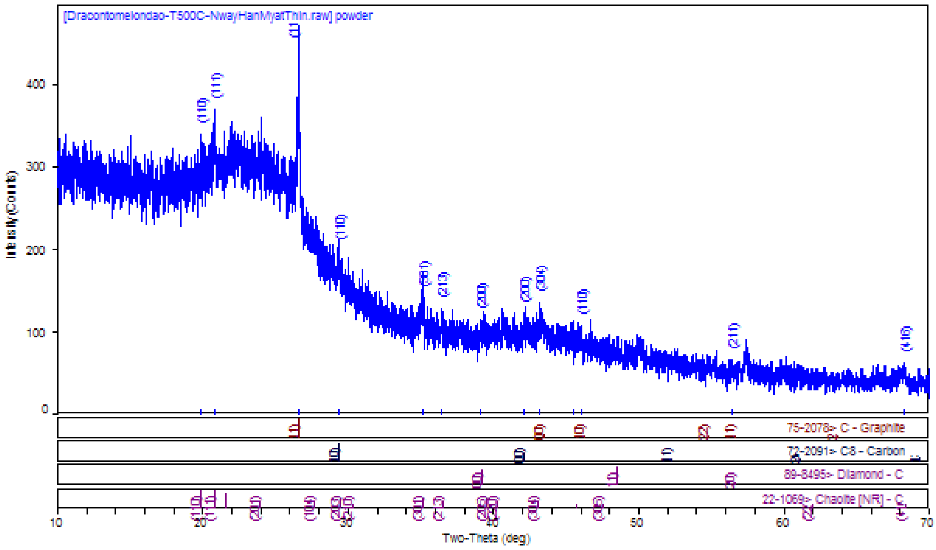

Figure 5 (b) XRD Pattern of Dracontomelon dao shell biocher prepared at 500℃

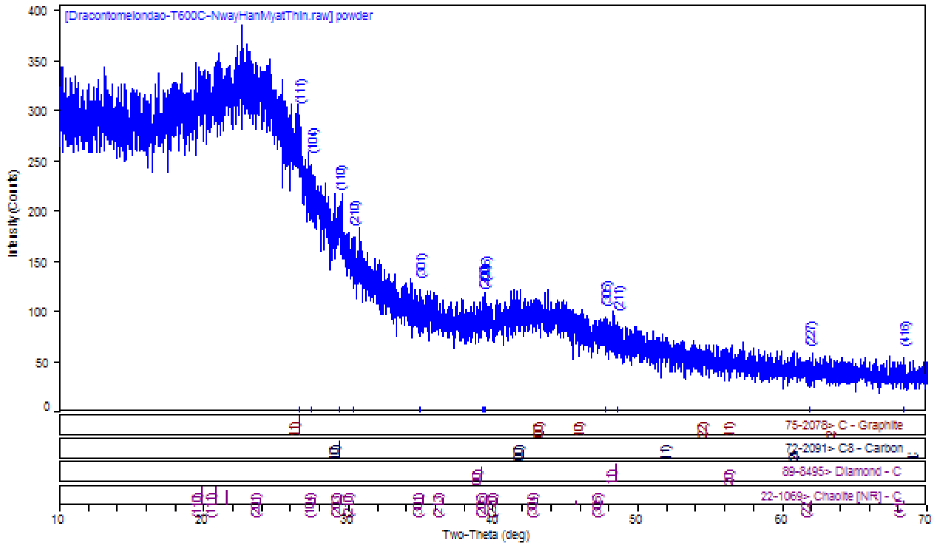

Figure 5 (c) XRD Pattern of Dracontomelon dao shell biocher prepared at 600℃

SEM Morphology of Dracontomelon Dao Fruit Shell Biochar

SEM micrographs for surface morphology of DD nut shell biochar at 400˚C, 500˚C,600˚C for 1h were shown in figure 6(a-c).It can be concluded that the microstructures of DD nut shell biochar were varying the pore sizes with different temperatures. The average pore sizes of the samples were found to be about 9.5µm in 400˚C, 7.9µm in 500˚C, 5.4µm in 600˚C respectively. All the samples presented well-defined pores structure and contained mesopore, micropore and macropore structures.

Table 2 Average Pore Diameter of Dracontomelon Dao Shell Biochar with Different Temperatures from SEM Image

Sr	Temperature (°C)	Time (*h*)	Average pore diameter (µm)
1	400	1	9.5
2	500	1	7.9
3	600	1	5.4

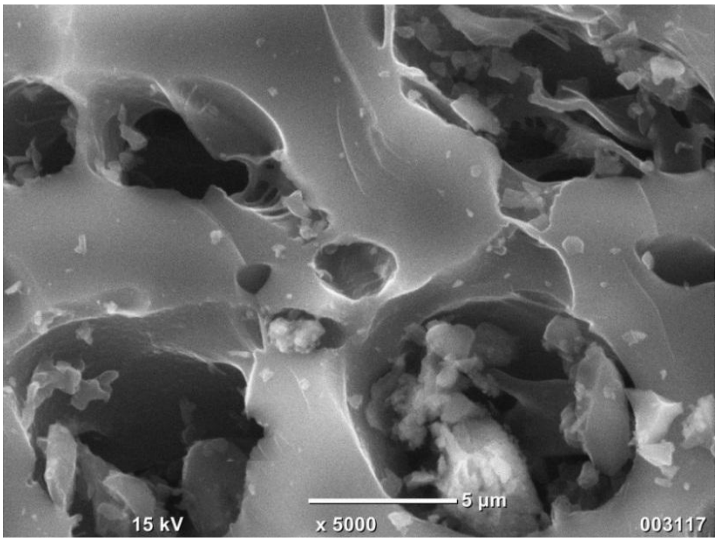

Figure 6(a) SEM photograph of Dracontomelon dao shell biocher prepared at 400℃

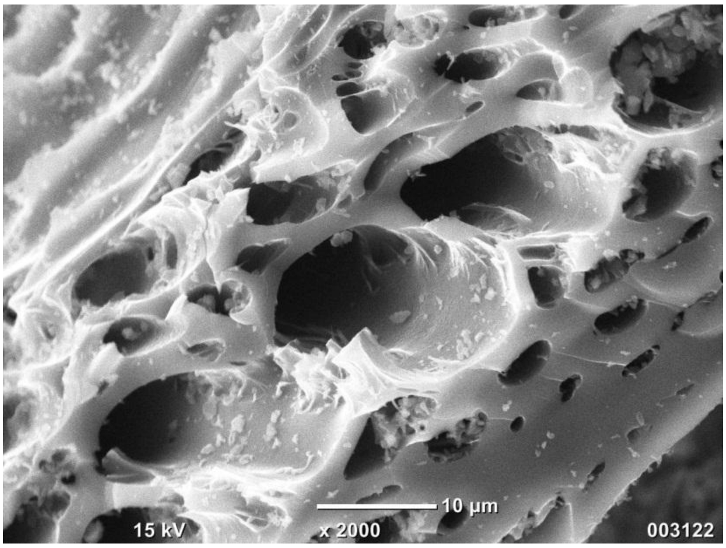

Figure 6 (b) SEM photograph of Dracontomelon dao shell biocher prepared at 500℃

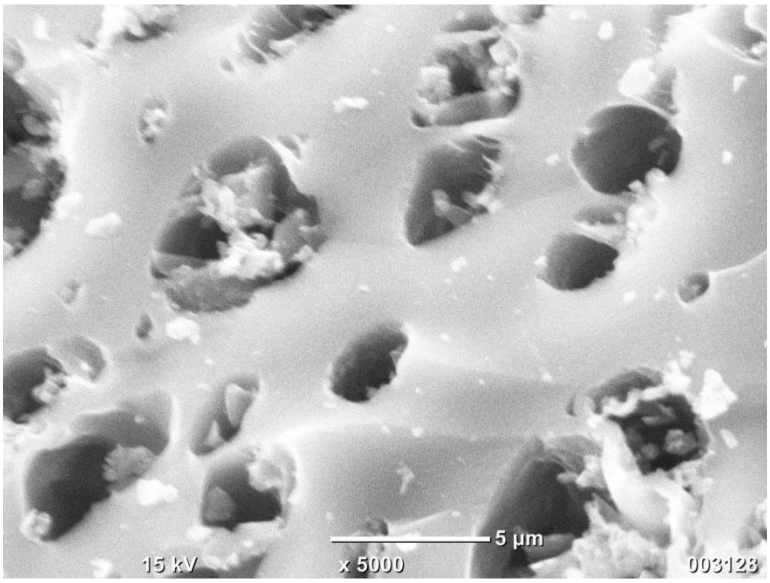

Figure 6 (c) SEM photograph of Dracontomelon dao shell biocher prepared at 600℃

FTIR spectrum Study of Dracontomelon Dao Shell Biocher

The surfaces chemistry of the sample was analyzed by identifying the surface functional groups the samples using Fourier transform infrared spectroscope. The spectra were recorded from 4000 to 400 cm^{-1} resolution in the mid-infrared region. The FTIR analysis demonstrated on different pyrolysis temperatures (400˚C, 500˚C,600˚C) of DD shell were shown in figure 7(a-c). For 400˚C, the first peak at 3179.57 cm-^{1} indicates O-H stretch bond carboxylic acids vibration. The two peaks that are located at (2346.09 cm^{-1}and 2112.57 cm^{-1} for 400˚C) and (2113.72 cm^{-1} and 1919.76 cm^{-1} for 500˚C) observed -C (triple bond) C-stretch alkynes vibrations. The peaks observed at 1577.67 cm^{-} ^{1}for 400˚C and 1573 cm^{-1} for 500˚C were indicated C-C stretch in ring aromatic vibrations. Also the peaks (1162.32 cm-^{1} for 400˚C and 1159.04 cm^{-1} for 500˚C) were found C-O stretch alcohols, carboxylic acid, esters, ether vibrations. The last peaks that are located at 748.15 cm^{-1} in 400˚C and 746.33 cm^{-1} in 500˚C showed the presence of C-H 'oop' bond with aromatics functional groups. FTIR results for 600˚C were shown in figure 7(c). The first two peaks at 2323.22cm^{-1} and 2083.83 cm^{-1} indicated the -C (triple bond) C-stretch alkynes vibrations. Out of these, the peak at 1000.42 cm^{-1} showed C-N stretch modes of aliphatic amines compound. According to FTIR analysis, -C triple bond C-stretching vibrations of alkynes group are consistent with all the samples. The polar group (-OH and CO) significantly decreased when heated to 600˚C. In fact, the functional groups observed on the biochers included, CH, OH, C≡C and C-O, were observed to biocher activities.

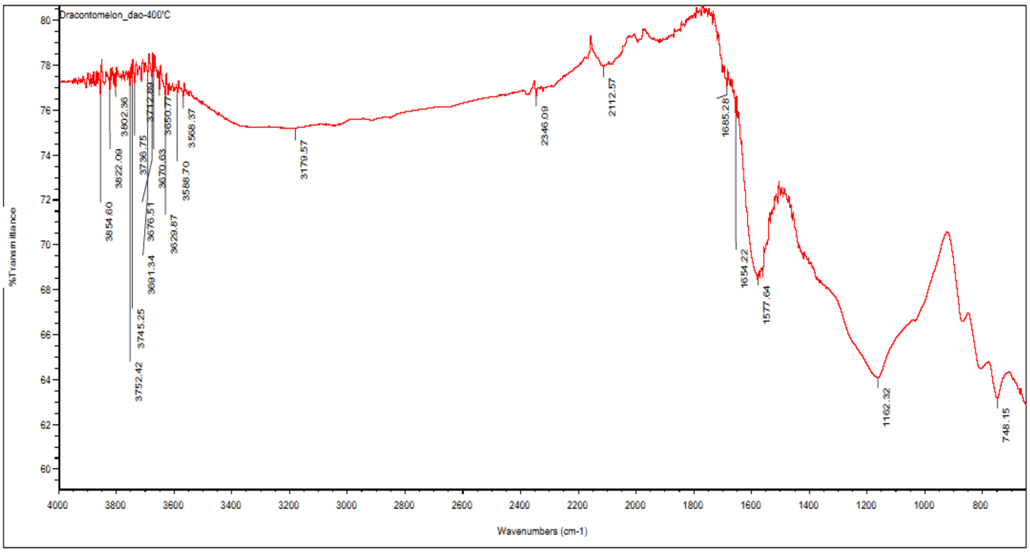

Figure 7 (a) FTIR analysis of Dracontomelon dao shell biocher at 400°C

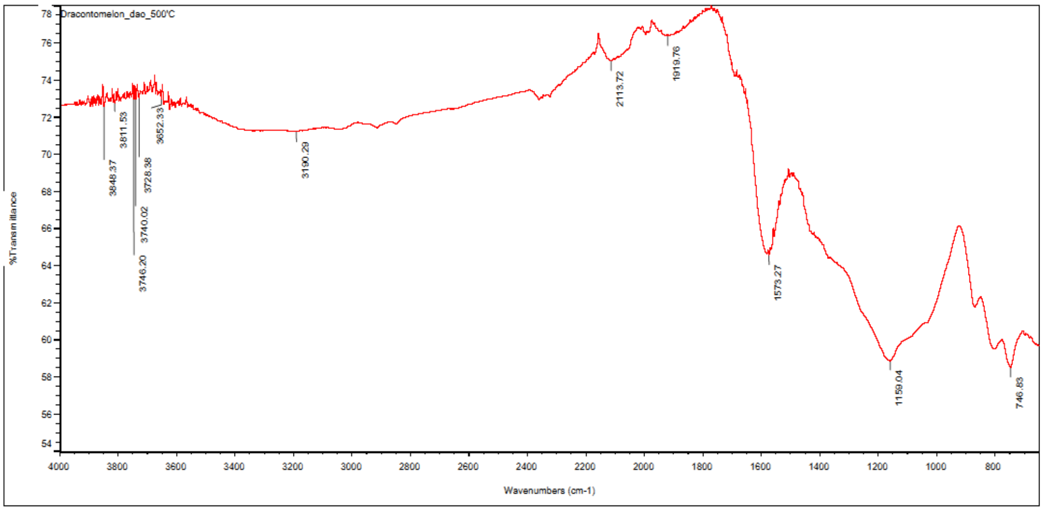

Figure 7 (b) FTIR analysis of Dracontomelon dao shell biocher at 500 °C

Figure 7 (c) FTIR analysis of of Dracontomelon dao shell biocher at 600 °C

Conclusion

The preparation and characterization of three biochars on different pyrolysis temperatures have been studied. According to XRD result, the biochar of three temperatures were found to be amorphous structure with little crystalline and they were matched with the peak of graphite, carbon, diamond and chaoite. The SEM images indicated that the average diameter of porous size becomes smaller when temperature increased. The FTIR spectrum analysis showed the functional groups decreased with the increasing of pyrolysis temperature. According to FTIR analysis, all of the absorption bands are due to hydroxyl group in cellulose, carbonyl groups of acetyl ester in hemicelluloses, and carbonyl aldehyde in lignin. By the three measurements on these three temperatures, the low temperature biochar types are more suitable for absorption area than the higher temperature biochar. The results highlighted the effect of pyrolysis temperatures on this three biochar present a simple, economical and environment-friendly method. According to such characteristics, it will be useful in the biochar application as soil amendment and absorption capacities. So the present work will be benefit in biochars for improving the growth and enhancing the renewable energy in Myanmar.

Acknowledgements

The authors would like to thank Dr Pho Kaung, Rector of University of Yangon for his kind permission to do this research paper.

I would like to express my sincere thanks to Professor Dr Khin Khin Win, Head of the Department of Physics, University of Yangon for her kind encouragement and permission to perform this research work.

I also would like to thank Professor Dr Aye Aye Thant, Professor Dr Myo Lwin, Professor Dr Yin MaungMaung, Professor Dr Than Zaw Oo, Department of Physics, University of Yangon, for their kind advice and suggestions for this research.

References

Harish .K.N (2013) , Archive of Applied Science Research 5 (2) 48

Jain.P.K et al, (2010), Optoelectronics and Advanced Materials, 4 (3) 299-304

Mathe.V.L et al., (2002), J. Master Sci ,25 (4) 347

Prasad.K et al., (1993), J. Master Sci,16 (6) 679

Redfern.S.A , (1996) ,J. Phys. Condens Matte, Vol. 8, PP-8267

Sik.Y et al, (2016) "Biochar: Production, Characterization and Application ". London, CRC Press.

Suryanarayana .C, M.C. Norton, (1998) " X-ray Diffraction, A Practical Approach" , Plenum Press, New York.

J. Myanmar Acad. Arts Sci. 2020 **Vol. XVIII.No.2C**

REEN SYNTHESIS AND CHARACTERIZATION OF ZINC OXIDE FROM *Ixora Coccinea* LEAF EXTRACT AND ITS APPLICATION

Htay HtayWin[1], Thin Thin Kyu[2], Khaing Nway Win[3] , Me Me Aung[4]

Abstract

Zinc oxide particle was synthesized from Ixora Coccinea Leaf (Pone Na Yeik) extract and zinc acetate by biological method. The product was confirmed by X-ray diffraction (XRD), and UV–Vis spectroscopy. Dye Sensitized Solar Cell (DSSC) was assembled by the green prepared ZnO and Ixora Coccinea petal (Pone Na Yeik flower) pigment. In this work, the green synthesis of zinc oxide was used as photoelectrode while carbon counter electrode was applied. After DSSC architecture, J_{SC} (short-circuit photocurrent), V_{OC} (open-circuit photovoltage), FF (fill factor) and η (efficiency) were investigated from the current - voltage (I-V) measurement.

Keywords: Green synthesis, Dye Sensitized Solar Cell, Photoelectrode, Fill factor and efficiency

Introduction

Among various semiconductor, Zinc Oxide is one of the most important semiconductor materials. It has with direct wide bandgap (3.2–3.37 eV) and it is a good transparency at room temperature. Moreover, due to large exciton binding energy of (60 meV), it has potential applications in optoelectronic devices such as solar cells (Barnali Ashe, 2011). Study of nano ZnO doped with various impurities has resulted in several publications leading to books, reviews and papers. Now most of the researchers are working on ZnO by changing the method of preparation to extract the novel character.(S. Yedurkar, C. Maurya, 2016).

Recently, the biosynthesis or green synthesis is an alternative synthesis method to prepare of ZnO using the plant extract. It depends on plant source and the organic compound in the crude leaf extract. Most plants have inherent capacity of reducing and capping of various metals and metal oxides nanoparticles which plays an important role in the bio-reduction and consequently formation of nanoparticles (C.M.Noorjahan, S.K.J Shahina, 2015). Synthesis of nanoparticles using different parts of the plants is quite novel, leading to truly green chemistry which is effective to low cost as there is no need to high pressure, energy, temperature and toxic chemicals (S. Yedurkar, C. Maurya, 2016).

Dye-sensitized solar cells (DSSCs) is a low-cost solar cell belonging to the group of thin film solar cells. They are based on the concept of photo sensitization of wide band gap mesoporous oxide semiconductor such as TiO_2, ZnO and SnO_2.

The performance of dye sensitized solar cells is mainly based on the dye as a sensitizer (Tao-Hua Lee, H J Sue ,2011).

Recently, there is a growing to develop environmentally friendly methods that does not use toxic materials in the synthesis procedures of ZnO particles. In this work, the biosynthesis of ZnO particles by using green Ixora Coccinea leaf extract was studied. These ZnO particles were used as photoelectrode of DSSC with Ixora Coccinea petal dye.

---

[1] Dr, Lecturer, Department of Physics, University of Yangon.

[2,4] Assistant Lecturer of Physics, University of Yangon.

[3] Lecturer, Department of Physics, University of Yangon.

Materials and Methods

Preparation of ZnO particles by biosynthesis method

Fresh leaves of Ixora Coccinea were cleaned with water to remove dust and other contaminations, followed by distilled water and air dried at room temperature. Leaves were finely chopped into small pieces. The aqueous extract of sample was prepared by boiling the freshly collected cut leaves (10 g), with 100 cm^3 of distilled water, at 60˚C for about 30 minutes, until the color of the aqueous solution changes from watery to light brown. Then the extract was cooled to room temperature and filtered using the filter paper.

For the synthesis of zinc oxide nanoparticles, 50 cm^3 of 0.5 M zinc acetate dihydrate solution was prepared using distilled water. 1 cm^3 aqueous leaf extract of Ixora coccinea was added into the above solution. In order to maintain the pH 12, 2.0 $mol{\cdot}dm^{-3}$ sodium hydroxide was used which resulted in a milky white aqueous solution. This was then placed in a magnetic stirrer for 2 hrs. The pale white precipitate was then taken out and washed over and over again with distilled water followed by ethanol to get free of the impurities. Then a pale white powder of zinc oxide particles was obtained after drying at 60˚C in oven about 6 hr. Graphical representation of the procedure is shown in Figure 1. The ZnO powder was checked by X-ray diffraction method (XRD) and to calculate the optical energy band gap by using UV-Vis spectroscopy method.

Ixora Coccinea Dye Extraction

25g petal of Ixora Coccinea (Pone Na Yeik) was ground and mixed with 50 ml of ethanol solvent. The extracted sample was stirred using magnetic stirrer about 30 min. The procedure continued with the filtration of the sample to remove residue. The absorption spectrum of these dye has been investigated by UV-Vis spectrophotometry.

Preparation of electrode

ZnO film on ITO substrate were deposited as follows, 1 g of biosynthesized ZnO powder and 3 ml ethanol were mixed well in agate mortar for one hour. The final mixture was stirred to obtain the desired ZnO paste. The electrode was immersed in the dye solution and then kept overnight at room temperature. Carbon powder was used as carbon catalyst counter electrode.

3 ml of ethanol was poured drop by drop into 1 g of carbon. After grinding for 1h, the carbon solution was obtained. The deposited carbon paste was dried on the hot plate for 15 min.

DSSC Architecture

The dye-sensitized ZnO electrode and the carbon counter electrode were assembled to form a solar cell. A drop of iodide electrolyte solution was sandwiched between the two slides and clipped together to form a complete cell. The conversion efficiencies were recorded under simulated solar light conditions.

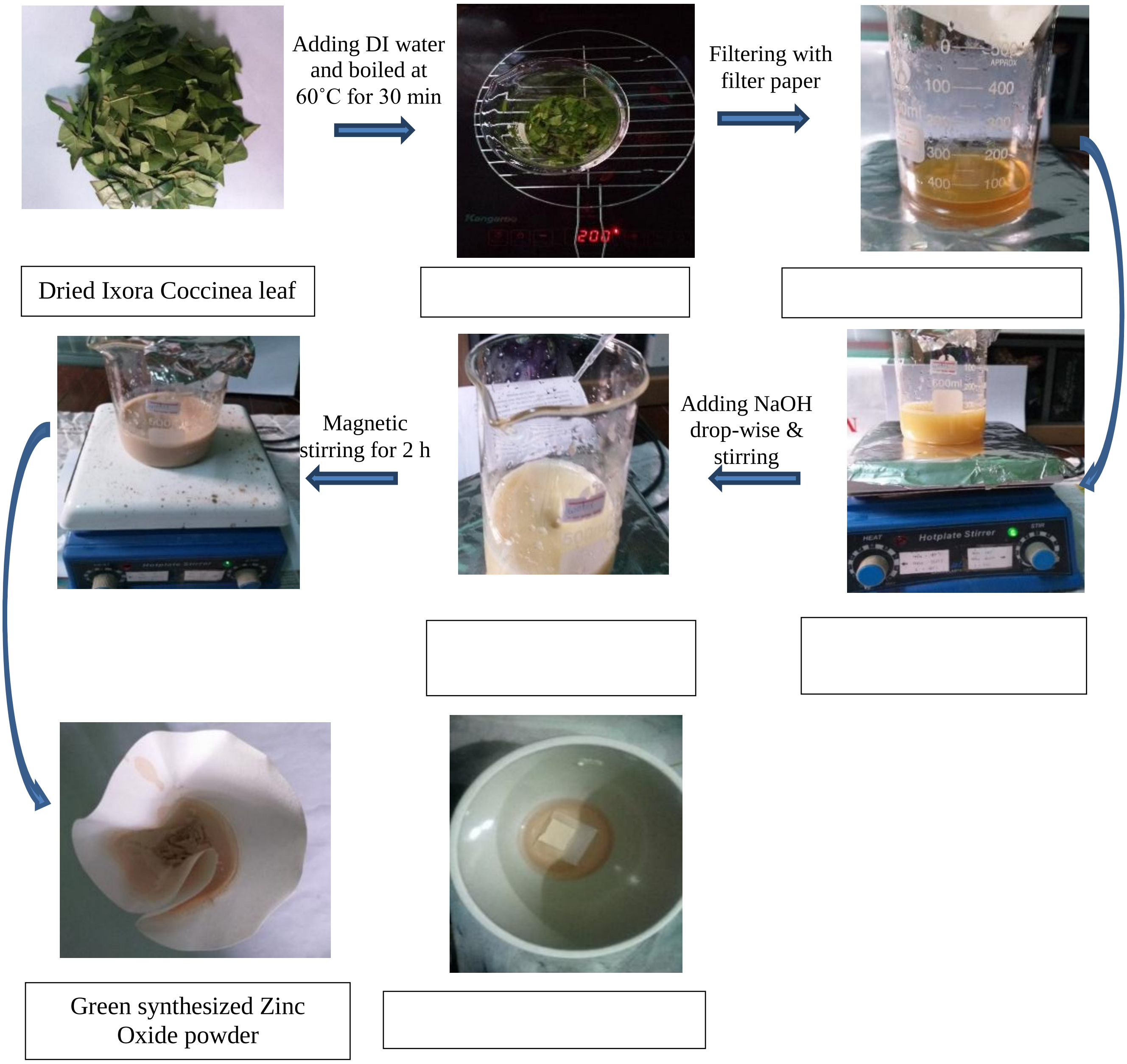

Figure 1 Experimental procedure of the preparation of green synthesized ZnO particles

Results and Discussion

XRD Analysis of biosynthesized ZnO powder

The XRD spectrum of biosynthesized ZnO powder is shown in Figure 2. Simple was scanned from 10°C to 70°C in diffraction angle 2θ. Seven distant peaks such as (100), (002), (101), (102), (110) ,(103)and (112) are formed on the profile. All of diffraction patterns were well match with JCPDS in ZnO library file. The sharp peaks of the XRD pattern indicated that the synthesized sample were well crystalline.

Moreover, the higher intensity peak observed at $2\theta = 37^{\circ}$ of the standard chart, referring to (101) reflection, confirms that the degree of crystallinity increased. The average crystallite size

(D), calculated from the most intense X-ray diffraction peak (101) using Scherrer's equation is 29 nm. The lattice parameters of the ZnO powders were a = b = 3.2549 nm, c= 5.2185 nm. The sample powder was successfully obtained with hexagonal structure. Thus, ZnO powder was successfully formed under these conditions by biosynthesis method.

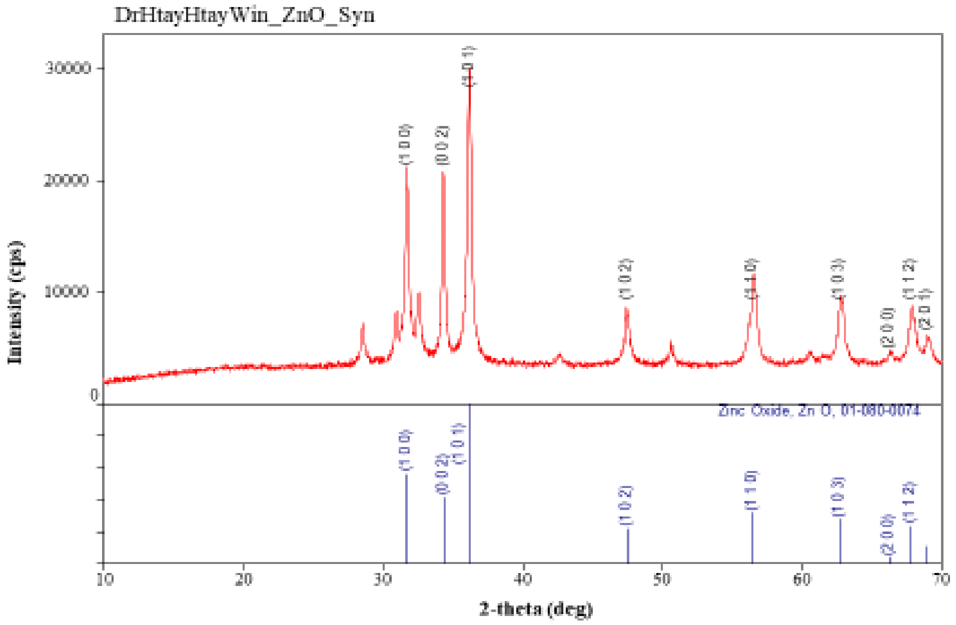

Figure 2 XRD spectrum of Zinc Oxide

UV-Vis Analysis of biosynthesized ZnO powder

The optical spectrum of biosynthesized ZnO powder is shown in Fig. 3 (a). In this figure, the optical absorption spectrum was well accepted and the absorption band was observed near ultraviolet region. The absorption peak located at 374.5 nm. The estimated optical band gap of ZnO powder is 3.31 eV.

Optical properties of Ixora Coccinea petal Dye

Fig. 3(b) showed the optical absorption spectrum of Ixora Coccinea petal dye. The maximum absorption peak was founded at 450 nm for Ixora Coccinea petal dye. So the absorption peak was in visible range. The energy band gap of these dye is 2.76 eV.

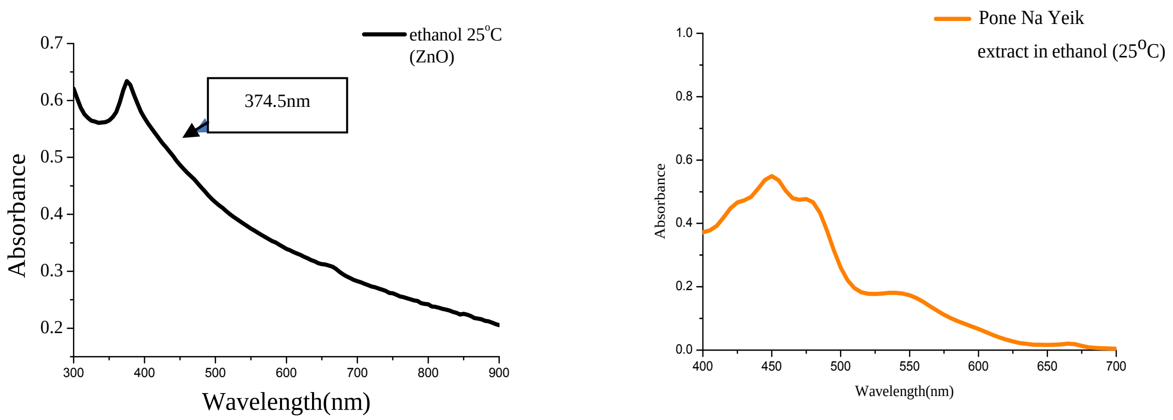

Figure 3(a) Optical absorption spectra of Zinc Oxide **(b)** Ixora Coccinea dye solution

Analysis of photochemical properties

Photochemical properties of fabricated DSSC were characterized by current voltage measurement. The experiment was carried under simulated solar light conditions. The current voltage characteristic of sample was showed in figure 4. From this figure, it was observed that the solar cell behavior. Ixora Coccinea extraction is favoured well attach of the dye to the semiconductor layer. Parameters such as short circuit current density (J_{sc}), maximum voltage (V_m), open circuit voltage (V_{oc}), conversion efficiency (η) and fill factor (FF) of DSSC immersed in natural dye tabulated in table 1.

Table 1 Photovoltaic performance of DSSC cell

Substrate	**ITO glass**
Photoelectrode	Biosynthesized ZnO
Counter electrode	carbon
Dye	Ixora Coccinea
J_m (mA/cm^2)	0.009
V_m (V)	0.240
J_{sc} (mA/cm^2)	0.017
V_{oc} (V)	0.461
Fill factor	0.276
Efficiency (%)	1.367

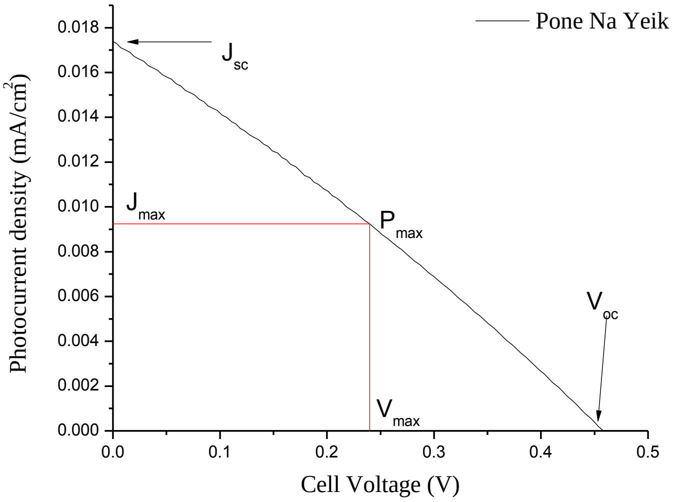

Figure 4 J-V characteristics of Ixora Coccinea dye sensitized ZnO based DSSC

Conclusion

In this paper, biological synthesis of zinc oxide sample using leaf extract of Ixora coccinea provided an environmental friendly, simple and efficient road for synthesis of the sample. Zinc Oxide sample has been successfully synthesized by using this method. X-ray diffraction confirmed the formation of a hexagonal phase which was the most stable form of zinc oxide at ambient conditions. The average crystallite size (D), calculated from the most intense X-ray diffraction peak (101) was 29 nm. The lattice parameters of the ZnO powders were a = b = 3.2549 nm, c= 5.2185 nm. The energy band gap of these powder was 3.31 eV. The natural dyes extracted from Ixora Coccinea petal was used to build dye-sensitized solar cells. The dyes showed sharp absorption peaks in the visible region, 400 – 700 nm. The maximum absorption peak was founded at 450 nm for Ixora Coccinea petal dye. The energy band gap of these dye was 2.76 eV. According to the experimental data resulted from energy band gap of the dyes extracted were quite promising candidates for dye sensitizers of DSSC. The conversion efficiency of fabricated cell was observed to be about 1.367 %. The solar energy to electrical conversion efficiency is very less, but the result obtained is academically interesting. From the experimental results, it was founded that the fabricated DSSC with green synthesis method for the preparation of crystalline zinc oxide targeted on the requirements for DSSC of low cost and eco-friendly.

Acknowledgements

We would like to thank Professor Dr Khin Khin Win, Head of Department of Physics, University of Yangon for her kind permission to carry out this work.

We also like to thank to all respectable Professors of Physics Department, University of Yangon for useful their advice me. We would like to give my special thanks to Professor Dr Yin Maung Maung, Department of Physics, University of Yangon and Professor Dr Than Than Win Department of Physics, Pinlon University for their encourage and support me during the undertaking of this work.

References

Barnali Ashe, (2011) "Investigation to observe the effect of zinc oxide and silver nanoparticles in biological system" PhD Thesis, pp 2

C.M.Noorjahan, S.K.Jasmine Shahina, Deepika, Summera Rafiq (2015) "Green Synthesis and Characterization of Zinc Oxide Nanoparticles from Neem (Azadirachta indicia)" vol 4, pp 5751-5753

Mohammed Isah Kimpa, Musa Momoh, Kasim Uthman Isah et al., (2012)"Photoelectric Characterization Dye Sensitized Solar Cell Using Natural Dye from Pawpaw leaf and Flame Tree Flower a Sensitizer", Material sciences and Applications, vol 3,pp 281-286

Michael Gratzel,(2003)"Dye Sensitized Solar Cells" Journal of Photochemistry and Photobiology Review, vol 4, pp 145

Snehal Yedurkar, Chandra Maurya, Prakash Mahanwar (2016), "Biosynthesis of Zinc Oxide Nanoparticles Using Ixora Coccinea Leaf Extract-A Green Approach" Open Journal of Synthesis Theory and Applications, vol 5, pp 1-14

Tao-Hua Lee, H J Sue and X Cheng, (2011) "Solid-state dye sensitized solar cells based on ZnO nanoparticle and nanorod array hybrid photoanode", Nano Res Lett., vol 6(1),pp 517

J. Myanmar Acad. Arts Sci. 2020 **Vol. XVIII.No.2C**

ANALYSIS OF OPTIMUM TILT ANGLE OF SOLAR POWER PLANT IN MINBU (MAGWAY REGION)

Min Zaw Lin*

Abstract

The photovoltaic (PV) panel performance is mainly influenced by its tilt angle, orientation, climatic conditions and geographic location of solar panels, which are used to get the maximum conversion of sunlight into solar electricity. In order to have maximum annual average incident solar energy on the surface of PV system, it is required to determine the optimum tilt angle. Optimization of tilt angle ensures the maximum energy generation output and area of PV modules were calculated. Several simplified design procedures for solar energy systems require monthly average meteorological data. In this paper proposes an algorithm to calculate the optimum tilt angle of solar panels method was developed by S. A. Klein by using NASA Solar Radiation Data Base, consisting of solar radiation and meteorological data all over the world. The output power of solar PV modules with the various incident angle of solar radiation was determined. According to the results, the average optimum angle (the best angle) of inclination of the solar panels is $\beta = 25^\circ$ for Minbu solar power plant in Magway region. After completion of study, an optimum plan can be formulated for practical set ups which can lead to maximum efficiency of solar power generation.

Keywords: photovoltaic (PV), solar panel, optimum tilt angle, solar radiation, solar energy, maximum output power

Introduction

Solar energy is the energy derived from the sun, when the sun's radiation reaches the earth's atmosphere; it is converted into other forms for the production of electricity. Solar energy resource data is necessary for the evaluation of the profitability of installing photovoltaic (PV) plants. The total solar radiation data is scarce in some locations, this is due to the absence of meteorological measurement stations and remote data collection networks, whose installation is expensive. Total measured solar radiation data are the best source of information for estimating average incident radiation necessary to calculate the productivity of an installed solar energy systems. In order to evaluate the production of a photovoltaic solar power plant, in a given region, must be made over a period of at least 11 years. In this paper, obtaining geometry information from National Aeronautics and Space Administration (NASA) surface meteorology and solar energy - available tables over 22-year average.

A critical parameter for installing fixed-tilt panels is the tilt angle, since PV panel output increases with increasing exposure to direct sunlight. Energy modelers also need to know the optimal tilt angle of a panel for calculating regional or global PV output in a given location or worldwide. Many studies have provided equations that allow for the theoretical calculation of the optimal tilt angle over time of a solar collector based on earth-sun geometry. Currently, many research works are carried out focusing on optimization of PV systems. The aim of this study was to propose an algorithm for the determination of the optimum tilt and orientation of a solar panel using a calculation model based on the orientation of a generic surface with respect to the position of the sun in the sky.

---

* Dr, Lecturer, Department of Physics, University of Yangon.

Radiation of the Sun

The sun radiates gargantuan amount of energy into solar system or universe, this energy travels at 3.0 x 108 m/s^2; thus being able to reach the earth's surface within eight minutes. Solar energy is considered renewable because it is constantly available (in the absence of weather conditions like winter, clouds, night, rainfall etc.) and it is replenished naturally.

Due to the rotation of the earth, only half of the earth is lit by sunlight at a time. Solar radiation comes in the form of electromagnetic wave which has wide spectrum. The longer the wavelength of the spectrum, the less energy it has and the shorter the wavelength the more energy it possess. Of all the spectrum of 6 wavelengths of the sun, only wavelength ranging between 0.29µm and 2.3µm reaches the earth's surface. Most of the solar energy which hits the surface of earth is reflected back into space.

Irradiance or insolation is the solar radiation intensity which falls on a surface. This quantity is measured or expressed in watts per meter square (W/m^2).The *global irradiance* is the solar radiation that reaches horizontal surface on the earth through the atmosphere. The following factors account for global irradiance.

Beam radiation (I_b): is the radiation that passes straight through the atmosphere and hits the earth's surface, hits the plane. It is also known as Direct radiation.

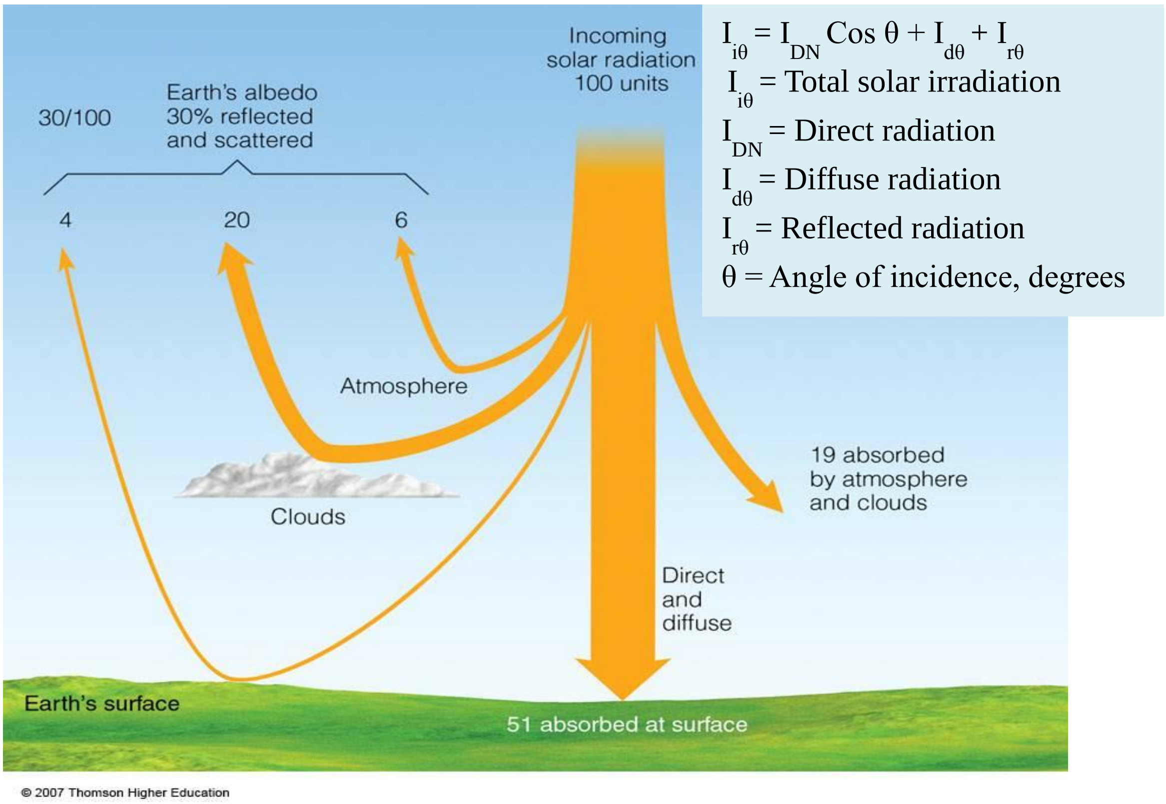

$I_{i\theta} = I_{DN} \text{Cos}\,\theta + I_{d\theta} + I_{r\theta}$

$I_{i\theta}$ = Total solar irradiation

I_{DN} = Direct radiation

$I_{d\theta}$ = Diffuse radiation

$I_{r\theta}$ = Reflected radiation

θ = Angle of incidence, degrees

© 2007 Thomson Higher Education

Figure 1.1 Solar radiation passes through the atmospheres *(awdet H.Mohammed*, 2007).

Diffuse radiation (I_d): in diffuse radiation, the solar radiation is scattered in all direction in the atmosphere and part of it arrives at the earth's surface.

Total radiation (I_t): is the sum of the beam and diffuse radiation, sometimes known as *global radiation*.

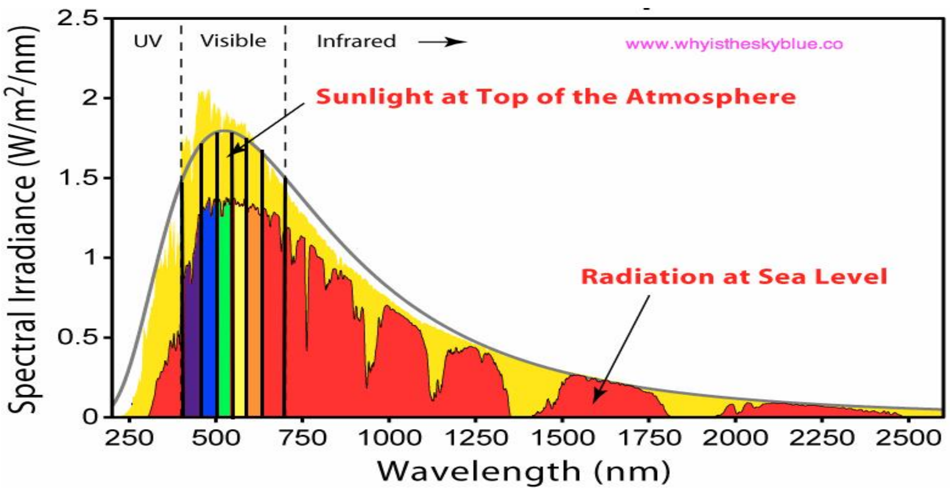

Figure 1.2. Solar radiation spectrum.

Solar potential in Myanmar

Myanmar has a tropical monsoon climate. The cooler, dry season lasts from November to April and the hotter, wet season from May to September or October. The weather is hottest from March-May, before the onset of the heaviest rains.

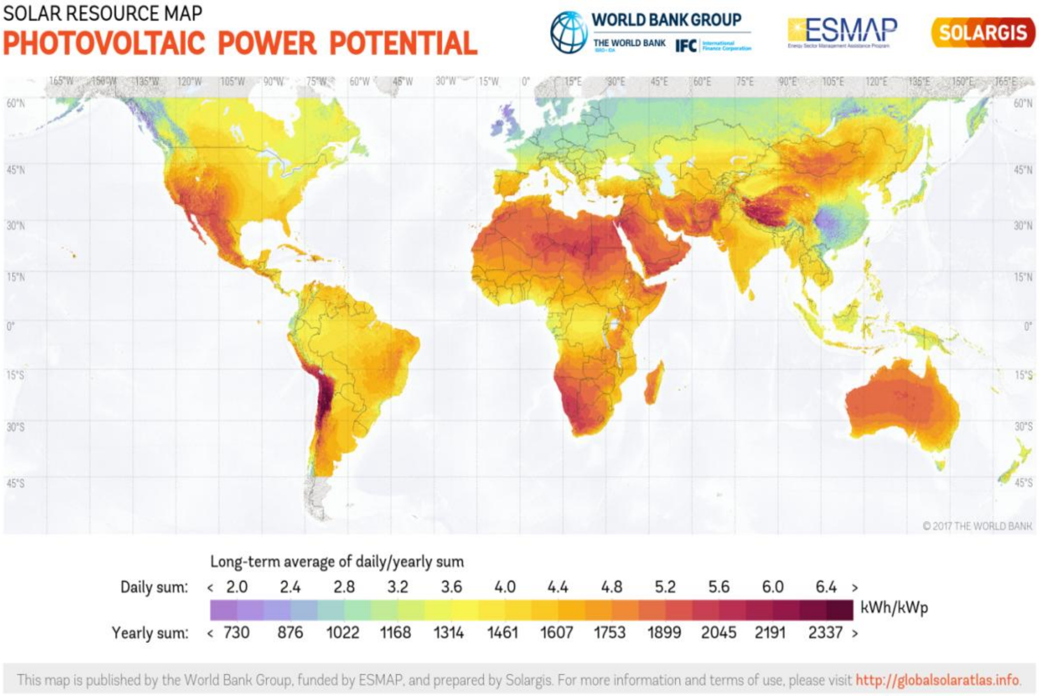

Figure 1.3. Global Photovoltaic Power Potential (World Bank Group, 2016).

The overall potential for solar power is estimated to be 51,973 terawatt-hours per year, with the highest potential in the central dry zones of the country. The former government signed two major solar power deals with foreign investors, both in 2014. US-based ACO Investment Group will invest USD 480 million to build two 150 MW solar plants near Mandalay, both of which are due to enter operation in 2016. Separately, Synergy Business Development Co Ltd (SBD), a local firm, together with its foreign partner have submitted a proposal to construct a

200MW solar power plant Meiktila Township, Mandalay Region to the MOEE, said U Lin Naing Oo, managing director of SBD.

According to the study on solar resources and solar PV potential in Myanmar, conducted by the World Bank, most of the population (75%-85%) lives within a 25-50 km radius of HV power lines, which overall are good premises for developing medium- and large-scale solar projects in the country.

Recently, Myanmar State Counsellor Aung San Suu Kyi is opened the first phase of a solar power plant project, which is the first in Myanmar and one of the biggest solar power plants in Southeast Asia, in Minbu Township, Magway Region on June 27. The first phase of the solar power plant located at a place of 800 acres of land space in Minbu Township, implemented under build-operate-transfer (BOT) system by the Green Earth Power (Myanmar) Company, initially added 40 megawatts (mw) to the national grid.

On completion of the remaining three phases of the four-phase 170 mw installed capacity, the plant would produce 350 million kilowatt-hours (kwh) per annum, distributing electricity to about 210,000 households. The electricity generated from the plant will be added to the national grid and cost around 12.5 cents per unit.

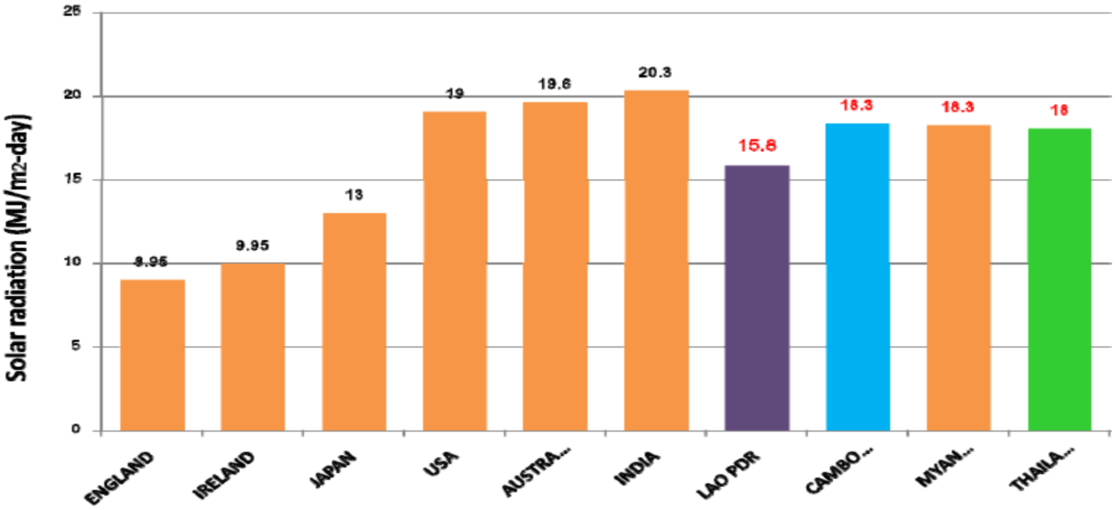

Figure 1.4 Comparison of average daily solar radiation per year (World Bank Group, 2016).

Electricity from the sun which is quite abundant in most of the developing countries is used in rural areas to meet basic electricity needs of a rural community. Today's electricity supply in Myanmar is generated by hydroelectric power plants and fuel generators. However, far from areas which are away from National Grids cannot enjoy the electricity generated by these sources. Since Myanmar is a land of plentiful sunshine, especially in central and southern regions of the country, the first form of energy-solar energy could hopefully become the final solution to its energy supply problem. Sunshine is plentiful during the dry season, averaging 7 to 10 hours a day. During the rainy season the weather is cloudier and daily sunshine amounts average only 3 to 4 hours a day.

Even though most electricity is produced from hydropower in Myanmar, the country has rich technical solar power potential that is the highest in the Greater Mekong sub-region; however, in terms of installed capacity Myanmar lags largely behind Thailand and Vietnam. The country aims to generate 8% of electricity through renewable energy sources-through wind and solar energy-by 2021 and 12% by 2025.

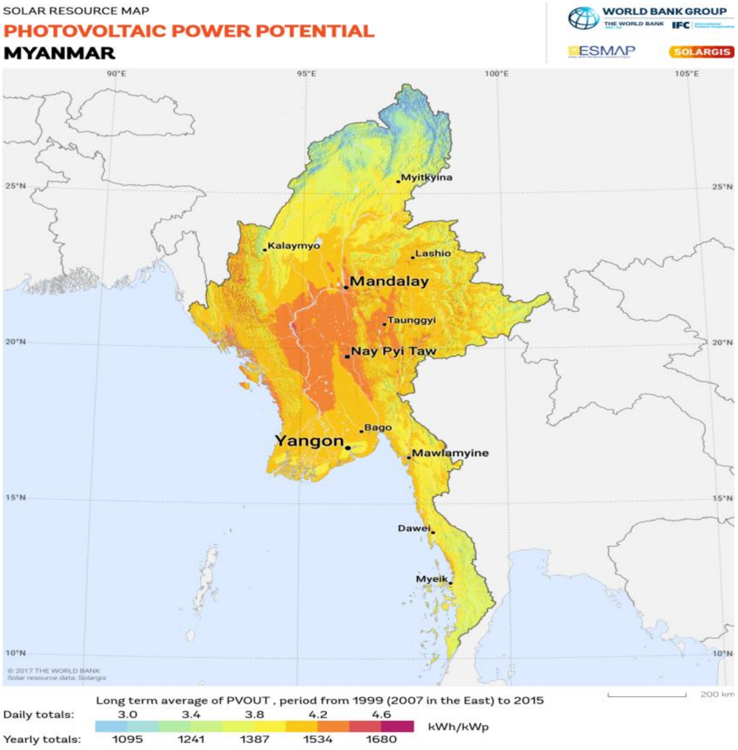

Figure 1.5. PV potential of Myanmar (World Bank Group, 2016).

S. A. Klein method (S. A. Klein, 1976**)**

Using this method we can calculate max output energy from solar incident radiation horizontally. The basic equation of this method :

Declination angle is calculated by the following equation

$$\delta = 23.45 \sin \left[360 * \frac{(284 + n)}{365} \right]$$

Where, n represents the day of the year and 1st January is accepted as the start [16, 18, 20, 21].

Incidence angle (θ) is the angle between the radiation falling on the surface directly and the normal of that surface.

$$\theta = \cos^{-1} [\cos(\delta).\cos(\emptyset).\ \cos(\omega) + \sin(\delta).\ \sin(\emptyset)]$$

Tilt angle (β) is the angle between the panels and the horizontal plane. This angle is south oriented in the Northern Hemisphere and north oriented in the Southern Hemisphere.

$$\beta = |\emptyset - \delta|$$

Where, $\varphi = latitude\ angle\ of\ location$

Global formula : E = A * r * H * PR
E = Energy (kWh)
A = Total solar panel Area (m^2)
r = solar panel yield (%)
H = Annual average irradiation on tilted panels
PR = Performance ratio, coefficient for losses
(range between 0.9 and 0.5, default value = 0.75)

Using some specification of Minbu solar power plant in figure 1.6.

Chinese company Jetion Solar has supplied PV modules to Minbu power plant, said to be the first such large-scale project in the country. Recently, an opening ceremony marked the completion of the first phase of electricity generation from Myanmar's first solar power plant, which has been added to the national grid to supplement the country's power needs. Located in Minbu Township, in upper Myanmar's Magwe Region, the Minbu Solar Power Plant was developed by Green Earth Power (Myanmar) under a build-operate-transfer (BOT) contract. It will have a total capacity of 170MW and the first stage complete, the plant is now capable of producing up to 40 MW of power.

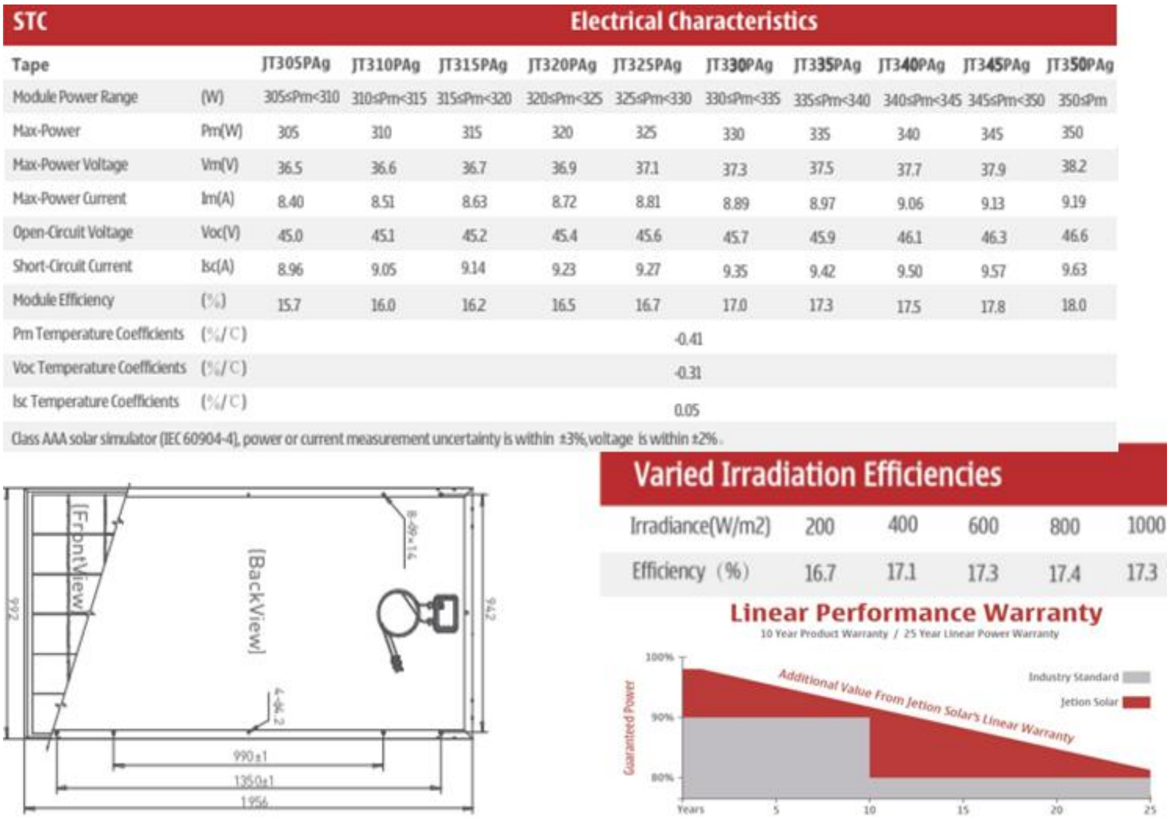

STC Electrical Characteristics

Tape		JT305PAg	JT310PAg	JT315PAg	JT320PAg	JT325PAg	JT330PAg	JT335PAg	JT340PAg	JT345PAg	JT350PAg
Module Power Range	(W)	305≤Pm<310	310≤Pm<315	315≤Pm<320	320≤Pm<325	325≤Pm<330	330≤Pm<335	335≤Pm<340	340≤Pm<345	345≤Pm<350	350≤Pm
Max-Power	Pm(W)	305	310	315	320	325	330	335	340	345	350
Max-Power Voltage	Vm(V)	36.5	36.6	36.7	36.9	37.1	37.3	37.5	37.7	37.9	38.2
Max-Power Current	Im(A)	8.40	8.51	8.63	8.72	8.81	8.89	8.97	9.06	9.13	9.19
Open-Circuit Voltage	Voc(V)	45.0	45.1	45.2	45.4	45.6	45.7	45.9	46.1	46.3	46.6
Short-Circuit Current	Isc(A)	8.96	9.05	9.14	9.23	9.27	9.35	9.42	9.50	9.57	9.63
Module Efficiency	(%)	15.7	16.0	16.2	16.5	16.7	17.0	17.3	17.5	17.8	18.0
Pm Temperature Coefficients	(%/℃)	-0.41									
Voc Temperature Coefficients	(%/℃)	-0.31									
Isc Temperature Coefficients	(%/℃)	0.05									

Class AAA solar simulator (IEC 60904-4), power or current measurement uncertainty is within ±3%,voltage is within ±2%.

Varied Irradiation Efficiencies

Irradiance(W/m2)	200	400	600	800	1000
Efficiency (%)	16.7	17.1	17.3	17.4	17.3

Figure 1.6 Specification of solar panel (JT310) of Minbu solar power plant.

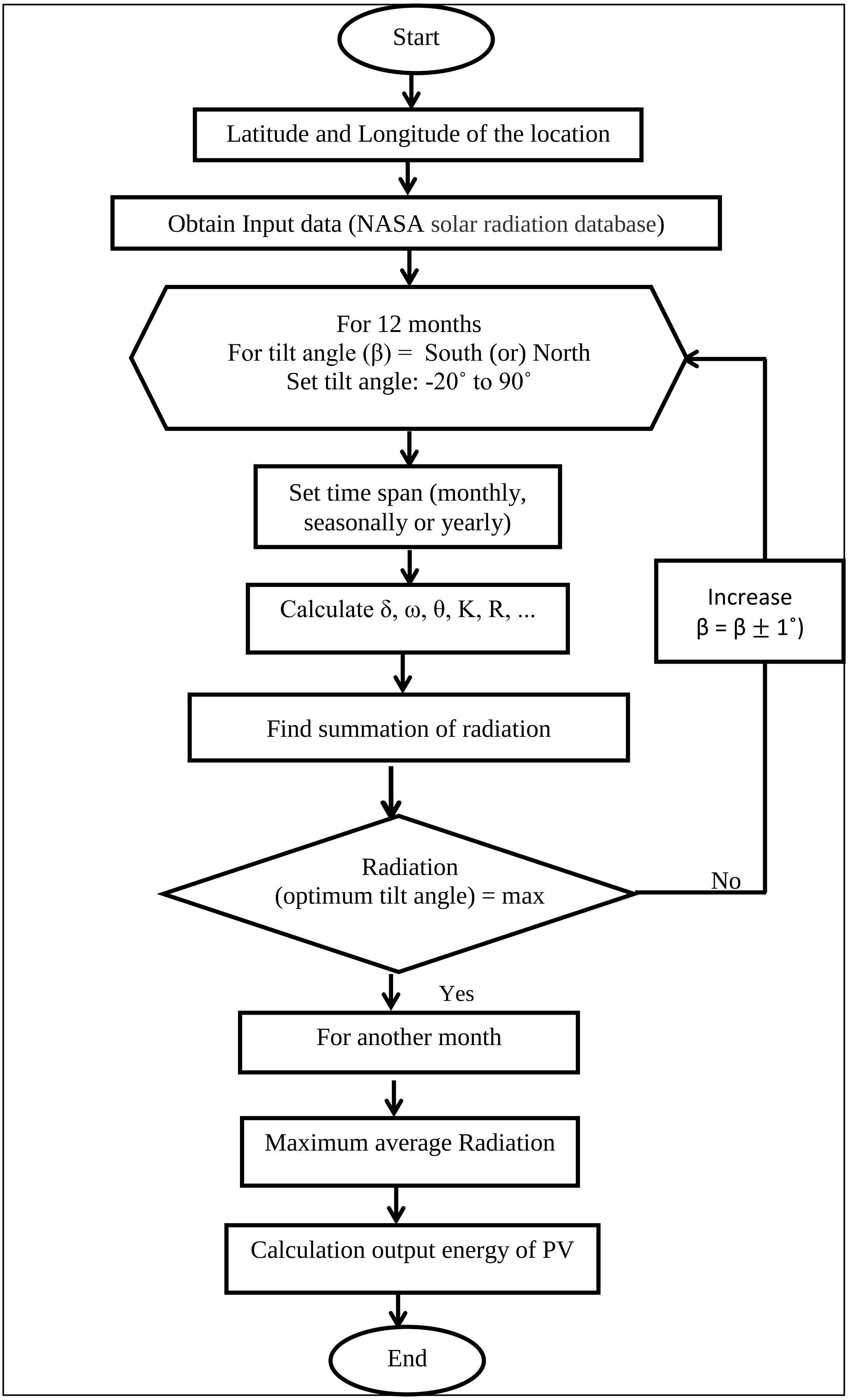

Figure 1.7 Optimization algorithm for PV panels tilt angle.

Calculation model are created for optimization of the tilt angle

In this research, obtaining geometry information from National Aeronautics and Space Administration (NASA) surface meteorology and solar energy - available tables over 22-year average. In this paper proposes an algorithm to calculate the optimum tilt angle of solar panels method was developed by S. A. Klein by using NASA Radiation Data Base.

Figure 1.7. is showing algorithm for the determination of the optimum tilt and orientation of a solar panel using a calculation model based on the orientation of a generic surface with respect to the position of the sun in the sky.

Several simplified design procedures for solar energy systems require monthly average meteorological data. In this paper proposes an algorithm to calculate the optimum tilt angle of solar panels method was developed by S. A. Klein by using NASA Solar Radiation Data Base, consisting of solar radiation and meteorological data all over the world for 22 years period. Figure 1.8 (a) and (b) showing Input data for calculation model for optimum tilt angle for Minbu solar power plant.

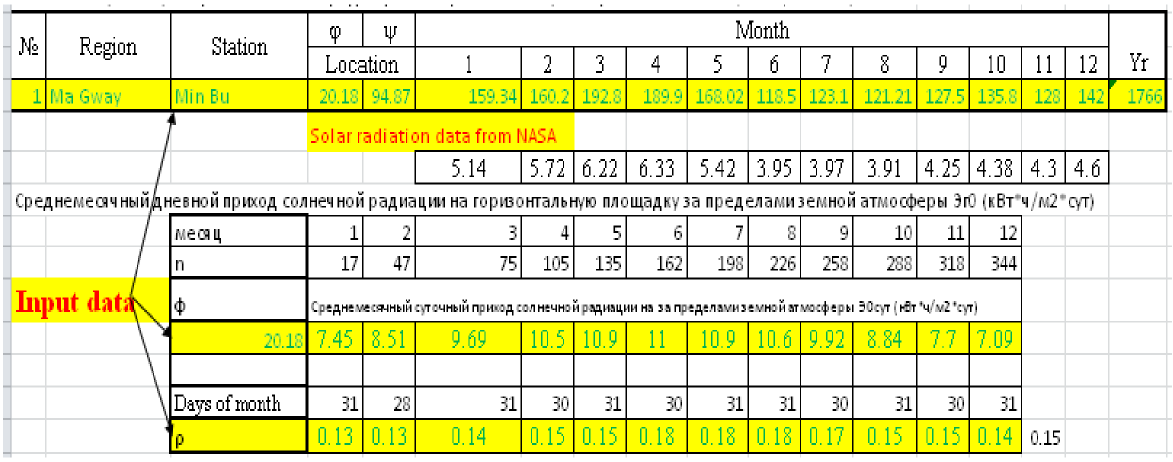

№	Region	Station	φ	ψ	Month												Yr
			Location		1	2	3	4	5	6	7	8	9	10	11	12	
1	Ma Gway	Min Bu	20.18	94.87	159.34	160.2	192.8	189.9	168.02	118.5	123.1	121.21	127.5	135.8	128	142	1766
			Solar radiation data from NASA														
					5.14	5.72	6.22	6.33	5.42	3.95	3.97	3.91	4.25	4.38	4.3	4.6	
Среднемесячный дневной приход солнечной радиации на горизонтальную площадку за пределами земной атмосферы Эг0 (кВт*ч/м2*сут)																	
		месяц	1	2	3	4	5	6	7	8	9	10	11	12			
		n	17	47	75	105	135	162	198	226	258	288	318	344			
Input data		ф	Среднемесячный суточный приход солнечной радиации на за пределами земной атмосферы Э0сут (кВт*ч/м2*сут)														
		20.18	7.45	8.51	9.69	10.5	10.9	11	10.9	10.6	9.92	8.84	7.7	7.09			
		Days of month	31	28	31	30	31	30	31	31	30	31	30	31			
		ρ	0.13	0.13	0.14	0.15	0.15	0.18	0.18	0.18	0.17	0.15	0.15	0.14	0.15		

Figure 1.8 (a) . Input data for optimum tilt angle by using Klein method.

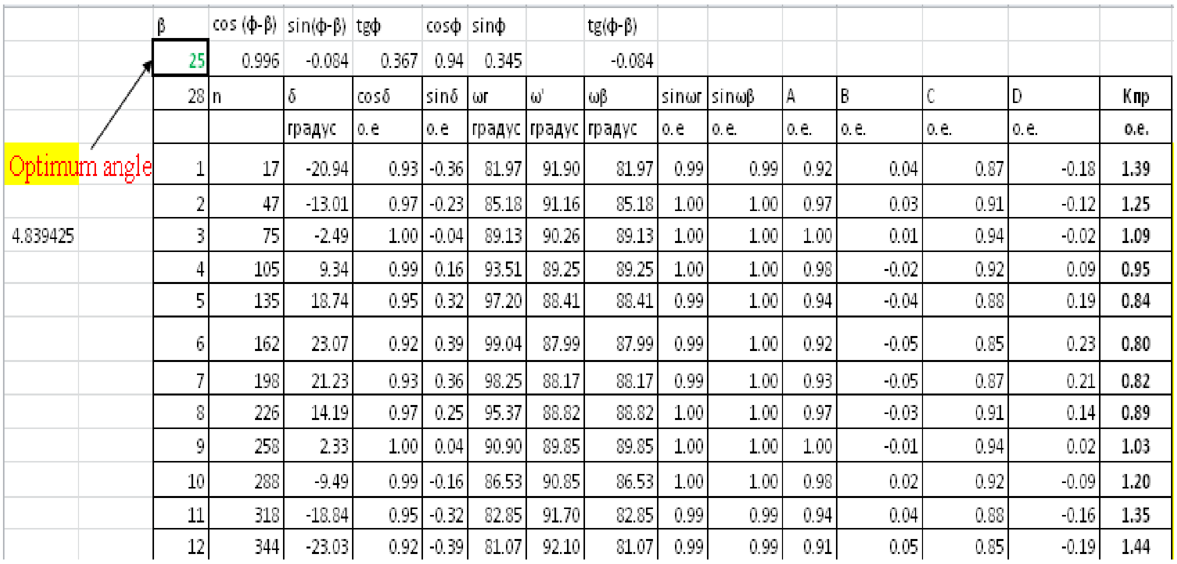

		β	cos (ф-β)	sin(ф-β)	tgф	cosф	sinф		tg(ф-β)							
		25	0.996	-0.084	0.367	0.94	0.345		-0.084							
		28	n	δ	cosδ	sinδ	ωr	ω'	ωβ	sinωr	sinωβ	A	B	C	D	Kпр
				градус	o.e	o.e	градус	градус	градус	o.e	o.e.	o.e.	o.e.	o.e.	o.e.	o.e.
Optimum angle		1	17	-20.94	0.93	-0.36	81.97	91.90	81.97	0.99	0.99	0.92	0.04	0.87	-0.18	1.39
		2	47	-13.01	0.97	-0.23	85.18	91.16	85.18	1.00	1.00	0.97	0.03	0.91	-0.12	1.25
4.839425		3	75	-2.49	1.00	-0.04	89.13	90.26	89.13	1.00	1.00	1.00	0.01	0.94	-0.02	1.09
		4	105	9.34	0.99	0.16	93.51	89.25	89.25	1.00	1.00	0.98	-0.02	0.92	0.09	0.95
		5	135	18.74	0.95	0.32	97.20	88.41	88.41	0.99	1.00	0.94	-0.04	0.88	0.19	0.84
		6	162	23.07	0.92	0.39	99.04	87.99	87.99	0.99	1.00	0.92	-0.05	0.85	0.23	0.80
		7	198	21.23	0.93	0.36	98.25	88.17	88.17	0.99	1.00	0.93	-0.05	0.87	0.21	0.82
		8	226	14.19	0.97	0.25	95.37	88.82	88.82	1.00	1.00	0.97	-0.03	0.91	0.14	0.89
		9	258	2.33	1.00	0.04	90.90	89.85	89.85	1.00	1.00	1.00	-0.01	0.94	0.02	1.03
		10	288	-9.49	0.99	-0.16	86.53	90.85	86.53	1.00	1.00	0.98	0.02	0.92	-0.09	1.20
		11	318	-18.84	0.95	-0.32	82.85	91.70	82.85	0.99	0.99	0.94	0.04	0.88	-0.16	1.35
		12	344	-23.03	0.92	-0.39	81.07	92.10	81.07	0.99	0.99	0.91	0.05	0.85	-0.19	1.44

Figure 1.8 (b). Calculation model for optimum tilt angle of PV panels.

The results of output energy as shown in figure 1.9 - 1.14.

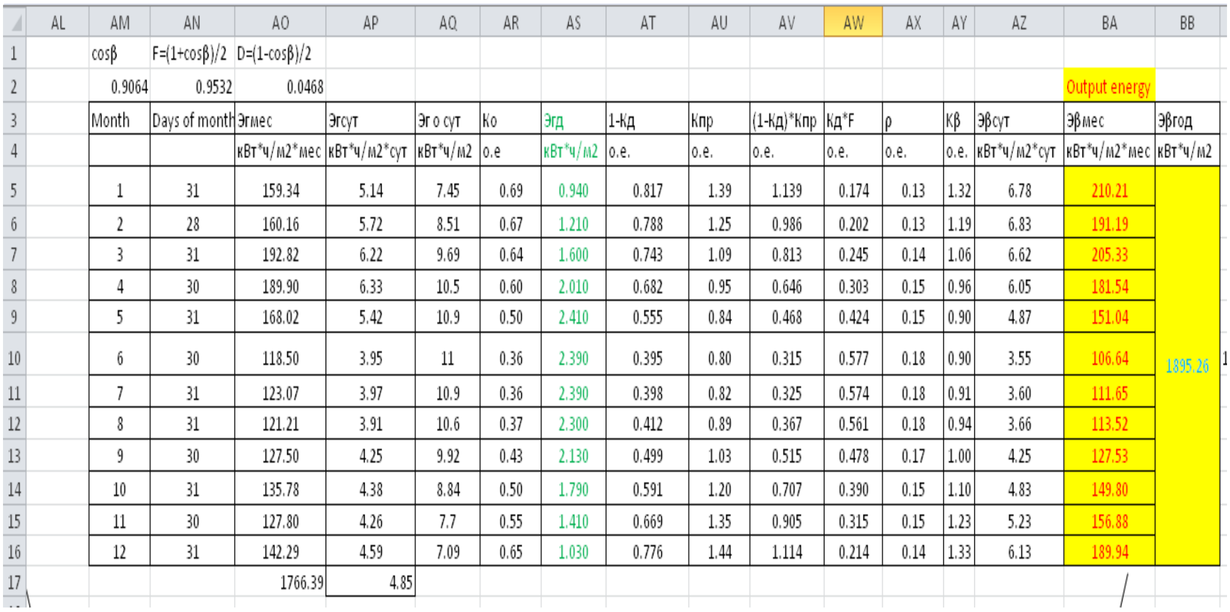

	AL	AM	AN	AO	AP	AQ	AR	AS	AT	AU	AV	AW	AX	AY	AZ	BA	BB
1		cosβ	F=(1+cosβ)/2	D=(1-cosβ)/2													
2		0.9064	0.9532	0.0468												Output energy	
3		Month	Days of month	Эгмес	Эгсут	Эг о сут	Ко	Эгд	1-Кд	Кпр	(1-Кд)*Кпр	Кд*F	ρ	Кβ	Эβсут	Эβмес	Эβгод
4				кВт*ч/м2*мес	кВт*ч/м2*сут	кВт*ч/м2	о.е	кВт*ч/м2	о.е.	о.е.	о.е.	о.е.	о.е.	о.е.	кВт*ч/м2*сут	кВт*ч/м2*мес	кВт*ч/м2
5		1	31	159.34	5.14	7.45	0.69	0.940	0.817	1.39	1.139	0.174	0.13	1.32	6.78	210.21	
6		2	28	160.16	5.72	8.51	0.67	1.210	0.788	1.25	0.986	0.202	0.13	1.19	6.83	191.19	
7		3	31	192.82	6.22	9.69	0.64	1.600	0.743	1.09	0.813	0.245	0.14	1.06	6.62	205.33	
8		4	30	189.90	6.33	10.5	0.60	2.010	0.682	0.95	0.646	0.303	0.15	0.96	6.05	181.54	
9		5	31	168.02	5.42	10.9	0.50	2.410	0.555	0.84	0.468	0.424	0.15	0.90	4.87	151.04	
10		6	30	118.50	3.95	11	0.36	2.390	0.395	0.80	0.315	0.577	0.18	0.90	3.55	106.64	1895.26
11		7	31	123.07	3.97	10.9	0.36	2.390	0.398	0.82	0.325	0.574	0.18	0.91	3.60	111.65	
12		8	31	121.21	3.91	10.6	0.37	2.300	0.412	0.89	0.367	0.561	0.18	0.94	3.66	113.52	
13		9	30	127.50	4.25	9.92	0.43	2.130	0.499	1.03	0.515	0.478	0.17	1.00	4.25	127.53	
14		10	31	135.78	4.38	8.84	0.50	1.790	0.591	1.20	0.707	0.390	0.15	1.10	4.83	149.80	
15		11	30	127.80	4.26	7.7	0.55	1.410	0.669	1.35	0.905	0.315	0.15	1.23	5.23	156.88	
16		12	31	142.29	4.59	7.09	0.65	1.030	0.776	1.44	1.114	0.214	0.14	1.33	6.13	189.94	
17				1766.39	4.85												

Figure 1.9 The results of output energy.

In my calculation, there are three types of optimum tilt angle for Minbu Solar power plant. They are : fixed-tilt angle, seasonally tilt angle and monthly tilt angle. Optimum fixed-tilt angle means you install your solar panels angle is all the time and you can not change the angle of solar panels. Seasonally optimum tilt angle means you can change your angle of solar panels in each season. Finally, monthly optimum tilt angle means you can change the angle of solar panels in each month.

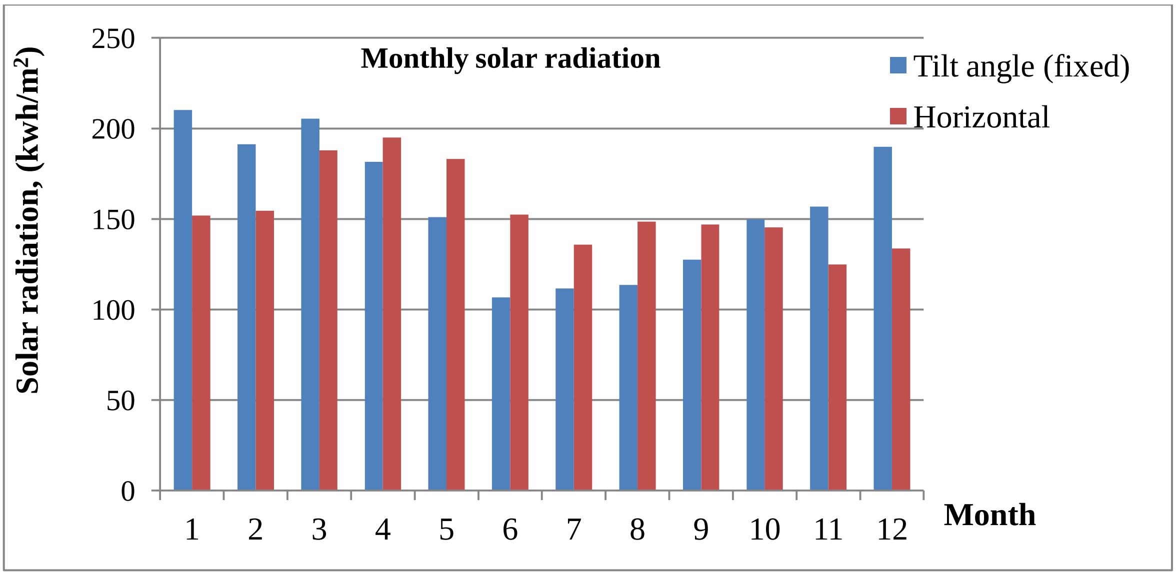

Figure 1.10 (a) Solar radiation for optimum tilt angle for Minbu solar power plant.

Total output solar radiation for horizontal (0˚) – 1860 kwh/m^2 and total output solar radiation for tilt angle (25˚) – 1895 kwh/m^2 respectively.

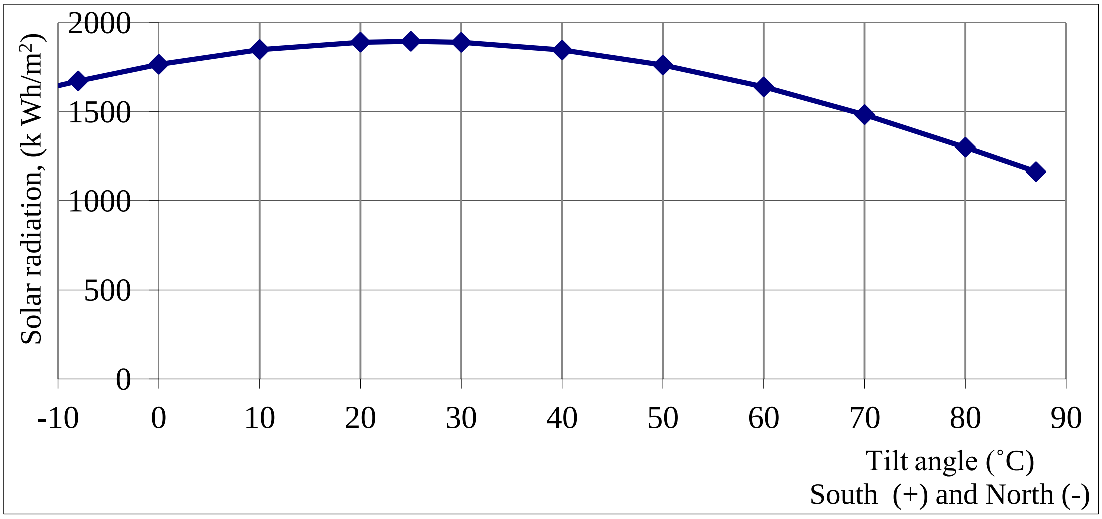

Figure 1.10 (b). Determination of the optimum fixed tilt angle for Minbu solar power plant.

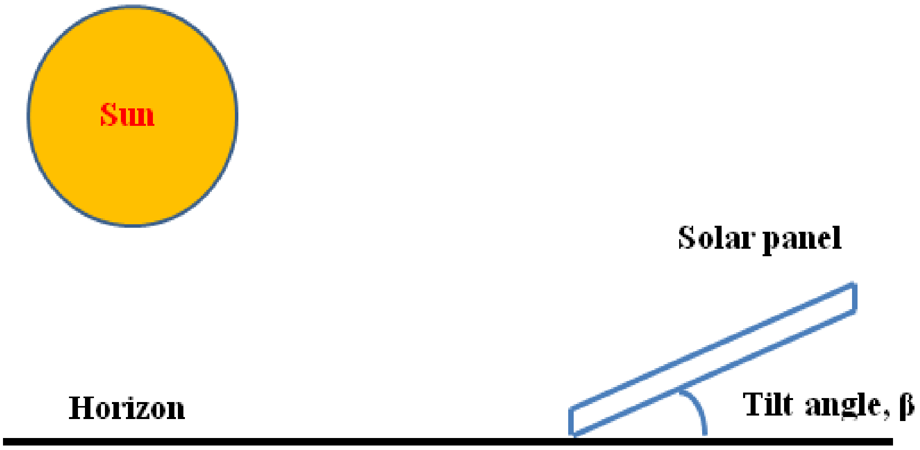

Figure 1.10 (c) Example optimum fixed tilt angle for Minbu solar power plant.

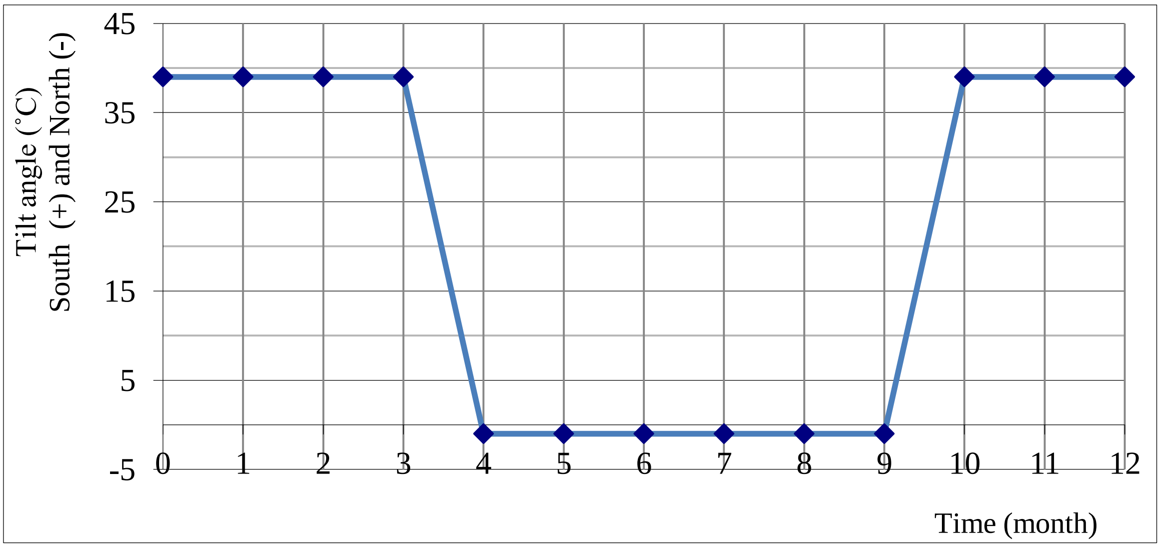

Figure 1.11 Determination of seasonally optimum tilt angle for Minbu solar power plant.

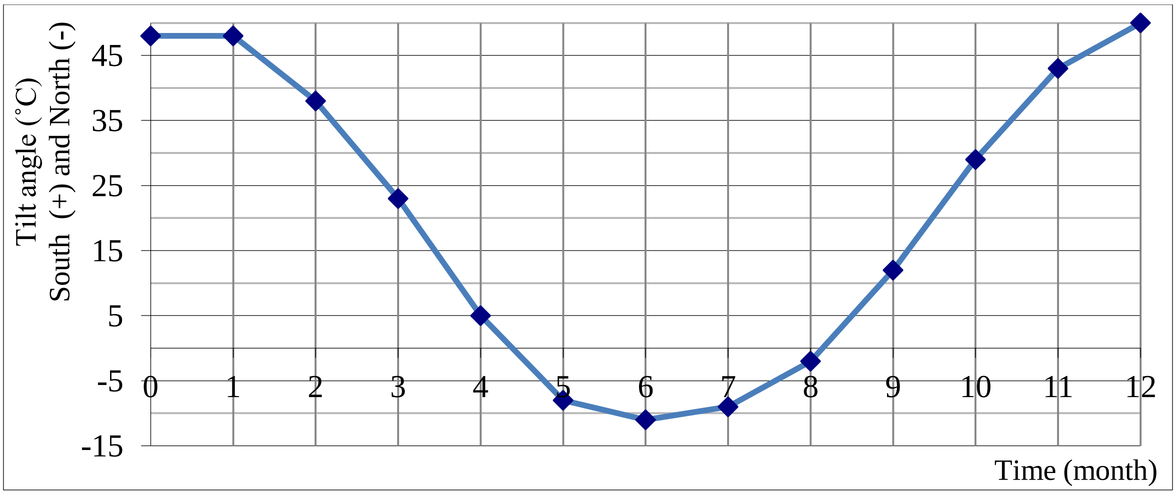

Figure 1.12 Determination of monthly optimum tilt angle for Minbu solar power plant

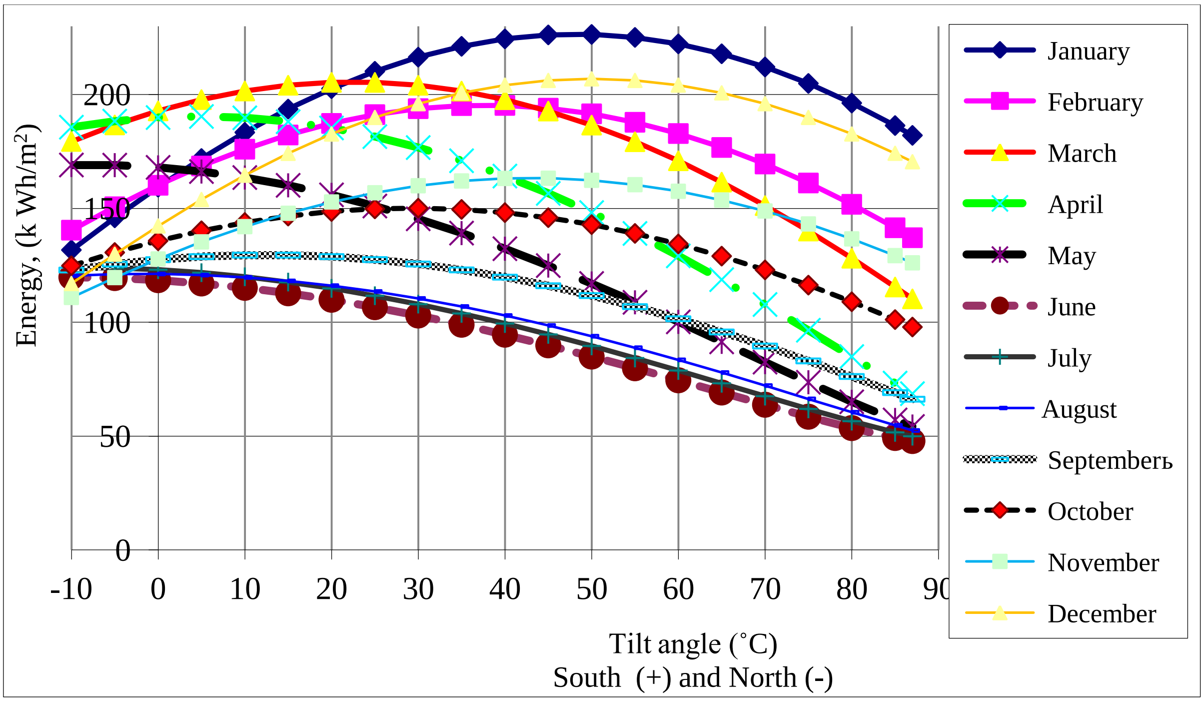

Figure 1.13 Monthly tilt angle optimization results (solar radiation and tilt angle) for Minbu solar power plant

For Minbu 170 MW solar power plant, the total number of PV modules are 548387.

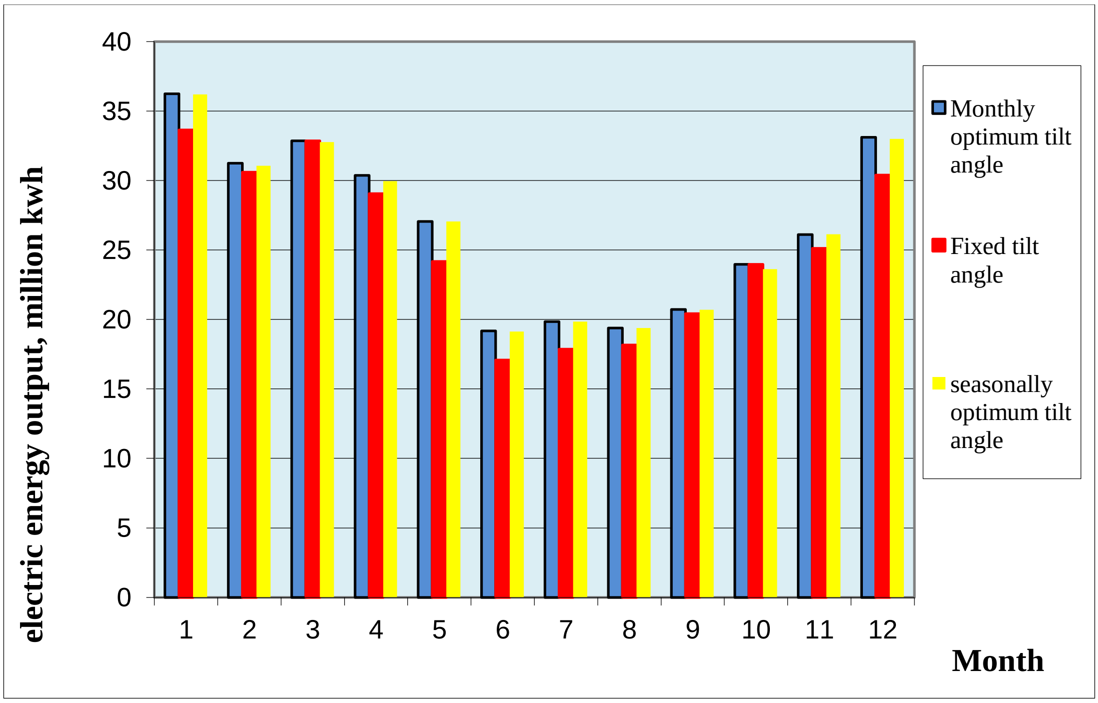

Figure 1.14. Output energy for Minbu solar power plant (fixed, seasonally and monthly optimum tilt angle)

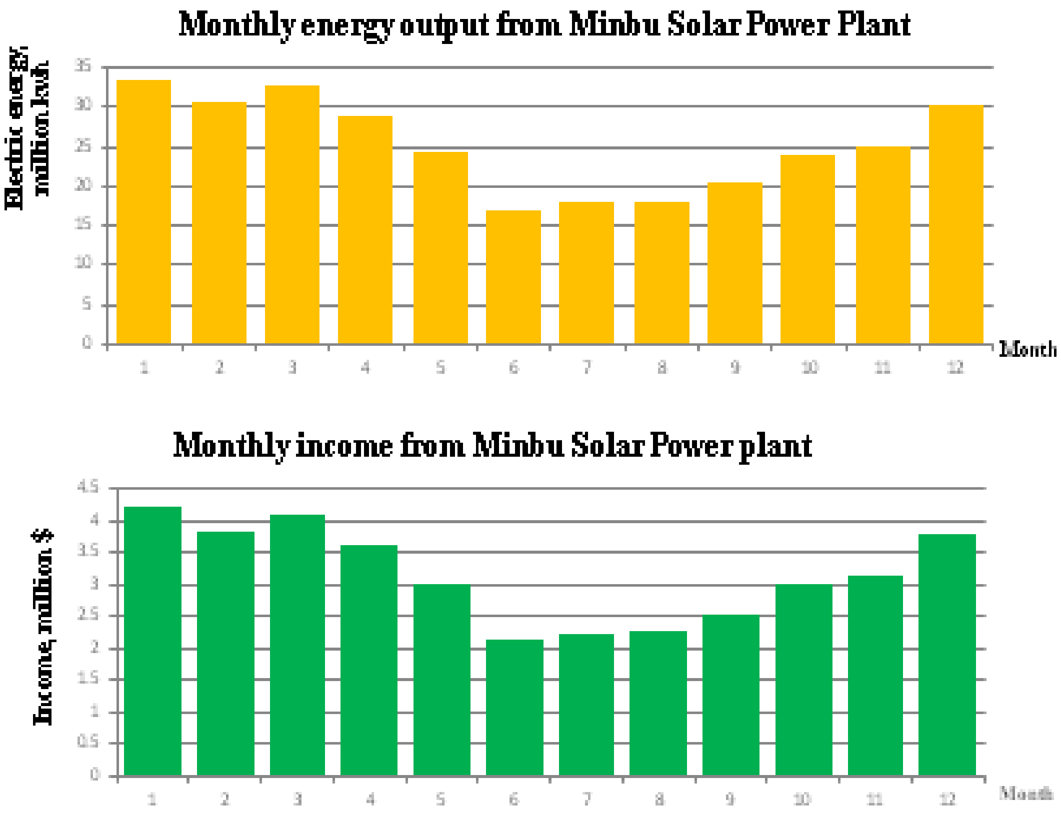

Figure 1.15 Energy output and income of Minbu Solar Power Plant (170 MW).

Conclusion

Myanmar is a land of plentiful sunshine, especially in central part of Myanmar. In research, proposed method we can calculate for output energy for various optimum tilt angle using Klein method. S. A. Klein method is very suitable for some regions which is near equator. From an economic point of view, the optimum tilt angle for Minbu solar power plant is $\beta = 25^{\circ}$ (fixed). Electricity tariff 12.5 cents is expensive for Myanmar. For example, Vietnam – 9.3 cents and Combodia - 9.1 cents. Minbu Solar power plant will generate electric output energy more than 300 million kwh and will receive income around 37 million $ per year. This calculation model will help how to determination of the optimum tilt angle and orientation of a solar panel any location of Myanmar. According to the results, economically the best optimum tilt angle for Minbu solar power plant $\beta = 25^{\circ}$. This solar power plant will generated solar energy about 302.5 million kWh per year.

Acknowledgements

The author would like to express sincere gratitude to Department of Higher Education, Ministry of Education, Myanmar, for guiding the good opportunities to do this research and for allowing to present this paper. Then, I specially wish to acknowledge to Rector Dr Pho Kaung and Pro-rectors, University of Yangon, Dr Khin Khin Win, Head of Department of Physics, University of Yangonm, for the encouragement.

I am deeply wished to express my gratitude to my teacher (A. U Aleksandroski and N. K Malinnyi from Moscow Power Engineering Institute, Department hydroelectricity and renewable energy resources, Russian Federation.

References

Awdet H.Mohammed, (2007). “Lecture Number 2 meteorology”, page 23.

Klein S. A., (1976). “Calculation of monthly average insolation on tilted surface”. Solar energy 19, (1977) and 20 (1978), University of Wisconsin - Madison, Madison, USA.

Min Zaw Lin, 2017. Dissertation of. the research and development of methods for reducing the power deficit in the energy sector of Myanmar, Russia, Moscow Power Engineering Institute (National Research University), Russia, Moscow.

Visarionov B. I. N. K Malinnyi. (2008). “Солнечная энергетика: учеб. пособие для вузов/ В.И. Виссарионов, Г.В.Дерюгина, В.А Кузнецова, – М.: Publish, Moscow Power Engineering Institute, Moscow, Russia.

World Bank Group, (2016). “Myanmar_PVOUT_poster-map_800x1200mm-300dpi_v20170127.tif”. Washington DC 20433, USA.

http://www.ultravioletphotography.com/content/index.php/topic/2323-sol-solar-radiation-spectrum/

http://en.jetion.com.cn/product/122.html

https://globalsolaratlas.info/downloads/myanmar

Ministry of electricity and energy, https://www.moee.gov.mm/

J. Myanmar Acad. Arts Sci. 2020 **Vol. XVIII.No.2C**

SOL-GEL SYNTHESIS AND CHARACTERIZATION OF Mn DOPED TiO_2 THIN FILMS

Saw Moh Moh Oo[1], May Kalayar Kyaing[2], San San Oo[3] and Hnin Yu Wai[4]

Abstract

Manganese (3%, 6%, 9% and 12%) doped titanium oxide, $MnTiO_2$ thin films were prepared by sol–gel synthesis and deposited onto the silicon substrates using spin coating technique. The morphologies of the Mn doped TiO_2 thin films were analyzed using scanning electron microscope (SEM) and the surface observation showed a rather good density of grains without cracks. The crystalline phase and particle size of the films were examined by X-ray diffraction (XRD) measurement. The calculated crystallite sizes (by Scherrer's relation), lattice constants and cell volumes were increased with increasing Mn doping percentage. Furthermore, capacitance-voltage measurements of all the films were performed with varying frequencies (0.1 kHz to 100 kHz) using a LCR meter and the effects of dopant concentration of manganese on the dielectric behavior in $MnTiO_2$ thin films were investigated.

Keywords: Mn doped TiO_2 thin films, Sol-gel synthesis, Dielectric behavior

Introduction

Titanium dioxide (TiO_2) is an important function material with good chemical stability, low cost, low toxicity, natural abundance and environmentally friendly nature. It is currently being intensively studied for various applications in environment and energy areas, such as, photocatalysts, pollutant cleansers, lithium ion batteries, supercapacitors, gas sensors, solar energy cells, and so forth. The materials' morphology has a great influence on their performance. TiO_2 nanoparticles are of particular interest in as much as they have been widely used in important technological applications. TiO_2 nanoparticles fabricated by anodisation, with highly ordered structures and large specific surface areas, are of enhanced or new properties compared to other morphologies. Modified TiO_2 nanoparticles, with better performances, have a wider range of applications, such as dye sensitized solar cell, catalys, etc.

The dye-sensitized TiO_2 solar cells are inexpensive and have high photon to electron conversion efficiency TiO_2 is probably the most investigated photocatalyst system and has been found to be capable of decomposing a wide variety of organics; it is becoming a promising material for lithium rechargeable batteries. Synthesis of transition metal oxide nanoparticles often involve water as solvent or reactant and thus result in particles with hydroxylated surfaces that influence properties of materials. Oxide nanoparticles lacking such hydroxylated surfaces are expected to have properties that are different from their counterparts, particularly in terms of their subsequent chemical behavior. The advanced materials chemistry goal is to synthesise TiO_2 crystals with required shape, which results in potential materials with shape dependent properties. Crystal surface energy is responsible for crystal growth rate. The surface energy of the crystals can be enhanced or reduced by surfactant adhesion which results in crystal growth.

As MnO_2 is one of the most promising pseudocapacitive materials with high theoretical specific capacitance and it is suitable for a pseudocapacitive electrode in hybrid system with

---

[1] Assistant Lecturer, Department of Physics, University of Yangon

[2] Assistant Lecturer, Department of Physics, University of Yangon

[3] Assistant Lecturer, Department of Physics, University of Yangon

[4] Assistant Lecturer, Department of Physics, University of Yangon

other active electrode materials like TiO_2. Metal ions doping is one of the effective approaches to improve the properties of TiO_2 nanoparticles. Whereas, there are few reports on the capacitance properties of Mn-doped TiO_2 nanoparticles. In this research, Mn-doped TiO_2 thin films were prepared by the solid state reaction method and their morphologies and structures were discussed in detail.

Experimental Details

Manganese (3%, 6%, 9% and 12%) doped titanium oxide; Mn-doped TiO_2 thin films were synthesized by solid state reaction method, using high purity (99.9% reagent grade) Mn and TiO_2 powders. These powders were weight on the basis of stoichiometric composition. The resultant, stoichiometric composition of the $Mn_xTi_{1-x}O_2$ (x = 0.03, 0.06, 0.09 and 1.2) powders were ground by agate mortar to obtain the homogeneity and annealed at 500°C for 1 hours. Each mixture was mixed with 2-methoxyethanol ($CH_3OCH_2CH_2OH$) solution and then heated up to 100˚C with indirect heat treatment for 1hr. Finally, homogeneous precursor solutions or coating solutions are obtained. The silicon substrates were cleaned by standard cleaning method. The resulting precursor solutions are deposited on silicon substrates by spin coating technique. After spin coating, deposited thin films are heat treated at 500˚C for 1hr. The surface morphology and the thickness of the films were analyzed by scanning electron microscope (SEM). The phase and crystallinity of the films were characterized by X-ray diffraction (XRD) analysis with Cu-$K_{\propto 1}$ radiation. The capacitance- voltage measurements and the dielectric properties of the films were carried by using LCR meter.

Results and Discussion

SEM Analysis

The surface morphologies and the cross sectional views of Mn-doped TiO2 thin films were evaluated using SEM as shown in Fig 1 (a-d). These results showed a well-developed grain size and dense microstructure in all samples. The effect of doping on grain size is usually interpreted in terms of dopant solubility and distribution of doping ions between the surface and interior parts of the grain. The values of the average grain sizes and thickness of the thin films were presented in Table 1.

Table 1 The values of the average grain sizes and thickness of manganese (3%, 6%, 9% and 12%) doped titanium oxide thin films

Thin film	Average Grain Size (μm)	Thickness (μm)
3% Mn doped TiO_2	0.26	4.2
6% Mn doped TiO_2	0.27	4.6
9% Mn doped TiO_2	0.22	5.5
12% Mn doped TiO_2	0.25	9.8

SEM image of Mn-doped TiO$_2$thin film **Cross sectional image Mn-doped TiO$_2$ thin film**

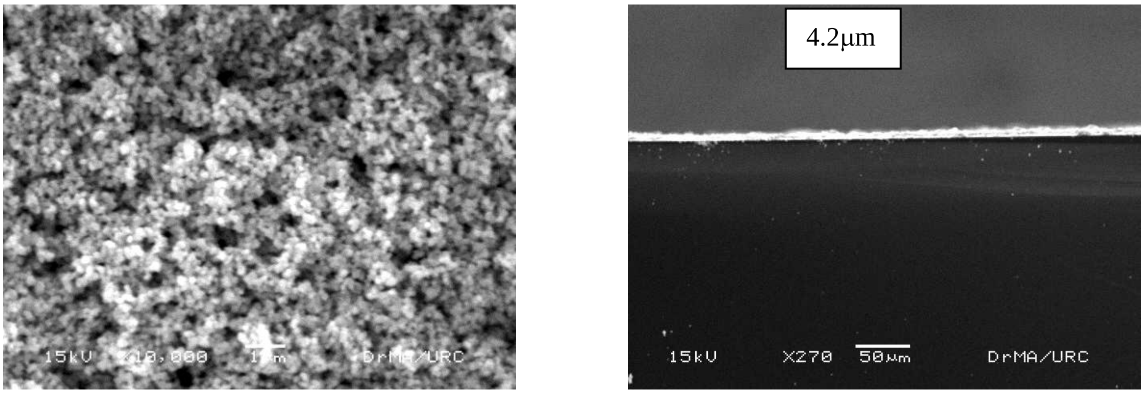

(a)For 3% Mn-doped TiO$_2$

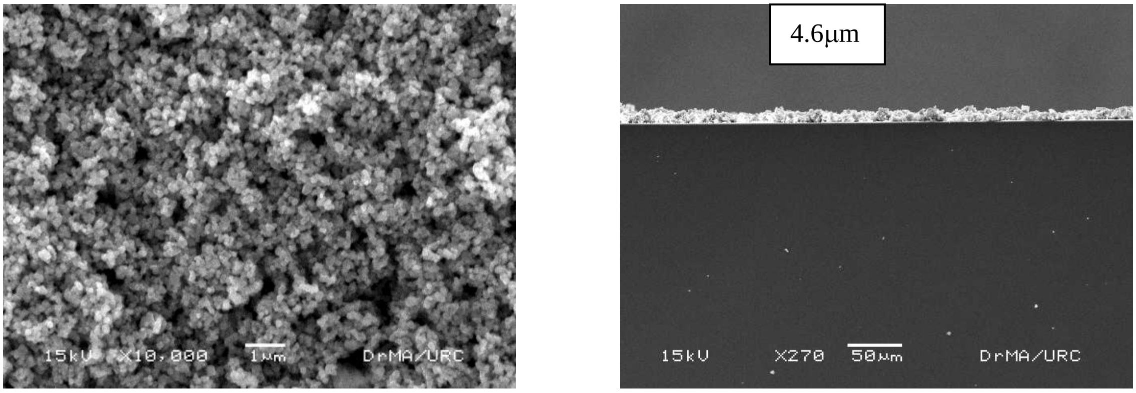

(b)For 6% Mn-doped TiO$_2$

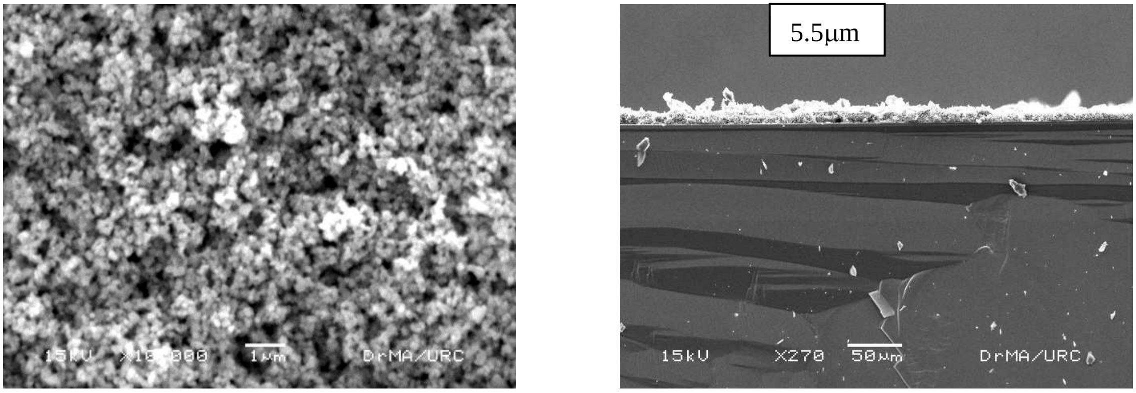

(c)For 9% Mn-doped TiO$_2$

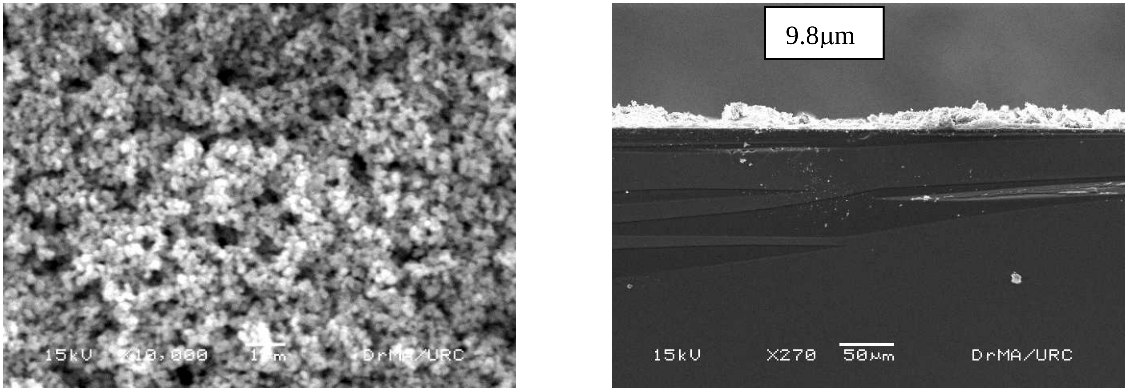

(d)For 12% Mn-doped TiO$_2$

Figure 1(a) Scanning Electron Microscopy (SEM) of Mn-doped TiO$_2$ thin films

X-ray Diffraction (XRD) Analysis

The crystal structures of Mn doped TiO_2 thin films were clarified by XRD measurements. Fig.2 (a-d) shows the X-ray diffraction patterns for Mn-doped TiO_2 nanoparticles with different weight percentages (3%, 6%, 9% and 12%). The samples were scanned from ($2\theta = 24.885 - 24.927$) using XRD machine with Cu source which has a wavelength of 0.154056 nm. The patterns of Mn-doped TiO_2 particles demonstrate its crystalline nature. All the peaks were indexed within the tetragonal system with body centred anatase phase, which crystal structure is composed of stacked edge sharing TiO_6 octahedra. The variation in the lattice parameters of Mn-doped TiO_2 thin films with change in dopant concentration may be attributed to the change in ionic radius. The XRD patterns showed that the increased dopant concentration leads to decrease in intensity of diffraction peaks with preferred orientation at (101) planes. The crystallite size was calculated using Scherrer's formula,

$$D = \frac{0.9\lambda}{\beta \cos\theta}$$

The intensity, peak positions (2θ), full width half maximum (FWHM), lattice parameters and crystallite sizes (D) of manganese (3%, 6%, 9% and 12%) doped titanium oxide thin films are listed in Table 2 (a-d).

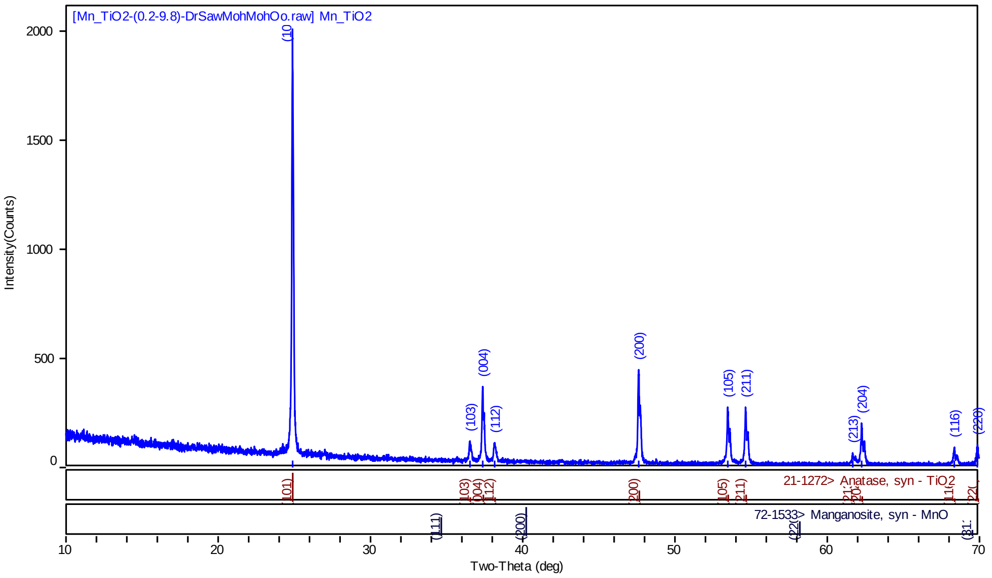

Figure 2(a) X-ray diffraction of 3% Mn-doped TiO_2 thin film

Table 2(a) (hkl) plane, full width half maximum (FWHM) and crystallite sizes (D) of 3% Mn-doped TiO_2 thin film

No	(hkl) plane	FWHM (deg)	Crystallite size D (nm)
1	(101)	0.138	56.214
2	(103)	0.163	46.279
3	(112)	0.209	40.219
Average crystallite size			47.571

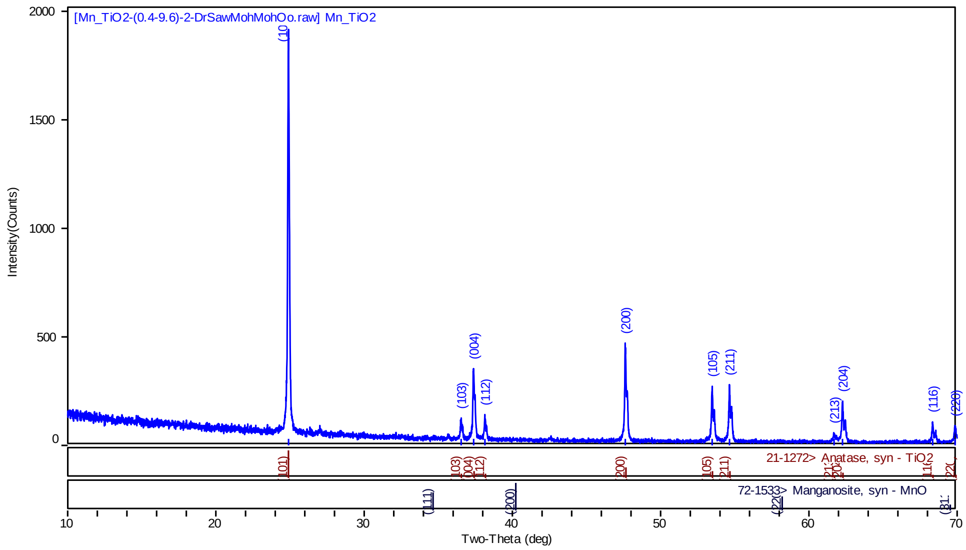

Figure 2 (b) X-ray diffraction of 6% Mn-doped TiO_2 thin film

Table 2(b) (hkl) plane, full width half maximum (FWHM) and crystallite sizes (D) of 6% Mn-doped TiO_2 thin film

No	(hkl) plane	FWHM (deg)	Crystallite size D (nm)
1	(101)	0.136	59.819
2	(103)	0.160	52.287
3	(112)	0.168	50.033
Average crystallite size			52.046

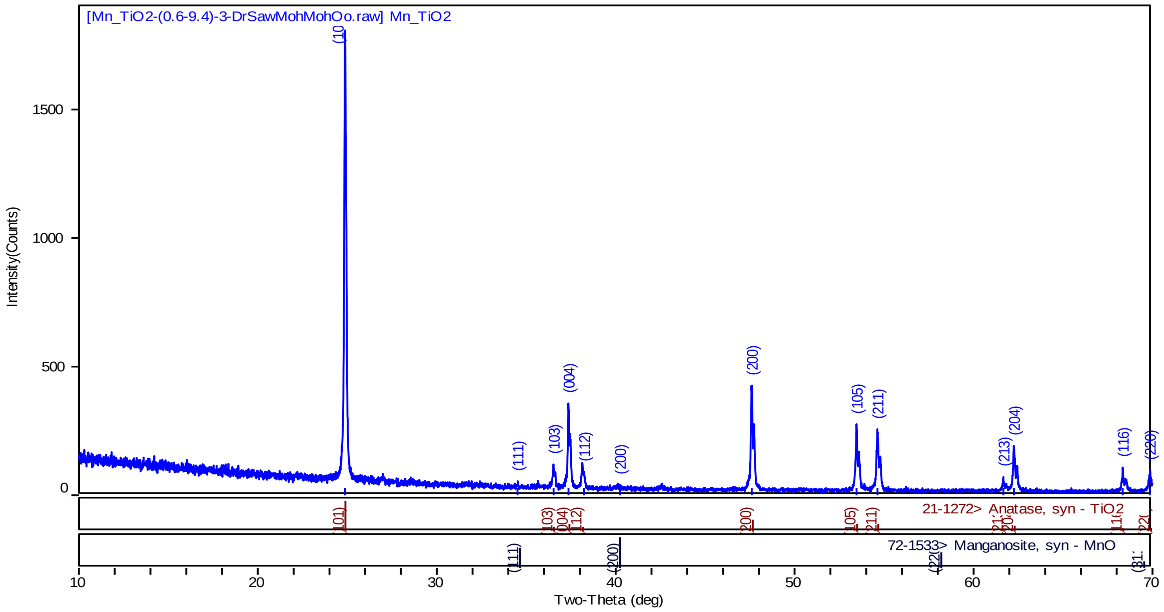

Figure 2 (c) X-ray diffraction of 9% Mn-doped TiO_2 thin film

Table 2 (c) (hkl) plane, full width half maximum (FWHM) and crystallite sizes (D) of 9% Mn-doped TiO_2 thin film

No	**(hkl) plane**	**FWHM (deg)**	**Crystallite size D (nm)**
1	(101)	0.138	58.950
2	(103)	0.134	62.397
3	(112)	0.251	33.496
Average crystallite size			51.614

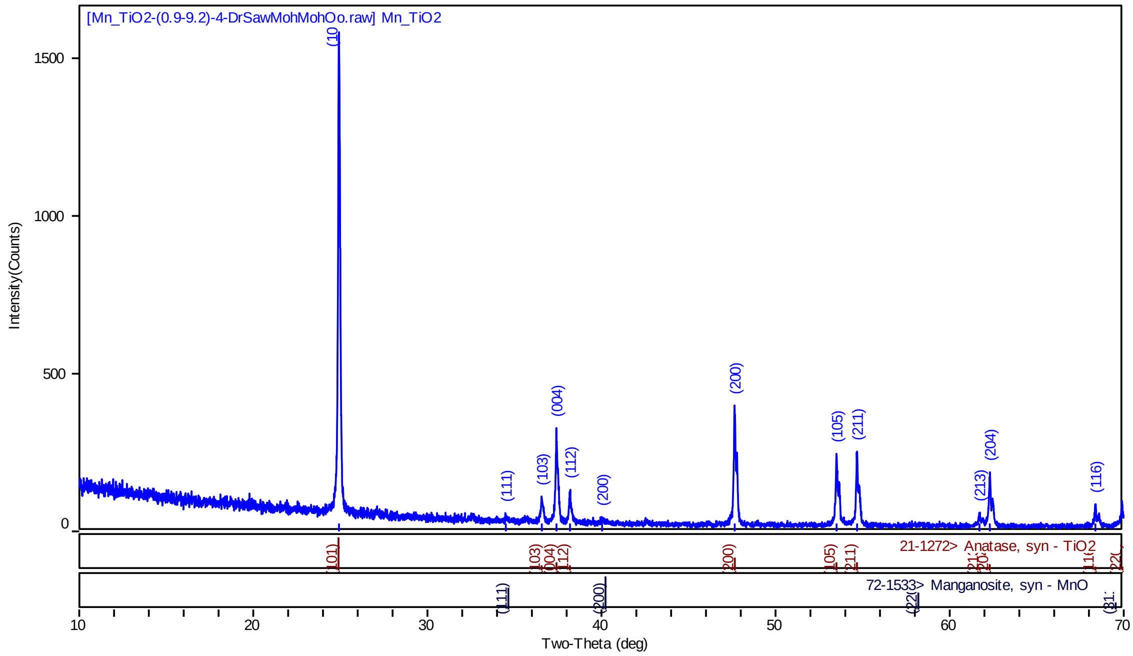

Figure 2 (d) X-ray diffraction of 12% Mn-doped TiO_2 thin film

Table 2 (d) (hkl) plane, full width half maximum (FWHM) and crystallite sizes (D) of 12% Mn-doped TiO_2 thin film

No	**(hkl) plane**	**FWHM (deg)**	**Crystallite size D (nm)**
1	(101)	0.153	53.175
2	(103)	0.183	45.719
3	(112)	0.162	51.892
Average crystallite size			50.262

Table 3 The intensity, peak positions (2θ), full width half maximum (FWHM), lattice parameters and crystallite sizes (D) of manganese (3%, 6%, 9% and 12%) doped titanium oxide thin films (101)

Thin Films	**Intensity (cps)**	**Peak positions (2θ)**	**FWHM**	**Lattice parameter**	**Crystallite size D (nm))**
3% Mn-doped TiO_2	1963	24.888	0.138	a =b= 3.8512 c = 9.5057	56.214
6% Mn-doped TiO_2	1868	24.900	0.136	a =b= 3.8488 c = 9.5121	59.819
9% Mn-doped TiO_2	1758	24.885	0.138	a =b= 3.8538 c = 9.4797	58.950
12% Mn-doped TiO_2	1540	24.927	0.153	a=b = 3.8487 c = 9.5064	53.175

Dielectric Properties

The dielectric constants of manganese (3%, 6%, 9% and 12%) doped titanium oxide, $MnTiO_2$ thin films were calculated from capacitance-voltage measurements at the frequency range of 0.1 kHz to 100 kHz. The dielectric constant varies with the applied voltage. The dielectric constant and dielectric loss of the films as function of applied voltage, Mn content and frequency are shown in Fig 3 (a-b). Dielectric constant (ε) can be calculated by the equations below,

$$C_0 = \varepsilon_0 A/t,$$

$$\varepsilon = C/C_0$$

where,

C = capacitance using the material as the dielectric in the capacitor,

C_0 = capacitance using vacuum as the dielectric

ε_0= Permittivity of free space (8.85 x 10-12 F/m)

A = Area of the plate/ sample cross section area

t = Thickness of the sample

The maximum value of dielectric constant was occurred at the 12% manganese doped titanium oxide thin film measured in a frequency range of 0.1 kHz. The dielectric constants of the films decrease with the increasing of dopant concentration are shown in Fig 3 (a-b) and the results are listed in Table 4.

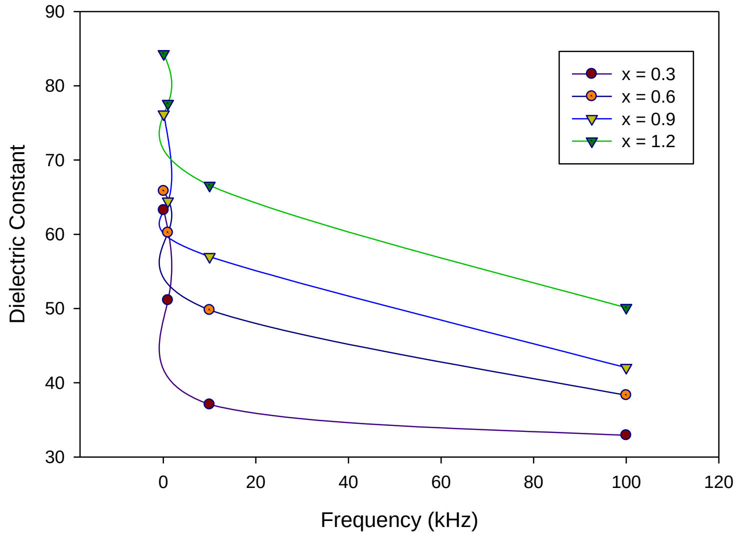

Figure 3 (a) The dependence of dielectric constant of manganese (3%, 6%, 9% and 12%) doped titanium oxide thin films as a function of frequency

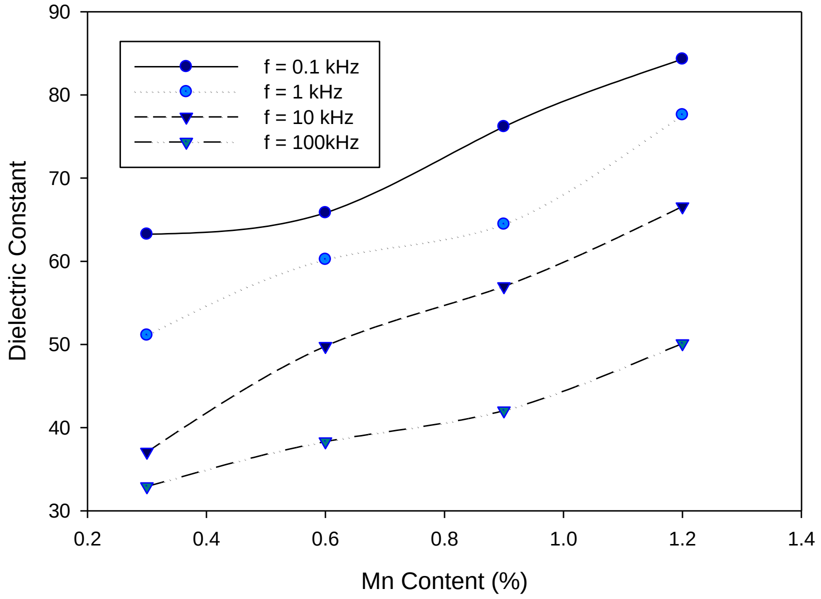

Figure 3 (b) The dependence of dielectric constant of the TiO_2 thin films on the Mn content

Table 4 The values dielectric constant of manganese (3%, 6%, 9% and 12%) doped titanium oxide thin films a function of frequency

	Dielectric Constant			
Thin Films	**f = 0.1 kHz**	**f =1kHz**	**f = 10kHz**	**f = 100kHz**
3% Mn doped TiO_2	63.2498	51.1118	37.0679	32.9160
6% Mn doped TiO_2	65.8172	60.2164	49.7984	38.3176
9% Mn doped TiO_2	76.1762	64.4514	56.9802	42.0378
12% Mn doped TiO_2	84.3017	77.5989	66.5661	50.1149

Conclusions

Manganese (3%, 6%, 9% and 12%) were doped titanium oxide, Mn-doped TiO_2 thin films were prepared by solid state reaction method and deposited onto the silicon substrates using spin coating technique. However, in 9% and 12% (over 6%) of Mn- doped TiO_2, the more Mn content, the less crystallite size. The crystallite size of the thin films calculated from XRD depending on the influence of Mn content. By the characterization of Scanning Electron Microscopy (SEM), grain sizes of the samples are in the range of 0.22 nm and 0.27 nm and it has been confirmed that the crack free and uniform surface of the films. XRD patterns indicated that all the films were well crystallized and tetragonal structure. The average crystallite size is around 57 nm and the largest crystallite size is 6% of Mn-doped TiO_2. The dielectric constants of the films increase with the increasing of dopant concentration of manganese. The maximum value of dielectric constant was occurred at the 12% manganese doped titanium oxide thin film measured in a frequency range of 0.1 kHz. These results showed a dependence of the structural and electrical properties of the TiO_2 films on the Mn concentration. According to the experimental result, TiO_2 films on the Mn Concentration with good dielectric properties can be used for measuring device in electronic applications.

Acknowledgements

The authors sincerely thank Professor Dr Khin Khin Win, Head of Department of Physics, University of Yangon, for her kind permission to carry out this research.

I would like to express my sincere thanks to Dr Myo Lwin, Professor, Department of Physics, Dr Ye Chan, Professor and Head, Universities' Research Center, Dr Aye Aye Thant, Professor, Department of Physics, Dr Yin Maung Maung, Professor, Department of Physics and Dr Than Zaw Oo, Professor, Universities' Research Center, University of Yangon, for their permission to this paper.

References

H. Li, Z. Chen, C.K. Tsang, (2014) "Electrochemical doping of anatase TiO2 in organic electrolytesfor high-performance supercapacitors and photocatalysts," *J. Mater. Chem. A*, 2, 229-236.

H. Wu, D. Li, X. Zhu, (2014) "High-performance and renewable supercapacitors based on TiO_2 nanotube array electrodestreated by an electrochemical doping approach," *Electrochim. Acta*, 116 , 129-136.

M.Z. Lin, H. Chen, W.F. Chen, (2014) "Effect of singlecation doping and codoping with Mn and Fe on the photocatalytic performance of TiO2 thin films," *Int. J. Hydrogen Energy*, 39, 21500-21511.

P. Roy, S. Berger, P. Schmuki, (2011) "TiO2 nanotubes: synthesis and applications," *Angew. Chem. Int.*, 50 , 2904-2939.

S. Liu, Z. Wang, C. Yu, H.B. Wu,(2013) "A flexible TiO2(B)-based battery electrode with superior power rate and ultralong cycle life, Adv. Mater." 25 , 3462-3467.

.

J. Myanmar Acad. Arts Sci. 2020 **Vol. XVIII.No.2C**

THE STRUCTURE CALCULATION OF K^-pp WITH Λ^*p MODEL

May Saw Ohn[1] and Khin Swe Myint[2]

Abstract

The purpose of this research is to investigate the structure of K^-pp system by using Λ^*p model, where Λ^* is a resonance state of K^-p system. To determine the binding energy of this system, Schrödinger equation is solved in two body system, which consists of Λ^* and proton. In our calculation, the Gaussian basis wave function is used to solve the Schrödinger equation. Phenomenologically constructed potential of Λ^*p interaction is used in this calculation. The experimental value for the binding energy of Λ^* is 27 MeV. By using theYamazaki and Akaishi phenomenological potential, the calculated result of the binding energy of K^-pp system from the Λ^*p threshold is 21.17 MeV and level width is 61 MeV. The binding energy of K^-pp system from $(K^- + p + p)$ threshold is $(\mathbf{21.17} + \mathbf{E}_{\Lambda^*}) = \mathbf{48.17\,MeV.}$ By using the DISTO experimental data, the calculated binding energy for K^-pp system from $\Lambda^* p$ threshold is 78.0457 MeV and level width is 118.4 MeV. The binding energy of K^-pp system from $(K^- + p + p)$ threshold is $(78.04 + E_{\Lambda^*}) = 105.04$ MeV. Thus, the calculated results for binding energy of K^-pp system are in good agreement with the calculated result of YA and experimental result of DISTO.

Keywords Power inverse iteration method, Two body system, Three body system.

Introduction

A "K^-pp"-like structure has observed in the d (π^+, K^+) reaction at 1.69 GeV/c. In this reaction Λ(1405) hyperon resonance is expected to be produced as a doorway to form the $K^- pp$ through the $\Lambda^* p \rightarrow K^- pp$ process.

Since this is a three-body system, several groups calculated the binding energy and width of K^-pp by applying various few-body calculation techniques such as variational and Feddeev type calculations. The obtained binding energies are scattered in a broad range: 10-20 MeV for shallow potential cases and 50-100 MeV for deep cases. The width would be as wide as 70 MeV because of the strong $\overline{K}N - \pi\Sigma$ coupling. In addition there could be non-mesonic absorption contributions of $\overline{K}NN \rightarrow \Lambda(\Sigma)N$.

The first experimental evidence of the K^-pp bound state was reported by the FINUDA collaboration in the stopped K^- absorption reactions on ^{6}Li, ^{7}Li and ^{12}C targets. They observed a lot of Λp pairs emitted in back-to-back, and found the invariant mass of the pair significantly lower than K^-pp mass threshold.

The binding energy of $115^{+6}_{-5}(\text{stat.})^{+3}_{-4}(\text{syst.})\,\text{MeV}$ and the decay width of $\Gamma = 67^{+14}_{-11}(\text{stat.})^{+2}_{-3}(\text{syst.})\,\text{MeV}$ were obtained. However, there was a theoretical criticism to interpret the observed structure as the K^-pp bound state. Experimental evidence was reported by

---

[1] Dr, Lecturer, Department of Physics, Taungoo University.

[2] Dr, Emeritus Professor, Department of Physics, University of Mandalay

the DISTO collaboration. They measured the missing-mass and invariant mass spectra in an exclusive reaction of $pp \rightarrow K^{+}\Lambda p$ at 2.85 GeV. The binding energy of 103 ± 3 (stat.) ± 5(syst.) MeV and the width of 118 ± 8 (stat.) ± 10 (syst.) MeV were obtained. However, they did not observe the signal at 2.50 GeV, may be due to the less production cross section of Λ (1405) at this energy.

The Λ(1405) is conventionally assumed to be a well-established resonance and to represent the I = 0, strangeness = –1, $J^{p} = \frac{1}{2}^{-}$ state within the L = 1 supermultiplet of the three-quark system. Lying roughly 30 MeV below the $\overline{K}N$ threshold, the resonance can only be observed directly in the $(\sum\pi)^{0}$ system of final states of production experiments. It was first reported by Alston et al. in the reaction $K^{-}p \rightarrow \sum 3\pi$ at 1.15 GeV/c and subsequently “seen” in several other experiments. However these observations suffered from

a. low statistics,

b. difficulties with the reconstruction of final states involving ∑ decays, and

c. the uncertainly in the removal of backgrounds, particularly that from

$\Sigma(1385) \rightarrow \sum\pi$ whose rate was badly know.

In fact, none of the experiments during the period 1962-1972 were able to demonstrate a convincing signal, to measure the precise mass and width, or to determine the quantum numbers.

The only experiment which has reported a respectable signal for Λ (1405) is that of Thomas et al. in the reaction $\pi^{-}p \rightarrow \sum\pi K$ at 1.69 GeV/c. Subsequently, Chao et al. demonstrated the importance of such data in constraining the multichannel analyses. Very recently, Dalitzetal have restated the debate on the nature of the Λ (1405) resonance and asked for more precise data on the production line-shape of the $\Lambda(1405) \rightarrow \sum\pi$. Currently, it is not known whether the interpretation of the Λ (1405) as a three-quark state is or is not consistent with its appearance as an unstable $\overline{K}N$ bound state.

Two- Body Calculations

In order to calculate the structure of two-body quantum system we solved Schrödinger equation.

$$HU = EU$$

$$(H_0 + V)\, U = EU$$

Where,

H= Hamiltonian operator

E= Energy eigen value

U = Eigen vector

H_0 = Kinetic energy operator

V = Potential energy operator

Since, the interaction between Λ^* and proton is central force, so we choose the spherical coordinate for the wave function

$$\Psi(\vec{r}) = R(\vec{r})\Theta(\theta)\Phi(\varphi)$$

where,

$R(\vec{r})$ is a radial part and $\Theta(\theta)\Phi(\varphi)$ is an angular part .

$Y_l^m(\theta,\varphi) = \Theta(\theta)\Phi(\varphi)$ is spherical harmonic which are well known.

We have to solve only the radial part $R(r)$ with the local potential type.

$$\left\{-\frac{\hbar^2}{2\mu}\frac{d^2}{dr^2} + \frac{\hbar^2}{2\mu}\frac{\ell(\ell+1)}{r^2} + V(r)\right\}U(r) = E\,U(r) ----------(1)$$

Where, $U(r) = r\,R(r)$

The reduced mass, $\mu = \dfrac{M_{\Lambda^*} M_p}{M_{\Lambda^*} + M_p}$

M_{Λ^*} =mass of Λ^*

M_p =mass of proton

Gaussian Basic Treatment

To solve the above equation, we will use the Gaussian Basis wave function.

$$U(r) = r^{\ell+1}\sum_j c_j\, e^{-\left(\frac{r}{b_j}\right)^2} --------------------------(2)$$

Where, c_j's are expansion coefficients and b_j's are range parameters which are adjusted in the calculations with

$$b_{j+1} = c\,b_j$$

$$b_N = c^{N-1}\, b_1$$

$$c = \left(\frac{b_N}{b_1}\right)^{\frac{1}{N-1}}$$

The Schrödinger equation becomes

$$\left\{-\frac{\hbar^2}{2\mu}\frac{d^2}{dr^2} + \frac{\hbar^2}{2\mu}\frac{\ell(\ell+1)}{r^2} + V(r)\right\}\sum_j c_j\, r^{\ell+1} e^{-\left(\frac{r}{b_j}\right)^2} = E\sum_j c_j\, r^{\ell+1} e^{-\left(\frac{r}{b_j}\right)^2}$$

$$\sum_j H_{ij}\, c_j = E\sum_j N_{ij} c_j$$

$$H_{ij} = T_{ij} + A^{\ell}_{ij} + V_{ij}$$

H_{ij} is the Hamiltonian matrix element

$$[H]\,[c] = E\,[N]\;[c]$$

Where, [H] and [N] are square matrices. [c] is column matrix. N_{ij}, T_{ij} and A^{ℓ}_{ij} are analytically solved by using standard integral form.

Calculation of Eigen Value

In the previous section, the Schrödinger equation can be written as the following matrix equation.

$$[H]\,[c] = E\,[N]\,[c]$$

$$[N]^{-1}\,[H]\,[c] = E\;[c]$$

$$[A]\,[c] = E\,[c]$$

Which is an eigen value equation with

$[A] = [N]^{-1}\,[H]$, $[N]$ is called the norm matrix and [H] is the Hamiltonian matrix. We are going to use the power inverse iteration method to calculate eigen values E with corresponding eigen vectors c.

Calculation of the Physical Quantities

We normalized wave function as $\int u^{*}\,u\,dr = 1$

$$u = A\sum_{j} c_j\, r^{\ell+1}\, e^{-\left(\frac{r}{b_j}\right)^2}$$ Where, A is the normalization constant.

$$\int A^{*}\sum_{i} c_i^{*}\, r^{\ell+1}\; e^{-\left(\frac{r}{b_i}\right)^2}\;\; A\sum_{j} c_j\, r^{\ell+1}\, e^{-\left(\frac{r}{b_j}\right)^2}\, dr = 1$$

$$|A|^2 = \sum_{i}\sum_{j} c_i^{*} c_j\, N_{ij} \;\; = 1$$

$$|A\,| = \frac{1}{\sqrt{\sum_{i}\sum_{j} c_i^{*} c_j\, N_{ij}}}$$

$$\mathbf{u}(\vec{\mathbf{r}}) = \mathbf{A}\sum_{\mathbf{j=1}}^{\mathbf{N}} \mathbf{r}^{\ell+1}\mathbf{c}_{\mathbf{j}}\, \mathbf{e}^{-\left(\frac{\mathbf{r}}{\mathbf{b}_{\mathbf{j}}}\right)^2} \text{ -------------------------- } (3)$$

With this normalized wave function, we have calculated the physical quantities which are average kinetic energy $\langle \hat{T} \rangle$, average centrifugal potential energy $\langle A_{ij}^{\ell} \rangle$ and average potential energy $\langle \hat{V} \rangle$. To find the average kinetic energy, we have the relation such that

$$\langle \hat{\mathbf{T}} \rangle = \langle \mathbf{u} | \hat{\mathbf{T}} | \mathbf{u} \rangle \text{ ---------------------------------(4)}$$

$$= \int u^{*}\, \hat{T}\, u\, dr$$

$$\langle \hat{T} \rangle = \int A^{*} \sum_{i} c_i^{*}\, r^{\ell+1}\, e^{-\left(\frac{r}{b_i}\right)^2} \left\{ -\frac{\hbar^2}{2\mu} \frac{d^2}{dr^2} \right\} A \sum_{j} c_j\, r^{\ell+1} e^{-\left(\frac{r}{b_j}\right)^2}\; dr$$

$$= |A|^2 \sum_{i} \sum_{j} c_i^{*}\; c_j T_{ij} \qquad \text{Where, } T_{ij} = -\frac{\hbar^2}{2\mu} \int r^{\ell+1} e^{-\left(\frac{r}{b_i}\right)^2} \frac{d^2}{dr^2} r^{\ell+1}\, e^{-\left(\frac{r}{b_j}\right)^2}\; dr$$

The average centrifugal potential energy, the relation can be expressed as

$$\langle \mathbf{A}_{\mathbf{ij}}^{\ell} \rangle = \langle \mathbf{u} | \mathbf{A}_{\mathbf{ij}}^{\ell} | \mathbf{u} \rangle \text{ -------------------------------(5)}$$

$$= \int u^{*}\;\; A_{ij}^{\ell}\, u\; dr$$

$$= \int A^{*} \sum_{i} c_i^{*} r^{\ell+1} e^{-\left(\frac{r}{b_i}\right)^2} \left\{ \frac{\hbar^2}{2\mu} \frac{\ell\,(\ell+1)}{r^2} \right\} A \sum_{j} c_j\;\; r^{\ell+1} e^{-\left(\frac{r}{b_j}\right)^2}\; dr$$

$$= |A|^2 \sum_{i} \sum_{j} c_i^{*} c_j A_{ij}^{\ell} \qquad \text{Where,} \quad A_{ij}^{\ell} = \int r^{2(\ell+1)} \left\{ \frac{\hbar^2}{2\mu} \frac{\ell\,(\ell+1)}{r^2} \right\} e^{-\left(\frac{1}{b_i^2} + \frac{1}{b_j^2}\right) r^2}\; dr$$

The average potential energy numerically, the relation can be expressed as

$$\langle \hat{\mathbf{V}} \rangle = \langle \mathbf{u} | \hat{\mathbf{V}} |\; \mathbf{u} \rangle \text{ -------------------------------(6)}$$

$$= \int u^{*}\, \hat{V}(r) u\; dr$$

$$= \int |A|^2 \sum_{i} c_i^{*}\; r^{\ell+1}\, e^{-\left(\frac{r}{b_i}\right)^2} \left(\bar{v}_0 + i\,\bar{\varpi}_0\right) \left(\frac{r}{b}\right)^2 e^{-\left(\frac{r}{b}\right)} \sum_{j} c_j r^{\ell+1} e^{-\left(\frac{r}{b_j}\right)^2}\; dr$$

$$= |A|^2 \sum_{i} \sum_{j} c_i^{*}\; c_j \int r^{2(\ell+1)}\; V(r) e^{-\left(\frac{1}{b_i^2} + \frac{1}{b_j^2}\right) r^2}\; dr$$

The relation of the root mean square radius,

$$\langle \bar{\mathbf{r}}^2 \rangle = \int \mathbf{u}^{*}\, \mathbf{r}^2\, \mathbf{u}\; \mathbf{dr} \text{ --------------------------------(7)}$$

$$\langle \bar{r}^2 \rangle = \int A^* \sum_i c_i^* \, r^{\ell+1} e^{-\left(\frac{r}{b_j^2}\right)} r^2 A \sum_j c_j r^{\ell+1} e^{-\left(\frac{r}{b_j^2}\right)} \, dr$$

$$\sqrt{\langle \bar{r}^2 \rangle} = \sqrt{|A|^2 \sum_i \sum_j c_i^* c_j \frac{(2\ell+3)!!}{2^{\ell+3}} \frac{\sqrt{\pi}}{\left(\frac{1}{b_i^2}+\frac{1}{b_j^2}\right)^{\ell+\frac{5}{2}}}}$$

Interactions

The elementary $\overline{K}N$ and NN interactions deduced semiempirically to obtain not only the binding energy and width but also the spatial and momentum distribution of the individual particles. Three-body calculations by showing that the $\overline{K}N$ complex potential, which is transformed from coupled-channels interactions, has very little energy dependence. Furthermore the result remains unchanged, even when the $\overline{K}N$ and NN interactions to vary in a wide range, as long as they reproduce the energy and width of Λ (1405). The predicted K^-pp is a compact nuclear system with a binding energy around 50MeV and a root-mean-square (rms) p-p distance of 1.9 fm. The K^-p pair (quasi- Λ^*) behaves like an atomic unit in a "molecule" of K^-pp, similarly to the mechanism of the Heitler-London scheme. Namely, a super strong nuclear force is caused by a migrating real $\overline{K}$ meson.

The Λ (1405) resonance state the I = 0 is bound state of $\overline{K}N$. Through the main part of is article the "classical" experimental values for the binding energy and width,

$$-B_k = E_{\overline{K}N}^{I=0} = -27 \text{ MeV}, \ \Gamma = 40 \text{ MeV}$$

The Λ^* data combined with the kaonic hydrogen shift (yielding a_{K^-p}) and Martin's $\overline{K}N$ scattering length ($a^{I=0}$ and $a^{I=1}$),

$$a_{K^-p} = (-0.78 \pm 0.15) + i\,(0.49 \pm 0.28)\text{fm}$$

$$a^{I=0} = (-1.70 \pm 0.07) + i\,(0.68 \pm 0.04)\text{fm}$$

$$a^{I=1} = (0.37 \pm 0.09) + i\,(0.60 \pm 0.07)\text{ fm}$$

Where used in a coupled-channels calculation to deduce the $\overline{K}N$ interactions of the following forms

$$v_{\overline{K}N}^{I} = v_D \exp\left[-\left(\frac{r}{b}\right)^2\right],$$

$$v_{\overline{K}N,\pi\Sigma}^{I} = v_{C_1} \exp\left[-\left(\frac{r}{b}\right)^2\right],$$

$$v^{I}_{\bar{K}N,\pi\Lambda} = v_{C_2} \exp\left[-\left(\frac{r}{b}\right)^2\right]$$, Where b = 0.66 fm and

$$v_{D}^{I=0} = -436\,\mathrm{MeV},\ v_{C_1}^{I=0} = -412\,\mathrm{MeV},\ v_{C_2}^{I=0} = \mathrm{none},\ v_{D}^{I=1} = -62\,\mathrm{MeV},$$

$v_{C_1}^{I=1} = -285\,\mathrm{MeV}$, $v_{C_2}^{I=1} = -285\,\mathrm{MeV}$.The two interactions, $v^{I}_{\pi\Sigma}(r)$ and $v^{I}_{\pi\Lambda}(r)$ are taken to be vanishing to simply reduce the number of parameters. This is justified because they are almost irrelevant in describing the $\bar{K}$ bound states.

The above coupled-channels interactions were used to derive equivalent single-channel $\bar{K}N$ potentials with imaginary parts in energy-independent forms, which is an appropriate way to obtain the decaying state of Kapur-Peierls as discussed below. The obtained complex potentials are

$$v_{\bar{K}N}^{I=0}(r) = (-595 - i83)\ \exp\left[-\left(\frac{r}{0.66}\right)^2\right],$$

$$v_{\bar{K}N}^{I=1}(r) = (-175 - i105)\ \exp\left[-\left(\frac{r}{0.66}\right)^2\right],$$

in units of MeV and fm. The same rage is assumed for I=0 and I=1. The interaction strength (V_0) and the rage (b) can be determined simultaneously because B and a_{K^-p} have different dependences on V_0 and b. Semiempirical $\bar{K}N$ interaction is consistent with the theoretically derived ones from meson-exchange and from chiral dynamics.

Nothing that the parameter b in the above Gaussian distribution is related to the rms distance R as $b = \sqrt{\frac{2}{3}}R = 0.816R$, the observed proton rms radius (R_p= 0.862 fm) to give a range parameter b = 0.70 fm, which is compatible with rage parameter (0.66 fm). The $\bar{K}N$ scattering amplitude by changing the range parameter b. The real and imaginary parts with b = 0.7 fm reproduce the chiral dynamics result very well, in spite of the strong claim by Oset and Toki that AY's scattering amplitudes are too large compared with those obtained from the chiral unitary approach of Oset and Ramos. Thus, the interaction rage deduced and used in AY is fully justified.

Table 1 Calculated potential parameters (V_0 and W_0 in MeV), energies (E_{K^-pp})and widths (Γ_{K^-pp}) of K^-pp in MeV, and the I=0 scattering length in fm with varied $\overline{K}N$ rage (b in fm), while reproducing Λ (1405).

b	**V_0**	**W_0**	E_{K^-pp}	Γ_{K^-pp}	**$A^{I=0}$ (fm)**
1.0	-316.5	-62.0	-49.5	66.5	-1.95+i0.45
0.9	-368.7	-67.0	-49.0	65.7	-1.89+i0.44
0.8	-439.6	-73.0	-48.3	64.4	-1.82+i0.44
0.7	-540.0	-81.0	-47.3	62.9	-1.75+i0.43
0.6	-689.5	-91.0	-45.8	60.3	-1.69+i0.43
0.5	-929.7	-105.0	-44.0	57.4	-1.62+i0.42
0.4	-1358.0	-128.0	-42.1	54.9	-1.55+i0.42
0.3	-2250.0	-162.0	-40.1	51.3	-1.48+i0.42

Results and Discussions

The structure of K^-pp nuclear cluster comprehensively by solving three-body system exactly in a variational method starting from the Λ(1405) resonance $(\equiv \Lambda^*)$ is a K^-p bound state. The prediction for the presence of K^-pp as a compact bound system with M = 2322 MeV/c^2, B_k = 48 MeV and Γ = 60 MeV remains unchanged by varying the $\overline{K}N$ and NN interactions widely as far as Λ (1405). The Λ^*- p system exists a compact doorway state propagating to K^-pp $(\mathbf{R}_{\Lambda^*p} \approx \mathbf{1.67\,fm})$.

The potential used in the calculation is $V^{opt}(r) = (\overline{v}_0 + i\overline{\omega}_0)\left(\frac{r}{b}\right)^2 \exp -\left(\frac{r}{b}\right)$

In Y-A potential, the value of $\overline{\mathbf{v}}_0 = -\mathbf{227.0\,MeV}$

$\overline{\boldsymbol{\omega}}_0 = -\mathbf{106.0\,MeV}$

b =0.30fm

By using Y-A potential, the calculated value of binding energy and level width for Λ^* p system are represented in table (2).

In DISTO potential, the value of $\overline{\mathbf{v}}_0 = -\mathbf{400.0\,MeV}$

$\overline{\boldsymbol{\omega}}_0 = -\mathbf{162.0MeV}$

b = 0.3 fm

By using DISTO (Defense Industrial Security Education & Training Office) experimental data, the calculated value of binding energy and level width forΛ^* p system are represented in table (3).

Then, average kinetic energy, average potential energy and root mean square radius values are calculated.

By using Y-A phenomenological potential and the DISTO experimental data, the calculated results of average kinetic energy, theaverage potential energy and the root mean square radius for Λ^* and p system are represented in table (4).

In the three body K^-pp system, Yamazaki-Akaishi calculated rms value between N and the $\overline{K}N$ is 1.67 fm. The calculated rms values are different because of using the different potential models.

Table 2 The calculated results of binding energy and level width of Λ^*p system for Yamazaki Akaishi potential.

Λ^*p potential	**BE (MeV)**	**Level Width (MeV)**
Y-A phenomenological potential [T.Yamazaki]	-21.00	61.00
Our Calculated Result	-21.168	60.76

Table 3 The calculated results of binding energy and level width of Λ^*p system for DISTO experimental data.

Λ^*p potential	**BE (MeV)**	**Level Width (MeV)**
DISTO Experimental Data [M. Maggiora et al]	-78.00	108.00
Our Calculated Result	-78.05	108.52

Table 4 Calculated results of kinetic energy, potential energy and root mean square radius For Λ^*p system.

	Kinetic Energy (MeV)	Potential Energy (MeV)	RMS (fm)
Y-A phenomenological Potential [T.Yamazaki]	43.90	-65.06	1.46
DISTO Experimental Data [M. Maggiora et al]	68.27	-146.32	1.11

Conclusion

Thus, the calculated results for binding energy of K^-pp system are in good agreement with the calculated result of YA and experimental result of DISTO. The calculated rms values are different because of using the different potential models. The Λ (1405) plays an essential role in forming the $\overline{K}$ nuclear clusters (KNC). A new window to Nuclear Physics would be opened up through the investigation of KNC.

Acknowledgement

I would like to thank Rector Dr Tin Tun, Pro-Rector Dr Mar Lar, Pro-Rector Dr Yee Yee Oo, Taungoo University for their permission to do this paper. I am very thankful to Professor Dr Nge Nge Khaing, Head of Physics Department, Taungoo University, for her kind permission to do this paper.

References

Hemingway R.J., (1985), Nucl. Phys. **B 253,** 742-752.

Ichikawa Y. et al., (2013), Prog. Theor.Exp. Phys. 8.

Maggiora M. et al., (2010), Nucl. Phys. **A 835,** 43-50.

Yamazaki T., (2007), Phys. Rev.**C 76,** 045201.

J. Myanmar Acad. Arts Sci. 2020 **Vol. XVIII.No.2C**

CALCULATION OF DEUTERON BINDING ENERGY WITH AND WITHOUT PARTIAL WAVE DECOMPOSITION METHODS

Aye Thida[1], Htun Htun Oo[2] and Aye Nyein Thu[3]

Abstract

In this paper, the binding energy of deuteron is calculated by using both with and without partial wave decomposition methods. Firstly, the time independent Schrödinger equation is transformed into Lippmann-Schwinger equation for two-body bound system. This equation is solved by using Gauss-Legendre integration method. In this calculation, Malfliet-Tjon III potential is used and derived the potential matrix element in momentum space. The binding energy of deuteron is calculated by using iterative method. From this research, it is found that our calculated deuteron binding energy by using with partial wave decomposition method is 2.2283 MeV and it is about 4 keV greater than the experimental result. Our calculated deuteron binding energy by using without partial wave decomposition method is 2.2335 MeV and it is about 9 keV greater than the experimental result. The experimental deuteron binding energy is 2.2245 MeV.

Keywords: Gauss-Legendre integration method, iterative method, Malfliet-Tjon III potential

Introduction

In 1931, Brige and Menzel suggested the existence of the first isotope of hydrogen. After a few months later American scientist H.C. Urey and his co-worker investigated the distilled sample of natural hydrogen for the optical atomic spectrum of ${}^{1}_{1}\mathrm{H}$ in a discharge tube. Isotopic separation to study the properties of deuterium quickly became an intense activity. The discovery of deuterium in 1932, coming before the discovery of neutron, was an experimental shock to theory. Deuteron, the simplest system of bound nucleon, the nucleus of deuterium atom contains one proton and one neutron. In 1932, it is discovered by Urey and his co-workers. The properties of deuteron in nuclear theory are as important as the hydrogen atom in atomic theory. It was shortly after the discovery of deuteron, Chadwick discovered neutron devoted in deuteron while he studied the deuterium. There is no man who immediately eliminates the confusion of proton and neutron. Because the previous model is persistent as a bound system of a proton and an electron. Based on this assumption, Heisenberg produced the first model of proton-neutron force. He assumed that the phenomenological potential could describe the proton-neutron force, and the neutron was a spin ½ particle like proton. The first idea about the nature of the nucleon-nucleon interaction came from Yukawa in 1935. He assumed that the strong interaction between two nucleons is carried by an interaction in quantum.

Deuterium is one of the only four stable nuclides with an odd number of protons and neutrons. Most odd-odd nuclei are unstable with respect to beta decay because the decay product are even-even, and are therefore more strongly bound, due to nuclear paring effects. Its benefits from having its proton and neutron coupled to a spin 1 state, which gives a stronger nuclear interaction. The corresponding spin 1 state does not exist in the two-nucleon or two-proton system due to Pauli’s exclusion principle which would require one or the other identical particle

---

[1] Dr, Lecturer, Department of Physics, Taungoo University

[2] Dr, Associate Professor, Department of Physics, Lashio University

[3] Daw, Assistant Lecturer, Department of Physics, Kalay University

with the same spin to have some other different quantum number, such as orbital angular momentum.

The standard approach in conventional nuclear theory is to treat the two-nucleon interaction in a phenomenological manner, that is, assume it to be derivable from a potential, and then set up a reasonable form for it in agreement with general theoretical considerations and experimental data. Most experimental data providing direct information on the potential concern with the two-nucleon system: neutron-proton (n-p), proton-proton (p-p) and neutron-neutron (n-n). The n-p system produces a bound state, whereas no bound state exists in p-p and n-n systems.

Calculations by Using Partial Wave Decomposition Method

Lippmann-Schwinger Equation for the Two-Body Bound System

The Lippmann-Schwinger equation is derived from the time independent Schrödinger equation. The time independent Schrödinger equation has the following form.

$$\hat{H}\Psi = E\Psi \tag{1}$$

But, $\hat{H}$ have kinetic energy $\hat{H}_0$ and potential energy $\hat{V}$ operators. So, Eq.(1) becomes

$$(\hat{H}_0 + \hat{V})\left|\Psi\right\rangle = E\left|\Psi\right\rangle \tag{2}$$

The Eq. (2) can be written as follows. It is Lippmann-Schwinger equation in ket form.

$$\left|\Psi\right\rangle = \frac{1}{E - \hat{H}_0}\left|\Psi\right\rangle \tag{3}$$

By multiplying Eq. (3) with $\left\langle p\ell m\right|$ from left and operating $\hat{p}^2$ on to Ψ gets

$$\left\langle p\ell m\middle|\Psi\right\rangle = \frac{1}{E - \frac{p^2}{2m}}\left\langle p\ell m\middle|\hat{V}\middle|\Psi\right\rangle \tag{4}$$

By inserting the completeness relation $\sum_{\ell' m'}\int p'^2\,dp'\left|p'\ell' m'\right\rangle\left\langle p'\ell' m'\right| = 1$ into Eq.(4),

$$\left\langle plm\middle|\Psi\right\rangle = \frac{1}{E - \frac{p^2}{2m}}\sum_{\ell' m'}\int p'^2 dp'\left\langle p\ell m\middle|V\middle|p'\ell' m'\right\rangle\left\langle p'\ell' m'\middle|\Psi\right\rangle \tag{5}$$

Since the local potential is consider, Eq. (5) becomes

$$\Psi_{\ell m}(p) = \frac{1}{E - \frac{p^2}{2m}}\sum_{\ell' m'}\int p'^2 dp'\,V_{\ell\ell' mm'}(p,p')\delta_{\ell\ell'}\delta_{mm'}\Psi_{\ell' m'}(p') \tag{6}$$

Since the potential is spherically symmetric, the index m can be dropped. It becomes

$$\Psi_\ell(\mathrm{p}) = \frac{1}{\mathrm{E} - \frac{\mathrm{p}^2}{2\mathrm{m}}} \int_0^\infty \mathrm{p}'^2 \mathrm{dp}'\, \mathrm{V}_\ell(\mathrm{p},\mathrm{p}') \Psi_\ell(\mathrm{p}') \tag{7}$$

The integral term in Eq. (7) can be transform into discrete form as follows:

$$\Psi_\ell(\mathrm{p_i}) = \frac{1}{\mathrm{E} - \frac{\mathrm{P_j^2}}{2\mathrm{m}}} \sum_{\mathrm{j=1}}^{\mathrm{N}} \mathrm{p_j^2} w_j\, \mathrm{V}_\ell(\mathrm{p_i},\mathrm{p_j})\, \Psi_\ell(\mathrm{p_j}) \tag{8}$$

The calculation of potential matrix element is presented in next section. The FORTRAN 90 code is written using Eq. (8) to find the deuteron binding energy. Malfliet-Tjon potential is used in this calculation. In writing numerical code, the potential is written as a function. Then Gauss points, Gauss weights and momentum range are prepared to use Gauss-Legendre integration method. Iterative method is used to find the binding energy of deuteron.

Calculation of Potential Matrix Element

Yukawa type Malfliet-Tjon potential has the following form

$$\mathrm{V(r)} = \mathrm{V_A} \frac{e^{-\mu_A r}}{r} + \mathrm{V_R} \frac{e^{-\mu_R r}}{r}$$

Where, $\mathrm{V_A}$, $\mathrm{V_R}$ = depth parameter and μ_A, μ_R = range parameter

The potential matrix element is

$$\mathrm{V}_\ell(\mathrm{p},\mathrm{p}') = \langle \mathrm{p}\ell\mathrm{m} | \mathrm{V} | \mathrm{p}'\ell\mathrm{m} \rangle \tag{9}$$

When the normalized equation is used, it becomes

$$\mathrm{V}_\ell(\mathrm{p},\mathrm{p}') = \frac{1}{2\ell+1} \sum_{m=-\ell}^{\ell} \langle \mathrm{p}\ell\mathrm{m} | \mathrm{V} | \mathrm{p}'\ell\mathrm{m} \rangle \tag{10}$$

By inserting the completeness relation into Eq. (10),

$$\mathrm{V}_\ell(\mathrm{p},\mathrm{p}') = \frac{1}{2\ell+1} \sum_{\mathrm{m}=-\ell}^{\ell} \int d\vec{\mathrm{p}}'' \int d\vec{\mathrm{p}}''' \langle \mathrm{p}\ell\mathrm{m} | \vec{\mathrm{p}}'' \rangle \langle \vec{\mathrm{p}}'' | \mathrm{V} | \vec{\mathrm{p}}''' \rangle \langle \vec{\mathrm{p}}''' | \mathrm{p}'\ell\mathrm{m} \rangle \tag{11}$$

The Eq.(11) can be written as

$$\mathrm{V}_\ell(\mathrm{p},\mathrm{p}') = \frac{1}{2\ell+1} \sum_{\mathrm{m}=-\ell}^{\ell} \int \mathrm{p}''^2 \mathrm{dp}'' d\hat{\mathrm{p}}'' \int \mathrm{p}'''^2 \mathrm{dp}''' d\hat{\mathrm{p}}'''\; \mathrm{Y}^*_{\ell\mathrm{m}}(\hat{\mathrm{p}}'') \frac{\delta(\mathrm{p}''-\mathrm{p})}{\mathrm{p}''\mathrm{p}}$$

$$\times \mathrm{Y}_{\ell\mathrm{m}}(\hat{\mathrm{p}}''') \frac{\delta(\mathrm{p}'''-\mathrm{p}')}{\mathrm{p}'''\mathrm{p}'} \langle \mathrm{p}'' | \mathrm{V} | \mathrm{p}''' \rangle \tag{12}$$

After solving Eq.(12), it becomes

$$\mathrm{V}_\ell(\mathrm{p},\mathrm{p}') = \frac{1}{4\pi} \int d\hat{\mathrm{p}} \int d\hat{\mathrm{p}}'\, \mathrm{P}_\ell(\hat{\mathrm{p}},\hat{\mathrm{p}}') \langle \mathrm{p} | \mathrm{V} | \mathrm{p}' \rangle \tag{13}$$

The Malfliet-Tjon potential which is expressed in coordinate space is used in this calculation. So this potential can be transformed into momentum space by using the completeness relation $\int d\vec{r}\,|\vec{r}\rangle\langle\vec{r}\,| = 1.$

$$\langle p|V|p'\rangle = \int d\vec{r} \int d\vec{r}\,' \langle \vec{p}\,|\,\vec{r}\rangle\langle\vec{r}\,|V|\,r'\rangle\langle r'\,|\,p'\rangle \tag{14}$$

For the local potential, it can be written as

$$\langle p|V|p'\rangle = \frac{1}{(2\pi)^3} \int d\vec{r}\, e^{i(\vec{p}\,'-\vec{p}).\vec{r}}\ V(r) \tag{15}$$

So, the potential matrix element is as follows:

$$\langle p|V|p'\rangle = \frac{4\pi}{(2\pi)^3} \int d\vec{r} \sum_{\ell m} i^{\ell}\, Y^{*}_{\ell m}(\hat{q}) Y_{\ell m}(\hat{r}) j_{\ell}(qr) V(r) \tag{16}$$

For $\ell = 0$, Eq. (16) becomes

$$\langle p|V|p'\rangle = \left[\frac{V_A}{2\pi^2} \frac{1}{\mu_A^2 + p^2 + p'^2 - 2pp'\cos\theta} + \frac{V_R}{2\pi^2} \frac{1}{\mu_R^2 + p^2 + p'^2 - 2pp'\cos\theta} \right] \tag{17}$$

Substituting Eq. (17) in Eq. (13) gets

$$V_{\ell}(p,p') = \frac{1}{4\pi} \frac{1}{2\pi^2} \int_0^{2\pi} d\varphi \int_0^{2\pi} d\varphi' \int_{-1}^{1} d\cos\theta \int_{-1}^{1} d\cos\theta'\, P_{\ell}(\cos\theta)$$

$$\times \left[\frac{V_A}{\mu_A^2 + p^2 + p'^2 - 2pp'\cos\theta} + \frac{V_R}{\mu_R^2 + p^2 + p'^2 - 2pp'\cos\theta} \right] \tag{18}$$

For $\ell = 0$, $P_0(x) = 1$ and let $\cos\theta = x$. Eq. (18) becomes

$$V_{\ell}(p,p') = \frac{V_A}{2\pi} \frac{1}{pp'} \ell n \left[\frac{\mu_A^2 + (p+p')^2}{\mu_A^2 + (p-p')^2} \right] + \frac{V_R}{2\pi} \frac{1}{pp'} \ell n \left[\frac{\mu_R^2 + (p+p')^2}{\mu_R^2 + (p-p')^2} \right] \tag{19}$$

A numerical code for the potential is written as a function using Eq.(19). In writing numerical code, the values of potential depth parameters (V_A and V_R) and range parameters (μ_A and μ_R) are used.

Calculations by Using Without Partial Wave Decomposition Method

Lippmann-Schwinger Equation for the Two-Body Bound System

Lippmann-Schwinger equation in ket form is

$$|\Psi\rangle = \frac{1}{E - \hat{H}_0} \hat{V} |\Psi\rangle \tag{20}$$

Multiplying Eq.(20) with $\langle\vec{p}\,|$ from left gets

$$\langle\vec{p}\,|\Psi\rangle = \langle\vec{p}\,| \frac{\hat{V}}{E - \hat{H}_0} |\Psi\rangle \tag{21}$$

After operating with $\hat{P}^2$ on to $|\Psi\rangle$, Eq.(21) becomes

$$\langle\vec{p}|\Psi\rangle = \frac{1}{E-\frac{P^2}{2m}}\langle\vec{p}|\hat{V}|\Psi\rangle \tag{22}$$

The completeness relation is inserted in Eq.(22) as follows,

$$\langle\vec{p}|\Psi\rangle = \frac{1}{E-\frac{P^2}{2m}}\int d\vec{p}'\langle\vec{p}|\hat{V}|\vec{p}'\rangle\langle\vec{p}'|\Psi\rangle \tag{23}$$

In Eq.(23) $\vec{p}$ has magnitude p and direction x. $\vec{p}'$ has magnitude p' and direction x'. Therefore it can be written as

$$\Psi(p,x) = \frac{1}{E-\frac{P^2}{2m}}\int d\vec{p}'V(p,p',y)\Psi(p',x') \tag{24}$$

To find out the relations between x, x' and y, the momentum $\vec{p}$ and $\vec{p}'$ are considered in the Cartesian diagram.

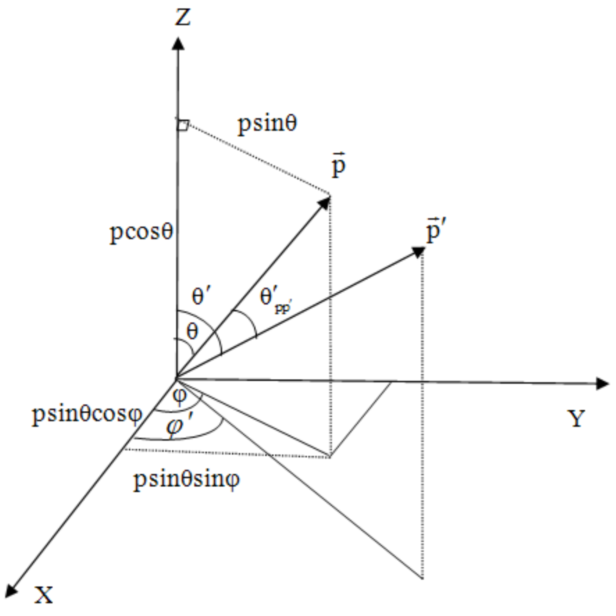

Figure 1 The momenta and in the Cartesian co-ordinate system

From the figure $\vec{p}$ $\vec{p}'$

$$\vec{p} = p\sin\theta\cos\varphi\,\hat{x} + p\sin\theta\sin\varphi\,\hat{y} + p\cos\theta\,\hat{z} \tag{25}$$

$$\vec{p} = p'\sin\theta'\cos\varphi'\,\hat{x} + p'\sin\theta'\sin\varphi'\,\hat{y} + p'\cos\theta'\,\hat{z} \tag{26}$$

We take scalar product of and and then

$$\cos\theta_{pp'} = \cos\theta\cos\theta' + \sin\theta\sin\theta' + \cos(\varphi-\varphi') \tag{27}$$

Let $\cos\theta = x,\ \cos\theta' = x', \cos\theta_{pp'} = y$

Eq.(27) can be written as

$$y = xx' + \sqrt{1-x^2}\,\sqrt{1-x'^2}\cos\left(\varphi - \varphi'\right) \qquad (28)$$

The arbitrary azimuthal angle for momentum $\vec{p}$ is chosen to be zero.

$$y = xx' + \sqrt{1-x^2}\,\sqrt{1-x'^2}\cos\varphi' \qquad (29)$$

Substituting Eq.(29) in Eq.(24) obtains

$$\Psi(p,x) = \frac{1}{E - \frac{P^2}{2m}} \int_0^\infty p'^2 dp' \int_{-1}^{1} dx' \int_0^{2\pi} d\varphi'\, V\left(p, p', xx' + \sqrt{1-x^2}\,\sqrt{1-x'^2}\cos\varphi'\right)\, \Psi\left(p', x'\right) \qquad (30)$$

The integral term in Eq. (30) can be transform into discrete form as follows:

$$\Psi\left(p_i, x_\ell\right) = \frac{1}{E - \frac{P_j^2}{2m}} \sum_{j=1}^{N_p} p_j^2 w_j \sum_{k=1}^{N_x} w_k\ V\left(p_i, x_\ell, p_j, x_k\right) \Psi\left(p_j, x_k\right) \qquad (31)$$

The calculation of potential matrix element is presented in next section. We write a FORTRAN 90 code using Eq.(31) to find the deuteron binding energy. Malfliet-Tjon III potential is used in this calculation. In writing numerical code, the potential is written as a function.

Calculation of Potential Matrix Element

The potential matrix element can be written as

$$V\left(p, p', y\right) = \langle \vec{p} | V | \vec{p}' \rangle \qquad (32)$$

The Malfliet-Tjon potential is expressed in coordinate space. So, it will be transformed into momentum space by using the completeness relation $\int d\vec{p}' |\vec{p}'\rangle\langle\vec{p}'| = 1$.

$$V\left(p, p', y\right) = \int d\vec{r} \int d\vec{r}\,' \langle \vec{p} | \vec{r} \rangle \langle \vec{r} | V | \vec{r}\,' \rangle \langle \vec{r}\,' | \vec{p}' \rangle \qquad (33)$$

It can be written as

$$V\left(p, p', y\right) = \frac{1}{(2\pi)^3} \int d\vec{r} \int d\vec{r}\,' e^{i(\vec{p}' - \vec{p}).\vec{r}}\, V(r)\, \delta\left(\vec{r}\,' - \vec{r}\right) \qquad (34)$$

By using the delta function properties, Eq. (34) becomes

$$V\left(p, p', y\right) = \frac{1}{8\pi^3} \int_0^\infty r^2 dr \int_0^\pi \sin\theta\, d\theta \int_0^{2\pi} d\varphi\, e^{i(\vec{p}' - \vec{p}).\vec{r}}\, V(r) \qquad (35)$$

After inserting the Malfliet-Tjon potential in Eq.(35), it can be written in the form

$$V\left(p, p', y\right) = \frac{V_A}{2\pi^2} \frac{1}{\mu_A^2 + \left(p' - p\right)^2} + \frac{V_R}{2\pi^2} \frac{1}{\mu_R^2 + \left(p' - p\right)^2} \qquad (36)$$

By defining as

$$V(p,x,p',x') = \int_0^{2\pi} d\varphi' \, V\left(p,p',xx' + \sqrt{1-x^2}\sqrt{1-x'^2}\cos\varphi'\right) \tag{37}$$

By substituting Eq.(36) in Eq.(37)

$$V(p,x,p',x') = \int_0^{2\pi} d\varphi' \frac{V_A}{2\pi^2}\frac{1}{\mu_A^2 + (p'-p)^2} + \int_0^{2\pi} d\varphi' \frac{V_R}{2\pi^2}\frac{1}{\mu_R^2 + (p'-p)^2} \tag{38}$$

Solving Eq (38) obtains

$$\begin{aligned} V(p,x,p',x') = {} & \frac{V_A}{\pi}\frac{1}{\sqrt{\left(\mu_A^2 + p'^2 + p^2 - 2pp'xx'\right)^2 - \left(-2pp'\sqrt{1-x^2}\sqrt{1-x'^2}\right)^2}} \\ & + \frac{V_R}{\pi}\frac{1}{\sqrt{\left(\mu_R^2 + p'^2 + p^2 - 2pp'xx'\right)^2 - \left(-2pp'\sqrt{1-x^2}\sqrt{1-x'^2}\right)^2}} \end{aligned} \tag{39}$$

The numerical code is written as a function using Eq.(39). In writing numerical code, the potential parameters shown in Table 1 are used.

Calculation of Eigen Value by Using Iterative Method

Let φ_i be the set of the possible state kets.

$$\varphi_i = \varphi_1 + \varphi_2 + \varphi_3 + \ldots\ldots + \varphi_n \tag{40}$$

$|\Psi\rangle$ is the total wave function of all state kets and which can be written as

$$|\Psi\rangle = \sum_{i=1}^{n} c_i \varphi_i \tag{41}$$

K be the square matrix and has the following property

$$K\varphi_i = \lambda_i \varphi_i \tag{42}$$

$$K|\Psi\rangle = \sum_{i=1}^{n} \lambda_i c_i \varphi_i \tag{43}$$

$$K^j|\Psi\rangle = \lambda_1^j c_1 \varphi_1 + \lambda_2^j c_2 \varphi_2 + \ldots\ldots\ldots + \lambda_n^j c_n \varphi_n \tag{44}$$

It is assumed that,

$$|\lambda_1| > |\lambda_2| > |\lambda_3| > \ldots\ldots > |\lambda_n|$$

Eq.(44) becomes

$$K^j|\Psi\rangle = \lambda_1^j\left(c_1\varphi_1 + \left(\frac{\lambda_2}{\lambda_1}\right)^j c_2\varphi_2 + \ldots\ldots + \left(\frac{\lambda_n}{\lambda_1}\right)^j c_n\varphi_n\right) \tag{45}$$

If j becomes large, all terms in the bracket approach to zero expect the first term. So Eq.(45) becomes

$$K^j|\Psi\rangle = \lambda_1^j c_1\varphi_1 \tag{46}$$

For (j+1)th iteration,

$$K^{j+1}|\Psi\rangle = \lambda_1^{j+1} c_1\varphi_1 \tag{47}$$

By taking the ratio of Eq.(46) and (47),

$$\frac{K^{j+1}|\Psi\rangle}{K^j|\Psi\rangle} = \frac{\lambda_1^{j+1}c_1\varphi_1}{\lambda_1^j c_1\varphi_1} = \lambda_1 \tag{48}$$

In this way the largest eigenvalue λ_1 is obtained. In order to apply the iterative method for partial wave decomposition, the Eq.(7) is rewritten again and let Kernel be K(E).

$$\Psi_\ell(p) = \frac{1}{E - \frac{P^2}{2m}} \int_0^\infty p'^2 dp' V_\ell(p,p')\Psi_\ell(p')$$

$$K(E) = \frac{1}{E - \frac{P^2}{2m}} \int_0^\infty p'^2 dp' V_\ell(p,p') \tag{49}$$

Therefore, it can be written as

$$|\Psi\rangle = K(E)|\Psi\rangle \tag{50}$$

Arbitrary value η which is the function of E is introduced into Eq.(50).

$$\eta|\Psi\rangle = K(E)\,|\Psi\rangle \tag{51}$$

When η becomes 1, Eq. (51) is equal to Eq.(50). Since the true energy eigenvalue E is not known, we start with an estimated energy and determine the corresponding eigenvalue η. Then the energy E is varied such that η approaches the value 1.

Technique of Energy Search Program

Now to search the binding energy, the natures of η and E are needed to know. The arbitrary energy is initialized using Eq.(7) for the calculation with partial wave decomposition method. The arbitrary input energy E_1 and E_2 are introduced. The E_1 and E_2 are upper bound and lower bound absolute value of energy. The input energy is define as $E = (E_1+E_2)/2$. If the value of η is less than 1, we set E_2 should be E and E_1 is kept. If η is greater than 1, we set E_1 should be E and E_2 is kept. Then, the η value is searched by iteration. According to this procedure, the gap between E_1 and E_2 is narrower and narrower and η approaches to 1. In this way, the value of η converges to 1 and the corresponding energy is obtained. It is true energy for the deuteron. This procedure is written in program code. For the calculation without partial wave decomposition method, Eq.(30) is used to calculate the deuteron binding energy. The parameter set for Yukawa type Malfliet-Tjon III potential is shown in Table 1. The discretization parameters which converge the deuteron binding energy by changing the number of grid points are shown in Table 2 and Table 3.

Table 1 The parameter set for Yukawa type Malfliet-Tjon III potential

V_A (MeV fm)	μ_A (fm^{-1})	V_R (MeV fm)	μ_R (fm^{-1})
- 626.822	1.55	1438.317	3.11

Table 2 The discretization parameters for partial wave decomposition

P_0 (fm^{-1})	p_{max} (fm^{-1})	p_{cut} (fm^{-1})	N_1	N_2	BE (MeV)
0.00	5.0	60.0	20	20	2.2283

Table 3 The discretization parameters for without partial wave decomposition

P_0 (fm^{-1})	p_{mid} (fm^{-1})	p_{max} (fm^{-1})	N_p	N_x	BE (MeV)
0.00	3.0	30.0	26	14	2.2335

Results

According to the numerical result, it is found that the binding energy of deuteron is 2.2283 MeV by using with partial wave decomposition method and 2.2335 MeV by using without partial wave decomposition method. Our calculated results are compared with the experimental result and the results calculated by other theoretical groups. Comparison of deuteron binding energies is shown in Table 4.

Table 4 Comparison of deuteron binding energies

Potential Types	Binding Energy (MeV)
Nijmegen I	2.2245
Nijmegen II	2.2245
Nijmegen 93	2.2245
CD-Bonn	2.2245
Malfliet-Tjon III	2.2300
Malfliet-Tjon IV	2.2300
Experimental result	2.2245
Malfliet-Tjon III (Our result using with partial wave decomposition method)	2.2283
Malfliet-Tjon III (Our result using without partial wave decomposition method)	2.2335

Discussion

Our calculated deuteron binding energy by using with partial wave decomposition method is 2.2283 MeV and it is about 4 keV greater than the experimental result and the results calculated by Nijmegen and CD-Bonn groups. This could be the fact that the potentials (Nijmegen I, Nijmegen II, Nijmegen 93 and CD-Bonn) which are used by theoretical groups are realistic potentials. These potentials are fitted to the experimental data and considered including spin and isospin. But the Malfliet-Tjon III potential which is used in this calculation is a phenomenological potential. This potential can be adjusted the parameter set. Our calculated result is in good agreement in two decimal places with the results calculated by Malfliet-Tjon group using Malfliet-Tjon type III and IV potentials. In this calculation spin and isospin are not considered. Only for S-state ($\ell = 0$) is calculated. Our calculated deuteron binding energy by using without partial wave decomposition method is 2.2335 MeV and it is about 9 keV greater than the experimental result and the results calculated by Nijmegen and CD-Bonn groups. Our calculated result is in good agreement in two decimal places with the results calculated by Malfliet-Tjon group. Our results calculated by using two methods are slightly different. This will be the fact that higher partial waves are needed to consider in the calculation by using partial wave decomposition method. But the deuteron binding is directly calculated and no need to consider partial waves in the calculation by using without partial wave decomposition method.

Conclusion

The two-body problem which is the simplest and one can understand the nucleon-nucleon interaction. Two-body forces are basic to study three-body and many-body problems. The Lippmann-Schwinger equation is used in the calculations of two-body bound state and scattering process. At low energies in the MeV and the few tenth of MeV region very few angular momenta contribute to the nucleon-nucleon (N-N) scattering process. Consequently a description using angular momentum decomposition is an adequate tool for carrying out scattering calculations. However, at intermediate energies, energies of a few hundred MeV and higher energies very many angular momenta contribute to the scattering amplitude. In these energy domains those individual contributions to the scattering amplitude for a fixed high angular momentum oscillate strongly in angle. The without angular momentum decomposition method is suitable for the studying of high energy N-N interaction.

Acknowledgements

The authors would like to thank Rector Dr Tin Tun, Pro-Rector Dr Mar Lar and Pro-Rector Dr Yee Yee Oo, Taungoo University for their permission to do this paper. The authors are also grateful to Professor Dr Nge Nge Khaing, Head of Department of Physics, Taungoo University for her permission during the preparing of this manuscript.

References

Bainbridge K.T., (1932), Phys. Rev. **41**, 115.

Birge R.T. and Menzel D.H., (1931), Phys. Rev. **37**, 1669.

Gargcon M. and Van Orden J.W., (2001), ar Xiv:nucl-th-**21,** 0102049.

Machleidt R., et.al, (2001), Phys. Rev **C 63**, 24001.

Malfliet R.A. and Tjon J.A., (1969), Nucl.Phys. A **127**, 161.

Urey H. C. et.al, (1932), Phys. Rev. **39,** 164.

J. Myanmar Acad. Arts Sci. 2020 **Vol. XVIII.No.2C**

PREPARATION AND CHARACTERIZATION OF SELECTED BIOCHAR FROM BIOLOGICAL WASTES

Thin Thin Kyu[1], Thinzar Lwin[2], Moe Min Min Aye[3],
Than Than Win[4], Yin Maung Maung[5]

Abstract

Biochar is a solid material that is produced by heat decomposition of biological wastes biomass. The experiments were carried out to study the characterization of the Coconut Husk and Areca nut Husk biochar. The Coconut Husk and Areca nut Husk were heated at 300˚C for 1h in muffle furnace and ground into the uniform powder. The most important properties that provide information about the fuel were proximate analysis such as moisture, ash content, volatile matter and fixed carbon contents. The fixed carbon content of Coconut Husk and Areca nut Husk were measured to be 10 mf wt%. The structural characterizations of Coconut Husk and Areca nut Husk biochar were identified by X-ray diffraction (XRD) technique. The Fourier transform infrared spectroscopy (FTIR) analysis showed the presence of a variety of functional groups of Coconut Husk and Areca nut Husk biochar. Scanning Electron Microscope images of the biochar were obtained for morphological features analysis.

Keywords: Biochar, Coconut Husk, Areca nut Husk, Proximate analysis, XRD, FTIR, SEM

Introduction

Biomass is biological material derived from living, or recently living organisms. In the context of biomass for energy this is often used to mean plant based material, but biomass can equally apply to both animal and vegetable derived material. [Mohammad Hariz A.R, etal. 2015] Biomass is non-fossilized and biodegradable organic material originating from plants, animals and microorganisms. This includes the products, byproducts, residues and wastes from agriculture, forestry, industrial and municipal wastes. [Qian, K, etal 2015] Pyrolysis conversion process is one of the prominent methods through which biomass is converted into three significant by-products namely solid char, bio-oil and gases. [Sukiran, M. A. B. 2008)] [Abnisa, F.,etal. 2013] Biochar is a solid carbon-rich product produced when biomass such as stalks, straw, wood, fruits, seeds and leaves is heated in a closed container without or limited presence of air. [Qian, K.; etal 2015] Biochar is produced during the pyrolysis of biomass materials. [Sulaiman, F., etal 2011] [Safaba aminu Aliyu., etal 2018] Biochar is a low-cost, carbon rich material derived from the thermochemical composition of lignocellulosic biomass in limited or absence of oxygen. Compared to other types of carbonaceous materials, biochar emerges as a new cost-effective and environmentally friendly carbon material with great potential of application in many different fields. [Ahmed Y. Elnour. etal 2019] The main objective of the present study is to investigate the preparation and characterization of biochar from coconut husk and areca nut husk at 300^{o}C. In order to utilize this biochar for further application, it is desirable to understand the most important pyrolysis indicator such as proximate analysis, i.e., information of moisture, ash content, volatile matter and fixed carbon content. Fourier transform infrared

---

[1] Dr, Assistant Lecturer, Department of Physics, University of Yangon

[2] PhD Student, Department of Physics, University of Yangon

[3] Dr, Associate Professor, Department of Engineering Physics, Dawei Technology University.

[4] Dr, Professor, Department of Physics, Ponglong University

[5] Dr, Professor, Department of Physics, University of Yangon

spectroscopy (FTIR), X-ray diffraction (XRD) and scanning electron microscopy (SEM) were also investigated.

Materials and Methods

Starting Materials

Two different feed stocks of coconut husk and areca nut husk were selected for the preparation of biochar. Raw feed stocks were collected from local environment and dried properly under natural conditions. After drying, the materials were cut into desirable size pieces and then dried in air oven in batches at 105°C for the removal of moisture. The dried coconut husk and areca nut husk pieces are then sent to ball mill for grinding. The product is then ground to smaller size and the finer product is separated using a sieve. Thus final particle size of ground coconut husk and areca nut husk are less than 1 mm. And then the pyrolysis temperature used in these study at 300 ºC. The conversion of coconut husk and areca nut husk biomass into biochar was shown in Figure 1 and 2. The flow diagram of the sample preparation of two biochar was shown in Figure 3.

Figure 1 Conversion of Coconut Husk biomass into Biochar

Figure 2 Conversion of Areca nut Husk biomass into Biochar

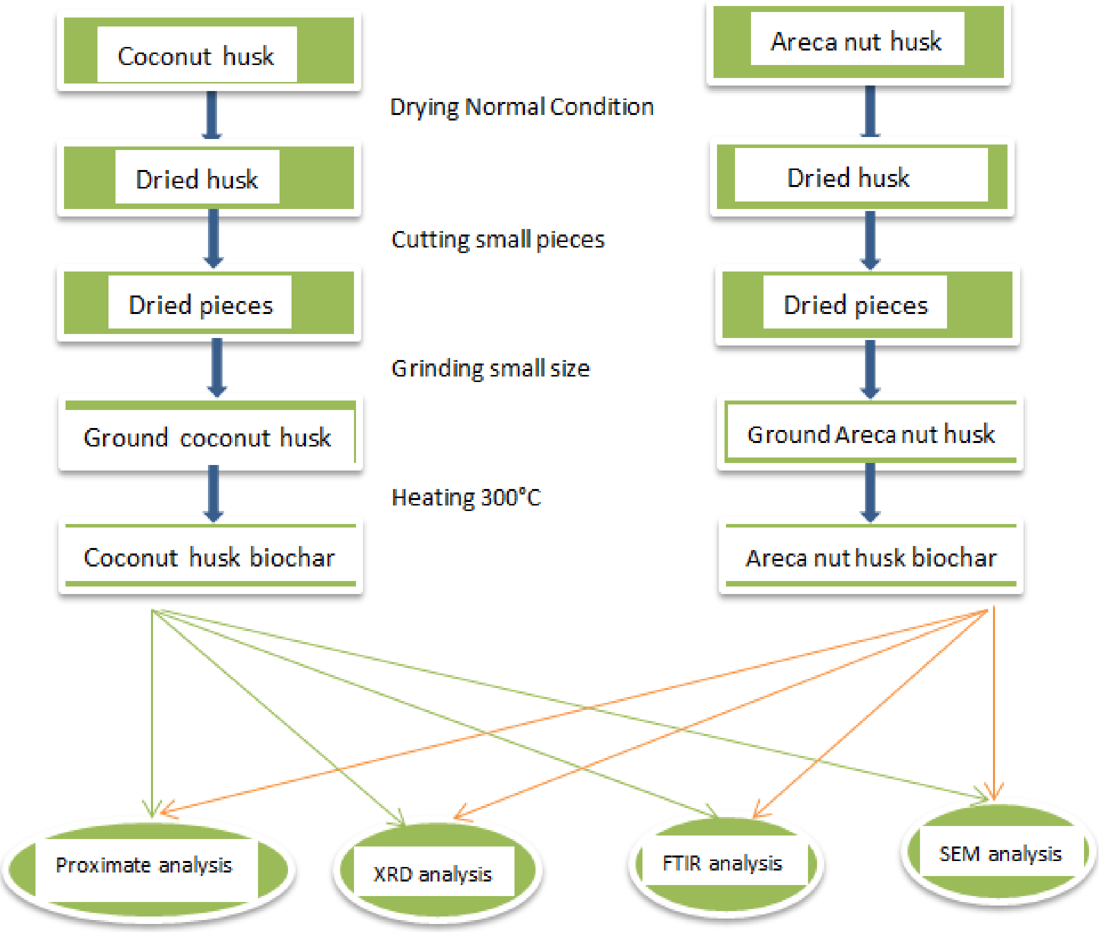

Figure 3 The flow diagram of the sample preparation of two biochar

Characterization of coconut husk and areca nut husk biochar

The biochar of coconut husk and areca nut husk were characterized to determine its fundamental properties by proximate analysis of moisture content, ash content, volatile matter content and fixed carbon content. Fixed carbon other than ash does not vaporize when heated in the absence of air. Fixed carbon is usually determined by subtracting the sum of the first three values that is moisture, ash, and volatile matter (weight percent from 100 percent).So, it is very important for economic reasons to know the moisture and ash contents of the material. The phase composition and crystal structure of the obtained carbon were analyzed on an X-ray diffractometer (Smart Lab) with (Cu/K-alpha1) radiation (λ = 1.54056°A) under a current of 50mA and a voltage of 40kV. Fourier Transforms Infrared Spectroscopic analysis of biochar was recorded on (Thermo-Scientific Nicolet iS5) spectrometer to determine its functional groups. The FTIR spectra were collected with a spectrometer using potassium bromide pellets and the wave number ranging from 400 to 4000 cm^{-1}. Surface morphology of biochar was identified by Scanning Electron Microscopy were obtained using an acceleration voltage of 15kV and a magnification x300 and x2000. (JEOL- BENCHTOP).

Results and Discussion

Proximate Analysis of coconut and areca nut husk biochar

In order to determine the volatile matter, fixed carbon and ash content in the biochar product of two different biomasses, coconut husk and areca nut husk, the proximate analysis was performed. The comparative results of the proximate analysis of the biochar are shown in Table 1. The results disclose that the proximate analysis of the coconut husk and areca nut husk were almost similar. However, areca nut husk contained a little higher moisture content than and lower than volatile matter content and ash content than coconut husk. The fixed carbon content of areca nut husk higher than coconut husk was observed.

Table 1 Proximate analysis for Coconut and Areca nut Husk

Sample	Moisture content (%)	Volatile matter content (%)	Ash content (%)	Fixed Carbon Content (%)
Coconut Husk	9.200	75.996	0.047	14.757
Areca nut Husk	9.307	68.380	0.028	22.282

XRD Analysis of Coconut Husk and Areca nut Husk Biochar

The XRD diffractogram of the coconut husk and areca nut husk biochar are represented in Figure 3 and 4 has shown several peaks, although the overall characteristic of the biochar is amorphous. There are a little sharp diffracted peaks were observed. The peaks at d spacing 3.1477°A and 2.2250°A (2Ө values 28.330° and 40.510°) are assigned to the presence of potassium chloride and it is consistent with coconut husk and areca nut husk biochar. These are indicated the presence of components, which were related to the crystalline forms of potassium chloride and other components of carbon and graphite peaks. The present data suggests that most of the amorphous carbon rich regions. It could be said that the coconut husk and areca nut husk biochar were amorphous material with little crystalline. The crystalline percent and amorphous percent of coconut husk and areca nut husk biochar were shown in Table 2.

Table 2 Crystallinity results of Coconut and Areca nut Husk biochar

Biochar	Crystalline (%)	Amorphous (%)
Coconut husk	3.66	96.34
Areca nut husk	5.39	94.61

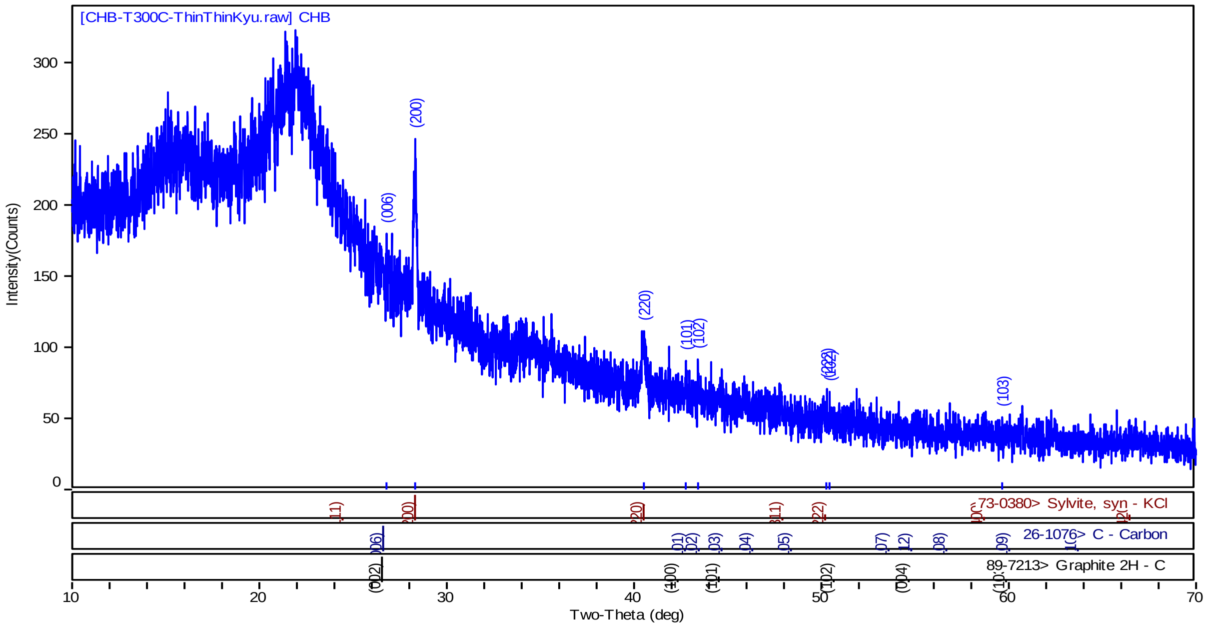

Figure 3 XRD analysis of Coconut Husk Biochar

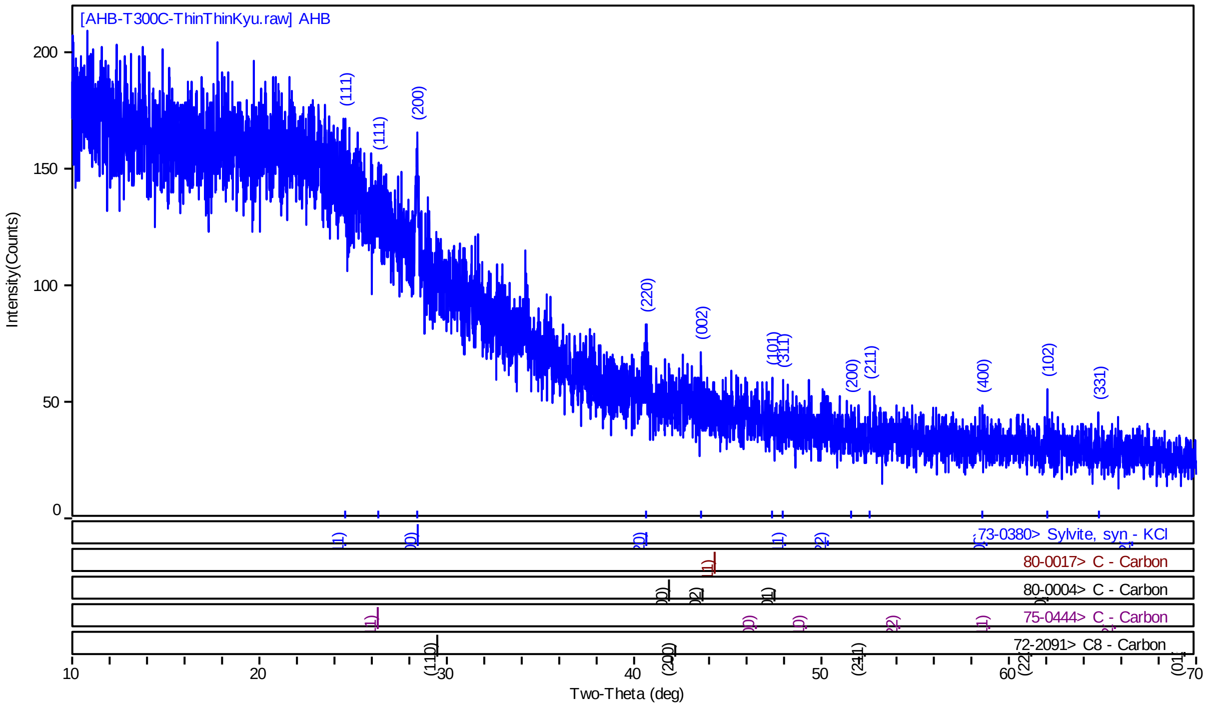

Figure 4 XRD analysis of Areca nut Husk Biochar

Functional group of Coconut Husk and Areca nut Husk Biochar

Fourier Transform Infrared spectroscopy (FTIR) is an important analysis technique which detects various characteristic functional groups present in biochar**.** The FTIR spectrum of biochar obtained from pyrolysis of coconut husk and areca nut husk at the pyrolysis temperature at 300 °C in one hour are shown in Figure 5 and 6. The O-H stretching vibrations at 3337.55cm^{-1}

and 3342.09cm^{-1} indicate the presence of phenols and alcohols and the C-H stretching vibrations at 2927.68cm^{-1} and 2930.02cm^{-1} indicate the presence of aromatic ring. A strong stretching vibration at 1700.99cm^{-1} shows the presence of C=O of carboxylic acid. A stretching vibration at 1594.29 and 1596.92 cm^{-1} shows the presence of C=C of alkenes. The C-O stretching vibration at 1212.63, 1104.36, 1029.34 and 1032.65cm^{-1} indicates the presence of alkanes. These functional groups are responsible for the sharp stretching vibration at 1029.34 cm^{-1} shows the presence of C-O stretching vibration and 1596.92 cm^{-1} show the presence of C=C strong stretching vibration. The different assignments of the FTIR spectra of coconut husk and areca nut husk biochar were summarized in Table 1 and 2.

Table 2 Peaks and functional groups from FTIR spectrum of Coconut Husk Biochar

Wave Number (cm^{-1})	**Type of vibration**	**Functional group**
3327.30	H–bonded O–H stretch (Broad strong band)	Alcohols, Phenols
2927.68	C–H stretch (strong)	Aromatic Rings stretching
1594.29	C=C stretch (medium)	Alkene
1508.09	C=C stretch(weak)	Aromatic Rings
1420.40	C–H (variable)	scissoring and bending
1212.63	C–O stretch	Aromatic
1029.34	C–O stretch (strong)	Ether

Table 3 Peaks and functional groups from FTIR spectrum of Areca nut Husk Biochar

Wave Number (cm^{-1})	**Type of vibration**	**Functional group**
3342.09	H–bonded O–H stretch (Broad strong band)	Alcohols, Phenols
2930.02	C–H stretch (strong)	Aromatic Rings stretching
1700.99	C=O stretch (strong)	Ketone , Carboxylic acid
1596.92	C=C stretch (medium)	Alkene
1508.30	C=C stretch(weak)	Aromatic Rings
1437.66	C–H (variable)	scissoring and bending
1204.75	C–O stretch	Aromatic
1104.36	C–O stretch (strong)	Alcohols, Ethers, Carboxylic acids
1032.65	C–O stretch (strong)	Ether

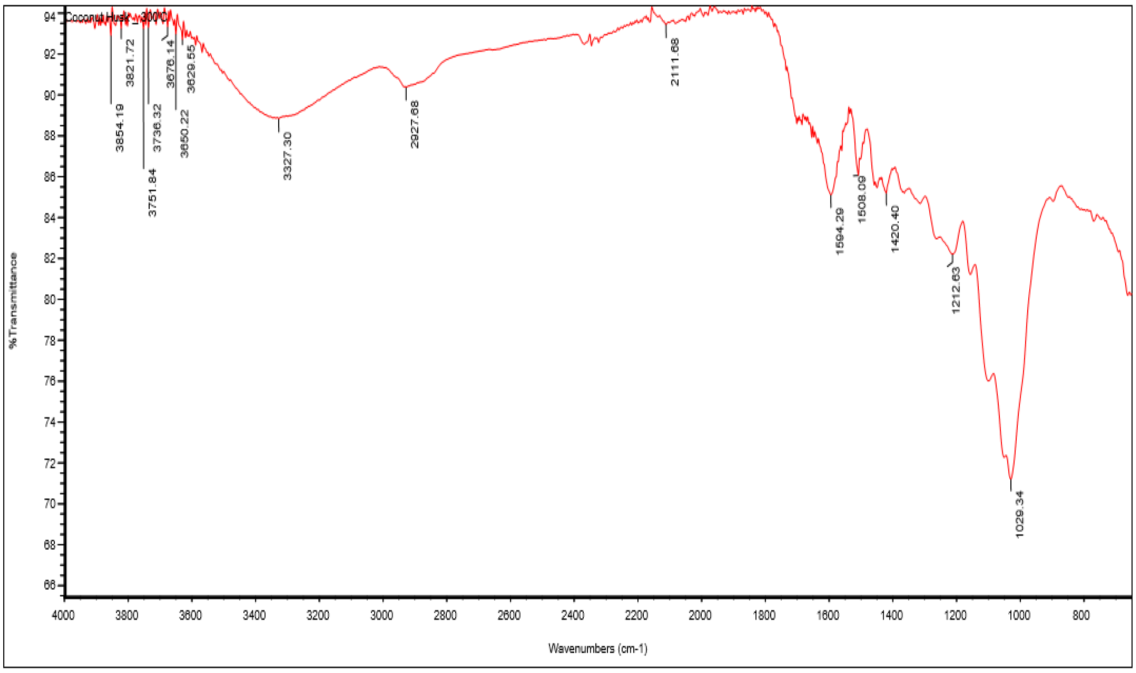

Figure 5 FTIR spectra of Coconut Husk Biochar

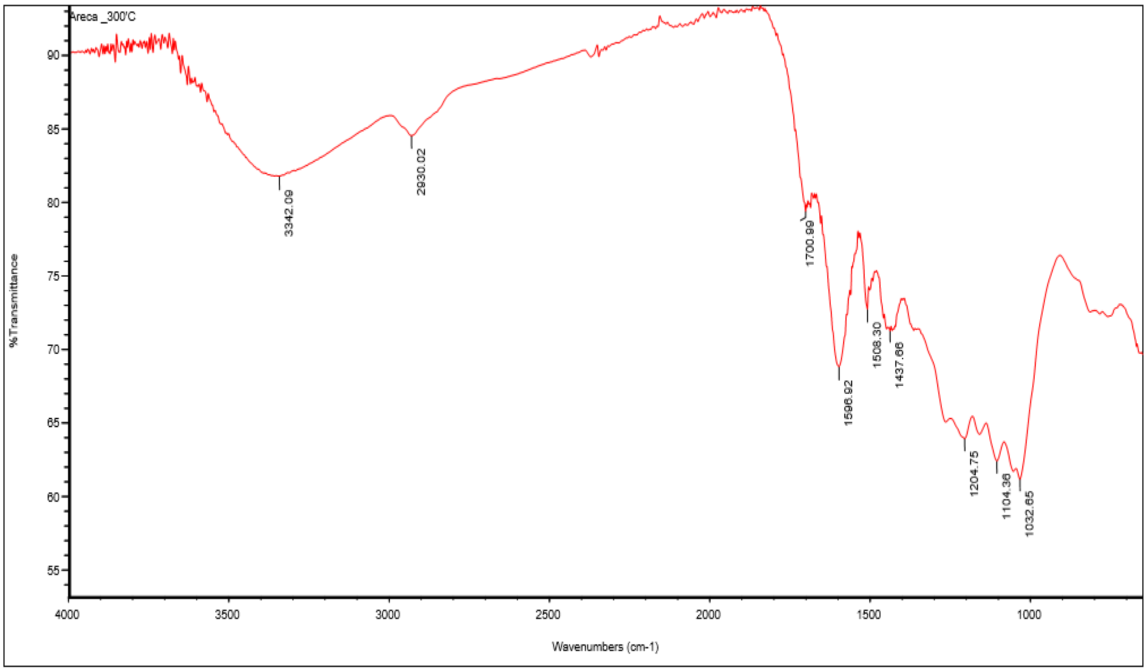

Figure 6 FTIR spectra of Areca nut Husk Biochar

Surface morphology structure of Coconut Husk and Areca nut Husk Biochar

The scanning electron microscopy (SEM) images of the prepared biochar samples of coconut husk and areca nut husk biochar are shown in Figure 7 and 8. The SEM images showed the variations in the porous structure of morphology. SEM image of coconut husk and areca husk biochar taken at 300 X and 2000X magnification. These two biochar image showed heterogeneous distribution of pores and rough texture. Presence of micropores and mesopores were detected. The size of the pores indicated that the volatile compounds had evaporated creating macro pores on the surface. The SEM images of areca nut husk biochar possess well-defined pores structure and the smooth wall dense surfaces. The size of the pores on a surface with varying diameters as follows the average diameter of coconut husk and areca nut husk was 2.20µm and 2.62µm respectively. As a result of these developed pores, that two biochar will have a high surface area.

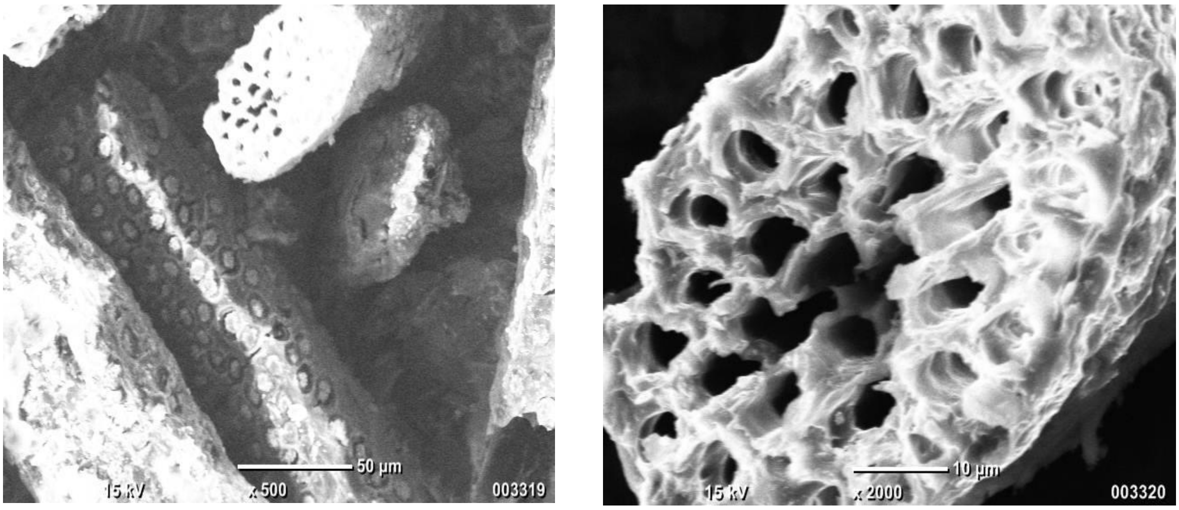

Figure 7 SEM image of Coconut Husk Biochar at (a) 500X and (b) 2000X magnification

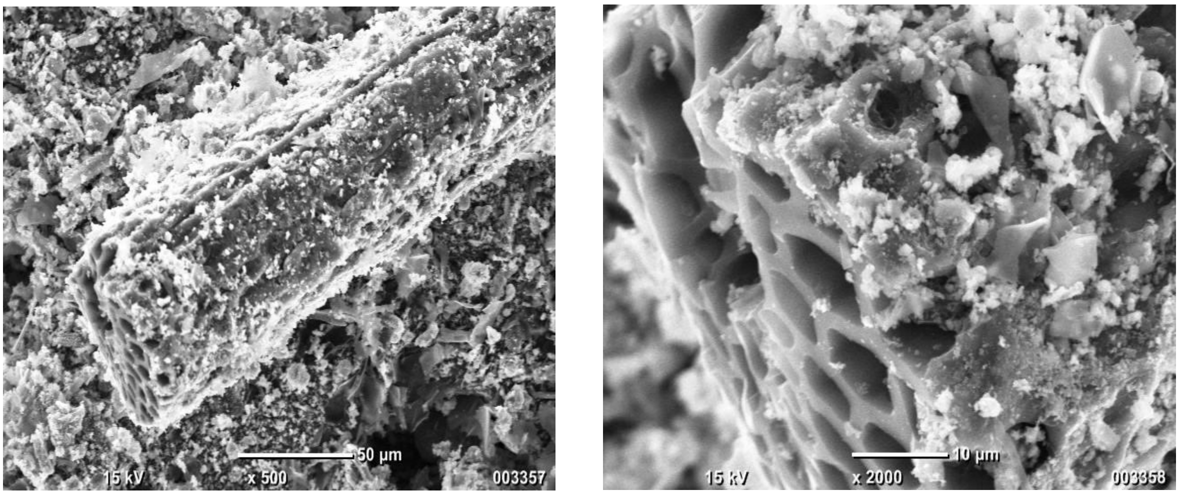

Figure 8 SEM image of Areca Husk Biochar at (a) 500 X and (b) 2000X magnification

Conclusion

Characterization of biochar derived from pyrolysis of coconut husk and areca nut husk were investigated. The results disclose that the proximate analysis of the materials were almost similar. A mineralogical study of the coconut husk and areca nut husk biochar by XRD revealed of amorphous mainly carbon, graphite were found. XRD spectra of two biochar peak in figure and there are two diffracted peaks were observed. It could be said that the two biochar were amorphous material with little crystalline. The most important observation was the difference in the number of oxygenated functional groups, on the surface of the two biochar as shown by FTIR analysis of two biochar peak The FTIR spectra of two biochar display the bands containing O-H, C-H, C=O and C-O stretch. Coconut husk biochar and areca nut husk biochar differed in their surface morphology in terms of pore size. These coconut husk biochar image showed heterogeneous distribution of pores and rough texture. Presence of micro-pores and mesoporous detected. The size of the pores indicated that the volatile compounds had evaporated creating macro pores on the surface. This study was carried out to provide basic information as to the possibility of reuse of biochar derived from different biomass of biological waste. According to the characterization of biochar obtained by coconut husk and areca nut husk biomass, we can conclude that such biochar can be suitable for different specific application and may be an effective way for recycling the waste resources.

Acknowledgement

I am highly grateful thanks Professor Dr Khin Khin Win, Head of Department of Physics, University of Yangon for her permission to do and her encouragement throughout this paper.

We also thank to members of Materials Science Lab, Department of Physics, University of Yangon, for kind supply of practical equipment.

References

Abnisa, F,etal. (2013) “Characterization of bio-oil and bio-char from pyrolysis of palm oil wastes” *BioEnergy Research* . 6,830-840

Ahmed Y. Elnour., etal (2019) “Effect of Pyrolysis Temperature on Biochar Microstructural Evolution, Physicochemical Characteristics, and Its Influence on Biochar/Polypropylene Composites” *Applied Science,* 9,1149

Angalaeeswari K and Kamaludeen SPB (2017) “Production and characterization of coconut shell and mesquite wood biochar” *International Journal of Chemical studies*, 5(4). 422-226

Mohammad Hariz A.R., etal.(2015) “Local Particles for production of rice husk biochar and coconut shell biochar: Production methods, product characteristics, nutrient and field water holding capacity” *J. Trop. Agric. and Fd. Sc.* 43(1) 91-101

Qian, K.; Kumar, A.; Zhang, H.; Bellmer, and Huhnke, R. (2015) “Recent advances in utilization of biochar” *Renewable and Sustainable Energy Reviews.* 42, 1055-1064. DOI: 10.1016/j.rser.2014.10.074

Safaba aminu Aliyu., etal (2018) “Combustion characteristics of palm pressed fibres biochar and sub-bituminous Malaysian coal*” Journal of Fundamental and applied Sciences,* Vol 4,(3) 334-337

Sulaiman, F., etal (2011) “Optimum conditions for mazimising pyrolysis liquids of oil palm empty fruit bunches” *Energy,* 36(5), 2352-2359

Sukiran, M. A. B. (2008) “Pyrolysis of empty oil palm fruit bunches using the quartz fluidized-fixed bed reactor” Master Thesis, University of Malaya Kuala Lukpur.

J. Myanmar Acad. Arts Sci. 2020 **Vol. XVIII.No.2C**

PHYSICSOCHEMICAL PROPERTIES OF SURGANE BAGASSE BIOMASS WITH ACTIVATED CARBON (ACs) AS RENEWABLE ENERGY

Zin Min Myat[1], Zin Min Tun[2], Than Than Win[3] and Yin Maung Maung[1]

Abstract

Biomass is an industry term for getting energy by burning wood, plants and animal waste and other organic matter in nature. In this research, sugarcane bagasse biomass has been used as a raw material for the preparation of different activated carbons. Sugarcane bagasse is a solid residue, consisting of the dry fibrous mass remaining after the juice is extracted, which can cause serious environmental problem if disposed inadequately. The aim of this study was to use the bagasse in the preparation of activated carbons (ACs) followed by pyrolysis at 300°C, 400°C, and 500 °C for 1 h respectively. The sugarcane bagasse biomass was characterized by instrumental analysis such as infrared spectroscopy (FTIR), X-ray Diffraction (XRD) and Scanning Electron Microscopy (SEM). Also, the pH and electrical conductivity (EC) of biomass was determined for physical properties. According to the experimental results, sugarcane bagasse biomass gave good strength results as well as the potential to be used as the source of energy. The results of this study present a simple, economical and environment-friendly method of improving the growth and enhancing the renewable energy in Myanmar.

Keywords - FTIR, XRD, SEM, sugarcane bagasse biomass

Introduction

Biochar can be used as fuel, for carbon sequestration, as activated carbon and soil amendment to reduce greenhouse gas emissions [Lehmann J et al 2006]. Activated carbon is a well-known as porous material, with large specific surface area, which is useful in various application of both gases and solutes from aqueous solution [Pragya P et al 2013]. The term biomass refers to all materials derived from living organisms (plants and animals). Biomass can be used as a material (such as food, timber products, fiber, fertilizer, chemicals, etc.) or energy. A wide range of biomass sources have been used to make biochar, including agricultural and food waste, woody plants and animal manures and waste from many industries. The application of biochar to soil can improve soil quality and plant growths. Properties of biochars are strongly dependent on biomass feed stocks and production conditions. Current study on the characterization of biochars mainly focused on their chemical functionality related to agricultural and environmental applications. Among them various types of biomass in our environment, optimizing studies were carried out on sugarcane bagasse as potential feedstock for biochar production.

Sugarcane is a member of the grass family. Sugarcane is a tree-free renewable resource and one of the most important agricultural plants that grown in hot regions [Rasula M G et al 1999]. Sugarcane is “carbon neutral” (i.e. emissions are equal to energy generated) and is the product of choice in the manufacture of bio-fuels due to its high energy conversion rate [Aigbodion V. S et al 2010]. Bagasse is lateral production of sugarcane that after treatment of sugarcane in the form of light yellow particles is produced. The bagasse ash is the remains of

---

[1] Dr, Assistant Lecturer, Department of Physics, University of Yangon

[2] Department of Physics, West Yangon University

[3] Department of Physics, Panlong University

fibrous waste after the extraction of the sugar juice from cane [Kawade U R et al 2013].In many tropical countries there are substantial quantities of bagasse and husks from rice both are rich in amorphous silica, which react with lime. The bagasse ash is a pozzolanic material that would otherwise require disposal. The chemical composition of this product are cellulous fibers, water and some soil soluble material such as cube sugar, by passing time cube sugar is converted alcohol also the evaporation of bagasse fiber produce the methane gas which can cause fire in some circumstance [Subramani T and Prabhakaran M 2015]. Sugarcane consists of 25-30% bagasse whereas sugar recovered by the industry is about 10%. Bagasse is also used as a raw material for paper making due to its fibrous content and about 0.3 tons of paper can be made from one ton of bagasse. Bagasse is a byproduct during the manufacture of sugar and it has high calorific value [Nuntachai Chusilp et al 2009]. It is utilized as a fuel in boilers in the sugar mills to generate steam and electricity.

Materials and method

Preparation of Sugarcane Bagasse Biochars

Raw materials of sugarcane bagasse samples for this study were obtained from release of cold and drink shops, North Okkalapa Township. The collected sugarcane bagasse were washed several times with distilled water to remove dust and impurities and then dried in an oven at 120 °C for 24 h to remove all moisture. The bagasse were cut into small pieces, grained and sieved to an average particle size and stored in air-tight containers to prevent moisture buildup and other infections. The samples for activation process were then pyrolysis in a muffle furnace for activation temperature of 300 °C, 400 °C and 500 °C respectively. After activation period of 1 h the sugarcane bagasse biomass were allowed to cool down to the room temperature. The physiochemical and mechanical properties of sawdust biomass were successfully investigated. The block diagram of biochar preparation of sugarcane bagasse was shown in figure 1. The sugarcane bagasse biochar were measured for the value of change in pH and EC measurement. The chemical properties, structural properties and morphology structure of sawdust biomass were characterized FTIR, XRD and SEM analysis.

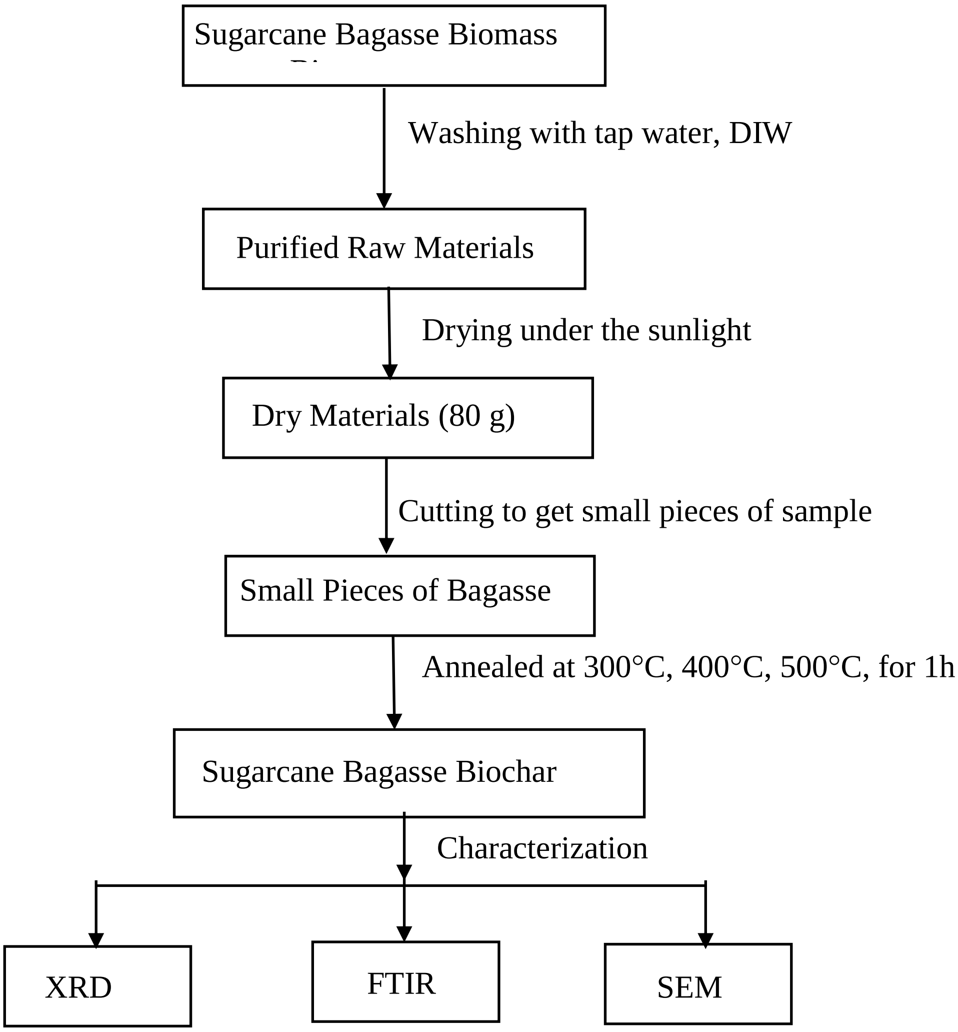

Figure 1 Block diagram of preparation of biochar Sugarcane Biomass

Biochar yield of Sugarcane Bagasse Biochar

In the preparation of biochar, the yield of biocahr is an important factor to be considered. The biochar yield (dry basis, %) is defined as the ratio of weight of biochar after pyrolysis (m_a (g)) to the weight of sugarcane bagasse before pyrolysis (m_b (g)) and is calculated by using the following equation,

$$\text{Biochar yield (\%)} = \frac{m_a\,(g)}{m_b\,(g)} \times 100\%$$

For all cases, the biochar yields of sugarcane bagasse biomass with various temperatures, the yields decreased sharply when the temperature was increased from 300°C to 500°C, and it decreased more slowly at increased temperatures. The variation of yield (%) is described in Table 1.

Table 1 Biochar Yield from Sugarcane Bagasse Biomass

Biochar	Pyrolysis Temperature (°C)	m_b(g)	m_a (g)	Biochar Yield (%)
Sugarcane bagasse Biomass	300	80	21.24	26..55
	400	80	17.42	21.78
	500	80	12.67	15.84

pH and Electrical Conductivity Analysis of Biochar

The pH testing of the sugarcane bagasse biochar were measured by pH meter Honiba F-51 (Japan). 2 g of dry biochar sample was dissolved 10 ml of deionized water for 15 min. Biochar was shaken with deionized water able at a constant temperature of 27 °C for 18 h. The pH values of the biochars in water ranged from slightly acidic 6.5 to alkaline 9.27. The value of pH increased considerably with the carbonization temperature from 300 °C to 500 °C. The value of pH slowly increased when the carbonization temperature was over 500 °C. The electrical conductivity is a measurement of the amount of soluble salts in biochar solutions, which is based on the principle that biochar solutions with a higher concentration of salts have a greater ability to conduct electricity. Electrical conductivity increases from 5.74 µS/cm to 7.49 µS/cm when the temperatures were increased. This is due to the presence of greater content in biochar prepared at higher pyrolysis temperature. Table 2 shows the pH value and EC measurement of sugarcane bagasse biochar. The graph of pH and EC measurement with different temperatures was shown in figure 2.

Table 2 The pH value and EC measurement of sugarcane bagasse biochar.

Temperature (°C)	pH value	EC (µS/cm)
300	6.5	5.74
350	7.8	6.21
400	8.89	6.61
450	9.15	7.01
500	9.27	7.49

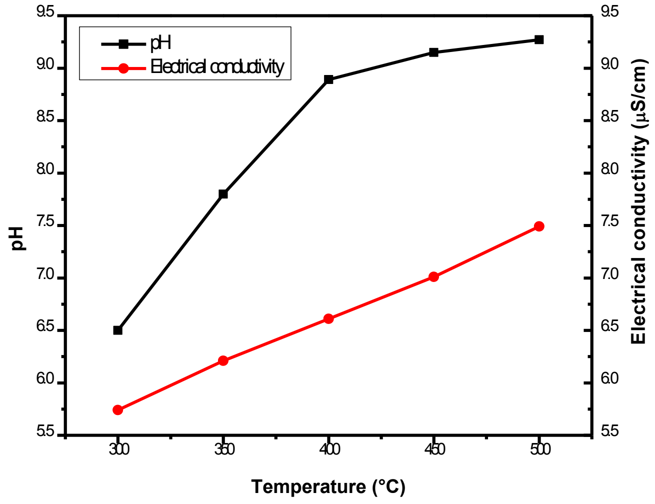

Figure 2 The graph of pH and EC measurement with different temperature

Results and Discussion

XRD Analysis of Sugarcane Bagasse Biochar

X-ray diffraction technique (XRD) is a powder technique for dimension of crystal structure, interplanar spacing by using X-ray beam. The sugarcane bagasse biochars were analyzed by XRD technique. According to XRD result, there are several diffracted peaks were observed. They were not perfectly identified. It could be say that the sugarcane bagasse samples were found to be amorphous structure with little crystalline. The absence of sharp peaks demonstrated the amorphous texture of the biochar sample. According to figure 3(a-c), it was examined that the dominant peaks were formed and they were matched with the peaks of carbon (graphite), diamond structure of carbon and chaoite structure. By analyzing XRD measurement, all the peak heights and peak position were in good agreement with library file of XRD machine.

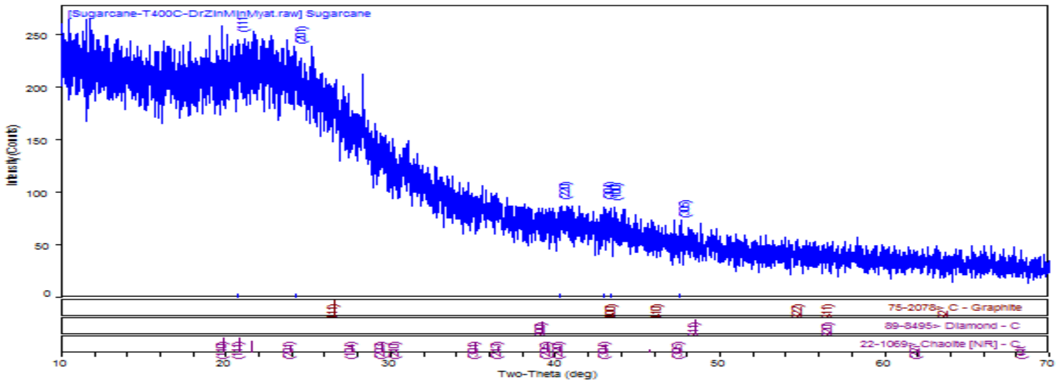

Figure 3(a) XRD Analysis of Sugarcane Bagasse Biochar at 300 °C

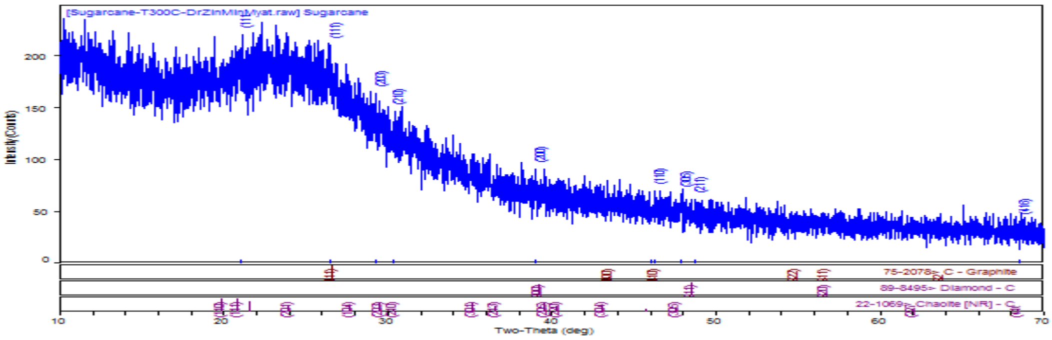

Figure 3(b) XRD Analysis of Sugarcane Bagasse Biochar at 400 °C

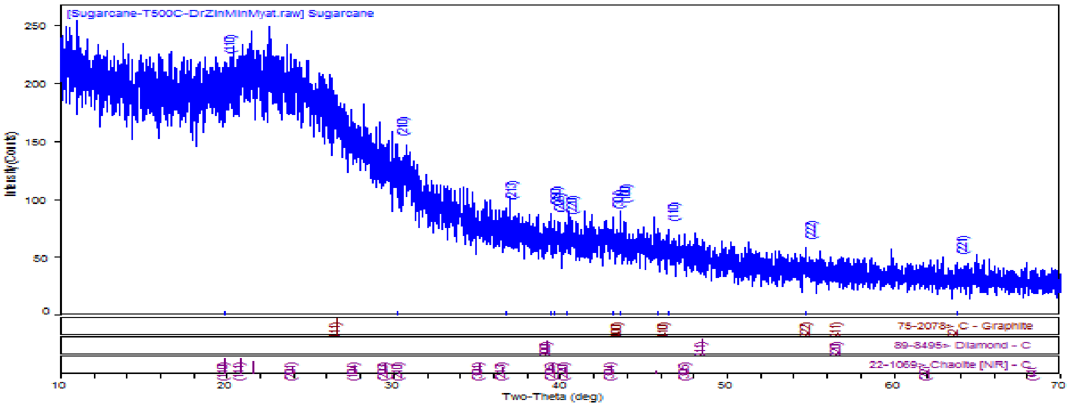

Figure 3(c) XRD Analysis of Sugarcane Bagasse Biochar at 500 °C

FTIR Analysis of Sugarcane bagasse biochar

Chemical functional groups were determined by Fourier Transform Infrared Spectroscopy (FTIR) analysis. The Fourier Transform Infrared Spectroscopy (FTIR) was used to characterize biochar because carbon impurities, water, functional groups and chemical properties can be detected that may modify the sequestration capability. FTIR spectroscopy was applied to measure the chemical properties and absorption of energy from the range of 4000 cm^{-1} - 400 cm^{-1} by studied samples. Figure 4 shows the FTIR analysis demonstrated the functional groups presented on sugarcane bagasse biochar types with various temperatures (SB-300 °C, SB-400 °C and SB-500). The functional groups of these biochar samples have found to be C-H stretching vibration, C ≡ C ring stretching and C = C stretching vibration respectively. The spectrum of these samples showed some characteristic bands related to physical and chemical changes. As shown in figure 4, the infra-red spectra of these biochar types are comparable but there are some changes in the functional groups depend upon its pyrolysis temperature. The water O-H stretch can occur in the SB-400 °C about 3841.46 cm^{-1}. The strong hydroxyl group can display in the SB-300 °C, SB-400 °C and SB-500 °C for about 3367.25 cm^{-1}, 3350.82 cm^{-1} and 3331.96 cm^{-1}. The N = H ring stretching is associated with all of the biochar types. The peak observed at 1586.53 cm^{-1}, 1573.71 $cm^{-1}$and 1573.07 $cm^{-1}$with SB-300 °C, SB-400 °C and SB-500 °C, respectively, corresponded to aromatic C = C ring stretching. The peak located at 1117.30 $cm^{-1}$and 1035.84 cm^{-1} for SB -400 °C and SB -500 °C, respectively, assigned to C-Cl stretching vibration of the alkyl halide groups. The presence of the band located at 824 cm^{-1}- 600 cm^{-1} showed a C - H out-of-plane bending modes of aromatic compounds in SB-300 °C, SB-400 °C and SB-500 °C biochar types. It was previously reported that different type of oxygen containing functional groups which existed in the raw sugarcane bagasse. According to FTIR analysis, all of the absorption bands in different temperature biochar types SB-300 °C, SB-400 °C and SB-500 °C are suitable for their absorption bands due to hydroxyl group in cellulose, carbonyl groups of acetyl ester in hemicellulose, and carbonyl aldehyde in lignin.

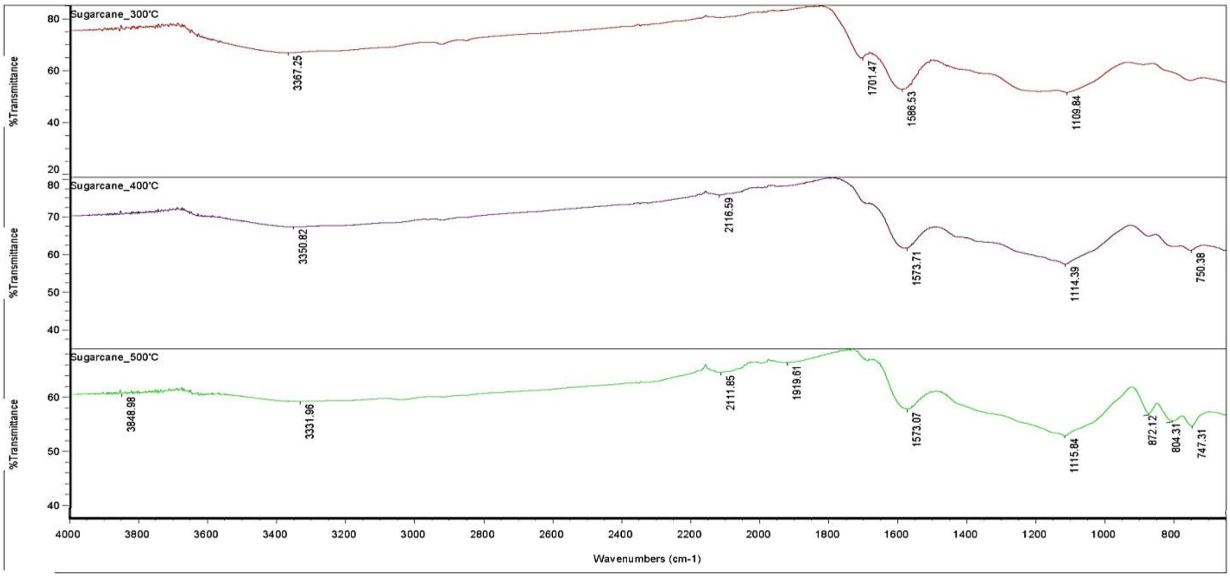

Figure 4 FTIR Analysis of Sugarcane Bagasse Biochar at 300 °C, 400 °C and 500 °C

SEM Analysis of Sugarcane bagasse biochar

SEM is one of the most versatile instruments available for the examination and analysis of the microstructure characteristics of a solid. The most important reason for using SEM is high resolution that can be obtained when bulk sample are examined. SEM micrographs for external morphology of sugarcane bagasse biochar at temperatures 300 °C, 400 °C and 500 °C for 1 h were shown in figure 5 (a-c). According to figure 5 (a), the clear porous nature had observed the sugarcane bagasse biochar at 300 °C and 400 °C. After increasing temperature, it was found that the sugarcane bagasse biochar had not clearly porous nature with macro- porous structure at 500 °C. From SEM analysis as shown in figure 5 (a-c), it can be observed that the microstructure of sugarcane bagasse biochar samples by varying the pore sizes with different temperatures. The average pore sizes of the samples were found to be about 6.7 µm at 300 °C, 10.2 µm at 400 °C and 11.7 µm at 500 °C respectively.

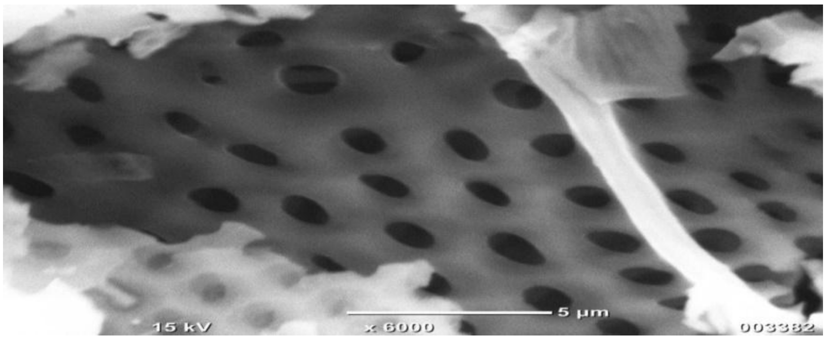

Figure 5 (a) SEM Analysis of Sugarcane Bagasse Biochar at 300 °C

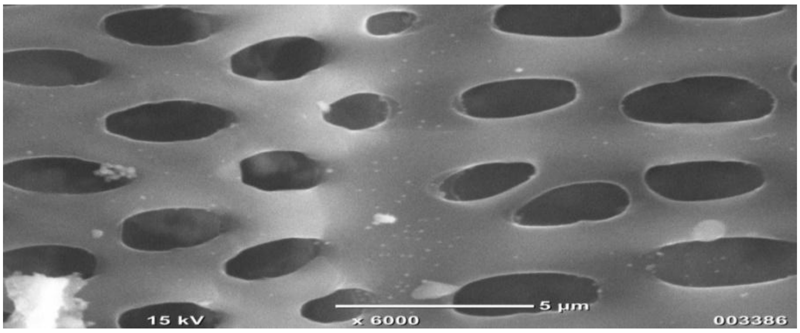

Figure 5 (b) SEM Analysis of Sugarcane Bagasse Biochar at 400 °C

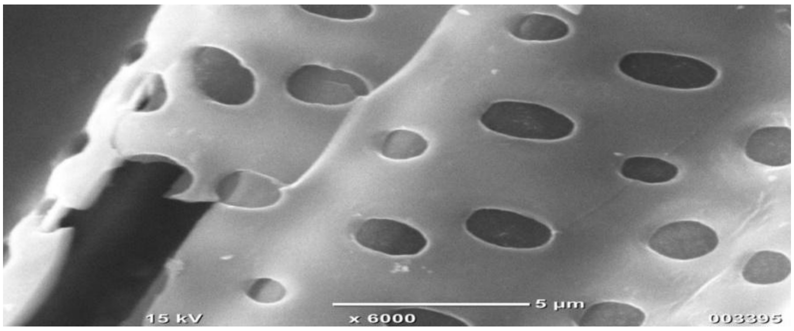

Figure 5 (c) SEM Analysis of Sugarcane Bagasse Biochar at 500 °C

Conclusion

The present investigation shows that the activated carbon obtained from sugarcane bagasse were prepared and characterized by studying physical, chemical and mechanical properties. In the physical properties measurements, the biochar yield % wt increased with increasing the carbonization temperatures. With the successive increase in temperature the pH and electrical conductivity (EC) values increased with elevated temperature. Sugarcane bagasse biomass provides the solution to use it and produce the low cost, energy efficient and clean energy in the form of briquetted biomass. According to FTIR analysis, low temperature, 300 °C biochar types is more suitable for their absorption bands due to hydroxyl group in cellulose, carbonyl groups of acetyl ester in hemicellulose, and carbonyl aldehyde in lignin. According to XRD result, the absence of sharp peaks demonstrated the amorphous texture of the biochar sample. They were not perfectly identified. It could be say that the sugarcane bagasse samples was found to be amorphous structure with little crystalline. XRD patterns of sugarcane bagasse were quite acceptable. Almost all the reflections were found to be consistent with carbon. SEM investigation showed that the macro- porous structure of sugarcane bagasse biochar. Sugarcane bagasse biomass can directly be used as a source of renewable energy because of their effective properties, environmental friendliness and low-cost production.

Acknowledgements

I would like to express my sincere gratitude to Professor Dr Khin Khin Win, Head of Department of Physics, University of Yangon, for her kind permission.

I would also like to mention my gratitude to Professor Dr Yin Maung Maung, University of Yangon for his encouragement on this research. This research was fully supported by the Department of Physics, University of Yangon, Myanmar (2018-2019).

References

Aigbodion V S et al (2010) Potential Utilization of Solid Waste (Bagasse Ash). *Journal of Minerals & Materials Characterization & Engineering*, 9 (1) 67-77

Govindarajan D and Jayalakshmi G (2011) XRD, FTIR and SEM studies on calcined sugarcane bagasse ash blended cement. Archives of Physics Research, 2(4)38-44

Howard et al (2002) "Healthy Villages A guide for communities and community health workers"

Kawade U R et al (2013) Effect of use of Bagasse Ash on Strength of Concrete. International Journal of Innovative Research in Science Engineering and Technology, 2(7)2997-3000

Lehmann J, Gaunt J and Rodon M (2006), " Biochar sequestration in terrestrial ecosystems –Areview" *Mitig. Adapt.Strat. Gl.* 11(2) 404-427.

Mohammed Abdullahi MU'AZU (2007) "Evaluation of Plasticity and partical Size Distribution Characteristics of Bagasse Ash on Cement Treated Lateritic Soil" Leonardo Journal of Sciences (10)137-152

Nuntachai Chusilp et al (2009) "Development of bagasse ash as a pozzolanic material in concrete" Asian Journal on Energy and Environment, 10 (03) 149-159

Pragya P, Sripal S, Maheshkumar Y (2013) "Preparation and Study of Properties of Activated Carbon Produced from Agricultural and Industrial Waste Shells" Journal of Chemical Science 3 (12), 12-15

Srinivasan R and Sathiya K (2010) "Experimental Study on Bagasse Ash on Concrete" International Journal for Service Learning in Engineering, 5 (2) 60-66

Srinivasan R & Sathiya K (2010) "Experimental Study on Bagasse Ash in Concrete" International Journal for Service Learning in Engineering, 5 (2) 60-66

Subramani T & Prabhakaran M (2015) "Experimental Study On Bagasse Ash In Concrete" International Journal of Application or Innovation in Engineering & Management (IJAIEM), 4 (5) 163-172

J. Myanmar Acad. Arts Sci. 2020 **Vol. XVIII.No.2C**

EXPERIMENTAL STUDY ON STRUCTURAL, MICROSTRUCTURAL AND ELECTRICAL CONDUCTIVITY OF MAGNESIUM DOPED NICKEL-COPPER-ZINC FERRITES

Kyaw Kyaw[1], Aye Aye Lwin[2], Moe Min Min Aye[3] and Win Kyaw[4]

Abstract

Magnesium doped Nickel-Copper-Zinc ferrites with the general formula $Ni_{0.6-x}Mg_xCu_{0.2}\ Zn_{0.2}Fe_2O_4$ (where x = 0.0 – 0.6 with the step of 0.2) were prepared by solid state reaction method. The samples were characterized by X-ray Diffractometry (XRD), Scanning Electron Microscopy (SEM) and temperature dependent electrical conductivity measurement. XRD confirmed the presence of spinel phase cubic crystalline as major phase of the as-prepared samples. The lattice parameters and average crystallite sizes of the samples were investigated from the observed XRD patterns. The samples were made into pellets and the temperature dependent dc electrical conductivities were studied by using two-probe method. Electrical conduction mechanism and the activation energy were studied. The obtained electrical conductivity results reveal that the samples (x = 0.0, 0.2 and 0.4) were normal ionic conductors and the sample x = 0.6 was superionic conductor at high temperature.

Keywords: $Ni_{0.6-x}Mg_xCu_{0.2}Zn_{0.2}Fe_2O_4$, solid state reaction, XRD, SEM, conduction mechanism, superionic conductor.

Introduction

Spinels of the type $M^{2+}M_2^{3+}O_4$ attract the research interest because of their versatile practical applications [Iftimie, (2006)]. In the case of M^{3+} = Fe, the resulting spinel ferrites having a general chemical composition of MFe_2O_4 (M = Mg, Ni, Cu, Zn, Mn, Co, Cd, etc.) are widely used as magnetic materials [Kony, (2004)].

The polycrystalline NiMgCuZn soft ferrites are suitable for core materials in microinductor applications. In view of the extensive applications of NiCuZn ferrite [Rajendra, (2014)], it is economical to replace Nickel with Magnesium and achieve desirable properties in NiMgCuZn ferrites. MgCuZn ferrite is a pertinent magnetic material suitable for high-frequency applications owing to its properties like high resistivity, fairly high Curie transition temperature, environmental stability, and low cost [Ramana, (2012)]. In the present work, Magnesium doped Nickel-Copper-Zinc ferrites, $Ni_{0.6-x}Mg_xCu_{0.2}Zn_{0.2}Fe_2O_4$ (where x = 0.0, 0.2, 0.4 and 0.6) were prepared by solid state reaction method and their structural, microstructural and electrical properties were investigated in the temperature range of 303 K – 773 K.

Materials and Method

Preparation of Samples

Magnesium doped Nickel-Copper-Zinc ferrites, $Ni_{0.6-x}Mg_xCu_{0.2}Zn_{0.2}Fe_2O_4$ (where x = 0.0, 0.2, 0.4 and 0.6) were prepared by solid state reaction method. Starting materials of Analytical Reagent (AR) grade Magnesium Oxide (MgO), Nickel Oxide (NiO), Copper Oxide

---

[1] Dr, Assistant Lecturer, Department of Physics, Taungoo University

[2] Dr, Associate Professor, Department of Physics, Loikaw University

[3] Dr, Associate Professor, Department of Physics, Technological University (Dawei)

[4] Dr, Associate Professor, Department of Physics, Pyay University

(CuO), Zinc Oxide (ZnO) and Ferric Oxide (Fe_2O_3) were used to prepare the samples. Then, the starting materials were weighed with desired stoichiometric compositions and mixed each other. The mixed starting materials were heated at 1000°C for 5 h in JLabTech Electric Oven. Figure 1 shows the flow diagram of the sample preparation process.

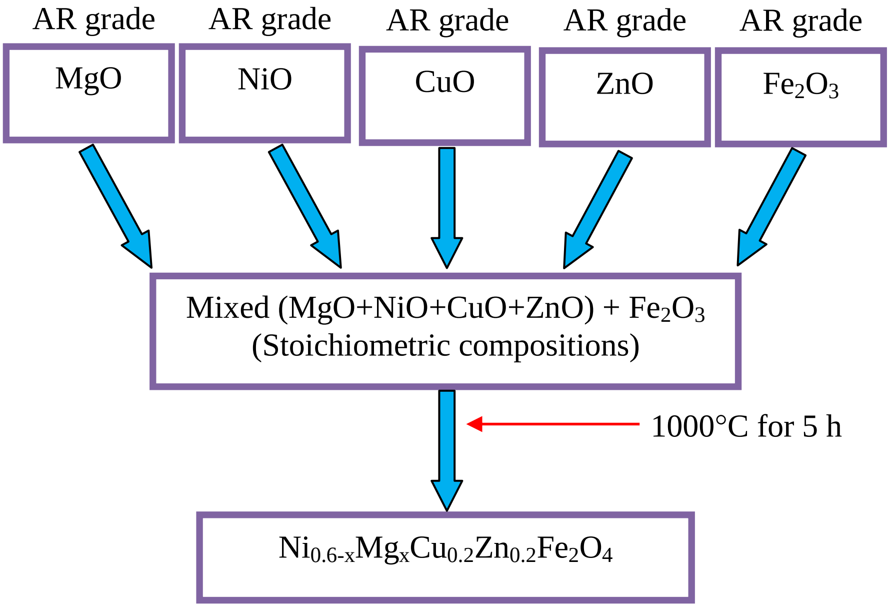

Figure 1 Flow-diagram of the $Ni_{0.6-x}Mg_xCu_{0.2}Zn_{0.2}Fe_2O_4$ sample preparation process

XRD and SEM Measurements

The crystalline phase formation, variation of the lattice parameters and estimation of the crystallite sizes of the Magnesium doped Nickel-Copper-Zinc ferrites, $Ni_{0.6-x}Mg_xCu_{0.2}Zn_{0.2}Fe_2O_4$ (where x = 0.0, 0.2, 0.4 and 0.6) were investigated by PC-controlled RIGAKU MULTIFLEX X-ray Diffractometer [Universities' Research Centre (URC), University of Yangon] using Ni-filter with CuK_α radiation, λ = 1.54056 Å. Microstructural properties of the samples were investigated by using JEOL JSM-5610LV SEM [Universities' Research Centre (URC), University of Yangon] with the accelerating voltage of 15 kV, the beam current of 50 mA and 5500 times of photo magnification.

Temperature Dependent Electrical Resistance Measurement

Firstly, the as-prepared samples were made into pellets by SPECAC hydraulic pellet-maker using 5 ton (~70 MPa). The electrical resistances of the samples were observed by using FLUKE 180 digital multi-meter in the temperature range of 303 K – 773 K by the use of DELTA A SERIES DTA-4896 Temperature Controller. The area and thickness of the pellets were 1.14×10^{-4} m^2 and 5.15 mm respectively. Experimental setup of the electrical conductivity measurement is shown in Figure 2.

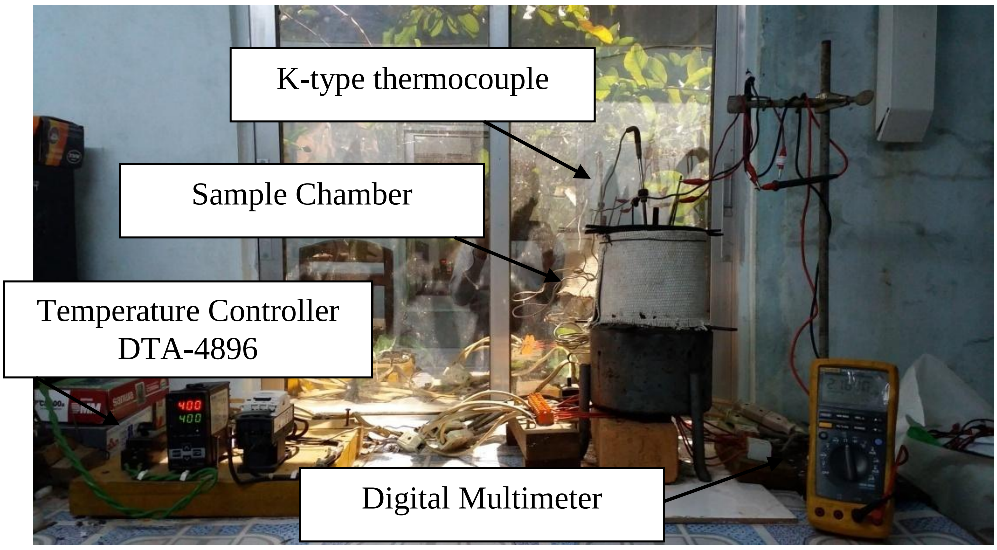

Figure 2 Experimental setup of temperature dependent electrical resistance measurement

Results and Discussion

Structural Investigation

The indexed powder X-ray diffraction patterns of the samples are shown in Figure 3. For phase identification of the samples, the collected diffraction lines were identified by using reference patterns of pure substances or JCPDS data files of (i) Cat. No. 22-1012>Franklinite - syn, $ZnFe_2O_4$, Cat. No. 88-1943>Magnesioferrite - syn, $MgFe_2O_4$, Cat. No. 25-0283> Cuprospinel, $CuFe_2O_4$ and Cat. No. 10-0325>Trevorite - syn, $NiFe_2O_4$ for x = 0.0, 0.2, 0.4 samples and (ii) Cat. No. 22-1012>Franklinite - syn, $ZnFe_2O_4$, Cat. No. 25-0283>Cuprospinel, $CuFe_2O_4$ and Cat. No. 10-0325>Trevorite - syn, $NiFe_2O_4$ for x = 0.6 sample.

XRD patterns show the formation of single phase cubic structure with dominant peak corresponding to (311) reflection indicating that the crystallites are preferentially oriented along (311) plane. The lattice parameters are evaluated by using crystal utility of the equation

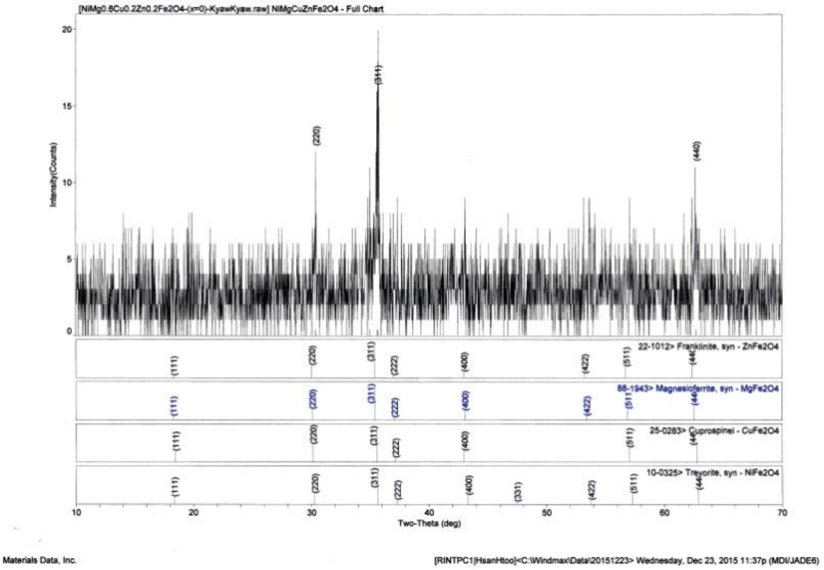

Figure 3 (a) XRD pattern of $Ni_{0.6-x}Mg_xCu_{0.2}Zn_{0.2}Fe_2O_4$ where x = 0.0

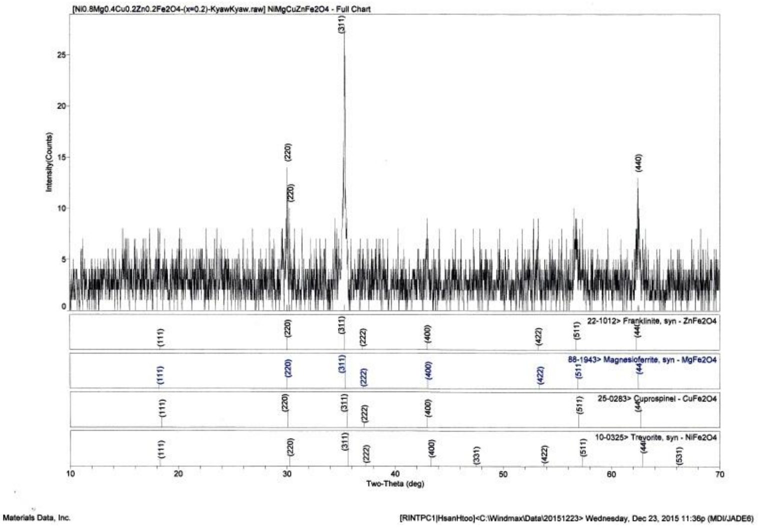

Figure 3(b) XRD pattern of $Ni_{0.6-x}Mg_xCu_{0.2}Zn_{0.2}Fe_2O_4$ where x = 0.2

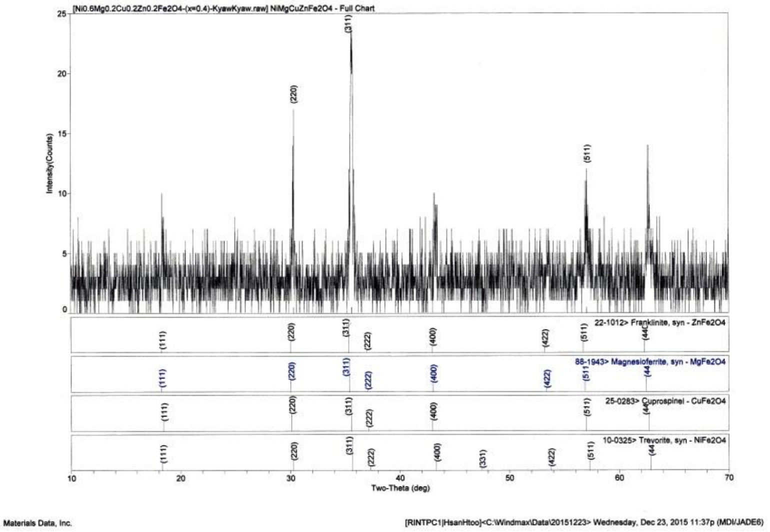

Figure 3(c) XRD pattern of $Ni_{0.6-x}Mg_xCu_{0.2}Zn_{0.2}Fe_2O_4$ where x = 0.4

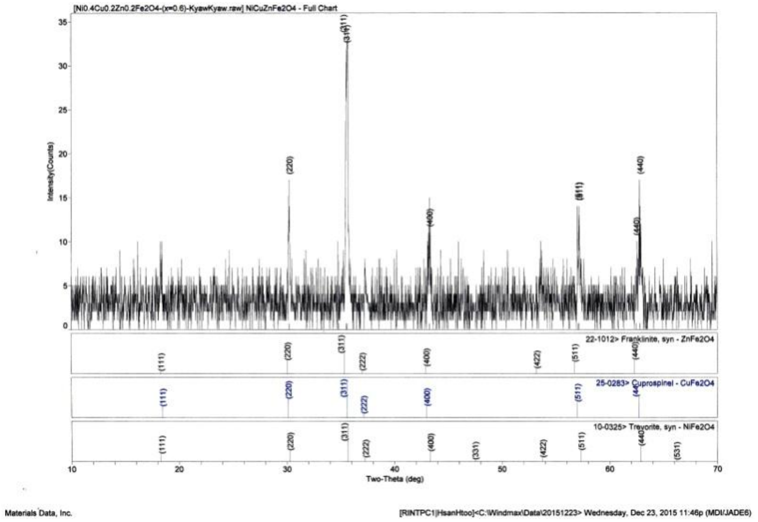

Figure 3(d) XRD pattern of $Ni_{0.6-x}Mg_xCu_{0.2}Zn_{0.2}Fe_2O_4$ where x = 0.6

Table 1 The lattice parameters and crystallite sizes of $Ni_{0.6-x}Mg_xCu_{0.2}Zn_{0.2}Fe_2O_4$

Sample (Contents x of Mg)	Obs. *a*=*b*=*c* (Å)	*D* (nm)
0.0	8.3518	46.54
0.2	8.3907	64.94
0.4	8.3599	45.69
0.6	8.3608	53.04

of $\frac{\sin^2\theta}{(h^2+k^2+l^2)}=\frac{\lambda^2}{4a^2}$ where θ is the diffraction angle (°), (hkl) is the miller indices, λ is the wavelength of incident X-ray (Å) and *a* is the lattice parameter of the samples (Å). The observed lattice parameters are tabulated in Table 1. Figure 4 shows the variation of the lattice parameters with Mg concentration of the samples. The lattice parameters of the samples were found to be alternated with increase in concentration of Mg due to the ionic substitution of Mg^{2+} on Ni^{2+} in the lattice sites. It can be simply explained as follows:

The atomic sites distribution of $Ni_{0.6-x}Mg_xCu_{0.2}Zn_{0.2}Fe_2O_4$ ferrites can be taken as $(Ni_{0.6-x}Cu_{0.2}Zn_{0.2}Fe)[Mg_xCu_{0.2}Zn_{0.2}Fe]O_4$ where the brackets ( ) and [ ] denote A-site and B-site respectively. Such cation distribution is based on the following facts:

(1) Ni^{2+} ions have a strong preference to occupy the A-site while Mg^{2+} ions have a strong preference to occupy the B-site.

(2) As for Mg-ion distribution, it is reported that Ni^{2+} ions strongly prefer to occupy the A-site for low Mg-concentration. However, for high Mg-concentration, it is suggested that the Ni^{2+} ions are either distributed between A-site and B-site or reside at the grain boundaries. Thus, according to the assumed cation distribution, increasing of the Mg-concentration from x = 0.1 to x = 0.3 leads Fe^{3+} content in A-site to decrease and that in B-site to increase.

Ramana, M.V. et al (2012) has reported that the lattice parameters of the $Ni_{0.6-x}Mg_xCu_{0.1}Zn_{0.3}Fe_2O_4$ (for x = 0.0, 0.1 and 0.2) ferrites are 8.36 Å, 8.38 Å and 8.35 Å respectively. Thus, in this work, the obtained lattice parameters are acceptable due to the agreement with the results of Ramana, M.V. et al (2012).

The crystallite sizes of the samples were estimated by using the Scherrer formula, $D=\frac{0.9\lambda}{B\cos\theta}$ where D is the crystallite size (nm), λ is the wavelength of incident X-ray (Å), θ is the diffraction angle of the peak under consideration at FWHM (°) and B is the observed FWHM (radians). The breadth of the Bragg peak is a combination of both instrument and sample dependent effects. To decouple these contributions, it is necessary to collect a diffraction pattern from the line broadening of a standard material such as silicon to determine the instrumental broadening. In this work, the instrumental effects on the breadth of the Bragg peak neglected. In the present work, the average crystallite sizes of the samples are also presented in Table 1. The obtained crystallite sizes are 46.54 nm for x = 0.0, 64.94 nm for x = 0.2, 45.69 nm for x = 0.4 and 53.04 nm for x = 0.6 respectively. It indicates the nanosized Cu-Mg ferrites materials. The variation of the crystallite sizes with Mg concentration of $Ni_{0.6-x}Mg_xCu_{0.2}Zn_{0.2}Fe_2O_4$ (for x = 0.0, 0.2, 0.4 and 0.6) ferrites is shown in Figure 4.

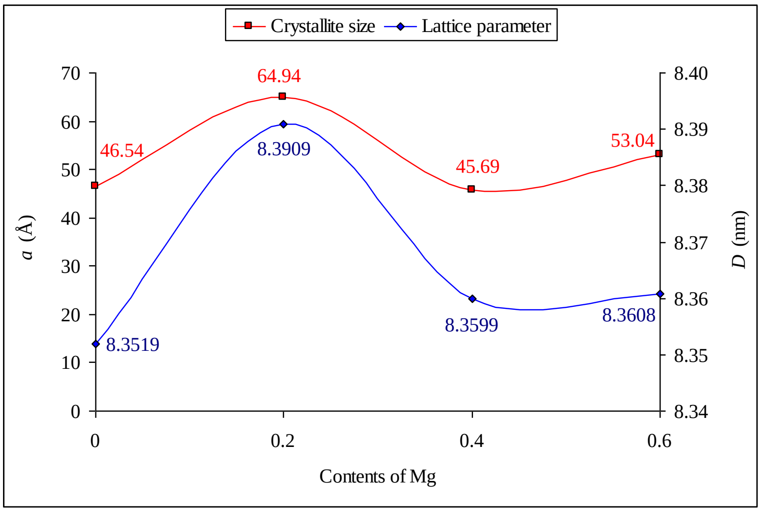

Figure 4 Variation of the lattice parameters and crystallite sizes with Mg concentration of $Ni_{0.6-x}Mg_xCu_{0.2}Zn_{0.2}Fe_2O_4$

SEM Analysis

Scanning Electron Microscopy (SEM) was employed for microstructural characteristics of $Ni_{0.6-x}Mg_xCu_{0.2}Zn_{0.2}Fe_2O_4$ (for x = 0.0, 0.2, 0.4 and 0.6) powders. Figure 5 shows the SEM micrographs of the samples.

As shown in observed SEM micrographs, generally, morphological features of the samples are spherical shape of different grain sizes. The grain sizes varied with the concentration of Mg^{2+} on NiCuZn ferrite.

In Figure 5(a), the grain sizes of the samples are in the range of 0.40 µm – 1.80 µm. Most of the grains are found to be non-homogeneous and some of the grains are composed of agglomerated particles. The area of the pores (porosity) is about 10% of the image.

As shown in Figure 5(b), the grain sizes of the samples are obtained as in the range of 0.20 µm – 0.50 µm. Some of the grains are agglomerated particles with poor grain boundary. The pore area is about 15% of the image.

In Figure 5(c), the grain sizes are in the range of 0.20 µm – 0.40 µm and thus the sample is the most homogeneous in the investigated samples. The pore area is about 5% of the image and it is the smallest area of pores with poor grain boundary of the sample.

In Figure 5(d), the grain sizes are 0.25 µm – 0.50 µm range. Most of the defects or the largest area of pores is found in the sample and it is about 40% area of the image. In this image, the grain boundary is also poor. The grain sizes of the samples are listed in Table 2.

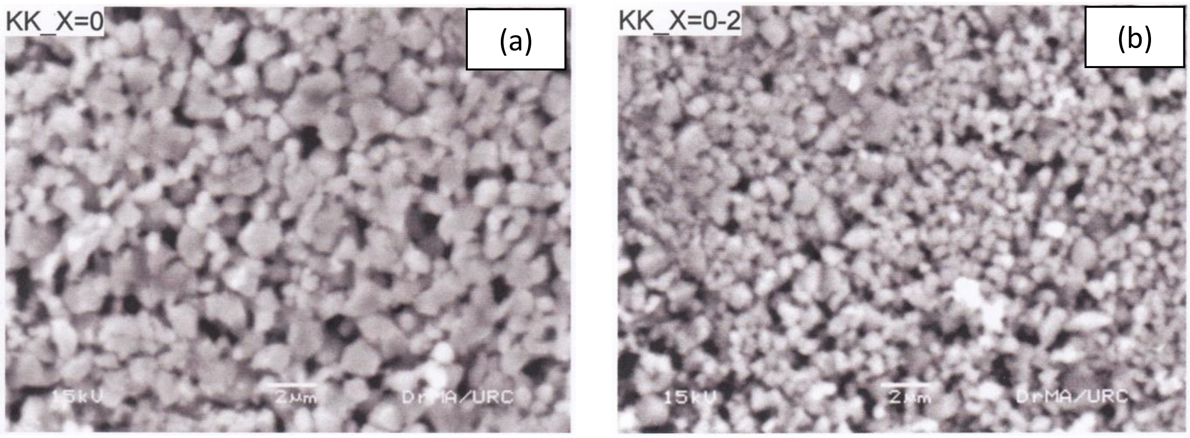

Figure 5. SEM micrographs of $Ni_{0.6-x}Mg_xCu_{0.2}Zn_{0.2}Fe_2O_4$ where (a) x = 0.0 and (b) x = 0.2

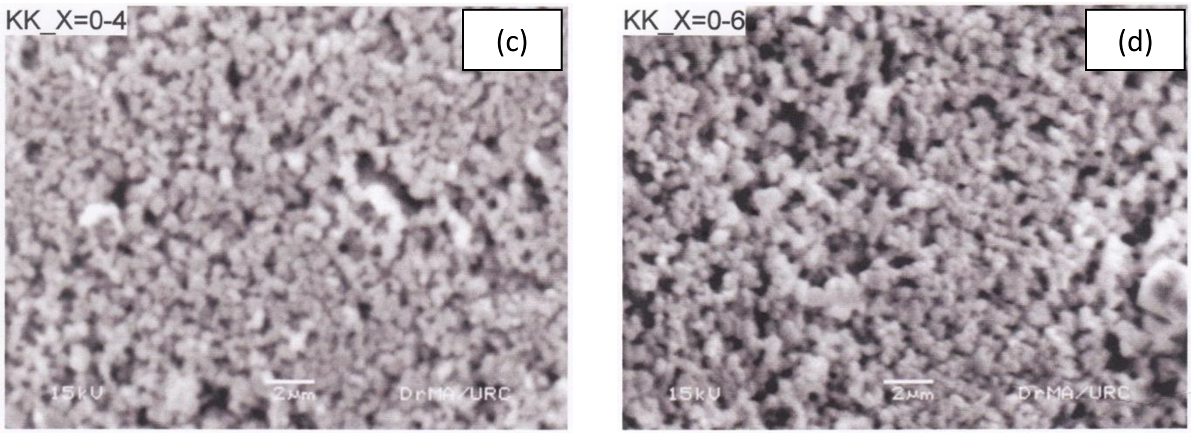

Figure 5 SEM micrographs of $Ni_{0.6-x}Mg_xCu_{0.2}Zn_{0.2}Fe_2O_4$ where (c) x = 0.4 and (d) x = 0.6

Table 2 Grain sizes of the $Ni_{0.6-x}Mg_xCu_{0.2}Zn_{0.2}Fe_2O_4$

Sample (Contents x of Mg)	Grain sizes (μm)
0.0	0.40 – 1.80
0.2	0.20 – 0.50
0.4	0.20 – 0.40
0.6	0.25 – 0.50

Temperature Dependence Electrical Conductivity Study

The superionic conductivity of the materials plays an important role in the class of solid electrolytes. Most of the spinel based compounds are well-known superionic conductors. The samples are cubic structures at room temperature. Since, the substances have been found to be characterized by a higher conductivity (10^{-5} - 10^{-4} S cm^{-1}) in the high temperatures due to the ionic motion caused by ionic-bond disorder (so called fast ionic conductors or superionic conductors).

Electrical conductivity of a ceramic with temperature obeys an Arrhenius expression $\sigma=\sigma_0 \exp(-E_a/kT)$, where σ is the conductivity, σ_0 is the pre-exponential factor, E_a is the activation energy for ionic conduction, k is the Boltzmann constant and T is the absolute temperature. In the present work, Arrhenius plots of the variation of dc electrical conductivity of the $Ni_{0.6-x}Mg_xCu_{0.2}Zn_{0.2}Fe_2O_4$ (for x = 0.0, 0.2, 0.4 and 0.6) samples are shown in Figure 6.

According to the theory of ionic conductivity, the slopes of the electrical conductivity in each of the ln σ vs. 1000/T graph, e.g., in Figure 6(a) (for x=0.0 or $Ni_{0.6}Cu_{0.2}Zn_{0.2}Fe_2O_4$),

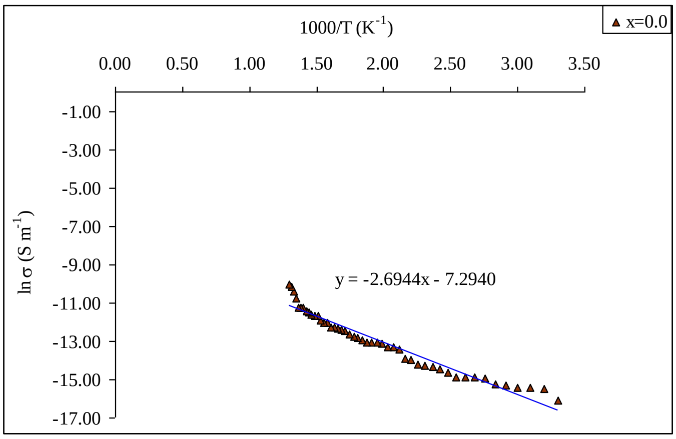

Figure 6 (a) Arrhenius plot of the ln σ versus 1000/T graph of the $Ni_{0.6-x}Mg_xCu_{0.2}Zn_{0.2}Fe_2O_4$ where x = 0.0

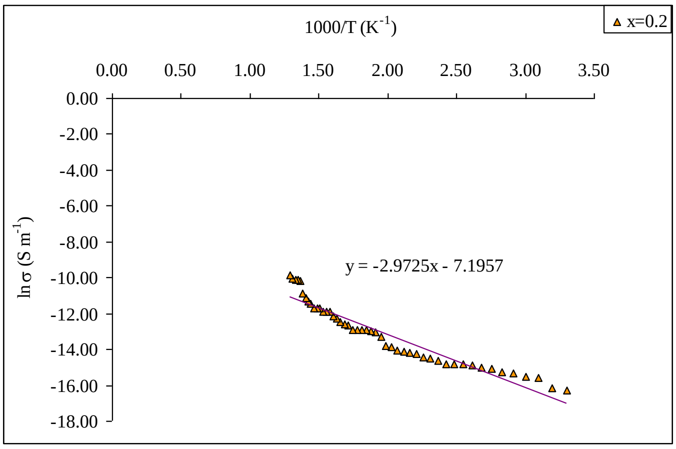

Figure 6(b) Arrhenius plot of the ln σ versus 1000/T graph of the $Ni_{0.6-x}Mg_xCu_{0.2}Zn_{0.2}Fe_2O_4$ where x = 0.2

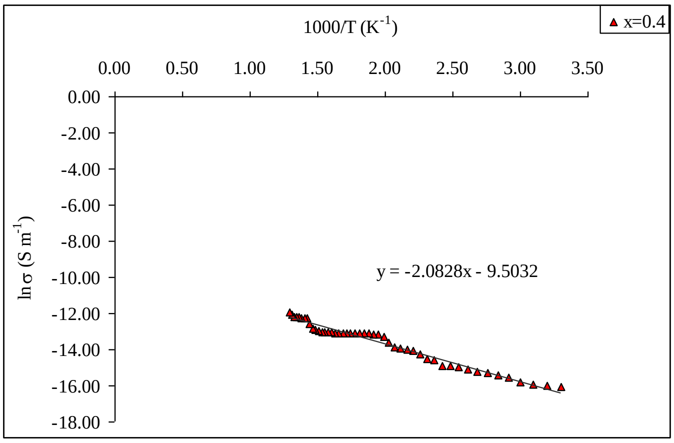

Figure 6 (c) Arrhenius plot of the ln σ versus 1000/T graph of the $Ni_{0.6-x}Mg_xCu_{0.2}Zn_{0.2}Fe_2O_4$ where x = 0.4

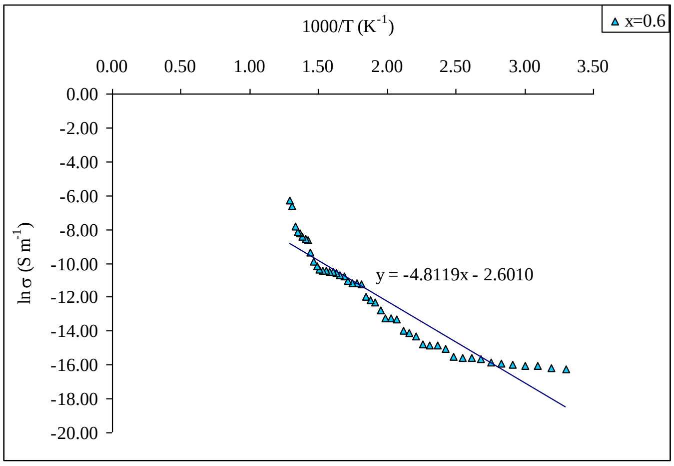

Figure 6 (d) Arrhenius plot of the ln σ versus 1000/T graph of the $Ni_{0.6-x}Mg_xCu_{0.2}Zn_{0.2}Fe_2O_4$ where x = 0.6

corresponding to the activation energy for creating of defect states due to the ionic motions of the sample. The electrical conductivity (σ) of the sample can be written in the form:

$$\sigma = \sigma_0 \exp(-E_a / kT)$$
$$\ln(\sigma) = -E_a / kT + \ln \sigma_0$$
$$= (-E_a / k)(1/T) + \ln \sigma_0$$

From Figure 6(a), the activation energy E_a can be obtained by using the slope of the ln σ versus 1000/T graph.

$E_a/k = 2.6944 \times 1000$

$E_a = 2.6944 \times 1000 \times k$

$E_a = 2.6944 \times 1000 \times 1.38 \times 10^{-23}$

$E_a = 3.7183 \times 10^{-20}$ J

$E_a = 0.2324$ eV

As shown in figures, the electrical conductivity of the samples increased with increase in temperature. The activation energies of the samples are listed in Table 3.

In general, for the ferrite samples, the activation energy is often associated with the variation of mobility of charge carriers rather than with their concentration. The charge carriers are considered as residing at the vacant sites and conduction occurs via a hopping process which depends upon the activation energy. Due to addition of Mg^{2+} inter ionic distance increase which enhances the barrier height encountered by the charge carriers during the hopping process and consequently, it enhances the activation energy.

Table 3 Slopes of ln σ vs. 1000/T graphs and the activation energies of the $Ni_{0.6-x}Mg_xCu_{0.2}Zn_{0.2}Fe_2O_4$

Sample (Contents x of Mg)	Slope of ln σ vs. 1000/T graph	Activation energy (eV)
0.0	2.6944	0.2324
0.2	2.9725	0.2564
0.4	2.0828	0.1796
0.6	4.8119	0.4150

According to literature of electrical conductivity, the electrical conductivity of a solid is $\sigma \geq 10^{-3}$ S m^{-1}, the sample is known as the solid electrolyte material or superionic conductor or fast ion conductor. From the observed experimental data of electrical conductivity measurements, the (x = 0.0, 0.2 and 0.4) samples are normal ionic conductors and the sample x = 0.6 is a superionic conductor at high temperature due to its electrical conductivity is 1.33×10^{-3} S m^{-1} at 763 K. The ln σ vs 1000/T curves of the samples indicate the charge carrier density which are generated as a consequence of thermal activated process of lattice defects, is increased up to end point temperature by increasing the concentration of the Mg^{2+}.

Conclusion

Magnesium doped Nickel-Copper-Zinc ferrites, $Ni_{0.6-x}Mg_xCu_{0.2}Zn_{0.2}Fe_2O_4$ (where x = 0.0, 0.2, 0.4 and 0.6) were successfully prepared by solid state reaction method. The as-prepared samples were characterized by XRD and SEM to study the effect of dopant concentration of Mg^{2+} structural and microstructural characteristics of Ni-Cu-Zn ferrites. The X-ray diffraction confirmed the presence of spinel type cubic crystalline as major phase of the as-prepared samples. The lattice parameters were found to be alternated with the increase in concentration of Mg. The crystallite sizes were estimated by using the Scherrer formula and nanosized ferrite crystallites of the samples were obtained and these were also alternated. From the SEM micrographs, the grain shapes of the samples are found to be spherical with non-uniform grain sizes. Most of the pores are appeared with different sizes of area. The grain sizes of the samples varied with the dopant concentration of Mg^{2+}. The grain size of the undoped material was found to be the largest one among the investigated samples. From the temperature dependence electrical conductivities results, the samples x = 0.0, 0.2 and 0.4 were normal ionic conductors and x = 0.6 sample was superionic conductor at the high temperature. Thus, the x = 0.6 sample can be used as the solid electrolyte material.

Acknowledgements

The authors would like to acknowledge Professor Dr Khin Khin Win, Head of Department of Physics, University of Yangon, for her valuable suggestion and comments for this work. I would like to thank Professor Dr Nge Nge Khaing, Head of Department of Physics, Taungoo University, for her kind permission to carry out this work.

References

Iftimie, N., Rezlescu, E., Popa, P.D. & Rezlescu, E. (2006) Gas sensitivity nanocrystalline nickel ferrite. JOURNAL OF OPTOELECTRONICS AND ADVANCED MATERIALS, 8(3), 1016-1018.

Kony, D.E. (2004). Dielectric Relaxation in Al - Substituted Ni - Cd Spinel Ferrites. Egypt Journal of Solids, 27, 285-296.

Rajendra, R., Pushpinder, B. & Rajlakshmi, N. (2014). Structural and Electrical Properties of Titanium Substituted Ni-Cu-Zn Ferrites. International Journal of Chemical and Physical Sciences, 3, 132-138.

Ramana, M.V., Reddy, N.R. & Kumar, K.V.S. (2012). Influence of Magnesium Substitution on Thermal and Electrical Properties of NiCuZn Ferrites for Microinductor Core Applications. Physics Research International, 10, 1-8.

J. Myanmar Acad. Arts Sci. 2020 **Vol. XVIII.No.2C**

STUDY ON STRUCTURAL, MICROSTRUCTURAL AND VIBRATIONAL CHARACTERISTICS OF NANOSIZED COBALT-ZINC ALUMINATES

Phyo Phyo Thida Aung[1], Aye Aye Lwin[2] and Win Kyaw[3]

Abstract

Nanosized Cobalt-Zinc Aluminates with the formula $Co_{1-x}Zn_xAl_2O_4$ (where x = 0.00, 0.25, 0.50, 0.75 and 1.00) were prepared by solid state reaction method by using Analytical Reagent (AR) grade CoO, ZnO and Al_2O_3. Structural, microstructural and vibrational characteristics of the samples were studied by XRD, SEM and FTIR spectroscopy. XRD patterns showed all characteristic peaks of the spinel structure and confirmed the phase formation indicating the absence the others impurity phases. The observed peaks perfectly matched with the crystalline phase of cubic spinel structure with the identification of satndard JCPDS. The crystallite sizes were estimated by using Debye-Scherrer's formula to examine the nanosized aluminates materials. SEM micrographs showed that the samples were cauliflower shapes and composed of agglomerated particles with poor grain boundary. FTIR spectra indicated that the stretching vibrations of divalent cations (ν_1-mode) and trivalent cations (ν_2-mode) of the samples. These two modes indicated that the vibrational characteristics of $Co_{1-x}Zn_xAl_2O_4$.

Keywords: $Co_{1-x}Zn_xAl_2O_4$, XRD, SEM, FTIR, cubic spinel.

Introduction

Numerous researches have shown that a characteristic of solid-state gas sensors is the reversible interaction of the gas with the surface of a solid-state material [Akbar, (2006)]. In addition to the conductivity change of gas-sensing material, the detection of this reaction can be performed by measuring the change of capacitance, work function, mass, optical characteristics or reaction energy released by the gas/solid interaction [Buchholt, (2011)].

Aluminates are chemical compounds consisting of ceramic materials based upon Aluminium Oxide as principal component. The materials based on the aluminates are potential candidates for modern technological applications due to their unique potential application in high density magnetic recording, microwave devices, magnetic fluids, heterogeneous catalysis and absorbent materials [Deraz, (2013)]. Spinel structure oxides constitute one of the most interesting classes of advanced ceramic materials due their intrinsic physical and chemical properties [Deraz, & Fouda, (2013)]. Among the spinel oxides, Cobalt Aluminate ($CoAl_2O_4$) and Zinc aluminates ($ZnAl_2O_4$) possess interesting properties for technological application [Ummartyotin, (2009)]. Specifically, Cobalt Aluminate ($CoAl_2O_4$) possesses important applications in various fields such as humidity sensor, gases sensor, catalyst in the oxidation reaction of benzyl alcohol, thermoelectric properties, photocatalyst for degradating the pollutants in aqueous solution, solar absorber, oxygen carrier in chemical-looping combustion and optical and dielectric properties [Abaide, (2015)].

$ZnAl_2O_4$ is a spinel type oxide, which have high chemical and thermal stability, high mechanical resistance and low surface acidity, being suitable for a wide range of applications, such as optical coating or host matrix, high temperature ceramic material, catalyst and catalyst

---

[1] PhD Candidate, Assistant Lecturer, Department of Physics, Taungoo University

[2] Dr, Associate Professor, Department of Physics, Loikaw University

[3] Dr, Associate Professor, Department of Physics, Pyay University

support [Battiston, (2014)]. The aim of this work was to prepare **C**obalt-Zinc Aluminates, $Co_{1-x}Zn_xAl_2O_4$ by solid state reaction method and their structural, microstructural and vibrational characteristics were reported by using XRD, SEM and FTIR spectroscopy.

Experimental Details

Preparation of Cobalt-Zinc Aluminates

Cobalt-Zinc Aluminates, $Co_{1-x}Zn_xAl_2O_4$ (where x = 0.00, 0.25, 0.50, 0.75 and 1.00) were prepared by solid state reaction method. Analytical Reagent (AR) grade Cobalt Oxide (CoO), Zinc Oxide (ZnO) and Aluminium Oxide (Al_2O_3) were used as the raw materials. The starting materials were weighed with desired stoichiometric compositions and mixed. The mixed powders were pre-heated at 950°C for 5 h and followed heated at 1100°C for 5 h in JLab Tech Electric Oven. Flow diagram of the sample preparation procedure is shown in Figure 1.

XRD, SEM and FTIR Measurements

X-ray diffraction (XRD) patterns of the samples were observed by PC-controlled RIGAKU MULTIFLEX X-ray Diffractometer [Universities' Research Centre (URC), University of Yangon] in the diffraction angle range of 10° – 70° using CuK_α radiation with Ni filter at 40 kV and 40 mA.

Microstructural characteristics of the samples were investigated by using JCM-6000Plus SEM [Department of Physics, West Yangon University] with the accelerating voltage of 15 kV and 5000 – 6000 times of photo magnifications.

FTIR transmission spectra of the samples with Potassium Bromide, KBr pellet were observed by PC-controlled SHIMADZU FTIR-8400 Spectrophotometer [Universities' Research Centre (URC), University of Yangon] at room temperature.

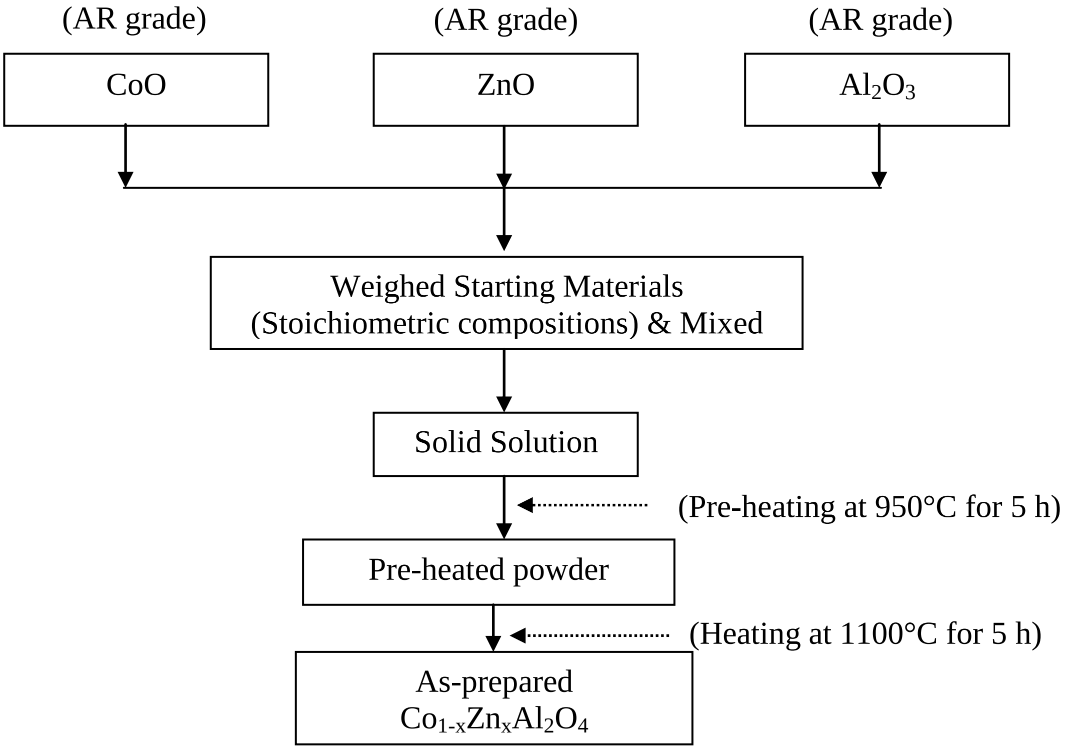

Figure 1 Preparation procedure of $Co_{1-x}Zn_xAl_2O_4$

Results and Discussion

Structural Analysis

Powder X-ray diffraction patterns of the samples are shown in Figure 2. The observed XRD lines were identified by using standard JCPDS (Joint Committee on Powder Diffraction Standards) data library files of Cat. No. 82-2252> Spinel – $CoAl_2O_4$ and Cat. No. 74-1138> Gahnite magnesian – $ZnAl_2O_4$. The patterns show all characteristic peaks of spinel structure and confirms the phase formation indicating the absence the others impurity phases. The observed peaks perfectly match with the crystalline phase of cubic spinel structure of spinel (JCPDS data library files: Cat. No. 82-2252 and Cat. No. 74-1138). As shown in the observed XRD patterns, the observed XRD lines are found to be agreed with standard JCPDS. It indicates that the appearance of the diffraction peaks demonstrate the single-phase spinel type cubic crystalline $Co_{1-x}Zn_xAl_2O_4$. The diffraction line of (331) plane (*) indicates the diffraction line of $ZnAl_2O_4$ and it appears at the Zn contents x = 0.50, 0.75 and 1.00.

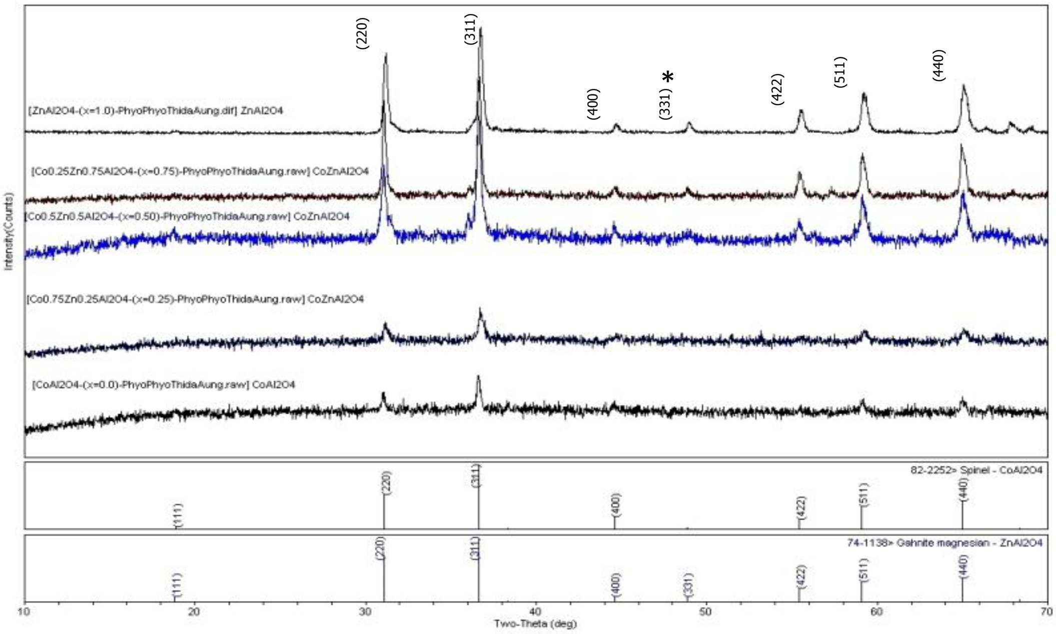

Figure 2 XRD patterns of $Co_{1-x}Zn_xAl_2O_4$

The lattice parameters are evaluated by using crystal utility of the equation $\frac{\sin^2\theta}{(h^2+k^2+l^2)}=\frac{\lambda^2}{4a^2}$, where "(hkl)" is the Miller indices, "λ' is the wavelength of incident X-ray (Å), "θ" is the diffraction angle of the peak (°) and "*a*" is the lattice parameter (Å).

The crystallite sizes of each of the samples were estimated by using Debye-Scherrer's formula, $D=\frac{0.9\lambda}{B\cos\theta}$, where "*D*" is the crystallite size (nm), "λ' is the wavelength of incident X-ray (Å), "θ" is the diffraction angle of the peak under consideration at FWHM (°) and "B" is the observed FWHM (radians). The experimental results of the calculated average lattice parameters, the observed lattice parameters and the crystallite sizes are tabulated in Table 1. It is seen that the crystallite sizes of the samples are nanosized crystalline materials.

Table 1 The lattice parameters and crystallite sizes of $Co_{1-x}Zn_xAl_2O_4$ samples

Sample (Contents x of Zn)	Obs. *a=b=c* (Å)	Cal. *a=b=c* (Å)	*D* (nm)
0.00	8.1404	8.1453	54.20
0.25	8.0879	8.0893	58.35
0.50	8.1122	8.1121	52.09
0.75	8.0880	8.0915	29.15
1.00	8.1064	8.1012	33.74

Microstructural Analysis

SEM micrographs of the samples are shown in Figure 3. Except the x = 1.00 sample, the observed SEM images of the samples generally reveal that the spherical shapes with poor grain boundary. As shown in SEM images of $Co_{1-x}Zn_xAl_2O_4$ (where x = 0.00, 0.25, 0.50, 0.75 and 1.00) samples, a large grain composed of many small grains of nearly spherical. The images show that the powder samples are composed of agglomerated particles. In each of the image, some pores formed due to the heat-treatment of the starting materials in the sample preparation process. The grain sizes of the samples are evaluated by the use of (equal bar code) same scale in length of corresponding representative bar of 5 μm. In this work, the obtained grain sizes are tabulated in Table 2. In these images of mixed aluminates samples, some pores were also found and they are larger area than pure aluminates samples. The pores serve as adsorption sites due to the heat-treatment of starting materials in the preparation of desired materials. Furthermore, it was found that the shape of the samples varied from the cauliflower to poly-face with the concentration of Zn^{2+} on $Co_{1-x}Zn_xAl_2O_4$ sample.

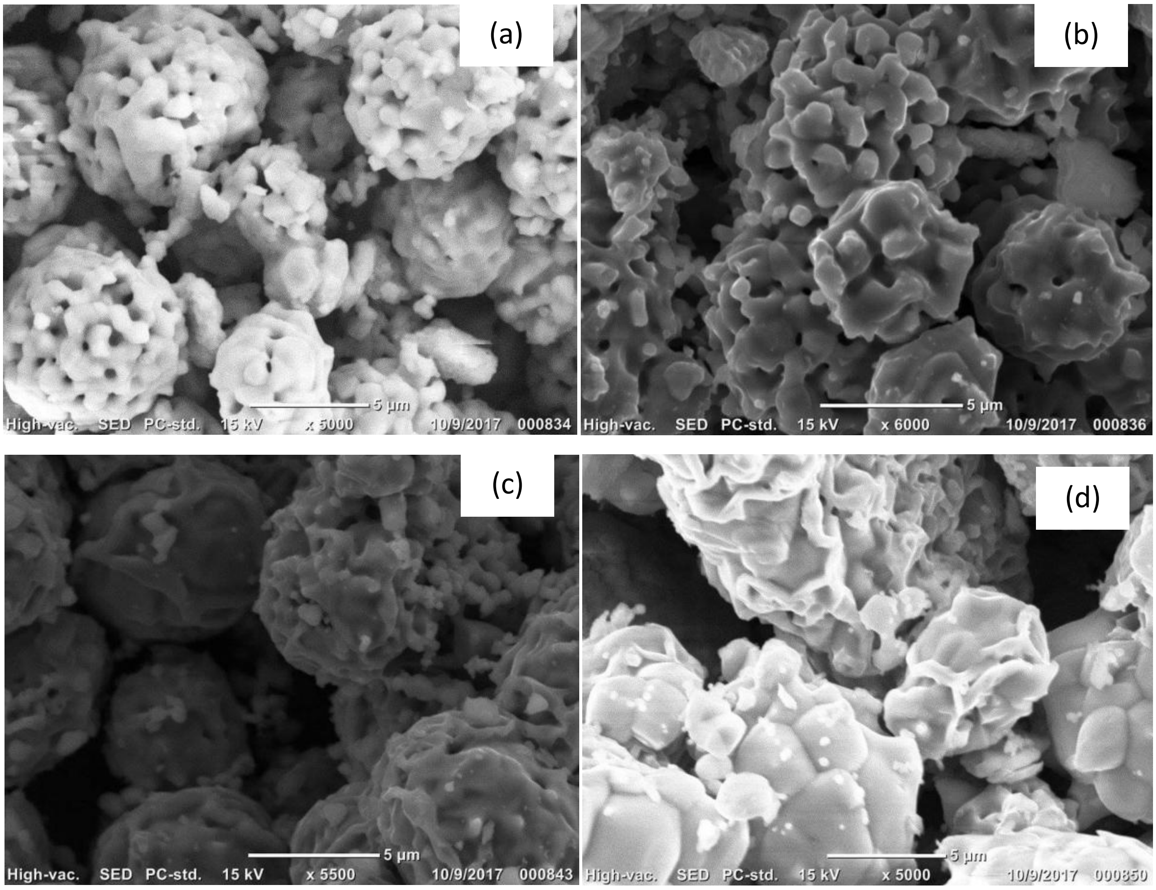

Figure 3 SEM micrographs of $Co_{1-x}Zn_xAl_2O_4$ where (a) x = 0.00, (b) x = 0.25, (c) x = 0.50 and (d) x = 0.75

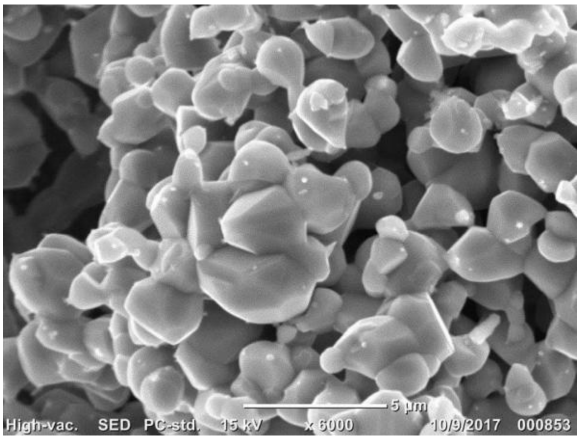

Figure 3(e) SEM micrograph of $Co_{1-x}Zn_xAl_2O_4$ where x = 1.00

Table 2 The grain sizes of $Co_{1-x}Zn_xAl_2O_4$ samples

Sample (Contents x of Zn)	Grain size (µm)
0.00	0.42 – 1.00
0.25	0.25 – 1.20
0.50	0.22 – 1.50
0.75	0.45 – 3.10
1.00	0.50 – 2.50

Vibrational Analysis

Spinels are generally formulated as AB_2X_4 that formally consider the structure as consisting of isolated ion of B and isolated AX_4 molecules. The spinel structure is cubic with eight molecules in the unit cell (Z = 8), and has the B atoms on octahedral sites D_{3d} symmetry, and the A atoms on tetrahedral sites of T_d symmetry. The oxygen atoms occupy C_{3v} sites. The coordination polyhedron around B is a regular octahedron. The vibrational frequencies of a molecule may be varied with the crystalline environments. Sometime the vibrational frequencies of octahedral site (B-atoms) and tetrahedral site (A-atoms) molecules are assigned as υ_2-mode and υ_1-mode respectively. These two modes are stretching vibrations of spinel type samples.

The standard vibrational frequencies (wavenumbers) of $CoAl_2O_4$ are mainly 658 cm^{-1} for A atoms on tetrahedral sites (assigned as υ_1-mode) and 494 cm^{-1} and 574 cm^{-1} for B atoms on octahedral sites (assigned as υ_2-mode). Vibrational frequencies of $ZnAl_2O_4$ are mainly appeared at 667 cm^{-1} for A atoms on tetrahedral sites (assigned as υ_1-mode) and 562 cm^{-1} and 510 cm^{-1} for B atoms on octahedral sites (assigned as υ_2-mode). In this work, FTIR transmission spectra of the samples are shown in Figure 4. In this Figure, the shifting of wavenumbers indicates with ellipses. These bands are clearly indicated that the increasing concentrations of $ZnAl_2O_4$ on $CoAl_2O_4$.

The observed absorption lines and corresponding vibrational characteristics of constituent molecules are identified by using standard wavenumbers of $CoAl_2O_4$ and $ZnAl_2O_4$. The detail assignments of observed wavenumbers and corresponding molecular vibrations are tabulated in Table 3. Furthermore, the observed spectral lines in the observed FTIR spectra corresponding to the optical properties of wavelength, frequency, oscillation time and energy of are also listed in Table 3.

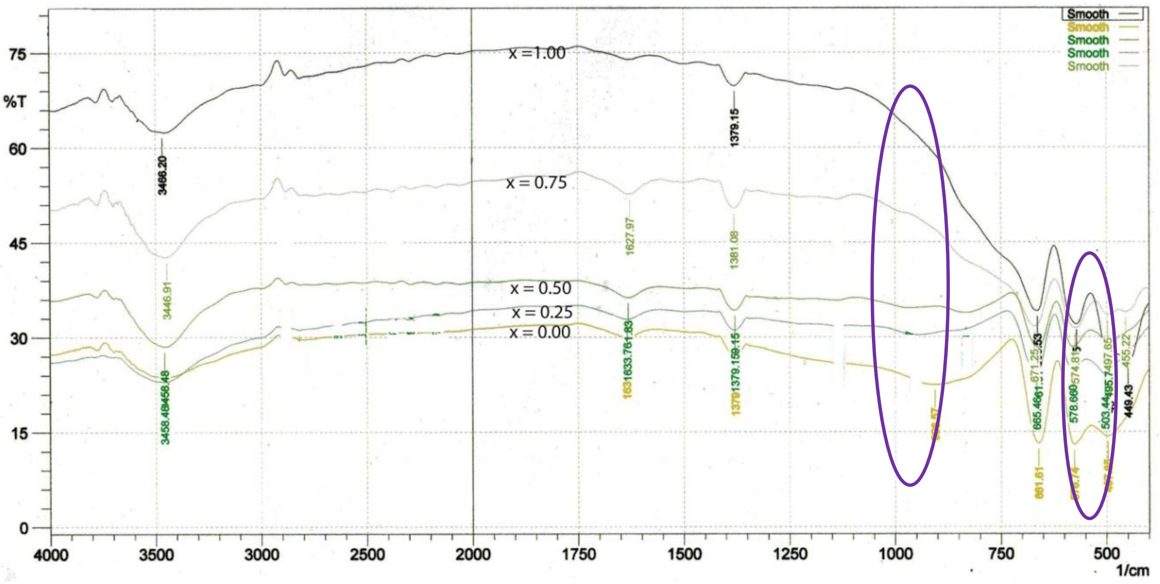

Figure 4 FTIR transmission spectra of $Co_{1-x}Zn_xAl_2O_4$

Table 3 (a)Vibrational properties of wavelength, frequency, oscillation time and energy of the $Co_{1-x}Zn_xAl_2O_4$ (where x = 0.00)

Wavenumber $\bar{\nu}$ **(cm^{-1})**	**Wavelength λ (nm)**	**Frequency υ (Hz)**	**Oscillation time τ (s)**	**Energy E (eV)**
498 (υ_2-mode)	20080	1.493E+13	6.698E-14	0.0618
577 (υ_2-mode)	17331	1.730E+13	5.781E-14	0.0716
662 (υ_1-mode)	15106	1.985E+13	5.039E-14	0.0822
907 (Com:)	11025	2.719E+13	3.678E-14	0.1126
1379 (Com:)	7252	4.134E+13	2.419E-14	0.1712

Table 3(b) Vibrational properties of wavelength, frequency, oscillation time and energy of the $Co_{1-x}Zn_xAl_2O_4$ (where x = 0.25)

Wavenumber $\bar{\nu}$ **(cm^{-1})**	**Wavelength λ (nm)**	**Frequency υ (Hz)**	**Oscillation time τ (s)**	**Energy E (eV)**
496 (υ_2-mode)	20161	1.487E+13	6.725E-14	0.0616
581 (υ_2-mode)	17212	1.742E+13	5.741E-14	0.0721
662 (υ_1-mode)	15106	1.985E+13	5.039E-14	0.0822
833 (Com:)	12005	2.497E+13	4.004E-14	0.1034
1379 (Com:)	7252	4.134E+13	2.419E-14	0.1712

Table 3(c) Vibrational properties of wavelength, frequency, oscillation time and energy of the $Co_{1-x}Zn_xAl_2O_4$ (where x = 0.50)

Wavenumber $\bar{\nu}$ **(cm^{-1})**	**Wavelength λ (nm)**	**Frequency υ (Hz)**	**Oscillation time τ (s)**	**Energy E (eV)**
503 (υ_2-mode)	19881	1.508E+13	6.632E-14	0.0624
579 (υ_2-mode)	17271	1.736E+13	5.761E-14	0.0719
665 (υ_1-mode)	15038	1.994E+13	5.016E-14	0.0825
1379 (Com:)	7252	4.134E+13	2.419E-14	0.1712

Table 3(d) Vibrational properties of wavelength, frequency, oscillation time and energy of the $Co_{1-x}Zn_xAl_2O_4$ (where x = 0.75)

Wavenumber $\bar{\nu}$ (cm^{-1})	Wavelength λ (nm)	Frequency υ (Hz)	Oscillation time τ (s)	Energy E (eV)
455 (υ_2-mode)	21978	1.364E+13	7.331E-14	0.0565
498 (υ_2-mode)	20080	1.493E+13	6.698E-14	0.0618
575 (υ_1-mode)	17391	1.724E+13	5.801E-14	0.0714
671 (υ_1-mode)	14903	2.012E+13	4.971E-14	0.0833
1381 (Com:)	7241	4.140E+13	2.415E-14	0.1714

Table 3(e) Vibrational properties of wavelength, frequency, oscillation time and energy of the $Co_{1-x}Zn_xAl_2O_4$ (where x = 1.00)

Wavenumber $\bar{\nu}$ (cm^{-1})	Wavelength λ (nm)	Frequency υ (Hz)	Oscillation time τ (s)	Energy E (eV)
449 (υ_2-mode)	22272	1.346E+13	7.429E-14	0.0557
492 (υ_2-mode)	20325	1.475E+13	6.780E-14	0.0611
571 (υ_1-mode)	17513	1.712E+13	5.842E-14	0.0709
664 (υ_1-mode)	15060	1.991E+13	5.024E-14	0.0824
1379 (Com:)	7252	4.134E+13	2.419E-14	0.1712

As shown in FTIR spectra, except the $ZnAl_2O_4$ or x = 1.00 sample, the band observed in the wavenumber range of about 1628 cm^{-1} – 1636 cm^{-1} indicates the bending vibration of H_2O molecules. Also the band observed in the wavenumber range of about 3447 cm^{-1} – 1466 cm^{-1} indicates the anti-symmetric stretching vibration of H_2O molecules. These bands are often appeared in the FTIR transmission spectra of KBr pellet method due to the distribution of humidity around the FTIR spectrophotometer.

Conclusion

Cobalt-Zinc Aluminates, $Co_{1-x}Zn_xAl_2O_4$ (where x = 0.00, 0.25, 0.50, 0.75 and 1.00) samples were successfully prepared by solid state reaction method. Structural, microstructural and vibrational characteristics were studied by XRD, SEM and FTIR spectroscopy. XRD patterns showed all characteristic peaks of the spinel structure and confirmed the phase formation indicating the absence the others impurity phases. The observed peaks perfectly matched with the crystalline phase of cubic spinel structure with the identification of satndard JCPDS. From the SEM micrographs, except the x = 1.00 sample, the grains shapes of others samples were spherical in shape and some particles were found as agglomerated with poor grain boundary. The pores serve as adsorption sites due to the heat-treatment of starting materials in the preparation of desired materials. The grain sizes were varied with the concentration of Zn. It can be said that the lattice substitution of Zn^{2+} on Co^{2+} in the samples. The grains were found to be gray colour and similar shapes (spherical and poly-face blocks). It indicates that the candidate materials are taken as the single phase and the results well confirmed from the XRD results. FTIR spectra showed that the vibrational characteristics of stretching vibrations of tetrahedral sites (A atoms, assigned as υ_1-mode) and octahedral sites (B atoms, assigned as υ_2-mode) of the AB_2X_4 [$Co_{1-x}Zn_xAl_2O_4$ sample] and their combination bands. It indicates that the candidate materials are taken as the single phase and the results well confirmed with structural phase identification of XRD results.

Acknowledgements

The authors would like to acknowledge Professor Dr Khin Khin Win, Head of Department of Physics, University of Yangon, for her valuable suggestion and comments for this work. I would like to thank Professor Dr Nge Nge Khaing, Head of Department of Physics, Taungoo University, for her kind permission to carry out this work.

References

Abaide, E.R., Anchieta, C.G., Foletto, V.S., Reinehr, B., Nunes, L.F., Kuhn, R.C., Mazutti, M.A. & Foletto, E.L. (2015). Production of Copper and Cobalt Aluminate Spinels and Their Application As Supports for Inulinase Immobilization. *Materials Research*, 18(5), 1062–1069.

Akbar, S., Dutter, P. & Lee, C. (2006). High-Temperature Ceramic Gas Sensors. *International Journal of Applied Ceramic Technology: A Review*, 3(4), 302–311.

Battiston, S., Rigo, C., Severo, E.C., Mazutti, M.A., Kuhn, R.C., Gundel, A. & Foletto, E.L. (2014). Synthesis of Zinc Aluminate ($ZnAl_2O_4$) Spinel and Its Application as Photocatalyst. *Materials Research*, 17(3), 734–738.

Buchholt, K. (2011). *Nanostructured materials for gas sensing applications*. Linkoping University: Sweden.

Deraz, N.M. (2013). Formation and Characterization of Cobalt Aluminate Nano-Particles. *International Journal of Electrochemical Science*, 8, 4036–4046.

Deraz, N.M. & Fouda, M.M.G. (2013). Synthesis, Structural, Morphological Properties of Cobalt-Aluminum Nano-Composite. *International Journal of Electrochemical Science*, 8, 2756–2767.

Ummartyotin, S., Sangngern, S., Kaewvalai, A., Koonsaeng, N., Manuspiya, H. & Laobuthee, A. (2009). Cobalt Aluminate ($CoAl_2O_4$) Derived from Co-Al-TEA Complex and Its Dielectric Behaviors. *Journal of Sustainable Energy & Environment*, 1, 31–37.

J. Myanmar Acad. Arts Sci. 2020 **Vol. XVIII.No.2C**

APPLICATION OF LQR CONTROL FOR TWO-WHEEL SELF-BALANCING ROBOT

Lwin Mg Mg Thwin[1], Ye Chan[2]

Abstract

The concept of two-wheel self-balancing robot is based on an Inverted pendulum (IP) on a cart. The control of an IP has been the most popular benchmark, among others, for teaching and researches in control theory and robotics. The implemented control technique is full state feedback control, Linear Quadratic Regulator (LQR). The LQR algorithm is essentially an automated way of finding an appropriate state-feedback controller. The full state system information about the position and velocity of the cart are obtained from encoder on dc motor and angular position and angular velocity of the pendulum are obtained from IMU sensor MPU6050. A complimentary filter was used to weigh the accelerometer and gyro signals together to determine the pitch angle. This two-wheel self-balancing robot was implemented by using the Arduino Mega microcontroller. The microcontroller can be programmed with the Mathworks® Simulink® program using the Rensselaer Arduino Support Package.

Keywords: Linear Quadratic Regulator (LQR), complementary filter, microcontroller

Introduction

Control theory and its applications continue to grow and expand into new areas of our lives. From driverless cars to electric grid management to financial modeling we see new applications almost daily. These advances require that education grows and adapts as well. The content of control theory curriculum also has to include these new topics and applications to keep up with technology [Brian Howard, (2015)].

Two wheel self-balancing robot is a complicated non-linear system. It has also become great consideration as a research entity because of the unstable character of the system. The two wheel self-balancing robot is based on the fundamental principle of Inverted pendulum. Inverted pendulum has many practical applications such as human walking robots, missile launchers, earthquake resistant building design etc. Development of control system for a two-wheel self-balancing robot has been a huge area of research for the past few years. This is mainly due to its nonlinear dynamics. It became an important test platform for the design and development of missiles, automobiles, space crafts, robots. The simplest method of control system is by using a PID controller [Keerthi Prakash, (2016)].

Simple PID controller cannot give the efficient solution to inverted pendulum single-mass system or inverted pendulum double-mass system, because these systems include nonlinearities, coupling, and uncertain dynamics [Yizhu Li, (2018)]. In this work, Linear Quadratic Regulator (LQR) was applied for two-wheel self-balancing robot. LQR is a well know method to determine the feedback gains of a dynamic system. It’s assumed that we have an optimal full-state feedback, i.e. that we can measure all of our states.

There will be only one axle connecting the two wheels and a platform will be mounted on that to make two-wheel self-balancing robot which can balance itself. To obtain this physical structure, two wheels are mounted with two dc motors in this work. The platform will not remain

---

[1] PhD Candidate, Assistant Lecturer, Department of Physics, Taungoo University

[2] Dr, Professor and Head, Universities’ Research Centre, University of Yangon

stable itself because the system is not stable. The control objective is to keep the two wheels robot in the upright position by using inertial measurement unit (IMU) sensors and optical encoder. At first we have decided to just balance the robot on its two wheels.

Mathematical Modeling

Mathematical model is required to design the control law. Therefore, Newton law based model of the IP has been derived. The IP consists of a moveable cart rail system and a swing-able pole connected to the cart. A free body diagram of an inverted pendulum mounted on a motor-driven cart is shown figure (1). Cart position is controlled with DC motor. The non-linear mathematical model of the IP is derived using the Newton law approach. Vertical force does not affect the cart position and the horizontal movement is controlled by the forces applied through DC motors [Katsuhiko Ogata, (2010)]. The obtained non-linear mathematical model of system is given by equations (1) and (2). The system state and parameters are explained in table (1) and system specifications are provided in table (2).

$$(M_c + m)\, \ddot{x} \; + ml\, \ddot{\theta} \cos\theta = ml\, \dot{\theta}^2 \sin\theta + u \tag{1}$$

$$(I + ml^2)\; \ddot{\theta} \; + \; ml \cos\theta\, \ddot{x} \; = mgl \sin\theta \tag{2}$$

Since the inverted pendulum must be kept vertical position, it can be assumed that θ and $\dot{\theta}$ are small quantities such that sin $\theta \cong \theta$, cos $\theta = 1$ and $\dot{\theta}^2\theta = 0$. Then the non-linear system equations (1) and (2) can be linearized to equation (3) and (4) [Liu, Jinkan, (2017)].

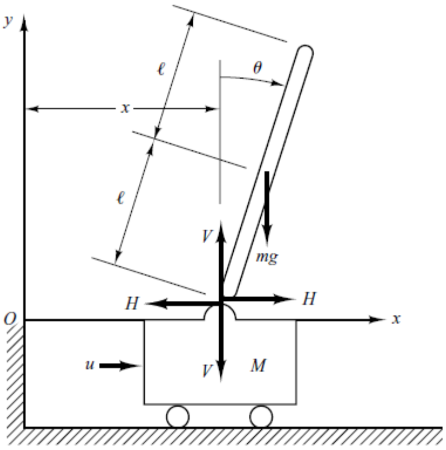

Figure 1 Free body diagram of inverted pendulum system

Table 1. The system states and parameters

Symbol	Description
M_c	mass of cart
m	mass of pendulum
l	length of pendulum
g	gravity
$\theta, \dot{\theta}, \ddot{\theta}$	angular position, angular velocity and angular acceleration of the pendulum rod from the vertical line
$x, \dot{x}, \ddot{x}$	cart position, velocity and acceleration respectively
u	control force applied to the cart
I	moment of inertia of the rod

Table 2 Parameter measurement values for the system

Symbol	Meaning	Value	Unit
M_c	Cart mass	0.46	kg
m	Pendulum mass	0.14	kg
L	Cart length	0.23	m
l	Length of pendulum	0.17	m
I	Inertia	$\frac{1}{12} mL^2$	kg/m^2
g	Gravity	9.8	m/s^2

$$\ddot{\theta} = \frac{m(m + M_C)gl}{(M_c+m)I + M_cml^2}\,\theta - \frac{ml}{(M_c+m)I + M_cml^2}\,u \tag{3}$$

$$\ddot{x} = -\frac{m^2gl^2}{(M_c+m)I + M_cml^2}\,\theta + \frac{I + ml^2}{(M_c+m)I + M_cml^2}\,u \tag{4}$$

The system equations can be reduced as follow.

$$\ddot{\theta} = t_1\theta + t_3u \tag{5}$$

$$\ddot{x} = t_2\theta + t_4u \tag{6}$$

where $t_1 = \frac{m(m + M_C)gl}{(M_c+m)I + M_cml^2}$, $t_2 = -\frac{m^2gl^2}{(M_c+m)I + M_cml^2}$,

$t_3 = -\frac{ml}{(M_c+m)I + M_cml^2}$ and $t_4 = \frac{I + ml^2}{(M_c+m)I + M_cml^2}$.

Let define as $x_1 = x$, $x_2 = \dot{x}$, $x_3 = \theta$ and $x_4 = \dot{\theta}$. Therefore,

$$\left.\begin{aligned} \dot{x}_1 &= x_2 \\ \dot{x}_2 &= t_2x_3 + t_4u \\ \dot{x}_3 &= x_4 \\ \dot{x}_4 &= t_1x_3 + t_3u \end{aligned}\right\} \tag{7}$$

Converting equation (7) to the equivalent state space form given as,

$$\dot{X} = A\mathbf{x} + Bu \tag{8}$$

where $\dot{X} = \begin{bmatrix}\dot{x}_1\\ \dot{x}_2\\ \dot{x}_3\\ \dot{x}_4\end{bmatrix}$, $\mathbf{x} = \begin{bmatrix}x_1\\ x_2\\ x_3\\ x_4\end{bmatrix}$, A = $\begin{bmatrix}0 & 1 & 0 & 0\\ 0 & 0 & t_2 & 0\\ 0 & 0 & 0 & 1\\ 0 & 0 & t_1 & 0\end{bmatrix}$ and B = $\begin{bmatrix}0\\ t_4\\ 0\\ t_3\end{bmatrix}$

x is the *n* dimensional state vector, **u** is the *m* dimensional input vector, **A** is the *n* × *n* system matrix and **B** is the *n* × *m* control matrix.

By using parameter measurement values from table (2), the system equation becomes

$$\begin{bmatrix}\dot{x}\\ \ddot{x}\\ \dot{\theta}\\ \ddot{\theta}\end{bmatrix} = \begin{bmatrix}0 & 1 & 0 & 0\\ 0 & 0 & -2.4877 & 0\\ 0 & 0 & 0 & 1\\ 0 & 0 & 62.7141 & 0\end{bmatrix}\begin{bmatrix}x\\ \dot{x}\\ \theta\\ \dot{\theta}\end{bmatrix} + \begin{bmatrix}0\\ 2.0897\\ 0\\ -10.6657\end{bmatrix}\mathrm{u(t)} \tag{9}$$

Stability

One of the first things we want to do is analyze the stability of the open-loop system (without any control). The poles or eigenvalues of the system matrix, *A*, determine the stability of the system. For this system based on the state space equation (9), the poles can be found simply by using Matlab command (poles = eig(A)). The poles or eigenvalues of opened loop system matrix are 0, 0, 7.9192 and -7.9192. The system has four poles with one in the right half plane which makes the system unstable. Therefore, a linear controller needs to be designed to force the poles in the left half plane.

Control Algorithm

Most single input, single output (SISO) systems can be adequately analyzed and controlled using basic transfer function techniques and PID type controllers. For systems that have multiple inputs and multiple outputs (MIMO) a more suitable type of control framework is called full state feedback. A full state feedback controller measures or estimates all of the system "states" and uses this "state" multiplied by a gain matrix to control the system.

The inverted pendulum based two-wheel self-balancing robot is an unstable and nonlinear system. In order to make the pendulum in upright position where the system will be stable, the suitable control algorithm has to be implemented.

Controllability and observability

The concept of controllability and observability were introduced by Kalman (1960) and play an important role in the control of multivariable systems. A system is said to be controllable if a control vector u(t) exists that will transfer the system from any initial state $x(t_0)$ to some final state x(t) in a finite time interval. A system is said to be observable if at time t_0, the system state $x(t_0)$ can be exactly determined from observation of the output y(t) over a finite time interval [Roland S. Burns, (2001)].

If a system is described by the following equations

$$\dot{X} = A\mathbf{x} + Bu$$

$$y = C\mathbf{x} + Du \qquad (10)$$

then a sufficient condition for complete state controllability is that the $\boldsymbol{n}\times\boldsymbol{n}$ matrix

$$M = [B{:}\ AB{:}\ \ldots{:}A^{n-1}B] \qquad (11)$$

contains $\boldsymbol{n}$ linearly independent row or column vectors, i.e. is of rank $\boldsymbol{n}$ (that is, the matrix is non-singular, i.e. the determinant is non-zero). Equation (11) is called the controllability matrix.

The system described by equations (10) is completely observable if the $\boldsymbol{n}\times\boldsymbol{n}$ matrix

$$N = [C^T{:}\ A^TC^T{:}\ \ldots : (A^T)^{n-1}C^T] \qquad (12)$$

is of rank n, i.e. is non-singular having a non-zero determinant. Equation (12) is called the observality matrix. The rank of controllability and observability matrix of a system model can be determined in Matlab using command rank(ctrb(A,B)) or rank(ctrb(sys)) and rank(obsv(A,C)) or rank(obsv(sys)) respectively.

Linear Quadratic Regular (LQR) Control

LQR is a linearized and optimal control technique which provides optimal gains for the systems. It is more suitable for the linear systems having no uncertainties or disturbances. The major benefit of this technique is that it gives the gains to minimize the cost function [Saqib Irfan, (2108)]. For an n^th^ order system the general cost function of LQR is given as,

$$J = \int_0^\infty [x^TQx + u^TRu]\, dt \qquad (13)$$

where, Q ∈ $R^{n\times n}$ is positive definite or positive semi definite Hermitian matrix or real symmetric matrix, R ∈ $R^{r\times r}$ is a positive definite Hermitian matrix or real constant number and J is always scalar quantity. The Q matrix is a weighting function for the states and R is weighting function for the inputs. LQR gain is computed as,

$$\mathrm{K} = R^{-1}B^{T}P \tag{14}$$

The Riccati equation is given in equation (15) to solve the optimal controller.

$$\mathrm{PA} + A^{T}P + Q - PBR^{-1}B^{T}P = 0 \tag{15}$$

The control law for the linear system is given as,

$$u = -K\mathbf{x} \tag{16}$$

$$\dot{X} = A\mathbf{x} - BK\mathbf{x}$$

$$\dot{X} = (A - BK)\mathbf{x} \tag{17}$$

Using Matlab to solve the equations, this controller had the following pole locations and gains. The controller parameters R = 0.3 and the diagonal values of Q matrix = [1, 1, 10, 1] are chosen to achieve good stability performance of the system. The poles and LQR gain matrix for the closed loop system are [-22.3818 -3.6206 -1.7162 -1.7162] and [-2.5820 -3.4896 -22.6641 -3.4435] respectively. Since all poles are in the left half plane, the system will be stable at pendulum upright position. Assuming it is possible to directly measure the entire state (i.e. y = **x**) implementing a state space controller is really simple. The state is simply multiplied by a control gain matrix KLQR and the result is fed back into the plant. As a block diagram for full state feedback control system is shown in figure (2).

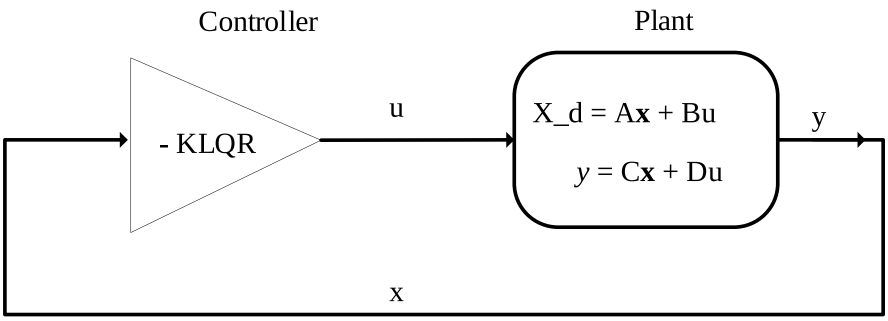

Figure 2 The block diagram of full state feedback control system

Results and Discussion

Implementation results

Simulink support package for Arduino hardware and Rensselaer Arduino support package had been installed to implement this research as prerequisite. The dynamics of the plant was sampled at fixed f_s = 200 Hz, which equals to the sampling frequency of the IMU sensors. Therefore, the microcontroller will execute the Simulink code every 50 milliseconds. The real time simulation involved in the proposed work was performed on Simulink, with simulation time of 30 s. But the following figures for the system response graphs are zoomed out to view clearly comparative study.

The controller from figure (2) was implemented as a Simulink model, shown in figures (3) and (4). The based part of two-wheel robot position, system state *x* can be obtained from the encoders on the motor and its velocity, system state *x_dot* is obtained from derivative block of *x* data. The Simulink diagram associated with robot position and velocity is shown in figure 3(a). Micro-Electro-Mechanical Systems (MEMS) package (MPU6050) is used to provide the rate of pitch angle $\dot{\theta}$, and pitch angle θ, as shown in figure 3(b). Measuring this pitch angle using the MPU6050 provided to be a challenging part of designing the controller. The accelerometers were relatively slow to respond and could not be used by themselves to measure pitch angle. The gyro signals have noise and a DC offset (bias) and could not be used alone to measure the angle.

A complimentary filter was used to weigh the accelerometer and gyro signals together to determine the pitch angle. Figure 4(b) shows the complimentary filter design used in the two-wheel robot. All four of the state variables are passed into a vector and multiplied by the LQR gain vector KLQR. The output of the gain is then passed onto the motor controller as shown in figure 4(a). The controller also includes logic to shut the motor off if the robot pitch angle is greater than 20° in either direction.

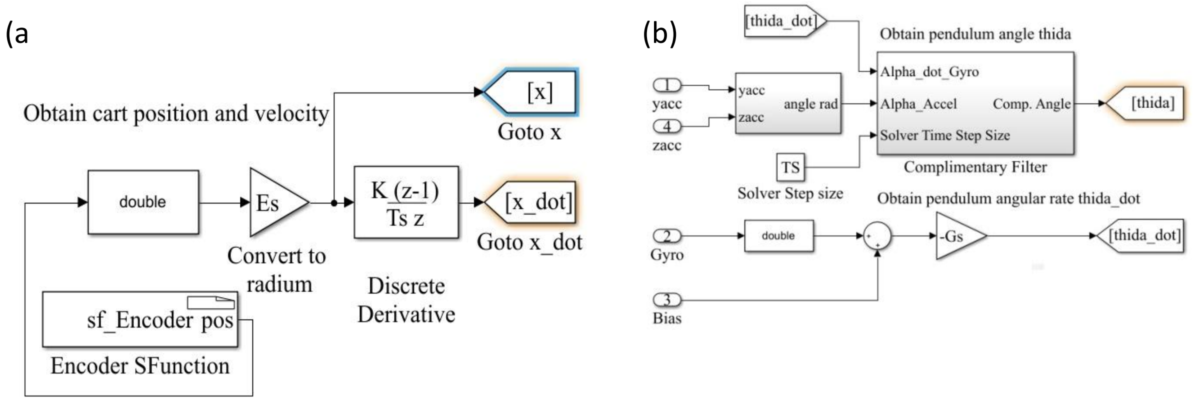

Figure 3 Simulink diagram for obtaining system state variables $[\ x\ \dot{x}\ \theta\ \dot{\theta}\ ]$

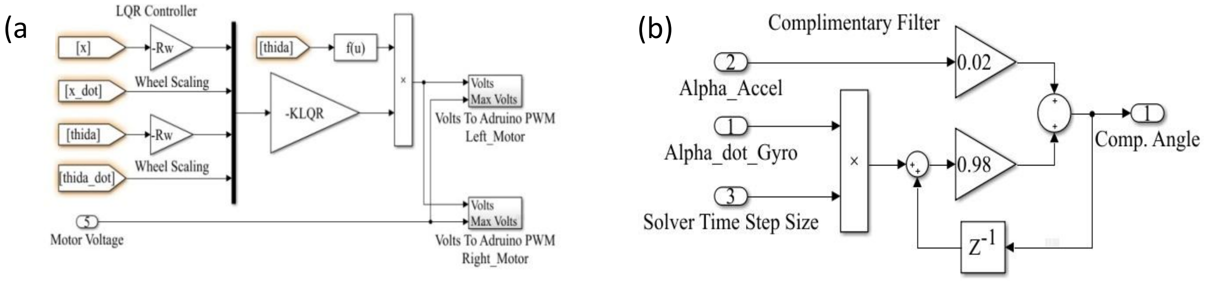

Figure 4 Simulink diagram for LQR controller and Complimentary filter

The desired dynamics system response can be set by adjusting the parameters Q and R values. The values of KLQR depend on both R and Q values. These LQR gain vector will affect the control input signal level, the system response and the robustness of the system.

The control input signal conditioning can be set by adjusting R value. By choosing a large value of R, the system will be operated with less energy i.e. low power consumption. Therefore, it is called expensive control strategy. If the very large value of R is used, the system cannot be responded fast enough to prevent the robot from falling. On the other hand, the system will be responded faster with the choosing of low value R. It is usually called cheap control strategy. The control signal is also become large and chattering. By using very low value of R, the system will become oscillate and unstable. Three different values of R, its corresponding KLQR gain values and the system response are compared in table (3). In this research, the optimum R value can be tuned manually with 0.3 for the constructed two-wheel robot which has the system parameter values given in table (2). Figure 5 (a), (b) and (c) are shown for the real time Simulink graphs of control signal, the pitch angles and the robot position values respectively.

Similarly, the Q values can hardly influence on the system response because it is a weighting function for the system state. In this two-wheel robot, there are four system variables, the position and speed of the based part of robot and the pitch angle and angular rate of the balanced robot. The specific system state response, $[\ x\ \dot{x}\ \theta\ \dot{\theta}\ ]$ can be tuned manually with the corresponding diagonal values of Q matrix, Q(1,1), Q(2,2), Q(3,3) and Q(4,4) respectively. By using larger value of Q, the system will try to stabilize with the least possible changes in the states. Alternatively, using the smaller value of Q will imply less influence about the changes in the states. The choosing for the best values of Q and R is a challenging part in LQR algorithm.

Table 3 The system response for different values of LQR gains

R	KLQR				Control Input	Chattering frequency	System Response
0.1	-3.1623	-4.9191	-27.8789	-4.9002	large	high	aggressive
0.2	-2.2361	-3.5604	-22.7021	-3.7581	↕	↕	↑
0.3	-1.8257	-2.9641	-20.5141	-3.2717			optimum
0.4	-1.5811	-2.6109	-19.2573	-2.9913			↓
0.5	-1.4142	-2.3708	-18.4254	-2.8054	small	low	delay

The real time pitch angle responses and the control signal u for different three diagonal values of Q matrix are compared as shown in figure (6). The small and large Q values are tuned manually to achieve the desired system performance. While the low values of Q (Q = [1, 1, 10, 1]) are used, the control signal is small and the system cannot robust. To obtain the robustness character, the larger Q values (Q = [6, 1, 150 3]) are tuned to compute the controller gain matrix but the system becomes jitter. The figure 6(a) and 6(b) are shown for the control signal and pitch angle response respectively. Since the high frequency switching is occurred at control signal, the robot will be jittered while balancing. This jitter effect may produce noise signal to the microcontroller. The experimental setup for real time simulation with Matlab Simulink and two-wheel balancing robot photos are shown in figure 7(a) and 7(b) respectively.

(a)

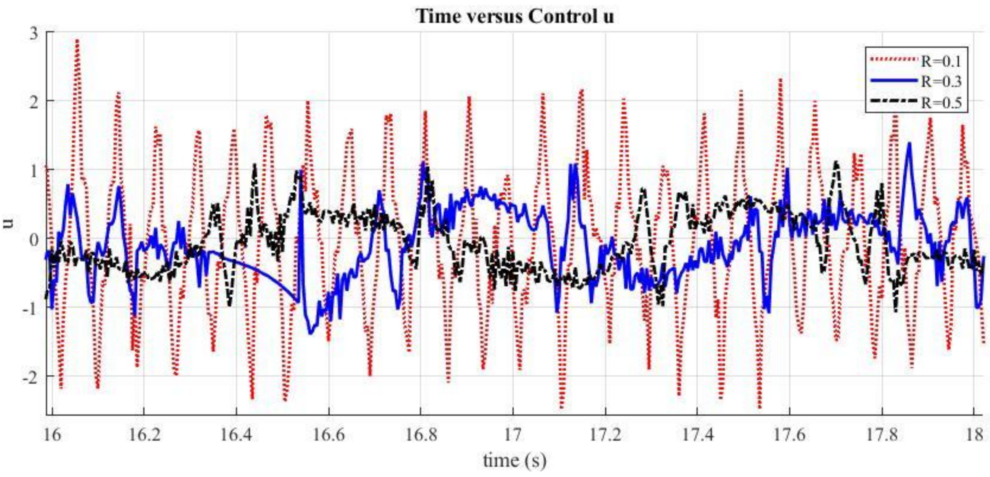

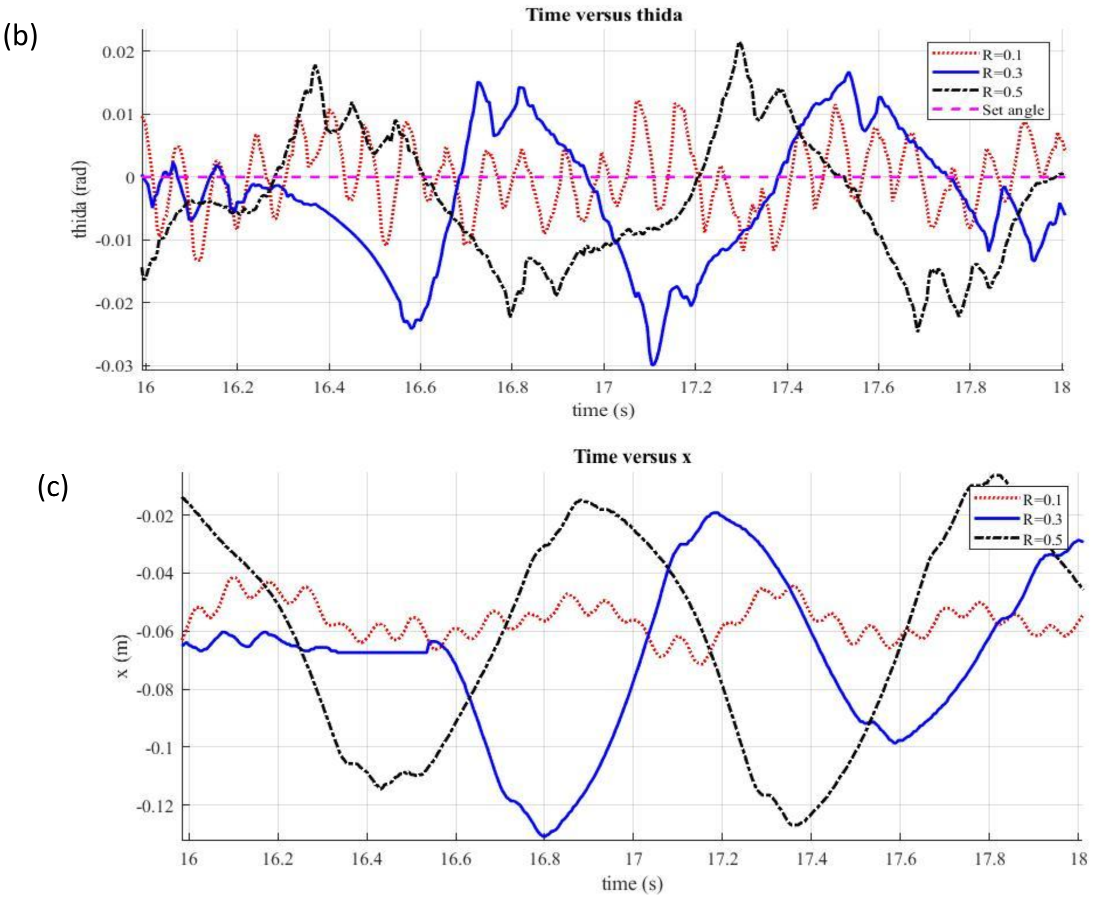

Figure 5 The control signal and system response compare results for three different R values

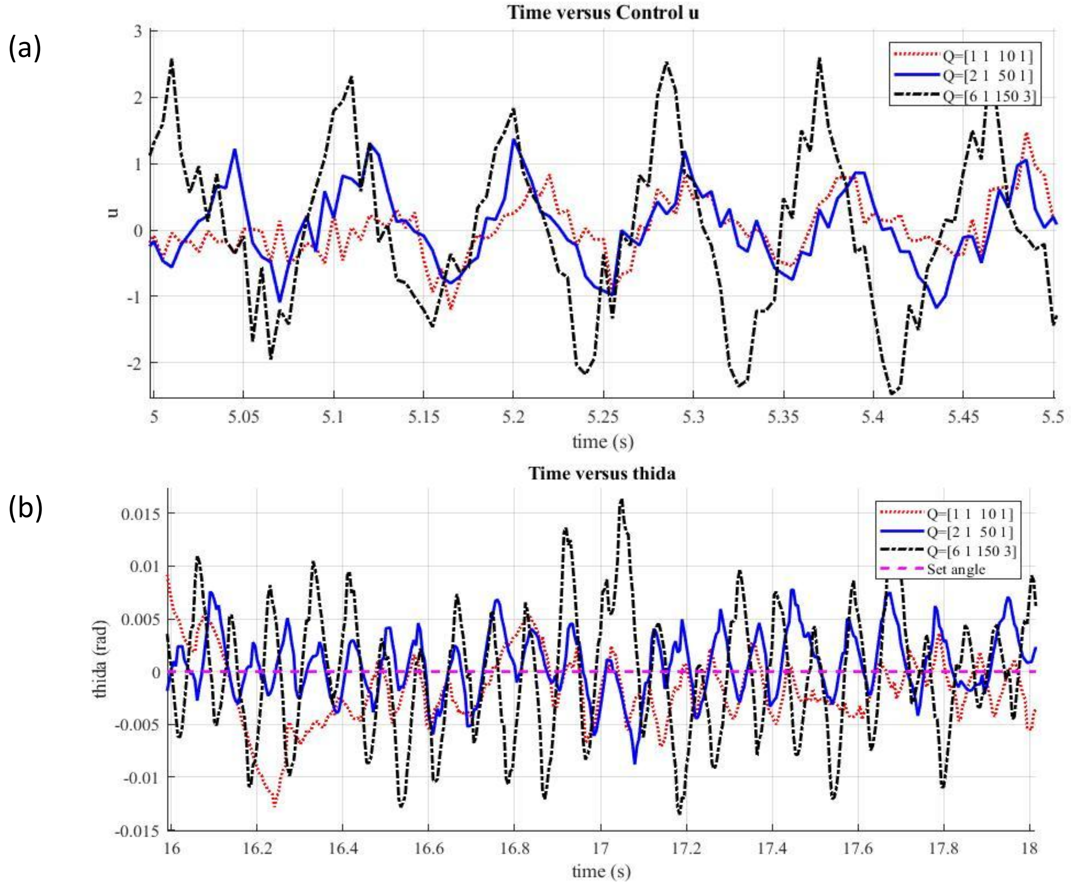

Figure 6 The control signal and system response compare results for three different Q values

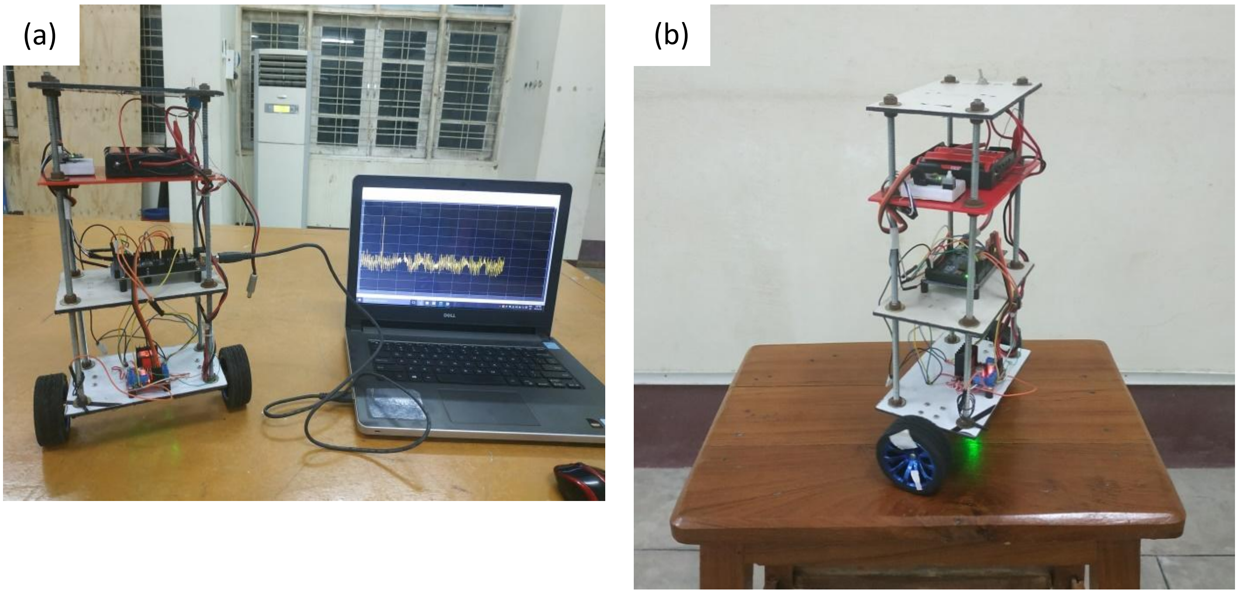

Figure 7 Two-wheel self-balancing balancing robot

Conclusion

In this research, two-wheel self-balancing robot was implemented by using state space control, LQR algorithm. The Rensselaer Arduino Support Package and Simulink support package for Arduino hardware were used not only to program for Arduino mega but also to analyze the performance of controller with real time simulation. Experimental results show that self-balancing can be achieved with LQR control in the vicinity of the upright position. The parameters Q and R values can be used as design parameters to penalize the state variables and the control signals. Since Q and R values are very sensitive variables, they are tuned carefully to provide desired system response. From this research, the MEMS gyro behavior suggests that Kalman filtering would be helpful in attenuating the noise from the gyro data. It is obviously that both sensor selection and signal conditioning are important to the performance of the control systems.

Acknowledgements

The authors would like to acknowledge Professor Dr Khin Khin Win, Head of Department of Physics, University of Yangon, for her valuable suggestion and comments for this work. I would like to thank Professor Dr Nge Nge Khaing, Head of Department of Physics, Taungoo University, for her kind permission to carry out this work.

References

Brian Howard & Linda Bushnell. (2015). Enhancing Linear System Theory Curriculum with an Inverted Pendulum Robot. *American Control Conference(ACC), IEE.*

Katsuhiko Ogata. (2010). *Modern Control Engineering,* Pearson Education, Inc., publishing as Prentice Hall, One Lake Street, Upper Saddle River, New Jersey 07458.

Keerthi Prakash & Koshy Thomas. (2016). A Comparative Study of Controllers for a TwoWheeled Self-balancing Robot. *International Journal of Advanced Research in Electrical, Electronics and Instrumentation Engineering.*

Liu, Jinkan. (2017). *Sliding Mode Control Using MATLAB*, Beihang University, Beijing, China.

Roland S. Burns. (2001). *Advanced Control Engineering*. Butterworth-Heinemann, Linacre House, Jordan Hill, Oxford OX2 8DP, 225 Wildwood Avenue, Woburn, MA 01801-2041, Department of Mechanical and Marine Engineering, University of Plymouth, UK.

Yizhu Li. (2018). *A Comparative Study on Several Control Strategies for Inverted Pendulum Systems*. Master thesis, The Department of Mechanical and Industrial Engineering, Northeastern University, Boston, Massachusetts.

J. Myanmar Acad. Arts Sci. 2020 **Vol. XVIII.No.2C**

STRUCTURAL INVESTIGATION OF PEANUT SHELL BIO-CHAR

Toe Toe Wai[1], Zin Min Myat[1], Shwe Sin Aung[1],
Nway Han Myat Thin[1], Than Than Win[2]

Abstract

Bio-char were prepared from peanut shell by thermal conversion of biomass. Peanut shells were dried in sun-shines to remove moisture. The dried peanut shells were ground to become powder and heated at 200 °C - 800 °C for 1 h respectively. After heating, bio-char was obtained. Structural properties of peanut bio-char were examine by X-ray diffraction (XRD). Scanning electron microscopy (SEM) was used to observe microstructure of bio-char. Functional groups in these bio-chars were investigated by Fourier transform spectroscopy (FT IR).

Keywords : Bio-char, XRD, SEM, FTIR

Introduction

Bio-char is a by-product of biomass pyrolysis (residues of crops, wood trees, turfgrass, animal, manure, etc) which is undertaken to generate energy[Lee, J.W *et al*., 2010]. Bio-char can be produced from almost of many types of feedstock as there are types of biomass including agricultural wastes, rice husks, bagasse, paper products…). Peanut shell is a kind of a agriculture waste and it is most available in many parts in Myanmar. It can be used as removal of pollutants from aqueous solution, for removal of heavy metal ions from aqueous medium, effect and perspectives for land reclamation, pollutants removal, carbon sequestration and soil amelioration. The pyrolysis is thermo chemical process and it converts the bio-waste into liquid, gas and solid product [Dmitri A 2011].

Biomass is conducive to environmental protection and sustainable development. Various kind of biomass has been transformed into porous carbon materials, such as corncob end straw rice husks, as well as banana leaves and stalks [Beguin, F. *et al*., 2014]. Porous activated carbon derived from peanut shells was used widely not only in the field of environmental protection as an efficient adsorbent to remove heavy metal ions and organic dyestuff in waste water but also in power sources such as lithium-/sodium- ion, batteries, and super-capacitor. [Georgin, J. *et al*., 2016]. Peanut shell is having different chemical composition, material morphologies, surface functionalities, carbon properties, which attracted great attention to utilise it as the precursor to produce the activated carbon [Hassan, A F. *et al*., 2014].

The activated carbon extracted from peanut shell can be utilised for the fabrication of electrode for energy storage devices like super capacitors and batteries [He, T. *et al*., 2015]. Biomass material not only contains abundant carbon, existing as cellulose, lignin and hemicelluloses, but also usually exhibits a unique hierarchical porous structure. Moreover, rational utilization of biomass is conducive to environmental protection and sustainable development. Therefore, the utilization of biomass to produce hierarchical porous carbon materials has become more and more attractive, especially for energy storage [Jiang Q. ed al 2016]. Until now, various kinds of biomass have been transformed into porous carbon materials, such as corncob and straw, rice husks, as well as batata leaves and stalks [Wer, X. *et al*., 2017].

---

[1] Dr, Assistant Lecturer, Department of Physics, University of Yangon

[2] Dr, Professor, Department of Physics, Panglong University

Peanut shell is having different chemical composition, material morphologies, surface functionalities, carbon properties, which attracted great attention to utilise it as the precursor to produce the activated carbon.

Chemically modified adsorbents have been prepared by treating raw peanut shells with three different chemical methods. Scanning electron microscope (SEM), Fourier transform in fared spectroscopy (FI TR), X-ray diffractometer (XRD) have been used to characterize these adsorbents.

Experimental Procedure

Peanut shells were collected from Ayeyarwady Division. The collected biomaterial was extensively washed with tap water to remove soil and dust. Washing process was repeated. They were dried in sunshine for 48 hours. The dried shells were cut into small pieces and heated in the muffle furnace. The peanut shells are annealed at (200 °C – 800 °C) for 1 hour respectively. Finally, the peanut shell bio-char were obtained. The block diagram of sample preparation of peanut- shell bio-char was shown in Fig 1.The prepared peanut-shell bio-char were characterized by using an X-ray Diffractometer (RIGAKA-RINT 2000). Each chars were grained for powder diffraction using Cuk$_\alpha$ radiation (40 kV,40 mA) from 10^o to 70^o (2 θ) with 0.1 strength size and 2 sec measurement interval. The surface morphology studies of bio-char were performed using Scanning Electron Microscopy (SEM). Fourier Transform Inferred Spectroscopy (FTIR) was examined in atmosphere using (Model- JEOL-6000). Absorbance spectrum (800-4000 cm^{-1}) was collected for each sample.

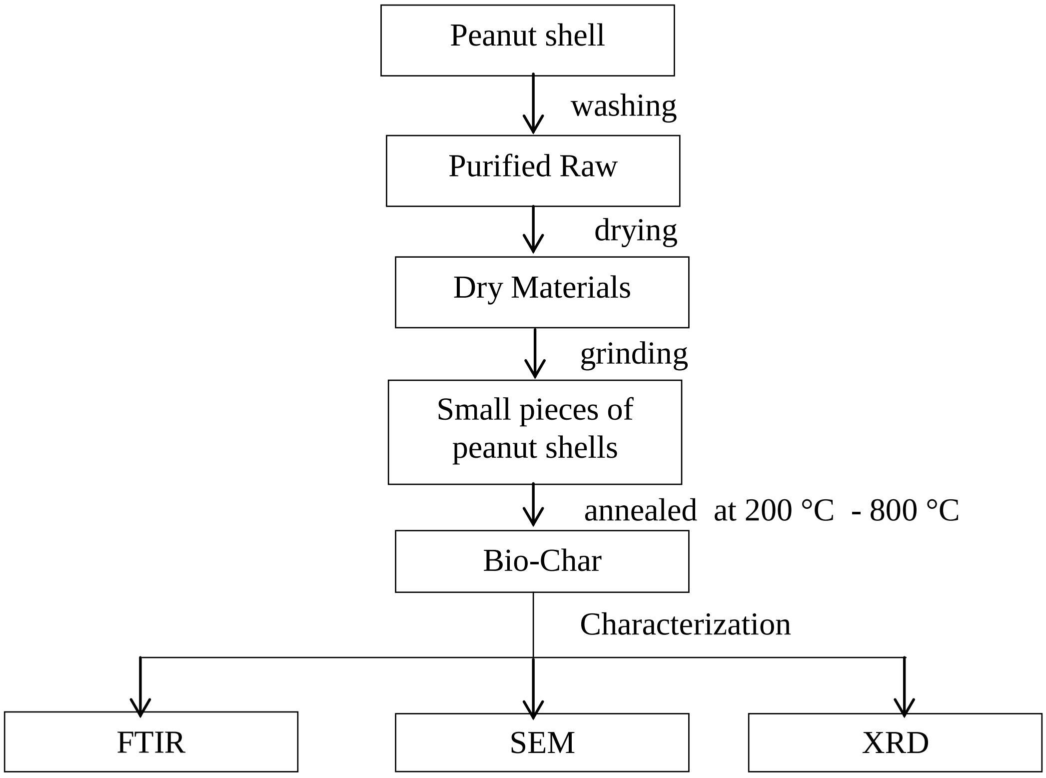

Figure 1 Flow Chart of Characterization of bio-char material

Results and Discussion

FTIR Analysis of Peanut shell Bio-char

FTIR spectroscopy was applied to measure the chemical properties and absorption of energy from the range of 800 cm^{-1}- 4000 cm^{-1} by studied samples. Spectral registration was examined with use of solid-state samples which is made of a complex organic material. The FTIR analysis demonstrated the functional groups presented on peanut shell bio-char. From the Fig. 2(a-d), an annealing temperature from 200 ºC to 500 ºC , the range at 3500-3200 cm^{-1} was shown O-H stretch and H bonded bond in alcohol, phenons functional group. And also stretch bands between 1534-1586 cm^{-1} were found in N-O asymmetric stretch nitro compound functional group and the peak at 1157 – 1200 cm^{1} formed to be C_O stretch alcohols, carboxylic acid, esters and ethers group. From the figure 2(e-g) the peak at 2260-2100 cm^{-1} is associated to C≡C stretch alkynes functional group. The functional groups of the peanut shell samples at 200 ºC to 500 ºC have found to be O-H stretch, N-O asymmetric stretch and C-O stretch alcohols, carboxylic acid, esters and ethers group . At 600 ºC to 800 ºC C≡C stretching vibration was occurred.

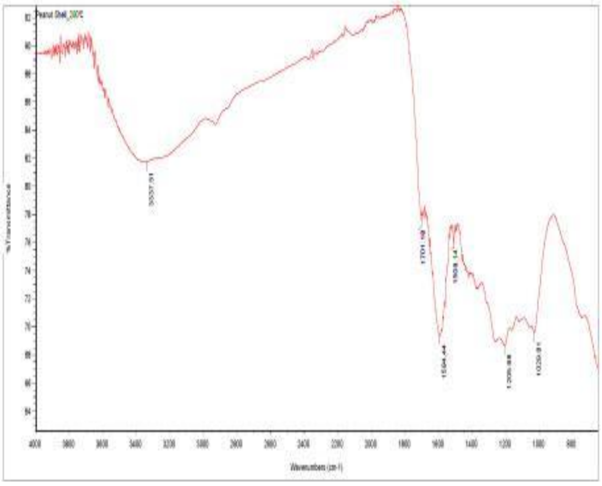

Figure 2(a) FT IR spectra of peanut shell bio-char at 200 ºC

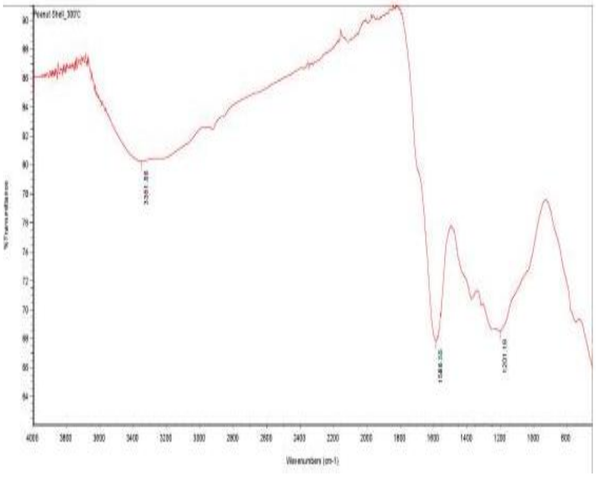

Figure 2(b) FTIR spectra of peanut shell bio-char at 300 ºC

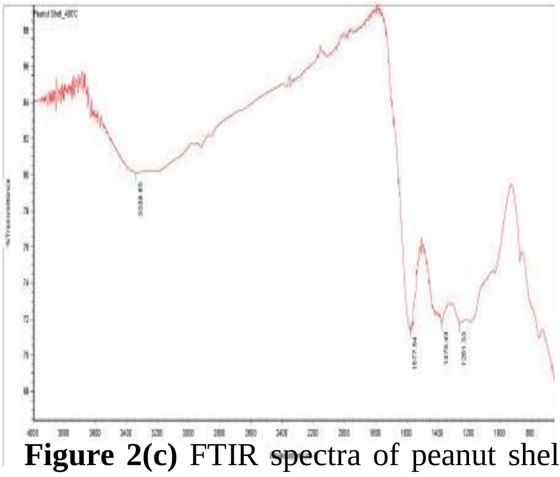

Figure 2(c) FTIR spectra of peanut shell bio-char at 400 ºC

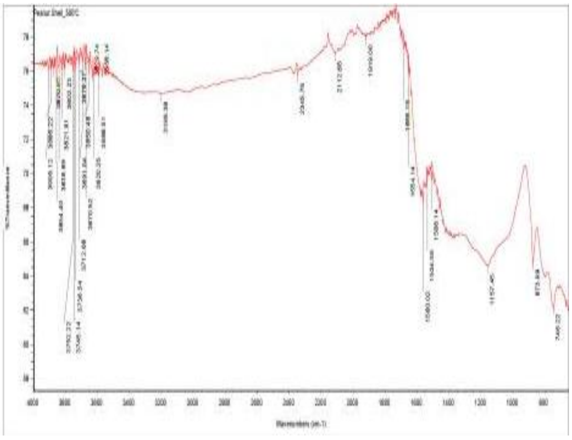

Figure 2(d) FTIR spectra of peanut shell bio-char at 500 ºC

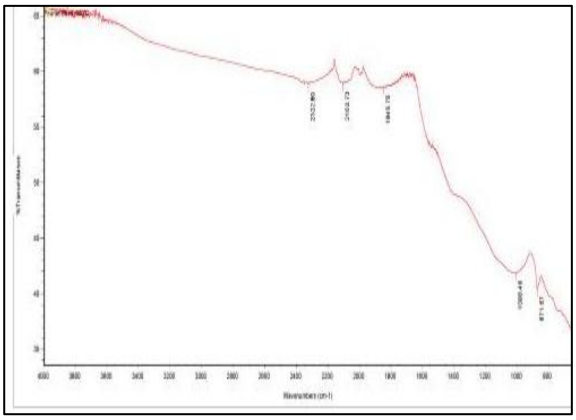

Figure 2(e) FTIR spectra of peanut shell bio-char at 600 ºC

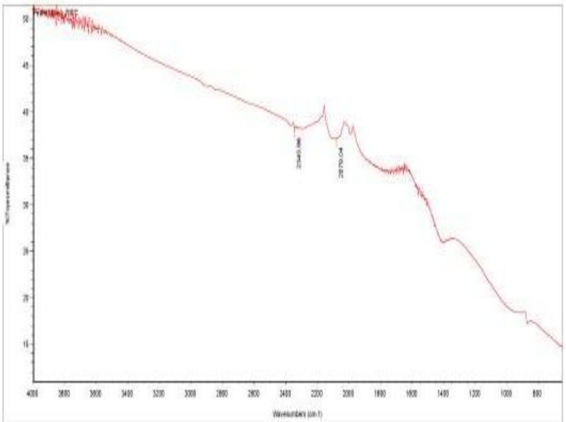

Figure 2(f) FTIR spectra of peanut shell bio-char at 700 ºC

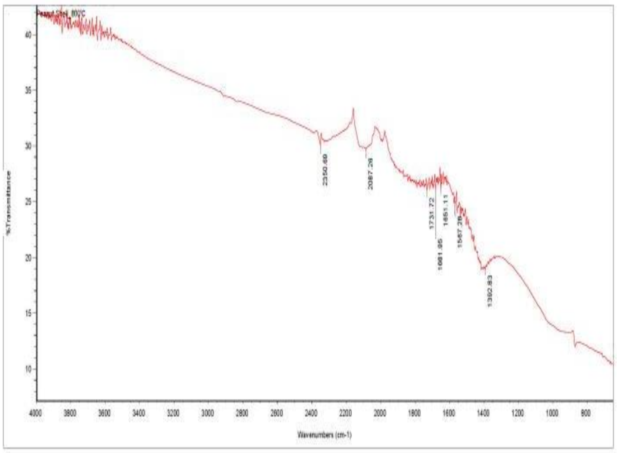

Figure 2(g) FTIR spectra of peanut shell bio-char at 800 ºC

SEM Analysis

Scanning electron micrographs for external morphology of peanut shell bio-char at temperatures 200 ºC to 800 ºC for 1 hour were shown in Fig. 4(a-b), the porous nature was found that the peanut shell bio-char had porous nature with micro-porous structure. From SEM images, it was found that the surface morphology and nature of pores size changes with different temperatures. From Figure 3(a – e) the pore size becomes smaller and smaller with increasing temperatures between 200 ºC and 600 ºC. At higher temperatures, 700 ºC and 800 ºC the pore sizes were very small and irregular in size. In 800 ºC, the crushed pieces of the peanut shell biochar became smaller due to the heat treatment and formed flakes layers. All figures exhibited the smooth in morphology, grain size and pores qualities of all samples were fabricated by pyrolysis method.

Table Average pore diameter of peanut shell biochar with different temperatures from SEM image

Sr	Temperature (°C)	Time (h)	average pore diameter (µm)
1.	200	1	8.39
2.	300	1	6.22
3.	400	1	5.80
4.	500	1	5.18
5.	600	1	3.40
6.	700	1	1.91
7.	800	1	1.72

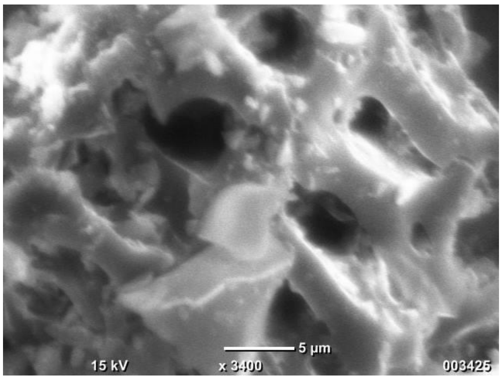

Figure 3(a) SEM image of Peanut Shell bio-char at 200 ºC

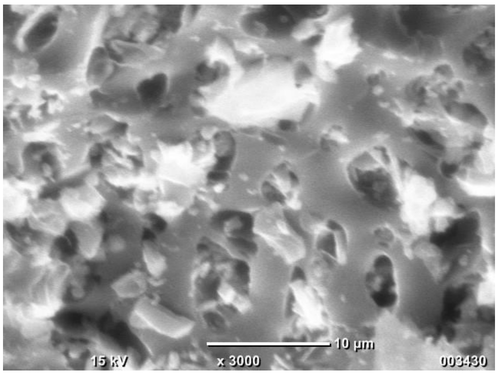

Figure 3(b) SEM image of Peanut Shell bio-char at 300 ºC

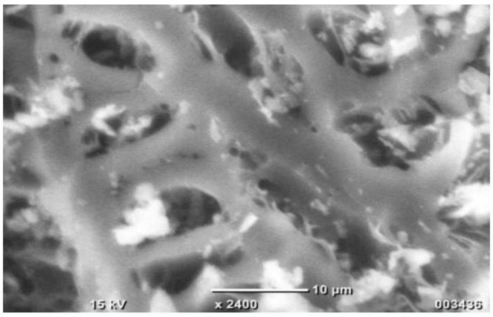

Figure 3(c) SEM image of Peanut Shell bio-char at 400 ºC

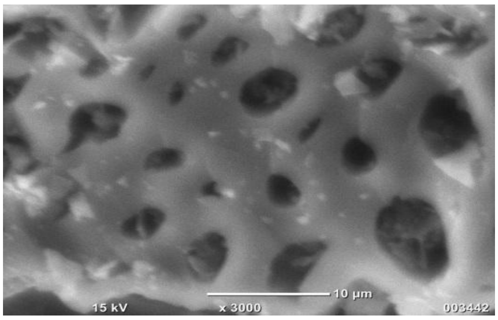

Figure 3(d) SEM image of Peanut Shell bio-char at 500 ºC

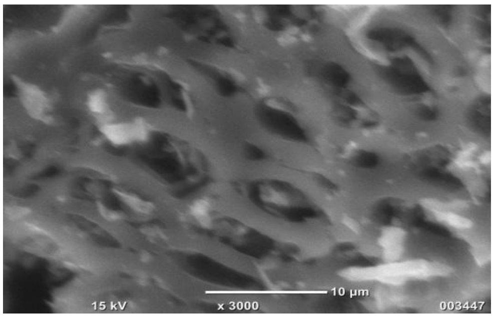

Figure 3(e) SEM image of Peanut Shell bio-char at 600 ºC

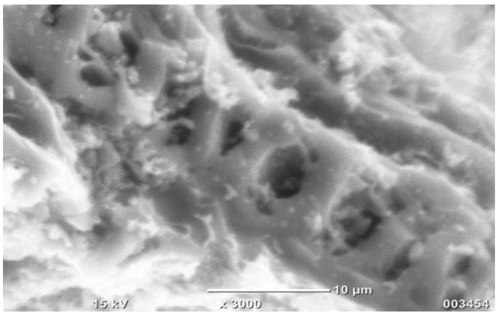

Figure 3(f) SEM image of Peanut Shell bio-char at 700 ºC

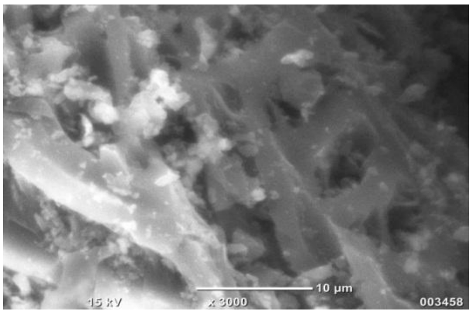

Figure 3(g) SEM image of Peanut Shell bio-char at 800 ºC

XRD Analysis

The peanut shell bio-char and were analyzed by XRD technique. The XRD spectra of peanut shell bio-char at 200 ºC to 800 ºC for 1 h were shown in Fig. 4 (a-g). According to XRD analysis, five diffracted peaks were observed. They were not perfectly identified. It could be said that peanut shell bio-char was amorphous material with little crystalline. It was found that five diffracted peaks were formed and they were matched with the peaks of Carbon, Graphite and diamond peaks.

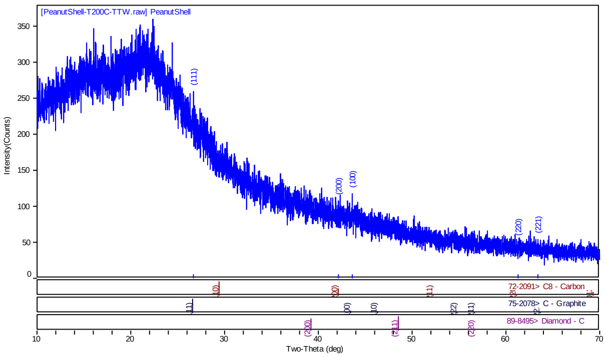

Figure 4(a) The XRD pattern of peanut shell bio-char at 200 ºC for 1 hr

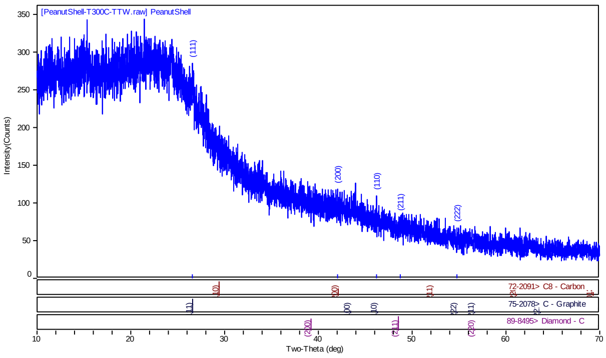

Figure 4(b) The XRD pattern of peanut shell bio-char at 300 ºC for 1 hr

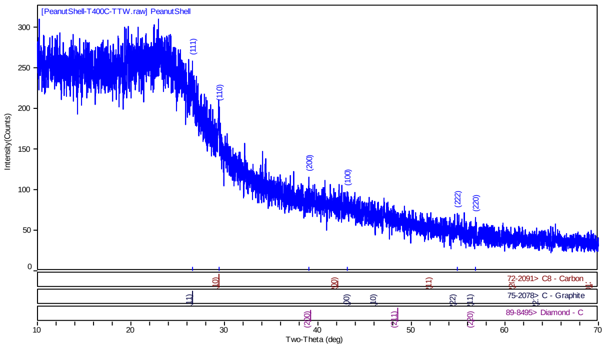

Figure 4(c) The XRD pattern of peanut shell bio-char at 400 ºC for 1 hr

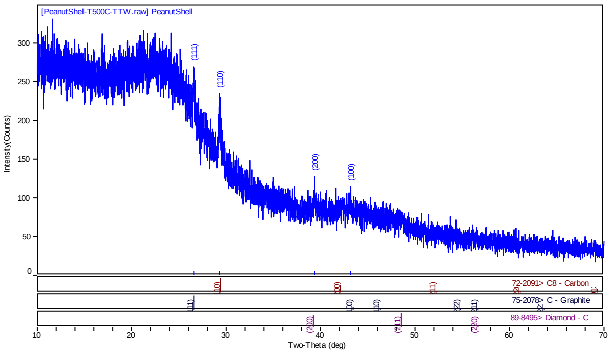

Figure 4(d) The XRD pattern of peanut shell bio-char at 500 ºC for 1 hr

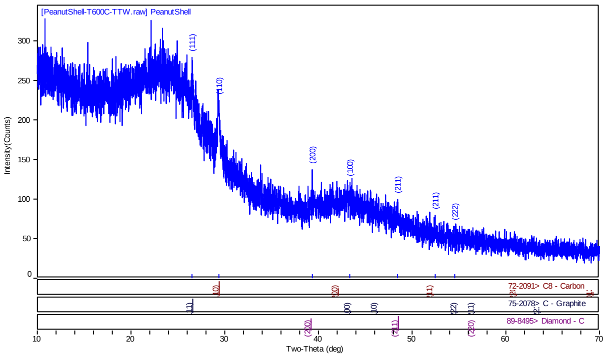

Figure 4(e) The XRD pattern of peanut shell bio-char at 600 °C for 1 hr

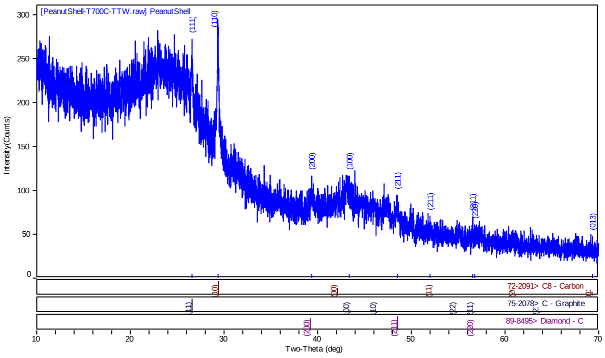

Figure 4(f) The XRD pattern of peanut shell bio-char at 700 °C for 1 hr

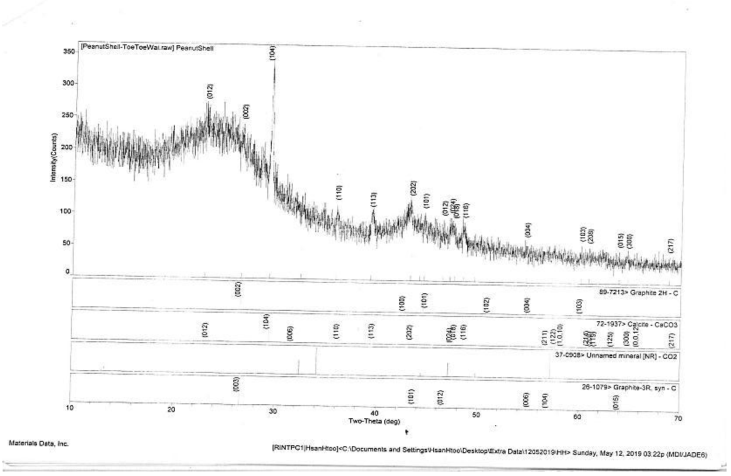

Figure 4(g) The XRD pattern of peanut shell bio-char at 800 °C for 1 hr

Conclusion

Bio-char are produced in a muffle furnace from the peanut shell of bio-mass. The .XRD spectra, SEM images and FTIR spectra of peanut shell bio-char were studied. As a result of XRD, the peanut shell bio-char at different temperatures (200 °C – 800 °C) were matched with carbon. From SEM image peanut shell bio-char could be said that it has porous nature. The Bio-char undertake a number of significant changes in chemical composition. These changes can easily be examined by FT IR analysis. The results suggested that the peanut shell bio-char can be used as an efficient quality for production of renewable sources based on activated carbon.

Acknowledgements

The authors would like to thank Dr Pho Kaung, Rector of University of Yangon for his kind permission to do this research paper.

I would like to express my sincere thanks to Professor Dr Khin Khin Win, Head of the Department of Physics, University of Yangon for her kind encouragement and permission to perform this research work.

I also would like to thank Professor Dr Aye Aye Thant, Professor Dr Myo Lwin, Professor Dr Yin Maung Maung, Professor Dr Than Zaw Oo, Department of Physics, University of Yangon, for their kind advice and suggestions for this research.

References

Beguin,F.V.Presser, A-Balducci and E.Frackowiak, Adv. Mater., 26(2014) 2219.

Dmitri A, 2011; Niruwan Syarif, 2012; Augustinova.J, 2013; Theodore Dickerson, 2013).

Georgin, J Dotto,G.L, Mazutti ,M.A. and Foletto , E.L, J.Environ. Chem.Eng., 4(2016)266.

Guo, P.Z. Ji, Q.Q. Zhang, L.L. Zhao, S.Y. and Zhao, X.S. Acta Physico-Chim.Sin, 27(2011)2836.

Hassan, A F. Youssef, A.M. "Preparation and Character; zation of microporous Naott activated carbon from hydrofluoric and leached rice husk and its application for lead (11) adsorption, AC carbon letters, 15(1)57-66,2014.

He, T. Ren, X. Nie, J. Ying, J. Cai, K. "Investigation of Imbalanced Activated carbon Electrode Super capacitors". International Journal of Electrochemistry, 201, 801-217, 2015.

Jiang, Q. Zhang, Z. Yin, Gou, S. Wang Z. S. and Feng, C. Appl.Susf.Su., 379(2016)73.

Lee, J.W, B.Hawkins, D.M.Day, D.C.Reicosky, 2010. Sustanablity: the capacity of 878 smokeless biomass phrolysis for energy production, global carbon capture and 879 sequestration. Energy and Environmental Science, 3:1695-1705.880.

Lee,S H.P.Jin, Y.T.Ahn and J.W.Chung, Water, Air & Soil Pollution, 226(2015)1.

Lv ,W. Wen, F. J. Xiang, Zhao, J. Li,L. Wang,L. Liu , Z. and Tian,Y. Electrochim. Acta, 176(2015)533.

Subramanian,V. Luo,C. Stephan,A.M. Nahm, Sabu Thomas, K.S. Wei,B. "Supercapacitors from Activated Carbon Derved from Banana Fibers." J.Phys-Chem. C,111,7527-7531,2007.

Wer, X. Li Y. and Gao, S. Mater, J. Chem.A,5 (2017)181

Wu, M.B. Li, R.C. He, X.J. Zhang, H.B. Sui W.B. and Tan, M.H. New Carbon Mater., 30(2015)86.

J. Myanmar Acad. Arts Sci. 2020 **Vol. XVIII.No.2C**

ELEMENTAL AND MICROSTRUCTURAL CHARACTERIZATIONS OF IRON CONCRETION

Khaing Nway Win[1], Htay Htay Win[2], Mar Mar Swe[3]

Abstract

A sample of Iron concreation is taken from the Moenyin Township, Kachin State. The elemental and characterization of this iron concretion are examined by utilizing XRD (X-ray diffraction) and EDXRF (Energy Dispersive X-ray Flurorescence) which are very useful for qualitative and quantitative analysis. The microstructural of iron concretion was studied by SEM(scanning electron microscopy). This study shows the different minerals in the sample and provide valuable information.

Keywords - Iron Concretion, XRD, EDXRF,SEM

Introduction

A concretion is hard, compact mass of matter formed by the precipitation of mineral cement within the spaces between particles and is found in sedimentary rock or soil. A iron concretion is the most abundant sedimentary rock. It is a rock composed mainly of clay size mineral grains and is also called a mud rock. It is a sedimentary rock that is usually from the compaction of at least 50 % silt and clay size particles. It can also contain organic material, iron oxide and heavy mineral grains. It is made up of very thin layers and has thin beds of either sandstone or limestone. The quantity of iron concretion depends on their thickness and extent, depth and pressure, fluid saturations, permeability and among other factors. Iron concretion can contain a wide range of minerals, although only the clay minerals and non clay mineral were found by X-ray diffraction. The type of clay found in iron concretion is a function of rock type and climate. A special variety of iron concretion is an iron rich material. A iron concretion was taken from Moenyin Township, Kachin State. Depositional environment was once thought to exert a considerable influence on clay mineralogy but it is now known that alteration of the clay framework does not occur, although there is a change in the exchangeable cation population. Rock type also plays its part in clay mineralogy. Illites probably derive from weathering of preexisting illites and chlorites from preexisting chlorites, thus certain rock type generate particular maineralogies. Black organics iron concretion are found in the earth. They can serve as a source rock for many oil and gas deposits. From the tiny particles of organic matter that were deposited with mud to form iron concretion. Iron concretion which are deposited in oxygen-rich environment often contain tiny particles of iron oxide or iron hydroxide minerals such as hematite, goethite or limonite. The presence of hematite can produce red iron concretion while the presence of limonite or goethite can produce yellow or brown iron concretion. High ratios of Fe^{+3}/ Fe^{+2} are associated with red colors and low with yellow or brown. Because the Fe^{+3}/ Fe^{+2} ratio is controlled by the oxidation state which in turn is controlled by the amount of organic matter in sediments, all color in iron concretion is ultimately controlled by the amount of organic matter present. The elemental analysis is characterized by using EDXRF (Energy Dispersive X-ray Fluorescence). The structural information is obtained by using the X-ray diffraction in the

---

[1] Dr, Lecturer, Department of Physics, University of Yangon

[2] Dr, Lecturer, Department of Physics, University of Yangon

[3] Dr, Lecturer, Department of Physics, University of Yangon

laboratory of UY. X-ray diffraction is widely used for the phase identification of a crystalline material and can provide valuable information. The objective of this experiment is to identify the different materials and grains size present in iron concretion.

Experiment

The range of particle size in the iron concretion is 16.12mm. The sample was made grounded to obtain powder by using pastel and motor. Experimental arrangement of sample preparation are shown in Figure 1(a-e). The elemental and structural characteristics are studied by X-ray diffraction (XRD) and energy dispersive X-ray fluorescence (EDXRF). Iron concretion was prepared by pressing into a pellet at 1 ton of dynamic pressure. The powder sample was put in the sample holder of the x-ray diffractometer and a test was conducted on it. The EDXRF spectrometer used was a tube excited system with molybdenum as anode, and silver in the secondary target arrangement. Figure 2 show as the x-ray diffractometers with interlocks and shielding. The beam function only with the door closed.

(a) (b)

Figure 1(a-b) Photographs of iron concretion

(c)

Figure 1(c) Photograph the diameter measurement of iron concretion

Figure 1(d) Sample preparation preparationpreations

Figure 1(e) Photograph of the top-view of as-prepared powder of iron concretion

Figure 2 photograph of X-ray diffractometers

Results and Discussion

X-Ray Diffraction (XRD) Analysis

X-ray diffraction is used to determine crystallinity of material. XRD uses the total X-ray scattering both the crystalline and amorphous phases to determine the crystallinity. The analysis of iron concretion powder was determined by using a X-ray Diffractomerter (Rigaku Miniflux 600). XRD was performed using monochromatic CuKα radiation (λ=1.54056Å¬) operated at 40kV (tube voltage) and 40mA (tube current). Sample was scanned from 10° to 70° in diffraction angle 2θ with a step-size of 0.02°. The X-ray diffractograms of iron concretion is shown in figure 3. The upper side of XRD profile was represented the observed profile while the lower side indicated the standard or reference JCPDS (Joint Committee on Powder Diffraction Standard) library file. On the XRD patterns, five peaks were clearly observed. They were (110), (120), (111), (221) and (151) respectively.

The crystallite size (G) was determined by Debye-Scherrer formula,

$$G = \frac{\beta\lambda}{B\cos\theta_B}$$

where, G = crystallite size (nm)

β = Scherrer constant ≈ 0.899

λ = wavelength of X-ray diffraction (1.54056Å)

B = FWHM (full width at half maximum peak)

θ_B = Bragg angle (deg)

The FWHM and crystallite size of iron concretion powder were shown in Table 1. The average crystallite size of iron concretion powder was in the range of 37.89 nm. The XRD measurement showed that all peaks of iron concretion were consisted with that iron concretion standard (JCPDS) file having a Al-substituted goethite.

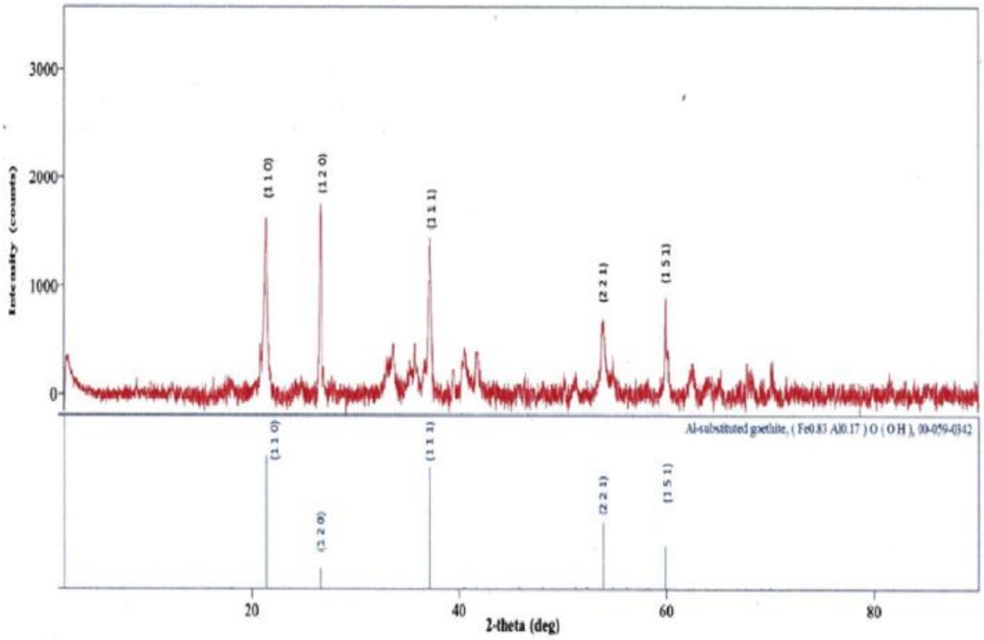

Figure 3 XRD pattern of iron concretion

Table 1 Crystallite size of iron concretion

No:	Peaks(hkl)	FWHM(deg)	Crystallite size (nm)
1	(110)	0.1647	49.03
2	(120)	0.1839	44.34
3	(111)	0.2194	31.16
4	(221)	0.2695	33.03
5	(151)	0.2870	31.91
		Average crystallite size	**= 37.89 nm**

EDXRF Analysis

The samples were collected from Moenyin Township, Kachin State. The samples were analyzed using EDXRF spectrometer at Universities' Research (URC) in University of Yangon. The spectrometer was operated at its optimum conditions. The spectrometer was operated at its optimum conditions. The detection unit is a Canberra Si (Li) detector with a resolution of 170eV at 5.9 keV. X-ray spectra were acquired on a PC-based MCA, Canberra S100. The sample was then irradiated for 3000s. The X-ray tube was operated at its optimized condition of 40 kV and 10mA. The EDXRF spectrum of the iron concretion was then recorded. It is shown in Figure 4.The concentration of elements contained in iron concretion sample, are listed in Table 2.

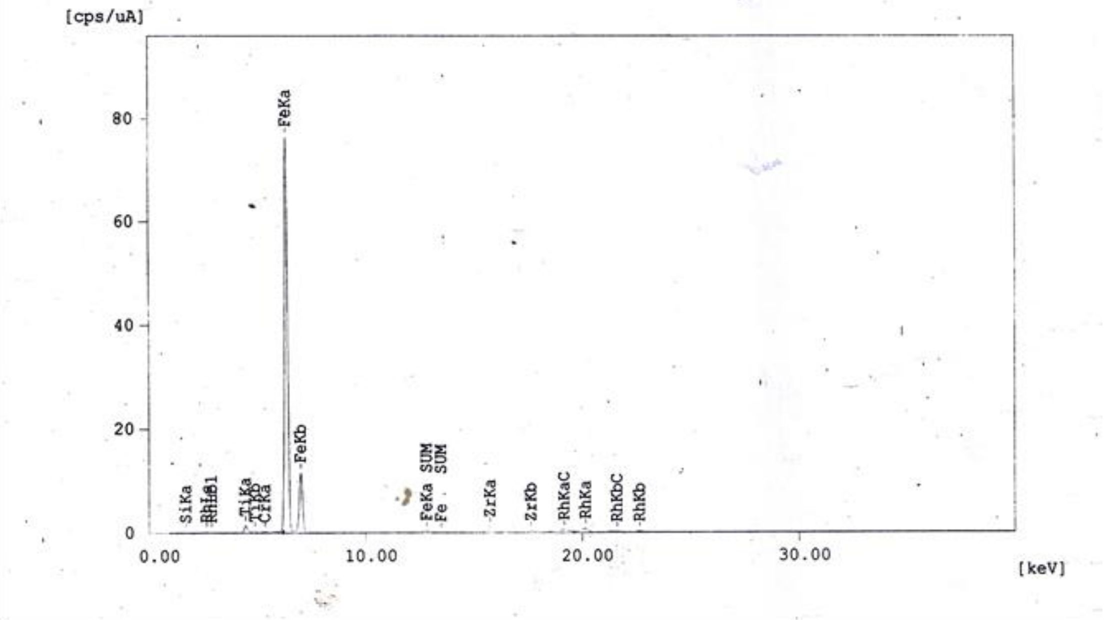

Figure 4 The EDXRF spectrum of iron concretion

Table 2 The elemental composition in iron concretions

Atomic No(Z)	Element	Concentration(%)
26	Fe	85.694
14	Si	11.017
81	Ti	2.473
40	Zr	0.706
24	Cr	0.110

Scanning Electron Microscopy (SEM) Analysis

The Scanning Electron Microscopy (SEM) is a type of electron microscope capable of producing high-resolution image of a surface iron concretion powder were obtained by calcination of the sample. Figure 5 showed the SEM analysis of iron concretion powder exhibit grained microstructure with small crystalline size. The grain size were calculated by using well known bar code system with Image J software. The average grain size of the sample powder was found to be about 1.145 µm. From the image, it was clearly found that the little amount of pores and grain growth pattern. This figure indicated that most of the grain size was regular structure and a few number of larggrain size was found. The sample powder appear with little agglomeration in light contrast with background particles. According to SEM, analysis, the SEM image was successfully implemented the smooth in morphology, grain size and particle quality of iron concretion powders.

Figure 5 The surface morphology of iron concretion

Conclusions

Iron concretion can contain large amounts of various minerals depending on its burial history and sedimentation. Elemental and structural characterizations of iron- concretion were characterized by XRD and EDXRF measurements Experimental results concluded as follows. XRD results show that the sample is Al-substituted goethite structure, their different crystalline structures make them distinct minerals. The mineral enthusiast chemical formula was Fe Al O(OH). EDXRF results show that the elemental compositions in iron concretion are Fe, Si, Ti, Zr, Cr are found in this sample. There were more concentration of iron in this sample. According to the SEM image the grain size was regular structure and a few number of large grain size was found. Goethite is a common weathering product of iron-bearing minerals. Iron concretion resists earthquake. So, it can be used for construction such as the wall, the ceiling and the building block. The research can be used as a fertilizer.

Acknowledgements

I wish to express my sincere thanks to Professor Dr. Khin Khin Win, PhD YU Head of Department of Physics, University of Yangon, for her kind permission and encouragement to carry out this research. I also like to thank to all respectable professors of physics department university of Yangon for useful their advise me.

References

He.,F and For Van Espen, P.J., Anal Chem, (1991) 63, 2237.

Jenkine,R,. Gould.,R.W and Geduke, D., (1981) "Quantitative X-ray Sp " (New York: Marcel Dekker)

Markowicz,A.A., and Van Grieken, R. E (1998) Anal Chem, 60, 28.

Van Grieken,R., Markowicz.,A and Torok,Sz., (1986) Anal Chem, 58, 825.

Website

1. www.spiritrockshoqp.com

2. https://en.m.wikpedia.org

J. Myanmar Acad. Arts Sci. 2020 **Vol. XVIII.No.2C**

PREPARATION OF TiO_2 PHOTO ELECTRODE FOR DYE- SENSITIZED SOLAR CELLS APPLICATION

Me Me Aung[1], Htay Htay Win[2], Thin Thin Kyu [3], Zin Min Myat[4]

Abstract

Green synthesis of TiO_2 nanoparticles was produced by Aloe Vera leaf. The structural properties of TiO_2 nanoparticles were characterized by X- ray diffraction (XRD). The chemical properties of TiO_2 nanoparticles were analyzed by Fourier Transform Infrared Spectroscopy (FTIR). The surface morphology and optical properties of TiO_2 nanoparticles were characterized by Scanning Electron Microscopy (SEM) and Ultraviolent Spectroscope (UV-Vis) measurements. According to experiment result, the extraction of Aloe Vera leaf dyne solution was performed and employed as natural dyne sensitizer in DSSC.

Keywords: TiO_2 Nanoparticles, Aloe Vera leaf Green Synthesis, XRD, FTIR, FESEM, UV-Vis.

Introduction

Nanoparticles (metal and metal oxides) of various types have been widely employed via physical and chemical methods. Nanoparticles are generally defined as particulate matter with at least one dimension that is less than 100 nm. Subgroups are examples of environmentally relevant types: inorganic nanoparticles and organic nanoparticles.

Titanium dioxide is solid inorganic substance, which is a white color metal oxide. TiO_2 is poorly soluble, non-flammable, thermally stable and not classified as hazardous according to the United Nations (UN) Globally Harmonized System (GHS) of Classification and Labeling of Chemicals.[Aadarsh Mishra, 2014] TiO_2 is formed by elements Titanium of atomic number 22 from IV B group and Oxygen of atomic number 8 from VI A group. It can exhibit three different phases in nano range at the different temperature, such as Anatase, Rutile and Brookite. Among these phases, Anatase has been proved to have extraordinary chemical and physical properties for environmental remediation.[Rajneesh Mohan, etal,2013] It is also having high quality properties, such as hydrophobicity, non-wettability and large band gap. Hence, it is used in the various industrial applications: dye sensitized solar cell, photo catalysis, self-cleaning, charge spreading devices, chemical sensors, microelectronics, electrochemistry, antibacterial products and textiles.[Saowaluk Boonyod, etal,(2011)]Different types of approaches are available for synthesis of titanium dioxide nano particles, those are solution Combustion, Sol-Gel, Hydrothermal, Solvothermal, Microwave Assisted, co-precipitation, Chemical Vapor Deposition and Green synthesis. The green synthesis process is eco-friendly technique due to use of extracts of plant (leave, flower, seed and peels), bacteria, fungi and enzymes for synthesis of titanium dioxide nanoparticles instead of large quantity of chemicals.[Vijaylaxmee Mishra, etal,(2014)] Green synthesis provides more advantages over physical methods and chemical methods because it is very cost effective, easy process and scalable for large scale production. This method not required high temperatures, high pressure, costly equipment and hazards chemicals.

---

[1] Dr, Assistant Lecturer, Department of Physics, University of Yangon

[2] Lecturer, Department of Physics, University of Yangon

[3] Assistant Lecturer, Department of Physics, University of Yangon

[4] Assistant Lecturer, Department of Physics, University of Yangon

The present work green synthesis of TiO_2 nanoparticles is based on the Aloe Vera plant extract. Aloe Vera is oldest medicinal plant ever known and a most applied medicinal plant, which is succulent plant species, the species is frequently cited as being used in herbal medicine since the beginning of the first century AD. It is a stem less plant growing to 60-100 cm (24-39 in) tall and the leaves are thick and fleshy, green to grey-green, with some varieties showing white flecks on the upper and lower stem surfaces.[Yuvasree. P., etal, 2013]The role of some inorganic elements like vanadium, zinc, sodium, potassium, magnesium, aluminum, iron, nickel, cadmium, copper, cobalt and manganese in the improvement of impaired glucose tolerance and their indirect role in the management of diabetes mellitus, hypoglycemic, wound healing and anti-inflammatory effects are being used, which contain both organic and inorganic constituents.

Experimental Procedures

Preparation of TiO_2 Nanoparticles

In various leaves, Aloe Vera leaves were collected from Gyobingauk Township, Bago Division, Myanmar. The leaves of Aloe Vera were separated from plant, which were washed thoroughly with tap water for three times and cut into small pieces. The raw materials were firstly weighed by electronic balance. Took 30g of the leaves into 100 ml distilled water boiled for 3hr at 80°C. The extract was filtered using filter paper. The filtrate was stored for the synthesis of nanoparticles. To synthesis the TiO_2 nanoparticles, dissolve 1.0 g of Titanium (IV) is opropoxide (TTIP) in 100 ml of distilled water. The mixture was kept under constant stirring on a magnetic stirrer for 4 hr continuously. At that time, added leaves extract drop wise under constant stirring up to achieve pH of solution became 7. The pH was measured using a pH test paper. In this process, and then separate this nanoparticles using filter paper. Obtained materials washed with water repeatedly to remove the by products. And then, the residual parts were dried at 160°C for 12 hours. After that the powder was put in the agate mortar and it was ground for 2 hr to reduce the particle size. In order to be dried, the nanoparticles were calcined at 500°C for 4 hr. The block diagram of preparation TiO_2 nanoparticles was shown in Figure1.The photos of sample preparation of TiO_2 nanoparticles from Aloe Vera leaves extract were shown in Figure 2.

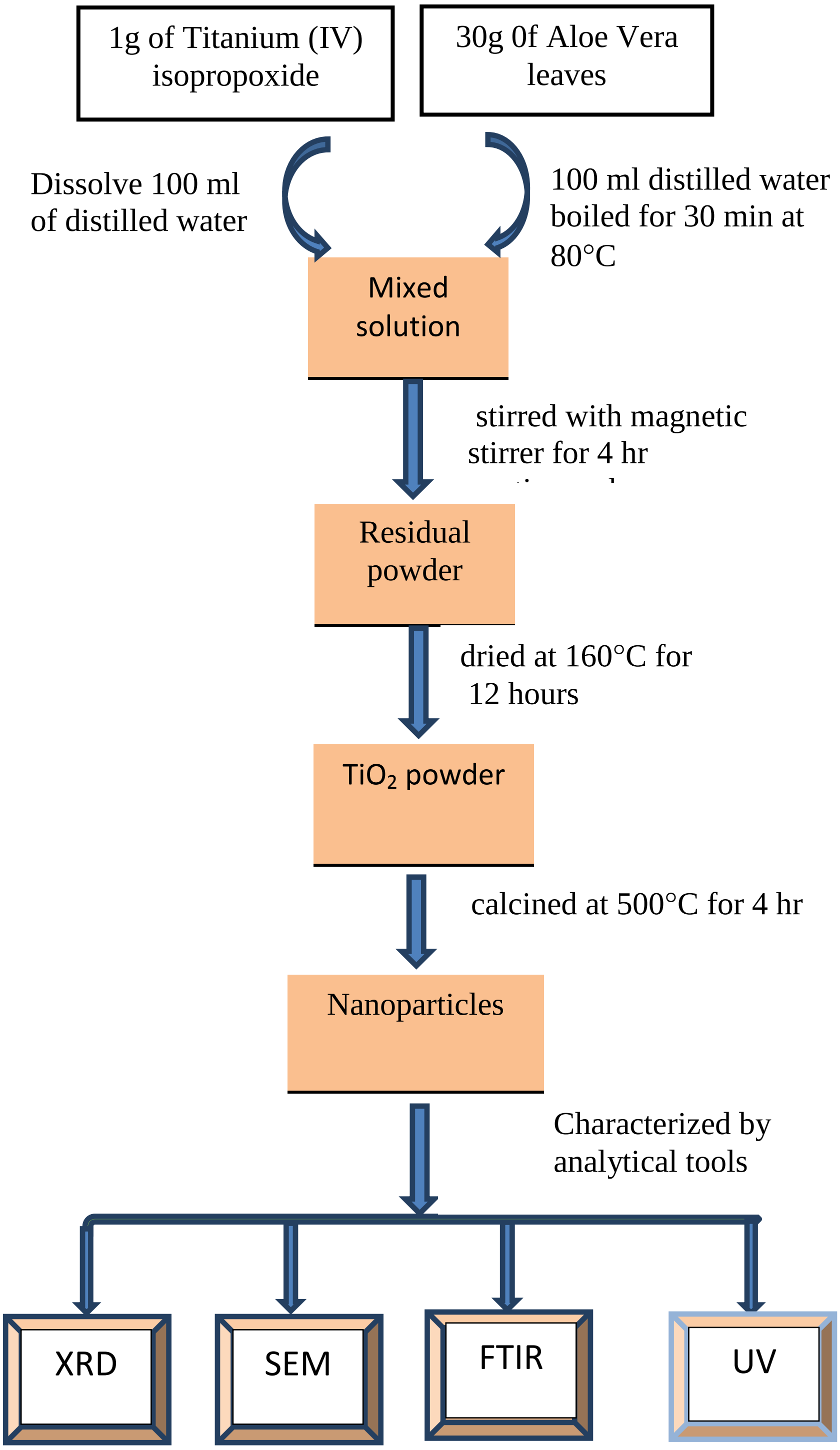

Figure 1 The block diagram of Preparation TiO_2 Nanoparticles

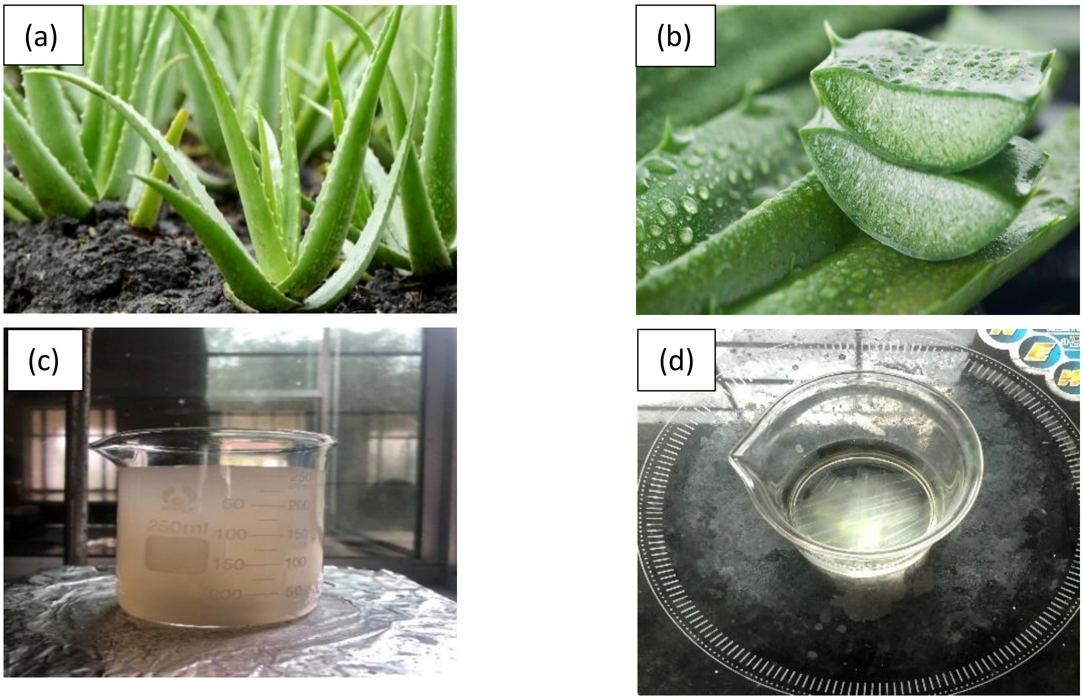

Figure 2(a) Aloe Vera plant, (b) Separated Pieces of Aloe Vera, (c) In Heating Process, (d) Juice of Leaves Extract

Characterization of TiO_2 nanoparticles

The crystal structure, lattic parameter and average crystallite size was measured by Brooker D8 X-ray diffractometer using Cu-kα-radiation (λ=0.154 nm). Grain size and morphology of the nanoparticles were observed estimated by S 3400 N Scanning Electron Microscope. FTIR analysis was employed to study the functional groups present in Titanium dioxide nanoparticles by SHIMIDUZU, JAPAN.UV-visible absorption spectra of TiO_2 nanoparticles were recorded on SHIMIDUZU, JAPAN 1800 sphectrophotometer.

Results and Discussion

XRD Analysis of TiO_2 Nanoparticles

The synthesized Titanium dioxide (TiO_2) nanoparticles obtained from green sythesis method at temperature 500°C is shown in Figure 3. All the peaks height and peaks position were good agreements with standard ICDD library file.On the TiO_2 XRD pattern, five peaks were clearly observed. XRD pattern of the (TiO_2) nanoparticles showed the present of anatase form which can be denoted at 2θ peaks at 25°, 38°, 48°, 55°, 62°,which are found to be (1 01), (1 0 3), (2 0 0),(1 0 5) and (2 1 3)respectively and confirmed the nanocrystallite nature. The (1 0 1) reflection peak becomes more intense and sharper and the crystal structure of TiO_2 was tetragonal. As the width of the peak increase size of particle size decrease, which resembles that present material in nano range. The lattice parameters were obtained a=b=3.7857 nm and c=9.5289 nm. The average crystallite size was measured by Debye – Schereer's equation as mentioned below.

$$D = \frac{K.\lambda}{\beta.Cos\ \theta}$$

Where D is the average crystallite size of the particles, K is Debye scherrer's constant (=0.94), λ is the wavelength of the CuKα- radiation (=0.154 nm), β is the full width half maximum (FWHM) of the peak, θ is the Bragg's angle. The average crystallite size was measured as 25.74 nm using the above formula.

Table 1 The comparison of crystallite size of TiO_2 nanoparticles

International Journal Values	K.Venkateswara Rao,etal,(IJARPS), 2015 crystallite size =20 nm
	Abdul Abdul Rahuman,etal,(APJOTM) ,2014 crystallite size =32.58 nm
Observed sample value	crystallite size =24.89 nm

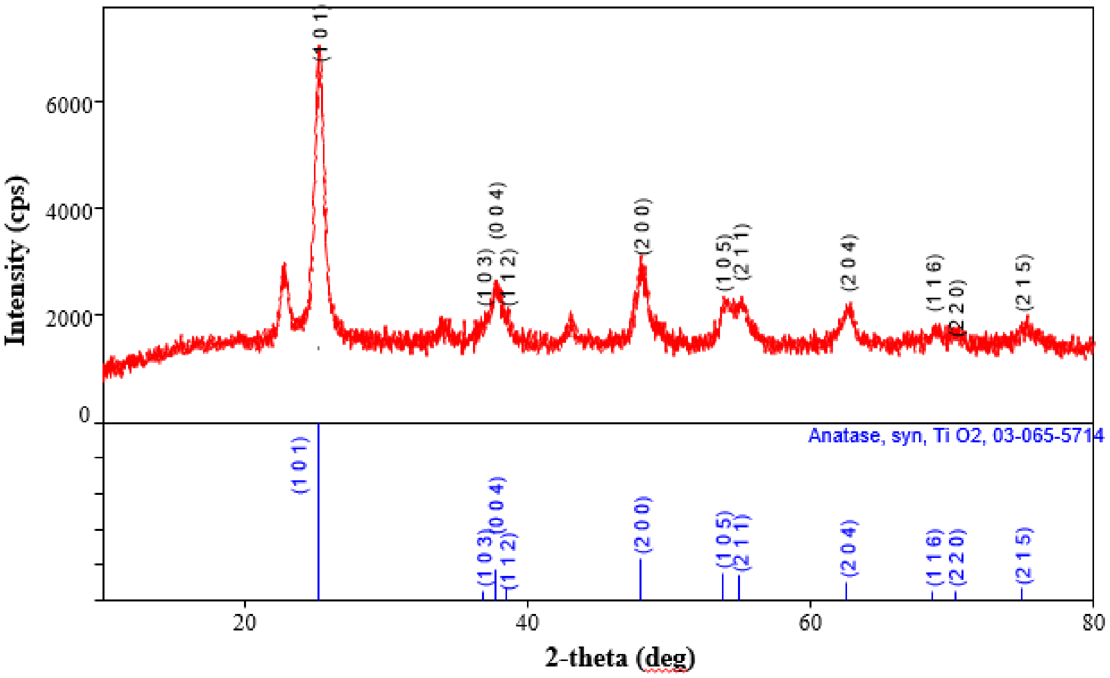

Figure 3 X – ray diffraction patterns of Synthesized TiO_2 NPs

SEM Analysis of TiO_2 Nanoparticles

The surface morphology features of synthesized TiO_2 nanoparticles were examined by Scanning Electron Microscope (SEM) shown in Figure 4. The average grain sizes were calculated by using well known bar code system with Image J software. Around the examined area, the grain size of TiO_2 was estimated to be 1.1723 µm. In addition overall observation of TiO_2 powder indicted a good microstructure with no discontinuities in terms of microracks. This figure indicated that most of the grain size was regular structure and a few number of large grain size were found. It looks fairly dense and rough. The morphology was still observed, becoming denser and smoother. The TiO_2 nanoparticles were showing irregular particles structure.

Figure 4 FESEM image of Synthesized TiO_2 NPs

FTIR Analysis of TiO_2 Nanoparticles

FTIR spectroscopy was applied to measure the chemical properties and absorption of energy from the range of 500-4000 cm^{-1} by studied samples. Figure 5 represents the FTIR spectra of green synthesis derived TiO_2. According to FTIR images in the functional group region, the outstanding wide absoration band is observed within 3500-3000 cm^{-1} region, corresponding to the axial OH deformation. This absorption is originated from variations of water present in samples. The samples present signal at 3438.70 and 1640.26 cm^{-1} in the spectra are due to the stretching and bending vibration of the –OH group. In the spectrum of pure TiO_2, the peaks at 491.88 cm^{-1} show stretching vibration of Ti-O and peaks at 1425.44 cm^{-1} shows stretching vibrations of Ti-O-Ti. Peaks at 3194.23cm^{-1} indicates the presence of amines, Peaks at 3294.53 cm^{-1} indicates the presence of Alkynes, Peaks at 1616.40 cm^{-1} indicates the presence of pyridines.

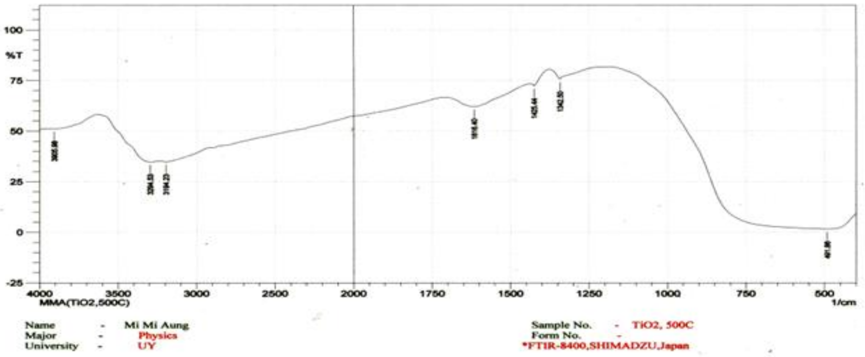

Figure 5 FTIR Analysis image of Synthesized TiO_2 NPs

UV-Vis Measurement of TiO_2 Nanoparticles

The optical band gap of the TiO_2 nanoparticles were examined using UV- Vis spectroscopy. The absorption spectrum of TiO_2 nanoparticles in the UV-Vis spectrum region ranging from 200 nm to 800 nm was shown in Figure 5. The optical bandgap is obtained by Tauc's equation, $\alpha h\upsilon = A\ (h\upsilon - E_g)^n$. where, A is constant , $h\upsilon$ is photon energy, E_g is the allowed energy band gap, n is ½ for allowed direct transition and n is 2 for indirect trasition. The extrapolation of the plot of $(\alpha h\upsilon)^2$ on the Y- axis as a function of($h\upsilon$) on the X - axis were provided a good estimate of the band gap of the material under investigation was shown in Figure

6. According to the absorption spectra, the energy band gap E_g for sample is 3.31 eV. The energy band gap of the standard sample is 3.2 eV and the energy band gap of prepare sample is similar to that of standard sample. It was found that the energy band gap is 3.2 eV in other research paper (“Green Synthesis of TiO_2Nanoparticles Using Aloe Vera Extract”, K. Ganapathi Rao, January 2015).

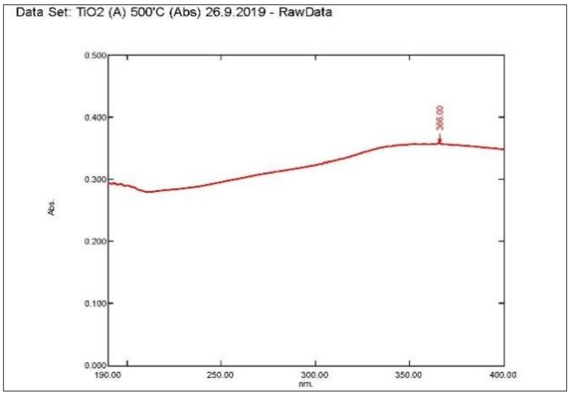

Figure 5 UV-Vis analysis of Synthesized TiO_2 NPs

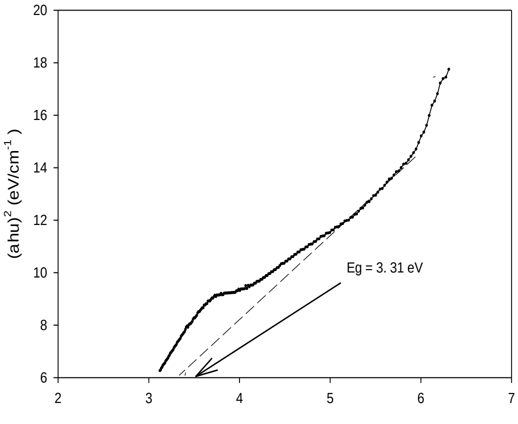

Figure 6 UV-Vis analysis of Synthesized TiO_2 NPs

Conclusions

In the research work, TiO_2 nanoparticles were successfully synthesized using green synthesis method. Then the prepared nanoparticles were characterized by modern analytical tools such as XRD, SEM, FTIR and UV- Vis. From XRD analysis average crystallite size of the sample was obtained 25.74 nm. It was observed that the tetragonal structure was formed. The tetragonal irregular particles structure was observed in SEM image. The average particle size was calculated 1.1723 μm with Image J software. The FTIR analysis confirmed the chemical composition of TiO_2 nanoparticles using Aloe Vera leaves extract corresponding to -OH group. The optical properties were studied by UV-Visible Spectroscopy it infers that the wavelength was 366 nm and energy band gap was 3.31eV. These above results showed that as prepared TiO_2 particles were in the nano range. According to the experimental result, synthesized TiO_2 nanoparticles can use in potential application as (DSSC).

Acknowledgements

This research was totally implemented at Department of Physics, University of Yangon in Myanmar (2018-2019).

References

Aadarsh Mishra, (2014),"Analysis Of Titanium Dioxide And Its Application In Industry", *Int. J. Mech.Eng. & Rob. Res.*, 3(3), 7pages.

Rajneesh Mohan, etal,(2013), "Water-dispersible TiO_2 nanoparticles via a biphasic solvothermal reaction method", *Nanoscale Research Letters*, 8(1),4 pages.

Saowaluk Boonyod,etal, (2011) ,"Antibacterial Activity of $TiO_2$and Fe^{3+} doped TiO_2 Nanoparticles Synthesized at Low Temperature", *Advanced Materials Research*, 214, 197.

Vijaylaxmee Mishra, etal, (2014) "A Review on Green Synthesis of Nanoparticles and Evaluation of Antimicrobial Activity",*International Journal of Green and Herbal Chemistry*, 3(1), 081.

Yuvasree. P., etal, (2013)," Biosynthesis of Silver Nanoparticles from Aloe vera Plant Extract and its Antimicrobial Activity Against Multidrug Resistant Pathogens", *Proceedings of the International Conference on Advanced Nanomaterials &Emerging Engineering Technologies*, Pp 84-86.

J. Myanmar Acad. Arts Sci. 2020 **Vol. XVIII.No.2C**

THE HETEROEPITAXIAL GROWTH OF π-CONJUGATED ORGANIC MOLECULES ON INORGANIC SINGLE CRYSTAL SAPPHIRE SUBSTRATE

Aye Myint Moh[1], Seiji Watase[2], Masanobu Izaki[3]

Abstract

The structure of organic semiconductor layers strongly affects the performance of the organic semiconductor-based devices such as organic thin film transistors (OTFTs), organic field effect transistors (OFETs), organic light emitting diodes (OLEDs) and organic photovoltaic cells (OPVs). The layer structure such as preferred orientation is controlled by the heteroepitaxial growth of organic molecules on different type of substrates. The π-conjugated organic semiconductor materials were deposited on single crystal sapphire substrate by vacuum thermal evaporation. The heteroepitaxial growth of π-conjugated n-type semiconductor of N, N'-dioctyl-3,4,9,10-perylenedicarboximide (PTCDI-C8) and p-type semiconductor of 2,7-dioctyl [1] benzothieno [3,2-b][1] benzothiophene (C8-BTBT) on single crystal Al_2O_3 sapphire substrates were investigated by X-ray diffraction analysis and atomic force microscopy observation. The (001) out-of-plane orientation of organic layers were developed on single crystal sapphire substrates for all prepared samples irrespective of the deposited organic materials we used in this research. The needle-shape PTCDI-C8 grains and layer-by-layer islands growth of C8-BTBT layers on (0001) C-sapphire substrate were observed in AFM observation. The PTCDI-C8 and C8-BTBT layers showed characteristic of its absorption spectra.

Keywords: π-conjugated organic molecules, heteroepitaxial growth, sapphire substrate, vacuum thermal evaporation

Introduction

The organic semiconductors have been successfully employed in electronics and optoelectronic devices such as organic field effect transistors (OFETs), organic light emitting diodes (OLEDs), and organic photovoltaic cells (OPVs). (C.D. Dimitrakopoulos, et al, 2001, 2002) (A. Facchetti, et al 2007), (C.W. Tang, et al, 1989), (H. Hoppe, et al, 2004), (T. Uemura, et al, 2009). In addition to that of devices, it is possible to be applied in application such as magnetoresistance devices. (F. Sawano, et al, 2005), (S. Sakai, et al, 2006). The device performance mainly relies on the crystal structure including the orientation and grain structure of the prepared-organic layers. (H.N. Tsao, et al, 2009), (F. Dinelli, et al, 2016). The structure has been controlled by optimizing the type of substrate materials as flexible substrates or metal substrates, in addition to orientation controlled substrates, (H. Huang, et al, 2016), (E.J. Kintzel, et al, 2006), and the growth containing the preparation processes and conditions such as substrate temperature, deposition rate, vacuum pressure and layer thickness. (L.Zhang, et al, 2015) (A. Andreev, et al, 2003).

Perylene derivatives of N, N'-dioctyl-3,4,9,10-perylenedicarboximide (PTCDI-C8) was potential material to fabricate in molecular based devices due to its mobility up to 0.6 $cm^2V^{-1}s^{-1}$. (P.R.L. Malenfant, et al, 2002). The 1D-PTCDI-C8 nanoribbons were prepared by a rapid transfer method, and the optical properties of this material made it possible to be utilized in

---

[1] Dr, Assistant Lecturer, Department of Physics, University of Yangon, Myanmar

[2] Osaka Municipal Technical Research Institute, Japan

[3] Graduate School of Engineering, Toyohashi University of Technology, Japan

optoelectronic circuitry and laser resonator. (C.O.N. Spectus, et al, 2008), (T. Abhijith, et al, 2015). The unit cell of the PTCDI-C8 was reported by the group of A.L. Briseno, et al, 2007 and (T.N. Krauss, et al, 2008) and it has triclinic lattice structure with two different values of lattice constants for the bulk and films of PTCDI-C8.

One of the BTBT derivatives of acceptor material, 2,7dioctyl [1] benzothieno [3,2-b][1] benzothiophene, is one of the promising materials to be used in photovoltaic and optoelectronic devices. It has been reported that high charge carrier mobility of ~ 43 $cm^2 V^{-1} s^{-1}$ were achieved in solution-based organic field effect transistor. We have reported that the (001)-2,7-dioctyl[1]benzothieno[3,2-b][1]benzothiophene (C8-BTBT) layers were grown on aluminium oxide Al_2O_3 and magnesium oxide MgO single crystal substrates and the electrical resistivity related the grain structure of C8-BTBT layers. (A.M. Moh, et al, 2018).

In this paper, we investigated the effect of substrate orientation of (0001) and type (single crystal aluminium oxide) on the growth and orientation of vacuum thermal evaporated-PTCDI-C8 and C8-BTBT layers, and also investigated the heteroepitaxial growth of π-conjugated organic semiconductor materials on (0001) C-Sapphire substrate with X-ray diffraction (XRD), atomic force microscopy (AFM), and optical absorption spectra measurement.

Experimental Details

The annealing was carried out in air for 1 hr at 1200 °C for (0001)- Al_2O_3 (C-Sapphire) sapphire substrates before deposition of organic semiconductor layers. (0001)-Al_2O_3 (C-Sapphire) substrate were cleaned with acetone, ethanol and deionized water for 15 min each in ultrasonic bath. After cleaning the substrates, it is dried at room temperature. After cleaning the substrates, the 100-nm-thick PTCDI-C8 and C8-BTBT layers were deposited at substrate temperature of 100 °C at a pressure around 4×10^{-5} Pa on single crystal substrates of (0001)-Al_2O_3 (C-Sapphire) substrate by a vacuum thermal evaporation system (ULVAC, VTS-350 ERH/M) connected with turbo molecular pump and oil-free scroll vacuum pump. The deposition rate 0.1 nm/s was controlled by a quartz crystal deposition control system (ULVAC, CRTM-6000G).

To characterize the heteroepitaxial growth of PTCDI-C8 and C8-BTBT layers, vacuum evaporated 100 nm-thick-semiconductor layers were prepared on C-Sapphire substrate at substrate temperature 100 °C. The thickness of the organic layers was determined by a surface profiler system (ULVAC, Dek Tak 150). The out-of-plane X-ray diffraction were performed at 2θ value from 5 degrees to 30 degrees by a $\theta/2\theta$ scanning technique using Rigaku RINT 2500 X-ray diffractometer at monochromatic CuKα radiation operated at 40 kV, 100 mA with a wavelength (λ = 0.154059 nm). Surface morphologies were observed by an atomic force microscopy (AFM, Shimadzu, SPM-9700 Kai) in dynamic mode in air. Absorption spectra measurements were performed using a UV-VIS-NIR spectrophotometer (HITACHI, U4100) with a reference of (0001) C-Sapphire bare substrate.

Results and discussion

X-ray diffraction method was performed to analyse the structure and orientation of the vacuum thermal-evaporated semiconducting layers prepared on (0001) C-sapphire substrate. The PTCDI-C8 possesses a triclinic lattice with a = 0.900 nm, b = 0.489 nm, c = 2.165 nm,

α = 95.0 degree, β = 100.7 degree, and γ = 112.8 degree, and the lattice parameters varied depending on the type of the PTCDI-C8 such as powder type and layer type. (A.L. Briseno, et al, 2007), (T.N. Krauss, et al, 2008), (T.N. Krauss, et al 2009). The Al_2O_3, C-sapphire substrate possesses a hexagonal lattice with a = 0.47589 nm, and c = 1.2991 nm. The lattice mismatch was estimated to be approximately 0.58% for a-axis and 2.68% for b-axis of PTCDI-C8 for the lattice relationship of $(001)_{\text{PTCDI-C8}}$ is parallel to the substrate of single crystal C-Sapphire (0001)Al_2O_3. Although the lattice mismatch varied in wide range between the substrate material of Al_2O_3 sapphire substrate and PTCDI-C8, but the lattice mismatch between the molecule of PTCDI-C8 and substrate did not affect the out-of-plane orientation of the PTCDI-C8 layers by the X-ray diffraction patterns.

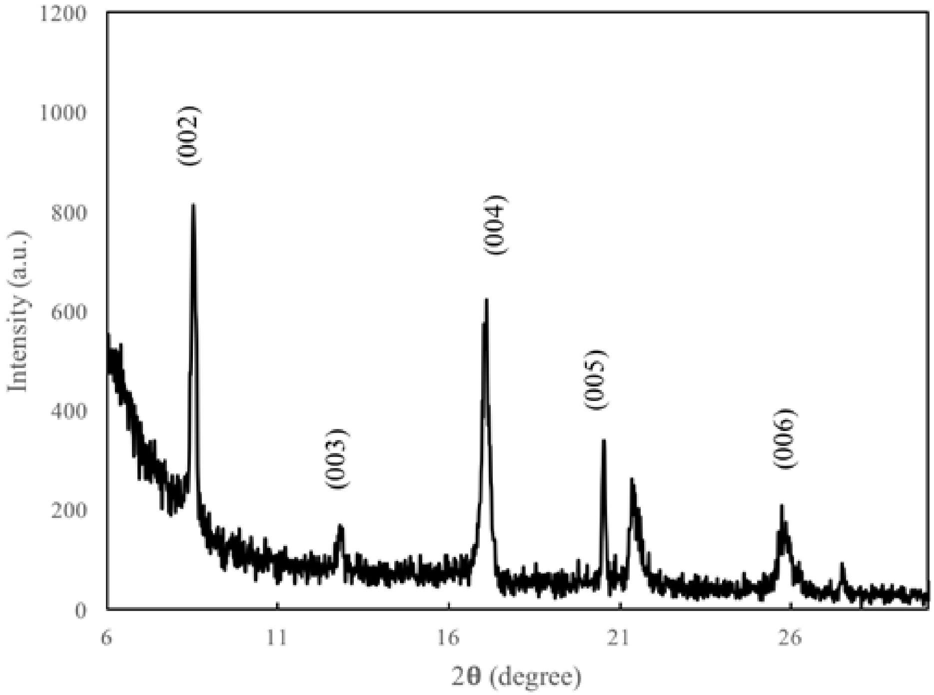

Figure 1 X-ray diffraction pattern of PTCDI-C8 layers prepared on C-sapphire substrate at 100 °C.

Figure 1 shows out-of-plane X-ray diffraction patterns for 100-nm-thick PTCDI-C8 layers prepared at substrate temperature 100 °C. The diffracted X-ray peaks could be observed from 8.4 degrees and each approximately 4.2 degrees, and these peaks were assigned as (002), (003), (004), and (005) planes, respectively. The peak at around 21 degrees which was originated from the single crystal C-sapphire substrate. The interlayer spacing d of the (002) plane of 100 nm thick vacuum thermal evaporated-PTCDI-C8 layers could be estimated to be 1.03 nm, which was close to 0.98 nm calculated from the lattice parameters mentioned above. It was confirmed from the out-of-plane X-ray diffraction patterns that PTCDI-C8 layers possessed the (001)-out-of-plane orientation, in which PTCDI-C8 molecules with almost upright standing position were preferably to grow on C-sapphire substrate. The lattice relationship between PTCDI-C8 layers and substrate materials could be identified as; $(001)_{\text{PTCDI-C8}}$ is parallel to the $(0001)_{\text{Al2O3}}$.

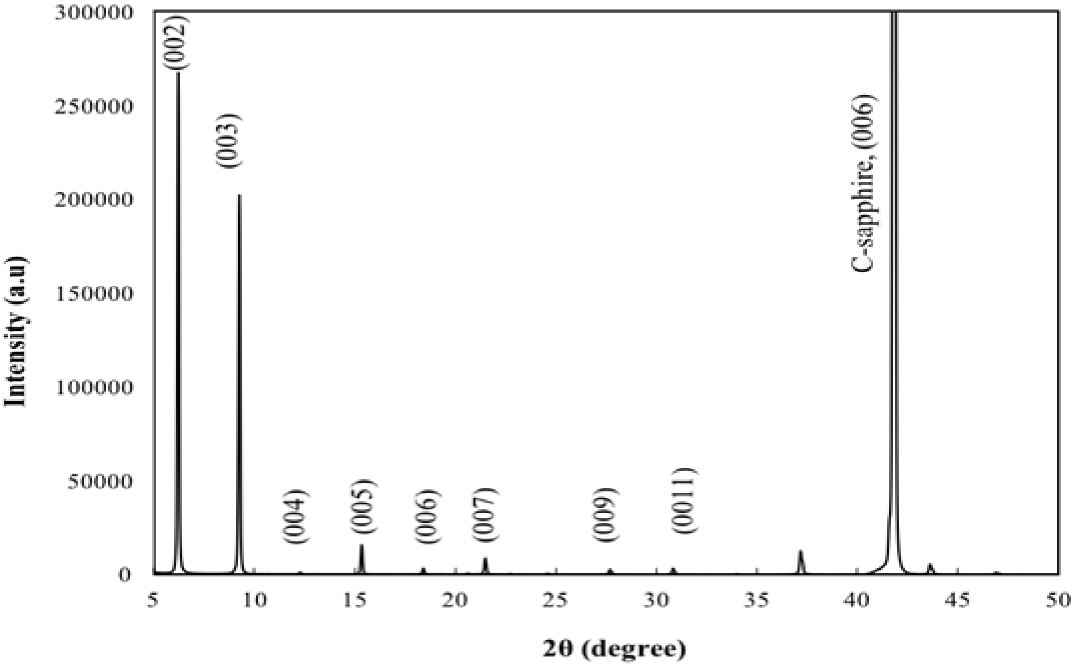

Figure 2 X-ray diffraction pattern of C8-BTBT layers prepared on C-sapphire substrate at 100 °C.

Figure 2 shows the X-ray diffraction pattern of 100 nm thick thermally evaporated- π-conjugated C8-BTBT molecules on C-sapphire substrate at substrate temperature 100 °C. Series of peaks could be assigned as (002), (003), (004), (005) etc, and planes of the C8-BTBT layer with the characteristic monoclinic lattice. The lattice mismatch was estimated to be approximately -24 and 4% on the a- and b-axes of C8-BTBT for the lattice relationship $(001)_{C8\text{-}BTBT}$ is parallel to that of the substrate material of $(0001)_{Al2O3}$. The growth mechanism governs by the strong π–π stacking between the molecules. Since the preferred orientation of the organic semiconducting molecules on C-sapphire substrate was (001) orientation without depending on the type of substrate.

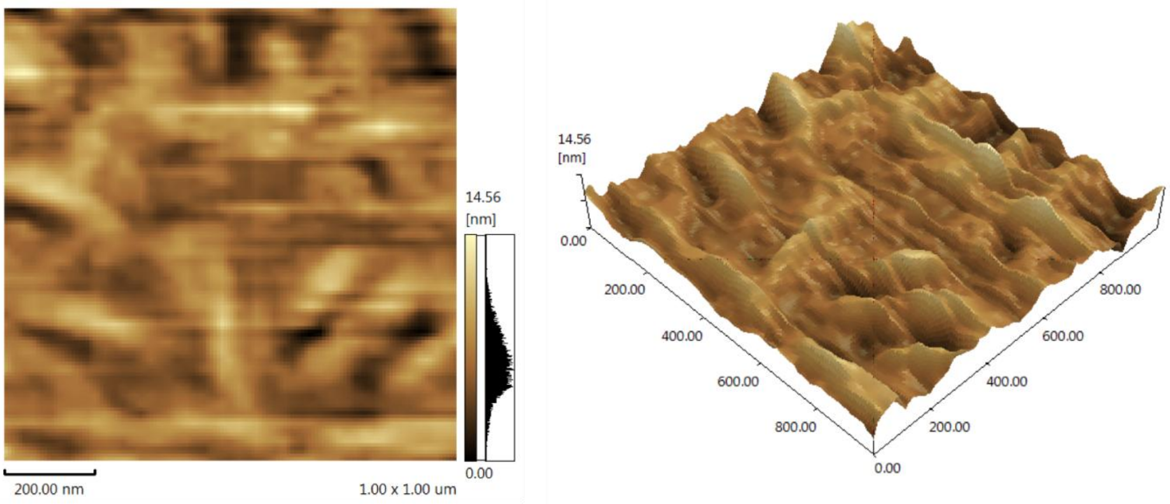

Figure 3 AFM images for 100-nm-thick-PTCDI-C8 layers prepared at substrate temperature of 100 °C.

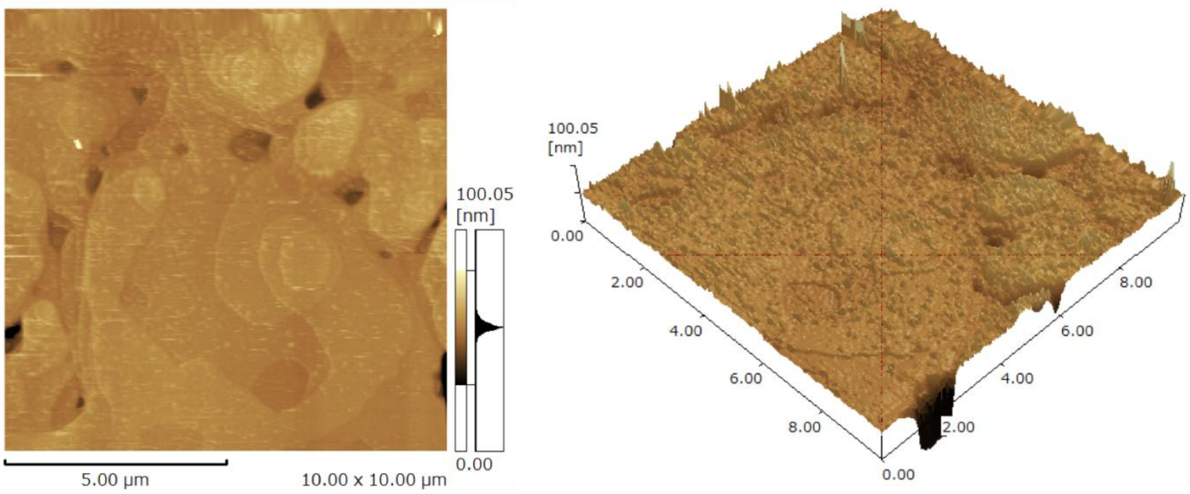

Figure 4 AFM images C8-BTBT layers prepared at 100 °C with the thickness of 100 nm.

The surface morphology of 100 nm-thick PTCDI-C8 and C8-BTBT layers prepared at 100 °C was observed by AFM. **Figure 3** shows AFM images for 100-nm-thick-PTCDI-C8 layers prepared at substrate temperature of 100 °C. Elongated needle-shape grains were formed over the C-sapphire substrate surface, and the grain length was estimated to be around 242 nm. The PTCDI-C8 layers possessed a relatively smooth surface with surface roughness (Ra) about 1.65 nm for prepared samples on (0001) C-sapphire substrate. The observed values show that the needle-shape grains grew with the smooth surface on growth of single crystal substrate. The needle-shape islands with the (001)-out-of-plane orientation were formed on the substrate by governing the π–π stacking. According to the experimental results, molecule-substrate interaction is weak and interaction between molecule-molecule is prominent.

Figure 4 shows AFM images of C8-BTBT layers prepared at 100 °C with the thickness of 100 nm. The layer by layer growth with several small islands were nucleated onto the early stage growth of continuous layers and the formation of continuous layer with several micro-meters wide, although some pores could be located between the coalescence islands. The surface roughness Ra could be estimated as 9.2 nm.

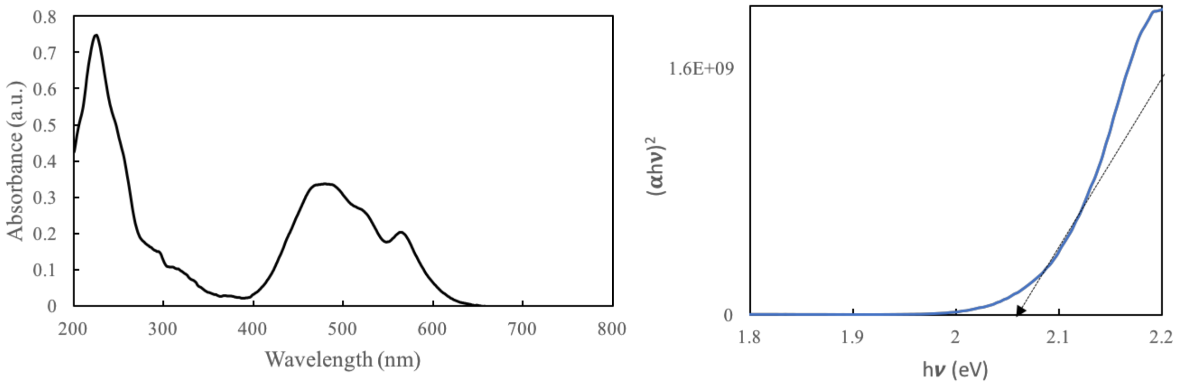

Figure 5 The optical absorption spectra for 100-nm-thick-PTCDI-C8 layers at 100 °C

Figure 5 shows the optical absorption spectra for 100-nm-thick-PTCDI-C8 layers at 100 °C. The PTCDI-C8 layers possessed three absorption peaks at the wavelength of 565 nm, 480 nm, and 228 nm and a weak shoulder at 525 nm. The spectra were almost the same in profile as that already reported for the PTCDI-C8 layer. (B. Mukherjee, et al, 2015). Since the C-sapphire substrate showed no absorption at wavelength from 200 to 700 nm, the absorption peaks at the wavelength of 228 nm also was originated from the PTCDI-C8 layers. The PTCDI-C8 layers showed an absorption edge at wavelength of 610 nm corresponding to the photon energy of 2.03 eV. The absorption edge wavelength was determined by extrapolating the linear line. The absorption coefficient was calculated from the absorbance at the wavelength of 228 nm and thickness, and value of 8.9×10^4 cm^{-1} for 100-nm-thick-PTCDI-C8 layers.

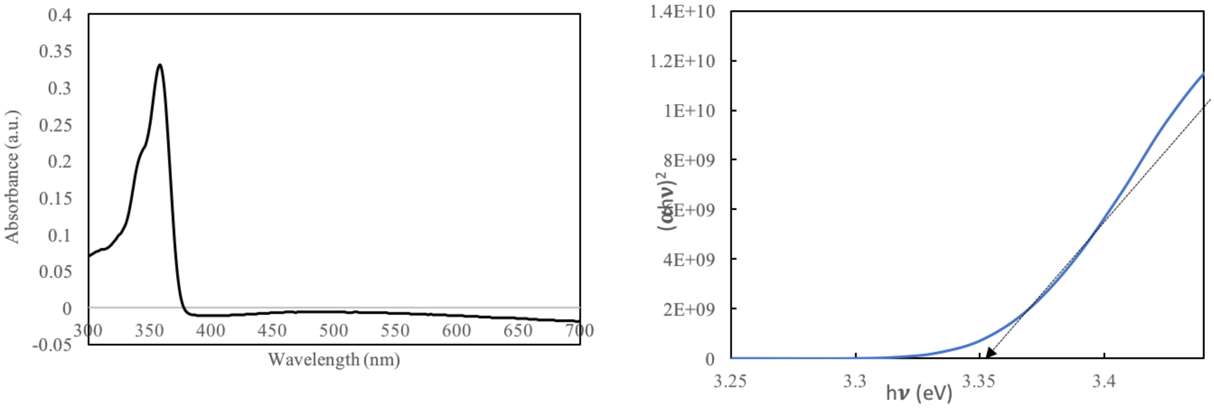

Figure 6 The optical absorption spectra for 100-nm-thick- C8-BTBT layers at substrate temperature 100 °C.

Figure 6 shows the optical absorption spectra for 100-nm-thick- C8-BTBT layers at substrate temperature 100 °C. The maximum absorption peak at the wavelength of 358 nm and a weak shoulder at the wavelength of approximately 340 nm could be estimated from absorption spectrum of prepared C_8-BTBT layer. The optical band gap energy of C8-BTBT layers was estimated to be 3.36 eV.

There was no effect of the atomic arrangement and lattice mismatch of (0001) Al_2O_3 C-Sapphire on the growth of the PTCDI-C8 layers, and C8-BTBT layers, the preferred orientation of (001) due to molecule-molecule interaction is stronger than those of molecule-substrate interaction. The growth of the PTCDI-C8 layers showed the similar growth to that of C8-BTBT layers.

Conclusions

π-conjugated organic semiconductors PTCDI-C8 and C8-BTBT layers were deposited on single crystal (0001) Al_2O_3, C-sapphire substrates by vacuum thermal evaporation technique. The (001)-out-of-plane orientation was developed on substrate material although there are large differences in the lattice mismatch. The needle-shape PTCDI-C8 grains and layer-by-layer of C8-BTBT islands growth were formed on C-Sapphire substrate. The optical band gap energy 2.03 eV of PTCDI-C8 and 3.36 eV of C8-BTBT were estimated from the absorption spectra of vacuum evaporated organic semiconductor layers. The results found in this experiment support the heteroepitaxial growth of organic semiconductors on the single crystal substrate without changing the orientation of deposited PTCDI-C8 and C8-BTBT, (001) preferred orientation on substrate which suggest that strong π-π bonding between molecules.

Acknowledgements

The authors are grateful to the financial support (Kakenhi, 16K12649) of Japan Society for the Promotion of Science (JSPS).

References

A. Andreev, R. Resel, D.M. Smilgies, H. Hoppe, G. Matt, H. Sitter, N.S. Sariciftci, D. Meissner, H. Plank, O. Zrzavecka, Oriented organic semiconductor thin films, Synth. Met. 138 (2003) 59–63. doi:10.1016/S0379-6779(03)00025-0.

A.Facchetti, Semiconductors for organic transistors, Mater. Today. 10 (2007) 28–37. doi:10.1016/S1369-7021(07)70017-2.

A. L. Briseno, S.C.B. Mannsfeld, C. Reese, J.M. Hancock, Y. Xiong, S.A. Jenekhe, Z. Bao, Perylenediimide Nanowires and Their Use in Fabricating Field-Effect Transistors and Complementary Inverters, Nano Lett. 7 (2007) 2847-2853. doi:10.1021/nl07149u.

A.M. Moh, K. Sasaki, T. Shinagawa, S. Watase, M. Izaki, Preferred orientation of 2,7-dioctyl[1]benzothieno [3,2-b][1]benzothiophene molecules on inorganic single crystal substrates with various orientations. Jpn. J. Appl. Phys. PV17001 (2018).

B. Mukherjee, Large photoresponse from a small molecule: Application in photodetector and pseudo-transistor, Optik (Stuttg). 126 (2015) 1258–1262. doi:10.1016/j.ijleo.2015.03.007.

C.D. Dimitrakopoulos, D.J. Mascaro, Organic thin-film transistors: A review of recent advances, IBM J. Reasearch Dev. 45 (2001) 11–27. doi:10.1147/rd.451.0011.

C.D. Dimitrakopoulos, P. Malenfant, Organic thin film transistors for large area electronics, Adv. Mater. 14 (2002) 99–117. doi:10.1002/1521-4095(20020116)14:2<99::aid-adma99>3.0.co;2-9.

C.O.N. Spectus, One-Dimensional Self-Assembley of Planar π-Conjugated Molecules : Adaptable Building Blocks for Organic Nanodevices, Acc. Chem. Res. 41 (2008) 1596-1608. doi:10.1021/ar800030w.

C.W. Tang, S.A. Vanslyke, Organic electroluminescent diodes, Appl. Phys. Lett. 51(1989) 913.doi:0003-6951/87/380913-03$01.00.

E.J. Kintzel, D.M. Smilgies, J.G. Skofronick, S.A. Safron, D.H. Van Winkle, Ultrathin film growth of p-phenylene oligomers on alkali halide substrates, J. Cryst. Growth. 289 (2006) 345–350. doi:10.1016/j.jcrysgro.2005.11.004.

F. Dinelli, M. Murgia, P. Levy, M. Cavallini, F. Biscarini, D.M. De Leeuw, Spatially Correlated Charge Transport in Organic Thin Film Transistors, Phys. Rev. Lett. 92 (2004) 7–11. doi:10.1103/PhysRevLett.92.116802.

F. Sawano, I. Terasaki, H. Mori, T. Mori, M. Watanabe, N. Ikeda, Y. Nogami, Y. Noda, An organic thyristor, Nature. 437 (2005) 522–524. doi:10.1038/nature04087.

H. Hoppe, N.S. Sariciftci, Organic solar cells: An overview, J. Mater. Res. 19 (2004) 1924–1945. doi:10.1557/JMR.2004.0252.

H. Huang, Y. Huang, S. Wang, M. Zhu, H. Xie, L. Zhang, X. Zheng, Q. Xie, D. Niu, Y. Gao, Van Der Waals Heterostructures between Small Organic Molecules and Layered Substrates, Crystals. 6 (2016) 113. doi:10.3390/cryst6090113.

H.N. Tsao, D. Cho, J.W. Andreasen, A. Rouhanipour, D.W. Breiby, W. Pisula, K. Müllen, The influence of morphology on high-performance polymer field-effect transistors, Adv. Mater. 21 (2009) 209–212. doi:10.1002/adma.200802032.

Joint Committee on Powder Diffraction Standards, Powder Diffraction File (International Data for Diffraction Data), No.00-042-1468.

Joint Committee on Powder Diffraction Standards, Powder Diffraction File (International Data for Diffraction Data), No. 00-004-0829.

L. Zhang, Y. Yang, H. Huang, L. Lyu, H. Zhang, N. Cao, H. Xie, X. Gao, D. Niu, Y. Gao, Thickness-dependent air-exposure-induced phase transition of CuPc ultrathin films to well-ordered one-dimensional nanocrystals on layered substrates, J. Phys. Chem. C. 119 (2015) 4217–4223. doi:10.1021/jp512613z.

P.R.L. Malenfant, C.D. Dimitrakopoulos, J.D. Gelorme, L.L. Kosbar, T.O. Graham, A. Curioni, W. Andreoni, N-type organic thin-film transistor with high field-effect mobility based on a N,N′-dialkyl-3,4,9,10-perylene tetracarboxylic diimide derivative, Appl. Phys. Lett. 80 (2002) 2517–2519. doi:10.1063/1.1467706

R. Rahimi, V. Narang, D. Korakakis, Optical and morphological studies of thermally evaporated PTCDI-C8 thin films for organic solar cell applications, Int. J. Photoenergy. 2013 (2013) 1-7. doi:10.1155/2013/205105.

S. Sakai, K. Yakushiji, S. Mitani, K. Takanashi, H. Naramoto, P. V Avramov, K. Narumi, V. Lavrentiev, Y. Maeda, Tunnel magnetoresistance in Co nanoparticle/Co–C60 compound hybrid system, Appl. Phys. Lett. 89 (2006) 113118. doi:10.1063/1.2354035.

T. Abhijith, M.Y. Ameen, V.S. Reddy, Synthesis of PTCDI-C8 one dimensional nanostructures for photovoltaic applications, IOP Conf. Ser. Mater. Sci. Eng. 73 (2015) 6–10. doi:10.1088/1757-899X/73/1/012052.

T.N. Krauss, E. Barrena, X.N. Zhang, D.G. de Oteyza, J. Major, V. Dehm, F. Würthner, L.P. Cavalcanti, H. Dosch, Three-dimensional molecular packing of thin organic films of PTCDI-C8 determined by surface X-ray diffraction., Langmuir. 24 (2008) 12742–12744. doi:10.1021/la8030182.

T.N. Krauss, E. Barrena, D.G. De Oteyza, X.N. Zhang, V. Dehm, F. Wu, H. Dosch, X-ray / Atomic Force Microscopy Study of the Temperature-Dependent Multilayer Structure of PTCDI-C 8 Films on SiO 2, J. Phys. Chem. C. 113 (2009) 4502–4506. doi:10.1021/jp808037w

T. Uemura, Y. Hirose, M. Uno, K. Takimiya, J. Takeya, Very high mobility in solution-processed organic thin-film transistors of highly ordered [1] benzothieno [3,2-b] benzothiophene derivatives, Appl. Phys. Express. 2 (2009) 6-9. doi:10.1143/APEX.2.111501.

Z.F. Yao, J.Y. Wang, J. Pei, Control of π-π Stacking via Crystal Engineering in Organic Conjugated Small Molecule Crystals, Cryst. Growth Des. 18 (2018) 7–15. doi:10.1021/acs.cgd.7b01385.

J. Myanmar Acad. Arts Sci. 2020 **Vol. XVIII.No.2C**

FABRICATION AND CHARACTERIZATION OF ZnO/Si FILM FOR SOLAR CELL APPLICATION

Khaing Khaing Min[1], Htet Htet Nwe[2], Yin Maung Maung[3] , Than Than Win[4]

Abstract

The crystalline state of undoped ZnO power was examined by X-ray diffraction (XRD) and Scanning Electron Microscopy (SEM). Zinc Oxide thin film was fabricated on the p- Si (100) substrate structure by single wafer spin processor at 500^{0}C and 600^{0}C. The surface morphology and microstructural properties were examined by Scanning Electron Microscopy (SEM). I-V characteristics (illuminated I-V) were investigated by monochromatic halogen lamp (100W). From the current and voltage characteristics under illumination, conversion efficiency (η_{con}) and fill factor (F_f) were observed for the cell. The results obtainted were quite suitable and application in used for solar cell application.

Keywords: Fine ZnO powder, spin coating, ZnO/Si substrate, I-V characteristics.

Introduction

A solar cell (also called a photovoltaic cell) is an electrical device that converts the energy of light directly into electricity by the photovoltaic effect. It is a form of photoelectric cell (in that its electrical characteristics e.g. current, voltage, or resistance vary when light is incident upon it) which, when exposed to light, can generate and support an electric current without being attached to any external voltage source.

The term "photovoltaic" comes from the Greek meaning "light", and from "Volt", the unit of electro-motive force, the volt, which in turn comes from the last name of the Italian physicist Alessandro Volta, inventor of the battery (electrochemical cell). The term "photo-voltaic" has been in use in English since 1849.

Solar panels on the International Space Station absorb light from both sides. These Bifacial cells are more efficient and operate at lower temperature than single sided equivalents. The efficiency of a solar cell may be broken down into reflectance efficiency, thermodynamic efficiency, charge carrier separation efficiency and conductive efficiency. The overall efficiency is the product of each of these individual efficiencies. A solar cell usually has a voltage dependent efficiency curve, temperature coefficients, and shadow angles.

The fill factor is defined as the ratio of the actual maximum obtainable power to the product of the open circuit voltage and short circuit current. This is a key parameter in evaluating the performance of solar cells. Typical commercial solar cells have a fill factor > 0.70. Grade B cells have a fill factor usually between 0.4 and 0.7. Cells with a high fill factor have a low equivalent series resistance and a high equivalent shunt resistance, so less of the current produced by the cell is dissipated in internal losses.

---

[1] Dr, Associate Professor, Department of Physics, Myingyan Degree College

[2] Assistant Lecturer, Department of Physics, Dagon University

[3] Professor, Department of Physics, University of Yangon

[4] Professor, Department of Physics, Pinlon University

[5] Professor, Department of physics, University of Yangon

Experimental Procedure

Preparation and Characterization of ZnO Powder

The material used in this research was undoped ZnO (Analar-grade) powder. The ZnO powder was added with some amount of ethanol (binding agent) and stirred for 30 min by using magnetic stirrer (500 rpm). The spherical shaped and fine powder was obtained by using ball milling and air-jet milling. The ZnO powder was performed by 3-step mesh-sieves to get uniform grain size. The crystallographic investigation and microstructural properties of ZnO powder were studied by using X-ray diffraction Scanning Electron Microscope.

Crystal structure and phase identification were examined by using RIGAKU model PINT 2000 X-ray diffractometer using CuKα radiation with wavelength of 1.54056 Ǻ. The diffraction patterns of powder specimens were identified by using JCPDS (Joint Committee on Powder Diffraction Standards) data book. The XRD profile of ZnO powder was shown in Fig 1. The upper site of this profile was given for observed ZnO while the lower site was represented as standard ZnO. According the profile, nine reflections were clearly formed with respective diffraction angles. They were (100), (002), (101), (102), (110), (103), (200), (112) and (201), respectively. The most intense peak was caused by the (101) reflection and indicating the polycrystalline nature. All observed reflections were well-matched with these of standard peaks. Thus the specimen was confirmed that the crystal structure of ZnO standard. The crystallite size of ZnO powder was obtained from the calculation and the value was 47.8426 nm.

Fig 2 showed the SEM image of ZnO powder. This image consisted of circular features known as rosette structure in microstructure. In addition, all grains were clearly formed. Furthermore, uniform grain distribution was also found and the grain size was measured to be 0.25 μm.

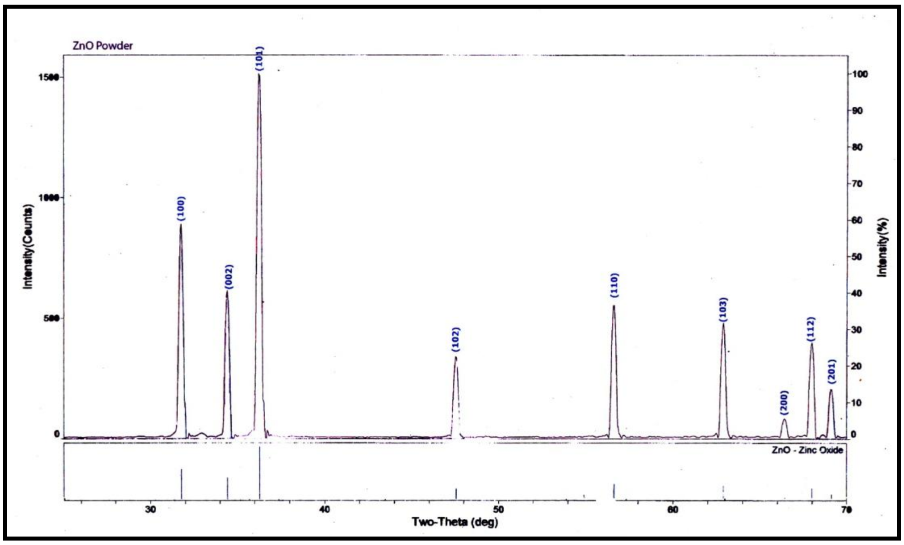

Figure 1 XRD profile of ZnO powder

Figure 2 SEM image of ZnO powder

Preparation of ZnO Solution

The ZnO solution was firstly prepared by mixing ZnO powder and ethanol solvent. The mixed solution was stirred with magnetic stirrer for 4h and refluxed at 110°C for 1h in a three-neck flask assembly to remove water of crystallization. Finally, ZnO precursor solution was obtained.

Preparation of Si Substrate

Defect-free and highly polished p-Si (100) (0.5cm x 0.5cm) wafer was used as a substrate. To remove the native oxide and contamination, cleaning process was made as follow:

(1) the Si wafer was washed in boiling acetone (60°C), then in boiled proponal (50°C) for 5 min to remove greasy film.

(2) it was immersed in nitric acid HNO_3 for 3 min in order to remove ionic contamination.

(3) it was etched in buffered hydrofluoric acid (34.6% NH_4F: 6.8% HF: 58.6%H_2O) for 2 min to remove oxide film.

(4) it was cleaned in DIW and dried on flat-oven at 100°C in a few minute.

Deposition of ZnO Film

ZnO sol solution was deposited on Si substrate by Single Wafer Spin Processer (WS-400BZ-6NPP/LITE). The substrate was placed on fragment adapter and the ZnO sol solution was poured onto substrate. The spin speed or rotational speed was set 2000 rpm and spinning time was 30 s. After spin coating, they were annealed at 500°C and 600°C for 1 h respectively. Eventually, ZnO/Si cells were formed at different process temperatures.

Table 1 ZnO film preparation condition

Substrate	Spin speed (rpm)	Spinning Time (s)	N_2 gas pressure (psi)	Vacuum (inches of Hg)	Annealing Temperature (^oC)
Si	2000	30	60	25.3	500, 600

Characterization of ZnO/Si Film

The XRD profiles of ZnO/Si Films with different temperatures were shown in Fig 3 & 4. The Brag angle 2θ value was measured between 10° and 70°. On the XRD pattern, fourteen peaks were clearly observed. Among these peaks, nine peaks were well-consisted with the JCPDS library file of # 89-7102> Zincite, Syn-ZnO. They were (100), (101), (002), (102), (110), (103), (200), (112) and (201) respectively. The most dominant peak was occurred at (101) reflection.

In this profile we considered within the defection limit from 10° to 70°. There were fifteen peaks in this profile. According to this profile, nine peaks were clearly formed and they were well–matched with JCPDS library file of # 89-7102>Zincite, syn-ZnO. The most intense peak was caused by the (101) diffraction plane. They were (100), (002), (101), (102), (110), (103), (200), (112) and (201) respectively. Theirs corresponding Bragg's angles were 31.616, 34.276, 36.098, 47.397, 56.444, 62.720, 66.225, 67.833 and 68.944, respectively. Remaining five profiles were well- matched with those of # 75- 0841> Si and 40-0932 > Si library. They were (300), (002), (330), (331)and (302) reflections. Their corresponding Bragg's angles were 35.869, 44.659, 51.900, 62.481 and 67.438. The (401) peak was caused at about 69.257 and couldn't be identified. Some important parameters for XRD patterns of ZnO/Si films were indicated in Table 2.

Table 2 Some important parameters for XRD patterns of ZnO/Si films

Annealing Temperature (^oC)	Lattice parameter (Å)		Lattice strain "c/a"	Crystallite size (nm)
	"a"	"c"		
500	3.22	5.18	1.60	53.96
600	3.21	5.17	1.61	46.26

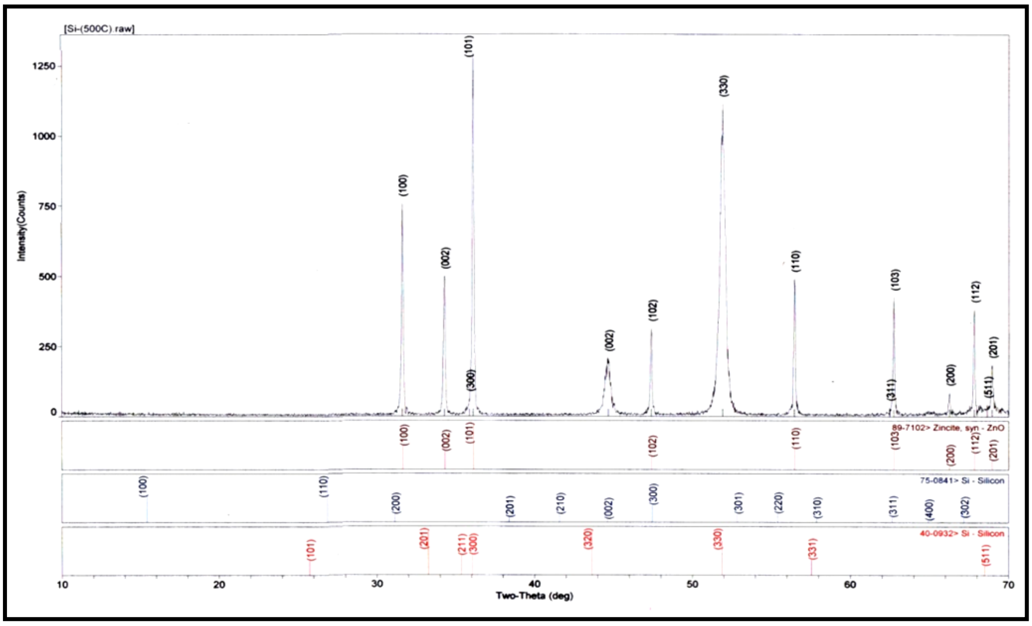

Figure 3 XRD profile of ZnO/Si film at 500°C

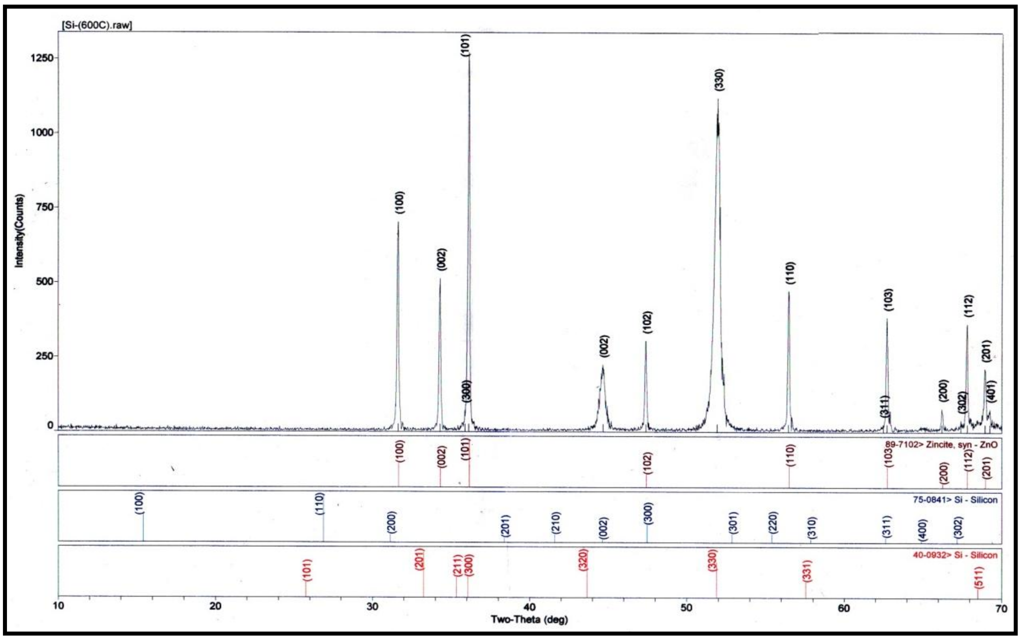

Figure 4 XRD profile of ZnO/Si film at 600°C

Microstructural Properties of ZnO/Si Films

Fig 5 & 6 showed the SEM microphotographs of ZnO/Si films at 500°C and 600°C. In these microphotographs, there were non cracking and some pores were formed among the crystalline grains. Grain sizes were little difference and they were measured by using well-known bar code system. The average grain sizes were determined to be 0.456 µm and 0.428 µm at 500°C and 600°C, respectively. The grain occurred at 500°C was oriented toward right site and uniform grain distribution was formed at 600°C. From the result, it was found that the grain size was the smallest for the annealing temperature at 600°C.

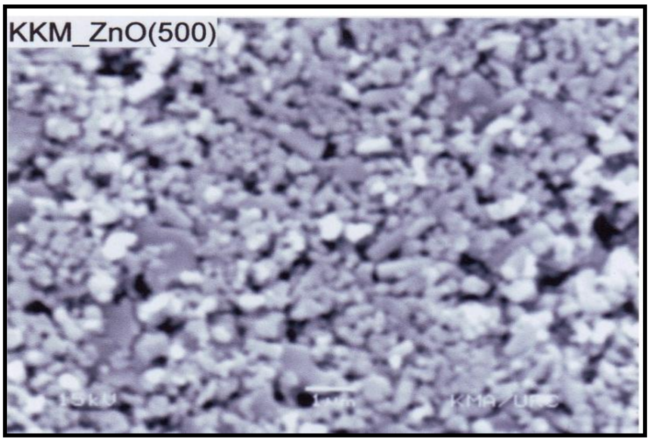

Figure 5 SEM image of ZnO/Si film at 500°C

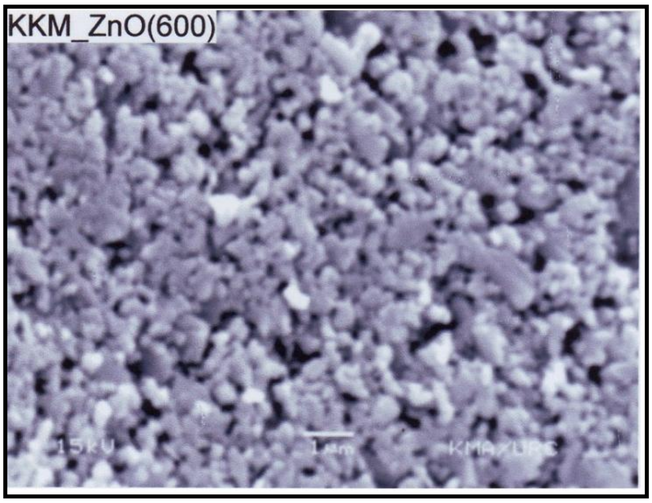

Figure 6 SEM image of ZnO/Si film at 600°C

Solar Cell Evaluation of ZnO/Si Films

Photocurrent and cell voltage were investigated by using a voltmeter (MULTMETER DT 9208) and an ammeter (FLUKE 196 SCOPEMETER). For illumination low pressure halogen lamp (100 watt) was used as a light source. A solar cell with a ZnO/Si structure provided power conversion efficiency (η) of 0.434 % and 0.497 % respectively. Fig 7 & 8 showed I-V curves of ZnO/Si thin films. The I-V characteristics of ZnO/Si films were indicated in Table 3.

Table 3 I_m, V_m, I_{sc}, V_{oc}, η_{con}, F_f of ZnO/Si films under illumination at 400 Lux

Annealing Temperature (°C)	**I_m(μA)**	**V_m (V)**	**I_{sc} (mA)**	**V_{oc} (mV)**	**η(%)**	**F_f**
500	0.918	1.001	1.039	1.167	0.434	0.758
600	0.917	1.147	1.035	1.337	0.497	0.760

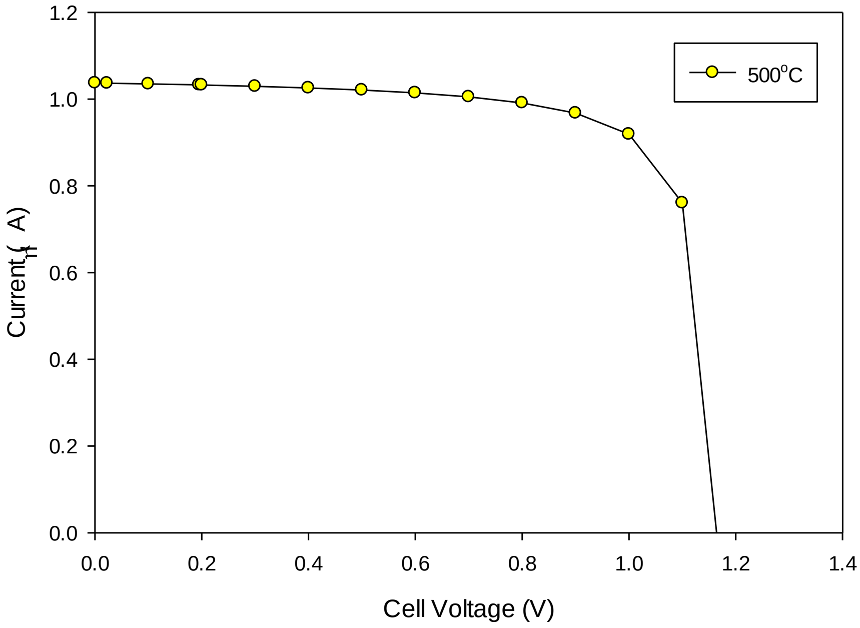

Figure 7 I-V curve of ZnO/Si at 500°C

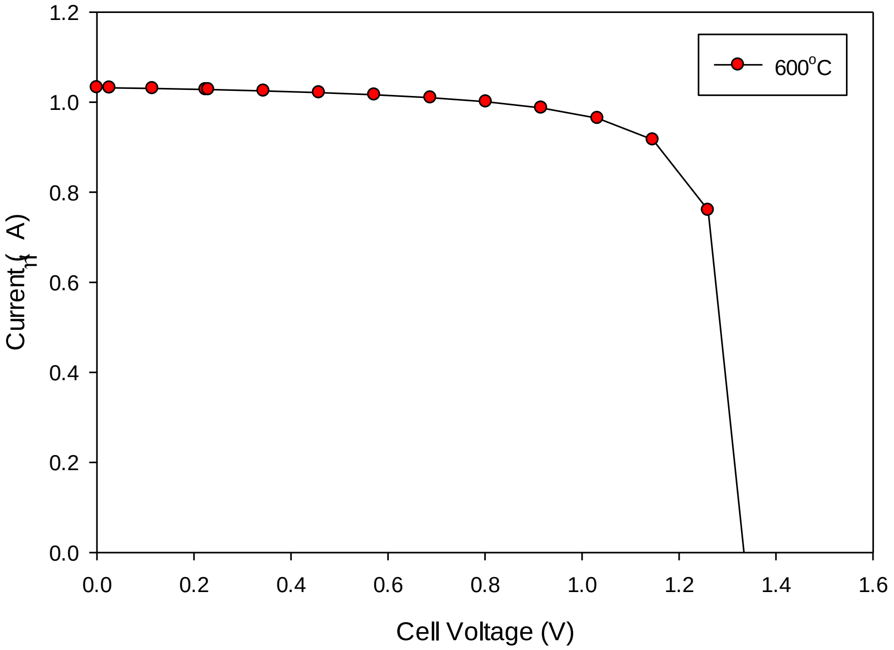

Figure 8 I-V curve of ZnO/Si at 600°C

Conclusion

The ZnO/Si films with different annealing temperatures have been successfully fabricated. The XRD result showed ZnO crystal structure with the crystallized size of 47.8426 nm. According to SEM result, ZnO powder exhibits circular shape with average grain size of 0.25 μm. The microstructural properties of ZnO/Si films were also confirmed by SEM technique and the average grain sizes were determined to be 0.456 µm and 0.428 µm at different annealing temperatures (500°C and 600°C), respectively. The I-V characteristics of ZnO/Si solar cells were measured under illumination condition. From the I-V graph, it was found that the power conversion efficiency (η) of 0.434 % and 0.497 % for ZnO/Si films with different temperatures. It was also found that the fabricated ZnO/Si films could be helped for thin film solar cell application.

Acknowledgements

One of the authors, Khaing Khaing Min would like to acknowledge Dr Tin Tin Yee Professor and Head of Department of Physics, Myingyan Degree College for her kind permission to carry out this work.

References

Alfred S (1849) “Elements of electro-biology” (London: Longman, Brown, Green, and Longmans)

Tsokos K. A. (2008) "Physics for the IB Diploma", (Cambridge, Cambridge University Press)

Perlin, J (2004) "The Silicon Solar Cell Turns 50" National Renewable Energy Laboratory Retrieved 5 October 2010

Mark Z et al (2009) Materials Science Poland 24 (2) 537

J. Myanmar Acad. Arts Sci. 2020 **Vol. XVIII.No.2C**

DYNAMICS AND SIMULATION OF THE GRAVITATIONAL COLLAPSE OF A NEUTRON STAR TO A BLACK HOLE

Thei` Theint Theint Aung[1], Kyaw Zall Linn[2]

Abstract

Using the highly non-linear differential equations, 3 +1 numerical relativity and Tolman-Oppenheimer-Volkoff equations, together with so called 1-log slicing condition (singularity avoiding gauge) it has been found that no real and coordinate singularity appears when the numerical simulations are carried out. Mass-Radius and Mass-Density visualization are implemented.

Keywords: Tolman-Oppenheimer-Volkoff equations, numerical simulations, Mass-Radius.

Introduction

Neutron stars are stellar remnants resulting from the gravitational collapse of a massive star during supernova event. Neutron stars are the most compact and smallest stars known to exist in the universe. Neutron stars are the end points of stellar evolution of massive stars whose corpse is not large enough to become a black hole. Black holes are even more compact than neutron stars: here, several solar masses are compressed within only a few kilometers "radius". They do not possess a distinct surface as such, but are delimited by a so-called event horizon which is the limit beyond which light cannot escape to infinity. General relativity is taken part in an important role in the formation of black holes and very important for the neutron stars. So the numerical simulations of gravitational collapse of rotating stellar configurations leading to the formation of black hole are a long standing problem in numerical relativity. This paper tries to simulate the collapse of a neutron star to a black hole. In the following the main theoretical concepts and basic equations required to understand the background of the gravitational collapsing of neutron star to black hole are discussed.

The Einstein Equations

The main theoretical concepts and the basic equations needed to understand the background of the gravitational collapse of neutron star to black hole are summarized. In connecting with the conservation laws for energy-momentum and rest-mass, Einstein's theory of general relativity is needed to solve the groundings of the differential equations. In highly nonlinear differential equation, the Einstein equations and the conservation laws are defined as follow

$$R_{\mu\nu} - \frac{1}{2} g_{\mu\nu} R = 8\pi T_{\mu\nu}, \tag{1}$$

$$\nabla_{\mu} \, T^{\mu\nu} = 0, \tag{2}$$

$$\nabla_{\mu} \left(\rho u^{\mu} \right) = 0. \tag{3}$$

---

[1] PhD Candidate, Assistant Lecturer, Department of Physics, Bago University

[2] Assistant Lecturer, Department of Physics, University of Yangon

Where $T_{\mu\nu}$ is the energy-momentum tensor, $R_{\mu\nu}$ is the Ricci tensor, which contains first and second derivatives of the space-time metric $g_{\mu\nu}$, ∇_μ is the covariant derivative and u^μ is the four velocity of the stars fluid. The Einstein equation describes in which way the space-time structure need to bend if energy-momentum is present. In this paper the energy-momentum, which curves space-time, arises from the large energy amount of the neutron star matter.

Tolman-Oppenheimer-Volkoff equations

The gravitational collapse of a neutron star to a black hole is depended on the equation of state (EOS), i.e. the relation between pressure and density in the neutron star interior (Lattimer & Pethick, 2004& Aaron Smith, 2012).To consider the mechanical structure of the neutron star is taken to be perfect fluid and spherical. For a perfect fluid, the energy momentum tensor is:

$$T^{\mu\nu} = \left(\rho + p\right) u^\mu u^\nu + p g^{\mu\nu} \tag{4}$$

The law of conservation of energy and momentum leads to

$$T^{\mu\nu}{}_{;\nu} = g^{\mu\nu}\partial_\nu p + \left[\left(\rho + p\right) u^\mu u^\nu\right]_{;\nu} + \left(\rho + p\right)\Gamma^\mu_{\nu\lambda} u^\nu u^\lambda = 0 \tag{5}$$

$$\nabla_\mu T^{\mu\nu} = 0,$$

For the spherically symmetric object, the space time is given by the Schwarzschild metric

$$ds^2 = -e^{2N(r)}dt^2 + e^{2\beta(r)}dr^2 + r^2 d\theta^2 + r^2\sin^2\theta d\phi^2 \tag{6}$$

where *N(r)* and *β(r)* are the metric functions depended on the radial coordinate r, t is the time component and *r, θ* and ϕ are the spatial component,

$$e^{2\beta(r)} = (1 - \frac{2Gm(r)}{r})^{-1} \tag{7}$$

and the *N(r)* can be expected from the following equation;

$$\frac{dN}{dr} = \frac{4\pi Gpr^3 + Gm(r)}{r(r - 2Gm(r))} \tag{8}$$

By taking the boundary condition, $\lim_{r\to\infty} e^{-2N(r)} = \lim_{r\to\infty} e^{2\beta(r)} = 1$

So, $$e^{2N(r)} = (1 - \frac{2Gm(r)}{r}) \tag{9}$$

If $r = R_s = 2MG$ the Schwarzschild radius, $m \equiv m(r)$ is star radius, $m\left(r\right) = \int_0^R 4\pi r^2 \rho(r) dr$ is mass of the sphere with radius *r*. Then the structures of spherical symmetric stars are computed utilizing the Tolman-Oppenheimer-Volkoff relativistic structure equations (i.e. TOV equations):

$$\frac{dP}{dR} = -\frac{G(m(r) + 4\pi r^3 P)(\rho + P)}{r(r - 2Gm(r))} \tag{10}$$

$$\frac{dm(r)}{dr} = 4\pi r^2 \rho(r) \tag{11}$$

Where *P* and *ρ* are the pressure and mass-energy density, and *m(r)* is the gravitational mass enclosed within a radius *r*. This connection is made by the equation of state of matter *P=P (ρ)* (the set of all spherical symmetric), in particular, an estimate for the maximum mass of the star can be obtained. These sets of nonlinear equations are for p(r) and m(r) from $r = 0$ for starting value of $p(r = 0) = p_0$ to the point $r = R$ where the pressure $p(r = R) = 0$. At that point R is the radius of the star. Since $p(r = R) = 0$, it is the vacuum outside of the star because the pressure gradually decreases outwards from the center. So there require that exterior metric should be Schwarzschild metric. Then the metric functions must be continuous at $r = R$:

Inside the star $$g_{rr} = (1 - \frac{2m(r)}{r})^{-1} \qquad (12)$$

and outside the star $$g_{rr} = (1 - \frac{2M}{r})^{-1} \qquad (13)$$

The total mass of the star is defined $M = m(r)$ (14)

Thus total mass of the star is determined by distant orbits, $$M = \int_0^R 4\pi r^2 \rho(r) dr \qquad (15)$$

Outside the distribution of mass, which terminates at the radius of star *R*, there is in vacuum with $p(r = R) = 0$ and Einstein equations give

$$g_{00}(r = R) = -(1 - \frac{2M}{r}) \qquad (16)$$

The important information which can be obtained by solving the TOV equation is the mass-radius relationship for a neutron star given a particular EOS model. If $r > R_s$, where *r* is the radius of star, and $R_s = 2MG$, i.e., the Schwarzschild radius, with the mass of the star *M* and the gravitational constant *G*. For $r < R_s$, the star becomes unstable and connected with gravitational collapse and likely to form a black hole. The 3-D variation of the gradient of the gravitational potential can be visualized in terms of radial function *r* and mass *m*.

The gravitational collapse of neutron star to black holes

To simulate the evolution of a collapse of a neutron star, the Einstein's equations are needed to reformulated and solve the time dependent problem numerically. This reformulation, the so called (3+1) split, starts by slicing the 4-dimensional manifold *M* into 3-dimensional space like hypersurface Σ_t. The space-time metric g_{ab} is then also divided into a purely spatial metric γ_{ij} and a lapse function *N* and a shift vector. Homogeneously, the line element may be written as

$$ds^2 = g_{ab} dx^a dx^b = -N^2 dt^2 + \gamma_{ij} \left(dx^i + \beta^i dt\right)\left(dx^j + \beta^j dt\right) \qquad (17)$$

where γ_{ij} and γ^{ij} is raise the lower indices of spatial tensors, *N* is the lapse function and β^i the shift vector and which is often referred to as the metric in 3+1 form(Baumgarte, 1998), here ds^2=-(proper time between neighboring spatial hypersurfaces)^2 +(proper distance between the spatial hypersurface)^2.

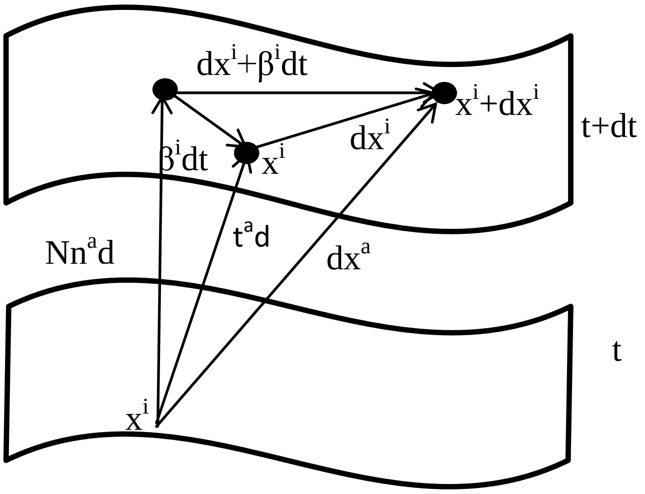

Figure 1 3+1 decomposition of spacetime

The coordinate label x^i moves through spacetime from one slice to another in a way given by the lapse N and shift β^i .Thus this equation can determine the invariant interval between neighboring points. The covariant components of metric g_{ab} are

$$g_{ab} = \begin{pmatrix} -N^2 + \beta^i \beta_i & \beta_i \\ \beta_i & \gamma_{ij} \end{pmatrix} \tag{18}$$

The lapse function *N* describes the difference between the coordinate time t and the proper time of a fluid particle. The shift vector β_i measures how the coordinates are shifted on the spatial slice if the fluid particle moves an infinitesimal time step further in figure. By using the above matric, the first order differential equation called ADM equations are reformulated. The ADM equations have two set of equations called constraint equations and evolution equations: the constraint equations are

$$R + K^2 - K_{ij}K^{ij} = 16\pi\rho \text{ (Hamiltonian constraint)} \tag{19}$$

and $$D_j K^{ji} - D_i K = 8\pi j^i \text{ (momentum constraint)} \tag{20}$$

the evolution equations are

$$\partial_t \gamma_{ij} = -2NK_{ij} + D_i\beta_j + D_j\beta_i \tag{21}$$

$$\begin{aligned} \partial_t K_{ij} = & -D_i D_j N + N\left(R_{ij} + KK_{ij} - 2K_{ik}K^k{}_j\right) + 4\pi N\left(\gamma_{ij}\left(S - \rho\right) - 2S_{ij}\right) \\ & + \beta^i D_k K_{ij} + K_{ik} D_j \beta^l + K_{kj} D_i \beta^k \end{aligned} \tag{22}$$

The shift terms in the last two equations arise from the Lie derivatives $\mathcal{L}_\beta \gamma_{ab}$ and $\mathcal{L}_\beta K_{ab}$. Here $\mathcal{L}_\beta$ is the lie derivative along the shift vector and that Ricci tensor R_{ij} is given be second spatial derivatives of the metric (Aaron Smith, 2012, Arnowitt et al., 1962, Arnowitt et al., 2008).

As a result this is not first order system. The constraint equations constraint the field variables on each spatial slice and the lapse and the evolution equations determine the time evolution of the fields from one spatial slice to the next.

Singularity avoidance conditions and 1- log slicing

In particularly, most of the modern 3+1 solution of the Einstein's equations adopt as hyperbole slicing condition a member of the so called Bona-Masso` family of slicing conditions(Bona C. et al, 2005), which can be generically written as

$$\left(\partial_t - \mathcal{L}_\beta\right) N = -KN^2 f\left(N\right) \tag{23}$$

where *f* is an arbitrary function and *f(N)>0.* By varying the expression of the generic function *f(N),* the slicing condition recovers a number of well-known slicing. The geodesic slicing condition also fulfills this relation with *f = 0.* If by setting *f =q/N* with q is an integer, the slicing condition obtains the generalized "1- log" slicing condition where $N = h\left(x^i\right) + \ln\gamma^{1/2}$, *h(x$_i$)* is positive but otherwise arbitrary time independent function. In practice, most numerical simulations set *f=2/N* lead to

$$\left(\partial_t - \mathcal{L}_\beta\right) N = -2KN \tag{24}$$

Substituting Eqn. (21) for *–KN*,

$$\left(\partial_t - \mathcal{L}_\beta\right) N = \partial_t \ln\gamma - 2D_i\beta^i \tag{25}$$

If normal coordinates are used, β=0, the above equation becomes

$$\partial_t N = \partial_t \ln\gamma \tag{26}$$

a solution of which is $$N = 1 + \ln\gamma \tag{27}$$

For this reason, a foliation whose lapse function obeys is called a 1-log slicing. Which has been shown to be very robust and well behaved not only in vacuum spacetimes representing black holes but also in spacetimes describing the neutron stars.

A coordinate system can be constructed by identifying the time coordinate vector with the Killing vector ξ^a, so

$$\xi^a = t^a = N_K n^a + \beta_K^a \tag{28}$$

N_K is called Killing lapsed and β_K^a is called Killing shift. For Schwarzschild spacetime, the foliated by slices of constant Schwarzschild time t, the Killing lapse can be identified

$$N_K = \frac{1 - M/(2r)}{1 + M/(2r)} \tag{29}$$

and the Killing shift as $\beta_K^r = 0$. But N_K is negative for *r >M/2.* Having the slicing lapse equal to the Killing lapse, $\partial_t N_K = \partial_t N_S = 0$ the slicing shift is equal to the Killing shift, then condition (24) reduces to

$$K = \frac{\beta_K^i \partial_i N_K}{2N_K} \tag{30}$$

This condition is stationary 1-log slicing. This condition can be employed for the construction of initial data. Besides this condition considered without the adventive term,

$$\partial_t N = -2NK \tag{31}$$

In this case the Killing lapse associated with a stationary slicing satisfied this condition only if the slices are maximal, i.e., if *K=0*. For Schwarzschild, the maximal slicing can be parameterized by a parameter C, the lapse is yield

$$N_K = (1 - \frac{2M}{R} + \frac{C^2}{R^4})^{1/2} \tag{32}$$

where *R* is an areal radius. For *C=0*, it give the slice of constant Schwarzschild time t. When applying the 1-log slicing, the right hand side *-2NK* is replaced by *–n f (N) K*, where n is some arbitrary number and *f (N)* some non-zero and finite function of *N*. Besides, 1+log slicing condition can be applied to binaries.

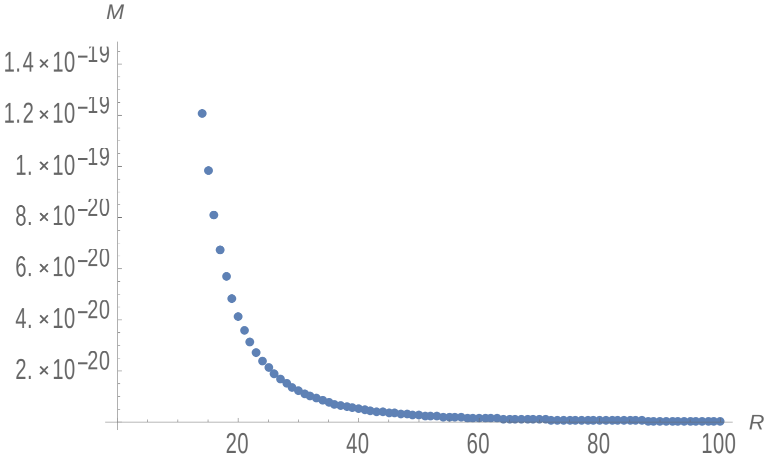

Figure 2 Mass-Radius relation of neutron star

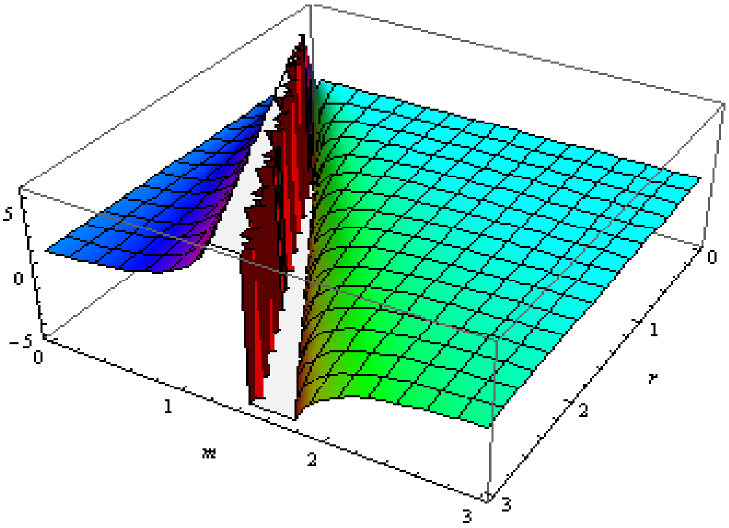

Figure 3 3D visualization of the gravitational potential with radius r and mass m

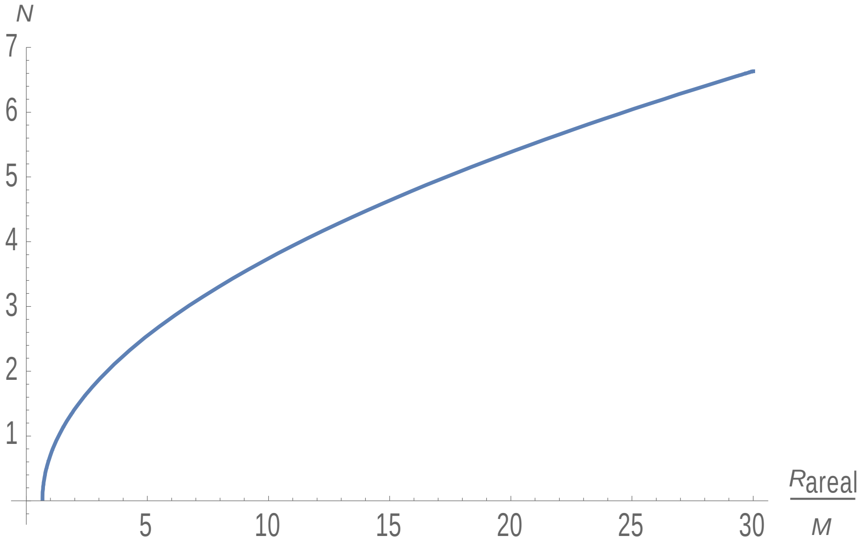

Figure 4 Graph of the lapse N for Schwarzschild in 1-log slicing

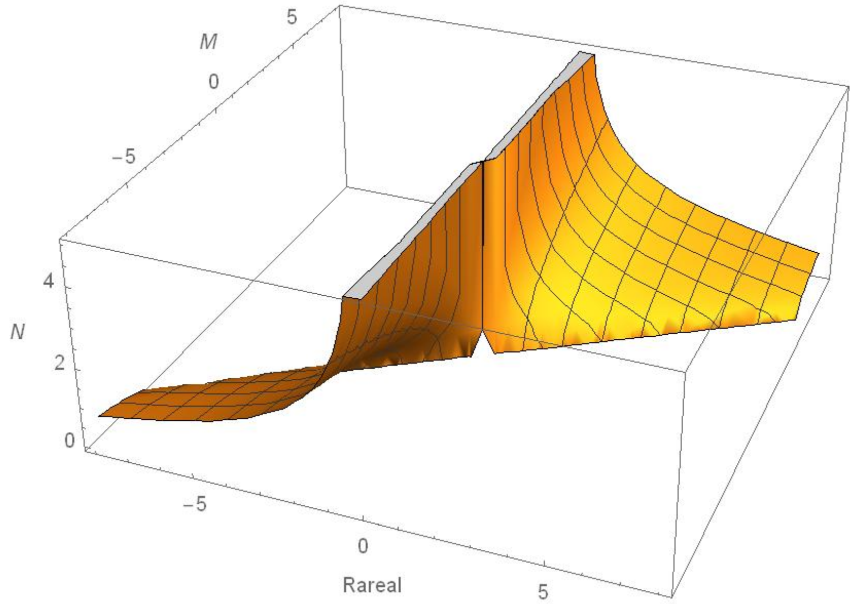

Figure 5 3D visualization of the lapse N in the 1-log slicing

Concluding Remarks

When the central density of a neutron star exceeds the maximal allowed value , the star collapses to a black hole and its radius shrinks until it reaches the value of the location of the event horizon of the corresponding black hole at r = 2M. . If $r > R_s$, where r is the radius of star, for $r < R_s$, the star becomes unstable and connected with gravitational collapse and likely to form a black hole and at $R_s = 0$ and R=2M (i.e., the Schwarzschild radius, with the mass of the star M), singularity point are formed. So, Figure 2 shows the relationship between mass and radius of the neutron star. Figure 3 show 3D visualization of the gravitational potential with radius r and mass m. To slow down the evolution near the real singularity, a singularly avoiding coordinates so called “1-log” slicing has been used fairly commonly. No real or coordinate singularity could appear in this gauge during the numerical evolution. Then, Figure 4 shows the graph of the lapse N for Schwarzschild in the 1-log slicing. When applying the 1-log slicing, Figure 5 shows 3D visualization of the lapse N in the 1-log slicing, which would avoid the singularity point where the gravitational fields are strongest.

Acknowledgements

I would like to express my sincere thanks to Professor Dr Khin Mar Ohn, Head of Department of Physics, Bago University, for her kind permission to carry out this research. I wish to show my sincere thanks to Professor Dr Khin Htoo, Department of Physics, Bago University, for her encouragement to carry out this research. Special thanks are due to Professor Dr Thant Zin Naing, Retired Pro-Rector (Admin), International Theravāda Buddhist Missionary University, for his valuable guidance and helpful advice to carry out this work.

References

Aaron Smith, (2012) “Tolman-Oppenheimer-Volkoff (TOV) Stars”, Department of Astronomy, The University of Texas at Austin, Austin.

Arnowitt, R., Deser, S. and Minser, C. W. (1962) “The dynamics of General Relativity”, New York. Papers.

Arnowitt .R, Deser, S. and Minser, C. W. (2008) “General Relativity and Gravitation”.

Baumgarte, (1998) “Lecture Note on Numerical Relativity”, unpublished.

Bona C., Lehner L. and Pen zuela-Luque C., (2005) “Geometrically motivated hyperbolic coordinate conditions for numerical relativity: Analysis**,** issues and implementations”, Phys, Rev. D 72, 104009.

Gourgoulhon Eric, (2007) “3+1Formalism and Bases of Numerical Relativity”, Lecture Notes, University Paris, France.

J. Myanmar Acad. Arts Sci. 2020 **Vol. XVIII.No.2C**

SPECTRAL FEATURES AND MUSIC SCALE OF MYANMAR BAMBOO XYLOPHONE

Htee Mu Wah[1], Ye Chan[2]

Abstract

Myanmar Bamboo Xylophone (Pattalar) is one of the famous Myanmar fixed-pitch musical instruments, which produce a pleasant sound. Pattalars have their own unique sound with unique parameters different from other musical instruments. The purpose of this paper is to analyzed spectral features of the sound of Pattlar with traditional tuning. The parameters of spectral features such as pitch, harmonics are extracted by short time Fourier transform (STFT). The accurate spacing of harmonic contents and spectral envelope are computed by cepstrum analysis. Then, the frequency contents of signal changes over time are visualized by spectrogram method. The tuning of Pattalar is studied by three different Pattalars with the music scale computed in a logarithmic unit called Cents. The resulting measurements are compared with the pervious measurements data reported by Professor J.West, Professor Dr Maung Maung Kha.

Keywords: STFT, Spectrogram, cepstrum, Pattalar, Myanmar music scale, Cents

Introduction

Myanmar Bamboo Xylophone (Pattalar) is one of the famous musical instruments have been existence during Innwa period (14th-15th century A.D). This is a fixed-pitch instrument including in idiophone class, which produce sounds through the vibration of their entire body. A Pattalar consists of three octaves, including 24 slates and they are made by 'Waboe' bamboo. Under the 24 slats, there is a wooden resonator to produce pleasant sounds. Pattalars are tuned in diatonic scale contains seven notes for an octave. The tuning of Bamboo Pattalar are studied from three different Pattalars and compared with Myanmar musical scale and traditional tuning of Pattalar reported by the previous researchers Robert Muriel. C Williamson (1956) and Dr Maung Maung Kha (1962). The music intervals between two successive notes are calculated in a logarithmic unit called Cents. The first one is a bamboo Pattalar made by Professor Dr Maung Maung Kha since 1962 and others two from Arts and Culture Club of University of Yangon [Muriel C Williamson, (2000)].

Pattalar has their own unique sound with unique parameters called timbre. The two general classes for identified timbre are temporal features and spectral features. In this paper, only spectral features are studied. The spectral parameters such as pitch, harmonics and their relative amplitudes are obtained by short time Fourier transform (STFT). The frequencies contents such as pitch, harmonics with their relative amplitudes varying over time are visualized by Spectrogram. The spectrum of the sound is very flat and it is confused to understand by containing a large numbers of harmonics. However, cepstrum has the ability to detect the harmonic pattern and an accurate indication of the harmonic spacing. Then, the spectral envelope is computed by cepstrum analysis, it is the important parameter for sound analysis, synthesis and classification timbre of musical instrument [R. B. Randall, (1987)].

---

[1] PhD candidate, Assistant lecturer, Department of Physics, Bago University

[2] Dr, Professor and Head, Universities' Research Centre, University of Yangon

Musical Scale of Bamboo Pattalar

Pattlars are tuned in a diatonic musical scale containing seven notes for an octave, athan-zin-hkun-napa` or 'set of seven sounds'. They are tuning in descending scale of diatonic (C B A G F E D), Tapauk, Hkun-napauk, Chauk- pauk, Nga-pauk, Lei`-pauk, Thone-pauk, Hna-pauk. However they are not really Western diatonic scale, the common note-set of Myanmar traditional notation can be described as a mixture of four Western tones and three neutral tones (tones lowered about a quarter tone), C D E* F G A* B*, asterisks indicate the neutral tones (Muriel Williamson). The musical interval can be measured in units called cents, mathematically expressed as

$$\text{cents} = 1200\log_2\left(\frac{f_1}{f_2}\right) = 3986 \times \log_{10}\left(\frac{f_1}{f_2}\right) \qquad (1)$$

From the above equation, f_1 and f_2 are the frequencies of the successive lower and upper notes. Table (1) shows the comparisons of music scale intervals between Western and Myanmar reported by the previous researchers (Dr Maung Maung Kha, 1963; U Khin Zaw, 1940; Muriel C. Williamson, 1956). Column (1) is C-major scale interval of Western music scale, Column (2) is nayin-lon scale of Myanmar traditional harp, Column (3) is the measurements of brass bar Pattalar reported by Professor J.West and Column (4) is the measurement of bamboo Pattalar reported by Professor Dr Maung Maung Kha [Muriel C Williamson, (2000)].

Table 1 The Comparison of Western music scale and Myanmar Music scale from Harp and Pattalar

Notes	Western (1)	Harp (2)	West (3)	Dr MMK (4)
C	1200	1200	1200	1213
B	1100	1050	1035	1071
A	900	900 (850)	889	890
G	700	700	717	700
F	500	500	534	511
E	400	350 (400)	373	380
D	200	200	199	186
C	0	0	0	0

Audio Recording and Spectrum Analysis

There are many background of study to analyze the music features and transform the sound of musical instrument to numerical data. The first step is recording process to achieve data as an audio file. In this work, individual notes of three different Pattalars are recorded by audio software Audicity with 44100Hz sampling frequency, 32-bit float sample format and .wav file. Figure (1) shows the recording of Pattalars from Arts and Culture Club of University of Yangon. The important parameters of spectral features such as pitch, harmonics and their relative amplitude of the sound signal are obtained by short time Fourier transform (STFT). Then, the spectrogram described time-frequency representation obtained by the magnitude of (STFT) and the intensity or amplitude of the harmonics spectrum are computed on a log scale (dB). The parameters of spectrogram such as window length, window type, hop-size, and segment length are choosing for finer time and frequency resolution. The cepstrum is logarithmic conversion of the original spectrum and has the ability to detect the periodic structures in a logarithmic spectrum, such as families of harmonics or sidebands with uniform spacing [R. B. Randall, (1987)].

The spectral envelope obtained by cepstrum windowing is defined as

$$Y_m = DFT[\underbrace{\omega.DFT^{-1}log(|X_m|)}_{\text{Real cepstrum}}]$$

where ω is a lowpass-window in the cepstrum domain. The log-magnitude spectrum of X_m is thus lowpass filtered (the real cepstrum of **x** is ''liftered'') to obtain a smooth spectral envelope. The unit of the cepstrum is quefrency, getting by the inversing of frequency, similarly cepstrum is the steaming from an inversion of spectrum, rahmonic from harmonic, lifter from filter and gamnitude from magnitude [Julius O. Smith III, (2011)]. All the processing is done by Matlab programming.

(a) (b) (c)

Figure (1) (a) Dr Maung Maung Kha's Pattalar (b) The first Pattalar from University of Yangon (c) The second Pattalar from University of Yangon

Result and Discussion

The fundamental frequencies or pitch of each musical notes for three different Pattlars are shown in table (2). By using equation (1) the music interval between two successive notes computed in cents is shown in table (3). The comparison of the music scale between Western diatonic, Myanmar traditional tuning and the resulting of three different Pattalars is shown in figure (2). However, figure (2) is only for middle octaves, in this figure the tuning of three Pattalars is not the same; they are varied about ±25 cents, less than a quarter tone. This is in the range between musical significant pitch changes (±25 cents) summarized by Muriel C. Willianson. But it is not for the lower and upper octave. From the computation data of table (3), some of notes especially in the lower octave varied closed to 100 cents, a semitone.

Figure (3) is the spectrogram of 1-Pauk 1 note with the segment length of 4096 samples Hanning window and 50% overlap ratio. In this figure, the fundamental frequency, harmonics with the relative intensity varying over time are represented by colored. The brighter color represents the higher intensity and the darker to the lower. The difference between spectrum and cepstrum is manily lie in the low quefrency parts of the cepstrum, which is dominated by formant characteristics. Figure (4) is the amplitude spectrum and amplitude cepstrum of 1-Pauk 1 note. Cepstrum described harmonic pattern and an accurate indication of the harmonic spacing, 72Hz corresponds to 13.9161ms, 48Hz corresponds to 20.8118 ms, 36Hz corresponds to 27.8277 ms and 28Hz corresponds to 34.4853 ms respectively. Figure (5) is the spectral envelope computed from real cepstrum. Firstly cepstrum coefficients are transformed back to the frequency domain. Then, the local maximum points are extracted from frequency spectrum and finally, spectral envelope is obtained by interpolation method.

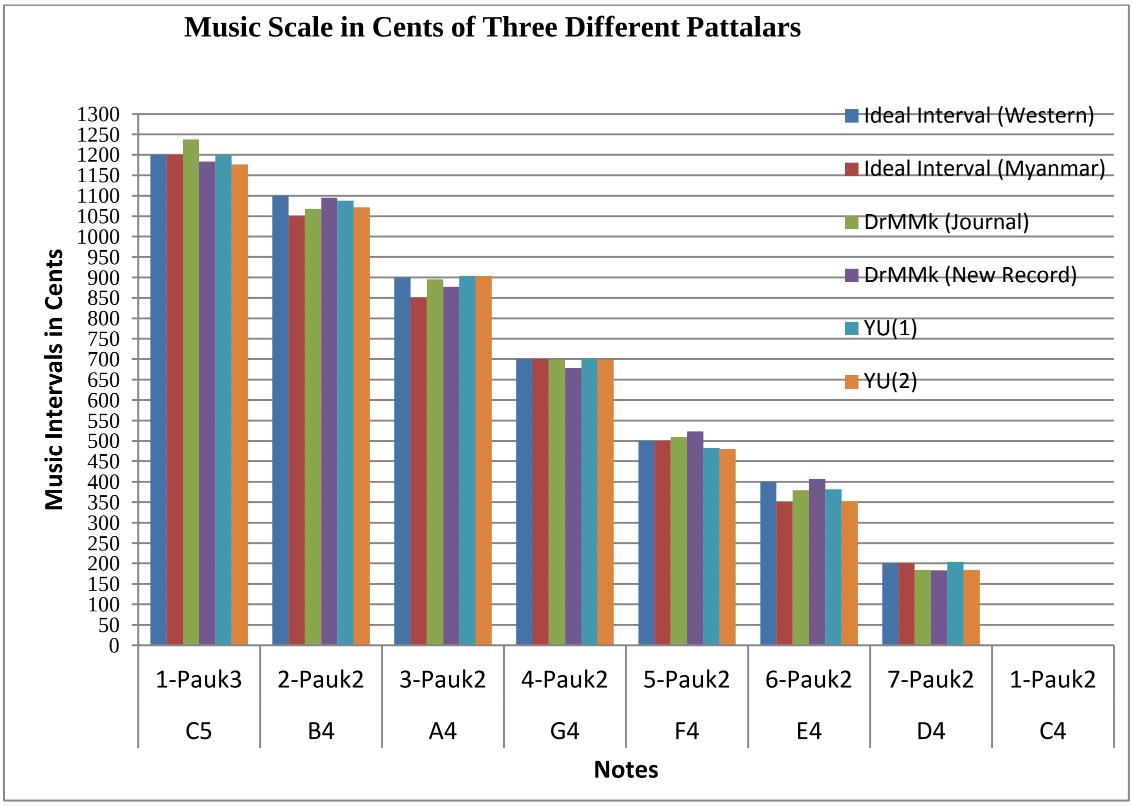

Figure 2 Music Scale in Cents of Three Different Pattalars

Table 2 Frequencies Tuning of Three Different Pattlars

Notes Western	Notes Myanmar	Dr MMK (Journal)	Dr MMK (New)	Yu (1)	Yu (2)
E6	6-Pauk4	1364	1354	1314	1330
D6	7-Pauk4	1222	1195	1180	1172
C6	1-Pauk4	1096	1053	1043	1044
B5	2-Pauk3	995	988	980	989
A5	3-Pauk3	884	872	878	877
G5	4-Pauk3	800	774	782	779
F5	5-Pauk	722	705	702	699
E5	6-Pauk3	661	656	658	655
D5	7-Pauk3	594	579	584	588
C5	1-Pauk3	543	516	527	524
B4	2-Pauk2	492	490	494	493
A4	3-Pauk2	445	432	444	447
G4	4-Pauk2	397	385	395	397
F4	5-Pauk2	356	352	348	350
E4	6-Pauk2	330	329	328	325
D4	7-Pauk2	295	289	296	295
C4	1-Pauk2	265	260	263	265
B3	2-Pauk1	243	246	242	248
A3	3-Pauk1	217	217	224	228
G3	4-Pauk1	194	191	194	195
F3	5-Pauk1	173	173	175	179
E3	6-Pauk1	160	164	163	170
D3	7-Pauk1	143	147	146	152
C3	1-Pauk1	128	121	129	138

Table 3 Music Scale in Cents of Three Different Pattlatrs

Notes Western	Notes Myanmar	Ideal Interval western (W)	Ideal Interval Myanmar (T)	Frequency-1 (Hz) Dr MMK (Journal)	Frequency-2 (Hz) Dr MMK (New)	Frequency (Hz) Yu (1)	Frequency (Hz) Yu (2)
E6	6-Pauk4	2800	2750	2828	2850	2772	2785
D6	7-Pauk4	2600	2600	2638	2634	2586	2567
C6	1-Pauk4	2400	2400	2450	2416	2373	2367
B5	2-Pauk3	2300	2250	2283	2306	2266	2274
A5	3-Pauk3	2100	2050	2079	2090	2076	2066
G5	4-Pauk3	1900	1900	1907	1884	1876	1861
F5	5-Pauk3	1700	1700	1730	1723	1694	1674
E5	6-Pauk3	1600	1550	1578	1599	1582	1562
D5	7-Pauk3	1400	1400	1393	1383	1376	1376
C5	1-Pauk3	1200	1200	1238	1184	1199	1177
B4	2-Pauk2	1100	1050	1068	1095	1088	1072
A4	3-Pauk2	900	850	895	877	904	903
G4	4-Pauk2	700	700	698	678	702	698
F4	5-Pauk2	500	500	510	523	483	480
E4	6-Pauk2	400	350	379	407	381	352
D4	7-Pauk2	200	200	185	183	204	185
C4	1-Pauk2	0	0	0	0	0	0
B3	2-Pauk1	-100	-150	-150	-95	-144	-114
A3	3-Pauk1	-300	-350	-345	-312	-277	-259
G3	4-Pauk1	-500	-500	-538	-532	-525	-529
F3	5-Pauk1	-700	-700	-736	-703	-703	-677
E3	6-Pauk1	-800	-850	-871	-795	-825	-766
D3	7-Pauk1	-1000	-1000	-1065	-984	-1015	-959
C3	1-Pauk1	-1200	-1200	-1256	-1320	-1229	-1126

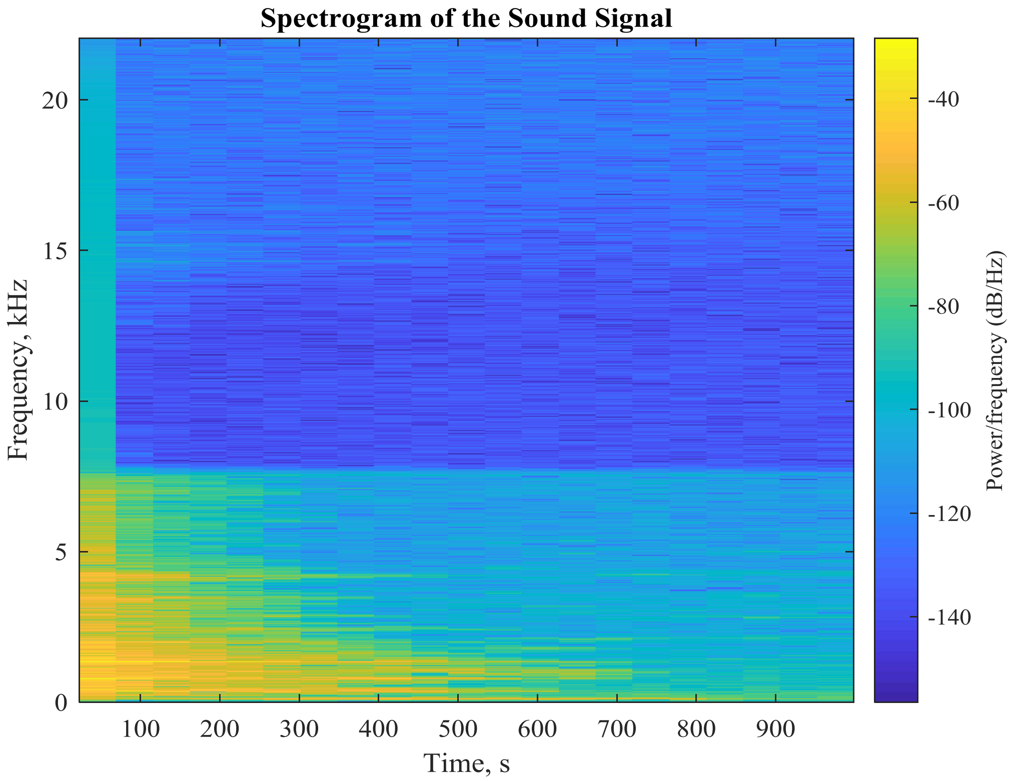

Figure 3 Spectrogram of the 1-Pauk1 note

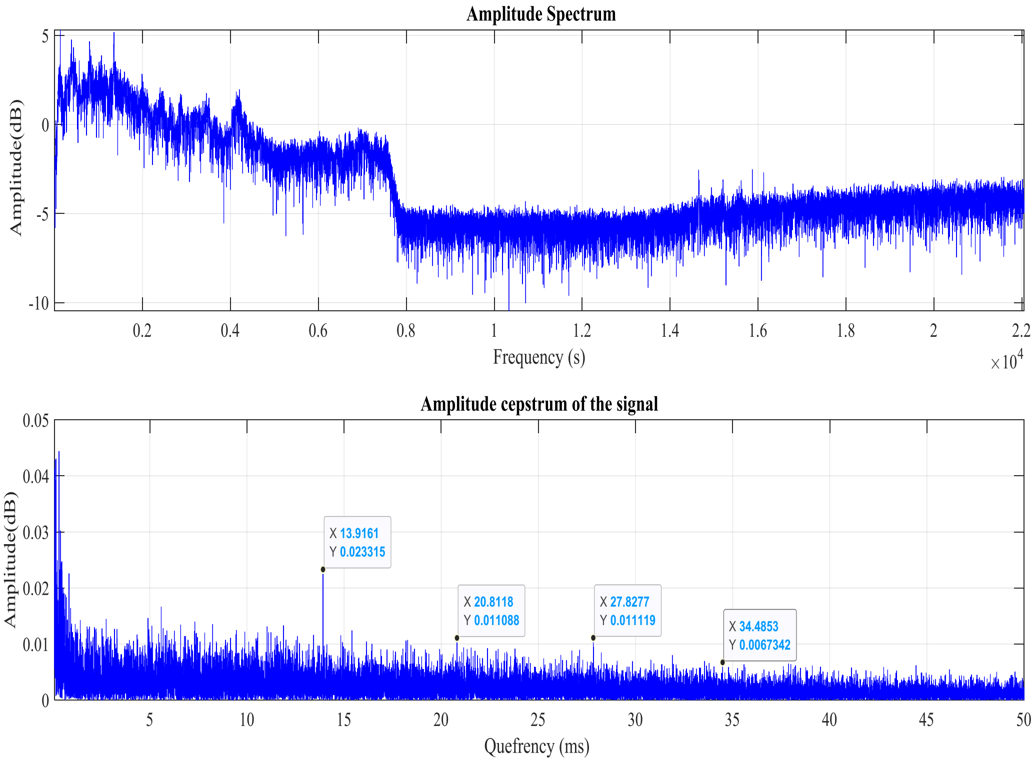

Figure 4 Amplitude Spectrum and Amplitude of Cepstrum of 1-pauk1 note

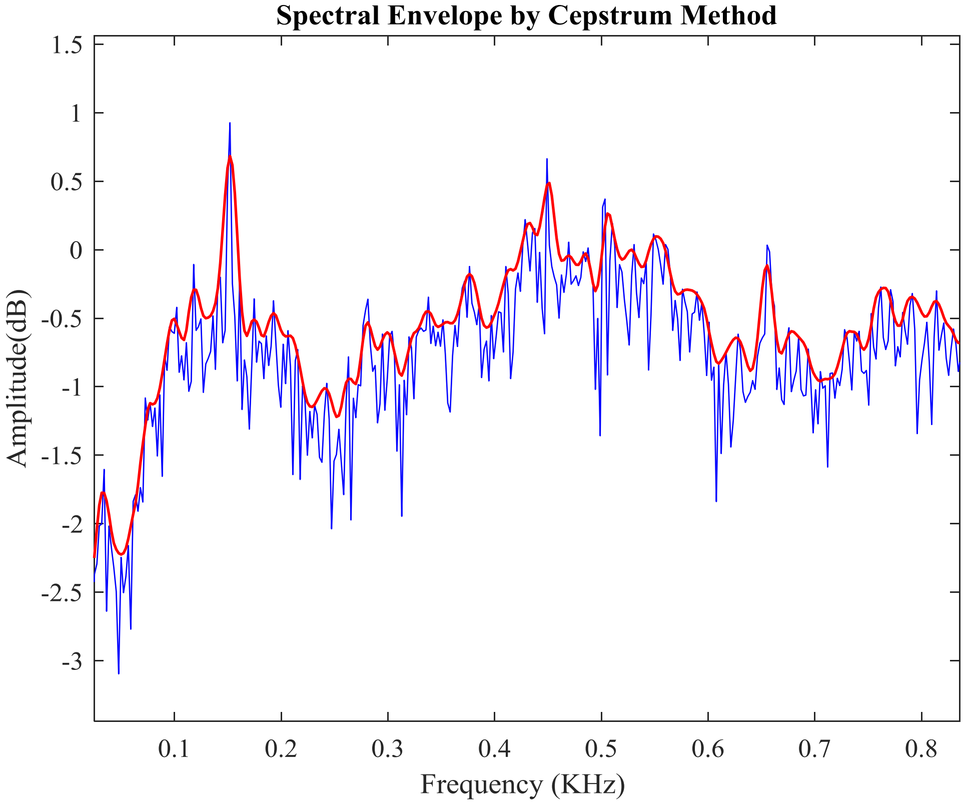

Figure 5 Spectral Envelope of 1-pauk1 note by Cepstrum Analysis

Conclusion

Although the music scale of the middle octave of three different Pattalars is varied in the range between musical significant pitch changes, less than a quarter tone, some of the notes of lower and upper octave are varied close to a semitone. Therefore, the tuning of bamboo Pattalar is not consistent. Quefrency domain represents periodic structures of logarithmic spectrum and thus an accurate indication of the harmonic spacing. Therefore the effect of harmonic family can be study clearly in cepstrum. Cepstrum components are manily lying in the low quefrency parts by shortpass lifterring each of the spectra. And only formants are left in the cepstrum. Therefore separated source and transmission path effects by quefrency contents are also one of the applications of the cepstrum. Spectral envelope can be used as filter coefficients for time-domain filtering and as a transfer function for frequency-domain filtering. It is also the important parameter to control the amplitudes of the partials for resynthesis.

Acknowledgements

I would like to express my sincere thanks to Professor Dr Aye Aye Tun, Rector, Bago University, Professor Dr Khin Mar Ohm, Head of Department of Physics, Bago University, for their kind permission to carry out this paper.

I would like to Thanks Professor Dr Khin Khin Win, Head of Department of Physics, University's of Yangon, for her kind permission to carry out this paper.

References

Julius O. Smith III, (2011) Spectral Audio Signal Processing, Centre for Computer Research in Music and Acoustic

Julius O. Smith III, (2007) Mathematics of Discrete Fourier Transform (DFT): with Audio Applications, second edition, Centre for Computer Research in Music and Acoustic

Li Tan, (2008), Digital Signal Processing Fundamentals and Applications, DeVry University

Muriel C Williamson, (2000) The Burmese Harp; Its classical music, tunings and modes,Centre for South - East Asian Studies, Northern Illinois University

Maung Maung Kha, (1963). An Acoustical Analysis of the Vibrations of Bamboo Bars Used in Pattalars, Journal of the Burma Research Society

R. B. Randall, (1987) Frequency Analysis, K Larsen and Sen A/S . DK-2600 Glostrup

Tin Win, U Khin Maung Tin, (2018) Investigating the Traditional Tunings of Saung Gauk (Burmese Arched Harp)

U Khin Zaw, (1940) Burmese Music, Journal of the Burma Research Society

J. Myanmar Acad. Arts Sci. 2020 **Vol. XVIII.No.2C**

PREPARATION AND CHARACTERIZATION OF MAGNESIUM COPPER MIXED FERRITE AND MAGNESIUM COPPER THIN FILM

Thinzar Wut Yee[1], Aye Aye Lwin[2], Win Kyaw[3] and Khin Mar Ohn[4]

Abstract

Magnesium-Copper mixed ferrite $Mg_{0.5}Cu_{0.5}Fe_2O_4$ was prepared by usual ceramic method at $1000^{\circ}C$ for 8h. Structural and microstructural characteristics of the sample were characterized by using X-ray diffraction (XRD) and Scanning Electron Microscopy (SEM). Temperature dependent electrical conductivities were investigated in the temperature range of 299K-573K region. Furthermore, $Mg_{0.5}Cu_{0.5}Fe_2O_4$ thin film was deposited on p-Si substrate by using thermal diffusion method at $500^{\circ}C$ for 1h.Microstructural characteristics and film thickness were examined by SEM. Current–Voltage (I-V) characteristics of the film were also investigated under the different illumination of visible light source.

Keywords: $Mg_{0.5}Cu_{0.5}Fe_2O_4$, XRD, SEM, Current-Voltage.

Introduction

Nanosize spinel ferrite particles have attracted considerable attention and continued efforts to investigate them for their technological importance to the microwave industries, high speed digital tap or disk recording, repulsive suspension for use in levitated railway systems, and magnetic refrigeration systems. The conventional way of preparing the ferrite is by solid-state reaction, which involves the mixing of oxides with intermittent grinding followed by high temperature sintering between 1300 and 1700°C. Though the process remains simple it has several drawbacks such as high reaction temperature, larger particle size, limited degree of homogeneity, and low sinterability.(Adam A, Ali Z, Andeltwab E & Abbas 2009)

Ferrite spinels have the formula $M(Fe_2O_4)$, where M is usually a divalent cation such as manganese (Mn^{2+}), nickel (Ni^{2+}), cobalt (Co^{2+}), zinc (Zn^{2+}), copper (Cu^{2+}), or magnesium (Mg^{2+}). M can also represent the monovalent lithium cation (Li^{+}) or even vacancies, as long as these absences of positive charge are compensated for by additional trivalent iron cations (Fe^{3+}). The oxygen anions (O^{2-}) adopt a close-packed cubic crystal structure, and the metal cations occupy the interstices in an unusual two-lattice arrangement. In each unit cell, containing 32 oxygen anions, 8 cations are coordinated by 4 oxygens (tetrahedral sites), and 16 cations are coordinated by 6 oxygens (octahedral sites). (Bhunia A & Bose D N 1998)

The antiparallel alignment and incomplete cancellation of magnetic spins between the two sublattices leads to a permanent magnetic moment. Because spinels are cubic in structure, with no preferred direction of magnetization, they are “soft” magnetically; *i.e.,* it is relatively easy to change the direction of magnetization through the application of an external magnetic field. (Candeia R A et al 2004)

In the present work, Magnesium-copper mixed spinel ferrite sample of $Mg_{0.5}Cu_{0.5}Fe_2O_4$ was first prepared by usual ceramic method and characterized by XRD, SEM, and temperature dependent electrical conductivity measurements to examine the phase formation and to study the

---

[1] Dr, Demonstrator, Department of Physics, Bago University, Myanmar

[2] Dr, Associate Professor, Department of Physics, Loikaw University

[3] Dr, Associate Professor, Department of Physics, Pyay University

[4] Dr, Professor & Head, Department of Physics, Bago University

structural, microstructural characteristics and electrical conductivity of the sample. Furthermore, $Mg_{0.5}Cu_{0.5}Fe_2O_4$ film was prepared on p-Si substrate by using thermal diffusion method and characterized by SEM and I-V characteristic measurements.

Experimental Procedure

Sample Preparation of Magnesium-Copper Mixed Spinel Ferrite

In this research, the starting materials of Magnesium Oxide (MgO), Copper Oxide (CuO), and Ferric Oxide, Fe_2O_3 were weighted with stoichiometric composition. The mixture powder sample was grounded by an agate motor for 3 h to be homogeneous and fine powders. The powders were annealed at 1000°C for 8 h in the vacuum chamber by using thermal resistive heating coil that controlled DELTA A Series Temperature Controller DTA4896. The K-type thermocouple (1300°C) was used as the temperature sensor to read-out the real temperature of the sample in the chamber. Finally, the Magnesium-copper mixed spinel ferrite, $Mg_{0.5}Cu_{0.5}Fe_2O_4$ was obtained. Experimental arrangement of the sample preparation system and the as-grown $Mg_{0.5}Cu_{0.5}Fe_2O_4$ sample are shown in Fig 1(a) and (b).

Figure1(a) Experimental arrangement of sample preparation system

Figure 1(b) Photograph showing the top-view of as-grown polycrystalline Magnesium-copper mixed spinel ferrite, $Mg_{0.5}Cu_{0.5}Fe_2O_4$

Preparation of $Mg_{0.5}Cu_{0.5}Fe_2O_4$/p-Si Thin Film

The obtained $Mg_{0.5}Cu_{0.5}Fe_2O_4$ powder is firstly grounded by agate motor for 1 h to be fine and homogeneous sample. 1 g of the sample and 2-methoxythanol are mixed. Obtained mixture is stirred and boiled at 100°C to get the sol state. Finally, this solution is cooled down at room temperature.

p-Si (100) wafers, dimension of (0.50 cm x 0.50 cm) are used as the substrates. These substrates are cleaned using standard wafer cleaning process. p-type silicon substrates are etched in HF:H_2O (1:5) for 10 minutes, immerse in deionized (DI) water for 10 minutes to remove native oxide. And then, the samples are immersed in acetone and methyl alcohol for 10 minutes to remove impurities. Then, the substrates are rinsed in deionized water for 10 minutes and the substrates are dried at room temperature.

After cleaning process, the precursor solution is coated onto substrates by screen-printing technique. Later, coated-layers are first dried at room temperature. The $Mg_{0.5}Cu_{0.5}Fe_2O_4$ material is deposited on p-Si at 500 °C for 1 h by using DELTA A Series Temperature Controller DTA4896 temperature controller in the vacuum condition of -150 mmHg in thin film fabrication chamber.

After the deposition, the $Mg_{0.5}Cu_{0.5}Fe_2O_4$/p-Si film was etched in the mixture of ethanol, DI-water and HCl (1:1:1) for 10 – 15 min to get the homogeneously surface of the film. Then, $Mg_{0.5}Cu_{0.5}Fe_2O_4$/p-Si thin film was dried at room temperature. Finally, $Mg_{0.5}Cu_{0.5}Fe_2O_4$/p-Si film was obtained. The flow-diagram of the $Mg_{0.5}Cu_{0.5}Fe_2O_4$/p-Si thin film is shown in Fig (2).

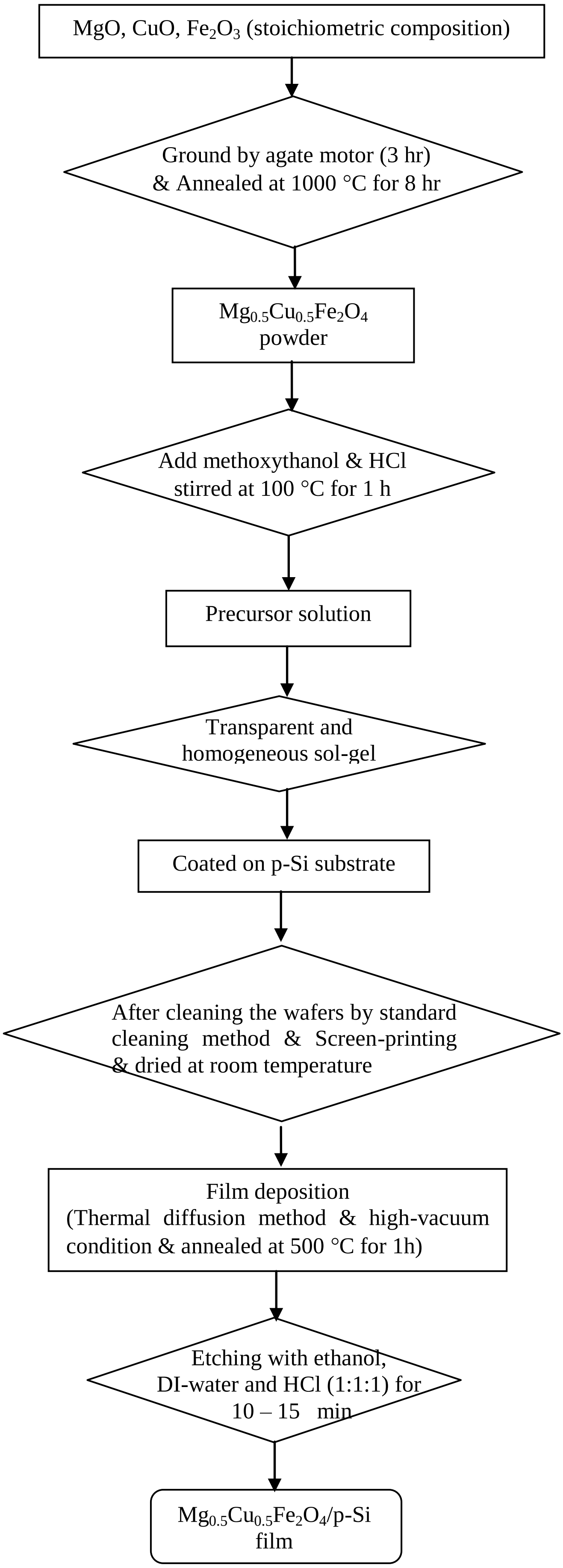

Figure 2 Flow-diagram of the $Mg_{0.5}Cu_{0.5}Fe_2O_4$/p-Si thin film

XRD Measurement

Structural analysis, lattice parameters determination and crystallite size estimation of the samples were investigated by using RIGAKU MULTIFLEX X-ray diffractometer using Ni-filter with CuK_{α} radiation, $\lambda = 1.54056$ Å.

SEM Measurement

The morphological features of Magnesium-copper mixed spinel ferrite, $Mg_{0.5}Cu_{0.5}Fe_2O_4$ powders and $Mg_{0.5}Cu_{0.5}Fe_2O_4$/p-Si film are investigated by using JEOL JSM-5610LV SEM with the accelerating voltage of 15 kV, the beam current of 50 mA and 10000 times of photo magnification.

Temperature Dependent Electrical Conductivity Measurement

The samples were firstly made into pellets by SPECAC hydraulic press using 5 ton (~70 MPa). The silver paste was made over the sample to ensure good electrical contacts. The electrical resistances of the samples were observed in the temperature range of 299K-573K by the use of CAHO SR-T903 Temperature Controller. Thicknesses of the samples were measured by digital Vernier Caliper and used as 3.11 mm each. The area of the pellet was 1.14×10^{-4} m^2. The electrical resistances of the samples were measured by using FLUKE 45 Dual-display digitalmulti-meter.

I-V Characteristic Measurement

Photovoltaic effect of $Mg_{0.5}Cu_{0.5}Fe_2O_4$/p-Si thin film has been investigated in dark condition (0 lux) and different illumination conditions by using (60 W) electric bulb light source. The light intensity sensor of Si-photodiode (LIGHTMETER 2330LX, SEW) was placed near the sample with parallel position to record constant intensity of light source throughout the measurement. The output photovoltage of the film was observed by FUKE FK9208D digital voltmeter.

I-V (Current – voltage) characteristics in dark and in illumination condition of the film were also measured between the bias voltages of -5 V and +5 V with the step voltage of 0.2 V. In this measurement, DT-830B and FUKE FK9208X were used as the digital ammeter and voltmeter. Photograph of the experimental arrangement of I-V characteristic measurement is shown in Fig 3.

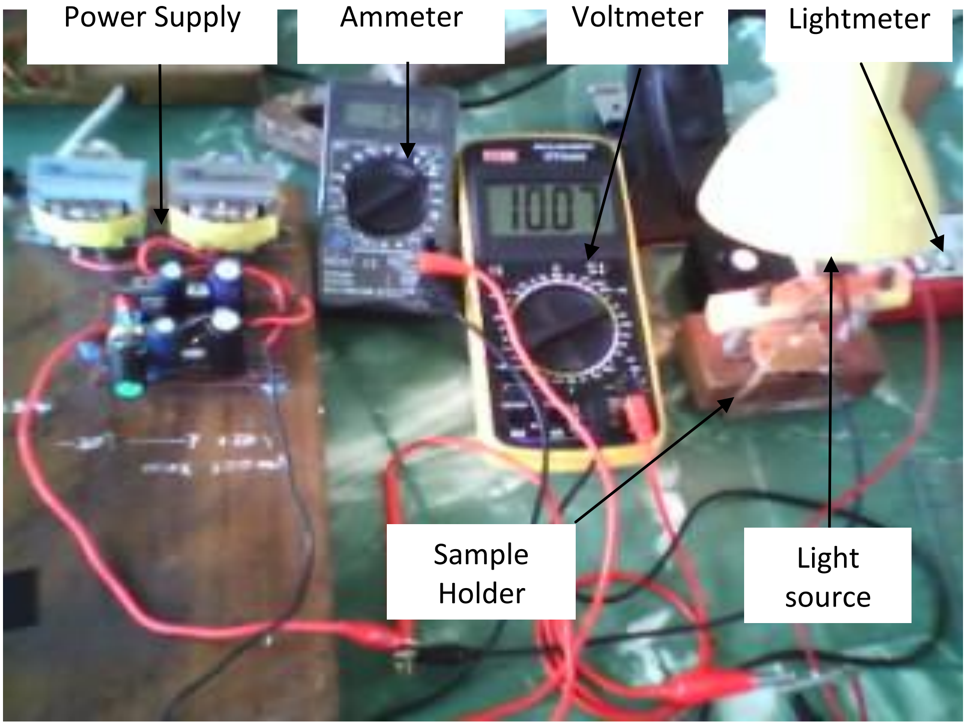

Figure 3 Photograph of the experimental arrangement of I-V characteristic measurement

Results and Discussion

XRD Analysis

Powder X-ray diffraction pattern of Magnesium-Copper mixed spinel ferrite, $Mg_{0.5}Cu_{0.5}Fe_2O_4$ is shown in Fig 4. XRD data of diffraction angle (2θ), atomic spacing (d), Miller indices (hkl), full width at half maximum (FWHM) and peak height of the sample are tabulated in Table 1. The collected XRD data are compared to those of JCPDS data library to identify the collected XRD pattern and to examine the single phase polycrystalline sample. Most of the collected diffraction lines are well assigned by JCPDS. From the XRD pattern, the material of $Mg_{0.5}Cu_{0.5}Fe_2O_4$ is found to single phase polycrystalline material belongs to cubic structure at room temperature. The lattice parameters are evaluated by using crystal utility of the equation of $\frac{\sin^2\theta}{(h^2+k^2+l^2)}=\frac{\lambda^2}{4a^2}$. Lattice parameters of the sample are $a = b = c = 8.28$ Å.

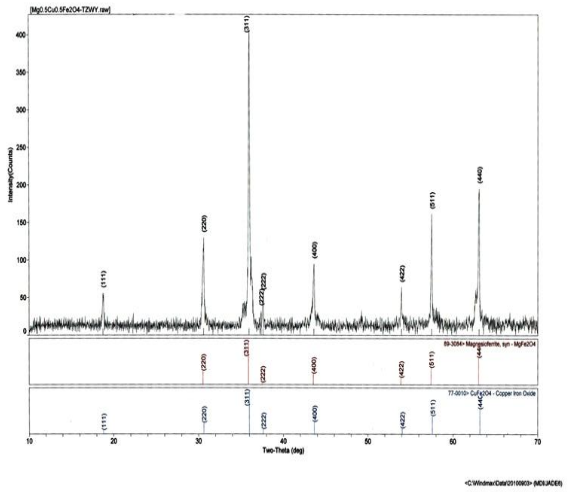

Figure 4 XRD pattern of Magnesium-Copper mixed spinel ferrite, $Mg_{0.5}Cu_{0.5}Fe_2O_4$

Table 1 **XRD data of Magnesium-copper mixed spinel ferrite, $Mg_{0.5}Cu_{0.5}Fe_2O_4$**

Line No	2θ (°)	(hkl)	d (Å)	FWHM (°)	I (%)
1	18.74	(111)	4.73	0.16	11.20
2	30.60	(220)	2.92	0.23	30.50
3	35.94	(311)	2.50	0.22	100.00
4	37.35	(222)	2.41	0.07	5.60
5	37.58	(222)	2.39	0.19	11.20
6	43.58	(400)	2.08	0.23	20.30
7	53.95	(422)	2.70	0.15	12.90
8	57.48	(511)	1.60	0.16	37.60
9	63.07	(440)	1.47	0.21	45.90

SEM Analysis

Morphological features of the samples are shown in Figure 5(a). It exposes that the grain shape of the sample is snow-like circular shape and the grain sizes are about 0.25 µm – 0.80 µm. Most of samples are found to be homogeneous and well grain boundary. SEM images of $Mg_{0.5}Cu_{0.5}Fe_2O_4$ film on p-Si substrate and the diffusion layer thickness of the $Mg_{0.5}Cu_{0.5}Fe_2O_4$ sample on p-Si are shown in Fig 5 (b) and (c). As shown in recorded SEM image (see Fig 5 (b)), the grain shape of the $Mg_{0.5}Cu_{0.5}Fe_2O_4$ layer is found to snow-like circular shape and crack free layer on p-Si substrate. As shown in observed diffusion layer thickness of the sample (see Fig 5 (c)), it is found that the layer boundary of the sample and substrate are found to homogeneous and the diffusion layer of the $Mg_{0.5}Cu_{0.5}Fe_2O_4$/p-Si thin film is about 3.14 µm. It is indicated that the$Mg_{0.5}Cu_{0.5}Fe_2O_4$ sample is successfully deposited on p-Si substrate by using thermal diffusion technique at 500 C for 1h in the vacuum chamber.

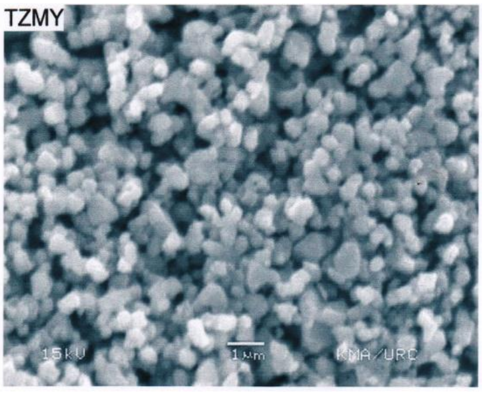

Figure 5(a). SEM image of Magnesium-copper mixed spinel ferrite, $Mg_{0.5}Cu_{0.5}Fe_2O_4$ powder

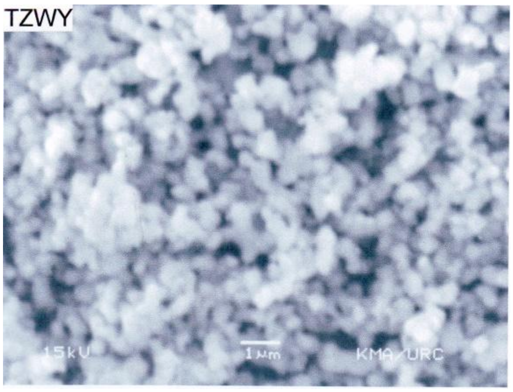

Figure 5(b) SEM image of $Mg_{0.5}Cu_{0.5}Fe_2O_4$/p-Si thin film

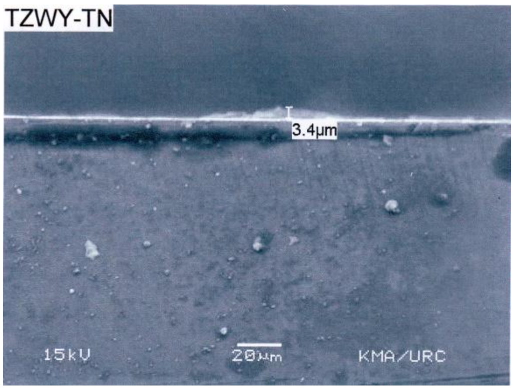

Figure 5(c) Diffusion layer thickness of $Mg_{0.5}Cu_{0.5}Fe_2O_4$/p-Si thin film

Temperature Dependent Electrical Conductivity

In the present work, Arrhenius plot of the variation of dc electrical conductivity of the $Mg_{0.5}Cu_{0.5}Fe_2O_4$ mixed spinel ferrite in the temperature range of 299 K - 573 K is shown in Fig 6.It shows that temperature dependent electrical conductivities of the sample are found to increase with increasing temperatures. Moreover, using the slope of the ln(σ) versus 10^3/T graph, the activation energy of the sample is calculated as 0.60 eV, according to the equation $\sigma = \sigma_0 \exp(-E_i / kT)$. From the experimental results of electrical conductivity, the $Mg_{0.5}Cu_{0.5}Fe_2O_4$ mixed spinel ferrite sample is a superionic conductor because its electrical conductivity is ($\sigma \geq 10^{-5}$ S cm^{-1}).

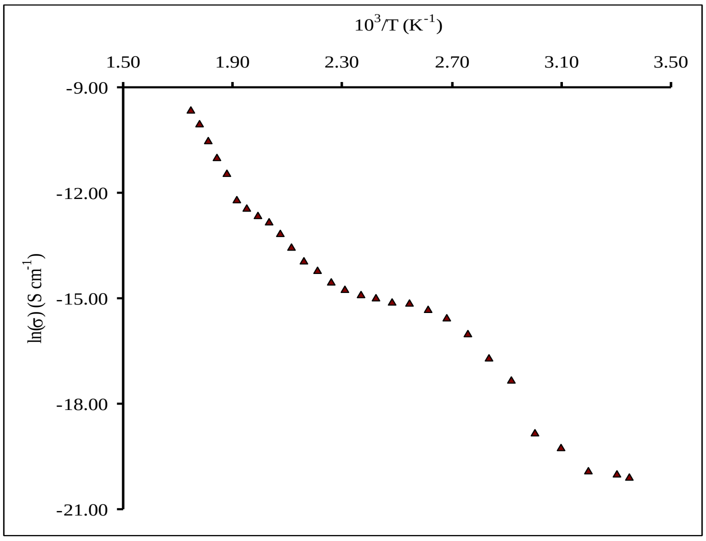

Figure 6 Arrhenius plot of the temperature dependent electrical conductivity of $Mg_{0.5}Cu_{0.5}Fe_2O_4$ mixed spinel ferrite

Current-Voltage Characteristic of $Mg_{0.5}Cu_{0.5}Fe_2O_4$/p-Si Thin Film

Current-voltage, I-V measurements of $Mg_{0.5}Cu_{0.5}Fe_2O_4$/p-Si thin film devices within the bias voltages of -5 V up to +5 V (Step Up) and +5 V down to -5 V (Step Down) under the different illumination conditions to investigate the photosensitive effect and loop character. Copper are used as electrodes for the top and bottom regions. I-V characteristic curves of the $Mg_{0.5}Cu_{0.5}Fe_2O_4$/p-Si thin film under dark (0 lux) and different illumination conditions of (250 lux (normal), 500 lux, 1000 lux, 1500 lux, and 2000 lux (60W, electric bulb light source) in the bias-voltage of -5 V - +5 V are shown in Fig 7(a) - (f). Among these curves, loop character of 1500 lux illumination condition is not found. Others I-V characteristic curves show the loop character of the sample in the positive bias regions.

The output current is exponentially increased with increasing bias voltage. Furthermore, comparison of the output currents as a function of (0 – 5 V) bias voltages in different illumination conditions is shown in Fig 7(g).Maximum output currents of the $Mg_{0.5}Cu_{0.5}Fe_2O_4$/ p-Si thin film at +5 V bias voltage in different illumination conditions are listed in Table 2.

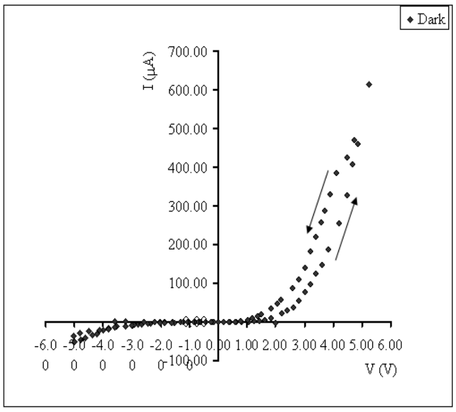

Figure 7(a) I-V characteristic curve of $Mg_{0.5}Cu_{0.5}Fe_2O_4$/p-Si thin film in dark (0 lux) condition

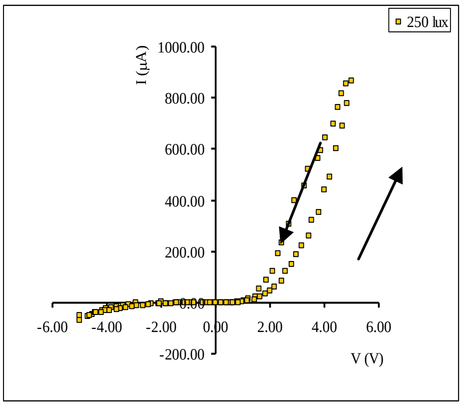

Figure 7(b) I-V characteristic curve of $Mg_{0.5}Cu_{0.5}Fe_2O_4$/p-Si thin film in ambient (250 lux) Illumination condition

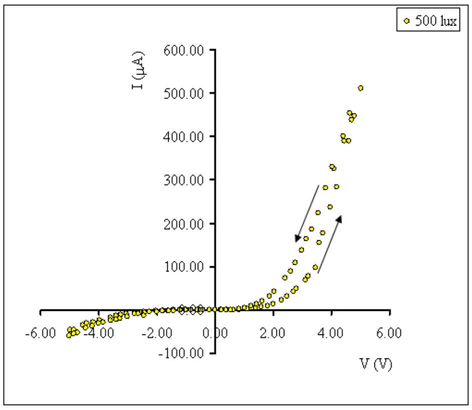

Figure 7(c) I-V characteristic curve of $Mg_{0.5}Cu_{0.5}Fe_2O_4$/p-Si thin film in 500 lux illumination condition

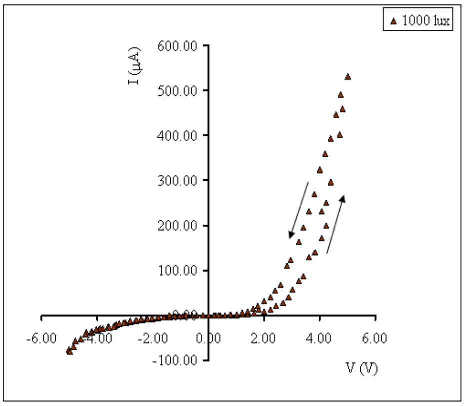

Figure 7(d) I-V characteristic curve of $Mg_{0.5}Cu_{0.5}Fe_2O_4$/p-Si thin film in 1000 lux illumination condition

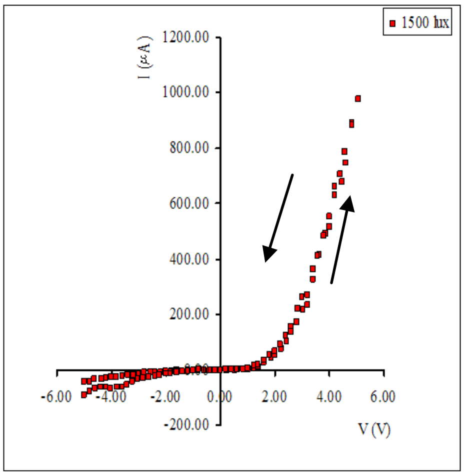

Figure 7(e) I-V characteristic curve of $Mg_{0.5}Cu_{0.5}Fe_2O_4$/p-Si thin film in 1500 lux illumination condition

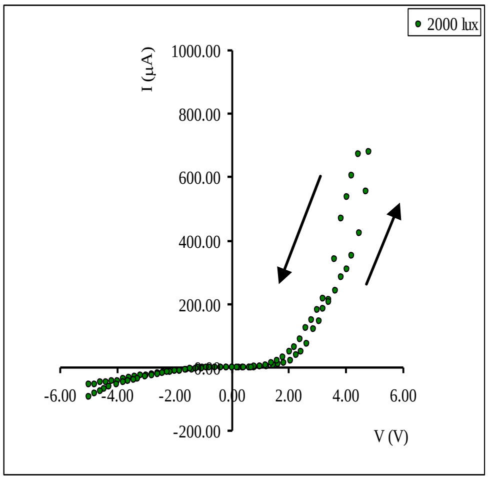

Figure 7(f) I-V characteristic curve of $Mg_{0.5}Cu_{0.5}Fe_2O_4$/p-Si thin film in 2000 lux illumination condition

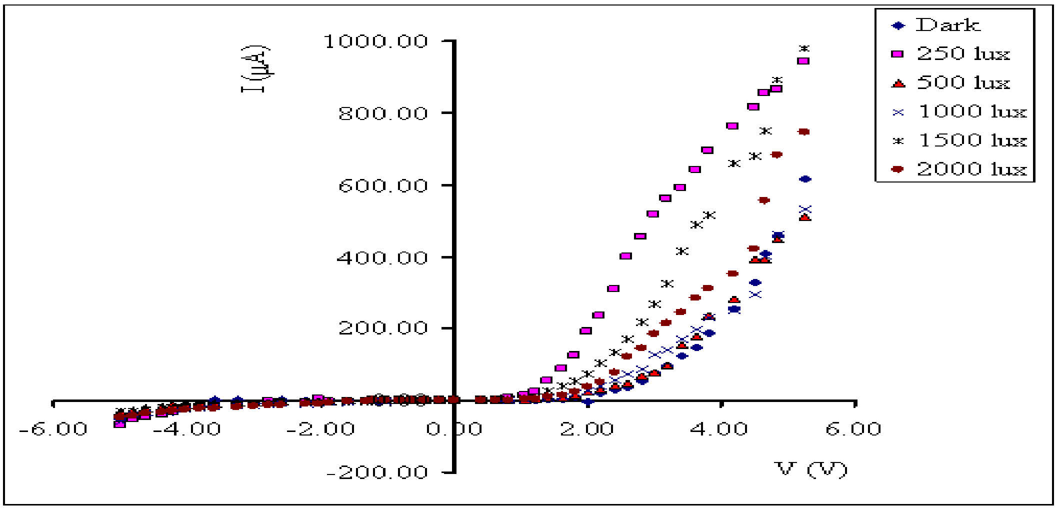

Figure 7(g) Comparision of the I-V characteristic curve of $Mg_{0.5}Cu_{0.5}Fe_2O_4$/ p-Si film in dark and in different illumination condition

Table 2 Maximum output currents of the $Mg_{0.5}Cu_{0.5}Fe_2O_4$/p-Si thin film at +5 V bias voltage in different illumination conditions

Sr No	Illumination (lux)	Output Current (μA)
1	0	616
2	250	943
3	500	512
4	1000	533
5	1500	979
6	2000	745

Conclusion

Magnesium-copper mixed spinel ferrite sample of $Mg_{0.5}Cu_{0.5}Fe_2O_4$ was prepared by usual ceramic method at 1000°C for 8 h in vacuum chamber.

Structural, microstructural and temperature dependent electrical conductivity of the as-grown $Mg_{0.5}Cu_{0.5}Fe_2O_4$ sample were reported by means of XRD, SEM and temperature dependent electrical conductivity measurements. From the XRD pattern, $Mg_{0.5}Cu_{0.5}Fe_2O_4$ mixed spinel ferrite belongs to cubic structure and the lattice parameters are $a = b = c = 8.28$ Å. It is found to single phase polycrystalline material. From the SEM micrograph, the grain shape of the sample is snow-like circular shape and the sizes are about 0.25 µm – 0.80 µm. Most of samples are found to be homogeneous and well grain boundary. From the temperature dependent electrical conductivity results, $Mg_{0.5}Cu_{0.5}Fe_2O_4$ is the superionic conductor at high temperature and the activation energy is also evaluated.

In addition, $Mg_{0.5}Cu_{0.5}Fe_2O_4$ was successfully deposited on p-Si substrate at 500°C for 1 h in the vacuum chamber by using thermal diffusion method. Morphological features and layers thickness of the film were investigated by SEM method. Electrical characterizations of the film were examined by I-V characteristic measurements in the bias-voltage of -5 V - +5 V under different illumination conditions. From the SEM micrograph, the grain shape of the $Mg_{0.5}Cu_{0.5}Fe_2O_4$ layer is found to snow-like circular shape and crack free layer on p-Si substrate. The diffusion layer thickness of the sample is about 3.14 µm.

The results of these studies are promising and suggested that Magnesium-copper mixed spinel ferrite, $Mg_{0.5}Cu_{0.5}Fe_2O_4$ based films are attractive for use as storage elements for ferromagnetic memory applications.

Acknowledgements

I would like to express my sincere thanks to Professor Dr Aye Aye Tun, Rector, Bago University, for her kind permission to carry out this research.

I wish to show my sincere thanks to Professor Dr Yin Yin Than, Pro-Rector, Bago University, for helpful advice and valuable guidance.

I would like to express my sincere thanks to Professor Dr Khin Mar Ohn, Head of Department of Physics, Bago University, for her kind permission to carry out this research.

I wish to show my sincere thanks to Professor Dr Khin Htoo, Department of Physics, Bago University, for her encouragement to carry out this research.

Special thanks are due to Professor Dr Win Kyaw, Associate Professor, Department of Physics, Pyay University, for his valuable guidance and helpful advice to carry out this research.

References

Adam A, Ali Z, Andeltwab E & Abbas Y (2009) “Journal of Ovonic Research”, Vol 2, 157-163

Bhunia A & Bose D N (1998) “Physics of Semiconductor”, Vol 5, 158-164

Bondyopadhyay A K (2010) “Nano Materials”, Vol 22, 162-167

Candeia R A et al (2004) “Materials Letters”, Vol 58, 169-174

J. Myanmar Acad. Arts Sci. 2020 **Vol. XVIII.No.2C**

ARDUINO BASED TEMPERATURE INDICATOR BY USING LM 35 TEMPERATURE SENSOR AND AN RGB LED

Hla Htay Win[1], Ar Kar[2], Htee Mu Wah[3], Ei Cherry Hlaing[4]

Abstract

The "Temperature Indicator Circuit" is mainly implemented by using Arduino Uno microcontroller board and LM35. The peripheral components are 16 x 2 LCD, HC05 Bluetooth module, android phone, RGB LED (common cathode type), buzzer, fan with motor and relay module. The output data is sent to LCD, an RGB LEDs and android phone from Bluetooth module. An LM35 temperature sensor is used for sensing environment temperature. Different temperature ranges will produce a different color on an RGB LED. The Arduino Uno microcontroller sends the calculated temperature to 16 x 2 LCD and RGB LED and the user by using appropriate commands of LM35 temperature sensor. The sketch for the microcontroller were written in the Arduino programming language, debugged, complied and burnt into the ATmega328P microcontroller using the Arduino integrated development environment (IDE).

Keywords : Arduino Uno,LM35, RGB LED,16 x 2 LCD.

Introduction

The Temperature Indicator circuit can be used as a temperature detector or a more accurate temperature signal indicator. The system is based on the working of temperature controller using LM35 as temperature sensor, RGB LED as signal indicator and LCD as show output signal range. LM35 sensor automatically senses the temperature and works normally within a particular temperature range. -10 to100°C temperature indicator circuit can be controlled with the help of a sensor and reported to the user' phone every time. The LM35 devices are precision integrated circuit temperature sensors whose output voltage is linearly proportional to the Celsius temperature scale.

An LED and buzzer alarm are used to indicate when the device crosses the set of hot temperature. In this research work, the RGB LED will change colors depending on the temperature of the surrounding environment. Bluetooth module, HC05 is a transceiver that realizes the connection between the smartphone and Arduino board. The block diagram of the system is shown in Figure 1.

---

[1] Dr, Lecturer, Department of Physics, Bago University

[2] Dr, Assistant Lecturer, Department of Physics, Bago University

[3] PhD Candidate, Assistant Lecturer, Department of Physics, Bago University

[4] Dr, Demonstrator, Department of Physics, Bago University

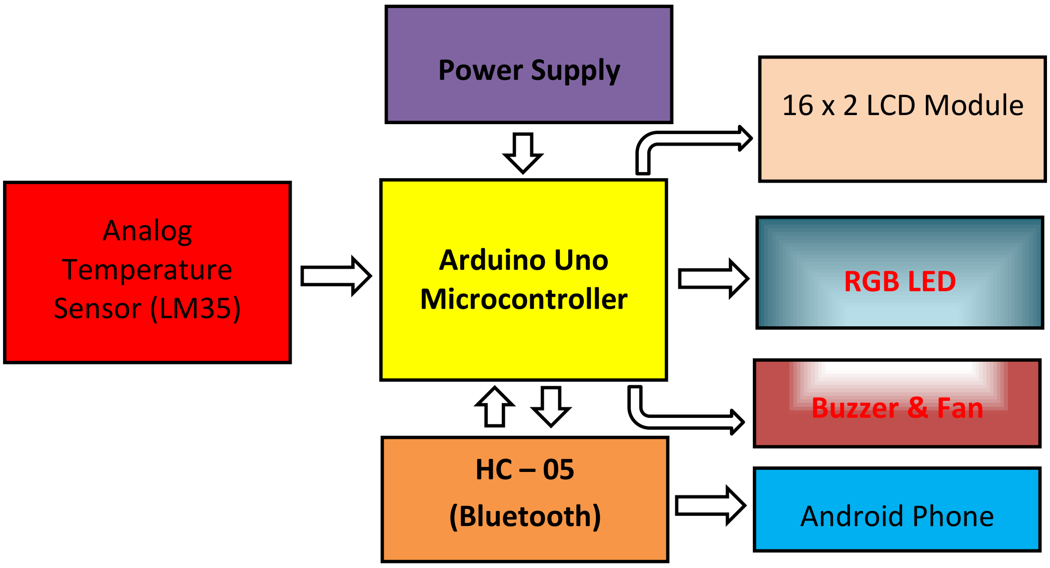

Figure 1 The block diagram of the temperature indicator circuit

Background Theory of the Temperature Indicator Circuit

Arduino Uno

Arduino Uno board is a microcontroller board based on Atmel Atmega328P 8-bit microprocessor. There are 14 digital input and output pins. 6 - pin of which can be used as pulse width (PWM) output. It has 6 Analog inputs and a 16 MHz quartz crystal or oscillator. Arduino Uno board has USB (universal serial bus) cable to connect to a computer, a power jack, an ICSP (In Circuit Serial Programming) header and a reset button.

Arduino is designed to sense the environment and/or surrounding by receiving input signal through sensors and communicates with its surrounding through actuators. Since the Arduino hardware and software is an open source, it has already many clones of Arduino hardware available with many exciting features, Arduino Uno board is used in this research. [BadamasiY., 2014]

Temperature Sensor LM35

A temperature sensor, LM35 is designed specifically to measure the hotness or coldness of an object. It is a precision temperature sensor with its output proportional to the temperature in °C. It can be measured more accurately than with a thermistor.

This sensor also possesses low self-heating and does not cause more than 0.1 °C temperature rise in air. The operating temperature range is from -55°C to 150°C. The LM35's low output impedance make interfacing to readout or control circuitry especially easy to use.[Arduino based digital temperature sensor,2016]

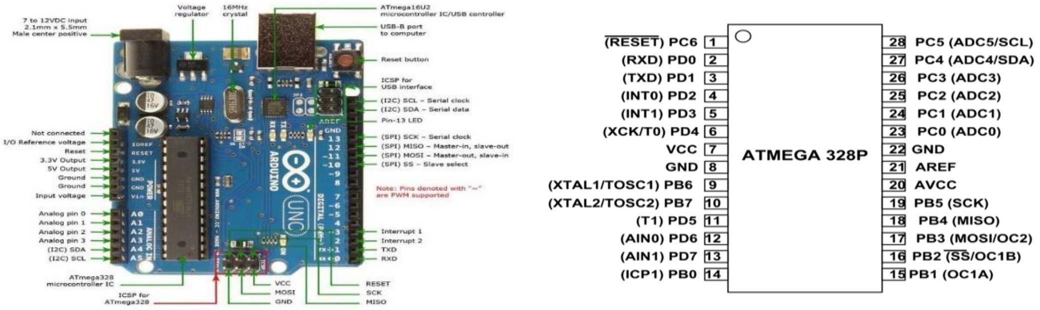

Figure 2 The photograph of Arduino Uno and pin diagram of the ATmega 328P

Figure 3 The photograph of and pin diagram of the LM-35 temperature sensor

Liquid Crystal Display (LCDs)

Liquid Crystal Display (LCDs) has 2 lines and can display 16 characters on each line. Nonetheless, when it is interfaced with the microcontroller, the messages can be scrolled with software to display information which is more than 16 characters in length.

The Arduino IDE allows the user to use LCD in 4-bit mode. This type of communication enables the user to decrease the pin usage on Arduino, unlike other the Arduino need not to be programmed separately for using it in 4-bit mode because by default the Arduino is set up to communicate in 4 bit mode. The 4-bit mode of LCD can be used in this circuit.[Pimpalgaonkar A.& at el,2013]

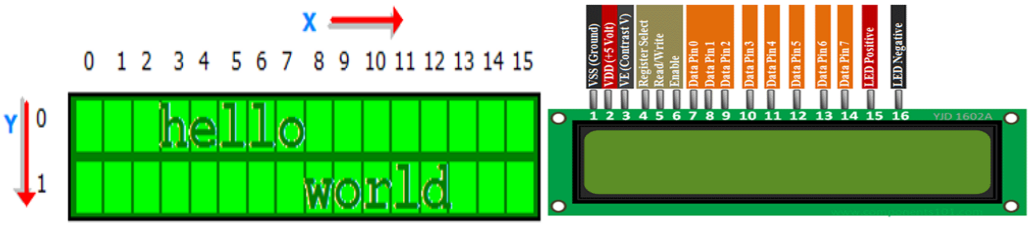

Figure 4 The position photograph and pin diagram of the 16x2 LCD display

HC05 Bluetooth Module

Bluetooth is a technology for wireless communication to apply long term. It is designed to replace cable connections. It uses serial communication to communicate with devices. It communicates with microcontroller using serial port (USART) and other devices. Usually, it connects small devices: mobile phones and TVs using a short-range wireless connection to exchange documents. Its frequency band is 2.45GHz. The connection can be point-to-point or multi-point where the maximum range is 9 meters or 30 feet. The data transfer rate is 1Mbps.

HC05 Bluetooth module provides switching mode between master and slave mode which means it able to use neither receiving nor transmitting data.[Cotta A.& at el,2016]

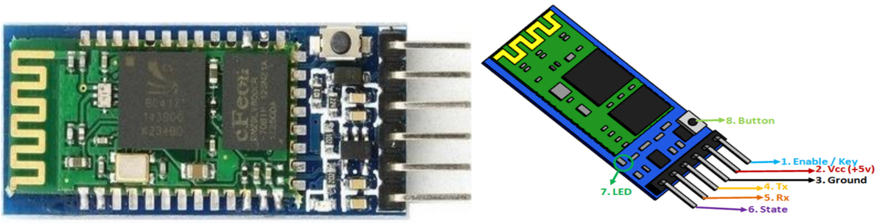

Figure 5 The photograph and pin diagram of the HC-05 Bluetooth module

RGB Light Emitting Diode

A light-emitting diode (LED) is a semiconductor light source that emits light when current flows through it. Electrons in the semiconductor recombine with electron holes to release energy in the form of photons. This is called electroluminescence. The color of the light (corresponding to the energy of the photons) is determined by the energy required for electrons to cross the band gap of the semiconductor. White light is obtained by using multiple semiconductors or a layer of light-emitting on the semiconductor device.[Mohdparvez A.,2017]

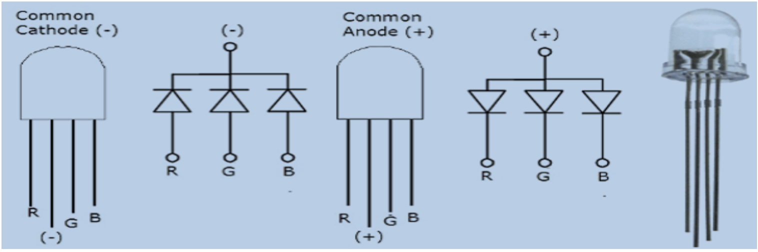

Figure 6 The photograph and pin diagram of the RGB LED

Construction of the circuit

The data pin of LM35 connects the A0 of Arduino Uno to take the output of the sensor. The RS, E, D4, D5, D6 and D7 of LCD pins connect the D13, A1 to A5 of Arduino Uno pins to show the current temperature in degree Celsius and conditions. The D9, D10 and D11 pins of Arduino connect each three-color pin of RGB LED to lit respective color according to the different temperature ranges. The buzzer pin connects the D5 of Arduino pin to alert hot temperature range. The fan with motor also connects the D8 of Uno to cool the surrounding temperature. The RX pin of the Bluetooth module is connected to the TX pin of the Arduino, and the TX of the Bluetooth module to the RX of the Arduino to communicate the user android phone. The power pin of each device connects the 5V pin of Arduino. Similarly, the ground pin of each device connects the GND pin of Arduino. The complete circuit diagram, photograph of the assembly of the temperature indicator and blue tooth android application are shown in Figure 7, 8 and 9.

Operation of the system

When the power supply applies to the system, a temperature sensor LM35 senses the surrounding temperature. It transfers the precision signal to the Arduino Uno microcontroller.

Arduino reads output voltage of temperature sensor by using Analog pin A0 and performs the calculation to convert this Analog value to a digital value of current temperature. After calculations, Arduino sends these calculated data's or temperature to 16x2 LCD and user's android phone simultaneously. RGB LED will produce the respective color according to the five different temperature ranges and the real surrounding temperature displays on the LCD screen and android phone. If the received temperature range (freeze) is below and equal 5°C, RGB LED produces white color. If the calculated temperature range (low or cold) is between above 5°C and 20°C, RGB LED becomes the blue color. If the normal range is between 20 and 30°C, RGB comes the green color. And then if the hot range is between 30°C and 40°C, the magenta color will open from RGB LED. If the very hot temperature range is above 40°C, the RGB will produce red color. The buzzer and fan will play and alert signal to the user's phone from Bluetooth when the temperature goes above 30°C. The several surrounding temperatures displayed on the user's phone screen all the time. The flow chart diagram of the temperature indicator circuit is as shown in Figure 10.

Results and Discussion

The research is a temperature sensor made with an Arduino Uno and LM35 sensor and a few other components. The working of the system starts with the LM35 sensor that senses the change in temperature of the surrounding and uses that temperature difference to produce a voltage signal which processes by the Arduino to give a digital output displaying the temperature of the surrounding. The system is to detect the temperature of the surroundings and display on the LCD screen and alert on the user's phone screen, fan and buzzer. The buzzer and fan will open if the sensor senses very hot (above 40°C) temperature range. The photographs of the different temperature range are shown in Figure 11 to Figure 14.

The system is successful in building a monitoring device which works as a thermometer for measuring temperature inside a building and outdoors. The performance of the system is accurate and reliable. Arduino based this device is the new possibilities for developing smart devices freely with low cost.

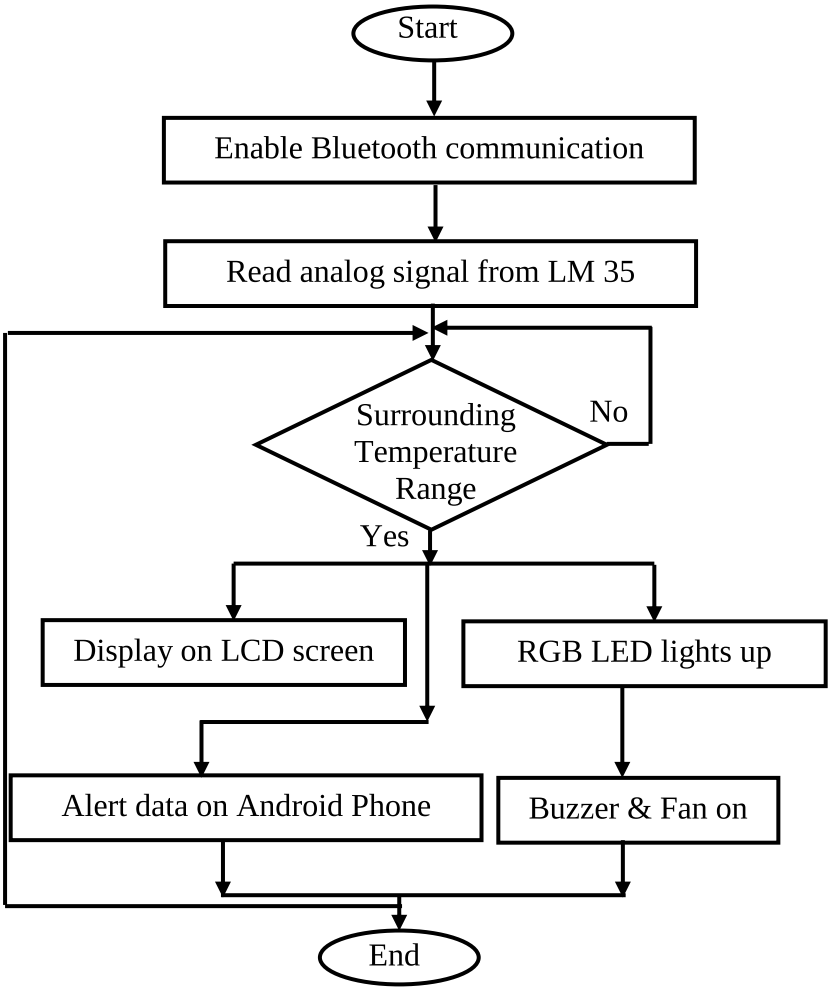

Figure 7 The Flow chart diagram of the temperature indicator circuit

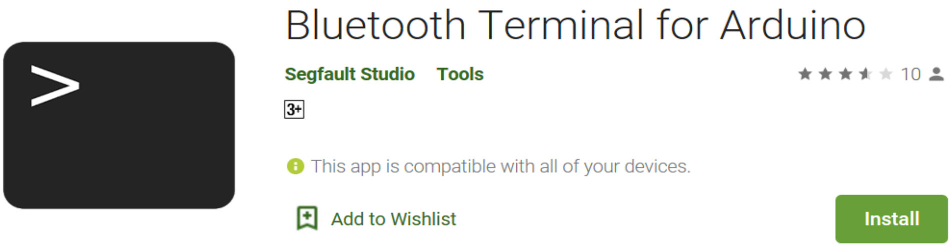

Figure 8 The photograph of Bluetooth android application for temperature data

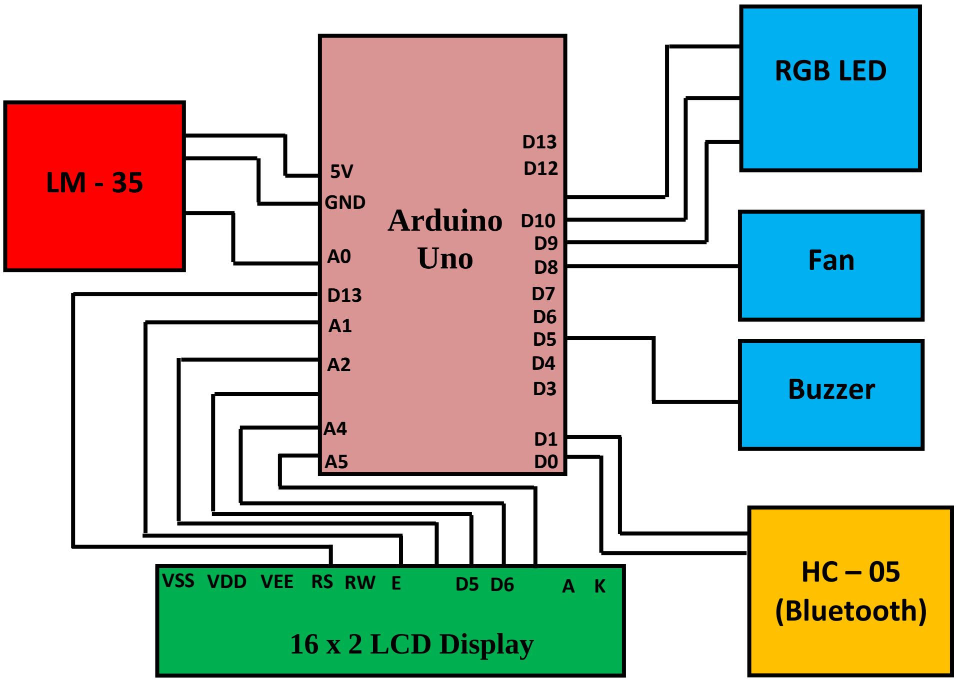

Figure 9 The complete diagram of the temperature indicator circuit

Figure 10 The photograph of the assembly of the temperature indicator circuit

```
HC-05: C3.65

HC-05: C
HC-05: C3.97

HC-05: °
HC-05: C3.97

HC-05: C
HC-05: C4.83

HC-05: °
HC-05: C4.19
```

Figure 11 The photograph of the Freeze (less than 5°C) temperature range of the system

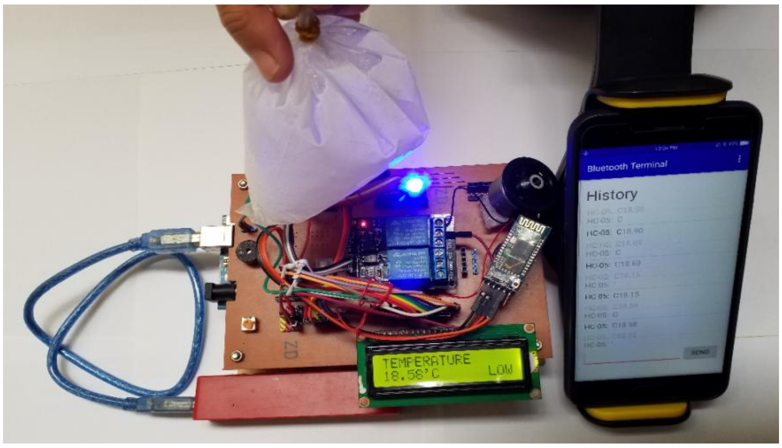

Figure 12 The photograph of Low (between above 5°C and 20°C) temperature rang of the system

Figure 13 The photograph of normal (between 20°C and 30°C) temperature range of the system

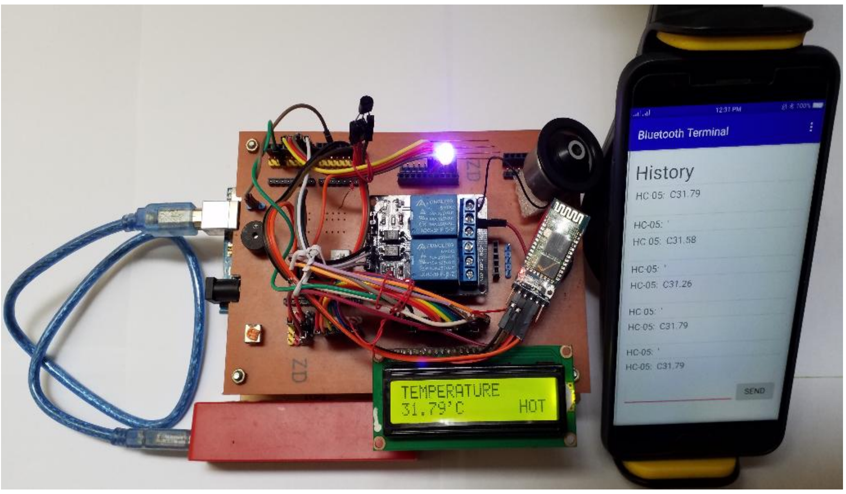

Figure 14 The photograph of the hot (between 30°C and 40°C) temperature range of the system

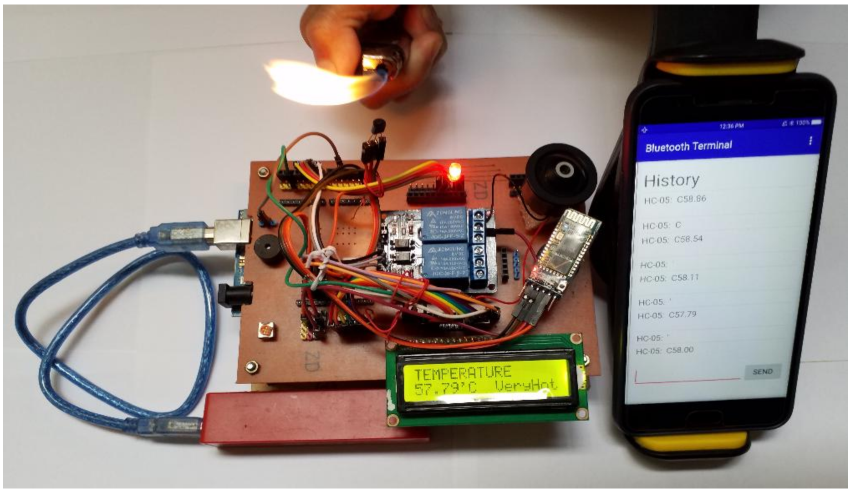

Figure 15: The photograph of the very hot (above 40°C) temperature range of the system

Conclusion

The Arduino based temperature indicator circuit can be divided into four sections: the first section (power supply) supplies the system, second section (sensor part) senses the heat by using temperature sensor LM35, third section (control part) converts the temperature value into a suitable number in Celsius scale which is done by Arduino, and last section (output part) of system displays and alerts temperature on LCD, android phone, RGB LED, fan and buzzer.

The temperature sensor on the other hand can be used to measure the safety limit temperature to prevent excessive temperature as a thermometer. The system is a very essential protection circuit and alert the hazardous heat. Therefore, it can be used in houses, offices, industries, a region of active volcano and etc.

Future Work

The Bluetooth is the communication technology of the wireless device. Its modules can transmit and receives the data wirelessly by using other devices. The HC05 Bluetooth module cannot sense a range of up to 9 meters (30ft). If the user is away from the 30ft, the connection lost. Therefore, this system will connect the GSM or Wi-Fi module to accept the temperature data later. And then it will add the Internet of thing (IOT) technology to communicate the data quickly and wide range.

Acknowledgements

I would like to thank Professor Dr Khin Khin Win, Head of Department of Physics, Yangon University for her constant support during this work.

I would also like to thank Professor Dr Khin Mar Ohn, Head of Department of Physics, Bago University for her useful advice and encouragement to complete work.

I would like to express sincere thanks to Dr Khin Htoo, Professor, Department of Physics, Bago University, for her helpful encouragement in the preparation of this work.

References

Arduino based digital temperature sensor, (2016). https://create.arduino.cc/projecthub/abishek-bhalaaji

Badamasi Y. A., (2014). "The working principle of an Arduino, Electronics, Computer and Computation".

Cotta A., Trupti Devidas N., and Devidas N. E., (2016) "Wireless Communication Using Hc-05 Bluetooth Module Interfaced with Arduino" International Journal of Science, Engineering and Technology Research (IJSETR), India, vol. 5, Issue 4, pp.869-872.

Michael M., (2014) " Beginning Arduino", Second Edition, California.

Mohdparvez A., Swamy S., Sukka B., Vijaya B. and S.V. Altaf, (2017) "Multiple Colour Generation by using RGB LED" International Journal for Scientific Research & Development, India, vol.5,pp.5-7.

Pimpalgaonkar A., Mansi Jha, Shukla N., Asthana K., (2013) "A Precision Temperature Controller using Embedded System", International Journal of Scientific and Research Publications, vol.3, no.12, pp.1-3.

J. Myanmar Acad. Arts Sci. 2020 **Vol. XVIII.No.2C**

FILTRATION PROCEDURE FOR ENVIRONMENTAL IMPACT ASSESSMENT OF AIR POLLUTANT

Lwun Htet Nay Aung [1], Win Zaw Myo Htet [2]

Abstract

Air quality issues are becoming of greater concern to the society because of the negative effects to human beings and the environment. This research was studied and purified the quality of pollutant air in northern Yangon District (Shwe Pyi Thar) from the aspect of physics in the area of environmental impact assessment (EIA). For the air purification process, washable or fiber pre-purifier, active carbon filter, and ultra violet lamp were used to constructed air filter. After using the filtration process, the data was analyzed by Scanning Electron Microscope (SEM). After that, the analyzed data were compared with the data of International Association for Impact Assessment's (IAIA) data. These analyzed data from the filtration process is slightly different with the International Association for Impact Assessment's (IAIA) data and the air filter can be widely used in industrial and air pollution problem. In this research presented a work effort to reduce CO_2 emissions through Carbon capture and storage mechanisms. Adsorption technique is followed to control the Carbon emissions from the burning of fossil fuels in automobiles, industries and using of fire wood.

Keywords: *washable or fiber pre-purifier, active carbon filter, and ultra violet lamp.*

Introduction

Air Quality Impact Assessment (AQIA) is a mechanism, which aids the efficient use of the air resource, where it is used, to identify, predict, and evaluate critical parameters and to identify the potential changes of air quality as a result of emissions from new proposed projects, to form a screening device for setting priorities in pollution control, to be used as a tool to test alternative project design at an early stage and aid the identification of the most suitable site in terms of benefit maximization and reduction of harmful effects. Finally, to identify the type of industry this can be accommodated in an area while maintaining good air quality.

An air filter is a device which removes solid airborne particles that are generally harmful to human health if haled in the lungs. Particles include things such as dust, powder, pollen, mold, fibers, germs etc. It is using physical and chemical processes with fibrous plated paper, foam, cotton, ionizers, activated charcoal, absorbents, chemicals, catalysts etc., and cleans the air to the designed breathable level and odor free for the intended user. Air filters are used in buildings, transportation, public areas and industries. There is air pollution due to the environmental conditions or nature of the process. Some of the popular air filers include:

- High- efficiency particulate absorption (HEPA) air filter- absorbs and clean 99.97% of airborne particles that have a size of 0.3 micrometers or larger, which are particularly sensitive for asthma patients.
- Ionizer air filter- uses ions to attract particles, dusts from a distance by magnetizing and neutralizing particles. It may not be very effective for a room with an asthma patient
- Active Charcoal air filter- filters fumes, cigarette smoke and some gaseous odors
- Germicidal ultra violet (UV) air filter-removes germs and viruses from the air by a special UV lamp.

---

[1] Lecturer, Department of Physics, Bago University

[2] Assistant Lecturer, Department of Physics, Bago University

Materials and Methods

Washable Fiber Pre-Filter

Washable fiber pre-filter is a semi-permeable paper barrier placed perpendicular to a liquid or air flow. It is used to separate fine substances from liquids or air. It is used in science labs to remove solids from liquids. This can be used to remove sand, dust, small particulate matter from environment. Filter paper has various properties. The important parameters are wet strength, porosity, particle retention, volumetric flow rate, compatibility, efficiency and capacity. There are two mechanisms of filtration with paper; volume and surface. By volume filtration the particles are caught in the bulk of the filter paper. By surface filtration the particles are caught on the paper surface. Filter paper is mostly used because even a small piece of filter paper will absorb a significant volume of liquid or gas.

The raw materials of fiber pre-filter are different paper pulps. The pulp may be from softwood, hardwood, fiber crops, and mineral fibers. For high quality filters, dissolving pulp and mercerized pulp are used. Most filter papers are made on small paper machines. In this research, cotton fiber was used for pre-filter. The size of the pre-filter is one square feet, width is 0.1 feet, which is located on the fourth layer of the air purification system. Therefore, the mechanisms of filtration process of the pre-filter have both volume and surface properties. The washable fiber pre-filter was shown in figure (1). After filtration process, the dust and small particulate matter was deposited in pre-filter, so the pre-filter is very dirty only in 2 weeks. This filter can wash by using the water, pressurized air, etc. And then, reuse for next filtration process until destroy.

Carbon and Sulphur Dioxide (CO_2) Scrubber or Filter

A carbon and sulphur dioxide scrubber are a type of filter that absorbs carbon and sulphur dioxide (CO_2). It is used to treat exhaust gases from industrial plants and automobile from exhaled air in life support systems. Carbon dioxide scrubbers are also used in air purification process. The Carbon dioxide scrubber or filter is very important in air purification process, because the ambient air is mostly consisting of CO_2 nearly 40% and the carbon dioxide is directly affected to environment, climate change and global warming. In this research, lime (calcium oxide) was used for carbon dioxide and sulphur dioxide, because lime is highly interaction with carbon oxide and sulphur dioxide.

Calcium oxide is a white crystalline solid with a melting point of 2572 ºC. It is manufactured by heating limestone, coral, sea shells, or chalk, which are mainly $CaCO_3$, to drive off carbon dioxide.

$$\mathrm{CaCO_3(s)} \xrightarrow{\text{500-600ºC}} \mathrm{CaO(s) + CO_2(g)}$$

This reaction is reversible; calcium oxide will react with carbon dioxide to form calcium carbonate. The reaction is driven to the right by flushing carbon dioxide from the mixture as it is released. At room temperature, the reaction of lime with carbon dioxide is very slow. It is speeded by mixing lime with water. When lime is mixed with water, it forms calcium hydroxide, called slaked lime.

$$\mathrm{CaO(s) + H_2O(I) \longrightarrow Ca(OH)_2(s)}$$

The reaction of calcium hydroxide with carbon dioxide is faster, producing a mortar that hardens more quickly. This reaction is also used for lime coating on the surface of aluminum sieve. After that reaction, carbon dioxide scrubbing process become as following equation.

$$\mathrm{Ca(OH)_2(s) + CO_2(g) \longrightarrow CaCO_3(s) + H_2O(I)}$$

Pollution control is a rapidly expanding consumer of lime. Lime is used in stack gas scrubbers to reduce sulfur dioxide emissions from power plants. Sulfur dioxide reacts with lime to form solid calcium sulfite.

$$\mathrm{SO_2(g) + CaO(s) \longrightarrow CaSO_3(s)}$$

So lime is very useful in chemical filtration process of sulphur dioxide, carbon dioxide and other chemical compounds. In this research, carbon and sulphur dioxide scubber which is made with calicium oxide coating on the aluminum sieve. Size of the scrubber is 1 feet squared and width is 0.1 ft and which is located in second layer of the air purification system. Carbon dioxide and sulphur dioxide filter was shown in figure 2.

Active Charcoal Carbon Filter

Carbon filtering is a method of filtering that uses a bed of activated carbon to remove contaminants and impurities, using chemical absorption. Each particle of carbon provides a large surface pore structure, allowing contaminants the maximum possible exposure to the active sites within the filter media. One pound (450 g) of activated carbon contains a surface area of approximately 100 acres (40 Hectares). Activated carbon works via a process called absorption, whereby pollutant molecules in the fluid to be treated are trapped inside the pore structure of the carbon substrate. Carbon filtering is commonly used for water purification, in air purifiers and industrial gas processing, for example the removal of siloxanes and hydrogen sulfide from biogas. It is also used in a number of other applications, including respirator masks, the purification of sugarcane and in the recovery of precious metals, especially gold. It is also used in cigarette filters. Active charcoal carbon filters are most effective at removing chlorine, sediment, volatile organic compounds (VOCs), taste and odor from water. They are not effective at removing minerals, salts, and dissolved inorganic compounds. Typical particle sizes that can be removed by carbon filters range from 0.5 to 50 micrometers. These particle size will use as part of the filter description. Charcoal is carbon & Activated charcoal is charcoal that has been treated with oxygen to open up millions of tiny pores between the carbon atoms. In this research, 225 gram of active charcoal carbon was used for active carbon filter, which's volume is $(1\times1\times 01)\ \mathrm{ft}^3$ and it is located in three layer of the air purification system. The active charcoal carbon filter was shown in figure 3.

Titanium Dioxide Filtration Process

In photocatalytic air purifiers, the catalyst that cleans the air is typical titanium dioxide and it's energized by ultraviolet light. UV is the short-wavelength light just beyond the blue-violet part of the electromagnetic spectrum that our eyes can detected. The UV light is exactly the right amount of energy to get titanium dioxide. Titanium dioxide film is covering the surface of a backing material called a substrate, which is usually made from a ceramic or a piece of metal (such as aluminum). There are three steps of process in the titanium dioxide catalyst in an air purifier breaks apart molecules of air pollution.

- When UV light shines on the titanium dioxide, electrons (the tiny, negatively charged particles inside atoms) are released at its surface. It's the electron that do the useful work for purification process.
- The electron interacts with water molecules in the air, breaking them up into hydroxyl radicals ($OH^{-)}$, which are highly reactive, short-lived, uncharged forms of hydroxide ions (OH^{-}).
- These small, agile hydroxyl radicals then attack bigger organic (carbon -based) pollutant molecules, breaking apart their chemical bonds and turning them into harmless substances such as carbon dioxide and water. This is a process of oxidation and that's why air purifiers that work this away are sometimes also described as PCO (photocatalytic oxidation) air cleaners.

In this research, titanium dioxide was coating on the aluminum sieve which area of 1square feet and width is 0.2mm. Sol-gel coating method was used for the coating of titanium on the aluminum sieve.

All chemicals to prepare TiO_2 powder modified sol (PMS) were used as received, polyethylene glycol, de-ionized water, nitric acid (60%) and P-25 powder. The precursor solution consisted of 70 g TTIP, 50g IPA and 9g PEG. The solution was stirred at room temperature for approximately 1 hour. Then the pre-mixed solution containing 30g IPA, 2g nitric acid and 4 g of de-ionized water was added drop-wise under vigorous stirring. Subsequently, P-25 powder was incorporated into a precursor sol solution. The loading concentrations of P-25 powder were 0, 10, 20, 40 and 80 g·L-1. After aging the solution at room temperature for 1 day, the pre-cleaned aluminum sieve was coated with P-25 powder modified TiO_2 sol-gel solution. The dip-coated specimens were dried at 65 ºC for 1 hour and then calcined at 300 ºC for 2 hours. Finally, Titanium dioxide photocatalytic filter was used for air purification process which is located on the first layer. The titanium dioxide filter was shown in figure 4.

Figure 1 Pre-Washable Filter

Figure 2 Calcium Oxide Filter

Figure 3 Active Charcoal Carbon Filter

Figure 4 Titanium Dioxide Filter

Designing of the Air Purification Process

Four types of filters were used for air purification process, which are titanium dioxide, calcium oxide, charcoal active carbon and pre-filter. These are main components of the air purification process. The titanium oxide filter is located on the first layer which is need to react with UV and air pollutants molecules in ambient air. Calcium oxide filter is located on the second layer of the system, that it is also called carbon dioxide and sulphur dioxide trap filter. In third layer, active charcoal carbon filter is located and react with other pollutant mineral in ambient air. Finally, pre-filter is located in last layer and this layer is last stage of the air purification process. In this design, function of the fan is to support the speed of the pollutant air from ambient to air purification system. Outlet air quality can determine by using the deposited test paper. The schematic diagram of the system was shown in figure 5.

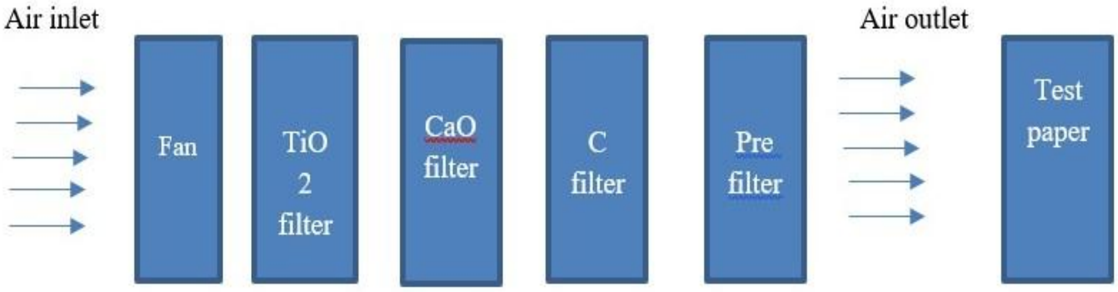

Figure 5 The Schematic Diagram of Air Purification System

Results and Discussion

Outlet air quality was determined by using two deposited test papers, these are test paper without purification process and another one is by using air purification system. These two figures were shown in figure 6(a) and 6(b). In the air purification test paper, the pollutant particles were less than the test paper without purification process. This amount of pollutant is within one month. Scanning Electron Microscope was using for particle analysing process. Figure 7(a) and 7(b) was shown the SEM image of the test papers. Image J software was used for particle counting and average size of particle analysis and those particles counting screen was shown in figure 8(a) and 8(b). Amount of the particle in air purification process test paper are 126 particles and average size of the particle is 108.230 pixels. Amount of the particle in without air purification process test paper is 274 particles and average size of the particles is 66.055 pixels. Amount of particle without air purification process test paper is larger than amount of particle in air purification process and also average size of the particle in without purification process is smaller than the size of particle in air purification process. On the other size, pixels amount of the 20 micro meter is 160 pixels, so the particle size of 108 pixels is 13.5 micro meter for filtration process and 8.25 micro meter for without filtration process. These data were analysed by using the Image J software, which is more affective of particle analysing software for scanning electron microscope image. So, air purification process is effective in this research because the purification process was reduced to particle amount of nearly 117 percent of particles and also size of the particle is increase 61.76 percent. These results are key of the air purification process.

Table 1 Comparison Results Data of Without Filtration Process and With Filtration

No.	Type of Paper	Number of Particles	Particle Size in Pixels	Particle Size in Micrometre
1	Without Filtration	274	66.055	8.25
2	With Filtration	126	108.23	13.5

Figure 6 (a) Test Paper with Air Purification Process

Figure 6 (b) Test Paper without Air Purification Process

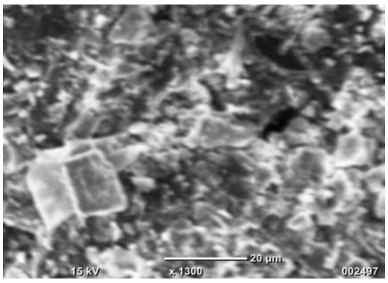

Figure 7 (a) SEM image of Air Purification Process Test Paper

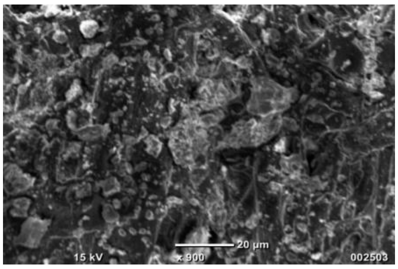

Figure 7 (b) SEM Image of without Air Purification Process Test Paper

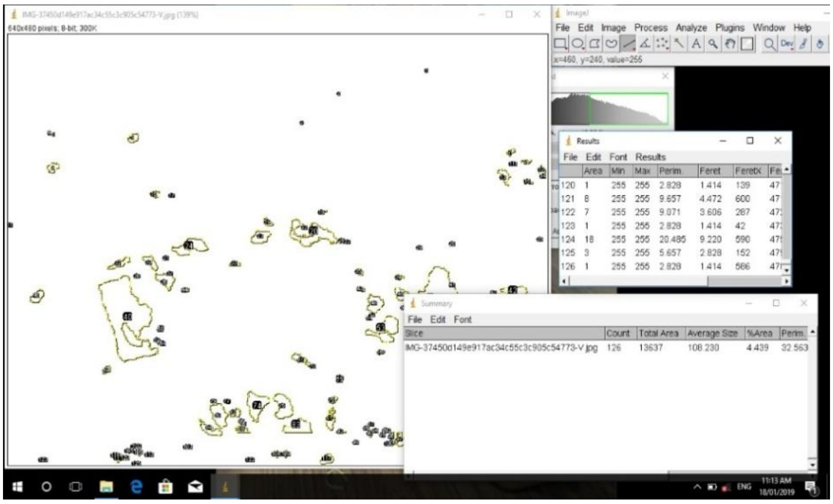

	Area	Min	Max	Perim.	Feret	FeretX	Fe
120	1	255	255	2.828	1.414	139	47
121	8	255	255	9.657	4.472	600	47
122	7	255	255	9.071	3.606	287	47
123	1	255	255	2.828	1.414	42	47
124	18	255	255	20.485	9.220	590	47
125	3	255	255	5.657	2.828	152	47
126	1	255	255	2.828	1.414	586	47

Slice	Count	Total Area	Average Size	%Area	Perim.
IMG-37450d149e917ac34c55c3c905c54773-V.jpg	126	13637	108.230	4.439	32.563

Figure 8(a) Particle Analysing of Air Purification Process Test Paper by Using Image J Software

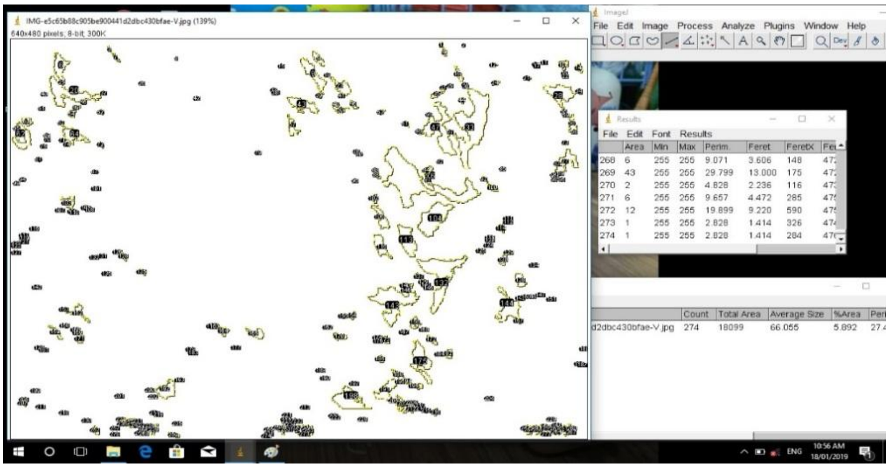

	Area	Min	Max	Perim.	Feret	FeretX
268	6	255	255	9.071	3.606	148
269	43	255	255	29.799	13.000	175
270	2	255	255	4.828	2.236	116
271	6	255	255	9.657	4.472	285
272	12	255	255	19.899	9.220	590
273	1	255	255	2.828	1.414	326
274	1	255	255	2.828	1.414	284

	Count	Total Area	Average Size	%Area
d2dbc430bfae-V.jpg	274	18099	66.055	5.892

Figure 8 (a) Particle Analysing of Without Air Purification Process Test Paper by Using Image J Software

Conclusion

The National Particle Component Toxicity (NPACZT) program concluded that all particles affect to health some way. Therefore, the kinds of the particle are not important but size of the particle is important in air quality. Particles less than 10 micrometer are the worst offenders. Particles larger than 10 micrometers can still irritate eyes, nose and throat as well. So, results of this research data are compared with the PM_{10} (particulate matter). Average size of the particle in air purification process is 13.5 micrometers. Therefore, the size of the particles is larger than the PM_{10}. In addition, the air purification process was reduced the amount of particle and increased the size of the particle. In this research, the titanium dioxide filter, calcium oxide filter, active charcoal filter and pre-washable filter are affective in air purification process. So, the air purification filter design can be used in air filtration process of industry, home and public access area.

Acknowledgements

I would like to express my sincere thanks to Dr Aye Aye Tun, Rector, Bago University, for her kind permission to carry out this research.

I would like to express my sincere thanks to Dr Yin Yin Than, Pro-Rector, Bago University, for helpful advice and valuable guidance.

I would like to express my sincere thanks to Professor Dr Khin Mar Ohn, Head of Department of Physics, Bago University, for her kind permission to carry out this research.

I would like to express my sincere thanks to my Supervisor Professor Dr Khin Khin Win, Head of Department of Physics, University of Yangon, for her kind permission and guiding to carry out this research.

References

Ahmad Y. J., and G.K. Sammy, (1987) "Guidelines to Environmental Impact Assessment in Developing Countries. UNEP Regional Seas Reports and Studies."

DEAT, (2006) "Government Gazette, National Environmental Management Air Quality." Act, 2004, No. 28899".

Lee N., (1995) "Environmental Assessment in European Union" a tenth anniversary project appraisal."

World Bank, (1993) "World Development report: investing in health. Washington, DC: The World Bank, Oxford University Press".

Welford R., (1996) "Corporate Environmental Management. Earth scan, London."

J. Myanmar Acad. Arts Sci. 2020 **Vol. XVIII.No.2C**

CONSTRUCTION OF MAXIMUM POWER POINT TRACKING WIND-SOLAR HYBRID CHARGE CONTROLLER

Win Zaw Myo Htet[1], Lwan Htet Nay Aung[2]

Abstract

Both wind and solar circuits are constructed by using an Arduino Uno that uses ATmega328P. ACS712 Hall Current Sensor and the voltage divider circuit are used to measure the input and output current and voltage of wind, solar and battery. PWM signal is provided by Arduino Uno to drive the MOSFETs via IR2110 MOSFET driver IC. High ampere dc relay is used to switch between dump load and wind circuit. The 4-lines LCD is used to display the voltage and the current of solar, wind and battery. The A/D module of an Arduino Uno is used to convert the output voltage and current from voltage divider and ACS712 into digital forms which are used as the reference values in the program. When battery is at maximum capacity, the controller will activate a relay that will send the excess power to a dump load resistor.

Keywords: hall current sensor, A/D module

Introduction

Research on MPPT controllers is becoming more popular as the interest in renewable energy technologies rises. In a PV system, when compared to the battery the energy produce by the panel(s) may be over or under. Not to waste energy, a buck or boost converter in a MPPT controller is used to gain higher power production efficiency. With a turbine, it is uncommon to have a steady input source because wind stays never steady. When the wind is strong and steady, it would be ideal to maximize the opportunity to harvest as much energy as possible through a buck converter. DC-DC converters with MPPT that provided the maximum power transfer are implemented. It can change the current and voltage levels so that the maximum power can be extracted from the PV array. Converting a given fixed load to a variable load is changing the voltage and current level. The whole circuit operation is shown as block diagram in Figure 1.

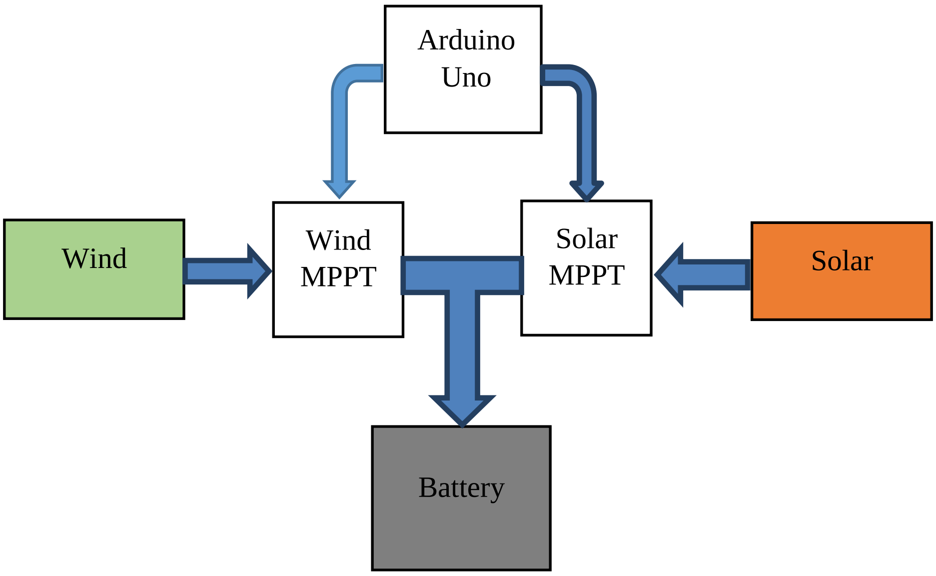

Figure 1 block diagram of MPPT hybrid charge controller

---

[1] Assistant Lecturer, Department of Physics, Bago University

[2] Lecturer, Department of Physics, Bago University

Controller Design

The diode and the capacitor on the input side filter noise that may be present. The input is read by the voltage divider and then passes through the ACS712 current sensor on both solar and wind. For this controller, the input is fed through a MOSFET if the voltage is high enough to meet the enable voltage, then it flows through the switching node. Pin 7 on the wind and pin 8 on the solar control the enabling and the disabling of the MOSFET. The Arduino begins setting up the hybrid MPPT controller by reading the defined variables and pins. It sets the digital pins 0, 6, 7, 8, and 11 to outputs. PWM signal or High/Low signal is given out by digital pins (0, 6, 7, 8 and 11). Since pins 0, 7, 8 are used as High/Low, they are initially given the Low (off) state not to allow flow from the output. The duty cycle has set limits not to allow either energy flow from the output and keep the bootstrap gate capacitor charged. The Arduino UNO sends a 62.5 kHz PWM signal from pin 6 and a 31.25 kHz PWM signal from pin 11 to the IR2110 high and low side drivers. The driver sends the same signal to the MOSFETs but amplifies the driving voltage to the MOSFET gate. The output voltage and current are measured and compared to the set values assigned within the program.

The duty cycle within the PWM equates to on/off time for the MOSFET. If the voltage from the output of DC-DC converter is above the maximum, the duty cycle will decrease until the output voltage matches the set limit. Conversely, if the DC-DC converter output voltage is less than the minimum limit set, the duty cycle will increase. If the input voltage from the solar panel and/or the wind turbine is less than the disable voltage or the current is less than the minimum, then the DC-DC converter will be disabled. If the system is disabled, it will be constantly checked by the Arduino till the system enabled. If the input voltages are greater than the enable voltage, it turns on the DC-DC converters. Figure 2 shows the circuit schematic for the hybrid controller and Figure 3 shows the photo of the hybrid controller circuit.

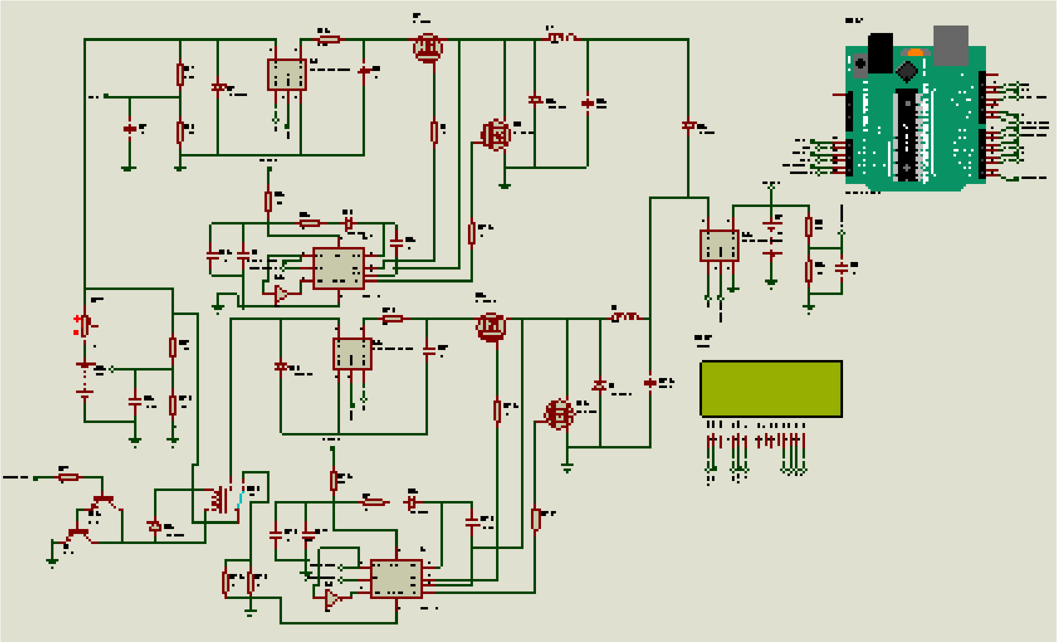

Figure 2 Hybrid MPPT charge controller circuit diagram

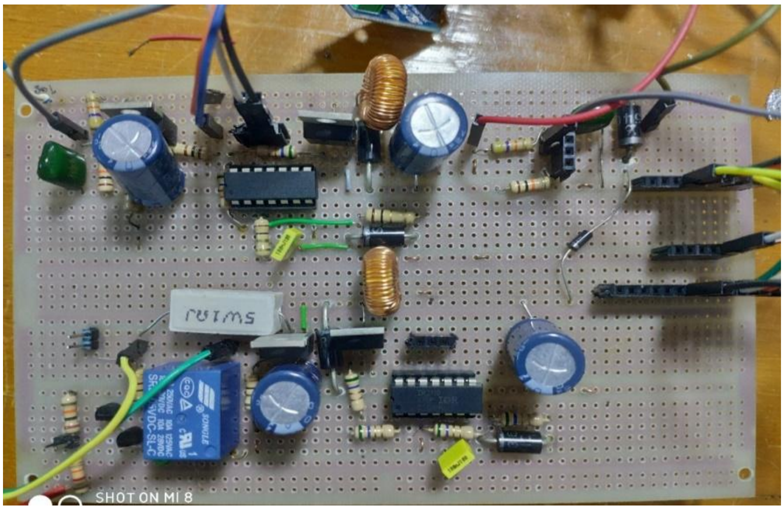

Figure 3 Photo of hybrid MPPT charge controller circuit

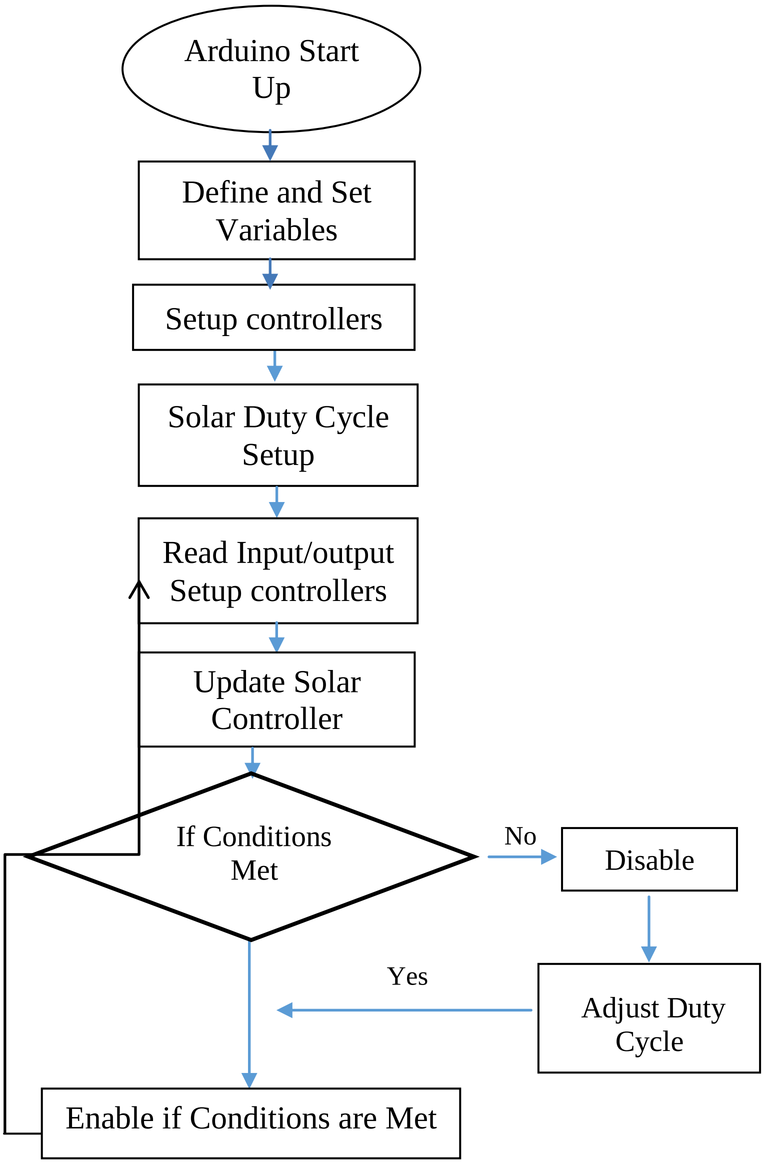

Figure 4 Flow diagram of control sequence

Operating Procedure

Once there is understanding of how the controller is designed to work, the next step is to have the circuit communicate with the controller. When the controller receives power from the UNO, it reads the defined conditions of the input and output sources. It begins to set up the controller by identifying which pins will provide an output and setting the PWM modes. It displays a welcome screen and then begins the infinite loop after setting up the controller. The loop contains three different parts, the first being to read the values at the input and output. Then, it begins the solar and wind updates; the Arduino controls the amount of duty being supplied through each PWM pin to correct the output voltage and input current.

It is necessary to set up a time delay because when operating on Fast PWM, the clock runs 64 times faster than normal. The delay will allow the Arduino to read at a normal pace. The duty cycle for the controllers needs to have a maximum and minimum level to protect the circuit. A voltage divider is used to produce a measurable voltage for the Arduino. The voltage multipliers are implemented to reflect the voltages before being reduced. Using an LCD display to show the values from the input and the output, the library Liquid Crystal is used to work with LCD screen.

The initial setup processes the hybrid MPPT controller goes through upon cycling on. The function pinMode sets the Arduino's pins to produce output. The "enable" pins, such Solar_Enable and Wind_Enable, are not defined to a PWM frequency but to a LOW or HIGH (on or off) through the function digital Write. The PWM pins need to be called upon to produce the fast PWM for pin 6 and the phase shift PWM for pin 11. This is done by setting the TCCR0A and TCCR2A registers then using the Output Compare (OCR0A and OCR2A) pin for the duty cycle, which is initially set to 0.

The enabling and the disabling parameters are set in phase, to ensure that the power is being delivered when it is needed and diverted away when it is not needed. Both buck converters need off time to keep the bootstrap capacitor for the upper MOSFET charged, so the duty cycle is set below 100% to ensure the capacitor is charged. If the bootstrap capacitor is not charged, the gate will turn off, creating a partially conducting state. A synchronous buck can eliminate the possibility of the voltage from the output to flow to the input by enforcing the duty cycle above 50%.

Measuring and Displaying Input and Output Values

The Arduino's microcontroller uses an analog to digital converter (ADC) that reads the voltage and converts it to a number between 0 and 1023. The circuit has a limit of 5V or it will overload. The voltage divider is used to measure anything above 5V, and the ACS712 converts the current to a voltage that is read the same way as the voltage divider. Each value is measured 16 times and then averaged. Once the values are read and averaged, it is then sent to the LCD screen.

Updating Solar and Wind DC-DC Converter

The Arduino begins the loop by reading the input and output values and then updating the controller for the wind and solar DC-DC converters based on the values. The Arduino decides to enable, disable, or update the duty cycle based on the state that the controller is in and the input/output values read. Wind and solar are nearly identical in the program design for disabling, enabling, and updating the duty cycle. The wind DC-DC converter has an additional condition if the turbine is producing more than 50V. The controller will disable the circuit and send it to the dump load resistors; this is to protect the components that are sensitive to voltages above 50V.

The Arduino begins by determining that the DC-DC converters are operating. If they are operating, then it will disable the DC-DC converters if the solar and wind voltages are less than their respective disable voltages, or the current is below the output's minimum. If the operating conditions are met, then the controller checks:

1. If the input voltages are less than the target voltages
2. If the output is greater than the output limit
3. If the input current is greater than the input maximum or
4. If the output current is greater than the output maximum

If one or more of these conditions are met, it will reduce the duty cycle by one until the desired output is met. If the voltages are greater than the target voltages and the output voltage is less than the minimum limit, then it will increase the duty cycle by one until the desired output is met. The Arduino will enable the DC-DC converters if previously disabled and the input is greater than the enable voltage. When in the enable state, it will measure and update the duty cycle by multiplying 255 by the output voltages over the input voltages.

Conclusion

The wind and solar hybrid charge controller circuit acts as a control circuit to regulate the process of wind turbine and solar panel battery charging process. These circuits can be constructed from discrete electronic components. The circuit operation is based on matching the wind and solar cell terminal load voltage to the appropriate number of battery cell units to be charged depending on the total power output of hybrid power source.

The advantage of using hybrid controller is controlling two systems of solar and wind energy simultaneously. The ability to control two systems with one controller is better for an overall production of energy, cost, and manageability at a slight expense to the efficiency. Developing a buck-boost converter for the wind MPPT controller would take advantage of both the lower and higher wind speed. Though the overall efficiency is less than that of a concentrated buck or boost controller, it would have more potential to produce power. To produce higher power from generator inductor size in controller must be increase due to frequency provided by Arduino. A larger inductor means less allowable current to flow before the inductor becomes over saturated, reducing the efficiency of the controller.

Acknowledgements

I would like to thank Professor Dr Khin Khin Win, Head of Department of Physics, University of Yangon and Professor Dr Khin Mar Ohn, Head of Department of Physics, Bago University, for her kind permission to carry out this work. And I also thank Professor Dr Khin Htoo, Department of Physics, Bago University for her encouragement. I am thankful for the valuable guidance and support provided by my co-supervisor Professor Dr Myo Lwin, Department of Physics, University of Yangon. I would like to express my sincere gratitude to my supervisor Dr Zaw Zaw Aung, Lecturer, Department of Physics, University of Yangon for his valuable advice and help. And my thanks also goes to U Thant Shwe, Lecturer, Department of Physics, Bago University, Dr Mie Mie Aye, Lecturer, Department of Physics, Dagon University for their help in programming and suggestion for this work. Without their guidance and feedback, the thesis work could not have been a success.

References

Allegro Micro Systems (2015, Nov) *Fully Integrated, Hall Effect-Based Linear Current Sensor IC with 2.1 kVRMS Isolation and a Low-Resistance Current Conductor*, ACS712 datasheet, [Revised June 2017].

Azevedo, J., Mendoca. F., (July, 2015) “Small scale wind energy harvesting with maximum power tracking,” AIMS Energy, Vol.3 no.3 pp.297-315. DOI:10.3934/ energy.2015.3.297.

Choudhary, D., Sexana, (2014) *A.R.DC-DC Buck-Converter for MPPT of PV System, International Journal of Emerging Technology and Advanced Engineering.*

ON Semiconductor (2013, Apr) LC selection Guide for the DC-DC synchronous Buck Converter.

Unknown Authors (2017, July) How to Design Battery Charger Applications that Require External Microcontrollers and Related System-Level Issues, Maxim Integrated https://www.maximintegrated.com/en/app-notes/index.mvp/id/680

J. Myanmar Acad. Arts Sci. 2020 **Vol. XVIII.No.2C**

AVERAGING SCHEMES FOR INHOMOGENEOUS UNIVERSE AND TIMESCAPE COSMOLOGIES

Nyein Thida[1], Han Win Than[2], Shwe Sin Oo[3], Aye Aye Mar[4], Thant Zin Naing[5]

Abstract

Timescape model is a phenomenological cosmology model without dark energy. By revisiting Einstein's strong equivalence principle and extending at the general average of the cosmological Einstein's equation, one can construct averaging schemes and timescape model. Detailed description of that timescape cosmology and expansion laws in general relativity within a covariant fluid approach have been studied. Physical interpretation of the results are carried out and visualizations of interesting results are implemented.

Keywords: Timescape model, dark energy, averaging schemes.

Introduction

Dark energy has been described as the biggest problem in cosmology. In a different perspective, dark energy is not the internal energy of a mysterious fluid, but a misidentification of those aspects of cosmological gravitational energy which by virtue of the equivalence principle cannot be localized: gradients in the energy associated with the varying curvature of space and the varying kinetic energy of the expansion of space. These are important aspects of gravitational physics in universe, which at the present epoch is very inhomogeneous, dominated by voids. (Adler. R, Bazin.M, Schiffer. M, 1975)

One uses the formalism of Thomas Buchert in taking account of backreaction in the evolution of Einstein's equations. One crucial insight is that gravitational energy and clock rates are defined with respect to a notion of infinity. Bound system where space is not expanding, including all galaxies live within finite infinity, but volume average positions in free expanding space lie beyond it there is a difference in gravitational energy and spatial curvature between the two locations. The differences were initially miniscule but are large today. Taking account of the initial conditions set by primordial inflation at the time of last scattering, when the cosmic microwave background was laid down, a quantitative model of the universe is developed. Relative to bound system observers, ideal observers at volume average positions in voids will measure an older age of the universe, a lower isotropy. These differences can be systematically quantified. On account of the variance in clock rates volume average observers in voids infer no apparent "cosmic acceleration", but observers in bound systems do. Apparent acceleration begins when the void volume fraction reaches 59%, at a redshift of order z = 0.5 to 1.0 (depending on whether one uses the CMB or supernovae as an estimator). The mystery of dark energy is explained purely in Einstein's theory, through a deeper understanding of those parts of general relativity, which Einstein himself recognised as being difficult: the understanding of gravitational energy, given that space itself is dynamical and may contain energy and momentum. (Buchert.T, 1999)

---

[1] Dr, Associate Professor, Department of Physics, Yangon University, Myanmar.

[2] Dr, Assistant Lecturer, Department of Physics, University of Yangon.

[3] Dr, Assistant Lecturer, Department of Physics, University of Yangon.

[4] Dr, Assistant Lecturer, Department of Physics, University of Yangon.

[5] Dr, Retired Pro-Rector (Admin) International Theravada Buddhist Missionary University, Yangon.

Although matter in the Universe was extremely uniform when the cosmic microwave background radiation formed, since then gravitational instability led to an increasingly complex hierarchy of structures at late epochs a cosmic web of voids with galaxies and clusters in sheets, filaments and knots. In the standard model of cosmology this hierarchy is treated by assuming an average background universe which expands uniformly, just as if no structures were present. The nonlinear growth of structure is then formally treated and simulates using Newtonian gravity only. In other words, the background evolution and the evolution of structure do not couple to each other, an idealization at odds with the very foundations of general relativity which generically demand a coupling between matter and geometry.

After that, Friedmann–Lemaître–Robertson–Walker (FLRW) model keeps spatial curvature uniform everywhere and decouples its evolution from that of matter, which is again not a generic consequence of Einstein's equations. The difference between an averaged generic evolution and an ideal FLRW evolution is usually called backreaction, and is potentially significant for interpreting observations of the actual inhomogeneous Universe. (Buchert.T, 1999)

Dark Energy and Dark Matter

In the standard model of cosmology one has to conjecture the existence of two constituents, if observational constraints are met, that both have unknown origin: first, a dominant repulsive component is thought to exist that can be modeled either by a positive cosmological constant or a scalar field, e.g. a so-called quintessence field. Besides this Dark Energy, there is, secondly, a non-baryonic component that should considerably exceed the contribution by luminous and dark baryons and massive neutrinos. The Dark Matter is thought to be provided by exotic forms of matter, not detected in (non-gravitational) experiments. According to the concordance model, the former converges to about ¾ and the latter to about ¼ of the total source of Friedmann's equations, up to a few percent that have to be attributed to baryonic matter and neutrinos (in the matter-dominated era).(Buchert.T, 2007)

Averaging Strategies: Different 'Directions' of Backreaction

The notion of averaging in cosmology is tied to space-plus-time thinking. Despite the success of general covariance in the four-dimensional formulation of classical relativity, the cosmologist's way of conceiving the Universe is evolutionary. This breaking of general covariance is in itself an obstacle to appreciating the proper status of cosmological equations. The standard model of cosmology is employed with the implicit understanding that there is a global spatial frame of reference that, if mapped to the highly isotropic Cosmic Microwave Background, is elevated to a physical frame rather a particular choice of a mathematical slicing of spacetime. (Witshire. D. L, 2007)

This point is raised as a criticism of an averaging framework, as if this problem were not in the standard model of cosmology. Again, the 'natural' choice for the matter model 'irrotational dust' is a collection of freely-falling continuum elements, now for an inhomogeneous continuum. For such a generalized collection of fundamental observers, the 4-metric form reads

$$^4g = -dt^2 + \, ^3g \, ; \;\; ^3g = \, g_{ab} \, dX^a \, \otimes dX^b \, ,$$

where latin indices run through 1…3 and X^a are local (Gaussian normal) coordinates. Evolving the first fundamental form ${}^3g$ of the spatial hypersurfaces along $\partial/\partial t =: \partial_t$ defines their second fundamental form

$$ {}^3K = K_{ab} dX^a \otimes dX^b \; ; \; K_{ab} := -\frac{1}{2}\, \partial_t \, g_{ab} \, , $$

with the extrinsic curvature components K_{ab}. Such a comoving (synchronous) slicing of spacetime may be considered 'natural', but it may also be questioned.[(Buchert.T, Ehlers.J, 1995]

Effective Description of Inhomogeneous Universe Models

Restricting attention to a universe filled with irrotational dust, i.e. irrotational pressureless matter, one spatially average the scalar parts of Einstein equations with respect to a collection of comoving (generalized fundamental) observers over a compact, rest mass preserving spatial domain D, and obtain the following set of equations

$$ \left(\frac{\dot{a}_D}{a_D}\right)^2 - \frac{8\pi G}{3}\langle e\rangle_D = -\frac{\langle R\rangle_D + Q_D}{6}, \tag{1} $$

$$ \frac{\ddot{a}_D}{a_D} + \frac{4\pi G}{3}\langle e\rangle_D = \frac{Q_D}{3}, \tag{2} $$

$$ \langle e\rangle^{\bullet}{}_D + 3\frac{\dot{a}_D}{a_D}\langle e\rangle_D = 0, \tag{3} $$

$$ \frac{1}{a_D^6}(Q_D a_D^6) + \frac{1}{a_D^2}(\langle R\rangle_D a_D^2)^{\bullet} = 0, \tag{4} $$

where a_D is the effective volume scale factor

$$ a_D(t) = \left(\frac{V_D(t)}{V_{D_i}}\right)^{1/3}, \tag{5} $$

with V_{D_i} the initial volume of the domain and $V_D(t)$ its volume at a proper time t, $\langle e\rangle_D = M a_D^{-3}/V_D$, the density of irrotational dust averaged over $D, \langle R\rangle_D$ the spatial scalar curvature averaged over D and Q_D the kinematical backreaction

$$ Q_D(t) := \frac{2}{3}\left\langle\left(\theta - \langle\theta\rangle_D\right)^2\right\rangle_D - 2\langle\sigma^2\rangle_D, \tag{6} $$

with θ the rate of expansion and $\sigma := \sqrt{\frac{1}{2}\sigma^{ij}\sigma_{ij}}$ the rate of shear with the shear tensor components σ_{ij}. Equations (1) and (2) govern the kinematics of the effective scale factor and equations (3) and (4) express the conservation law for the dust matter and the backreaction terms, respectively.

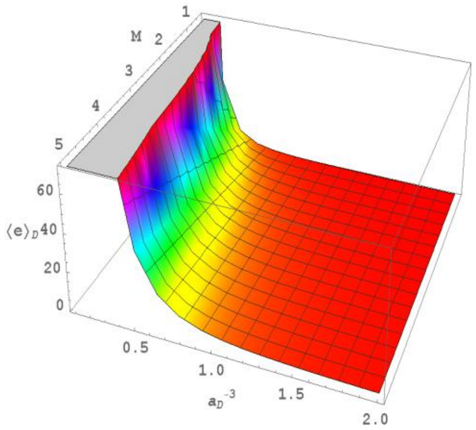

Figure 1 The evolution of density of irrotational dust in terms of mass and scale factor.

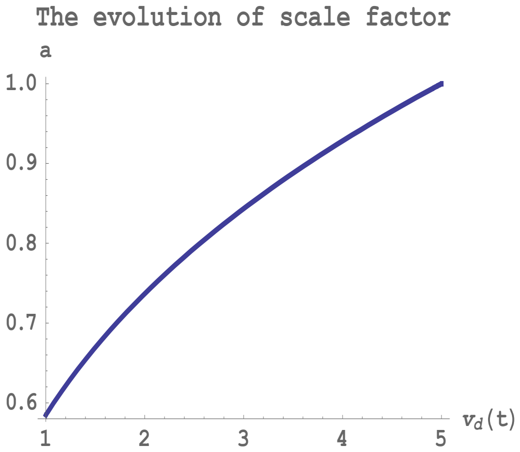

Figures 2 The evolution of scale factor with $V_D(t)$.

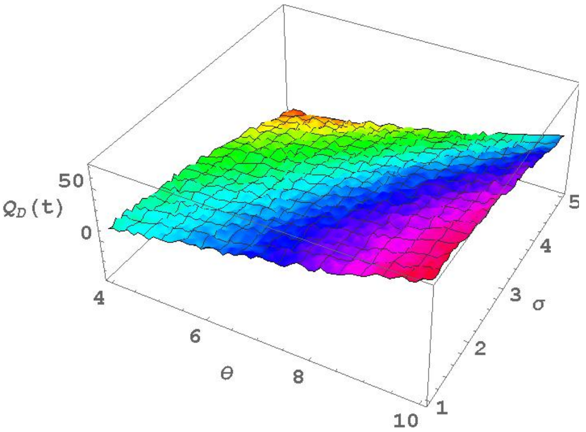

Figure 3 Variation of Kinematical Backreaction with expansion scalar and shear.

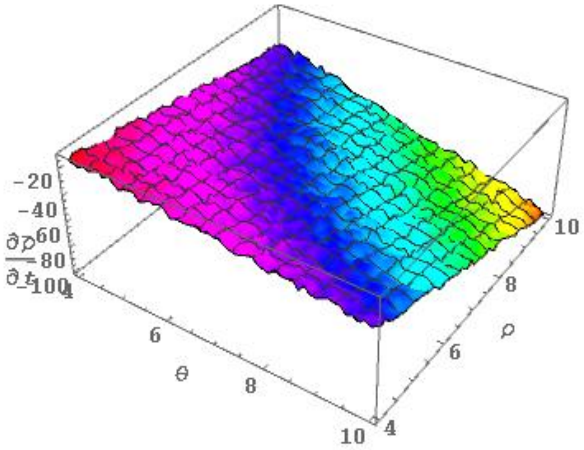

Figure 4 Time evolution of energy density in terms of scalar and density.

General Expansion Law in Newtonian Cosmology

Non Commutation Time Evolution and Averaging

Let us consider a portion of the Universe D (t) with volume $V(t)$. Henceforth, one concentrates on the expansion which one describes by the local expansion scalar $\theta = \nabla.\vec{v}$. Introducing the scale factor via the volume, $a_D \coloneqq V^{1/3}$, one can write the spatial average of θ on the domain D as

$$\langle\theta\rangle_D = \frac{1}{V}\int_D d^3 x\, \theta = \frac{\dot{V}}{V} = 3\,\frac{\dot{a}_D}{a_D} \qquad (7)$$

As written in (7) the spatial average can be calculated as a simple Euclidean volume integral over the domain *D*, the mail advantage of a Newtonian treatment. The subscript *D* indicates that the averages (as well as the scale factor) depend on morphological properties of the spatial such as content, shape and connectivity.

One evaluates the evolution of the average in a tube of trajectories of fluid elements, i.e., one introduces a Lagrangian mapping $\vec{f_t}\,:\,\vec{x}=\vec{f}\left(\vec{X}\,,t\,\right)$ which sends fluid particles from their initial (Lagrangian) position $\vec{X}$ to their final (Eulerian) position $\vec{x}$. One uses the Jacobian of this mapping, $d^3=\mathrm{J}d^3X$, J: = det $\left(\frac{\partial f_i}{\partial X_k}\right)$, to transform spatial averages to volume integrals in Lagrangian space:

$$\langle\theta\rangle_D=\frac{1}{V}\int_{D(t)}d^3\,x\,\theta(\vec{x},t)=\frac{1}{V}\int_{D(t_0)}d^3\,X\,\mathrm{J}\left(\vec{X},t\right)\theta\left(\vec{X},t\right). \tag{8}$$

Using the Lagrangian time-derivative, $\frac{d}{dt}:=\frac{\partial}{\partial t}+\nabla.$, one obtains the nonlinear commutation rule. (Buchert. T, Ehlers. J, 1995)

$$\frac{d}{dt}\langle\theta\rangle_D-\langle\frac{d}{dt}\theta\rangle_D=\langle\theta^2\rangle_D-\langle\theta\rangle^2{}_D. \tag{9}$$

Equation (9) shows that the evolution of the average and the average over the evolved field do not commute, their difference being given by the nonlinear fluctuation term on the right hand side.

The Generalized Friedmann Equation

Averaging Raychaudhuri's equation for the evolution of the expansion scalar, the scale factor a_D is found to obey the general expansion law. (Carroll, S. M., 2004)

$$3\frac{\ddot{a}_D}{a_D}+4\pi G\,\frac{M_D}{a_D^3}-\,\Lambda=-\mathbf{Q} \tag{10}$$

where the source term **Q** depends on the fluctuation term in (2.3) and the magnitudes of rotation (ω) and shear (σ) of the flow,

$$\mathbf{Q}:=\frac{2}{3}\left(\langle\theta\rangle^2{}_D-\langle\theta^2\rangle_D\right)+2\langle\sigma^2-\omega^2\rangle_D \tag{11}$$

$\mathrm{M_D}$ denotes the total mass contained in D .

Eq. (11) may be rewritten as a standard Friedmann equation for the actual source term $\langle\varrho_{eff}\rangle_D$:

$$4\pi G\,\langle\varrho_{eff}\rangle_D\coloneqq4\pi G\langle\varrho\rangle_D+\mathbf{Q}, \tag{12}$$

where $\langle\varrho\rangle_D=M_D/a_D^3$ is the pure average matter density. Eq. (12) shows that, for irrotational flows ,the additional "dynamical mass" is a positive term which adds to the matter density, if σ^2 is larger than the fluctuation $\langle\theta\rangle^2{}_D-\langle\theta^2\rangle_D=\langle(\theta-\langle\theta\rangle_D)^2\rangle_D\geq0$. This suggests to add the source term **Q** to the list of dark matter candidates: strongly sheared inhomogeneities could "fake" an additional density which leads to an overestimate of the density parameter.

Integrating eq.(11) with respect to time yields the generalized form of Friedmann's differential equation:

$$\frac{\dot{a}_D^2+k}{a_D^2}-\,\frac{8\pi GM_D}{3a_D^3}-\frac{\Lambda}{3}=\,\frac{1}{3a_D^2}\,\int_{t_0}^{t}dt'\,\mathbf{Q}\frac{d}{d\acute{t}}\,a_D^2. \tag{13}$$

Averaging Globally Homogeneous (Isotropic) Universes

One now assumes that a global Hubble flow exists on some large scale A and that the expansion-factor on that scale obeys Friedmann's differential equation Eq.(13) for (**Q = 0**);

on the scale A we write $a_D \equiv a$. Splitting the velocity gradient $v_{i,j}$ into its Hubble part and a peculiar-velocity gradient $v_{i,j} = H(t)\,\delta_{i,j} + v_{i,j}$, where H(t) = $\frac{\dot{a}}{a}$, one obtains:

$$\theta = 3H + \nabla.\vec{u} \tag{14}$$

After averaging, the last equation leads to a relation Between the Hubble function H(t), the “effective Hubble function" $H_D(t) := \frac{\dot{a}_D}{\dot{a}_D}$, and the peculiar-velocity field $\overrightarrow{u}(\vec{x}, t)$:

$$H(t) = H_D(t) - \frac{1}{3} a_D^{-3} \int_{\partial D(t)} \vec{d}\,S.\vec{u}\,. \tag{15}$$

H_D may be interpreted as that Hubble function which is inferred from the (possibly anisotropic and rotational) dynamics of the spatial domain D. (This interpretation is possible if statistical averages of many such spatial domains are considered, but at present, one only measures one member of such an ensemble.) Accordingly, the source term **Q** can be split into its Hubble part and deviations thereof and transformed into surface integrals over the boundary $\partial D(t)$. (Rosanen. S, 2006)

$$3\frac{\ddot{a}_D}{a_D} + 4\pi G\frac{M_D}{a_D^3} - \Lambda = -\frac{2}{3}\left(a_D^{-3}\int_{\partial D} \vec{d}\,S.\vec{u}\right)^2 + a_D^{-3}\int_{\partial D} \vec{d}S.(\vec{u}\,\nabla.\vec{u} - \vec{u}.\nabla\vec{u})\ . \tag{16}$$

Averaging and Schemes

The idea that the large scale universe is homogeneous and isotropic necessarily entails an implicit notion of averaging on these large scales. If g denotes the metric, Γ the Christoffel connection and E[g] the Einstein tensor for the metric g, the one has the relations

$$\Gamma \sim \partial g\ ;\ E[\,g\,] \sim \partial\Gamma + \Gamma^2\,, \tag{17}$$

with ∂ denoting spacetime derivatives. The Einstein equations are therefore

$$E[\,g\,] = T, \tag{18}$$

with T denoting the energy-momentum tensor of the matter components. Now, irrespective of any details of the averaging operation, one notes that

$$E[< g >] - < E[g] > \sim < \Gamma >^2 - < \Gamma^2 > \neq 0\ , \tag{19}$$

with the angular brackets denoting the averaging. The FLRW solution would amount to solving the equations $E[< g >] = < T >$. In general, therefore it is not true that averaging out the fluctuating inhomogeneities leaves being the FLRW solution, since what one is actually left with is

$$E[< g >] = < T > -C\ ;\ C \sim < \Gamma^2 > - < \Gamma >^2\,, \tag{20}$$

and the homogeneous solution that we are looking for will depend on the details of the correction terms C. The second cause for concern comes from observations. It has now been established beyond a reasonable doubt, that the FLRW metric confronted with observations indicates an accelerating scale factor. (Witshire. D. L, 2007)

Buchert’s Spatial Averaging

The most straightforward and intuitively clear application of Buchert’s spatial averaging is in the case when the matter source is a pressure “dust” with an energy-momentum tensor

$T^{ab} = \rho u^a \ u^b$, with u^a the dust 4-velocity which satisfies $u_a u^a = -1$. Assuming further that the dust is irrotational, the 4-velocity will be orthogonal to 3-dimensional spatial sections and the metric can be written in “synchronous and comoving” coordinates (in which $u^a = 1, \vec{0}$)as

$$ds^2 = -dt^2 + h_{AB}(t, \vec{x}) dx^A \ \ dx^B \qquad (21)$$

The expansion tensor Θ^A_B is given by $\Theta^A_B = (1/2) h^{AC} \dot{h}_{CB}$ where the dot refers to a derivative with respect to time *t*. The traceless symmetric shear tensor is defined as $\sigma^A_B \ \equiv \Theta^A_B - (\Theta/3) \ \delta^A_B$ where $\Theta = \Theta^A_A$ is the expansion scalar.

The scalar equations are the Hamiltonian constraint (3.6a) and the evolution equation for Θ

$$^{(3)}R + \frac{2}{3}\Theta^2 - 2\sigma^2 = 16\pi G\rho \, , \qquad (22)$$

$$^{(3)}R + \dot{\Theta} + \Theta^2 = 16\pi G\rho \, , \qquad (23)$$

where $^{(3)}R$ is the Ricci scalar of the 3-dimensional hypersurface of constant *t* and σ^2 is the rate of shear defined by $\sigma^2 \equiv (1/2)\sigma^A_B \sigma^B_A$. Eqns. (22) and (23) can be combined to give Raychaudhuri’s equation

$$\dot{\Theta} + \frac{1}{3}\Theta^2 + 2\sigma^2 + 4\pi G\rho = 0 \, . \qquad (24)$$

The continuity equation $\dot{\rho} = -\Theta\rho$ which gives the evolution of ρ, is consistent with Eqns. (23) , (24). One only consider the scalar equations, since the spatial average of a scalar quantity can be defined in a gauge covariant manner within a given foliation of spacetime. For the spacetime described by (24), the spatial average of a scalar $\psi(t, \vec{x})$ over a comoving domain $\mathcal{D}$ at time *t* is defined by

$$< \Psi >_{\mathcal{D}} = \frac{1}{V_D} \int_D d^3x \sqrt{h} \, \psi \, , \qquad (25)$$

where h is the determinant of the 3-metric h_{AB} and V_D is the volume of the comoving domain given by $V_D = \int_D d^3x \sqrt{h}$. The following commutation relation then holds

$$< \Psi >_{\mathcal{D}} - < \dot{\Psi} >_{\mathcal{D}} = \ < \Psi\Theta >_{\mathcal{D}} - < \Psi >_{\mathcal{D}} < \Theta >_{\mathcal{D}} \, , \qquad (26)$$

which yields for the expansion scalar Θ

$$< \Psi >_{\mathcal{D}} - < \dot{\Theta} >_{\mathcal{D}} = \ < \theta^2 >_D - < \Theta >^2_D \, . \qquad (27)$$

Introducing the dimensionless scale factor $a_D \equiv (V_D / V_{Din})^{1/3}$ normalized by the volume of the domain $\mathcal{D}$ at some initial time t_{in} , we can average the scalar Einstein equations (22), (23) and the continuity equation to obtain

$$\left(\frac{\dot{a_D}}{a_D}\right)^2 = \frac{8\pi G}{3} < \rho >_D - \frac{1}{6}(\mathcal{Q}_D + < R >_D), \qquad (28)$$

$$\left(\frac{\ddot{a_D}}{a_D}\right) = -\frac{4\pi G}{3} < \rho >_D + \frac{1}{3}\, \mathcal{Q}_D \ , \qquad (29)$$

$$< \rho >_D = - < \Theta >_{\mathcal{D}} < \rho >_D = \ -3\frac{\dot{a_D}}{a_D} \ < \rho >_D \ . \qquad (30)$$

Concluding Remarks

It is concluded that timescaping nature of cosmology can be more smoothly applicable to fundamental cosmological entities such as scale factor and density parameters and extendable to different time evolution settings. Some interesting visualization of the results are implemented using Mathematica software.

Acknowledgements

I would like to thank Dr Khin Khin Win, Professor and Head, Department of Physics, University of Yangon, for her kind permission and encouragements to carry out this work. I would like to express my gratitude to Professor Dr Aye Aye Thant, Professor, Department of Physics, University of Yangon, for her kind encouragements to undertake this research paper. Special thanks are due to Professor, Dr Thant Zin Naing, Retired Pro-Rector (Admin), International Theravāda Buddhist Missionary University, for his valuable guidance and helpful advice to carry out this work.

References

Adler. R, Bazin.M, Schiffer. M, (1975) *Introduction to General Relativity*. New York: Mc.Graw-Hill.

Buchert.T, (1999) *On Average Properties of Inhomogeneous Fluids in General Relativity: Dust Cosmologies*.

Buchert.T, (2007) *Dark Energy from Structure: a Status Report*.

Buchert.T, Ehlers.J,(1995) *Averaging Inhomogeneous Newtonian Cosmologies.*

Carroll, S.M., (2004) *Introduction to General Relativity Spacetime and Geometry*, San Francisco, Adddison Wesley.

Rosanen. S, (2006) *Accelerated expansion from structure formation*.

Witshire. D. L, (2007) *Exact solution to the averaging problem in cosmology* Physical Review Letter, 99, 251101.

Witshire. D. L, (2007) *Cosmic clocks, cosmic variance and cosmic averages*, New I. Phys. 9,377

J. Myanmar Acad. Arts Sci. 2020 **Vol. XVIII.No.2C**

STUDY ON STRUCTURAL AND DIELECTRIC PROPERTIES OF Sr DOPED $PbTiO_3$ FERROELECTRIC MATERIALS

Yee Yee Oo[1], War War Thin[2]

Abstract

We used spin coating to fabricate a Sr doped $PbTiO_3$ thin film on n-Si subtract. By means of X-ray diffraction and scanning electron microscopy analyses, it was confirmed that tetragonal structure at an as-synthesized state. The variations of capacitance (C) with frequency at different temperatures were also observed. It was found that the capacitance was frequency dependent at all temperatures but almost independent in the high frequency range beyond 3 kHz. From the variation of dielectric loss (tanδ) with frequency it was seen that tanδ values increase rapidly with frequency and attains a minimum value. Reverse C-V characteristics exhibited a linear $1/C^2$ versus V plot, from which a built-in potential of 0.71 V-0.85 V were deduced.

Keywords: Sr doped $PbTiO_3$ thin film, X-ray diffraction, scanning electron microscopy, Reverse C-V characteristics

Introduction

Ferroelectric thin films have been developed widely in recent years due to their potential applications including infrared detectors, actuators, and nonvolatile memories etc. Among the ferroelectric materials, lead titanate family such as $PbTiO_3$, $PbZrTiO_3$, $PbLaTiO_3$ . . . . are desirable for these applications due to the high dielectric constant, and large remnant polarization (Pontes.F.M et al, 2004). They have large spontaneous polarization and the ability to switch polarization direction. Ferroelectrics with perovskite structure (ABO_3), such as barium titanate and lead titanate are the most popular oxides because of their great properties for use in thin film capacitors, electronic transducers, actuators, high-k dielectrics, pyroelectric sensors, and nonlinear optics (Jun Wang et al, 2010). A perovskite solid solution of $PbTiO_3$ and $SrTiO_3$ (PST) exhibits the high dielectric constant of $PbTiO_3$ and the lattice stability of $SrTiO_3$ (Kyoung-Tae Kim at al, 2002).

$PbTiO_3$ reaches ferroelectric at room temperature and its Curie point is found to be at 490°C,as reported first by Shirane et al. and independently, by Smolenskii.

The structure of $PbTiO_3$, at room temperature, involves a tetragonal distortion from the pervosktite lattice, and its compound is amorphous with tetragonal (Ming-Chi Hsu et al, 2006). Nanosized PST powders have also been receiving great interest due to their novel physiocochemical properties (S. Sriram, M et al, 2009).

In this work, growth mechanism of Sr (6mol%) doped $PbTiO_3$ thin film devices is presented. Structural and microstructural properties, frequency dependent of dielectric properties, reverse C-V characteristics of the thin film devices are investigated.

Experimental Details

Sample Preparation

The raw materials of PbO, TiO_2 and $Sr(NO_3)_2$ are first weighed according to the stoichiometric formula. These powder materials are mixed to form $Pb_{1-x}Sr_xTiO_3$ with x= 0.06

---

[1] Dr, Associate Professor, Department of Engineering Physics, Technological University (Maubin)

[2] Department of Physics, West Yangon University

molar ratio. The mixture powder is ground by agate mortar to obtain the homogeneity and the primary heat treatment at 750°C for 1 hr. After that the crystalline powder is ground by agate mortar for second time in the same way as before. This sample is heat treated at 750°C for 1hr.

2-metoxyethanol ($CH_3OCH_2CH_2OH$) is added to the powder and then stirred and heated in a vessel with water-bath at 100°C for 1hr. The homogeneous precursor solution is obtained and ready to deposit into substrates. Before deposition, Si substrates are cleaned with standard semiconductor cleaning process. The Si substrate with dimension (1cm x1cm) are used as substrate and washed with dilute HF: DW (1:5) to remove native oxide and dry at room temperature. They are immersed in acetone for 5 minutes and dry at room temperature. After that, the precursor solution is deposited on Si substrates by spin coating technique. Later, layers are first dried at room temperature and annealed at 500°C, 550°C, 600°C, 650°C, and 700°C, respectively by conventional annealing process. Deposition procedures are carried out in the clean chamber. Finally, $Pb(Sr)TiO_3$, PST thin films are obtained. Crystallographic investigation of the films is examined. Microstructural properties of films are determined. Dielectric properties and reverse C-V characteristics of the thin film devices are investigated.

Results and Discussion

Structural Characterization

The x-ray diffraction is a convenient method to identify an unknown sample by determining its crystal structure and comparing it with a repository of standard powder diffraction patterns. XRD is performed using monochromatic Cu K_α radiation (λ=1.54056 Å) operated at 40kV (tube voltage) and 20mA (tube current). Sample is scanned from 10° to70° in diffraction angle, 2θ with a step-size of 0.02°. The XRD profiles are recorded and shown in Fig. 1(a-e). There are 14 peaks on pattern of all films and agree with the typical $PbTiO_3$ pattern of single phase perovskite structure. From the profile, it is clear that all XRD images are not remarkably different in variation nature. It is obvious that, all XRD profiles show no preferred orientation and polycrystalline. The intensity of (101) reflection is much stronger than that of remaining 13 $PbTiO_3$ peaks. It means dopant Sr ions are partially occupied into Pb-site in $PbTiO_3$ structure.

The (001) peak is occurred as first refraction of XRD spectra in all films. It is found that, all XRD profile shows pure $PbTiO_3$ structure. As the a-axis, (100) is formed as 2nd peak on XRD profile for all fabricated sample. Temperature dependence of a-axis, c-axis and c/a are evaluated and collected in table 1. Ions of alkali-earth metals, Sr^{2+} which has ionic radius 1.27 Å is frequently used to substituted Pb^{2+} (with an ionic radius of 1.32Å). Using element substitution, one can change properties of the piezoelectric ceramic, but still maintain its perovskite structure.

The width of the peaks in a particular phase pattern provides an indication of the average crystallite size. Large crystallite gives rise to sharp peak, while the peak width increase as crystallite size reduced. The average grain size, G is also estimated from the half-width of the x-ray diffraction peaks. Peak broading also occurs as results of radiations in d-spacing caused by micro-strain. However, the relationship between broading and diffraction angle, 2θ is different from that of crystallite size effects making it possible to differentiate between the two phenomena. The FWHM values of dominant reflections are found to be 0.00942, 0.00748, 0.00536, 0.00489 and 0.00359 for respective specimens. As it is shown in table, it is significantly obvious that the crystallite size variation is inversely changed compared to that of FWHM. These values were collected and listed in table 2.

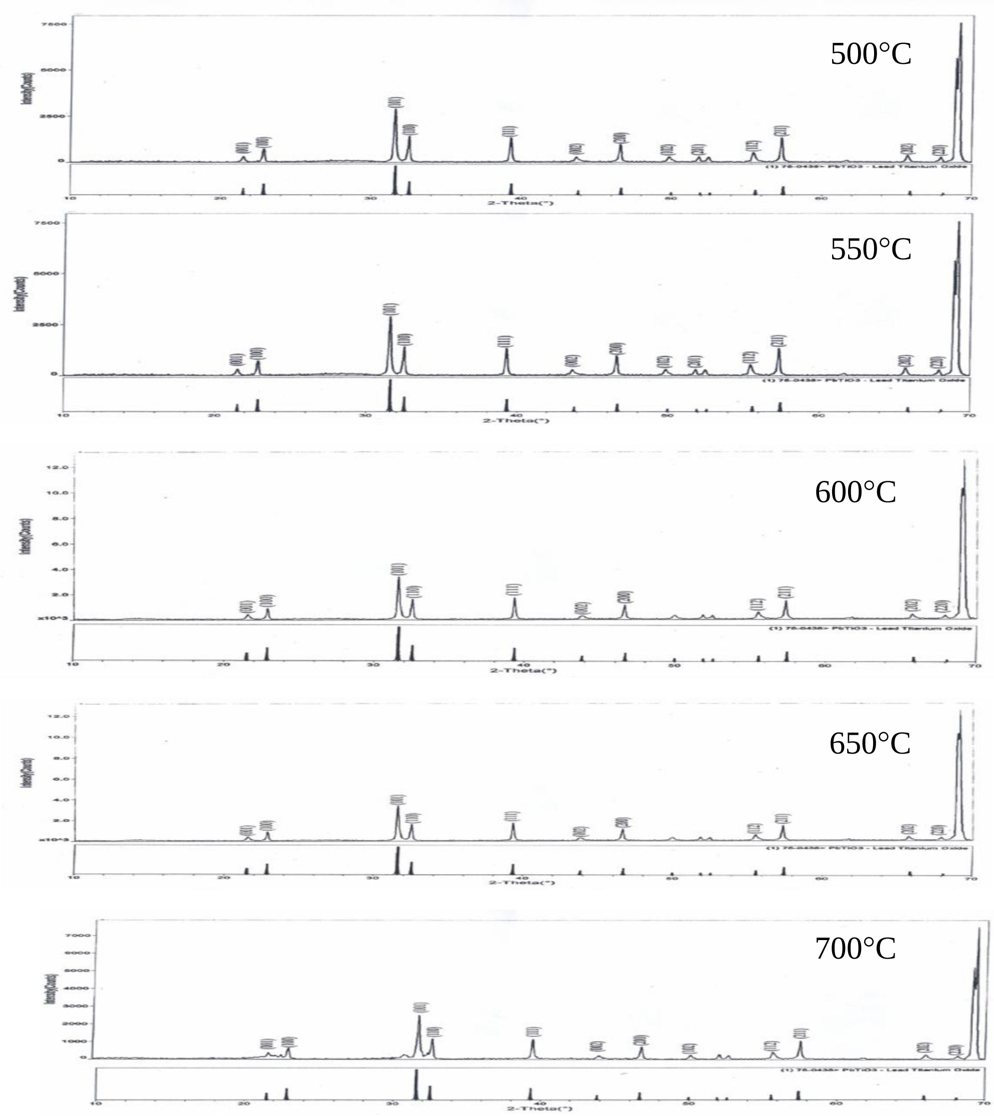

Figure 1 XRD patterns of Pb(Sr)TiO_3 TFD at process temperature (a) 500^oC (b) 550^oC (c) 600^oC (d) 650^oC (e) 700^oC

Table 1 Temperature dependence of lattice parameters (a and c) and c/a

Temperature(^{0}C)	a (Å)	c (Å)	c/a
500	3.9870	4.1284	1.0354
550	3.7982	4.1436	1.0909
600	3.9872	4.1339	1.0367
650	3.9971	4.1289	1.0329
700	3.7850	4.1304	1.0912

Table 2 FWHM and crystallite size of all fabricated sample

Temperature(^{0}C)	FWHM(deg)	crystallite size(nm)
500	0.00942	93.77
550	0.00748	147.15
600	0.00536	179.22
650	0.00489	213.47
700	0.00359	235.99

Microstructural Characterization

SEM investigation of Sr (6 mol %) doped $PbTiO_3$ films annealed at changing the process temperatures are shown in Fig. 2(a - e). The surface of the films became fairly dense after annealing at process temperatures from 500ºC to 700ºC. Fig. 2(a) shows bubble like morphology is observed in Sr (6 mol%) doped PST thin film device at process temperature 500ºC. The grain sizes are not uniform but also crack free. The grain size is found to 3.953 µm. Fig. 2 (b) shows the SEM photograph of Sr (6mol %) doped PST thin film device at process temperature 550ºC. From this Fig., it is clear that the grain sizes of this film are not uniform but crack free. The grain size is found to be 3.66 µm. From the Fig. 2 (c - e), it is obvious that, grain sizes are not uniform, crack free and no pin- hole arrangement.

Grain sizes of Sr (6 mol %) doped PST thin film devices at various process temperatures are listed in table 3. The increase of pore and grain-growth are observed with the increase of process temperature from 550ºC to 650ºC. The maximum grain size is at process temperature 650ºC. It is observed that the grain-size varies with process temperatures.

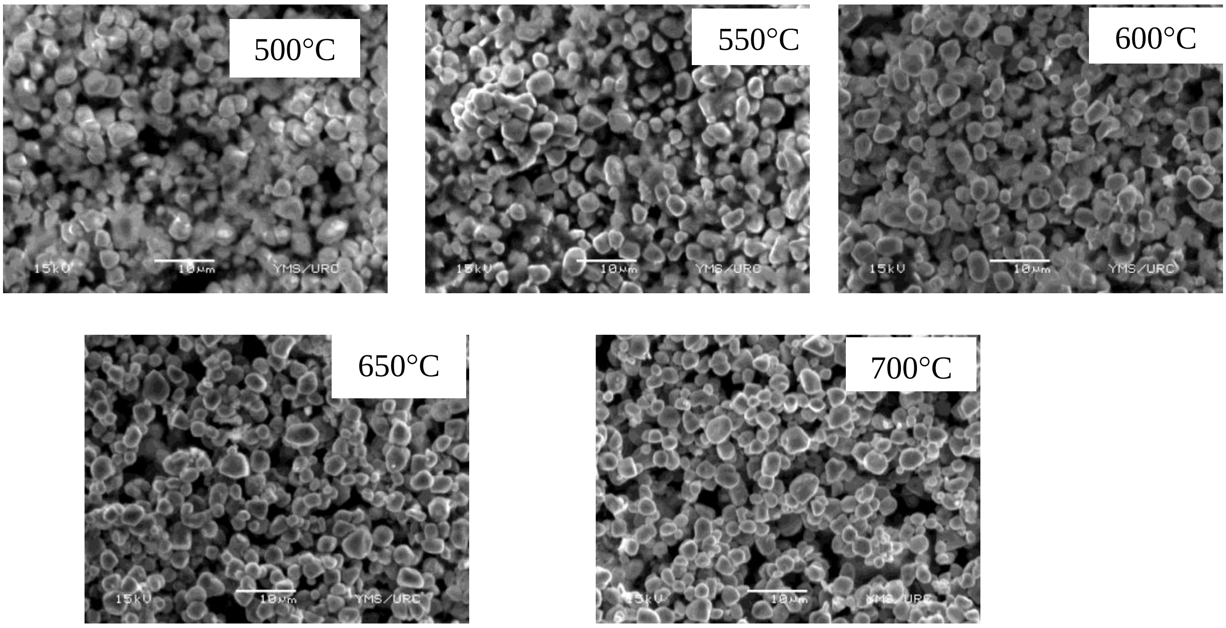

Figure 2 SEM photograph of PST thin film device at process temperature (a) 500°C (b) 550°C (c) 600°C (d) 650°C (e) 700°C

Table 3 Average grain size of $Pb(Sr)TiO_3$:Si thin film devices

Temperature (°C)	Grain size (µm)
500	3.953
550	3.666
600	3.820
650	4.353
700	4.313

$1/C^2$ – V Characterization

C-V measurements are performed in the region of -4 V to +4 V at 100 kHz frequency. From this measurement, $1/C^2$ – V characteristics of these films are also studied.

A plot of $1/C^2$ as a function of V is a straight line whose intercept on the voltage axis gives V_{bi} and the slope can be used to determine the effective dopant concentration N_i. Fig.3 (a-e) display $1/C^2$-V characteristics of $Pb(Sr)TiO_3$:Si thin film devices at process temperature 500°C, 550°C, 600°C, 650°C and 700°C, respectively. The results of the $1/C^2$ -V characteristics of $Pb(Sr)TiO_3$:Si thin film devices at room temperature measured at frequency of 100 kHz. The value of the built-in voltage, dopant concentration and depletion layer width have been calculated and described in Table 4. The values of V_{bi} is the highest at process temperature 600°C and the lowest at process temperature 700°C. The measurement of N_I is the highest at process temperature 500°C and the lowest at process temperature 650°C. Depletion layer width (W) is increase with increasing process temperature. So, W is the highest at process temperature 700°C and is the lowest at process temperature 500°C.

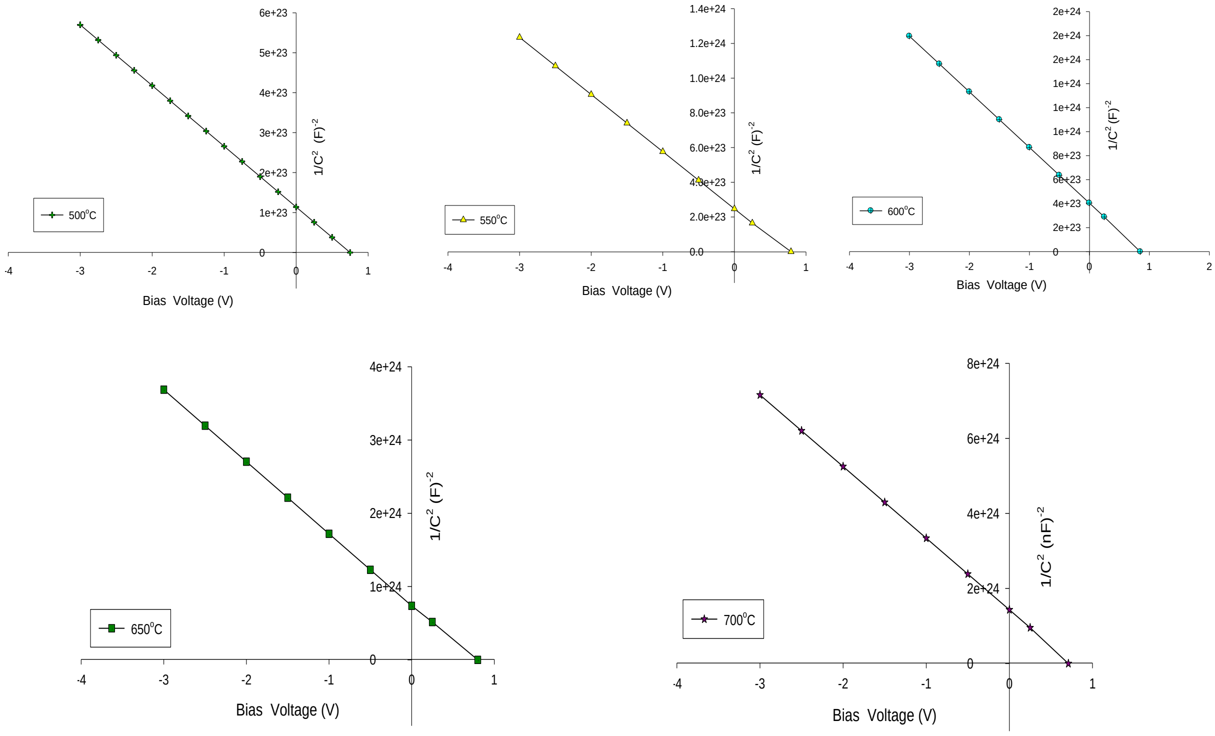

Figure 3 $1/C^2$-V characteristic of $Pb(Sr)TiO_3$:Si thin film devices at process temperature 500°C (b) 550°C (c) 600°C (d) 650°C (e) 700°C

Table 4 Built-in voltage, dopant concentration and depletion layer width of Pb(Sr)TiO_3:Si thin film devices

Process Temperature (^oC)	V_{bi}(V)	N_i (cm^{-3})	W (cm)
500	0.75	7.83x 10^{15}	7.92x 10^{-5}
550	0.79	3.64x 10^{15}	1.16x 10^{-4}
600	0.85	2.56x 10^{15}	1.40x 10^{-4}
650	0.80	1.12x 10^{15}	2.01x 10^{-4}
700	0.71	6.2x 10^{15}	2.80x 10^{-4}

Dielectric Properties Characterization

The AC parameter such as capacitance "C" and dissipation factor "D" are measured using LCR meter (Quad Tech, 1730 digibridge) and Cu electrode in the frequency range 1kHz to 100kHz at zero bias.

Frequency dependence of capacitance of Pb(Sr)TiO_3:Si thin film devices (TFDs) at various process temperatures is depicted in Fig. 4. Measurements are performed at zero bias. From this figure, it is obvious that capacitance decreases with increasing frequency. It is due to "RC" time effect. Capacitance versus ln f characteristic measurement of this devices at various process temperature is described in Fig. 5. From this figure, the value of capacitance decreases with increasing frequency.

Dielectric constant (ε_r) versus ln f characteristic measurement of Pb(Sr)TiO_3:Si TFDs at various process temperature is demonstrated in Fig. 6. From this characteristics, ε_r decreases with increasing frequency. Dielectric loss (tanδ) is the ratio of imaginary part of the dielectric constant to the real part of the dielectric constant. The frequency dependence of tanδ at various process temperatures is depicted in Fig. 7. From the figure, tanδ increases with increasing frequency.

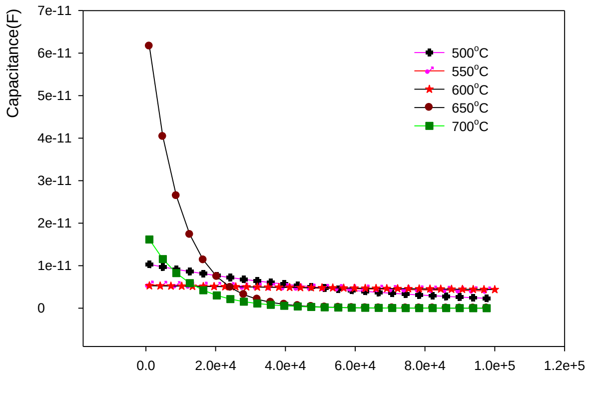

Figure 4 Capacitance - Frequency characteristic of Pb(Sr)TiO_3:Si thin film devices

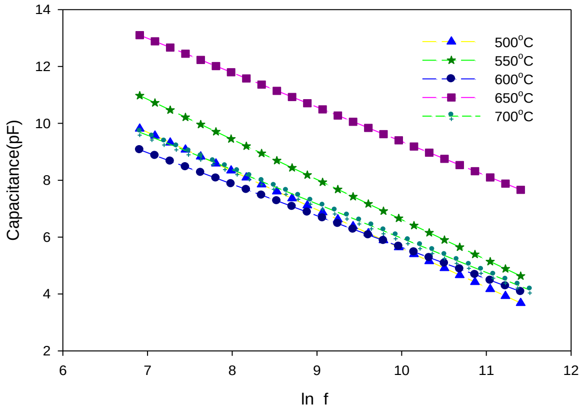

Figure 5 C-ln f characteristic of Pb(Sr) TiO_3:Si thin film devices

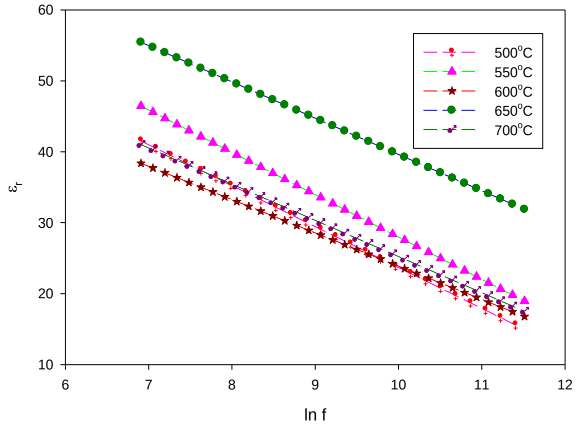

Figure 6 ε_r - ln f characteristic of $Pb(Sr)TiO_3$:Si thin film devices

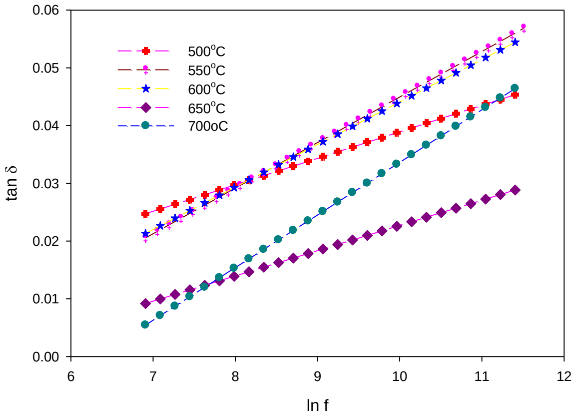

Figure 7 tan δ–lnf characteristic of $Pb(Sr)TiO_3$:Si thin film devices

Conclusion

Preparation and characterization of Sr doped lead titanate thin film devices have been investigated. In XRD profiles of $Pb(Sr)TiO_3$, there are 14 peaks on pattern of all films and agree with the typical $PbTiO_3$ pattern of single phase perovskite structure. And, it is clear that all XRD images are not remarkably different in peak formation. All XRD profiles show no preferred orientation and polycrystalline. Using element substitution, one can change properties of the piezoelectric ceramic, but still maintain its perovskite structure. SEM investigation of $Pb(Sr)TiO_3$ TFDs are annealed at changing the process temperatures had been studied. The increase of pore and grain-growth are observed with the increase of process temperature from 550ºC to 650ºC. The maximum grain size is at process temperature 650ºC. C-V characteristics of $Pb(Sr)TiO_3$:Si thin film are examined by using Cu electrode and Quad Tech LCR Digibridge meter model 1730. Measurements are performed in the region of -4 V to +4 V at 100 kHz frequency. From this measurement, $1/C^2$ – V characteristics of these films had been also studied. The value of built-in voltage V_{bi} for Si based thin films should be less than 1 V at room temperature (300 K). The V_{bi} values of $Pb(Sr)TiO_3$:Si thin film are followed the above condition. So, $Pb(Sr)TiO_3$:Si thin film are acceptable for diode application. The AC parameters such as capacitance "C" and dissipation factor "D" are measured using LCR meter (Quad Tech, 1730 digibridge) and Cu-electrode in the frequency range 1 kHz to 100 kHz at zero bias. The variations of dielectric constant and dielectric loss of ceramic had been investigated. It is found that, RC time effect is observed in frequency dependence of the dielectric constant characteristics.

Acknowledgements

We would like to express our gratitude to Rector Dr Daw Kyawt Khin for his permission to submit in this research paper. We also thank to members of Materials Science Lab, Department of Physics, University of Yangon, for kind supply of practical equipments.

References

Jun Wang,Xinchang,Mufit Akinc ang Zhiqun Lin,14th June (2010), "Synthesis and Characterization of perovskite $PbTiO_3$ nanoparticles with solution processability", Journal of Materials Chemistry,vol.20,pp.5945-5949.

Kyoung-Tae Kim and Chang-Il Kim∗, (September 2002), "Dielectric Properties of $(Pb,Sr)TiO_3$ Thin Films Prepared by Using the Sol-Gel Method", Journal of the Korean Physical Society, Seoul, vol.41, No. 3,pp.377-380.

Ming-Chi Hsu,Yu-Ming Sun,Ing-Chi Leu, and Min-Hsiung Hona (2006), "Structural and Electrical Characterizations of $PbTiO_3$ Thin Films Grown on $LaNiO_3$-Buffered $Pt/Ti/SiO_2/Si$ Substrates by Liquid Phase Deposition", Journal of The Electrochemical Society, vol 153(11), pp 60-65.

Pontes.F.M,Leite.E.R,Nunes.M,S,J,Pontes.D.S.L,Longo.E,Magnani.R,Pizani.P.S,Varela.J.A,(2004), "Preparation of $Pb(Zr,Ti)O_3$ thin film by soft chemical route", Journal of the European Ceramic Society, vol. 24, pp.2969-2976.

S. Sriram, M. Bhaskaran,D.R.G. Mitchell,K.T. Short,A.S. Holland and A. Mitchell (2009), "Microstructural and Compositional Analysis of Strontium-Doped Lead Zirconate Titanate Thin Films on Gold-Coated Silicon Substrates", Journal of Microscopy and Microanalysis, vol 15, pp 30-35

J. Myanmar Acad. Arts Sci. 2020 **Vol. XVIII.No.2C**

FABRICATION AND CHARACTERIZATION OF $ZnTiO_3$ BASED PEROVSKITE SOLAR CELL ON ITO SUBSTRATE

Thida Win [1], Than Than Win [2] and Yin Maung Maung [3]

Abstract

Firstly $ZnTiO_3$; Zinc titanate powder was successfully prepared by a solid state reaction method. After that $ZnTiO_3$ perovskite solar cell was fabricated by titanium dioxide (TiO_2) layer as the electron transporter layer (ETL) and CuO as the hole transport layer (HTL).Indium doped Tinoxide (ITO) was used as a substrate. In this research, fabrication of ZTO based perovskite solar cell was investigated. From J-V characteristics, efficiency (ɳ) and fill factor were evaluated under illuminated condition. The conversion efficiency 2.12% of ZTO perovskite solar cell was found. By using fabrication and characterization, this structure ZTO based perovskite solar cell was useful in solar cell application.

Keywords: $ZnTiO_3$ perovskite, solid state reaction, efficiency (ɳ) and fill factor

Introduction

Most of the renewable energy from wind, micro-hydro, tidal, geothermal, biomass, and solar are converted into electrical energy. Solar technologies use the sun to provide heat, light, electricity, etc for domestic and industrial applications. The best conversion efficiency of most commercially available solar cells is in the range 10-20% [Green, Martin A, 1982]. Perovskites are emerging as a new generation of photovoltaic materials. The transition metal oxide such as TiO_2, their perovskite structures $ZnTiO_3$, is widely used in optical and microelectronic applications because of their excellent mechanical, optical and insulating properties. Up to now, perovskite films have been formed by film deposition approaches such as spin-coating, sequential deposition of the inorganic and organic precursor, and co-evaporation of the precursors [Burschka, J et al 2013- Liu, M et al 2013]. There are three compounds that exist in the ZnO-TiO_2 system: $ZnTiO_3$ with a hexagonal limonite structure (h-$ZnTiO_3$), Zn_2TiO_4 with a cubic spinel crystal structure, and $Zn_2Ti_3O_8$ with a cubic defect spinel structure [Bartram, S.F et al 1961]. $Zn_2Ti_3O_8$ has been observed as a low-temperature form of h- $ZnTiO_3$ that exists at $T < 820$ °C [Steinike, U et al 1997], and is only produced based on the Zn_2TiO_4 phase [Kim, H.T et al 2001]. It is known that h- $ZnTiO_3$ decomposes into Zn_2TiO_4 and rutile TiO_2 at $T > 945$ °C [Dulin, F.H et al 1960], However, perovskite crystallizes very rapidly, so it is very challenging to form uniform, continuous, and leakage-free perovskite films by solution methods [Liu, M et al 2013] . In this study, fabrication of the $ZnTiO_3$ perovskite solar cell was carried out by spin coating method.

Experimental Procedure

Powder preparation for Zinc Titanate ($ZnTiO_3$)

In this research, ZnO and TiO_2 were chosen as the starting materials. Firstly ZnO and TiO_2 powder with stoichiometry (ZnO: TiO2= 1:1molar ratio) were mixed. Ethanol was added to

---

[1] Associate Professor Engineering Physics Department, Technological University (Toungoo)

[2] Professor, Department of Physics, Pinlong University

[3] Professor Department of Physics, Yangon University

the mixture powders. Zinc titanate ($ZnTiO_3$; ZT) powders were prepared by a solid state reaction method. And then the mixture solution stirred with the magnetic stirrer and milled with the ball milling machine for 12 hr. After that the powders were dried and sieved to form uniform particles size. And then ZT powders were heated at various calcination temperatures, ranging from 500 ºC to 850 ºC for 2 h at a heating /cooling rate of 5 ºC/min. After the sample was annealed at 850 ºC, $ZnTiO_3$ crystals were successfully obtained. The phase formation was identified by X-ray diffraction (XRD). Similarly, CuO and TiO_2 were checked to observe successfully forms. After that, $ZnTiO_3$ (850 ºC), TiO_2 and CuO were chosen for futher investigation.

Perovskite Solar Cell Fabrication

Perovskite solar cells were fabricated in two major architectures, p-i-n and n-i-p type. We fabricated perovskite solar cells with a n-i-p type. The solar cell device consisted of layers of conductive material, titanium dioxide (TiO_2), perovskite zinc titanate ($ZnTiO_3$) and Copper (II) Oxide (CuO) as in Figure 1.The fist layer was an electrically conductive indium doped tin oxide (ITO). The next layer was the electron transport layer (ETL) for which we used titanium dioxide (TiO_2). The ETL was responsible for extracting the excited electrons out of the perovskite material and transporting them to the electrically conductive layer. After that this substrate was annealed at 160°C for 30 minutes. Next was the light absorbing perovskite layer where electrons and holes were generated. At that time, the annealing temperature 200°C was used to form perovskite layer deposition. After the perovskite, we deposited a hole transport layer (HTL) and for this layer, we used CuO, which collects and transports the holes to the anode. After that, this substrate is then annealed at 110°C for 30 minutes. In this method, each layer was coated by using the spin-coater. The substrate is rotated at a very high speed (between 1500-3000 rpm), while the precursor solution is dropped onto the rotating substrate in each step. Finally silver back contact was used as the electrode for the device.

Result and discussion

XRD Analysis

X-ray powder diffraction is a rapid analytical technique used for phase identification of crystalline material and can provide information on unit cell dimensions. Based on the results of XRD, calcinations were carried out from 500 ºC to 850 ºC for 2 h. After annealed from 500 ºC to 850 ºC, in the temperature at 500 ºC and 600 ºC the precursor of ZnO and TiO_2 were detected. A high parity of the cubic perovskite phase was discovered in powders annealed at 700 ºC, 800 ºC and 850 ºC. The comparison of XRD pattern for $ZnTiO_3$ powders at 500 ºC, 600 ºC, 700 ºC, 800 ºC and 850 ºC is shown in Figure 2. XRD spectrums of TiO_2 and CuO were found in Figure 3(a) and 3(b). Some crystallographic information about the powder $ZnTiO_{3,}TiO_2$ and CuO were collected and listed in Tables 1.1~ 1.3. These tables also gave the crystallite size and average crystallite size of powders. Five most intense diffracted peaks are observed on XRD spectrum. While the upper site of XRD spectrum indicated the observed XRD spectrum and the lower site showed the JCPDS (Joint Committee on powder Diffraction Standards) Library file. All identification peaks were well matched with those of JCPDS library file.

SEM analysis

The microstructure of $ZnTiO_3$ powders were observed by SEM. The grain sizes were measured by using well known bar code system. Figures 4(a) ~ (c) are SEM images of $ZnTiO_3$, TiO_2 and CuO. According to SEM images, the grains were uniformly distributed on the experimental area of SEM microphotograph. The shape of grain was examined to be circular shape. The average grain sizes were estimated to be 364 nm at 850 ºC for $ZnTiO_3$. Some porosity was found on all SEM images and they were porous structure.

UV-Vis Analysis

Figure 5 (a), 6 (a), 7 (a) show the absorption spectrums of $ZnTiO_3$, TiO_2 and CuO film. The optical transmittance range and transparency cut off wavelength of the crystal are important factors for optical applications. Figures 5 (b), 6 (b) and 7 (b) show the optical properties of $ZnTiO_3$, TiO_2 and CuO. The optical band gap (Eg) was evaluated from the absorption spectrum and the optical absorption coefficient (α) near the absorption edge. The optical band gap and absorption edge of $ZnTiO_3$ film are presented in Table 1.4.

J-V Analysis

To examine the PV behavior of $ZnTiO_3$ perovskite solar cell fabricated, J-V characteristics were measured under illumination. J- V curve showed the photovoltaic behavior as in Figures 8. It meant the open-circuit voltage and short-circuits current (V_{oc}-J_{sc}) characteristics. From J-V characteristics curve, the current at maximum power point (J_m) and the voltage at maximum power point (V_m) were measured. Short-circuit current, Maximum Current, Open-circuit voltage, Maximum Voltage, Fill factor and Efficiency of $ZnTiO_3$ Perovskite Solar Cells were measured and calculated at Table 1.5.

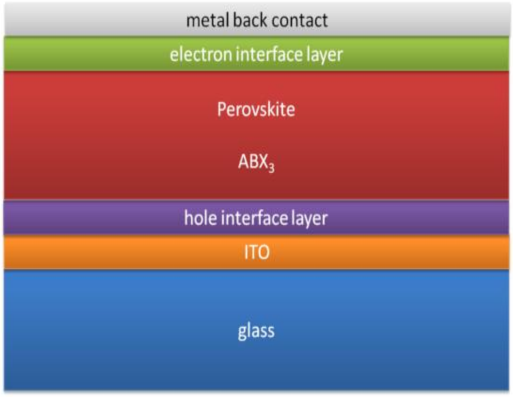

Figure 1 Generic structure of a standard (non-inverted) perovskite solar cell

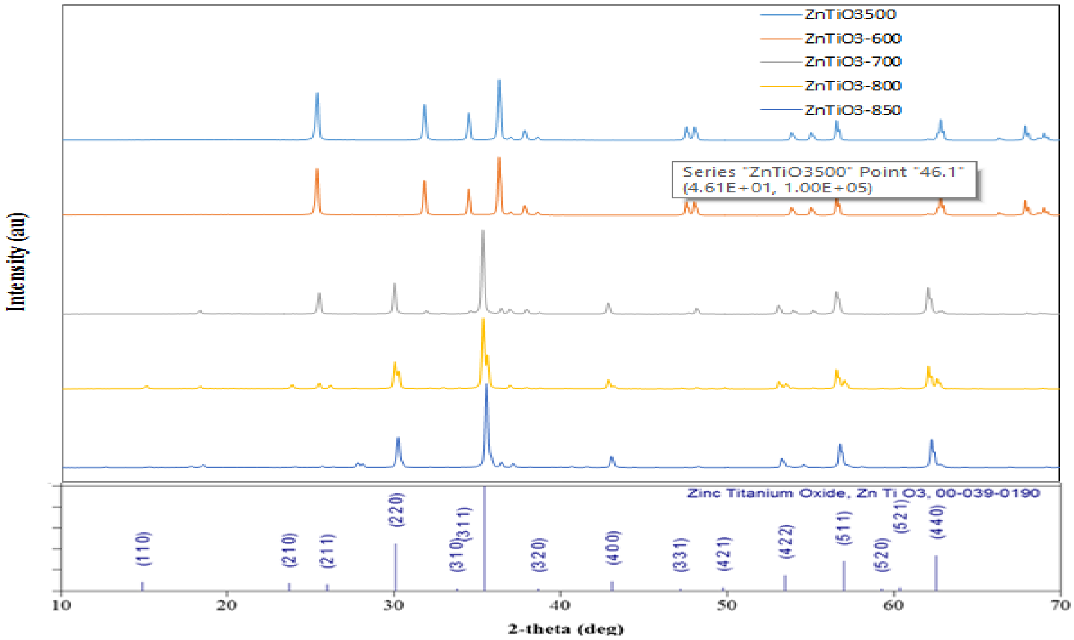

Figure 2 Comparison XRD patterns of $ZnTiO_3$ powders at 500 ºC, 600 ºC, 700 ºC, 800 ºC 850 ºC for 2 h

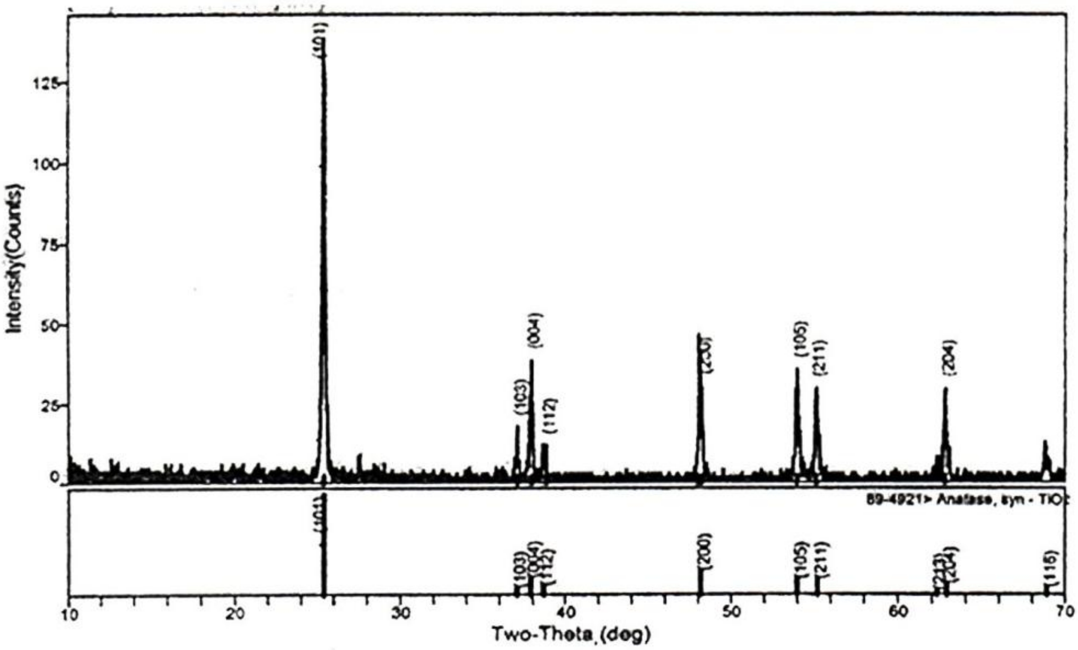

Figure 3 (a) XRD spectrum of TiO_2 powder

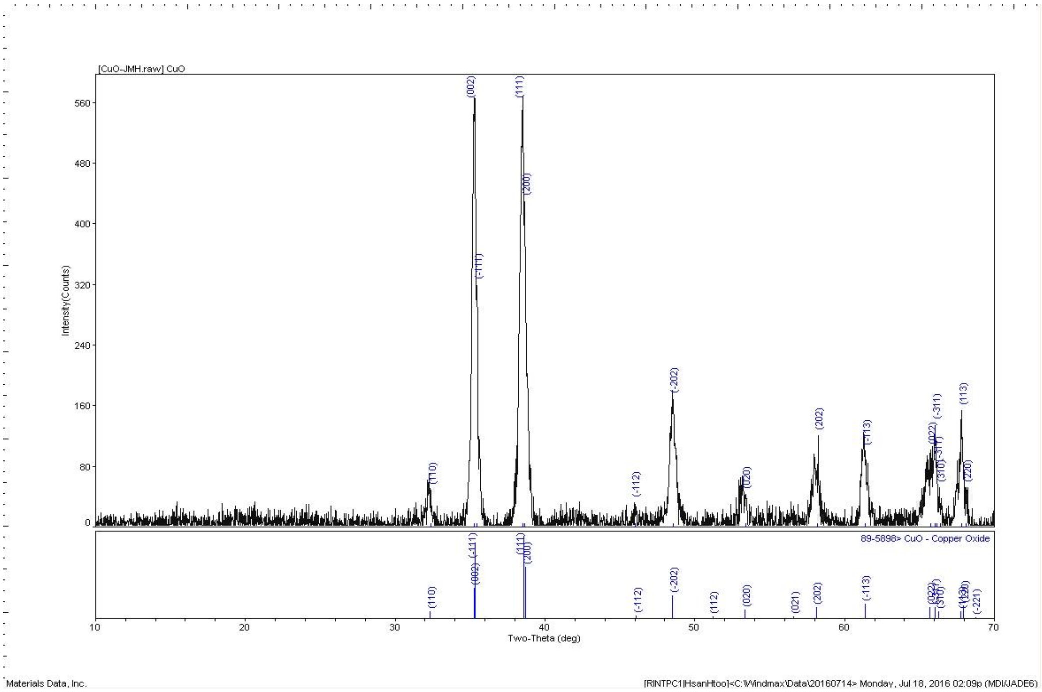

Figure 3(b) XRD spectrum of CuO powder

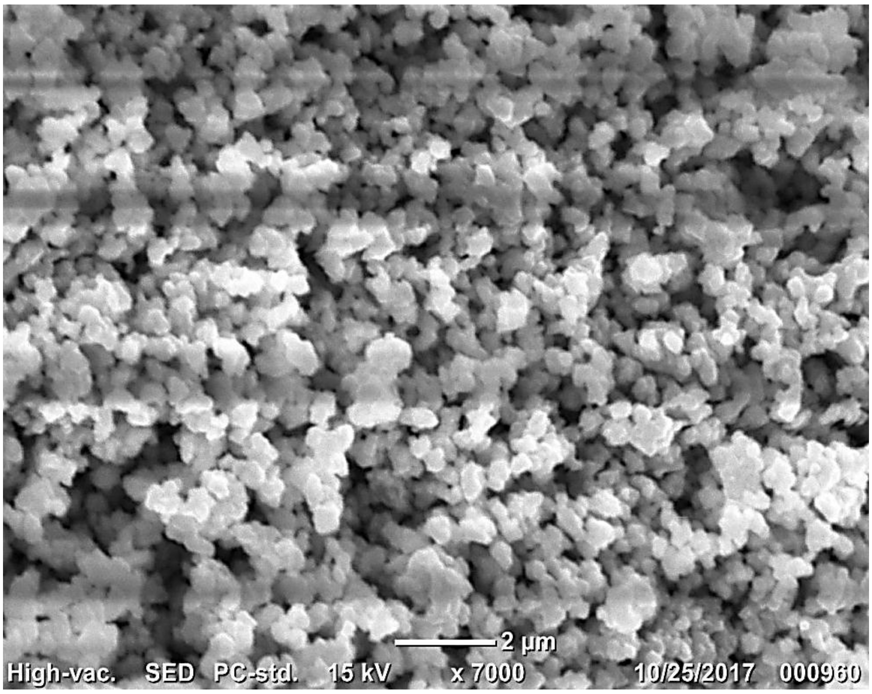

Figure 4 (a) SEM image of $ZnTiO_3$ powder at 850ºC for 2 h

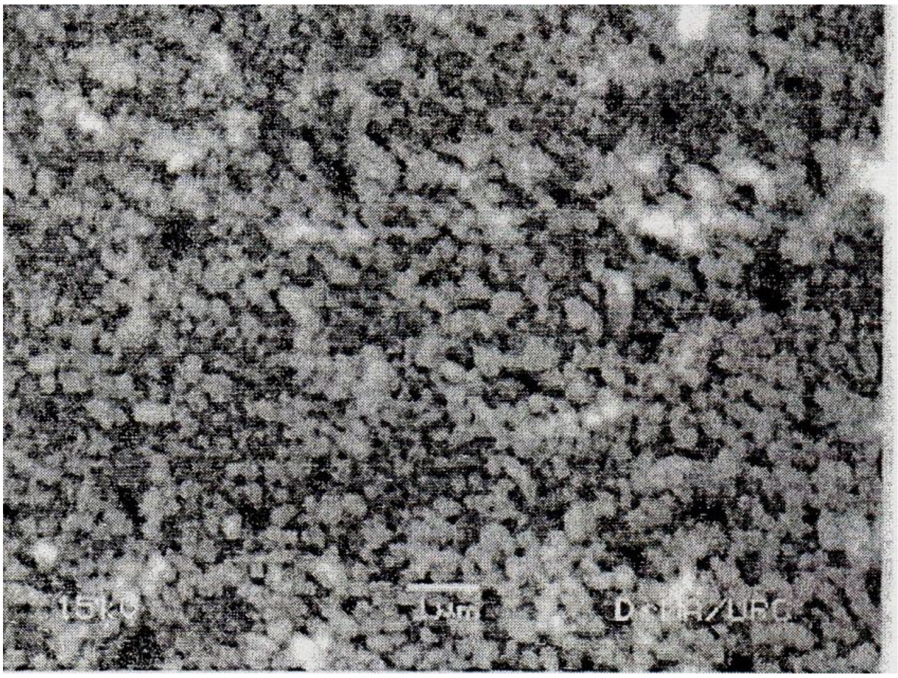

Figure 4(b) SEM image of TiO_2 powder

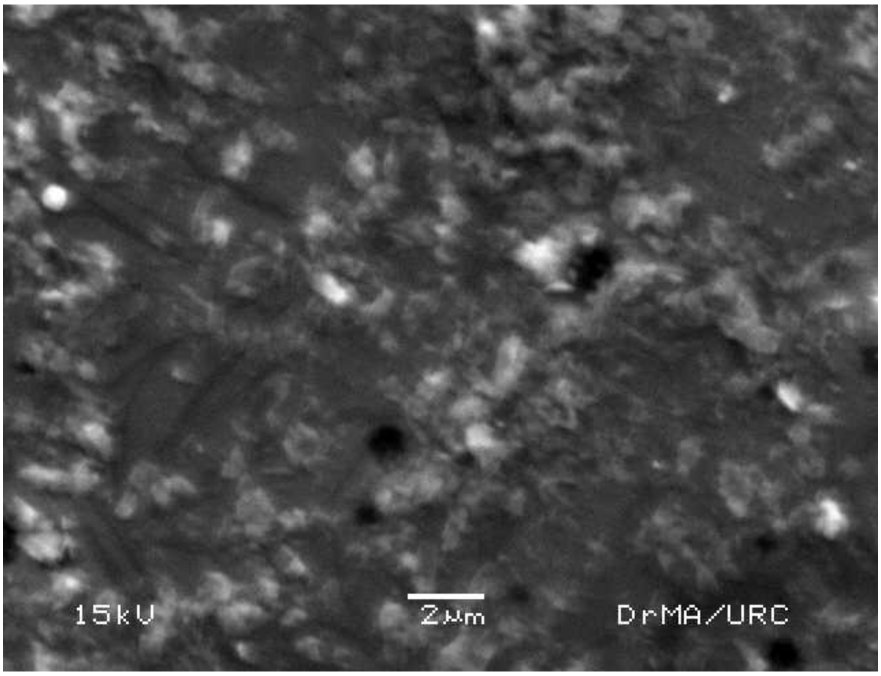

Figure 4(c) SEM image of CuO powder

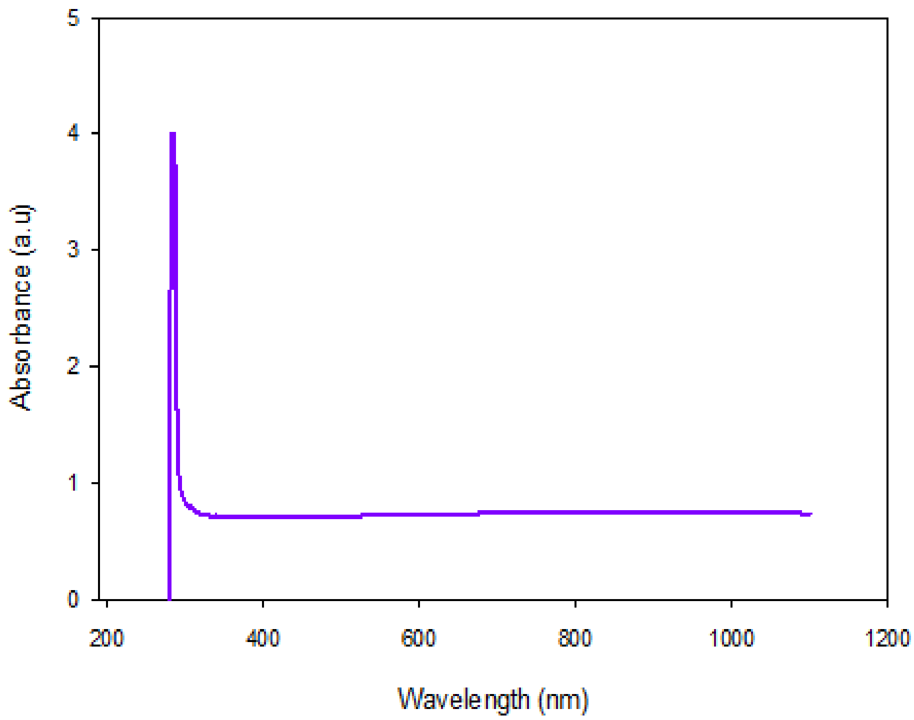

Figure 5 (a) The absorption spectrums of $ZnTiO_3$

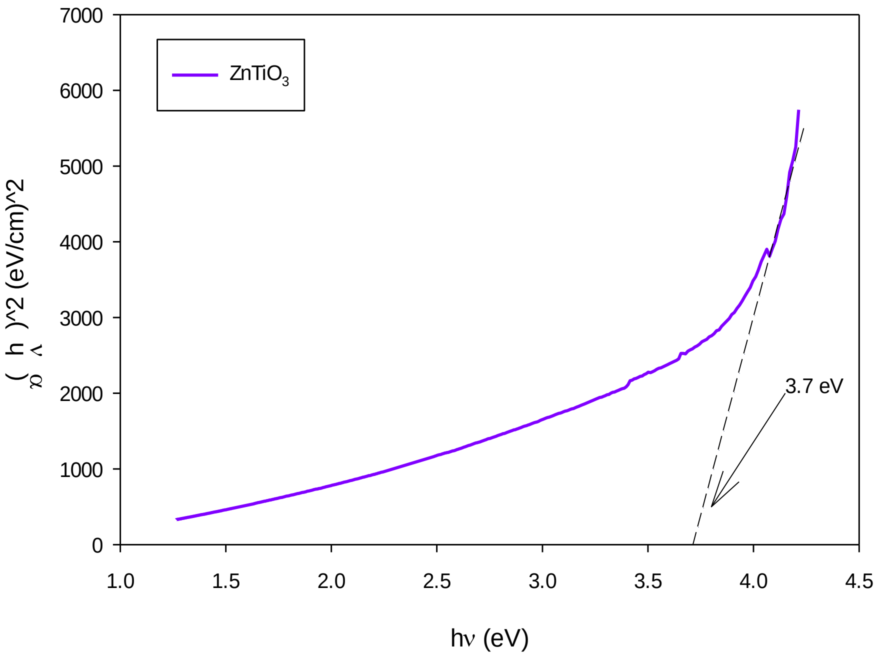

Figure 5 (b) Optical energy band gap of $ZnTiO_3$

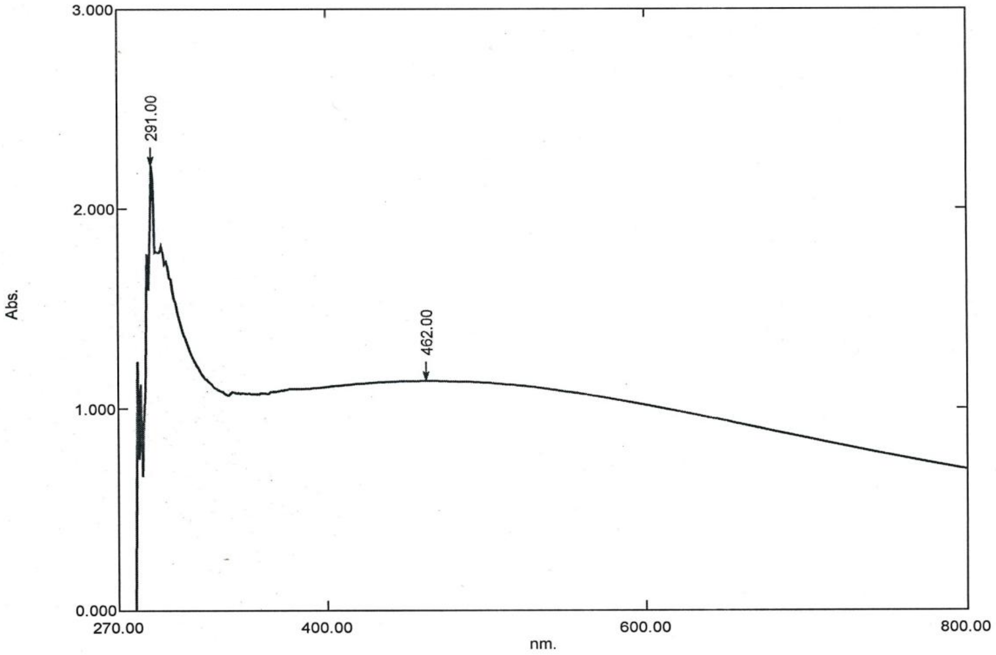

Figure 6 (a) The absorption spectrums of TiO_2

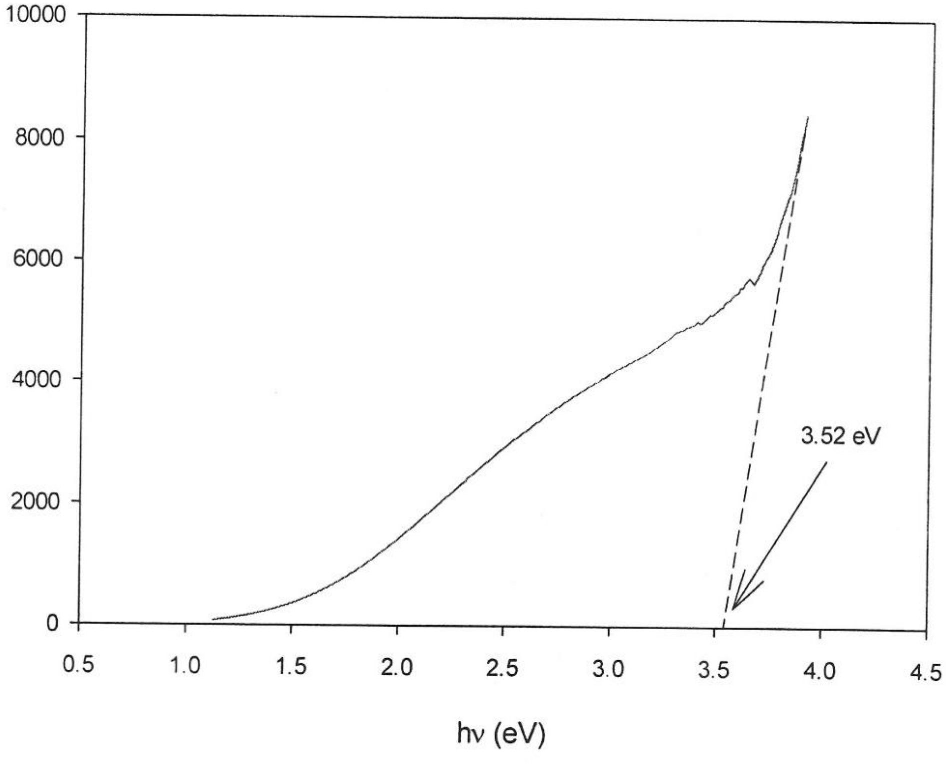

Figure 6 (b) Optical energy band gap of TiO_2

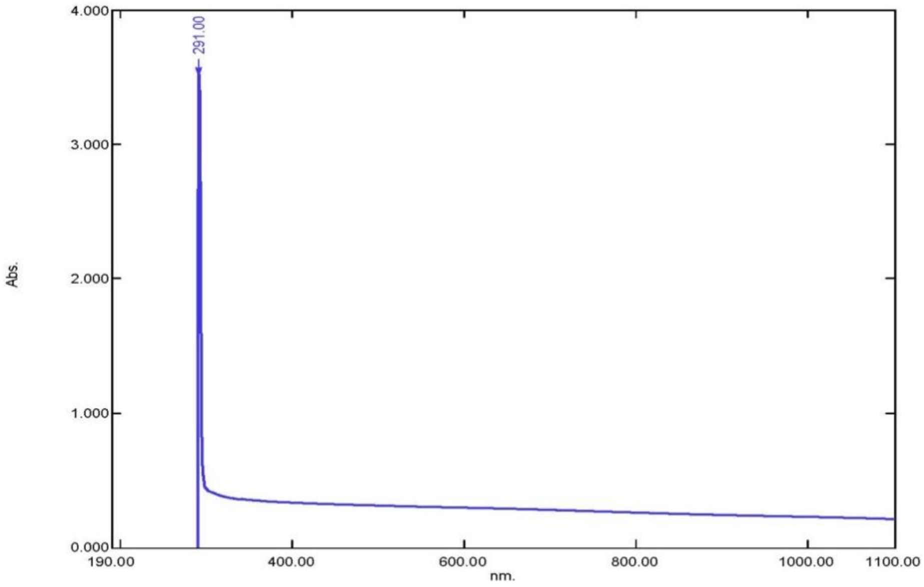

Figure 7 (a) The absorption spectrums of CuO

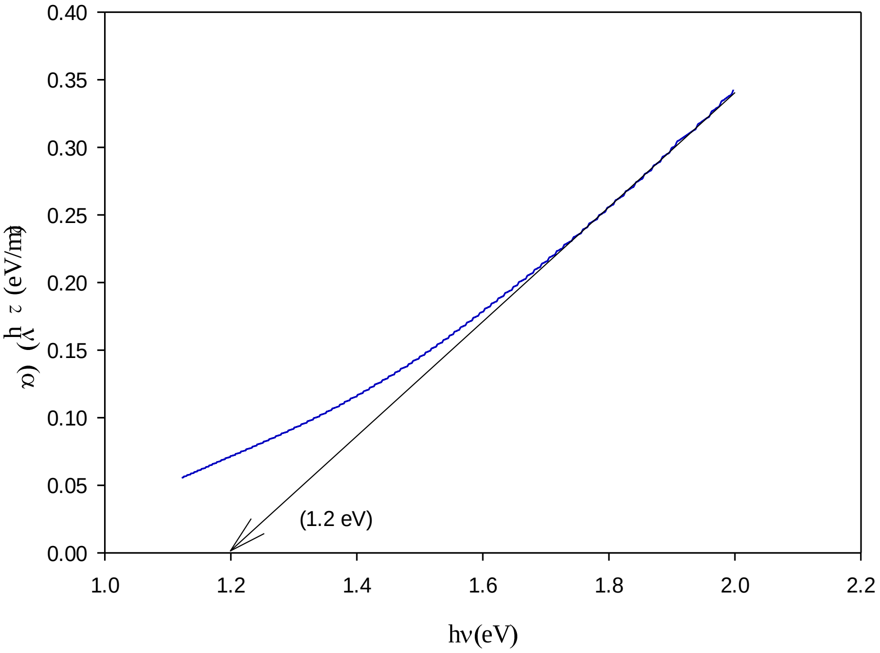

Figure 7 (b) Optical energy band gap of CuO

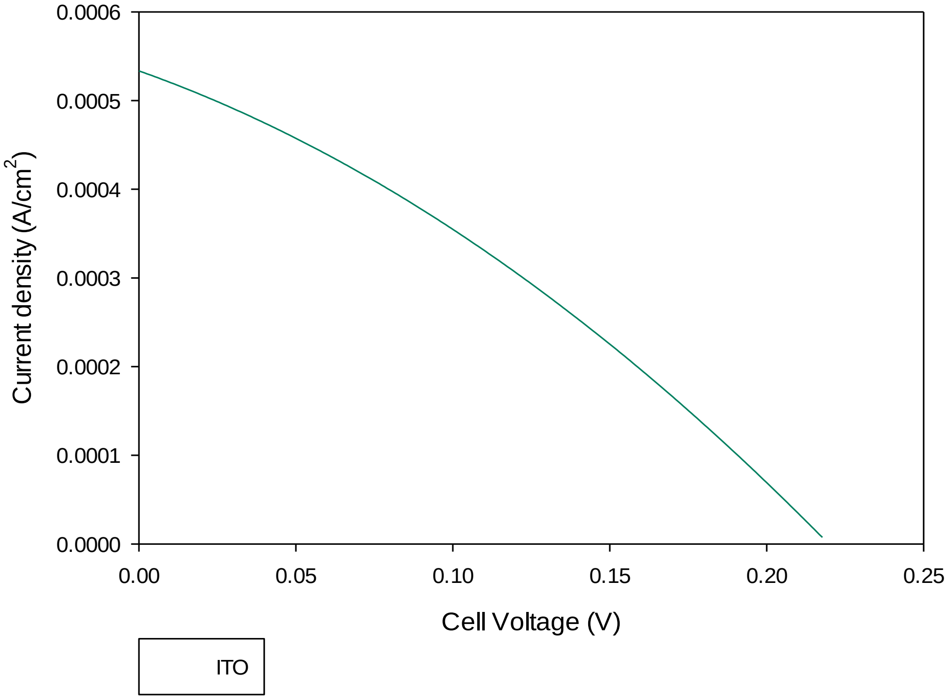

Figure 8 Current density – voltage curve for $ZnTiO_3$ perovskite solar cell with ITO (Indian doped tin oxide) substrate

Table 1.1 Crystallite size of $ZnTiO_3$ powder at 850°C for 2 h

No	Peak	2 θ	FWHM (deg)	Crystallite size (nm)
1	220	30.175	0.179	45.91
2	311	35.4721	0.166	50.18
3	422	53.699	0.18	49.41
4	511	57.214	0.193	46.83
5	440	62.795	0.288	32.23
	Average crystallite size			44.91

Table 1.2 Crystallite size of TiO_2

No.	Peaks	2 θ	FWHM (deg)	Crystallite size (nm)
1	101	25.355	0.207	39.340
2	103	37.013	0.181	46.293
3	0 04	37.846	0.200	42.000
4	112	38.643	0.260	32.370
5	200	48.143	0.211	41.250
6	105	53.973	0.236	37.760
7	211	55.184	0.212	42.270
8	204	62.810	0.243	38.290
	Average crystallite size			39.949

Table 1.3 Crystallite size of CuO powder

No	Peak	2θ	FWHM (deg)	Crystallite size (nm)
1	111	38.513	0.339	24.79
2	002	35.281	0.320	26.02
3	110	32.400	0.056	14.75
4	113	67.804	0.218	43.85
5	202	58.195	0.161	56.40
	Average crystallite size			33.16

Table 1.4 Optical band gap energy and Absorption edge

Sample	Optical band gap (eV)	Absorption edge (nm)
$ZnTiO_3$	3.7	284
CuO	1.2	291
TiO_2	3.52	291,462

Table 1.5 Short-circuit current, Maximum Current ,Open-circuit voltage, Maximum Voltage, Fill factor and Efficiency of $ZnTiO_3$ Perovskite Solar Cells

Solar Cell	Jsc (A)	J_{max} (A)	Voc (V)	V_{max} (V)	Fill factor (%)	Efficiency (%)
ITO	5.34E-04	3.35E-4	0.2172	0.1065	30.8	2.12

Conclusion

The perovskite structure of $ZnTiO_3$ was formed at 700 ºC, 800 ºC and 850 ºC. As the detail analysis of the phase by XRD, $ZnTiO_3$ was successfully formed at 700 ºC, 800 ºC and 850 ºC. SEM analysis of $ZnTiO_3$ showed advantageous microstructure with the appropriate pores, materials ratio and applications in the electronic industry as catalysts and color pigments. From the SEM results, it was found that all SEM images were porous structures. Small TiO_2 particles were formed on glass substrate. As a result of UV-vis spectroscopic measurement, the optical band-gap of TiO_2, CuO and $ZnTiO_3$ were examined according their wavelengths. Therefore, light energy can absorb easily. From J-V characteristics of $ZnTiO_3$ perovskite solar cell with ITO (Indian doped tin oxide) substrate showed the photovoltaic behaviour. The efficiency of $ZnTiO_3$ perovskite solar cell with ITO substrate is 2.12 %.The efficiency of $ZnTiO_3$ 2.12% is quite satisfied and credible compared with other photovoltaic applications (in Nature Energy,2019). The result of fill factor (30.8%) showed that $ZnTiO_3$ perovskite solar cell with ITO substrate exhibited a promising application in the preparation of perovskite solar cell.

Acknowledgements

I would like to thank Rector Dr Pho Kaung, University of Yangon, for his kind permission to carry out this research.

I am greatly indebted to Professor Dr Khin Khin Win, Head of Department of Physics, University of Yangon, for her kind permission to carry out this research.

References

A. Green, Martin (1982) Solar Cells; Operating Principles, Technology, andSystem Applications, Prentice-Hall Inc, pp xii and pp 62-184.

F.H. Dulin, D.E. Rase, (1960) J. Am. Ceram. Soc. 43, 125.

H. T. Kim, S. H. Kim, S. Nahm, J.D. Byun, and Y. Kim,(1999) "Lowtemperature sintering and microwave dielectric properties of zinc metatitanate-rutile mixtures using boron," *Journal of the American Ceramic Society*, vol. 82, no. 11, pp. 3043–3048.

J. Burschka, N. Pellet, S. Moon, R. Humphry-Baker, P. Gao, M. K. Nazeeruddin, and M. Gr¨atzel (2013) *Sequential deposition as a route to high-performance perovskite-sensitized solar cells*, **Nature 499**, pp. 316–319,.

M. Liu, M. B. Johnston, and H. J. Snaith (2013) *Efficient planar heterojunction perovskite solar cells by vapour deposition*, **Nature 501**, pp. 395–398.

S.F. Bartram, R.A. Slepetys, J. Am. Ceram. Soc. 44 (1961) 493.

U. Steinike, B. Wallis, Cryst. Res. Technol. 32 (1997) 187.

J. Myanmar Acad. Arts Sci. 2020 **Vol. XVIII.No.2C**

NUCLEON SINGLE-PARTICLE ENERGY LEVELS IN ^{51}Fe AND ^{51}Mn MIRROR NUCLEI

Aye Aye Min[1], Nang Khin Saw Aung[2] and Khin Swe Myint[3]

Abstract

In this paper, both the neutron and proton single-particle energy levels of A=51 mirror nuclei, ^{51}Fe and ^{51}Mn have been investigated by solving non-relativistic Schrödinger equation within the framework of Numerov method. In this calculation, phenomenological Woods-Saxon potential with spin-orbit interaction has been applied. Coulomb interaction is also taken into account for proton single-particle model approach. We also found that proton single-particle energy levels are higher than the neutron single-particle energy levels due to the effect of Coulomb repulsion. Moreover, there is some energy discrepancy between ^{51}Fe and ^{51}Mn mirror nuclei for proton single-particle model. This is due to the fact that the number of protons and neutrons are interchanged in the mirror nuclei. Moreover, the total root-mean-square radii of these mirror nuclei have also been investigated and the calculated values are found to be 3.57 fm for ^{51}Fe and 3.56 fm for ^{51}Mn respectively. We also observed the peculiar behavior in the relation between the binding energies and root-mean-square radii. Furthermore, the one nucleon and two nucleons separation energies have been investigated.

Keywords: mirror nuclei, single-particle energy levels, Numerov method

Introduction

Investigation of the structure and energy levels of nuclei is the basic understanding of nuclear properties and nucleon-nucleon interaction. Thus, many nuclear models such as Fermi gas model, liquid drop model, single-particle shell model and cluster model have been introduced to develop the better understanding of the nuclear properties. Among nuclear models, single-particle shell model is one of the most fruitful model in order to probe the nuclear properties (Bakhshabadi, F. and S. Mohammadi,, (2015), Giv, B.N. and S. Mohammadi, (2017)). Nowadays, the study of mirror nuclei (Machleidt, R. and H. Muther, (2001)) is an interesting issue to understand the charge symmetry breaking effect. The mirror nuclei have the same nucleon numbers and therefore they should have identical nuclear interaction due to properties of nuclear force. But the symmetry is being mainly broken due to spin orientation and the effect of Coulomb interaction. The study of this symmetry breaking reveals the details of structure of the mirror nuclei. In this paper, the nucleon single-particle energy of A=51 mirror nuclei, ^{51}Fe and ^{51}Mn, was investigated within the shell model approach.

Mathematical Formulation

(a) Numerov Method for Numerical Calculation

In this research work, the neutron and proton single-particle energies of A=51 mirror nuclei have been studied within the framework of shell model approach. To investigate the nucleon single-particle energy level, one-body Schrödinger radial equation will be used.

---

[1] Dr, Associate Professor, Department of Natural Science, University of Computer Studies (Magway)

[2] Master of Research Student, Department of Physics, University of Mandalay

[3] Rector (Rtd.), University of Mandalay

$$\frac{d^2u(r)}{dr^2}+k(r)\,u(r)=0 \text{ or } u''(r)=-k(r)\,u(r), \text{ where } k(r)\equiv\frac{2M}{\hbar^2}\left[E-V(r)-\frac{\hbar^2}{2M}\frac{\ell(\ell+1)}{r^2}\right] \qquad (1)$$

In this equation, k(r) is the kernel of the equation, M is the mass of nucleon single-particle, and V(r) is the potential of the single nucleon in the field of remaining core nucleus and u (r) is the reduced radial wave function. Equation (1) can be solved by means of Numerov method. In this method, the r range (r) is split into N points according to $r_n = r_{n-1} + h$ where h is the step and then the wave function and kernel of the equation can be rewritten as $u_n \equiv u(r_n) = u(r_{n-1}+h)$ and $k_n \equiv k(r_n) = k(r_{n-1}+h)$. Then, we can expand $u(r)$ by using Taylor series,

$$u_{n+1} \equiv u(r_n+h) = u(r_n)+hu'(r_n)+\frac{h^2}{2}u''(r_n)+\frac{h^3}{6}u'''(r_n)+\frac{h^4}{24}u^{iv}(r_n)+0(h^5) \qquad (2)$$

$$u_{n-1} \equiv u(r_n-h) = u(r_n)-hu'(r_n)+\frac{h^2}{2}u''(r_n)-\frac{h^3}{6}u'''(r_n)+\frac{h^4}{24}u^{iv}(r_n)+0(h^5) \qquad (3)$$

By adding equations (2) and (3), we obtain

$$u(r_n+h) = 2\,u(r_n)-u(r_n-h)-h^2\,k(r_n)\,u(r_n)+\frac{h^4}{12}u^{iv}(r_n) \qquad (4)$$

Similarly, the second-order derivative of the wave function can also be written as

$$u''_{n+1} \equiv u''(r_n+h) = u''(r_n)+hu'''(r_n)+\frac{h^2}{2}u^{iv}(r_n)+\frac{h^3}{6}u^{v}(r_n)+0(h^6) \qquad (5)$$

$$u''_{n-1} \equiv u''(r_n-h) = u''(r_n)-hu'''(r_n)+\frac{h^2}{2}u^{iv}(r_n)-\frac{h^3}{6}u^{v}(r_n)+0(h^6) \qquad (6)$$

As the same procedure of equation (2) and (3), the following equation can be obtained.

$$h^2u^{iv}(r_n) = -k(r_{n+1})\,u(r_{n+1})-k(r_{n-1})\,u(r_{n-1})+2k(r_n)\,u(r_n) \qquad (7)$$

By substituting equation (7) into equation (4) and solving, we get the following equations.

$$u_n = \frac{2\left[1-\frac{5h^2}{12}k_{n-1}\right]u_{n-1}-\left[1+\frac{h^2}{12}k_{n-2}\right]u_{n-2}}{\left[1+\frac{h^2}{12}k_n\right]} \qquad (8)$$

$$u_{n-1} = \frac{2\left[1-\frac{5h^2}{12}k_{n}\right]u_{n}-\left[1+\frac{h^2}{12}k_{n+1}\right]u_{n+1}}{\left[1+\frac{h^2}{12}k_{n-1}\right]} \qquad (9)$$

The above two equations are the forward and backward recursive relations in order to find the wave function for our consideration system. Therefore, when we calculate the wave function by using the forward-backward technique, it is necessary to give two initial values for each direction and the two solutions at the origin and the asymptotic solution at $r \to \infty$ are $u(r \to 0) = r^{-\ell}$ and $u(r \to \infty) = e^{-\alpha r^2}$, α = constant. The first derivative wave function is

$$u'_n = \frac{1}{2h}\left[\left(1+\frac{h^2}{6}k_{n+1}\right)u_{n+1} - \left(1+\frac{h^2}{6}k_{n-1}\right)u_{n-1}\right] \tag{10}$$

Since both $u_{out}(r)$ and $u_{in}(r)$ satisfy in a homogeneous equation, their normalization can always be chosen so that they are set to be equal at the r_c point. At the matching point r_c the eigen functions must all satisfy the continuity conditions as the following.

$$(u_{out})_{r_c} = (u_{in})_{r_c},\ (u'_{out})_{r_c} = (u'_{in})_{r_c} \tag{11}$$

We can define a G(E) function at r_c whose zeros correspond to the energy eigenvalues as;

$$G(E) = \left[\frac{u'_{out}}{u_{out}}\right]_{r_c} - \left[\frac{u'_{in}}{u_{in}}\right]_{r_c}. \tag{12}$$

Firstly, we give a trial energy "E" as an input at r = 0 and this energy is increased according to the equation $E_n = E + \Delta E$ where ΔE is the energy step within the N points. For each E_n, their eigen functions u_{out} and u_{in} can be calculated at the r_c point and build the G(E) function. We carefully looked for and checked a change of sign in the value of G(E) function. When we find it, we perform a fine tuning closing the energy range until the required tolerance. The correct energy eigen value and corresponding eigen function can be obtained simultaneously if the value of G(E) function is zero or very close to zero. In this calculation, we choose that the matching point is N/3.

(b) Derivation of Normalized Wave function

The outwards and inwards functions is directly obtained from the recursive formulas as $u_{out}(r)$ and $u_{in}(r)$ respectively.

The physical eigen functions $u_{out}(r)$ and $u_{in}(r)$ can be rewritten as

$$u_{out}(r) = A\,\Phi(r),\ u_{in}(r) = B\,I(r) \tag{13}$$

where A and B are constant. Their respective derivatives are

$$u'_{out}(r) = A\,\Phi'(r),\ u'_{in}(r) = B\,I'(r) \tag{14}$$

By substituting equation (13) and (14) in equation (11) respectively, we obtain as

$$(A\Phi)_{r_c} = (BI)_{r_c} \text{ and } (A\Phi')_{r_c} = (BI')_{r_c} \tag{15}$$

and performing the difference of the above equations, we get $A = \left[\frac{I - I'}{\Phi - \Phi'}\right]_{r_c} B \equiv f_c B$, where f_c = scaling factor. Therefore, the above equation is the relation between the constant A and B. We have already got outwards (Φ) and inwards functions (I) from the recursive formulas. After obtaining their derivatives, we can find the value of constant A. The value of constant B can be acquired after getting the value of A. Therefore, equation (14) can be rewritten as $u_{out}(r) = f_c B\ \Phi(r)$, $u_{in}(r) = B\ I(r)$, and B is the global factor that must be taken into account in the normalization process. Moreover, normalized constant "B" can be obtained by using the normalization conditions: $\int_0^{r_{max}} \left|u_\ell(r)\right|^2 dr = \int_0^{r_c} \left|u_{out}(r)\right|^2 dr + \int_{r_c}^{r_{max}} \left|u_{in}(r)\right|^2 dr = 1$. The global factor "B" is as $B = \frac{1}{\sqrt{N}}$, where, N = $\left[\ f_c^2 \int_0^{r_c} \left|\Phi(r)\right|^2 dr + \int_{r_c}^{r_{max}} \left|I(r)\right|^2 dr\ \right]$. Therefore, the normalized eigen functions becomes, $u_{out}(r) = \frac{1}{\sqrt{N}} f_c\ \Phi(r)$ from r = 0 fm to r_c point and $u_{in}(r) = \frac{1}{\sqrt{N}} I(r)$ from r = r_c fm to r_N point. The above wave functions are the normalized forward and backward wave functions in order to investigate the properties of nucleon single-particle states.

Potential for Nucleon Single-particle

In order to calculate nucleon single-particle energy levels, we considered that the nucleon moves freely in an average potential well generated by the other nucleons. The phenomenological Woods-Saxon central potential including spin-orbit interaction (Min, A.A. et al., (2014)) was applied in this calculation. Therefore, Woods-Saxon potential including spin-orbit term for $j = \ell + \frac{1}{2}$ state and $j = \ell - \frac{1}{2}$ state are:

$$V(r) = \frac{-V_0}{1+e^{(r-R)/a}} - V_{so}\left(\frac{\hbar}{m_\pi c}\right)^2 \left(\frac{1}{2}\ell\right)\frac{1}{ra}\frac{e^{\frac{(r-R)}{a}}}{\left(1+e^{\frac{(r-R)}{a}}\right)^2} \tag{16}$$

$$V(r) = \frac{-V_0}{1+e^{(r-R)/a}} + V_{so}\left(\frac{\hbar}{m_\pi c}\right)^2 \left(\frac{1}{2}(\ell+1)\right)\frac{1}{ra}\frac{e^{\frac{(r-R)}{a}}}{\left(1+e^{\frac{(r-R)}{a}}\right)^2}. \tag{17}$$

The above two potentials can be used in order to calculate nucleon single- particle energy levels for each orbital angular momentum states of our consideration system. The value of V_0, V_{so} and a are described in reference. It is also necessary to consider the Coulomb potential for the proton single-particle state. Since the core nuclei are not the point charged particles, the finite size Coulomb potential will, therefore, be used. Coulomb potential can be divided into three regions (i) the potential at a point outside the nucleus (r > R), (ii) the potential at on the surface of the nucleus (r ≥ R) and (iii) the potential inside the nucleus (r < R). By applying Gauss's theorem, we can derive Coulomb's potential for each region as $V_{Coulomb}(r) = Z_1 Z_2 \alpha\hbar c \frac{1}{r}$ (for $r \geq R$) and $V_{Coulomb}(r) = Z_1 Z_2 \alpha\hbar c \frac{1}{2R}\left[3 - \frac{r^2}{R^2}\right]$ (for $r \langle R$),

where Z_1 and Z_2 are charge of the single proton and core nucleus, α is the fine structure constant.

Calculation of Root-mean-square Radii and Nucleon Separation Energies

After getting the normalized wave function, we can calculate the root-mean-square radii of mirror nuclei, ^{51}Fe and ^{51}Mn. The root-mean-square radius of the nucleon single-particle in each state can be obtained as $\langle r^2 \rangle = \langle u(r) | r^2 | u(r) \rangle$. In this equation, u(r) is the wave function of the corresponding states. The total root-mean-square radii of A=51 mirror nuclei (Rmst) can be deduced by using the following equation as $\mathrm{Rmst} = \sqrt{\left(\frac{x_1}{x_2}\right)}$, where, $x_1 = \sum_i (2j_i + 1) \langle r^2 \rangle_i$ and $x_2 = \sum_i (2j_i + 1)$. The one-neutron and one-proton separation energies can be expressed as $S_n = B(Z,N) - B(Z\,,N-1)$ and $S_p = B(Z,N) - B(Z-1\,,N)$.

Based on the above equations, two-neutron separation energy and two-proton separation energy are $S_{2n} = B(Z,N) - B(Z,N-2)$ and $S_{2p} = B(Z,N) - B(Z-2\,,N)$. By using the above equations, one nucleon and two nucleon separation energies can be calculated.

Results and Discussions

In this paper, the nucleon single-particle energy levels of A=51 mirror nuclei, ^{51}Fe and ^{51}Mn, have been investigated by using Woods-Saxon potential with spin-orbit interaction. In this calculation, Numerov method has been applied. The accuracy of this method has already checked by using harmonic oscillator potential model for ^{12}C. The calculated numerical results are in good agreement with the analytical results. As a first step, the single-nucleon potentials have been analyzed. Fig. 1 (a) is the total potential of nucleon single-particle having the various spin-orbit coupling states in the nuclear medium. We found that the interaction range is about 8.0 fm for Woods-Saxon prescription. Moreover, the nucleon single particle field strongly depends upon the spin-orbit coupling. Therefore, the spin-orbit interaction for various orbital angular momenta have been plotted in order to recognize the behavior of this interaction and it is shown in Fig. 1 (b). From our graph, we can clearly see that the spin orbit potential for the Jackknife case gives the attractive interaction while that of the stretched spin case provides the repulsive interaction. In addition, there is no attractive or repulsive interaction in the nuclear interior but the spin-orbit potential is peaked near the nuclear surface.

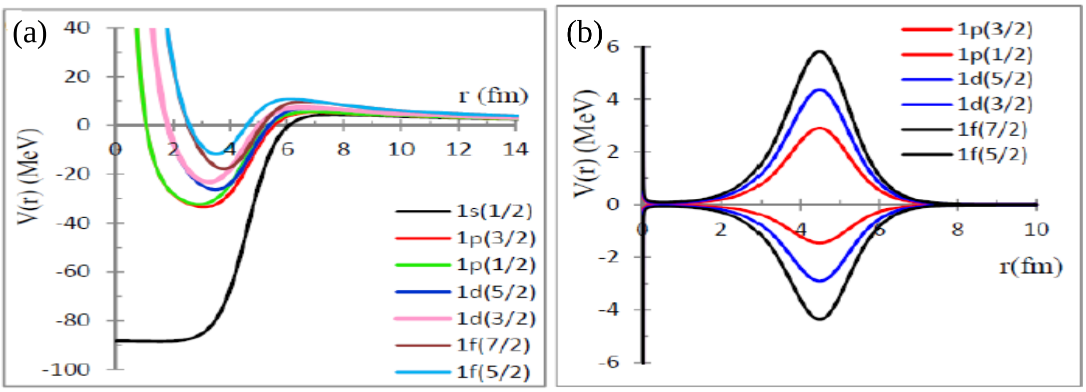

Figure 1 (a) Nucleon single-particle potential in the nuclear medium and (b) spin-orbit interaction for each state

The systematic energy level diagrams for neutron and proton single-particle energy levels in A= 51 mirror nuclei, ^{51}Fe and ^{51}Mn, are also displayed in Fig. 2 (a) and (b) respectively.

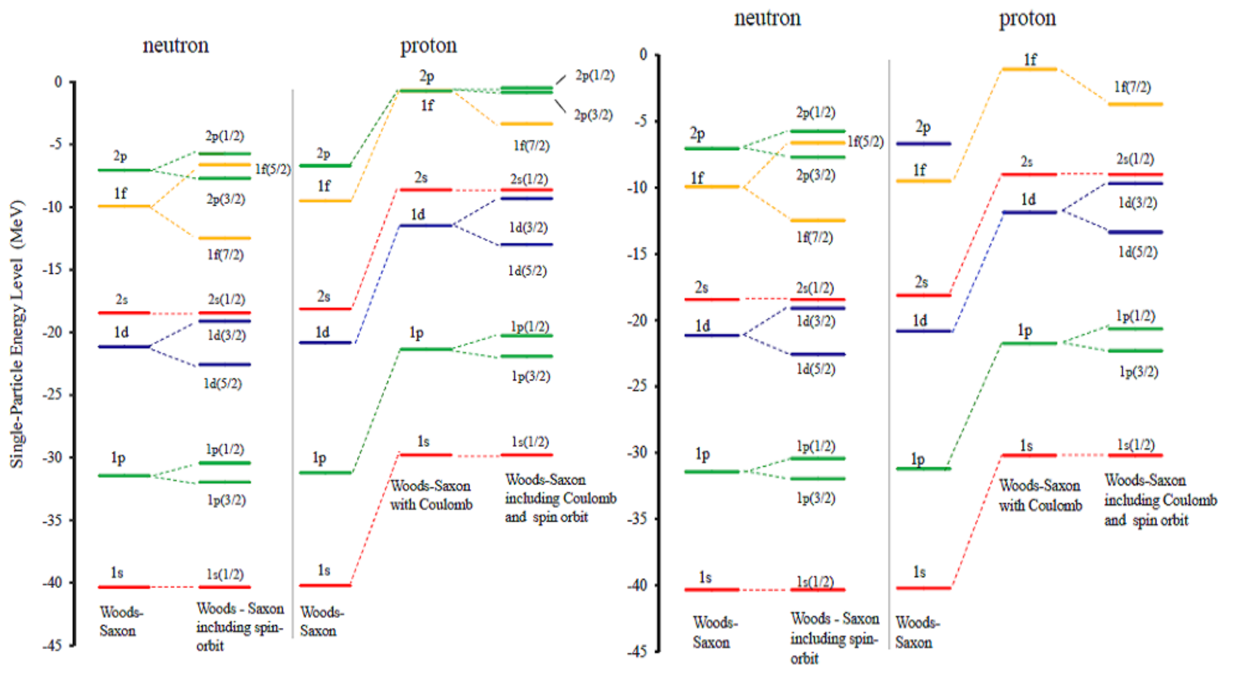

(a) (b)

Figure 2 Single-particle energy level (a) in ^{51} Fe (b) ^{51}Mn

The neutron single-particle energy levels are the same for A= 51 mirror nuclei. However, proton single-particle energy levels are higher than the neutron single-particle energy levels due to the effect of Coulomb repulsive interaction between proton and core nuclei. Moreover, we can also see that proton single-particle energy levels have some energy discrepancy between ^{51}Fe and ^{51}Mn mirror nuclei. This is due to the fact that the number of protons and neutrons are interchanged in the mirror nuclei. In order to understand the difference in energy level qualitatively, we plotted it which is also called the Coulomb energy difference in ^{51}Fe and ^{51}Mn mirror nuclei. Fig. 3 (a) and (b) show the energy difference between neutron and proton single-particle model and the Coulomb energy difference in the mass number A= 51 mirror nuclei.

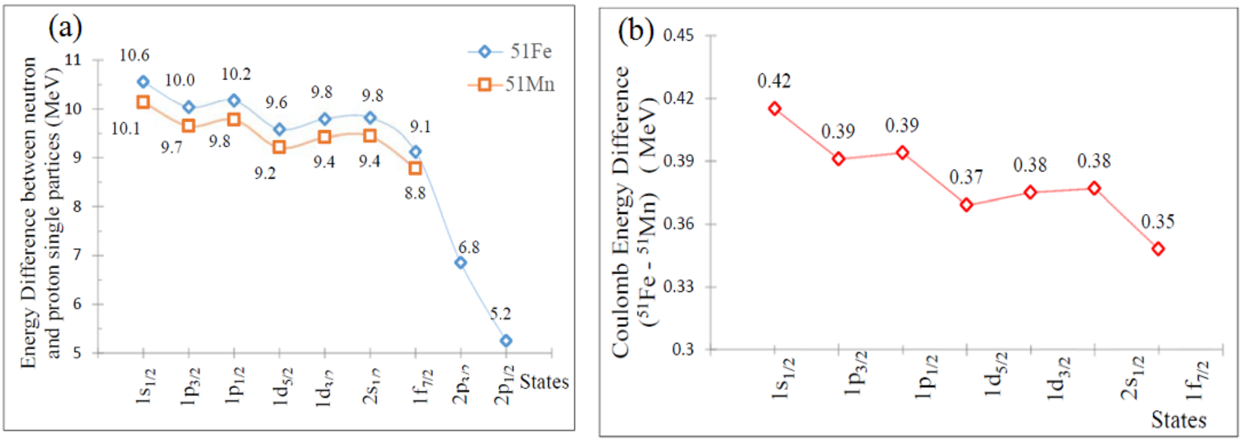

Figure 3 (a) Energy difference between neutron and proton single-particle model (b) Coulomb energy difference in A= 51 mirror nuclei.

The root-mean-square radii of A=51 mirror nuclei have also investigated for various nucleon single-particle states and the results are expressed in Tables (1) and (2).

Table 1 Neutron single-particle energy levels of A=51 mirror nuclei

Single-particle state	Single-particle energy (MeV) (Woods-Saxon pot. only)	rms distance (fm)	Single-particle state	Single-particle energy (MeV) (Woods-Saxon pot.+ LS pot.)	rms distance (fm)
1s	-40.34	2.63	$1s_{1/2}$	-40.34	2.63
1p	-31.44	3.17	$1p_{3/2}$	-31.96	3.20
			$1p_{1/2}$	-30.43	3.07
1d	-21.15	3.59	$1d_{5/2}$	-22.57	3.64
			$1d_{3/2}$	-19.11	3.52
2s	-18.44	3.51	$2s_{1/2}$	-18.44	3.51
1f	-9.91	4.00	$1f_{7/2}$	-12.48	4.04
			$1f_{5/2}$	-6.61	3.96
2p	-7.04	4.20	$2p_{3/2}$	-7.69	4.16
			$2p_{1/2}$	-5.74	4.26

According to our calculated results, the root-mean-square radii gradually increased with decreasing energy values within the frame work of Woods-Saxon interaction and this interaction including Coulomb interaction. But, when the spin-orbit interaction is switched on, we observed the peculiar behavior in the relation between the binding energies and root-mean-square radii. In order to understand this strange behavior clearly, the potential and the corresponding wave function for ^{51}Fe have been plotted for various states.

These plotted figures is described in Fig 4. (a) and (b). The attractive interaction strength which possesses the total spin $J = \ell + s$ is stronger than that having $J = \ell - s$. The stronger interaction strength gives the greater binding energy. Moreover, the spin-orbit attractive potential works near the nuclear surface.

Table (2) Proton single-particle energy levels of ^{51}Fe and ^{51}Mn

Nuclide	states	Single-particle energy (MeV) (Woods-Saxon +Coulomb)	states	Single-particle energy (MeV) (Woods-Saxon +Coulomb + LS coupling)	rms distance (fm)	Total rms distance (fm)
^{51}Fe	1s	-29.79	$1s_{1/2}$	-29.79	2.70	3.57
	1p	-21.35	$1p_{3/2}$	-21.92	3.27	
			$1p_{1/2}$	-20.26	3.18	
	1d	-11.48	$1d_{5/2}$	-12.99	3.71	
			$1d_{3/2}$	-9.31	3.60	
	2s	-8.62	$2s_{1/2}$	-8.62	3.53	
	1f	-0.71	$1f_{7/2}$	-3.35	4.14	
			$1f_{5/2}$	-	-	
	2p	-0.73	$2p_{3/2}$	-0.85	4.56	
			$2p_{1/2}$	-0.49	4.73	
^{51}Mn	1s	-30.20	$1s_{1/2}$	-30.20	2.70	3.56
	1p	-21.74	$1p_{3/2}$	-22.31	3.26	
			$1p_{1/2}$	-20.65	3.17	
	1d	-11.85	$1d_{5/2}$	-13.35	3.71	
			$1d_{3/2}$	-9.69	3.60	
	2s	-8.99	$2s_{1/2}$	-8.99	3.49	
	1f	-1.06	$1f_{7/2}$	-3.70	4.13	
			$1f_{5/2}$	-	-	
	2p	-	$2p_{3/2}$	-	-	
			$2p_{1/2}$	-	-	

Furthermore, single-nucleon wave functions for $J=\ell+s$ are more shifted to the outer region than that having spin state $J=\ell-s$ and that is why the root-mean-square radius of nuclei for each spin state is larger although the binding energy is large. These effects could explain why both the rms value and binding energy are large. The total root-mean-square radius of A=51 mirror nuclei have been investigated. The calculated results are 3.57 fm for ^{51}Fe and 3.56 fm respectively.

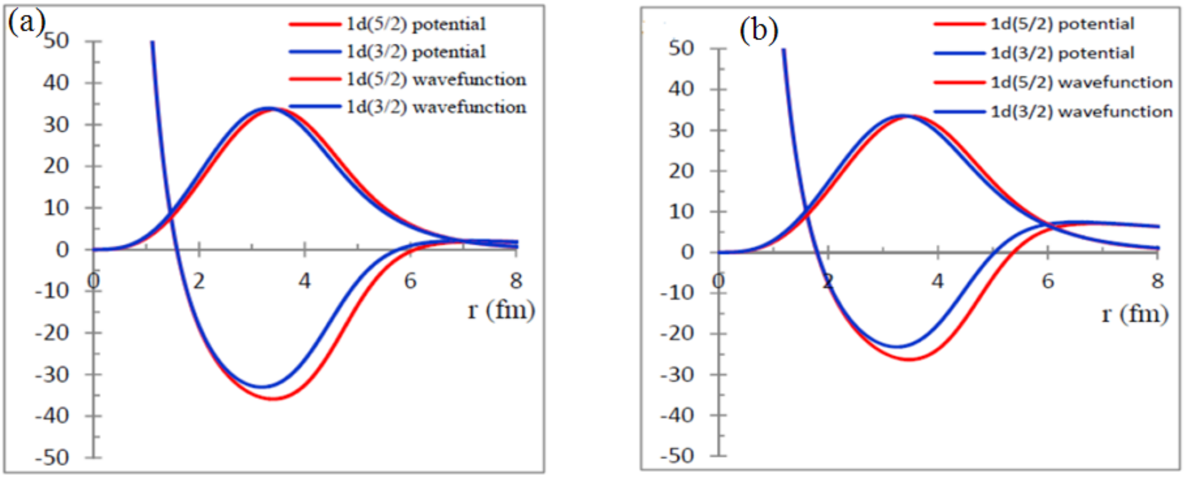

Figure 4 (a) Neutron and (b) proton single-particle wave functions and potentials for 1d state in ^{51}Fe

Moreover, we have calculated one nucleon separation energies and two nucleon separation energies for A=51 mirror nuclei by using the binding energies data (Audi, G. et al., (2012)) and the results are shown in Table (3). According to our results, although mass numbers are the same for the mirror nuclei, the nucleon separation energies are not the same. We found that the proton separation energies for ^{51}Fe are smaller than that for ^{51}Mn but the neutron separation energies are conflict with the proton separation energies.

Table 3 Nucleon separation energies for ^{51}Fe and ^{51}Mn

Nuclide	Neutron Separation Energy (MeV)		Proton Separation Energy (MeV)	
	One-neutron SE	Two- neutron SE	One-proton SE	Two-proton SE
^{51}Fe	13.83	31.65	4.91	9.50
^{51}Mn	13.69	26.75	5.27	14.86
Difference	0.14	4.90	-0.36	-5.36

For the neutron separation energy case, the difference energy values between ^{51}Fe and ^{51}Mn are 0.14 MeV and 4.90 MeV respectively for one-neutron and two-neutron separation energies. For proton separation energy case, the differences for one-proton and two-proton separation energies are found to be -0.36 MeV and -5.16 MeV correspondingly.

Conclusion

In this research work, nucleon single-particle energy levels of A=51 mirror nuclei, namely ^{51}Fe and ^{51}Mn have been investigated by solving one-body Schrödinger equation with the use of phenomenological Woods-Saxon central potential including spin-orbit interaction. According to our results, the calculated shell structure of neutron single particle are the same for A= 51 mirror nuclei but that of proton single particle have some discrepancy. This shell structure and some energy difference in proton single-particle energy levels of ^{51}Fe and ^{51}Mn mirror nuclei comes from the different number of protons in the mirror nuclei although the mass numbers are the same. In order to understand the difference in energy level, the Coulomb energy differences have been investigated qualitatively. We can conclude that the larger the value of the orbital angular momentum, the smaller Coulomb energy difference is. For the same orbital angular momenta case, the Coulomb energy difference for stretched spin state is greater than that for jackknife state. In addition, nucleon separation energies have been investigated. This present work is not only to understand the nuclear shell structure but also to recognize how to apply the simple and good numerical Numerov's method.

Acknowledgements

The authors would like to thank Dr Soe Lin Aung, Rector, University of Computer Studies (Magway), for his encouragement and to acknowledge Professor Dr. Y. Akaishi, KEK, Japan, for his valuable advice.

References

Bakhshabadi, F. and S. Mohammadi, (2015) "Calculation of the Energy Levels of Phosphorus Isotopes (A=31 to 35) by Using OXBASH Code." Americ. J. Mod. Phys. 4(3-1), pp.15-22.

Giv, B.N. and S. Mohammadi, (2017) "Calculating Energy Levels in ^{49}Mn/^{49}Cr Mirror Nuclei with OXBASH Code." SciencePG 5(5), pp.70-73.

Machleidt, R. and H. Muther, (2001) "Charge symmetry breaking of the nucleon-nucleon interaction: ρ-ω mixing versus nucleon mass splitting." Phys. Rev. C 63 034005, pp.1-10.

Min, A.A. et al., (2014) "Single-particle Energy Levels of ^{34}Si, ^{35}P and ^{36}S." Univ. Res. J. **7**(4), pp.25-36.

J. Myanmar Acad. Arts Sci. 2020 **Vol. XVIII.No.2C**

SYNTHESIS AND CHARACTERIZATION OF ZnO NANOPARTICLES AT DIFFERENT CALCINATION TEMPERATURES BY SOL-GEL METHOD

San San Wai[1], Khin Lay Thwe[2], Su Su Hlaing[3]

Abstract

In this work, zinc oxide nanoparticles were synthesized by using sol-gel method at calcination temperatures of 400˚C and 500˚C. Sol-gel method is the simplest method and has the ability to control the particle size and morphology through systematic monitoring of reaction parameters. Zinc oxide nanoparticles were synthesized via sol-gel method using zinc acetate dihydrate [$Zn(CH_3COO)_2.2H_2O$] as a precursor and methanol as a reagent. Distilled water was used as solvent medium and ammonia was used to adjust the pH value. And then the obtained samples were characterized by X-ray Diffraction (XRD) to confirm the formation of ZnO phase, which showed that it had this type of hexagonal wurtzite structure. In the comparison of the crystalized sizes of the samples, the sample calcinated at 500˚C have smaller crystalized size than the sample calcinated temperatures at 400˚C. The Scherrer's equation was used to calculate the crystalized size of the ZnO powder. And then, scanning electron microscopy (SEM) was used to observe the surface morphology of obtained ZnO nanoparticles.

Keywords: Sol-gel method, Zinc acetate dehydrate, ZnO nanoparticles, XRD, SEM

Introduction

Nanotechnology represents one of new sciences that promise to provide a broad range of novel uses and improved technologies for numerous applications. One important reason behind the intense interest is that nanotechnology permits the controlled preparation of nanomaterials where at least one dimension of the structure is less than 100 nm. Schematic illustration of structural dimensionality of nanomaterials with expected properties is shown in Figure 1. Synthesis of metal nanoparticles with specific properties is a newly established research area that attracts a great deal of attention. There are several methods for synthesis of metal nanoparticles. Among the metal nanoparticles, Zinc Oxide is the semiconductor material with high chemical stability, strong photo sensitivity and non-toxicity property and is widely used in antibacterial materials . Compared with ordinary Zinc Oxide powder, Zinc Oxide nanoparticles have a large specific surface area and small size effect and show wide applications . Several different methods can be used to control the size distribution of semiconductor and metal nanoparticles to obtain monodisperse samples. Common synthetic methods of ZnO nanostructures are shown in Figure 2. Most of the ZnO crystals have been synthesized by traditional high temperature solid state method which is energy consuming and difficult to control the particle properties. ZnO nanoparticles can be prepared on a large scale at low cost by simple solution-based methods such as chemical precipitation, sol-gel synthesis and solvothermal / hydrothermal reaction. So in the present work, ZnO nanoparticles are synthesized by using sol-gel method. And the obtained ZnO nanoparticles were characterized by X-ray Diffraction (XRD) and scanning electron microscopy (SEM).

---

[1] Assistant Lecturer, Department of Physics, Computer University, Myeik

[2] Dr, Lecturer, Department of Physics, University of Yangon

[3] Dr, Assistant Lecturer, Department of Physics, University of Yangon

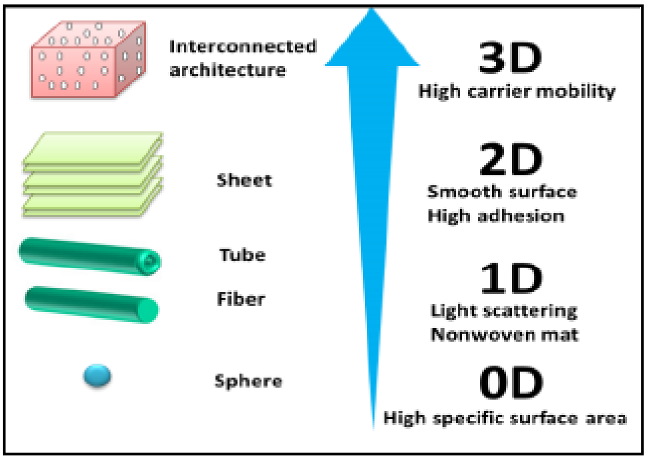

Figure 1 Schematic illustration of structural dimensionality of nanomaterials with expected properties

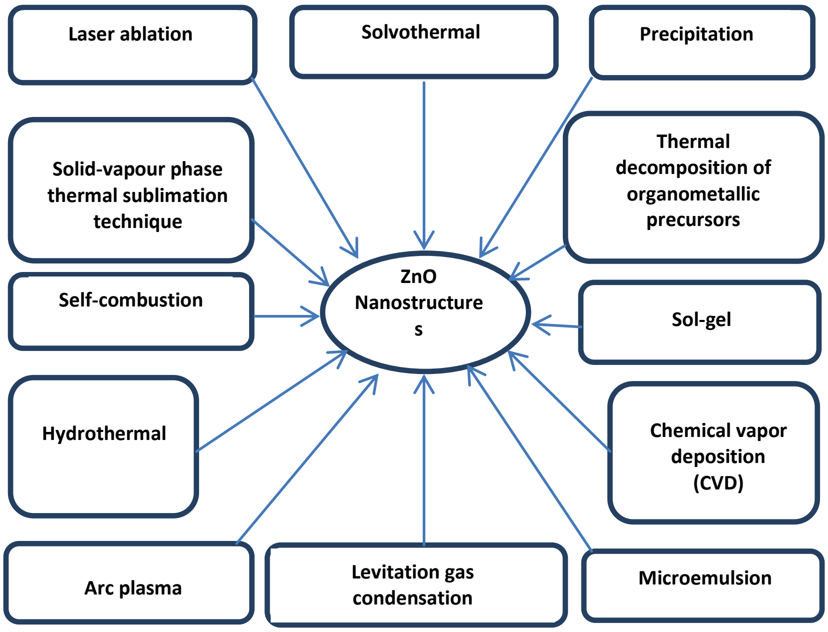

[Shaheed, M. A, et. al, J. Environ. Anal. Chem, 2015]

Figure 2 Common synthetic methods of ZnO nanostructures

Materials and Methods

(1) Synthesis of ZnO Nanoparticles

Synthesis of zinc oxide by sol-gel is one of the most successive methods for producing large-area and good quality ZnO nanostructures with suitable precursor. The main parameters for ZnO synthesis by sol-gel are precursors, reagents and experimental parameters. Most commonly used ZnO precursors are zinc acetate dihydrate, zinc nitrate hexahydrate and zinc acetylacetonate hydrate. Synthesis of ZnO using sol-gel consists of three processes: stirring, heating and annealing.

Synthesizing ZnO nanoparticles via sol-gel technique includes the use of materials such as zinc acetate dihydrate [$Zn(CH_3COO)_2.2H_2O$], methanol (CH_3OH) and distilled water. Zinc acetate dihydrate was used as precursor and methanol was used as a reagent. Distilled water was used as a solvent medium and ammonia (NH_3) was used to adjust pH value of solution between 9 and 11. The materials used in synthesizing ZnO nanoparticles were shown in Figure 3.

In order to prepare a solution, methanol (1 M) is made into 0.6 M to dilute and 13 g of zinc acetate dihydrate was weighed using a weighing balance. After that, 13 g of zinc acetate dehydrate ($Zn(CH_3COO)_2.2H_2O$) was dissolved with a 100 ml of methanol (0.6 M) under continuous stirring for 15 min. The mixed solution was stirred with a magnetic stirrer at 80˚C for 10 min to form transparent solution; its pH was adjusted by adding dropwise 5 ml of ammonia per 5 min. After 23 ml of ammonia have been added to the solution, pH value was 10. After adjusting the pH, the solution was heated at 100˚C for 30 min under stirring and then the temperature was increased up to 150˚C until gelation occurred. And white precipitate was formed after the solution evaporated. The precipitates were washed four times with methanol. And then the washed precipitates were dried at 190˚C for 15 min and annealed at 500˚C and 400˚C for 3 hrs in furnace. Finally, zinc oxide powder was obtained. Figure 4 shows the flow scheme of preparation of ZnO nanoparticles and Figure 5 shows the procedures of ZnO nanoparticles.

Figure 3 The materials used in synthesizing ZnO nanoparticles

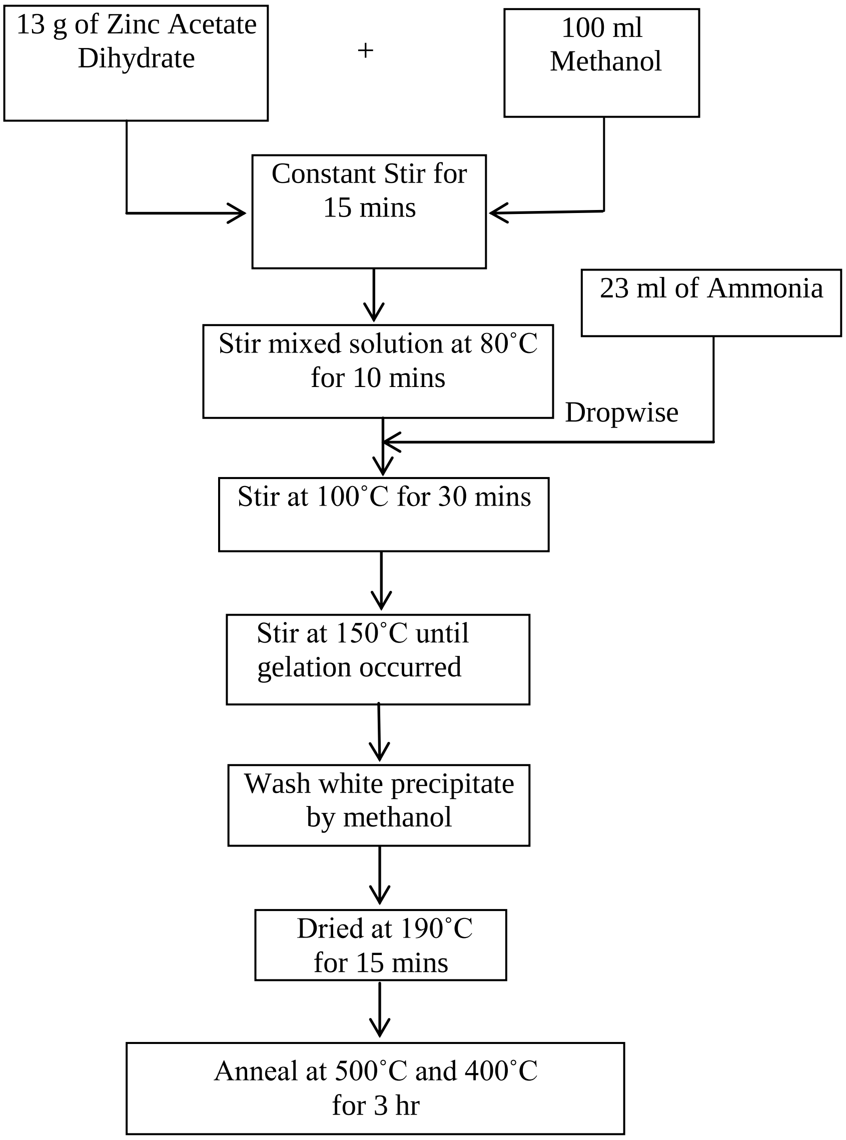

Figure 4 The flow scheme of preparation of ZnO nanoparticles

Figure 5 The procedures of ZnO nanoparticles

(1) X-ray Diffraction (XRD)

The synthesized ZnO powder was characterized by powder X-ray diffraction (XRD: RIGAKU-RINT 2000 X-ray Diffractometer). The X-ray diffraction data were recorded by using CuK_{α} radiation ($\lambda = 0.154056$ nm). The average crystallite size of the sample was estimated with the help of Scherrer's equation using the diffraction intensity of the peak.

$$D = \frac{0.94\lambda}{B\cos\theta}$$

where λ is the wavelength, B is the full width at half- maximum (FWHM) and θ is the diffraction angle.

(2) Scanning Electron Microscopy (SEM)

Scanning Electron Microscope (SEM) [JEOL - 6000] was used to observe the surface morphology of obtained ZnO nanoparticles. This SEM is scanning electron microscope with a high resolution. The scanning electron microscope is a type of electron microscope that creates various images by focusing a high energy beam of electrons onto the surface of a sample and detecting signals from the interaction of the incident electrons with the sample's surface. The type of signals gathered in a SEM varies and can include secondary electrons, characteristic X-rays, and back scattered electrons. In a SEM, these signals come not only from the primary beam impinging upon the sample, but also from other interactions within the sample near the surface. The SEM is capable of producing high-resolution images of a sample surface.

Results and Discussion

(1) XRD Analysis

The XRD pattern of the ZnO powder was recorded in the diffraction angle range 10˚ to 70˚. The Bragg's reflections in Figure 6 and 7 which were corresponded to the (100), (002), (101), (102), (110), (103), (200), (112) and (201) planes, respectively, after comparing them with the data in the JCPDS card 65-3411. They have been investigated that the orientation of (101) plane was favorable in hexagonal wurtzite structure for 500 ˚C and 400˚C. The standard lattice parameters 'a' and 'c' were a = 3.2 Å and c = 5.2 Å. But the lattice parameters 'a' and 'c' calculated from XRD were found to be a = 3.2475 Å and c = 5.2045 Å for 500˚C and a = 3.2462 Å and c = 5.2066 Å for 400˚C.So, both standard and experimental lattice parameters are in very good agreement for two samples. The average crystallite size of ZnO nanoparticles for two temperatures were presented in Table 1.

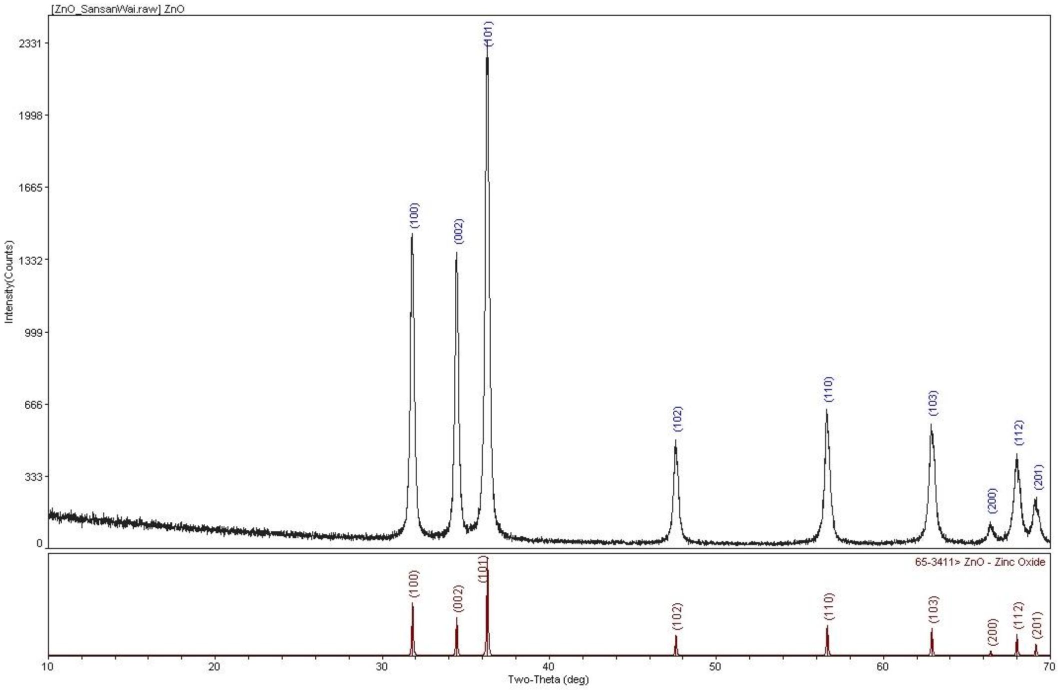

Figure 6 XRD pattern of ZnO nanoparticles powder at calcination temperature 500˚C

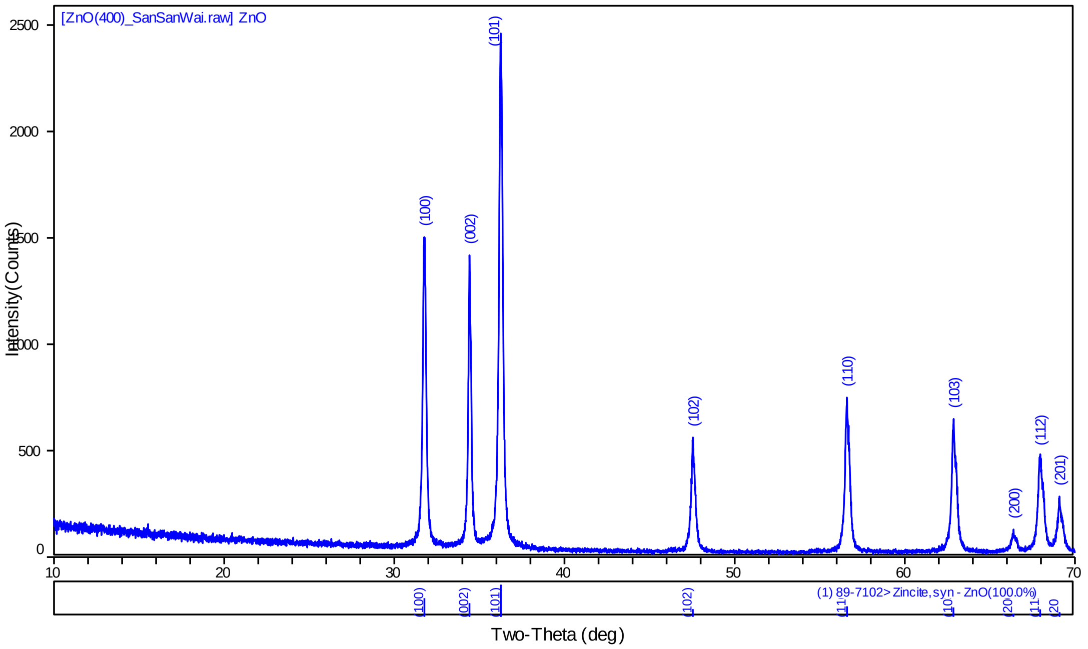

Figure 7 XRD pattern of ZnO nanoparticles powder at calcination temperature 400˚C

Table 1 The average crystallite size of the obtained ZnO powder

Sample	Average crystallite size, D (nm)	lattice parameter 'a'	lattice parameter 'c'
At 500˚C	26.61	3.2475 Å	5.2045 Å
At 400˚C	35.07	3.2462 Å	5.2066 Å

(2) SEM Investigation

SEM images also confirmed the formation of ZnO nanoparticles. The SEM micrographs of the synthesized ZnO powder were shown in Figure 8 and Figure 9. In Figure 8, the average grain size of ZnO nanoparticles at 500°C was 261 nm. It was found that the minimum grain size of ZnO nanoparticles was 117 nm and the maximum grain size of ZnO nanoparticles was 444 nm. In Figure 9, the average grain size of ZnO nanoparticles at 400°C was 31.533 µm. It was found that the minimum grain size of ZnO nanoparticles was 12.649 µm and the maximum grain size of ZnO nanoparticles was 124.724 µm.

The images showed most of the particles were spherical in shape with smooth surface, however some agglomerated particles were also presented. Agglomeration was understood to increase linearly with annealing temperature and hence some degree of agglomeration at this temperatures (500°C and 400°C) appears unavoidable.

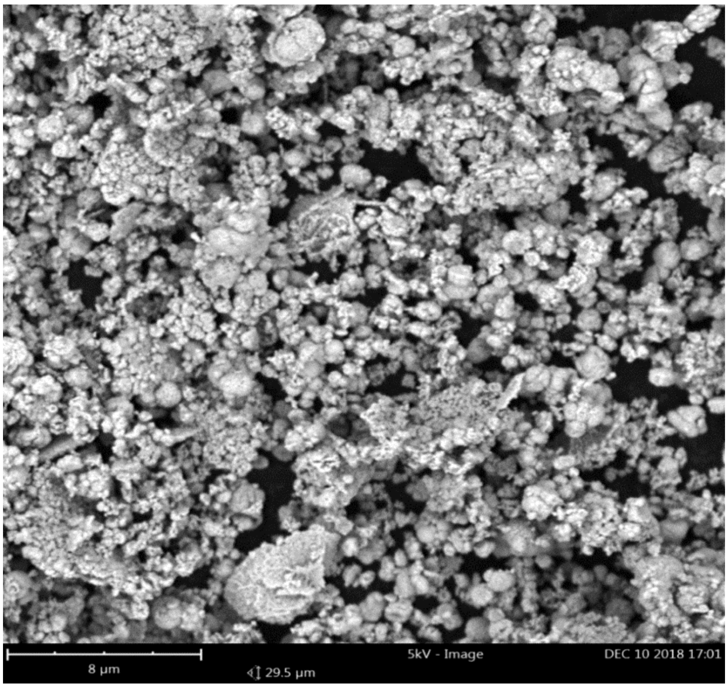

Figure 8 SEM micrograph of the synthesized ZnO powder at 500˚C

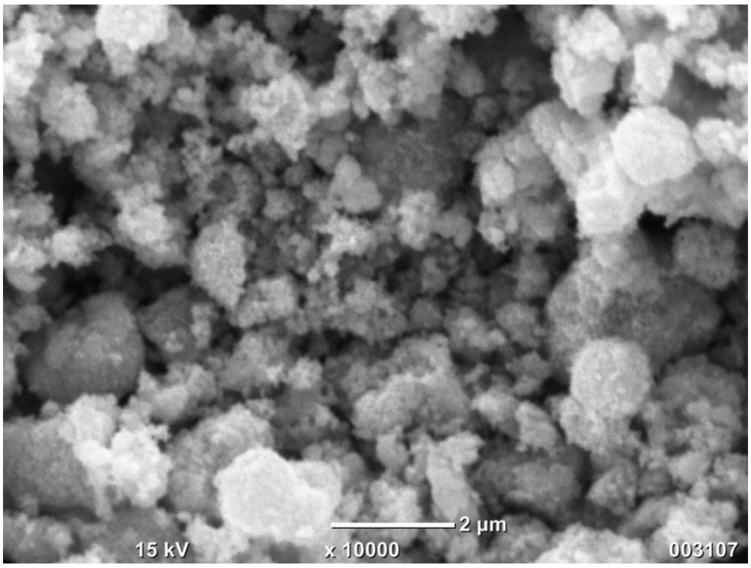

Figure 9 SEM micrograph of the synthesized ZnO powder at 400˚C

Conclusion

ZnO nanoparticles were successfully synthesized by sol-gel method using the materials such as zinc acetate dihydrate [$Zn(CH_3COO)_2.2H_2O$], methanol (CH_3OH), ammonia and distilled water. The obtained samples were characterized by using XRD for phase analysis. From the XRD profiles for the samples, it confirmed the presence of hexagonal wurtzite structure. The average lattice parameter 'a' and 'c' of ZnO nanoparticles were found to be 3.2475 Å and 5.2045 Å. So, both standard and experimental lattice parameters are in very good agreement. The average crystallite size of the sample was estimated with the help of Scherrer's equation using the diffraction intensity of the peak. It was found that the average crystallite size of ZnO nanoparticles was 26.61 nm for 500˚C and 35.07nm for 400˚C. The temperature increases, the crystallite size decreases. The morphological properties of the obtained samples were also characterized by using SEM. According to the SEM micrographs, the average grain size were 261 nm for 500˚C and 31.533 µm for 400˚C. It was found that ZnO nanoparticles were spherical in shape with smooth surface. Most of the nanoparticles were well-dispersed and some aggregates exhibited nanoscale features.

Future Plan

In the area of water purification, nanotechnology offers the possibility of an efficient removal of pollutants and germs. Today nanoparticles, nanomembrane and nanopowder used for detection and removal of chemical and biological substances. Nanomaterials reveal good result than other techniques used in water treatment because of its high surface area (surface/volume ratio). So, the antibacterial behavior of ZnO nanomaterials will be studied. They can be developed as antibacterial agents to improve the water quality. Then, ZnO nanomaterials will be applied in water and waste water treatment processes.

Acknowledgements

The authors are very grateful to Dr Thandar Win, Professor and Principal of University of Computer Studies (Myeik) for her kind permission to carry out this work.

References

Bari, A. R., Shinde, M. D., Vinita, D. & Patil, L. A. (2009). “Effect of Solvents on the Particle Morphology of nanostructured ZnO”, *Indian Journal of Pure & Applied Physics,* Vol.47.

Hasnidawani, J. N., Azlina, H. N., Norita, H., Bonnia, N. N., Ratim, S.&Ali, E. S. (2016). “Synthesis of ZnO Nanostructures Using Sol-Gel Method”, *Procedia Chemistry,* Vol.19.

Lingna, W. & Mamoun, M. (1999). “Synthesis of zinc oxide nanoparticles with controlled morphology”, *J. Mater. Chem.,* Vol. 9.

McNeil, S. E. (2005). “Nanotechnology for the biologist”, *J. Leuko. Bio.,* Vol. 78.

Moezzi, A., McDonagh, A. M. & Cortie, M. B. (2012). “Zinc oxide particles: Synthesis, properties and applications”, *J. Chem. Eng.,* Vol. 1.

Shaheed, M. A. & Hussein, F. H. (2015). “Preparation and Applications of Titanium Dioxide and Zinc Oxide Nanoparticles”, *J. Environ. Anal. Chem.,* Vol. 2.

Zhang, J., Sun, L. D., Yin, J. L., Su, H. L., Liao, C. S. & Yan, C. H.(2002).“Control of ZnO Morphology via a Simple Solution Route”, *Chem. Mater.*, Vol. 14.

J. Myanmar Acad. Arts Sci. 2020 **Vol. XVIII.No.2C**

EFFECTIVE AND EFFICIENT REMOVAL OF METHYLENE BLUE DYE BY ZEOLITE ADSORBENTS

Su Mon Oo[1], Hla Toe[2] and Cho Cho Thet[3]

Abstract

The application of mordenite zeolite and composite fiber as an adsorbent for the removal of aqueous methylene blue (MB) dye at room temperature was investigated. Effects of operational parameters including different contact time and different initial concentrations (C_i) of dyes on removal efficiency and adsorption amount of MB were determined. The characterization tools such as Fourier transform infrared (FT-IR), X-ray diffraction (XRD) and scanning electron microscope (SEM) were performed in order to identify the functional group, study the crystal structure and investigate the microstructure of zeolite adsorbents. Adsorption parameters were found out to be well fitted into *Langmuir* adsorption isotherm. The present work suggests that zeolite adsorbents could effectively remove MB dye. Thus, zeolites are good candidates for the removal of such organic pollutants.

Keywords: adsorbents, composite fiber, methylene blue (MB) dye, isotherm and zeolite.

Introduction

Dyes and pigments are used to apply colors for textile industry. There are nearly 800,000 tons of dyes per year in the dyeing process. In textile industry, about 10-15% of these dyes are lost during operation. Synthetic dyes are used in numerous industries such as textile, paper printing, food, pharmaceutical, leather and cosmetics. The presence of dyes can manufacture highly toxic compounds through many reactions that can cause very dangerous health problems such as allergies, tumors, and cancers in humans [Mohamed A et al, (2017)]. There are many more synthetic dyes than natural dyes. Among them, methylene blue MB ($C_{16}H_{18}ClN_3S$) is one of the most widely used dyes in some industries such as wood, linen and silk. 10 to 200 mg/L concentrations of MB are usually discharged into the environment. It is a cationic dye which is extremely resistant to be heat and light and hardly break down due to its complex structure. By exposing this dye to human, it can suffer serious damage to the eye and trouble breathing [Ahmad et al, 2019]. Even at low concentration, wastewater in organic dyes is very harmful to organisms.

There are several treatments to separate or decompose the pollutants in wastewater. The major treatments are followed in chemical precipitation/co-precipitation, membrane filtration, bio-degradation, and adsorption for heavy metals and dye [Shikha et al, (2017)]. Among these treatments, precipitation and biodegradation treatment have deficiency in high concentration level wastewater that causes fast saturation of adsorbents [Masaru et al, (2017)]. In contrast, adsorption is more economical and reliable treatment, which is one of the most effective physical processes for the decolorization of textile wastewater. Adsorption is the adhesion of atoms, ions or molecules from a gas, liquid or dissolved solid to a surface. This process creates a film of the adsorbate on the surface of the adsorbent. The mechanism of adsorption involves the adsorption of adsorbate molecules on the surface of the adsorbents through molecular interactions and

---

[1] Assistant Lecturer , Department of Physics, University of Computer Studies (Banmaw)

[2] Associate Professor, Department of Physics, University of Yangon

[3] Associate Professor, Department of Physics, Myeik University

diffusion of adsorbate molecules from the surface into the interior of the adsorbent materials either by monolayer or multilayer [Moustafa et al, (2012)]. Adsorption phenomenon depends on various factors such as pH, temperature, adsorbent dose, size and surface morphology. It also depends on the concentration and structure of adsorbate.

There are many adsorbents to remove the pollutants of wastewater. Among them, zeolites offer numerous advantages over liquid catalysts since they offer less or no corrosion, no waste or disposal problems, high thermostability and easy setup of continuous processes [Melkon et al, (2016)]. Zeolites are microporus, aluminosilicate minerals commonly used as commercial adsorbents and catalysts. Zeolites are natural or synthetic crystalline aluminosilicates with ion exchanging properties and bearing a negatively charged honeycomb framework of microspores into which molecules may be adsorbed for environmental decontamination and to catalyze chemical reactions. The main advantages of zeolites over conventional catalysts are due to the great acid strength they can have and to their great adaptability to practically all types of catalysis [N.O.Omisanya et al, (2012)]. Although zeolite powder can easily remove MB, it is difficult to separate powder from the aqueous MB solution. To overcome these problems, zeolite-composite fiber adsorbents using wet spinning method for decontamination of MB has been prepared. The treatment of such fibrous adsorbents is cheaper energy costs while membrane treatment increases energy costs through high-pressure operation although its separation efficiency is high. The advantage of fibrous adsorbents is high removal efficiency of heavy metal ions because it has small mesh structures consisting of small fiber filaments [U. Wingenfelder et al, (2005)]. In this work, zeolite adsorbents, both of powder and composite fiber, were used to remove the synthetic MB dye and investigated the removal efficiency of MB depending on contact time and initial concentration of MB.

Materials and Methods

Zeolite fibers were prepared by wet spinning process [Masaru et al, (2017)]. Zeolite concentration in the dispersion of poly ethersulfone (PES) in N methyl-2-pyrrolidone (NMP) solution was 50 wt%. Typically, 9 g of zeolite powder and 5 g of PES were dissolved in 11 ml NMP doped solution. Thus, weight ratio of PES to NMP is 1:2.333 and zeolite powder content was 50 wt % in PES in NMP solution. Then, the mixture was continuously stirred with constant speed at 50 ºC to prepare the blending solution. Blending solution containing zeolite powder was extruded through a spinneret at 3 ml/min using a high-pressure gear pump (GP Driving Unit CDS-18G-0.8; Kyowa Fine Tech. Co. Ltd). The extruded spinning solution was introduced into a water bath located at a distance of 10 cm below the nozzle. Then, the extruded spinning solution was coagulated at the room temperature in water to form zeolite fibers due to phase-transition. In the phase-transition condition, the PES and zeolites of the doped solution were both coagulated simultaneously in the water. However, NMP is not coagulated. They were kept underwater to remove the solvent from the resultant fiber. Finally, fibers were treated with excess hot water at 90 °C three times to eliminate the remaining NMP and they were stored in a wet condition at the room temperature until they are used.

Time dependence adsorption test

Time dependence adsorption test was performed in order to identify the possible rapidness of MB by adsorbents and to obtain the optimum time for complete removal of the dye (Fig. 1). Amount of 0.1 g of zeolite powders and fibers are added in 50 ml of MB solution having a concentration of 5 ppm in a rotary shaker operated at 200 rpm for 0.5, 1, 2, 3, 4, 5, 6, 7, 8, 9, 10, 11, 12, 24, 36, 48 and 60 h at the room temperature (27 °C) .Then, the solution was filtered by using the Smith filter paper (110 mm) for the filtration of the adsorbent from the aqueous solution.

Concentration dependence adsorption test

Concentration dependence adsorption test was investigated for different concentration of MB (Fig. 2). 0.1 g of dosage were added in 50 ml of MB solution having different concentration of (1, 5, 10, 20, 30, 40 and 50 ppm) in a rotary shaker operated at 200 rpm for zeolite powders (10 h) and composite fibers (48 h).Then, the solution was filtered by using the Smith filter paper (110 mm) for the filtration of the adsorbent from the aqueous solution. The final concentration of above two adsorption tests was determined by an UV-Vis spectrometer. The removal percentage and adsorption amount q_e of MB were calculated using the following equations.

$$\mathrm{Removal\%} = \frac{C_i - C_e}{C_i} \times 100 \tag{1}$$

$$q_e = \frac{(C_i - C_e)V}{m} \tag{2}$$

where

C_i = initial concentration (mg/L or ppm)

C_e = equilibrium concentrations (mg/L or ppm)

q_e = equilibrium adsorption amount of MB (mg/g)

m = mass of adsorbents (mg)

V = volume of the solution (ml)

Characterization of Adsorbents

The characterization tools such as Fourier transform infrared (FT-IR) 8400 Shimadzu spectrophotometer within the wave number from 4000 cm^{-1} to 650 cm^{-1}, X-ray diffraction (XRD) RIGAKU-RINT 2000 and scanning electron microscope (SEM) JEOL-JSM 5300 LV were performed in order to identify the functional group, study the crystal structure and investigate the microstructure of zeolite adsorbents.

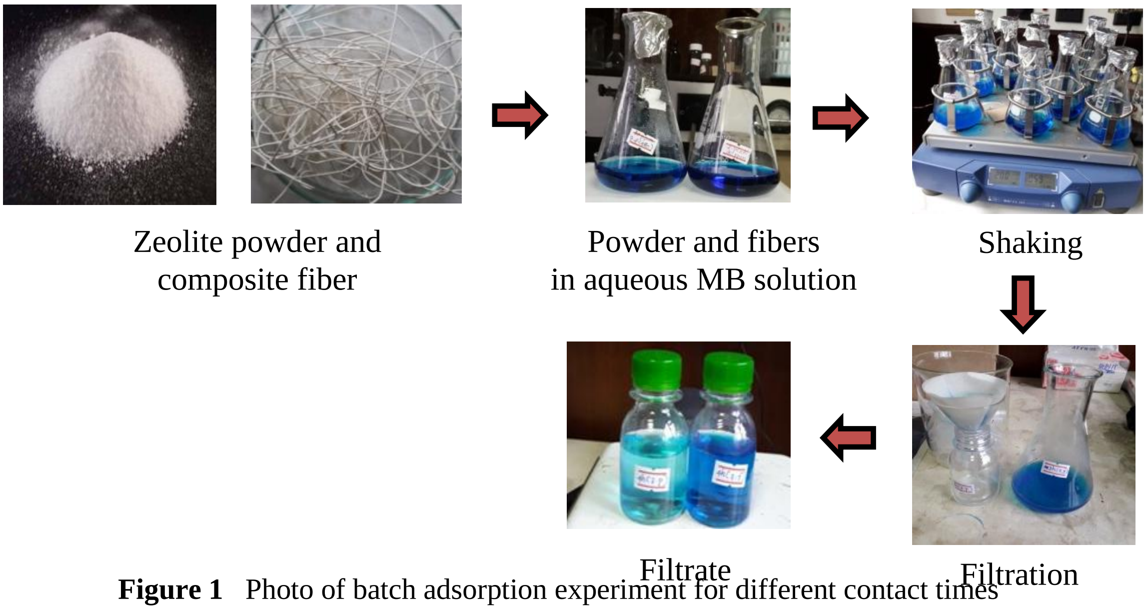

Figure 1 Photo of batch adsorption experiment for different contact times

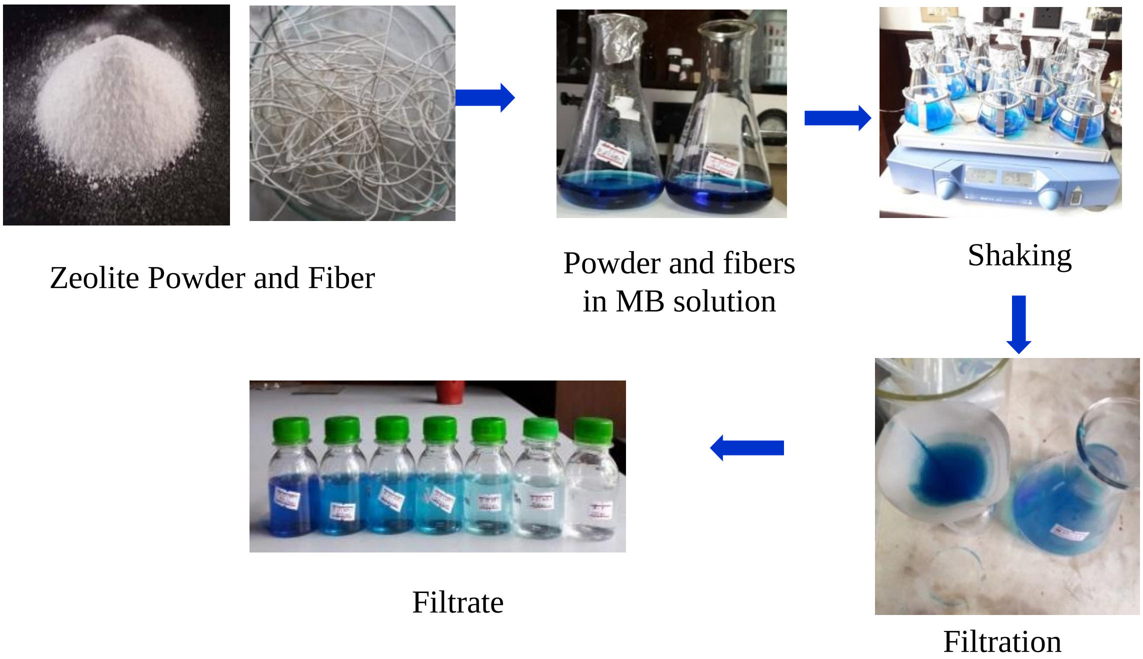

Figure 2 Photo of batch adsorption experiment for different initial concentrations

Results and Discussion

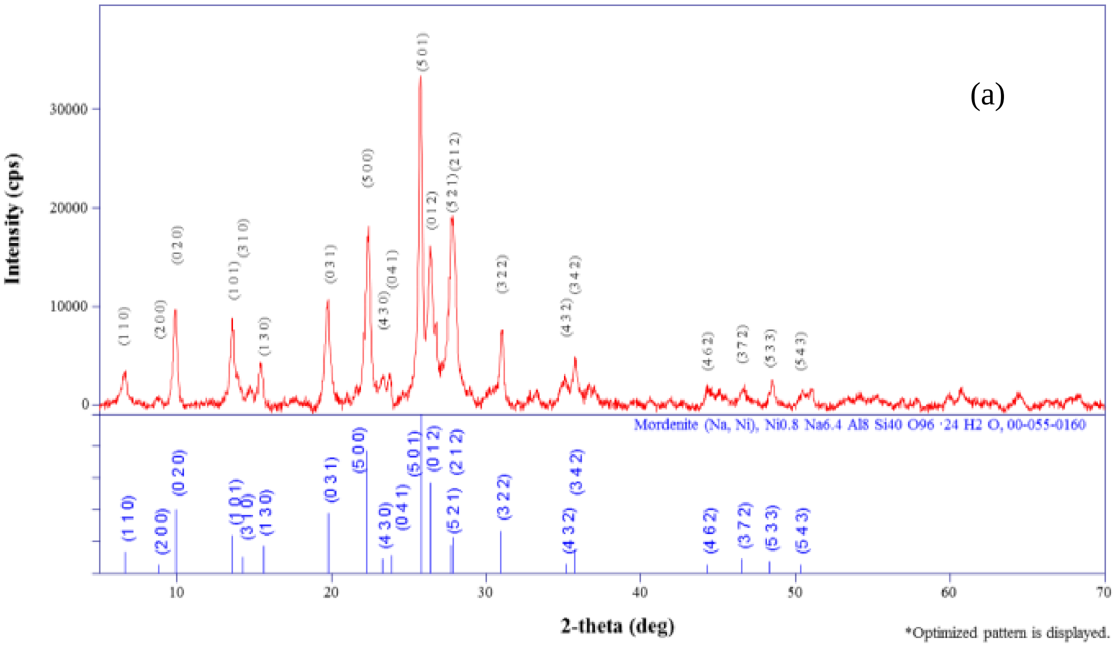

Figure 3(a) XRD spectrum of zeolite powder

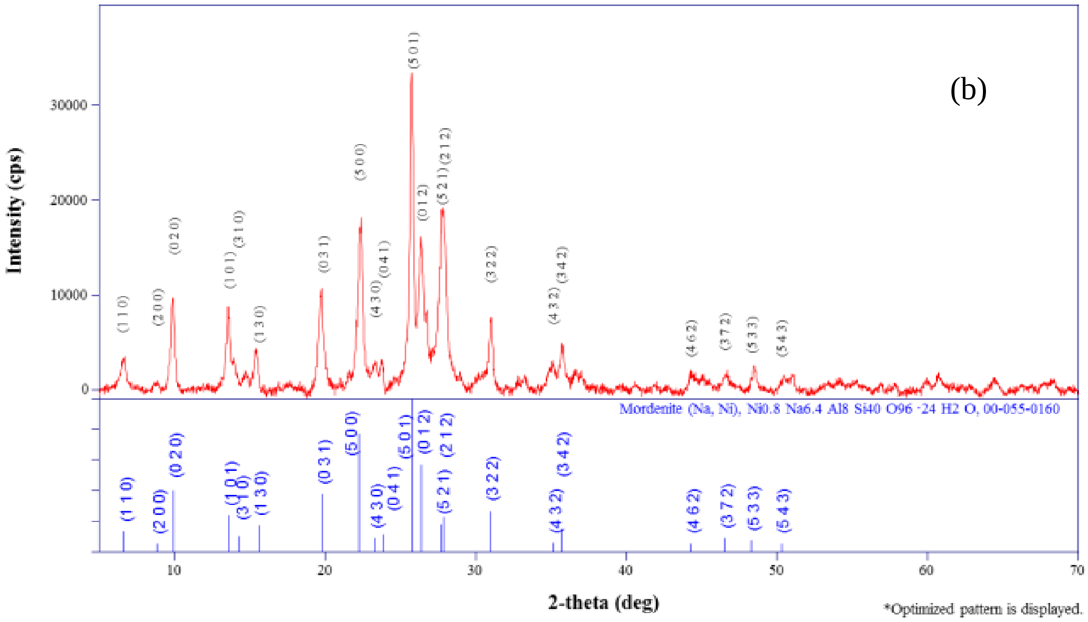

Figure 3(b) XRD spectrum of zeolite composite fiber

XRD spectrum of powder and fiber are presented in Fig.3 (a) and (b). According to the standard library file, the sharp crystalline peaks for both mordenite zeolite and the composite fibers were observed. No shift peak between the mordenite zeolite and the composite fibers was also occurred. It implies that the zeolite did not affect any changes in the crystalline structure of composite fibers.

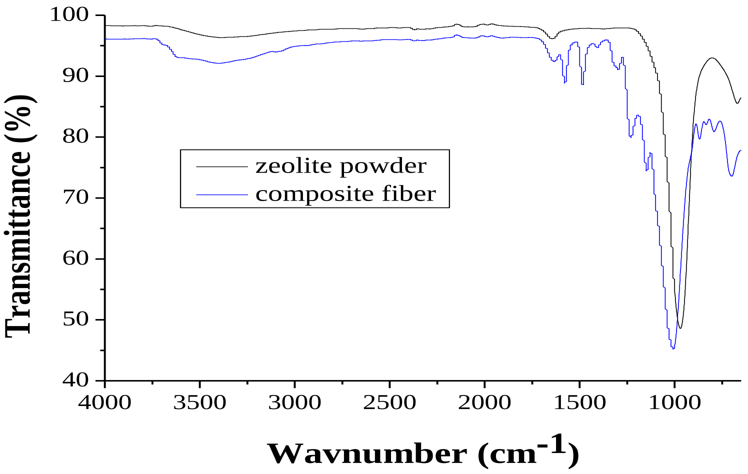

Figure 4 FT-IR spectra of zeolite powder and the composite fiber

Fig.4 shows the FT-IR spectra of zeolite powder and the composite fibers. The broad peaks at 3400 cm^{-1} in the spectra of both samples were attributed to O-H stretching vibration. For the composite fibers, the bands appeared at 1580 and 1490 cm^{-1} were assigned to the C=C stretching vibration. The peaks at 1630 and 1640 cm^{-1} in powder and fiber were due to O-H bending vibration. The peaks from 1150 to 1240 cm^{-1} were attributed to >S (=O)$_2$ stretching vibration. The intense broad peaks of Si-O and Al-O stretching vibration were observed at 1010 cm^{-1} in the zeolite fiber and at 968 cm^{-1} for composite fiber. Symmetric T-O-T vibrations (T=Si, Al) were found at the peaks 697 and 789 cm^{-1} of composite fibers [Moustafa et al, (2012)].

Fig. 5(a) is SEM micrograph of zeolite fiber with porous structure before the treatment of adsorption. In this figure, the zeolite powders were well distributed in the PES network with a sponge structure of the composite fibers. However, the pores in these fibers after the treatment of adsorption were closer than before adsorption as shown in Fig. 5(b). It implies that MB was well adsorbed by fibers. As the result, dye was successfully removed from the aqueous solution by fibers.

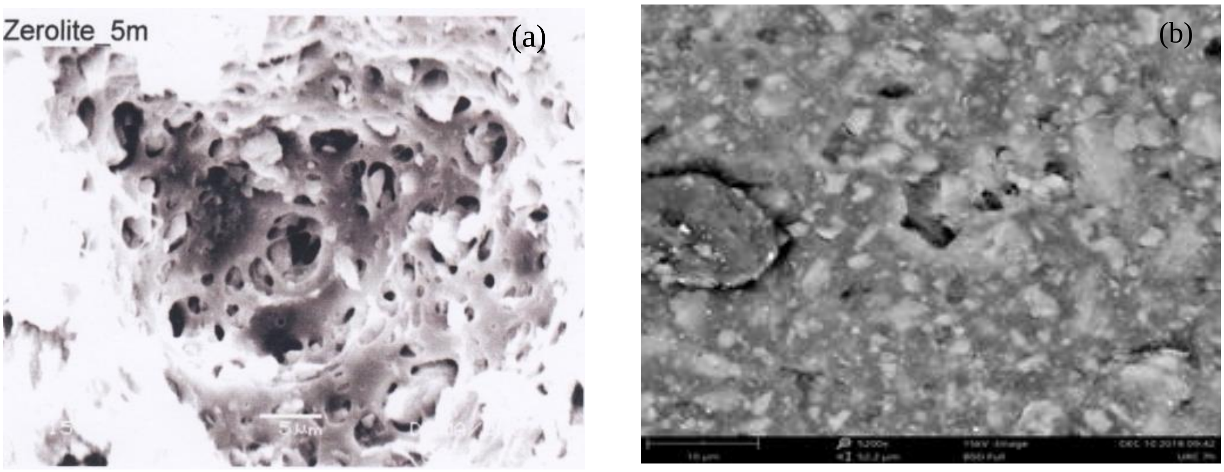

Figure 5. SEM images of zeolite composite fiber (a) before and (b) after adsorption process

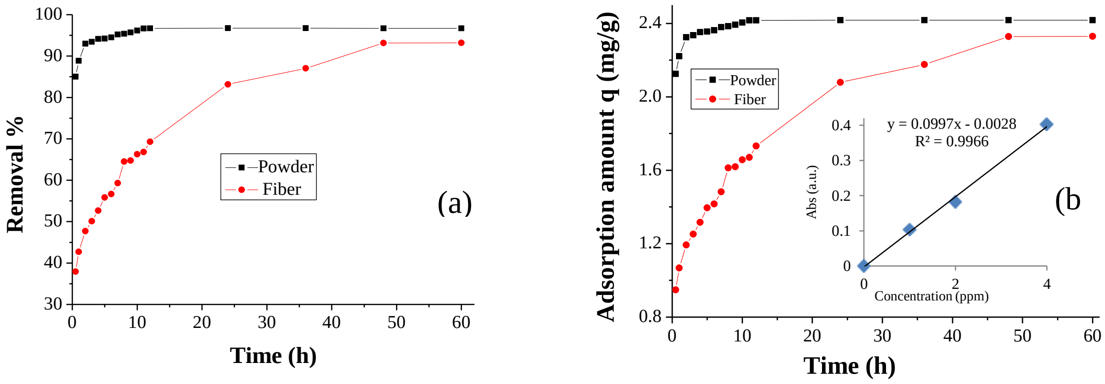

Figure 6(a) Graph showing the removal % and **(b)** adsorption amount of MB depending on different contact time (C_i=5 ppm). Inset shows calibration curve for this adsorption test.

Contact time dependence adsorption test was performed in order to study the effect of contact time on the adsorption behavior of MB by adsorbents. Fig. 6(a) shows the graph of removal percent depending on different contact time for zeolite powder and fiber on MB. The adsorption of MB to the zeolite powders was drastically increased until the contact time 10 h and then it became saturation. On the other hand, the adsorption of MB to the composite fibers were gradually increased and saturated at the contact time 48 h. As a result, zeolite powder and fiber could remove MB over 90 % for initial concentration 5 ppm of MB and dosage amount of adsorbent 0.1 g. Fig. 6(b) represents the equilibrium adsorption amount (q_e) of MB depending on different contact times of adsorption for both adsorbents. The equilibrium adsorption amounts were found out to be 2.41 mg/g and 2.33 mg/g after contact time 10 h for powder and 48 h for fiber. Thus, zeolite powder has faster adsorption capacity than fiber for C_i 5ppm of MB.

Concentration dependence adsorption experiment was carried out in order to investigate the effect of C_i on the adsorption properties of MB by both adsorbents. In this test, the experimental parameters including amount of dosage 0.1 g, volume of solution 50 ml and contact time 10 h for powder and 48 h for fibers were fixed. However, concentration of MB was varied from 1 to 50 ppm. The results were shown in Fig. 7. It was found out that adsorption capacity were dependent on concentration of MB. At low concentration of MB, the removal percent for both adsorbents were almost the same as shown in Fig. 7(a). However, a gradually decreasing in removal efficiency with increasing C_i of MB was occurred. In addition, it is remarkabe to note that powder is more effective than fibers for the removal of MB at higher concentration.

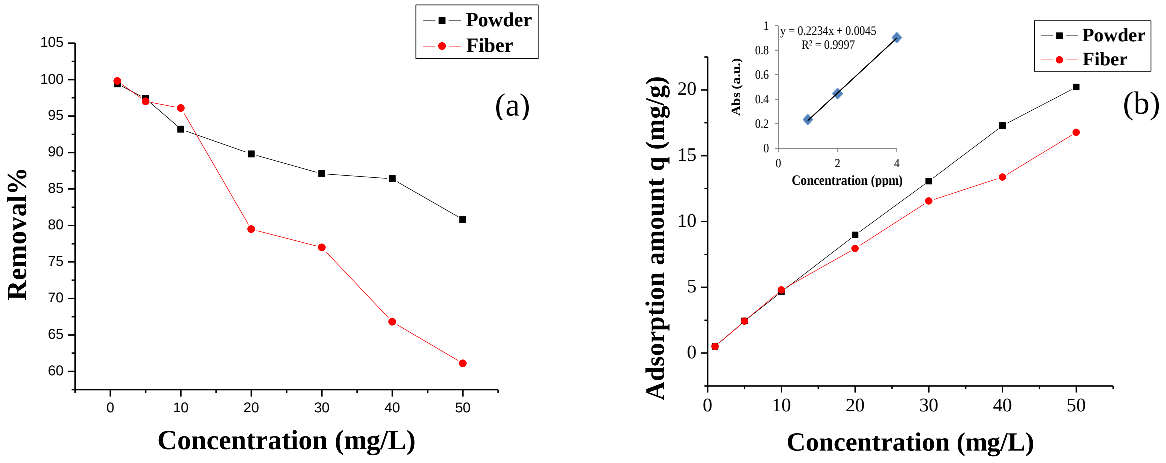

Figure 7 (a) Graph showing the removal % and **(b)** adsorption amount of MB depending on different initial concentrations Inset shows calibration curve for this adsorption test.

The adsorption amount q_e depending on different values of C_i have been conducted in order to investigate the equilibrium adsorption mechanism of dyes on adsorbents. Fig.7(b) illustrates the equilibrium adsorption amount (q_e) with different initial concentrations. Adsorption amount of MB by the powders and composite fibers were gradually increased until contact time was 10 h and 48 h. The adsorption isotherm based on experimental results has been determined. According to results, experimental adsorption isotherms of MB were well agreed with the *Langmuir* adsorption isotherm as shown in Fig.8.

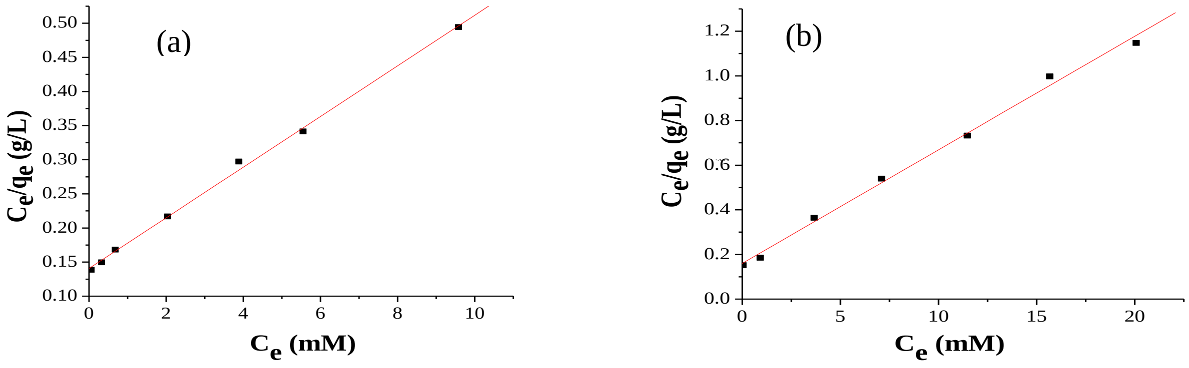

Figure 8. *Langmuir* isotherm plot for zeolite powder (a) and (b) composite fibers.

Conclusions

The adsorption behavior of MB on the adsorbents, zeolite powder and zeolite composite fibers, was investigated by doing the batch adsorption experiments. The effects of contact time and initial concentration were investigated. The contact time was firstly determined at the fixed experimental parameters including the amount of dosage 0.1 g, initial concentration 5 ppm and volume 50 ml of MB solution in order to obtain the optimum contact time for adsorption capacity. The maximum removal 96 % for powder and 91 % for fibers were obtained during the contact time 10 h and 48 h respectively. Secondly, the effect of initial concentration on adsorption behavior at the optimum contact times was studied. Both adsorbents can remove over 90 % at low concentration, 1, 5 and 10 ppm. Therefore, zeolite powder and composite fiber were effective and efficient adsorptivity for the removal of MB at low concentration. The adsorption isotherm of MB was well fitted into *Langmuir* isotherm model. Thus, zeolite based adsorbents can be applied to remove the organic pollutants.

Acknowledgements

I am greatly indebted to Dr Khin Khin Win, Professor and Head of Department of Physics, University of Yangon for her kind permission to carry out this research work. I am sincerely grateful to Dr Ye Chan, Professor, Universities' Research Center (URC), for his encouragement and permission to carry out research at URC and supporting of research facilities. I am deeply thankful to my supervisor Dr Hla Toe, Associate Professor, Department of Physics, University of Yangon, for his valuable advice. I do specially thank you to my co-supervisor, Dr Cho Cho Thet, Associate Professor, Department of Physics, Myeik University, for her valuable comments and suggestions.

References

Ahmad Badeenezhad, Abooalfazl Azhdarpoor, Shima Bahrami and Saeed Yousefinejad, (2019)"Removal of methylene blue dye from aqueous solutions by natural clinoptilolite and clinoptilolite modified by iron oxide nanoparticles, molecular simulation," VOL. 45, NO. 7, 564–571.

Masaru Ohshiroa,b, Kohtaroh Nakamotoa, Takaomi Kobayashia, (2017) "Mordenite zeolite- Polyethersulfone composite fibers developed for decontamination of heavy metal ions," Journal of Environmental Chemical Engineering 5, 513–525.

Melkon Tatlier***a*** , Çiğdem Atalay-Oral***a*** ***, (***2016) "Crystallization of Zeolite A Coatings from Natural Zeolite," *Materials* Research. 19(6), 1469-1477.

Mohamed A. Hassaan, Ahmed El Nemr. (2017) "Health and Environmental Impacts of Dyes: Mini Review," American Journal of Environmental Science and Engineering, Vol. 1, No. 3, pp 64-67.

Moustafa E. Moustafa, Ehab A. Abdelrahman, Hisham M. Aly, (2012) "Synthesis of mordenite zeolite in absence of organic template," Advanced Powder Technology 23, 757–760.

N. O. Omisanya, C.O. Folayan, S.Y. Aku and S.S. Adefila, (2012) "Synthesis and characterization of zeolite for adsorption refrigeration application," Pelagia Research Library, Advances in Applied Science Research, 3 (6):3746-3754.

Shikha Sharma, Deepak Pathania, Pardeep Singh,(2017)"Removal of methyleneblue by adsorption onto activated carbon developed from Ficus carica bast," Arabian Journal of Chemistry 10, S1445-S1451.

U. Wingenfelder, C. Hansen, G. Furrer, R. Schulin, (2005) "Removal of heavy metals from mine waters by natural zeolites," Environ. Sci. Technol. 39, 4606–4613.

J. Myanmar Acad. Arts Sci. 2020 **Vol. XVIII.No.2C**

AUTOMATIC ANTIBACTERIAL CLOTHES DRYER SYSTEM UTILIZING ULTRAVIOLET (UV) LAMP

Khin Mar Win[1], Tun Soe[1] & Nan Thazin[2]

Abstract

The antibacterial clothes dryer system is designed and constructed for killing the bacteria which make the bad smell in clothes. The system contains the clothes holder attached with motor dryer and ultraviolet (UV) lamp with a keypad lock. It is also designed to control the bacterial killing time and drying time of the wet clothes. The hardware of the lock system is designed and simulated by the Proteus 8.6 software and it is constructed by using PIC16F887 microcontroller, an 8 MHz crystal oscillator, 4×4 keypad, 16×2 LCD module, ultraviolet (UV) antibacterial Lamp, piezo sounder, relay, some active and passive components. The firmware for the lock system is written by Mikro Basic Pro programming language. The system permits to operate the UV antibacterial lamp for twenty minutes and motor dryer for thirty minutes as the instruction of the controlled program as soon as the keypad lock is unlocked. The presence of bacteria in clothes is observed by EC-1001-P-HLED Eco Blue microscope. The observation results show the antibacterial process in clothes is very effective by using ZW30S19W UV lamp.

Keywords: PIC16F887, 8 MHz crystal oscillator, Ultraviolet (UV) antibacterial Lamp, 16×2 LCD, Mikro Basic Pro programming language

Introduction

A clothes dryer is a well known appliance intended to be dried the clothes. The internal temperature of the clothes dryer is above the room temperature and it dries the wet clothes in a short time interval. Ultraviolet (UV) light has been known, to kill the bacteria by destroying some of the bacterial organisms. UV light is electromagnetic radiation with a wavelength shorter than that of visible light, but longer than X-rays, in the range 10 nm to 400 nm, and energies from 3 eV to 124 eV. A UV lamp is a source of germicidal ultraviolet radiation. A cylindrical instant start UV lamp emitting a wavelength of 253.7 nm is considered suitable for use in the present research work. Although literature on UVC damage is scarce since it is relatively benign in the natural form, it is the most dangerous form industrially. It can cause damage to eyes in as little as 3 seconds and DNA damage to all biological surfaces. The UV light created by human is very dangerous when it directly deposits on the eye or skin, especially child. The most common injuries of UVC are corneal burns and erythema or severe skin burns and excessive exposure to UVC causes skin cancers as UVA and UVB. Chronic exposures to acute intense UVC can lead to cataract formation and retinal damage [Mofidi, A. A. (2001)]. The UV hazards are listed in Table (1).

UV light is preferably housed within an impact resistant housing which includes a UV reflecting surface that functions to protect the light and to direct the UV light generally downward, e.g. to cast the light outside the cabinet [Katara G. (2008)]. By providing UV lamp to be full and complete distribution of UV light throughout the clothes dryer makes the efficient bacteria killing process. There is also a control system which controls the specified period of the illumination of the UV light and automatically turn off the function of the system. The system is used in killing bacteria in clothes that make the bad smell in clothes. The basic idea of

---

[1] Dr, Associate Professor, Department of Engineering Physics, Mandalay Technological University

[2] Dr, Professor, Department of Engineering Physics, Mandalay Technological University

microcontroller is to collect all the input and output peripheral in one single circuit and it is suitable for this research work. The system design is to construct a clothes dryer with antibacterial system and to kill the bacteria from clothes with ultraviolet (UV) antibacterial lamp. The block diagram of the automatic antibacterial clothes dryer system is as shown in Figure (1).

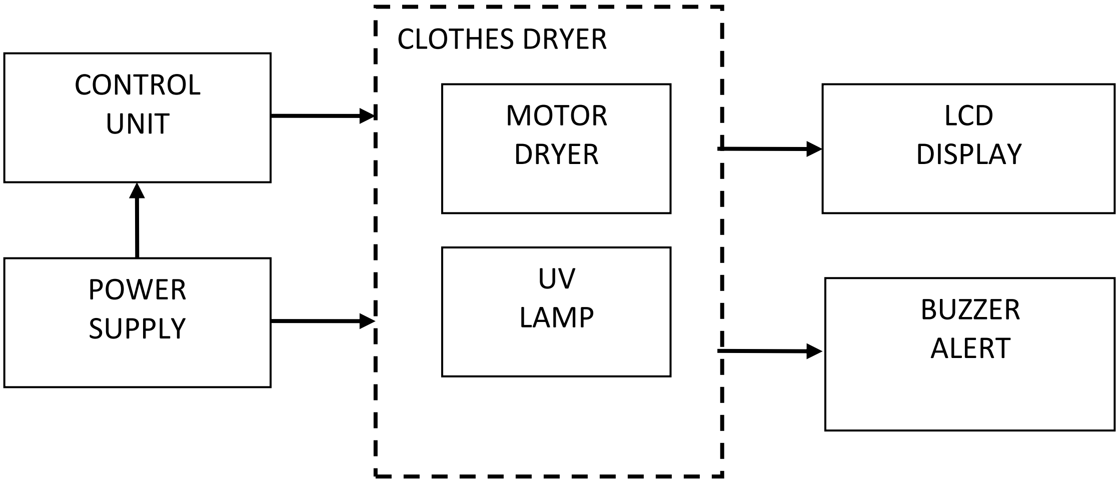

Figure 1 Block diagram of automatic antibacterial clothes dryer system

Table 1 UV hazards

Band	Wavelength	Primary Visual Hazard	Other Visual Hazards	Other Hazards
UV-A	315-400nm	cataracts of lens	skin cancer, retinal burns	
UV-B	280-315nm	corneal injuries	cataracts of lens, photokeratitis	erythema, skin cancer
UV-C	100-280nm	corneal injuries	photokeratitis	erythema, skin cancer

Materials and Method

UVC lamp

Mercury UVC devices use low-pressure mercury gas bulbs that primarily emit a strong narrow band of the UVC spectrum at 253.7 nm. The UVC lamp can be applied in disinfection kitchen cabinet, microwave oven and air condition etc. They are also used in hospital, school, hotel, home and office to disinfect. In this research work, ZW30S19W UV lamp is used according to the technical parameters as shown in Table (2). The photograph of the ZW30S19W UV lamp is as shown in Figure (2) and it is made up of pure quart glass materials filled with mercury.

Table 2 Technical parameters of ZW30S19W UV lamp

Parameters	**Specifications**	**Parameters**	**Specifications**
Diameter	19 mm	Power	30 W
Length	894.6 mm	UV intensity	107 μW/cm^2
Voltage	129 V	Wavelength	253.7 nm
Current	300 mA	Life span	8000 h

Ultraviolet Disinfection Testing

Antibacterial agents inhibit the growth of bacteria and may rapidly kill them by disrupting one or more of their essential cellular functions. Depending on the type of antibacterial agent, the mechanism of activity may result in: inhibition of the production of proteins or cell wall materials, inhibition of DNA replication, and disruption of cell membrane activities that maintain chemical balance. In bacteria killing process, the UV light penetrates the cell walls of bacteria, virus and protozoa as shown in Figure (3). The UV energy permanently alters the DNA of the microorganism. Microorganisms are inactivated and unable to reproduce or infect after depositing the UV light.

Design and Construction of the System

The constructed keypad based secure ultraviolet (UV) antibacterial lamp system comprises the control unit, the input unlock unit, and the ultraviolet (UV) antibacterial lamp unit including clothes holder with UV reflection system. The clothes dryer holder is designed to make cabinet based on foldable metal frame and the waterproof cloth in dimension (90×48×48) cubic centimeter. The inner waterproof walls are covered with silvery UV reflecting clothes with the purpose of reflecting the UV light inside the cabinet. The photograph of the constructed antibacterial clothes dryer is as shown in Figure (4).

The UV light created by human is very dangerous when it directly deposits on the eye or skin, especially child. Because of this fact, it needs to operate by an authorized person who can handle it safely. Only this authorized person know the input password of this system can prevent the unnecessary danger from harmful UV light. The controlled circuit connection of PIC16F887 microcontroller is tabulated in Table (3).

Table 3 Controlled circuit connection of PIC16F887 microcontroller

PIC16F887	**Controlled Circuit**	**PIC16F887**	**Controlled Circuit**
pin#1($\overline{MCLR}$)	LCD VDD	pin#27(RD4)	Keypad R0
pin#8 (RE0)	speaker	pin#28(RD5)	Keypad R1
pin#19 (RD0)	Keypad C0	pin#29 (RD6)	Keypad R2
pin#20 (RD1)	Keypad C1	pin#30 (RD7)	Keypad R4
pin#21 (RD2)	Keypad C2	pin#33 (RB0)	LCD D4
pin#22 (RD3)	Keypad C3	pin#34(RB1)	LCD D5
pin#25 (RC6)	Motor dryer	pin#35(RB2)	LCD D6
pin#26 (RA7)	UV lamp	pin#36(RB3)	LCD D7
pin#12, 31 (VSS)	Ground	pin#37(RB4)	LCD RS
pin#11,32 (VDD)	Power	pin#38(RB5)	LCD EN

The Operation of the Lock Circuit

The hardware of the lock circuit operates according to the instruction sets of the controlled program. The program starts with blinking "Hello!" word three times and asking for “Enter Password". Enter the password and press "OK" key. If the user can enter correct password, the Green LED will ON and LCD will display "Correct". If the entered password is incorrect, LCD will display “Incorrect..." "Try Again" and the Red LED will ON.

User can press "Undo" key to delete the entered error key. If password is correct, LCD will show Port pins in first row as 1 2 3 4 5 6 7 8 and in second row as 0 0 0 0 0 0 0 0. The user can press any key if he wants to open and/or close. The password is 12345678. If the entered password is wrong 3 times, and then the alarm will activate. The printed circuit design for antibacterial clothes dryer is as shown in Figure (5). The simulation screen capture and the lock circuit are shown in Figure (6). The program flow is as shown in Figure (7).

Discussion

The American Conference of Governmental Industrial Hygienists (ACGIH) recommended exposure limits 1.0 J/cm^2 for periods lasting less than 1000 seconds, and 1.0 mW/cm^2 for periods lasting greater than 1000 seconds. For UVC, threshold limit values are 250 mJ/cm^2 at 180 nm and 3.1 mJ/cm^2 at 275 nm. At certain wavelengths, UV is mutagenic to bacteria, viruses and other microorganisms. Particularly at wavelengths around 260-270 nm, UV breaks molecular bonds within microorganism DNA, producing thymine dimers that can kill or disable the organisms.

Mercury-based lamp, ZW30S19W emits UV light at the 253.7 nm line and we choose it for antibacterial agent. The design and implementation of Ultraviolet (UV) antibacterial lamp control system is presented practically with photos and demonstration circuit. The circuit can provide effective bacteria killing system for the clothes by using ZW30S19W UV antibacterial lamp. The disinfection process on napkin by ZW30S19W UV lamp for twenty minutes (1200 seconds) is as shown in Figure (7). The results are observed by Eco Blue microscope (EC-1001-P-HLED) of set up arrangement with (1000×) magnification as shown in Figure (8). According to the observation and results as shown in Figure 9 (a-d), it is found that the constructed UV antibacterial system is very effective in killing bacteria.

The UVC is dangerous for skin so that all exposed skin should be covered with opaque material including face, neck, head, hands, and arms when the system is operate. It is difficult to do so, to overcome this difficulty, the UV lamp is installed in a fully covered or envelope cabinet. The inner walls of the cabinet are designed by UV reflecting surfaces. The application of UVC in this research work follows the UVC guidelines and information for the safe use of Ultraviolet Radiation.

Conclusion

The purpose of this research work is just want to kill the bacteria in clothes and don’t want to get any harmful effect. But the ultraviolet light, UVC is danger for human when it exposed to eye and skin. The constructed system is designed that the UV light is not allowed to reach the outside of clothes holder and it can just reflect inside the clothes holder. The clothes holder is foldable and it contains a heater beneath floor. It takes thirty minutes to dry the wet clothes and twenty minutes (1200 seconds) to kill the bacteria inside the clothes holder.

Therefore, the time to dry the clothes is sufficient time to kill the bacteria in clothes. The clothes holder has three clothes hangers in it and it can kill bacteria in three clothes simultaneously. This clothes holder can operate only by the use of correct password to open the lock switch. Thus it can be used effectively and safely.

Future Work

The observation and analysis of the presence of the bacteria, viruses, dust mites, fungus, mold and other pathogens in clothes will carry on by the use of scanning electron microscope for more detailed purpose.

Acknowledgements

The authors would like to acknowledge Professor Dr Khin Khin Win, Head of Department of Physics, University of Yangon, for her kind permission to carry out this work. The authors also would like to be thankful to Sayargyi U Shwe Than, Principal Scientist (Rtd), Department of Atomic Energy, Ministry of Science and Technology for his valuable suggestions and introduction to programming language.

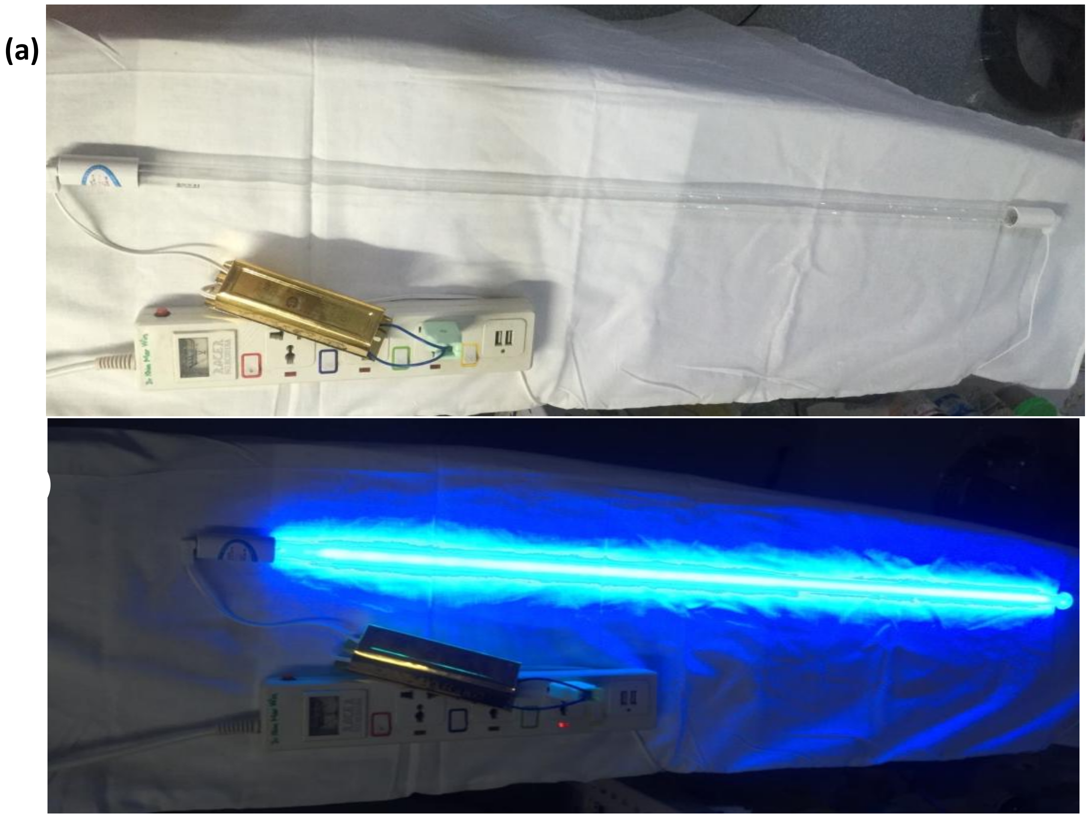

Figure 2 Photograph of the ZW30S19W UV lamp (a) testing circuit connection (b) emitting UV radiation in 253.7 nm wavelength and 107 µW/cm^2 intensity

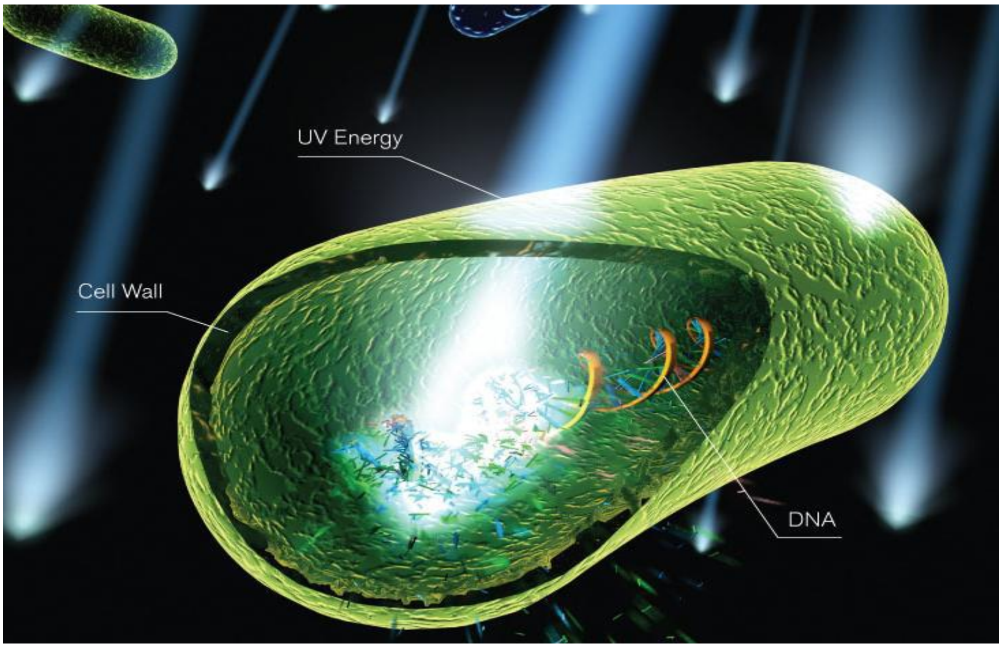

Figure 3: The UV light penetrates the cell walls of bacteria and breaks molecular bonds within microorganism DNA [www.trojanuv.com]

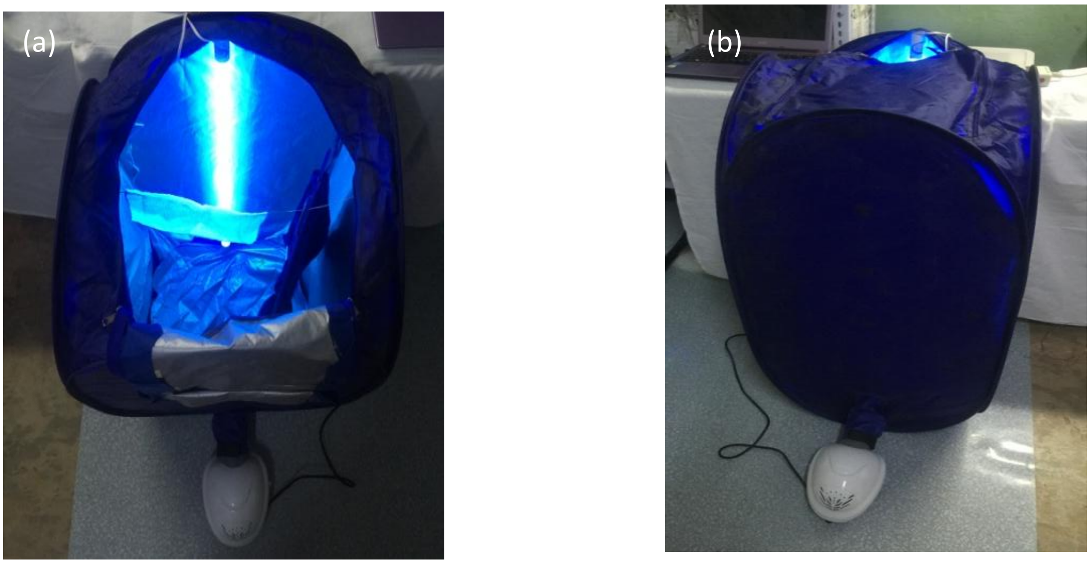

Figure 4 Photograph of (a) inner view and (b) outer view of antibacterial clothes dryer

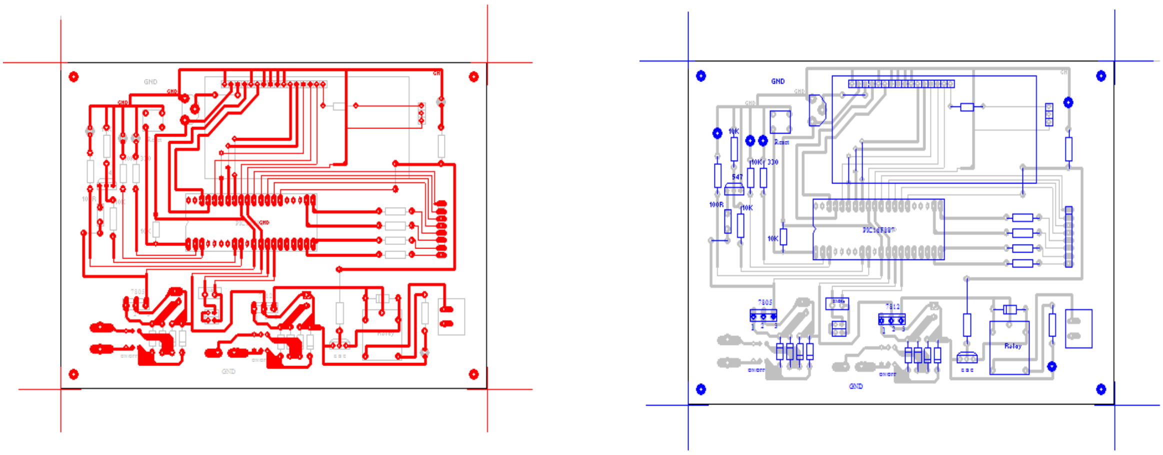

Figure 5 Printed circuit design of (a) soldering side view (b) component side view of the control lock for antibacterial clothes dryer

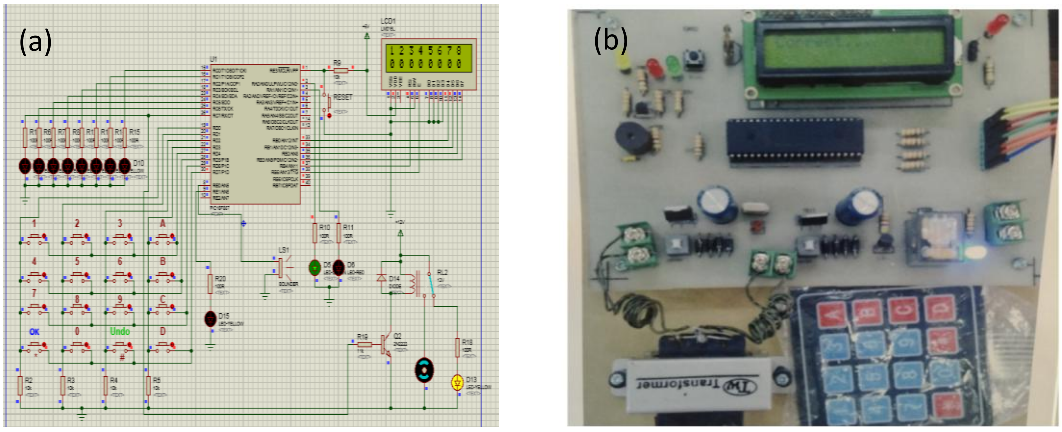

Figure 6 Antibacterial clothes dryer system (a) simulation screen capture and (b) control lock circuit

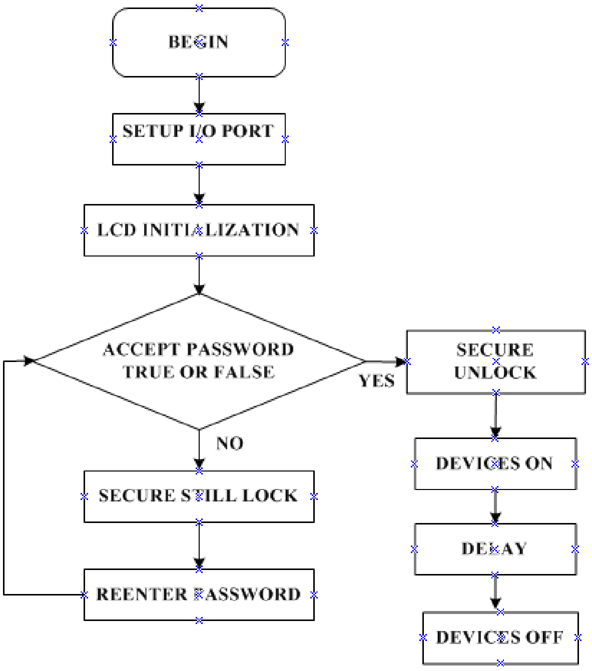

Figure 7 Flowchart diagram of the source code

Figure 8 Disinfection process on napkin by ZW30S19W UV lamp for twenty minutes (1200 seconds)

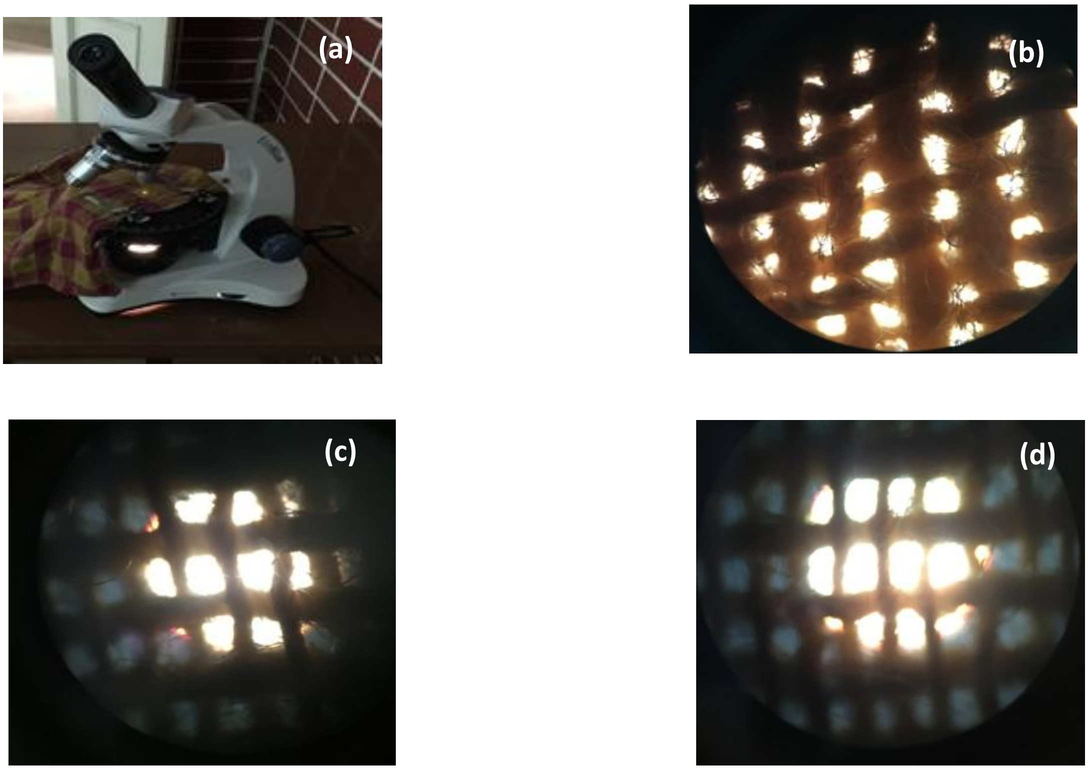

Figure 9: (a) Observation on presence of bacteria (mite dust) under EC-1001-P-HLED Eco Blue microscope (b) on dirty napkin fabric before wash (c) on clean napkin fabric after wash (d) after 1200 seconds disinfection process by ZW30S19W UV lamp

References

Diarah, R. S., C. O. Osueke, & D. Egbune. (Jan. 2014), “Microcontroller Based Code Locking System with Alarm.” *Journal of Electrical and Electronics Engineering,* Vol. 9, pp.09-17

Katara G., N. Hemvani, S. Chitnis, V. Chitnis & D. S. Chitnis. (2008). “Surface Disinfection by Exposure to Germicidal UV Light.” *Indian Journal of Medical Microbiology*, 26 (3): pp.241-242

Mofidi, A. A., H. Baribeau, P. A. Rochelle, R. Deleon, B. M. Coffey, & J. F. Green. (2001) “Disinfection of Cryptosporidium Parvum with Polychromatic UV Light”. *Journel of AWWA,* 93:6:95.

Morowitz, H. J. (1950) “Absorption Effects in Volume Irradiation of Microorganisms”. Science, 111:229

J. Myanmar Acad. Arts Sci. 2020 **Vol. XVIII.No.2C**

RADON MEASUREMENTS OF WATER SAMPLES AT SOME LAKES FROM MANDALAY REGION

Tun Soe[1], Khin Mar Win[1] & Nan Thazin[2]

Abstract

The aim of the present work is to carry out the radon concentration of water at some lakes from Mandalay Region and annual dose received by the people. Water samples from Sedawgyi, moat of Mandalay, Kandawgyi and Taungthamann were collected. Radon level in raw water (40 mL) was measured with RAD7 continuous radon monitor. By verification of the results, it can be checked out whether the WHO recommended permissible level (100 pCi/L) was exceeded or not. Mean radon concentration of the water samples are 10.6 pCi/L, 16.0 pCi/L, 10.7 pCi/L, 8.0 pCi/L and do not exceed the safe limit level. However, continuous monitoring of radon concentration is basic description of public water safety.

Keywords: Radon, RAD 7, water at some lakes, Mandalay region

Introduction

Nowadays, radon concentration has been interested for radiological safely because of radon is a radioactive gas for which both ingestion and inhalation present health risks, therefore radon in air and water has become a public health concern. Radon is produced continuously in soil, rocks and water source through alpha decay of Uranium, Thorium and Actinium series and Radium. Radon and its progenies emit alpha particles –USEPA Report (2003). RAD7 was designed to detect alpha particle only, so we will emphasize alpha radiation. Environmental Protection Agency (USEPA) established a voluntary program to promote radon awareness, testing and reduction and has warns the public that any radon has some risk of causing lung cancer therefore should always try to reduce the radon level in water and air – USEPA Report (2017). The recorded values of radon concentration in water are within the safe limit of 300pCi/L or 11.1 Bq/L (US Environmental Protection Agency) and 100pCi/L or 3.7Bq/L (WHO) were recommended –USEPA Report (1999). Many studies have been done to measure radon in water from different places around the world due to radon health hazard. They were showed the other samples more than the EPA recommended safe limit of 300pCi/L or 11.1Bq/L. Radiological health hazards associated with natural radionuclide and their progenies due to the consumption of water. Safe and effective ways to reduce radon content in water is needed for public water safety as any radon has some risk of causing lung cancer and stomach cancer. Radon content in public using lakes water has not been tested in Mandalay region yet. This experimental study was to determine the natural radon content in public lakes water from Mandalay region and then to compare the Radon concentration level in lake water at recommended safe limits.

RAD7 Radon Detector

Every nucleus of radon-222 eventually decays through the sequence polonium-218, lead-214, bismuth-214, polonium-214, and lead-210. With each transformation along this path the nucleus emits characteristic radiation: alpha particles, beta particles, or gamma rays, or combinations of these – Gruber, Maringer, & Landstetter (2009). The RAD7 was designed to

---

[1] Dr, Associate Professor, Department of Engineering Physics, Mandalay Technological University

[2] Dr, Professor, Department of Engineering Physics, Mandalay Technological University

detect alpha particles only, so we will emphasize alpha radiation.Radon-222 is an inert gaseous alpha-emitter that does not stick to or react with any materials. It has a half-life of 3.82 days. A particular radon nucleus may decay at any time, but it is most likely to decay between now and 8 days (two half-lives) from now –K.Badham, R.Mehra & R.G.Sonkawade (2010). There are several types of continuous radon monitors on the market. Nearly all of these are designed to detect alpha radiation, but not beta or gamma radiation. Why? Because it is very difficult to build a portable detector of beta or gamma radiation that has both low background and high sensitivity. Three types of alpha particle detectors are presently used in electronic radon monitors: 1. Scintillation cells or "Lucas cells" 2. Ion chambers 3. Solids state alpha detectors. Each of these types has advantages and disadvantages relative to the others. All of these types can be used for low background alpha particle counting. The DURRIDGE RAD7 uses a solid state alpha detector. A solid state detector is a semiconductor material (usually silicon) that converts alpha radiation directly to an electrical signal. One important advantage of solid state devices is ruggedness. Another advantage is the ability to electronically determine the energy of each alpha particle. This makes it possible to tell exactly which isotope (polonium-218, polonium-214, etc) produced the radiation, so that you can immediately distinguish old radon from new radon, radon from thoron , and signal from noise. This technique, known as alpha spectrometry, is a tremendous advantage in sniffing, or grab-sampling, applications. Very few instruments other than the RAD7 are able to do this - DURRIDGE (2015). A distinction should be made between true, real-time continuous monitors, and other instruments and devices. With a continuous monitor, you are able to observe the variation of radon level during the period of the measurement. This can sometimes show big swings in radon concentration and may allow you to infer the presence of process influencing the level. For good data, it is important that there be sufficient counts to provide statistically precise readings. Devices which give just a single, average reading, or whose precision is inadequate except after a long measurement time are not, in this sense, continuous monitors. Another important parameter is background. This is the reading given by the instrument when there is no radon in the air sample. For low level continuous monitoring, it is necessary that the background be extremely low and stable. Because of the high quality alpha detector, and unique real-time spectral analysis, the RAD7 background is vanishingly small, and is immune to the build-up of lead-210, which plagues other instruments – DURRIDGE (2012).

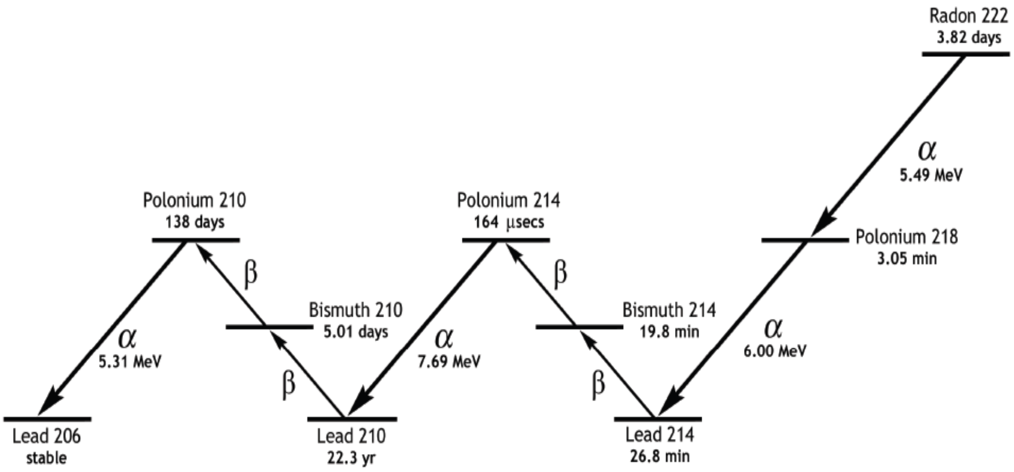

Figure 1 Radon decay sequence

Sample Collection

In this paper, four lakes were selected to include all different parts of the Mandalay region, namely Sedawgyi, moat of Mandalay, Kandawgyi and Taungthamann on January 30th 2019 (Wednesday).The altitude of the samples collected area is about 80 meter or 260 feet above sea level. Altogether four lakes were selected purposively because of these area public using these water. The samples were collected within evening of one day because the half-life of radon is 3.8 days. The locations of sample collected were described by Google maps of Figure (2), (3), (4), (5) and (6). Approximately 60ml of raw water samples are collected from each lake directly with quality control procedure. Before taking water samples, each sample container rinsed with distilled water.

Figure 2 The Google map of sample collected area in Mandalay region

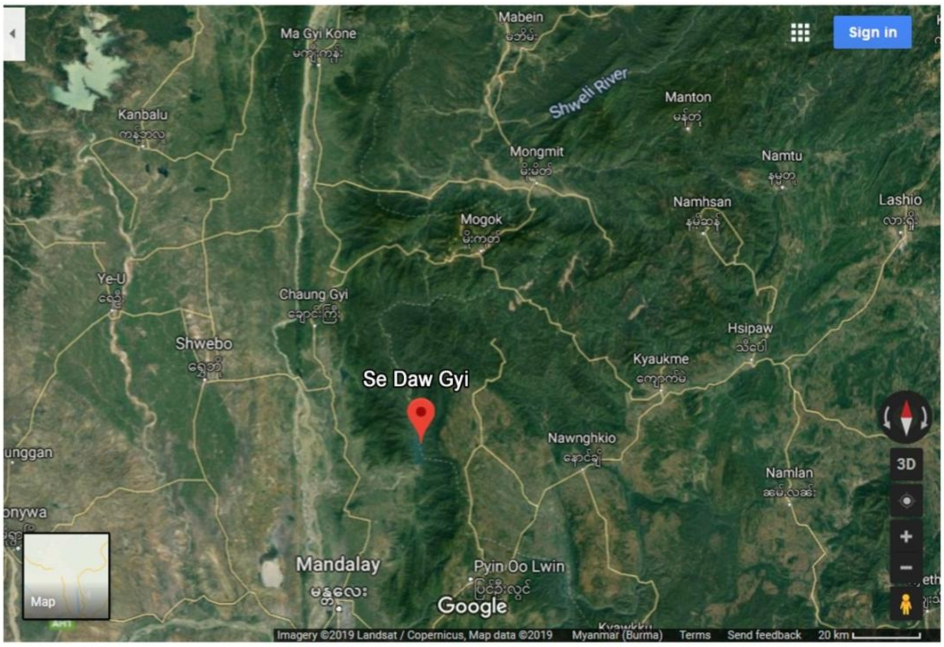

Figure 3 The location of Sedawgyi lake in Google map

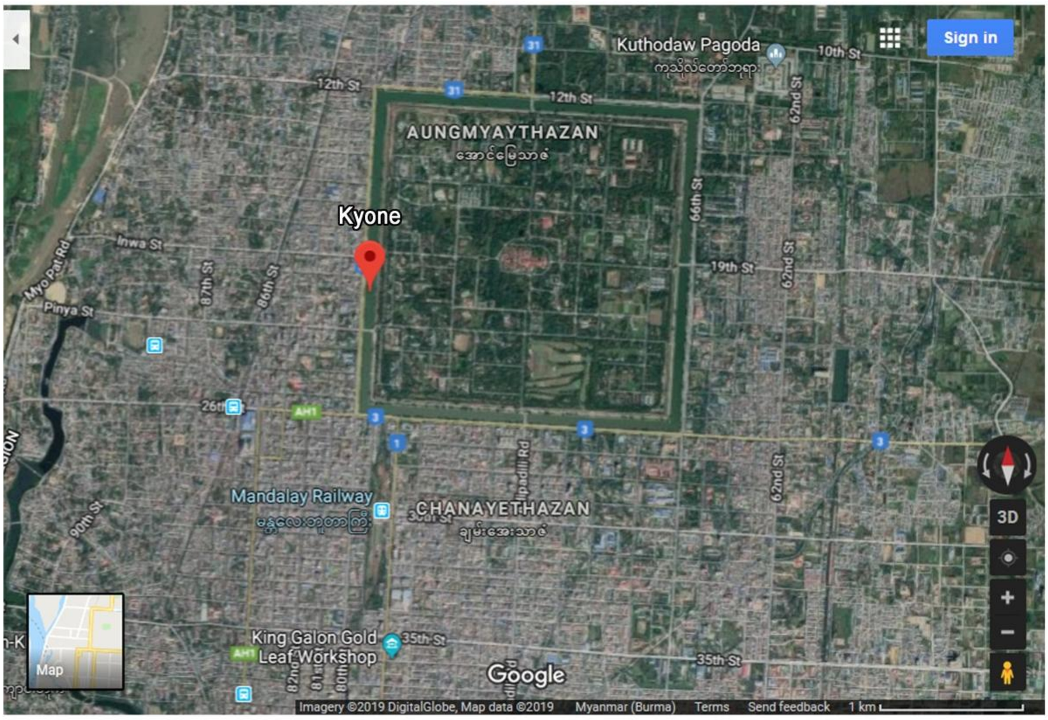

Figure 4 The location of moat of Mandalay in Google map

Figure 5 The location of Kantawgyi in Google map

Figure 6 The location of Taungthamann lake in Google map

Measurement of radon concentration in water samples

Radon content level in raw water (40ml) was measured onsite using by RAD7, Electronic Radon Detector. RAD7 connected to a RAD-H_2O accessory (DURRIDGE Co.Ltd USA) as shown in Figure (7). RAD 7 is a well calibrated, fast and accurate radon detector. After the 10 minutes purging the inner RAD7 detector, it was connected the tested water sample glass vial. Before the test, on the RAD7 go to setup water Protocol depending on water glass vial is being used and started. Data printed at the end of 4 cycles (30 minutes), and a summary, bar chart and cumulative spectrum was printed at the end of the run – DURRIDGE CO-Ltd-USA (2014). Four synthetic spectrums were describe for four water samples, as shown in Figure (8), (9), (10) and (11). Radon content level in water sample in mean, standard range of specific activity and median values were computed using by CAPTURE Software of RAD7, DURRIDGE Co-Ltd-USA. Data analysis was analyzed by Microsoft Excel and SPSS software.

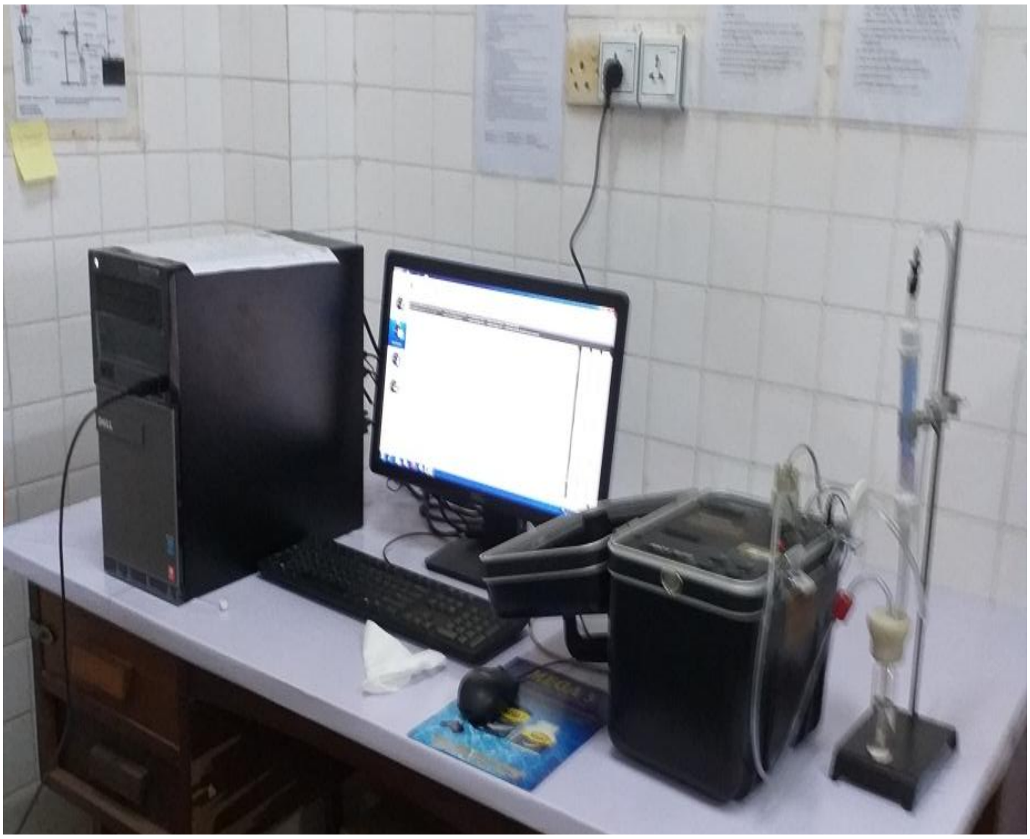

Figure 7 Measurement of radon concentration in water samples by RAD7 detector

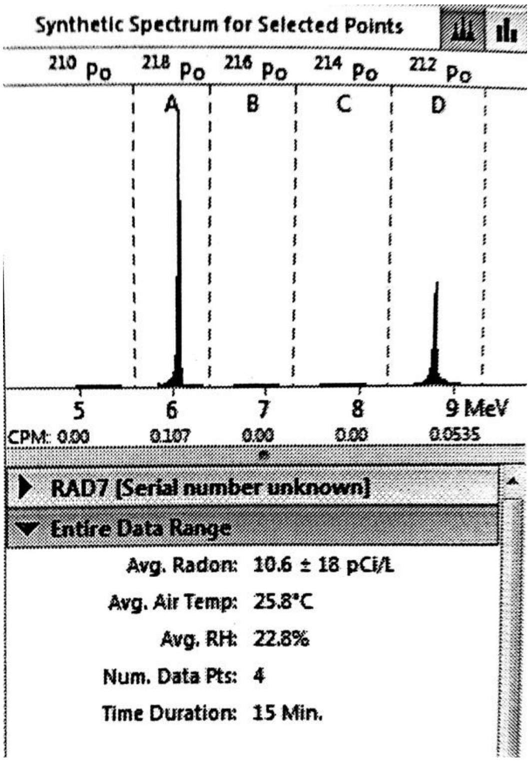

Avg. Radon: 10.6 ± 18 pCi/L
Avg. Air Temp: 25.8°C
Avg. RH: 22.8%
Num. Data Pts: 4
Time Duration: 15 Min.

Figure 8 Illustration of synthetic spectrum and entire data range of water samples from Sedawgyi lake

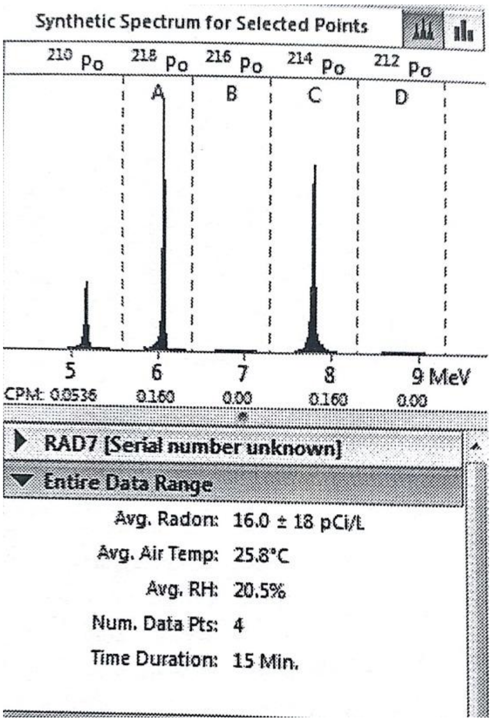

Avg. Radon: 16.0 ± 18 pCi/L
Avg. Air Temp: 25.8°C
Avg. RH: 20.5%
Num. Data Pts: 4
Time Duration: 15 Min.

Figure 9 Illustration of synthetic spectrum and entire data range of water samples from moat of Mandalay

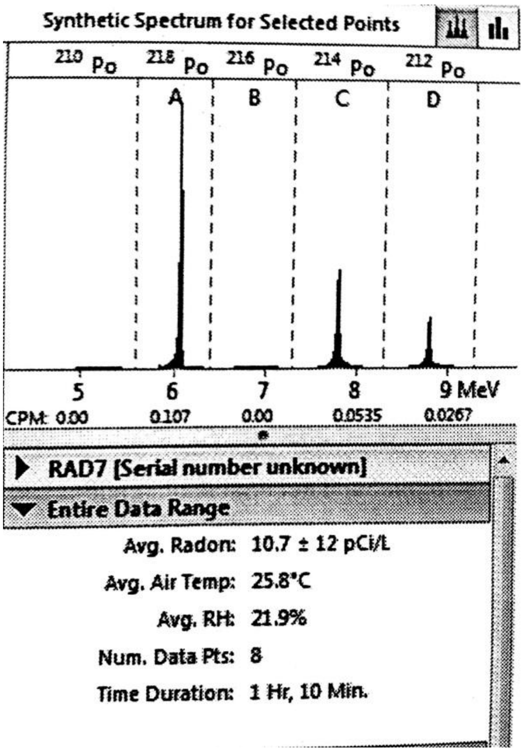

Avg. Radon: 10.7 ± 12 pCi/L
Avg. Air Temp: 25.8°C
Avg. RH: 21.9%
Num. Data Pts: 8
Time Duration: 1 Hr, 10 Min.

Figure 10 Illustration of synthetic spectrum and entire data range of water samples from Kandawgyi lake

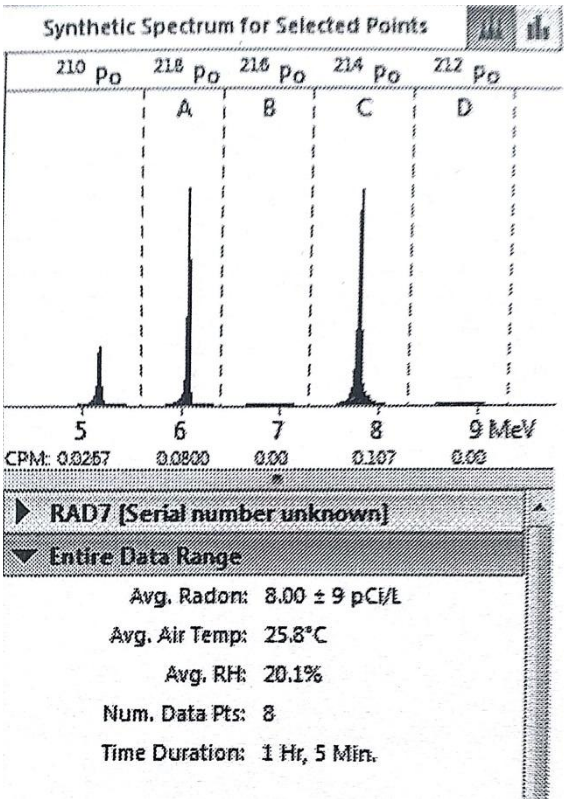

Avg. Radon: 8.00 ± 9 pCi/L

Avg. Air Temp: 25.8°C

Avg. RH: 20.1%

Num. Data Pts: 8

Time Duration: 1 Hr, 5 Min.

Figure 11 Illustration of synthetic spectrum and entire data range of water samples from Taungthamann lake

Results and Discussion

In this study, the calculated values of Radon concentration in tested 4 samples from selected lakes were described with a Table (1) and the graph of Figure (12). The highest radon concentration was found in moat of Mandalay (16.0 pCi/L) and the lowest radon concentration was found in Taungthamann (8.0 pCi/L). This research highlighted the no risk of radiation exposure from tested 4 water samples to community. Collected water samples of selected lakes contained lower radon concentration in selected place of Mandalay region and that is public safe limit level. Despite the reported radiological risk associate with the exposure to radon and its progenies, the level of awareness of the present of this cancinogenic radionuclide in lake water from selected are of Mandalay region is low. WHO-2009 and international Commission on Radiological Protection (ICRP-2009) has recommended for the public safe limit radon concentration is 100 pCi/ L received from radon and its progenies above which it can be health hazards.

Table 1 Mean radon concentration and range of specific activity of four water samples

No	Locations	Mean Radon Concentration (pCi/L)	Range of specific activity(pCi/L)
1	Sedawgyi	10.6	± 18
2	Moat of Mandalay	16.0	± 18
3	Kandawgyi	10.7	± 12
4	Taungthamann	8.0	± 9

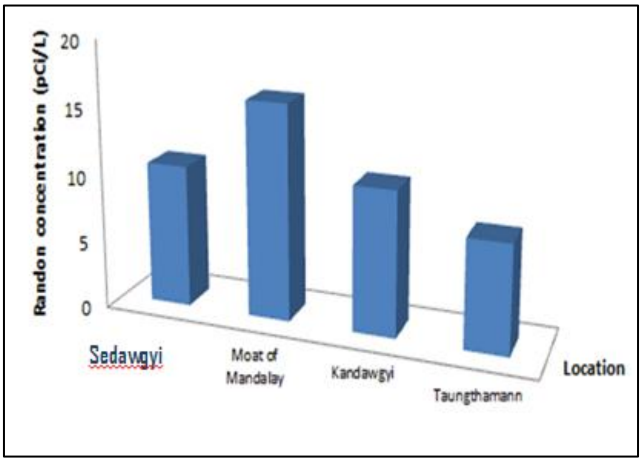

Figure 12 The radon concentration of water samples for four lakes

Conclusion

Knowledge of the distribution of radionuclide levels is important to the public safety and it is also necessary to know simple knowledge of safe and effective ways to reduce radon content in water. The present study will link to ongoing radiological studies on the other area providing information on natural radionuclide level of water. The current research work provides the information on natural radon concentration of water which can be used in developing intervention programs for household different water sources and storage strategies. This research showed that there is a low risk of radon exposure to community living in Mandalay region.

Acknowledgement

We are greatly indebted of Dr Kyi Thar Myint, Retired Professor, Department of Physics, West Yangon University, for her valuable suggestions in this research work.

References

DURRIDGE (2012)RAD7 RADON DETECTOR User Manual. DURRIDGE Company Inc., Boston.

DURRIDGE,C. (2015). Radon in water accessory. Revision 2015-07-28 edition.

Environmental Protection Agency, office of ground water and drinking water rule, (1999) “technical fact sheet EPA 815-F-99-006”. Washington DC.

Gruber,v., Maringer, F. J., & Landstetter, C.(2009).Radon and other natural radionuclides in drinking water in Austria: measurement and assessment. Applied Radiation and isotopes, 67,913-917.

http://www.epa.gov/radiation/images/radon-cancer-vs-other.jpg.

http://www.durridge.com/documentation/RADH$_2$O manual.pdf

K . Badham, R.Mehra and R.G. Sonkawade, (2010). “ Radon gas and its radioisotopes” Inadian Journal of Pure and applied Physics, Vol.48,pp.508-511.

US Environment Protection Agency, office of Radiation and Indoor Air, (2003) “Assessment of risk from radon in homes”. Washington DC.

J. Myanmar Acad. Arts Sci. 2020 **Vol. XVIII.No.2C**

THE AUTOMATIC INCLIENE PLANE TO MEASURE THE COEFFICIENT OF STATIC FRICTION FOR TEACHING AID

Phyu Phyu Mar[1], Ayethidar Aung[2], Mya Hnin Su[3]

Abstract

Today one of core science subject being offered in Myanmar schools is Physics and it forms the basis for the nations technological Subject and human resource development. This paper discusses the improvement of teaching aid in practical works. The automatic finding of the coefficient of static friction is designed by using inclined planed and Arduino technology. It is simple and very affective to describe the basic principle of static friction. The data are collected easily, show clearly and précised and accurate. The measured time is quickly done by this method. This design can be supported affectively in teaching to understand and linking between Physical Phenomenon, theory and practical for students in all educational fields.

Keywords: Automatic, Arudino nano, Education, Employment, Productivity, Physics, Technology, Teaching aid, Stepper motor

Introduction

In Myanmar there is a lot of need to provide society and human resources. To develop the education teaching methods and teaching aids are important. So teaching aids are the useful things to discuss and demonstrate the Theory and Law clearly. Among them finding of coefficient of static friction using the incline plane is included. In this paper “the automatic finding of coefficient of static friction using Arduino IDE” is used to find the coefficient of static friction by using of Inclined plane for teaching aid. Because of Arduino, its open source software is very popular today. So people are liked to use the Arduino IDE for research and the projects and invention of the news in various ways such as domestic used, economic used and for teaching aids. In this experiment, It will use a IR sensor do study static friction on the wooden block. Determine the relationship between force of static friction and due to the weight of an object. Use the Arduino microcontroller and IR sensor to independently measure the coefficient of static friction compare it to the previously measured value.

Theory and Components

When a surface of one body moves with respect to the surface of another when they are in contact, it must overcome a resisting force. This resisting force is called friction. In this paper “the automatic finding of coefficient of static friction using Arduino IDE” is used to find the coefficient of static friction by using of Inclined plane for teaching aid.

---

[1] Dr, Lecturer, Department of Engineering Physics, Yangon Technological University

[2] Dr, Associate Professor, Department of Engineering Physics, Yangon Technological University

[3] Dr, Professor and Head, Department of Engineering Physics, Yangon Technological University

Theory and Components

Theory of the Incline Plane

An incline plane is a sample machine that has its surface inclined at an angle with the horizontal. It consists mainly of a smooth plank of wood or metal rails. It is used to lift or roll heavy objects from one level to another. It permits the raising of heavy loads by application of smaller forces than would have been employed in resisting them vertically.

If a plane horizontal surface with a block resting on it be gradually tilted a certain angle of inclination will be reached when the block will begin to slide down the incline. This particular angle of inclination of the plane with the horizontal at which the block just begins to slide down is known as "**angle of friction**". Forces acting on the block placed on an inclined plane its weight mg, the normal reaction, N and the force of static friction F_S. At the angle θ at which it static to slide down, the static friction $F_s = mg \sin \theta$ and the normal reaction $N = mg \cos \theta$ show in Figure 1 a.

$$F_s \infty N$$

$$F_s = \mu_s N$$

$$\mu_s = \frac{F_s}{N} \qquad (1)$$

$$\mu_s = \frac{f_s}{N} = \frac{mg\sin\theta}{mg\cos\theta} = \tan\theta \qquad (2)$$

Eq (1)& (2)

$$\mu_s = \frac{Friction\ of\ force}{Normal\ Reaction} = \tan\theta$$

Thus μ_s can simply be found by determining tan θ from the measurement of h and a Figure 1.b.

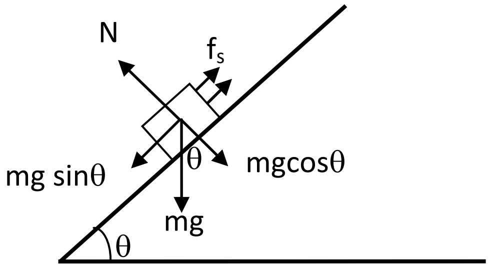

Figure 1a Forces on the block on an incline

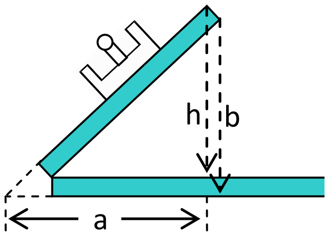

Figure 1b Determination of tan θ

2.2 Arduino Nano Board

The Arduino Nano shown in Figure 2, is one of the smallest and yet most exciting breadboard-friendly boards available on the market today. It's become exceptionally popular with beginner programmers thanks to its excellent functionality and the sheer variation of potential applications. Based on the ATmega328P, this tool is fantastic for those who wish to improve their programming skills and create some interesting and unusual projects. While the item does not come with a DC power pack, it benefits from a mini-USB cable for power, and that means it can be use with any PC or laptop device. This Nano board is used for to control the whole project and command the other devices.

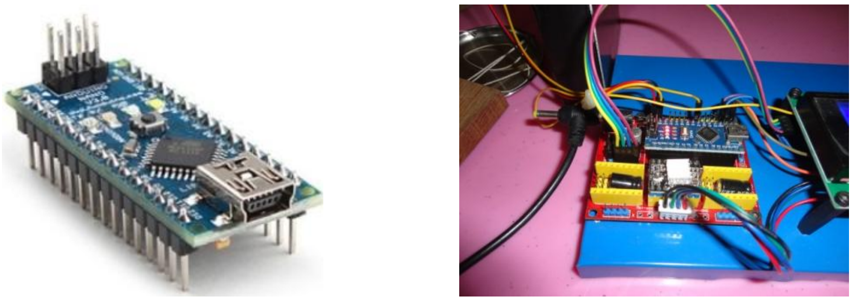

Figure 2 The Arduino Nano Board and using in the circuit

2.3 Developing and Measuring Equipment for Kinetic Friction Using Arduino Board Garbl CNC Shield

A CNC shield shown in Figure 3 is inserted to the Arduino microcontroller to start / stop and connection of stepper drivers easy. It is compatible with the G-Code interpreter firmware called GRBL. It supports maximum of four stepper drivers to run four stepper motors. It can support a maximum of 36 volts and setting the micro stepping is easy with a shield. This CNC shield is used for to control the motor.

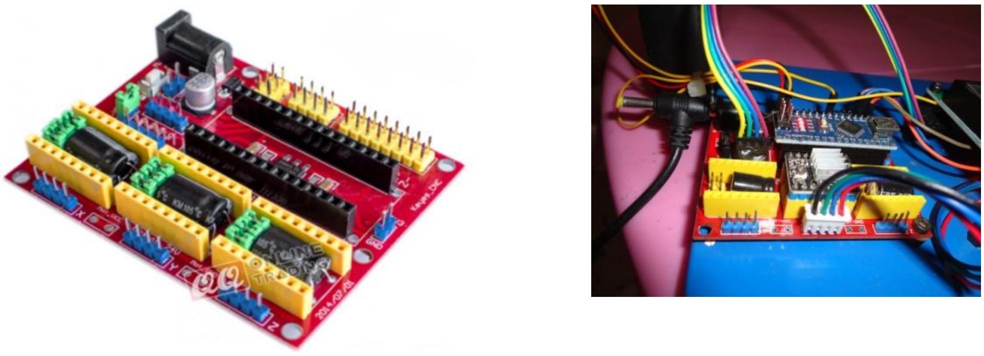

Figure 3 The CNC Arduino Garbal Shields and its application

2.4 Stepper Motor using the rising and falling of the incline plane

Stepper motors shown in Fig (4) is used for their high working ability and precision level. Unlike DC motors, the stepper motors are brushless, synchronous electric motors that can divide a full in both directions. It has a capability of holding torque at zero speed, and precise digital control without any feedback system depending on the overall size of the project and application. The stepper motors are constant power devices. As speed increases the torque decreases, so we'll have to try to find a happy medium for the need to drive our CNC machine. Stepper motors come in different types and multiple coil winding. In the project the stepper motor is used for raising the incline plane to detect the coefficient of static friction. This motor is controlled by the Arduino Garbal shields to raise or lower the incline plane.

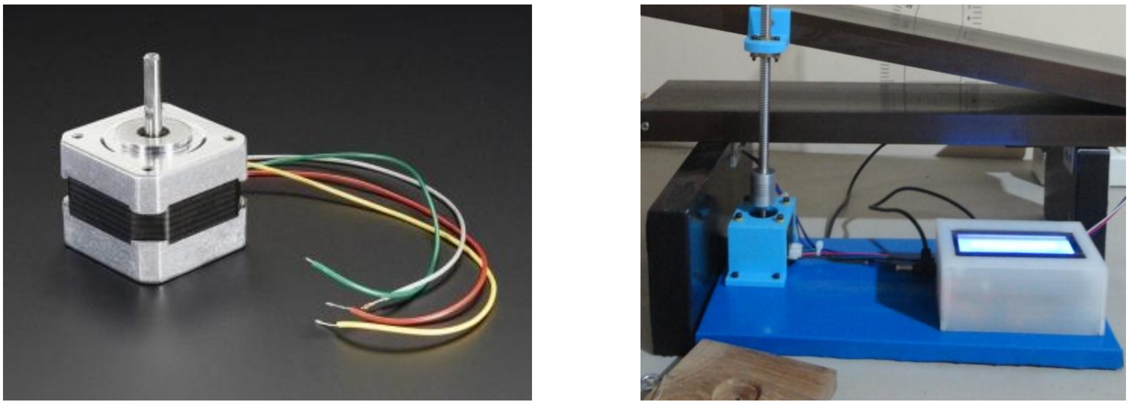

Figure 4 The JLB 17HS1362 Stepper Motor and its application in incline plane

2.5 Motor Driver using for the control of the stepper motor

The Big Easy Driver shown in figure 5 is a stepper motor driver board for bi-polar stepper motors up to 2A/phase. It is based on the Allegro A4983 or A4988 stepper driver chip, which is the next version of the Easy Driver board. This design is robust enough to handle most medium-sized stepper motors. This driver is used to control the motor to raise the incline plane or down the plane and to stop when it reaches the home condition.

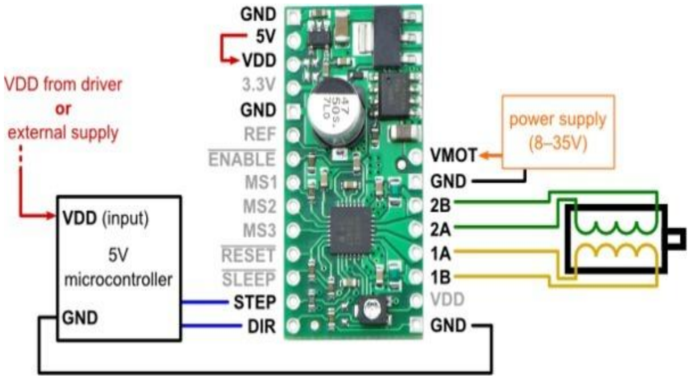

Figure 5 The Motor drivers

2.6 4-Line Liquid Crystal Display (LCD) using for the display device of the incline plane

The HD44780U dot-matrix liquid crystal display controller and driver LSI displays alpha numeric, Japanese kana characters, and symbols. It can be configured to drive a dot-matrix liquid crystal display under the control of a 4-bit or 8-bit microprocessor. Since all the functions such as display RAM, character generator, and liquid crystal driver, required for driving a dot-matrix liquid crystal display are internally provided on one chip, a minimal system can be interfaced with this controller/driver.

New Liquid Crystal Display is a collection of libraries that can handle almost all HD44780 compatible displays interfaces shown in figure 6. It has a number of benefits over the default library, including the ability to handle screens with an I2C adapter.

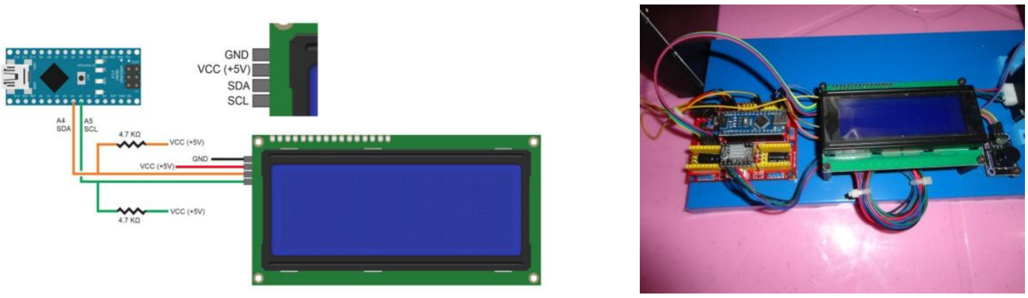

Figure 6 Arduino and 4-Line LCD interface with I2C and using Limit Switch in the incline plane circuit

2.7 Limit Switch Using for the home position of the incline plane

A **limit switch** , shown in figure 7, is an electromechanical device that consists of an actuator mechanically linked to a set of contacts. When an object comes into contact with the actuator, the device operates the contacts to make or break an electrical connection. They are also sensors that when a component is touching it or not. They can be used to prevent mechanisms from moving too far in one direction or another.

Figure 7 Limit Switch and using Limit Switch in the incline plane

2.8 IR sensor using for the detecting device of the object

IR Sensor or Infrared Sensor ,shown in Figure 8, has two main parts, IR Transmitter and IR Receiver. The work of IR transmitter or Infrared transmitter is to transmit the infrared waves whereas the work of IR receiver is to receive these infrared waves. IR receiver constantly sends digital data in the form of 0 or 1 to V_{out} pin of the sensor. In the project LM393 is used. This signal informs the Arduino Nano whether the object is ready position or not. If the object is very far away the sensor or not in detectable position there is no signal emit to the data pin. If so the Arduino can't command the motor to start. The LCD show that "the object is not detecting". When the object is repaired to ready condition, user can press the button switch, the motor start to move and raise the incline plane. When the object is start to move, the sensor can't meet the object, if so the motor stop and the Arduino gives the angle of the present position. The detail of the working capital is described in the following section.

Figure 8 LM 393 IR Sensor and sensing the object and out of sensing the object

Experimental Methodology

The Figure 9 shows the circuit implementation of the automatic incline plane. The coefficient of static friction in incline plane is calculated by the Arduino based programming method. The finding of the coefficient is written in the program. The 4 line LCD displayed the result of the coefficient. The control of LCD is written in “Liquid Crystal-PCF8574.h” header files. The data are given out form the output device LCD. It shows the value of coefficient, running conditions and pulse condition, and the object is detected or not. On /off switch control the starting and pause.

But the stopping is done by the Infrared Sensor gives the sensing of the object pan is detect. If the object is detected, the IR sensor gives the pulse to the Arduino control Board and the stepper motor can start to run. The stepper count is done by the program and can be calculated the tangent angle. If the object is start to move the IR sensor gives the pulse to stop the motor and the Arduino gives the coefficient of static friction of the plane by calculating the program. If the user repress the button switch the motor start to rotate backward and return to home position. ” The comparison of finding in coefficient of static friction in Arduino based incline plane and manual incline plane are compared in the following section. There are Two forms of data analysis. The first for different faces and the second for wood incline and Aluminum incline plane are described in the following section.

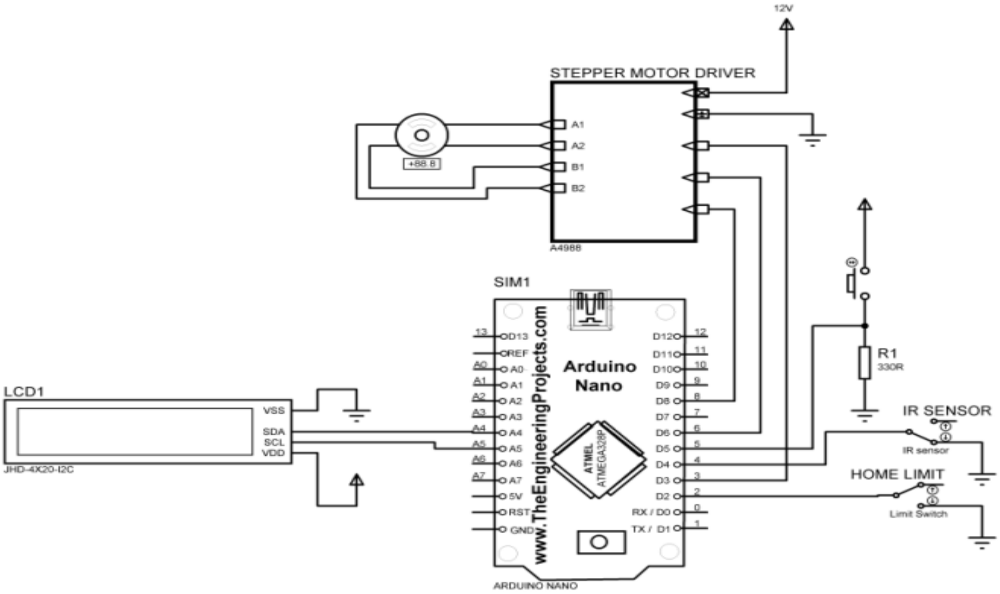

Figure 9 The Circuit Diagram of the Incline plane

Analysis Results and Discussion

The finding of coefficient of static friction by manual is changed by the human reaction time. If the human is sense correctly the result will include the error. To avoid this error the repeated experiment must be done. So the time is the factor to complete the experiment. The automatic finding of the incline plane can be found the result in a short time. The compares of data from Manual and Automatic are shown in the following table (1) and table (2). These results are depend on the research environment such as temperature, pressure, and air flow directions. So, if the accurate data are needed the conditions for the research must be in constant conditions. The actual data and photos are comparing the results are shown in Table (3).

Table 1 The compares of Data from Manual and Automatic incline plane with different surfaces on Aluminum

Material name	**Manual**		**Automatic**	
	θ(Degree)	**Coefficient of static friction**	**θ (Degree)**	**Coefficient of static friction**
Wood	30	0.577	29.7	0.57
plastic	31	0.601	30.85	0.59
paper	35	0.700	34.5	0.687
Rough wood	38	0.781	37.2	0.759

Table 2 The compares of data from Manual and Automatic incline plane with difference loads on Aluminum

Sr. No	**Total weight In Tray(g)**	**Manual**		**Automatic**	
		measured angle(Degree)	**μ_s=tanθ**	**measured angle(Degree)**	**μ_s=tanθ**
1.	50	20	0.364	16.65	0.30
2.	60	22	0.466	16.73	0.30
3.	70	26	0.487	16.55	0.30
4.	80	25	0.466	16.97	0.31
5.	90	18	0.325	17.39	0.31
6.	100	16	0.287	16.76	0.3

Table 3 The result counting of automatic incline plane with different weight

Weight in Tray(g)	**50g**	**60g**	**70g**	**80g**	**90g**	**100g**
Running condition					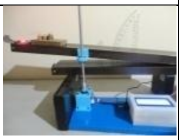	
Result	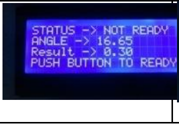 STATUS -> NOT READY ANGLE -> 16.65 Result -> 0.30 PUSH BUTTON TO READY	 STATUS -> NOT READY ANGLE -> 16.73 Result -> 0.30 PUSH BUTTON TO READY	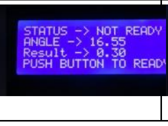 STATUS -> NOT READY ANGLE -> 16.55 Result -> 0.30 PUSH BUTTON TO READ	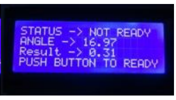 STATUS -> NOT READY ANGLE -> 16.97 Result -> 0.31 PUSH BUTTON TO READY	 STATUS -> NOT READY ANGLE -> 17.39 Result -> 0.31 PUSH BUTTON TO READY	 STATUS -> NOT READY ANGLE -> 16.76 Result -> 0.30 PUSH BUTTON TO READY

The automatic incline plane in testing condition is shown in Fig 10. The importance of precaution is that the testing condition is kept in constant temperature and pressure.

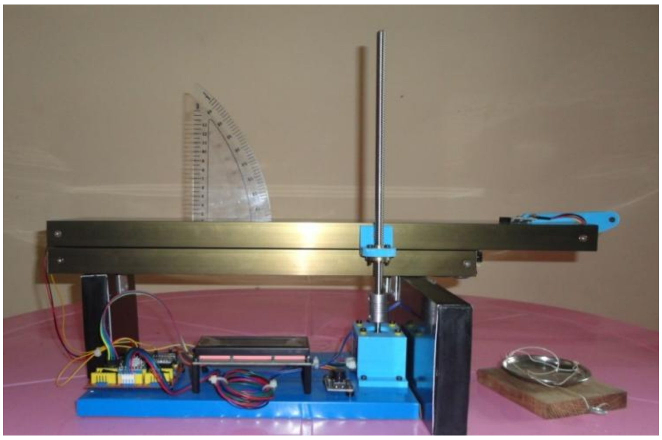

Figure 10 The testing condition of the automatic incline plane

Conclusions

The automatic incline plane is used to measure the coefficient of static friction are rugged classroom- proven technology that are well supported and easy to use. It provides consistent, high quality results for the demands of the classroom. From the above Method, the data are clearly seen that the automatic incline plane is more accurate and precise. Because the error percent of the automatic incline plane is relatively small and the measure time is at the constant because of the stepper motor rotation time. Detectors without a mode the switch do not proper detect objects closer than 2cm. As the result such detectors must be farther across from experiment than described in the student’s notes. In constant, detector with a mode switch will detect be object as also as 3cm. Ideally an experiment with be set up so that the target is nearly this close at the point of closest approach, giving the best possible data. Sometimes a target may not supply a strong reflection of the IR sensor. But the results are very good support to understand in describing about the friction. It includes many Arduino sketches (Programs) that can be used as a starting point of the projects. These sketches were intentionally kept simple, so that the analog without getting overwhelan with complex details. The following Figure 11 shows the Final running condition of the automatic incline plane.

Figure 11 the automatic incline in running condition

Acknowledgement

I would like to gratefully acknowledge the enthusiastic supervision of Dr. Aye Aye Kyu and Dr. Mya Hnin Su during this work. I also thanks to Prof. Dr. Ye Chan for his valuable advice to motivate to make the project. I also deeply thanks to Dr. Aye Thida Aung for her actively helps and giving precious advice and supervise. I am grateful to all my friends for being the kindly helps on my works in this project. I would like to especially thank my department staffs for their care and attention. Finally, I am forever indebted to my parents for their understanding, endless patience and encouragement when it was most required.

References

Embedded Controllers Using C and Arduino/ 2E, James M. Fiore, Version 2.1.0, 27 March 2019, Embedded Controllers

"Physics for Science and Engineers with Modern Physics", Serway and Jeweet, Cengage Learning; 10 edition (January 1, 2018)

Arduino cool, Jonathan OxerHugh Blemings, 2016 Vxlabs. (2018) *Which jumper to set on the ITEAD XBee shield v1.1 for use with a 3.3V Arduino* [Accessed 25th October 2017]

www.https://components101.com/arduino-nano

https://www.orientalmotor.com/stepper-motors/index.html

Implementing the model-view-view model pattern, [Online]. Available: https: // msdn.microsoft.com/en-us / library/ff798384.aspx

https://www.orientalmotor.com/stepper-motors/stepper-motor-drivers.html

https://www.instructables.com/id/3020-CNC-Arduino-GRBL-CNC-Shield

EFFECT OF pH LEVEL ON THE FORMATION OF SILICA AEROGEL SYNTHESIZED FROM RICE HUSK ASH

Ei Shwe Sin Oo[1], Myo Aung[2] & Ye Chan[3]

Abstract

Silica aerogel has been synthesized from rice husk ash via water glass solution by using sol-gel method. The synthesized silica aerogel at different pH level are characterized by X-ray diffraction (XRD) to analyze the structure formation of silica aerogel. The function group of the products are characterized by Fourier Transform Infrared Spectroscopy (FTIR). The particle sizes of silica aerogel are characterized by scanning electron microscopy (SEM). XRD result shows that the silica aerogel particles prepared at pH 7 has the capability to extract complete SiO_2 from rice husk ash with a great quantity of amorphous silica. SEM result indicates that the particle size of the silica aerogel increases at pH 5 and pH 9 and decrease at pH 7. The results show that the synthesis of silica aerogel from rice husk ash has porous structure and the particle size of silica aerogel depend on the effect of pH level.

Keywords: rice husk ash, silica aerogel and sol-gel method

Introduction

Aerogel is a synthetic porous ultralight material derived from a gel, in which the liquid component for the gel has been replaced with a gas. Aerogels have a porous solid network that contains 90% of air pockets taking up the majority of space within the material. The lack of solid material allows aerogel to be almost weightless. The term aerogel was introduced by Kistler in 1931 to define gels in which the liquid is replaced by a gas without the collapse of the polymer network. Nicknames include frozen smoke, solid smoke, solid air, solid cloud, blue smoke owing to its translucent nature and the way light scatters in the material (Tadjarodi A. et al., 2012). Aerogels possess remarkable properties such as high specific surface area and low thermal conductivity (Chen Q., 2017).

There are three most common types of aerogels such as silica, carbon and metal oxides. Among them, silica aerogel is most often used experimentally and in practical applications. Silica aerogels exhibit many unique properties, which include very high inner surface area, low sound velocity, high optical transparency, low refractive index, extremely and low thermal conductivity. Because of their special properties, silica aerogels have been widely investigated in various fields, find its applications in aerospace and aeronautic, thermal insulation, acoustic barrier materials, and more recently in catalyst products (Guangwu L., & Yangang L., 2016).

Silica aerogels contain more than 90% air and less than 10% solid silica. An aerogel is made by the so called “sol-gel process”. The first precursor used to obtain an aerogel was sodium silicate, resulting in the so called water glass solution. During this process, organic compounds containing silica undergo a chemical reaction producing silicon oxide (SiO_2). This mixture is a liquid at the creation of the reaction, and becomes more and more viscous as the reaction proceeds. When the reaction is completed, the solution loses its fluidity and the whole reacting mixture turns into a gel. This gel consists of a three-dimensional network of silicon oxide filled

---

[1] Assistant Lecturer, Engineering Science Department, Mawlamyine Technological University

[2] Lecturer, Universities’ Research Centre, University of Yangon

[3] Professor and Head, Universities’ Research Centre, University of Yangon

with the solvent. During the special drying procedure, the solvent is extracted from the gel body leaving the silicon oxide network filled with air. This product is called silica aerogel (Rakesh P. Patel, 2009).

Most commonly used raw materials for preparation of silica aerogels are tetraethylorthosilicate (TEOS), tetramethylorthosilicate (TMOS), and sodium silicate solution (water glass). These raw materials are more expensive and also carcinogenic. Therefore, for large-scale industrial production and for drug delivery applications, it is preferable to replace these conventional inorganic-based raw materials with an inexpensive, biocompatible, nontoxic and readily available bio-source as the raw material. Rice husk, an agricultural waste from rice mill industry, has a high silica content (~80 - 90%) and is easily available in large quantity (Kumar R. S., 2013).

In order to reduce the cost of fabrication and realize the commercial production of silica aerogels, green and cheap silica sources are very necessary. Rice husk ash are industrial wastes released by factories and thermal power plants, which consist of high content of silica. If these wastes could be converted into highly valuable silica aerogels, the environmental pollution problem caused by a stack of rice husk ash will be reduced greatly. Horticultural waste (e.g. waste leaves) could be another silica sources with 13% - 48% of silica content (Yanru L. et al., 2018).

In this study focus on the effect of pH level on the formation of silica aerogel by extracting pure silica from rice husk ash (RHA). This synthetic method provides economic benefits for the mass production of silica aerogel because it uses low-cost raw materials. The outermost layer of paddy rice is composed of about 20 wt% paddy grain, and silica comprises 20 wt% of the husk. Rice husk ash (RHA), which is produced as a by-product of combustion, contains amorphous silica. The silica aerogel has been synthesized according to the water glass solution and the effect of pH on the structure and size of silica aerogel nanoparticles was investigated.

Materials and Methods

Synthesis of Silica Aerogel from Rice Husk Ash

The rice husk (RH) was collected from a local rice mill, Yakhainekone, Mawlamyine, Mon State. Unwanted fine dust materials were removed through air-blowing separation technique and then washed properly to remove the physically adhered impurities using tap water. After successive washing, RH was dried in an air at room temperature for 72 hr to get clean and dry RH. The percentage of moisture content was measured by heating 1 gram of rice husk for 1 hr at 110°C (ASTM D3172-89). The amount of volatile materials was evaluated by heating 1 gram of the sample for 7 min at 950°C (ASTM 3175-02). Its ash content was determined by heating 1 gram of the sample for 4 hr at 750°C (ASTM 3174-02) which is shown in Table 1. The rice husk was firstly dried at 700°C for 6 hr, and grounded to pass the 150 µm sieve. The energy dispersive X-ray fluorescence (EDXRF) analysis of rice husk ash (RHA) was listed in Table 2. The rice husk ash (RHA) contains 77.34% silica, 15.98% potassium and small amount of others, such as Ca, Mn, Fe, Zn, etc. The silica aerogel was synthesized by using rice husk ash as precursor is shown in Figure 1. Five grams of RHA was mixed with 150 mL of 1 mol/L NaOH aqueous solution. The mixture was heated to 60°C for 1.5 hr with magnetic stirring. Finally, the water glass solution was obtained by filtering out the rice husk ash. The synthesis of aerogels was started with the gelation of water glass under different pH levels such as pH 5, pH 7 and pH 9 by using sulfuric acid drop by drop. The prepared gel was aged at room temperature for 24 hr. To remove sodium sulfate obtained from the neutralization stage, the aged gel was washed three times, each time kept in deionized water for 4 hr. Then, the pretreated silica gel was directly dried at 40℃ for 2 days to yield the silica aerogel powder (Ban G., 2019). The reaction occurred as the following equation.

$$\underset{\text{(Ash)}}{SiO_2} \quad + \quad \underset{\text{(Caustic soda)}}{2\ NaOH} \longrightarrow \underset{\text{(Sodium silicate)}}{Na_2SiO_3} \quad + \quad \underset{\text{(water)}}{H_2O}$$

$$\underset{\text{(Sodium silicate)}}{Na_2SiO_3} \quad + \quad \underset{\text{(Sulfuric acid)}}{H_2SO_4} \longrightarrow \underset{\text{(Silica)}}{SiO_2} \quad + \quad \underset{\text{(Sodium sulfate)}}{Na_2SO_4} \quad + \quad \underset{\text{(water)}}{H_2O}$$

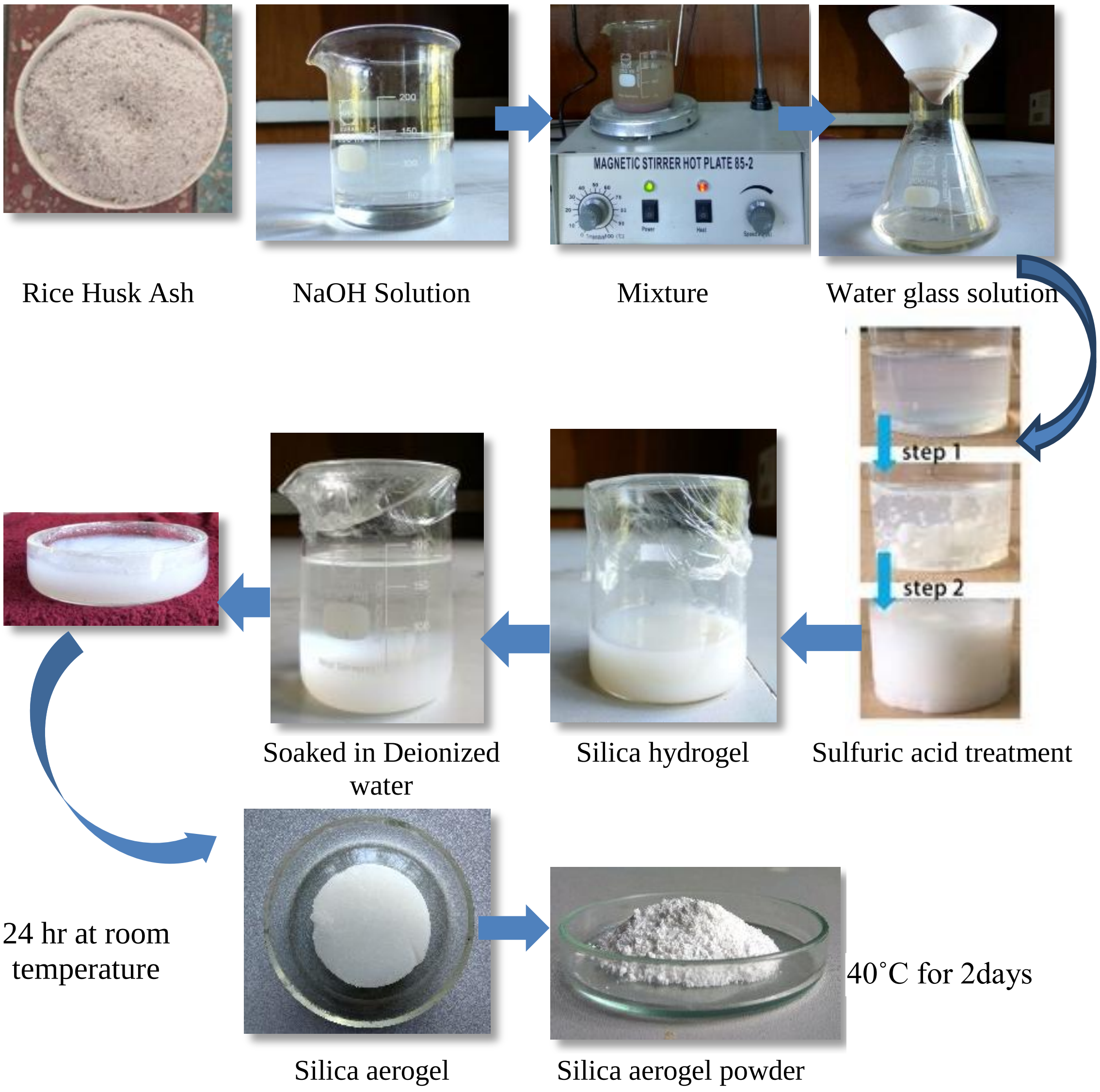

Figure 1 Synthesis of silica aerogel powder from rice husk ash

Table 1 Physical characterization of rice husk

Sample	Moisture	Volatile matter	Ash
Rice Husk (%)	10	65	25

Table 2 Elemental Analysis of rice husk ash

Elements	Si	K	Ca	Mn	Fe	Zn	Cu	Rb	Sr
Weight Percent (wt%)	77.344	15.989	3.526	1.446	1.326	0.170	0.092	0.068	0.040

Results and Discussion

Fourier Transform Infrared Spectroscopy Analysis

The FTIR spectrum of silica aerogel powder at different pH level is presented in Figure 2. The absorption peaks at 3450 cm^{-1} and 1641 cm^{-1} are due to stretching and bending vibrations of water molecules. The absorption peaks at 1091 cm^{-1} correspond to the Si−O−Si asymmetric stretching vibrations. The absorption peak at 471 cm^{-1} and the 800 cm^{-1} are corresponding with O-Si-O bending vibrations and the Si-O-Si symmetric stretching vibrations. The FTIR spectrum show almost the same patterns at different pH level such as pH 5, pH 7 and pH 9. Thus, it is confirmed that one can produce silica aerogel from rice husk ash.

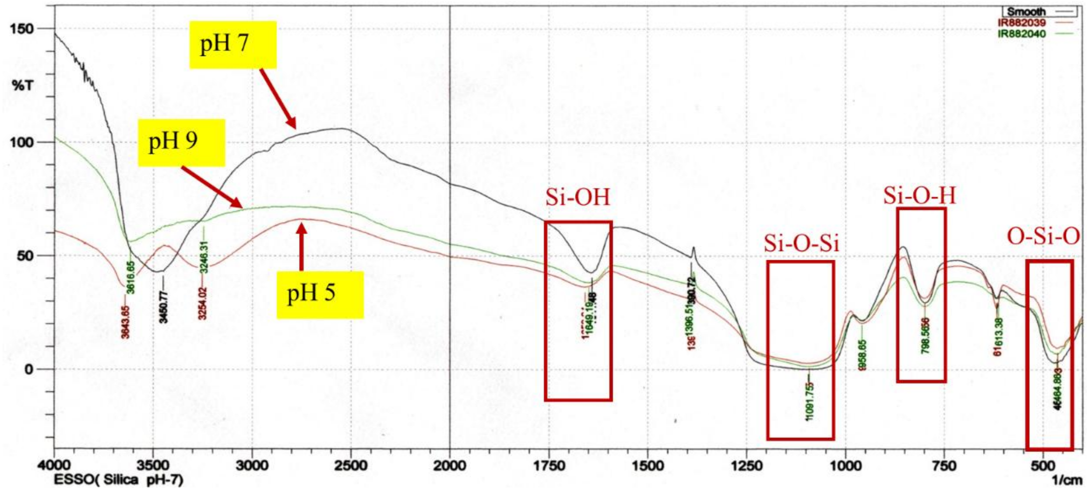

Figure 2 FTIR spectrum of silica aerogel at different pH levels

Characterization of Silica Aerogel Powder by XRD

The silica aerogel powder (SA) were synthesised at three different pH levels of pH 5, pH 7 and pH 9 to investigate the effect of pH on the quality of extract silica aerogel and particle size. The gelation time was greatly influenced by the pH level. Therefore, the gelation time decrease when the pH level increase. The XRD spectrum of product sample at pH 5, the chemical reaction is not completely and have more residual of Na_2SO_4 as shown in Figure 3(a). But the pH 7 and pH 9 , there is no chemical residual are found. The completely gelation occurred at these pH level since act as amorphous structure. The SA processing at pH 7 and pH 9, the spectrum appears as broaden with at 2θ = 22°, which indicating amorphous structure as shown in

Figure 3(b) and Figure 3(c). According to the Figures, the peak at 32˚ and 34˚ show that a few amount of Na_2SO_4 residual impurities trapped in the pores of the gel network after washing deionized water. The synthesis of silica aerogel prepared at pH 7 and pH 9 have the capability to extract more SiO_2 from rice husk ash.

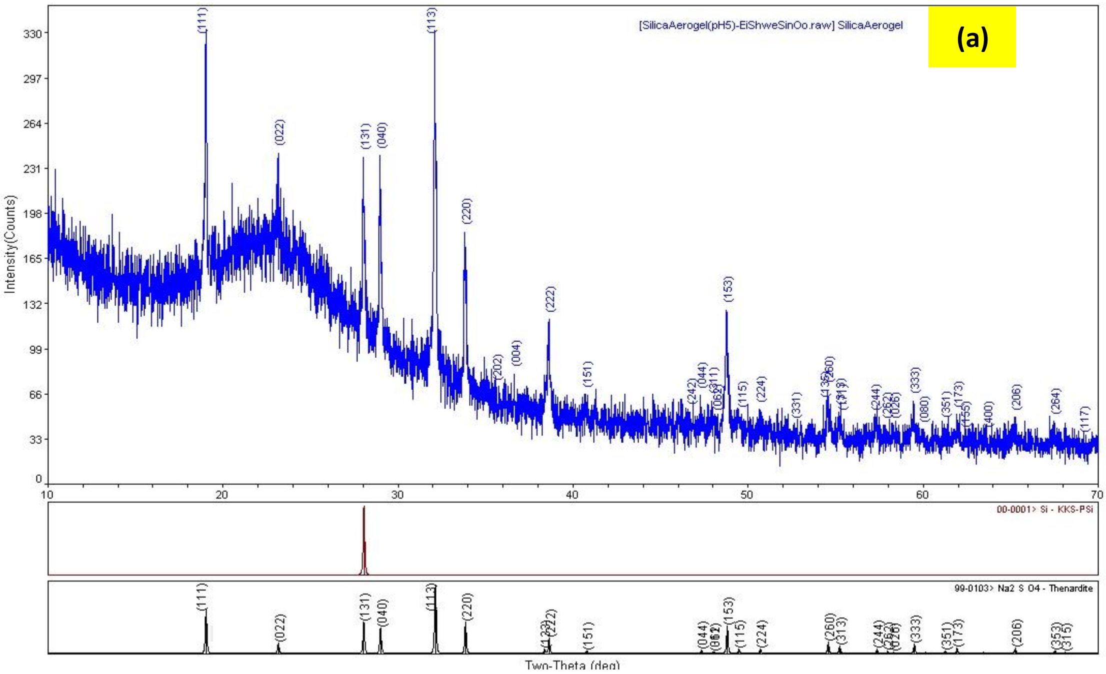

Figure 3 (a) XRD spectra of silica aerogel powder at pH 5

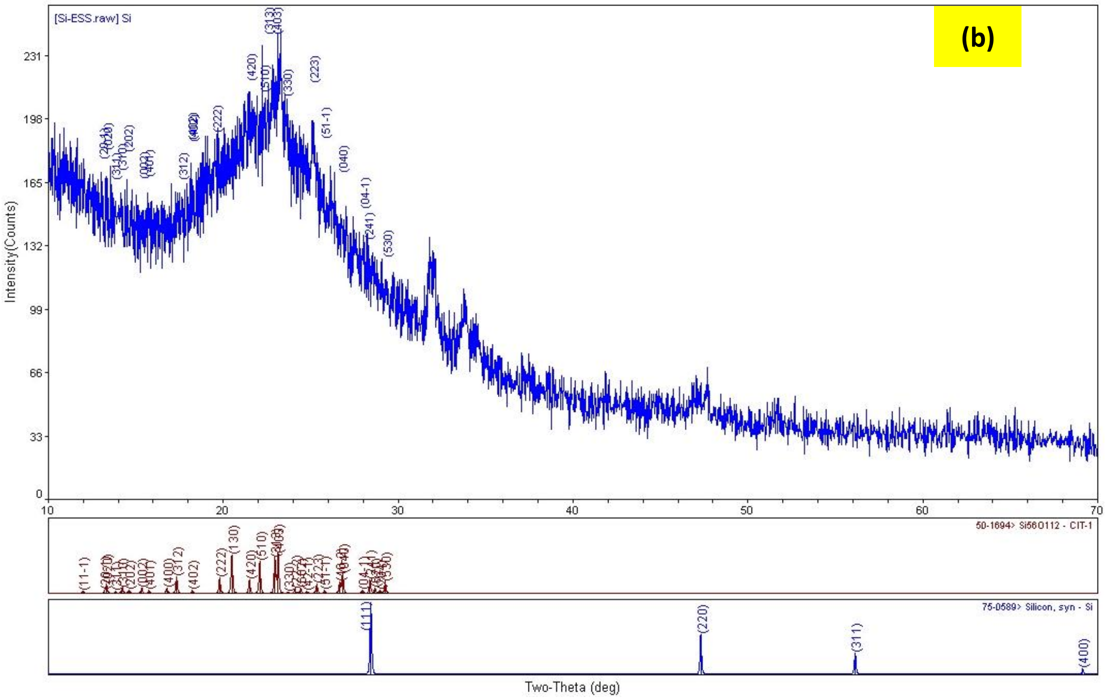

Figure 3 (b) XRD spectra of silica aerogel powder at pH 7

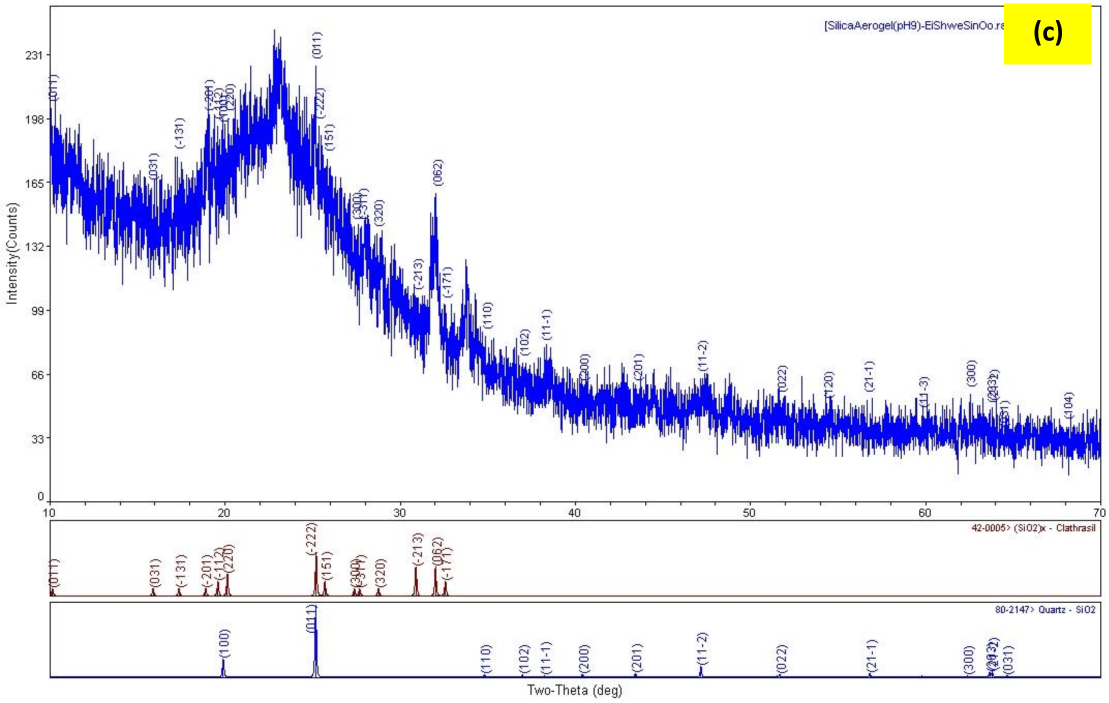

Figure 3 (c) XRD spectra of silica aerogel powder at pH 9

Characterization of Silica Aerogel Powder by SEM

The scanning electron microscope (SEM) images of silica aerogel powder synthesized at three pH levels are shown in Figure 4. The sample synthesized at pH 5 is found as flakes and is not well disperse as particles to be analyzed. At pH 7 and pH 9, the particles are although aggregate, individual particle can be distinguished and interconnect with each other to form a porous network. The average particle sizes are shown in Table 3. According to the Figure, silica aerogel had a uniform size varying from ~ 88 nm to ~ 75 nm in size at 7 and 9 pH levels. It can be concluded that the size of the silica aerogel increased at pH 5 and decreased at pH 7 and pH 9. At pH 7, silica aerogel showed nano particles in size and good morphology than others.

Table 3 Average particle size of silica aerogel

Product Sample	Average particle size
PH 5	90 nm (flakes)
pH 7	75 nm
pH 9	88 nm

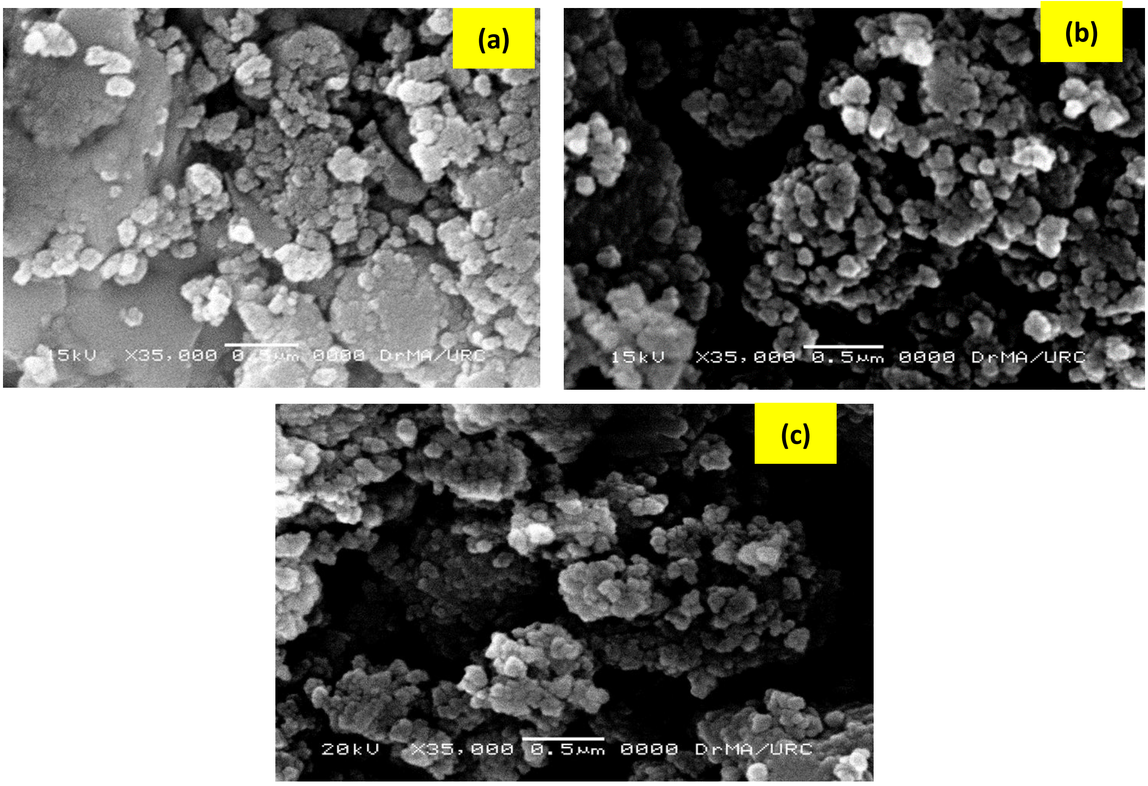

Figure 4 SEM micrographs of silica aerogel powder at (a) pH 5 (b) pH 7 and (c) pH 9

Conclusion

The silica aerogel was synthesized from rice husk ash via water glass solution by sol-gel method. Rice husk, a biomass resource left after threshing rice, is considered as economical raw material for large-scale production of silica aerogel due to its high silica content. In this study, fabrication of silica aerogel from rice husk ash under a relatively simple process was conducted with an eco-friendly, re-usable, cost-effective and safe approach compared to the conventional method. Silica aerogel was prepared by amorphous silica extracted in the form of sodium silicate from rice husk ash, and the silicate was then neutralized to form silica gel by the sol–gel process. The smallest nanoparticles size of silica aerogel synthesized using pH 7 and pH 9 showed more aggregate than large particles which are synthesized using pH 5. The silica aerogel synthesized at pH 7 showed porous structure and the smallest particle size compared with others. Therefore, the adjustment of pH level plays important role in the formation and sized silica aerogel.

Acknowledgement

The authors are grateful to Dr Khin Khin Win, Professor and Head of the Department of Physics, University of Yangon for her kind permission to carry out this work.

References

Ban G., Song S., Woon Lee H. & Taik Kim H., (2019), “Effect of Acidity Levels and Feed Rate on the Porosity of Aerogel Extracted from Rice Husk under Ambient Pressure”, *Journal of Nanomaterials,* vol. 9

Chen Q., Wang H.& Sun L., (2017), “Preparation and Characterization of Silica Aerogel Microspheres”, *Journal of Material (Basel),* vol.10(4)

Guangwu L., & Yangang L., (2016),“ Preparation and Characterization of Silica-titania Aerogel Monoliths by Sol-gel Method”, *16th International Conference on Nanotechnology,* Japan

Kumar R. S., Vinjamur M., & Mukhopadhyay M., (2013), “A Simple Process to Prepare Silica Aerogel Microparticles from Rice Husk Ash”, *International Journal of Chemical Engineering and Applications,* vol. 4(5)

Rakesh P. Patel, Nirav S. Purohit & Ajay M. Suthar, (2009), “An Overview of Silica Aerogels”, *International Journal of ChemTech Research,* vol.1, No.4, pp. 1052-1057

Tadjarodi A., Haghverdi M.& Mohammadi V., (2012), “Preparation and Characterization of Nano-Porous Silica Aerogel from Rice Husk Ash by Drying at Atmospheric Pressure”, *Journal of Materials Research Bulletin,* vol. 47, pp. 2584-2589

Yanru L., Hai H., & Xijiang Y., (2018), “Silica Aerogel as Super Thermal and Acoustic Insulation Materials”, *Journal of Environmental Protection,* vol.9, pp.295-308

J. Myanmar Acad. Arts Sci. 2020 **Vol. XVIII.No.2C**

DESIGN AND CONSTRUCTION OF THE INTENSITY BASED SOLAR TRACKING SYSTEM USING PIC 16F887 MICROCONTROLLER

Kalayar Win[1], Ni Ni Win[2]

Abstract

Solar energy is abundantly available Renewable Energy Source harnessed in all areas of the world and it is available every day. Energy produced by Photovoltaic system is used in many industrial and domestic applications. The sun position can be tracked based on the intensity of light and the power generating capability of the system can be increased. This paper presents the hardware implementation of the solar tracking system by using PIC microcontroller. An efficient and accurate DC motor control system is used to increase the system efficiency and reduces the solar cell system cost. The proposed automatic DC motor control system based on PIC 16F887A microcontroller is used to control the photovoltaic (PV) modules. This DC motor control system will track the sun rays in order to get maximum power point during the day using direct radiation. A photo cell is used to sense the direct sun radiation and feedback a signal to the PIC 16F887A microcontroller, and then the decisions are made through the microcontroller and send a command to the DC motor control system to achieve maximum power generation. The proposed system is demonstrated through simulation results. Finally, using the proposed system based on PIC microcontroller, the system will be more efficient, minimum cost, and maximum power transfer is obtained.

Keywords: DC Gear Motor, LDR, PIC 16F887A Microcontroller, PV cell

Introduction

One of the most important problems facing the world today is the energy problem. This problem is resulted from the increase of demand for electrical energy and high cost of fuel. The solution was in finding another renewable energy sources such as solar energy, wind energy, potential energy etc. Nowadays, solar energy has been widely used in our life, and it's expected to grow up in the next years. Solar energy has many advantages:

1. Need no fuel
2. Has no moving parts to wear out
3. Non-polluting & quick responding
4. Adaptable for on-site installation
5. Easy maintenance
6. Can be integrated with other renewable energy sources
7. Simple & efficient [Macagnan MH, F Lorenzo and C Jimenez , 1994]

As the range of applications for solar energy increases, so does the need for improved materials and methods used to harness this power source. There are several factors that affect the efficiency of the collection process. Major influences on overall efficiency include solar cell efficiency, intensity of source radiation and storage techniques. The materials used in solar cell manufacturing limit the efficiency of a solar cell. This makes it particularly difficult to make considerable improvements in the performance of the cell, and hence restricts the efficiency of

---

[1] Lecturer, Department of Engineering Physics, Technological University (Maubin)

[2] Associate Professor. Department of Physics, Magway University

the overall collection process. Therefore, the most attainable method of improving the performance of solar power collection is to increase the mean intensity of radiation received from the source. There are three major approaches for maximizing power extraction in medium and large scale systems. They are sun tracking, maximum power point (MPP) tracking or both. A solar tracker is a device that is used to align a single P.V module or an array of modules with the sun. Although trackers are not a necessary part of a PV system, their implementation can dramatically improve a system's power output by keeping the sun in focus throughout the day. Efficiency is particularly improved in the morning and afternoon hours where a fixed panel will be facing well away from the sun rays. PV modules are expensive and in most cases the cost of the modules themselves will outweigh the cost of the tracker system. Additionally a well designed system which utilizes a tracker will need fewer panels due to increased efficiency, resulting in a reduction of initial implementation costs. The dual axis solar tracking system is implemented in this research work. Block diagram of the intensity based solar tracking system is shown in Figure 1.

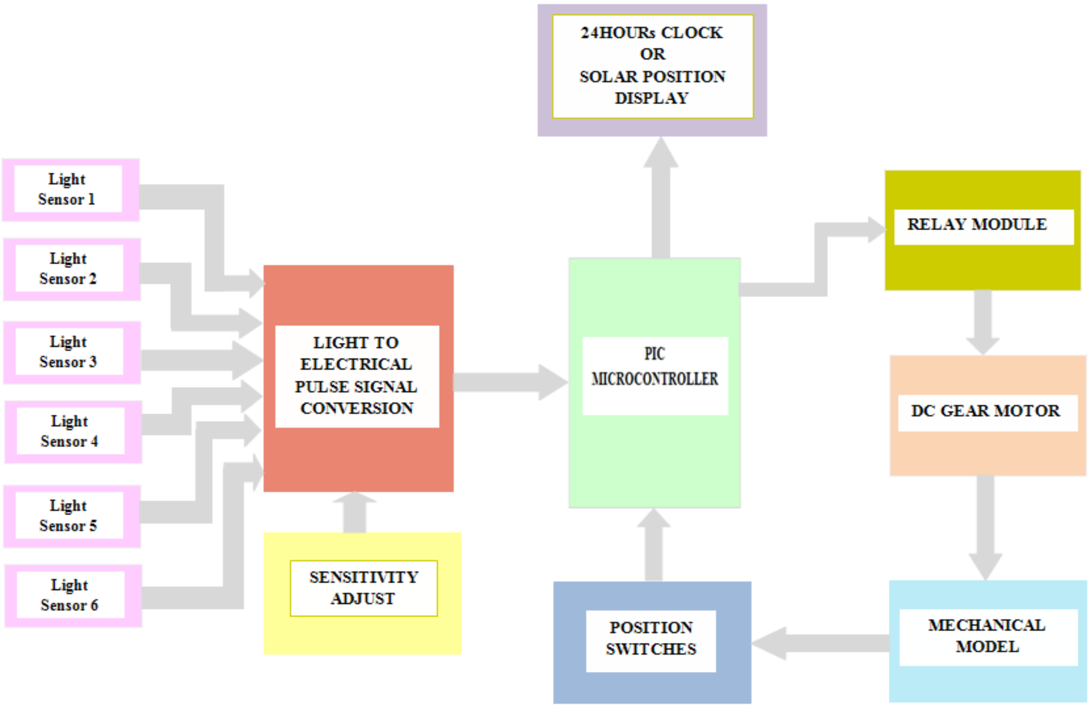

Figure 1 Block diagram of the intensity based solar tracking system.

Fundamentals, Materials & Methods

Solar Tracker Fundamentals

A solar tracker is a device that is used to align a single P.V module or an array of modules with the sun. Although trackers are not a necessary part of a P.V system, their implementation can dramatically improve a system's power output by keeping the sun in focus throughout the day. Efficiency is particularly improved in the morning and afternoon hours where a fixed panel will be facing well away from the suns rays. P.V modules are expensive and in most cases the cost of the modules themselves will outweigh the cost of the tracker system. Additionally a well designed system which utilizes a tracker will need fewer panels due to increased efficiency, resulting in a reduction of initial implementation costs.

Types of Solar Trackers

There are many different types of solar tracker which can be grouped into single axis and double axis models.

Single Axis Trackers: Single axis solar trackers can either have a horizontal or a vertical axle. The horizontal type is used in tropical regions where the sun gets very high at noon, but the days are short. The vertical type is used in high latitudes (such as in UK) where the sun does not get very high, but summer days can be very long. These have a manually adjustable tilt angle of 0 - 45 °and automatic tracking of the sun from East to West. They use the PV modules themselves as light sensor to avoid unnecessary tracking movement and for reliability. At night the trackers take up a horizontal position.

Dual Axis Trackers: Double axis solar trackers have both a horizontal and a vertical axle and so can track the Sun's apparent motion exactly anywhere in the world. This type of system is used to control astronomical telescopes, and so there is plenty of software available to automatically predict and track the motion of the sun across the sky. Dual axis trackers track the sun both East to West and North to South for added power output (approx 40% gain) and convenience. [Gay, CF; Wilson, JH & Yerkes, JW, 1982]

Hardware Components Required For the System

PV Panel: Solar panel absorbs the energy from the sunlight and convert it in to heat or electricity. A 12volts, 10 Watts Solar panel is used for this system. Four LDR’s are place on the four sides of the solar panel and another two LDR are placed at the bottom of solar panel to generate output that will be applied to the microcontroller.

Photosensor (LDR) : A photo sensor or light-dependent resistor (LDR) or photocell is a light controlled variable resistor. In the dark, a LDR can have a resistance as high as a few megaohms (MΩ), while in the light, a LDR can have a resistance as low as a few hundred ohms. Light dependent resistor OPR12 is used in the System. It is a photoconductive cadmium sulphide cell and its output is connected to the Analog input of the Microcontroller. The change in the resistance in the LDR is converted in to changes in output voltage that can be sensed by analog input of the microcontroller. Schematic symbol and voltage divider circuit of a LDR is shown in Figure 2.[Scherz P]

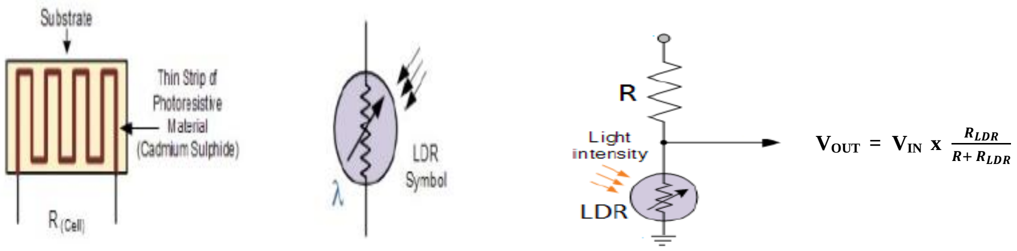

$$V_{OUT} = V_{IN} \times \frac{R_{LDR}}{R + R_{LDR}}$$

(a) (b)

Figure 2 (a) Schematic symbol of a photo resistor. (b) Voltage divider using LDR.

Control Unit : The PIC 16F887A microcontroller with FLASH memory has been used in this system because data are retained even when the power is switched off. Its features are the PIC16F887 incorporates 256 bytes of EEPROM data memory, 368 bytes of RAM, and program memory of 8K. Apart from self-programming capability, it also contains 2 Comparators, 10-bit Analog-to-Digital (A/D) converter with 14 channels, and capture, compare and PWM functions. Pin connection diagram of a PIC 16F887A microcontroller IC is shown in Figure 3. [Bates, Martin P]

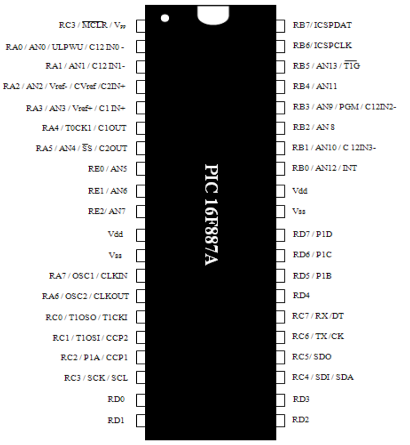

Figure 3 Pin connection diagram of a PIC 16F887A microcontroller IC.

DC Gear Motor : DC Gear Motor is used for the suggested system. This motor will rotate the Solar panel according to the Sun’s maximum intensity position. The specifications of DC Gear Motor used in this system are shown in Table 1.

Table 1 Specifications of DC Gear Motor used in this system

Voltage	**12 V**
Continuous Current	0.5 A
Output Power	7 W
Torque	100
Speed (RPM)	3800 RPM

Relay circuit using in DC Motor’s direction control : A relay based DC motor controller works with an H-bridge arrangement. With an H-bridge circuit, the polarity across a load can be altered in both directions.

Power Supply Unit: The regulated +5V , dc power supply is used for DC motor driver and microcontroller units. The voltage regulator IC 7805 is applied in this power supply unit. The line voltage 220V, ac is transformed to 12V,ac by using 12V ac step-down transformer. Step-down ac voltage is converted to unregulated dc voltage by using full wave rectifier and filter circuit. This dc voltage is applied to DC gear motor.

Software and System Design

The program for the intensity based solar tracking system is written in CCS C language. The C program is converted into machine code (HEX code) by using MPASM assembler. After converting the HEX code, MPLAB simulation is essentially needed to execute properly for the source code. The window of simulation on program execution is shown in Figure 4. The HEX code is downloaded into the MCU by the use of the programmer circuit.

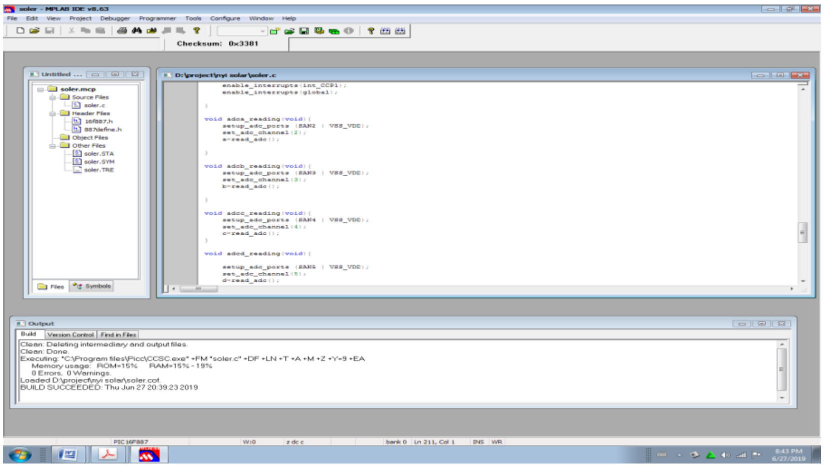

```
    enable_interrupts(int_CCP1);
    enable_interrupts(global);

}

void adca_reading(void){
    setup_adc_ports (SAN2 | VSS_VDD);
    set_adc_channel(2);
    a=read_adc();

}

void adcb_reading(void){
    setup_adc_ports (SAN3 | VSS_VDD);
    set_adc_channel(3);
    b=read_adc();

}

void adcc_reading(void){
    setup_adc_ports (SAN4 | VSS_VDD);
    set_adc_channel(4);
    c=read_adc();
}

void adcd_reading(void){

    setup_adc_ports (SAN5 | VSS_VDD);
    set_adc_channel(5);
    d=read_adc();
```

```
Clean: Deleting intermediary and output files.
Clean: Done.
Executing: "C:\Program files\Picc\CCSC.exe" +FM "soler.c" +DF +LN +T +A +M +Z +Y=9 +EA
    Memory usage:   ROM=15%     RAM=15% - 19%
    0 Errors,  0 Warnings.
Loaded D:\project\nyi solar\soler.cof.
BUILD SUCCEEDED: Thu Jun 27 20:39:23 2019
```

Figure 4 The window of simulation on program execution

The simulation window of the intensity based solar tracking system is illustrated in Figure 5. The type of microcontroller used in this circuit is PIC16F887A. This type of microcontroller has 14 ADC channel, and four channels (AN2, AN3, AN4, AN5) are used to read the analog signal of the cadmium sulfide (CdS) photocells, the photocell sensors are used to measure light intensity. The two horizontal LDR 1&2 are used for azimuth sensing and the two vertical LDR 3&4 are used for the declination sensing. Remaining two LDRs, LDR 5&6 are parallel with LDR 3&2. Position limit switches (S1 through S2) are connected to Port C (RC4 through RC7) of PIC 16F887A.It is used to limit the solar tracker position. Relay module is connected to Port C (RC0 through RC3). RC0 and RC1are used to control the solar panel azimuth motion and RC2 and RC3 are declination motion. These outputs (RC0 through RC3) are used to control the relay module. The outputs of the relay module control the two DC gear motors. Two DC gear motors are used to achieve maximum power output of the intensity based solar tracking system. The purpose of relay module circuit is to achieve DC gear motor control in two directions. Four seven segment LED display is used to display the 24 hour clock or solar panel position. Microcontroller output PORT B (RB0 through RB7) is connected to four seven segment (LED display segment) and PORT D output (RD4 through RD7) is used for digit control. Three push button switches (S5 through S7) are setting adjust, hour adjust and minute adjust. These three switches are also used to control the solar tracker position.

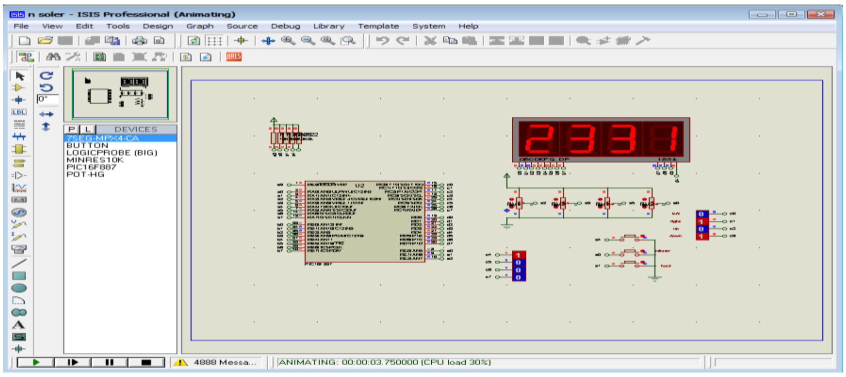

Figure 5 Simulation window of the intensity based solar tracking system.

The sequence for tracking algorithm main program of the intensity based solar tracking system for this project is illustrate in the flow chart(Figure 6) below.

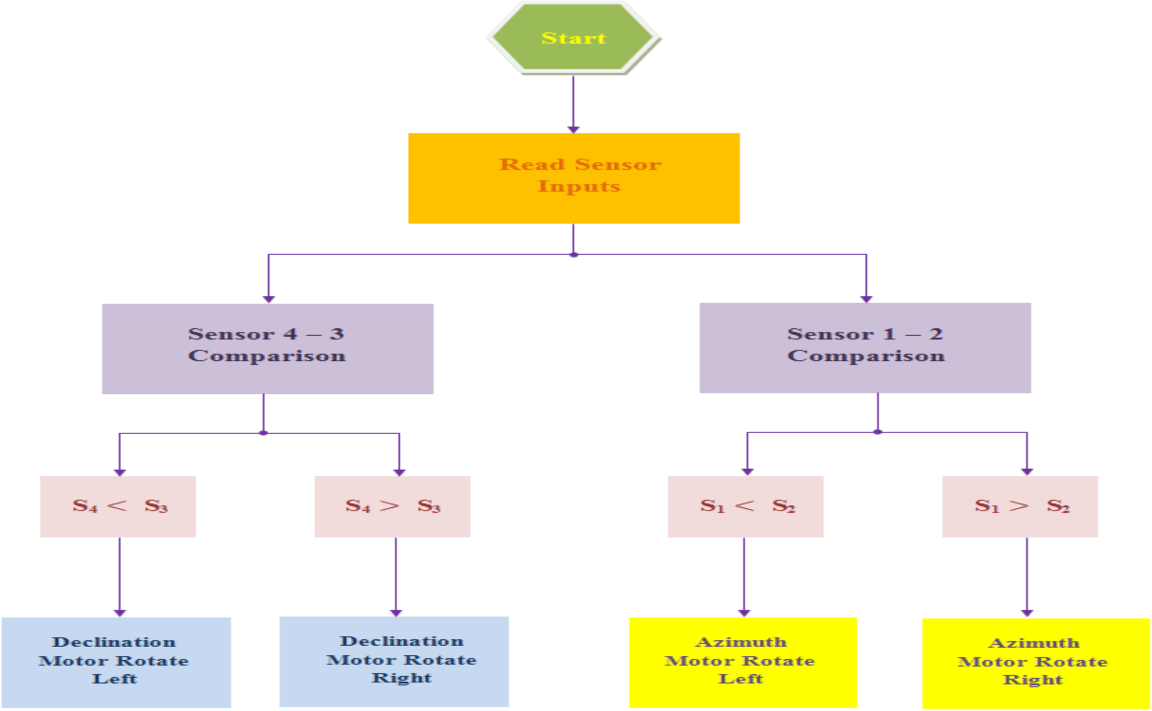

Figure 6 Flowchart of tracking algorithm for intensity based solar tracking system.

Results and Discussion

When sun light exposes to the solar panel, the angle at which the sun's rays meet the surface of the solar panel determines how well the panel convert the incoming light into electricity. The narrower the angle, the more energy a PV panel can produce. Solar tracker helps to minimize this angle by working to orient the panel, so that light strikes them perpendicular to this surface. The intensity of the sun light varies with time and location. The sun position can be tracked based on intensity of sun light and the power generating capability can be increased. This research paper describes the solar tracking system with 2 degree of freedom (dual axis solar tracker). This type of solar tracking system is designed to maximize solar energy collection throughout the year. It can track seasonal variations (north-south motion) in the height of the sun in addition to normal daily (east- west) motion of the sun.

Testing setup

Testing setup for intensity based solar tracking system is shown in Figure 7. LDR's placed at the solar panel detects the light intensity and based on the output, microcontroller will give the pulse to the driver circuit of motor .Based on the intensity, the DC geared motor drive the solar panel towards the maximum intensity position. The complete setup was exposed to the sunlight to check the operation of the system. Quantity of sunlight that reaches the solar panel is detected by LDR placed at the panel. Panel gets activated by the DC gear motor in response to the output of LDR, so that the panel aligned with sun's direction. This operation will be done by completing the three stages. The first stage was conversion of luminous intensity in to electrical signal (Voltage). The second stage that controls the actuation and decision making is made here. Movement of the panel using a DC gear motor was done at the last stage that is driver stage.

LDRs are used as Light sensors because its resistance varies with light. Microcontroller receives the voltage from the LDR and it activated the motor so that panel gets aligned. DC gear motors are used in this system because this motor will provide high torque, high precision and high speed.

Figure 7 Testing setup for intensity based solar tracking system

Testing of the System and Results

The designed solar tracking system was tested from morning 8 AM to 5 PM. The variation of the intensity of sunlight offers the several output voltages and currents throughout a day. The power output and varying intensity of the solar tracking system are listed in the following table 2.

Table 2 Measured Output of the solar tracking system versus intensity of the light

Time	Intensity of light (lx)	Output Voltage (V)	Output Current (A)	Output Power (W)
8:00 AM	2156	12.2	0.31	3.782
	1496	11.5	0.23	2.645
	1250	10.7	0.19	2.033
Average	1634	11.5	0.24	2.790
9:00 AM	2874	12.9	0.28	3.623
	2324	12.6	0.25	3.140
	1845	11.9	0.2	2.380
Average	2348	12.5	0.24	3.034
10:00 AM	3865	13.6	0.34	4.621
	2940	13.2	0.28	3.688
	2100	12.8	0.20	2.550
Average	2968	13.2	0.27	3.600
11:00 AM	4012	14.0	0.39	5.452
	3655	13.6	0.36	4.885
	3565	13.5	0.33	4.439
Average	3744	13.7	0.36	4.920
12:00 Noon	4562	14.9	0.4	5.952
	4950	15	0.39	5.733
	4876	15	0.39	5.967
Average	4796	15	0.39	5.884
1:00 PM	3690	14	0.36	4.855
	3420	13	0.33	4.422
	3374	13	0.33	4.369
Average	3495	13	0.34	4.547
2:00 PM	3565	13.6	0.34	4.610
	3542	12.5	0.3	3.750
	2712	12	0.26	3.120
Average	3273	12.7	0.3	3.806
3:00 PM	2871	10.5	0.26	2.730
	2341	9.2	0.25	2.308
	2540	9.6	0.25	2.400
Average	2584	9.8	0.25	2.790
4:00 PM	2421	9.5	0.23	2.185
	2300	9.0	0.20	1.800
	2240	8.6	0.20	1.720
Average	2320	9.0	0.21	1.897
5:00 PM	2343	8.5	0.20	1.700
	2240	7.4	0.18	1.332
	1548	6.1	0.17	1.037
Average	2044	7.3	0.18	1.344

Comparative Analysis

Comparative analysis was made between fixed axis solar system and dual axis solar tracking system. The results are given in Table 3. Figure.8 shows the relation between intensity of light and output power of the comparison results of dual and fixed axis solar system..

Table 3 Comparison results of the dual axis and fixed axis solar system

Dual Axis Solar Tracker			Fixed Axis Solar System		
Time	Intensity of Light (lx)	Output Power (W)	Time	Intensity of Light (lx)	Output Power (W)
8:00 AM	1634	2.79	8:00 AM	550	0.45
9:00 AM	2348	3.034	9:00 AM	1548	1.275
10:00 AM	2968	3.6	10:00 AM	2240	1.62
11:00 AM	3744	4.92	11:00 AM	2324	3.12
12:00 Noon	4796	5.884	12:00 Noon	3365	4.05
1:00 PM	3495	4.547	1:00 PM	3754	3.900
2:00 PM	3273	3.806	2:00 PM	2230	2.3
3:00 PM	2584	2.79	3:00 PM	880	0.98
4:00 PM	2320	1.897	4:00 PM	550	0.55

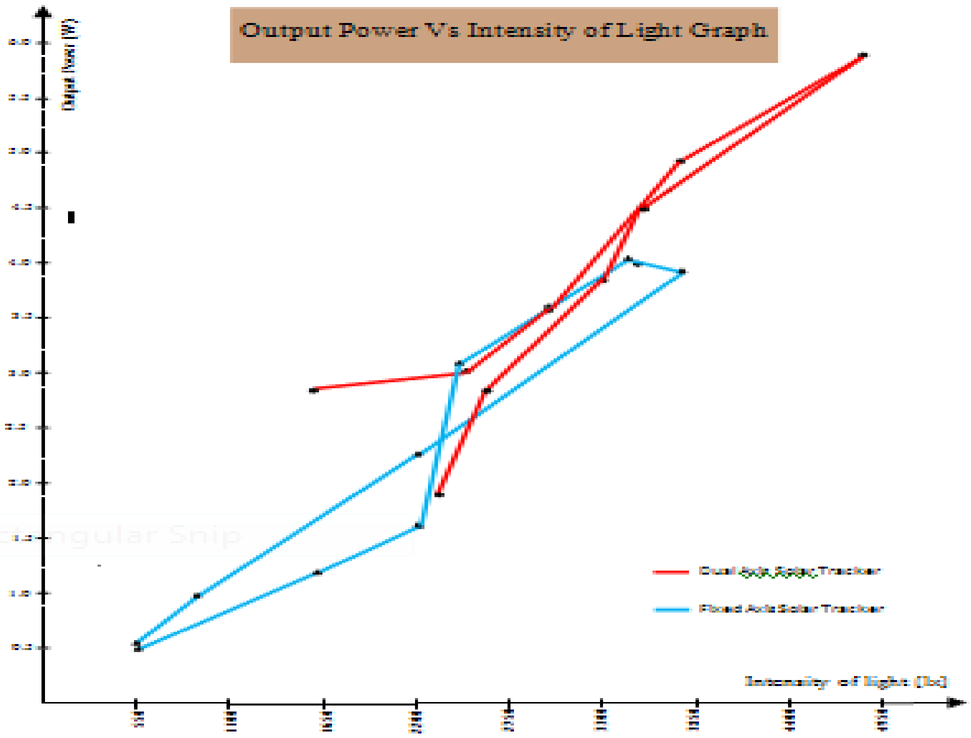

Figure 8 The relation between intensity of light and output power of the comparison results of dual and fixed axis solar system..

Average power output for the fixed tracking is 1.83 W whereas with tracker, it is 3.45 W. The suggested system produces more power (47%) than the fixed axis solar tracking system.

Conclusion

Intensity based solar tracking system (dual axis solar tracker) using PIC microcontroller has been proposed in this paper. The performance of the dual axis solar tracking system is better than static and because it saves the losses of the intensity of sun rays due to daily and seasonal variation in the sun's path. No matter where the sun is in the sky, dual axis trackers are able to angle themselves to be in direct contact with the sun. At high latitude locations, where the sun's position in the sky varies dramatically between summer and winter months, this solar system gives benefits to maximize the solar production and collect enough power for proper usage. An efficient and accurate DC gear motor control system is used to increase the efficiency of the system and reduce the cost. The system is completely automatic and maintenance cost is also less. This system can be designed to accommodate more number of panels so that the power output can be increased in future.

Acknowledgement

I am greatly indebted to Associate Professor Dr. Yee Yee Oo, Head of the Engineering Physics Department, Technological University (Maubin) due to her permission to undertake this piece of research. I am also extremely greatful to Dr. Ni Ni Win, Associate Professor, Physics Department, Magway University for her helpful suggestions during the preparation of this paper. I would like to especially thank to U Nyi Nyi Win for his guidance and kind help throughout this work.

References

Bates, Martin P "Programming 8-bit PIC Microcontrollers in C with interactive Hardware Simulation", (www.pic micros.org.UK).

Gay, CF; Wilson, JH & Yerkes, JW (1982) "Performance advantages of two-axis tracking for large flat plate photovoltaic energy systems". Conf. Rec. IEEE Photovoltaic Spec. Conf.16:1368.

Macagnan MH, F Lorenzo and C Jimenez. "Solar Radiation.(1994)" Midrib International Journal of Solar Energy, vol 16.

Saxena AK and V Dutta, "A Versatile Microprocessor based Controller for Solar Tracking Photo Voltaic Specialist" Twenty first Conference of IEEE, vol 2.

Scherz P," Practical Electronics for Inventors", Copyright 2000 The Mc Graw-Hill Companies, Inc.

J. Myanmar Acad. Arts Sci. 2020 **Vol. XVIII.No.2C**

DETERMINATION OF DENSITY DISTRIBUTION AND ROOT MEAN SQUARE RADII FOR LIGHT NUCLEI USING WOOD-SAXON AND HARMONIC OSCILLATOR POTENTIAL

Tin Mar Yu[1,] Khin Swe Myint[2]

Abstract

The main purpose of this study is to investigate the nuclear charge density distribution corresponding proton, charge, neutron, matter and root mean square radii for light nuclei such as ^{4}He, ^{12}C and ^{16}O. A detail series of calculations were carried out using the single particle reduced radial wave function and radial wave function by **Numerov method**. The density distributions and root mean square radii of neutron, proton, matter and separation energies for stable nuclei have been calculated by using Woods-Saxon potential and Harmonic- Oscillator potential with **FORTRAN LANGUAGES**. In order to compare the calculated results of density distributions, root mean square radii and separation energies for light nuclei with the experimental data and other literatures.

Keywords: Stable nuclei, density distributions, root mean square radii, separation energies, Woods-Saxon and Harmonic-Oscillator potential.

Introduction

The radial distribution of nuclear charge, matter and the spatial extant of atomic nuclei have received great attention. They are important to explore sizes and shapes of nuclei, besides to test the validity of the nuclear single-particle wave functions used especially in density folding models. The study of nuclear neutron and proton density distributions are essential quantities in understanding both nuclear structure and reactions.

The distribution of charge density and charge radii can be measured accurately from high energy electron elastic scattering, but such scattering is so far limited to stable or long-lived isotopes, besides, the measurements of muonic X-rays transitions are precise method for determining charge radii. Information about matter density distributions are obtained from experiments on elastic hadron scattering. Harmonic Oscillator potential is not accurate to describe the nuclear central confining potential because the potential continues to give a contribution even for much larger r and does not become zero, besides the radial wave functions obtained from HO have a Gaussian fall-off behaviour at large r which does not reproduce the correct exponential tail.

Elton and Swift generated wave functions in a parameterized single-particle local potential and adjusted the parameters so as to fit the shape of the wave functions to elastic electron scattering data and the eigen energy to the proton separation energies in the 1p and 2s-1d shell nuclei. Gibson et. al. studied the ground state of the ^{4}He nucleus using the single-particle phenomenological model. Wave functions were generated from a potential whose parameters are chosen to reproduce the correct neutron separation energy. The proton separation energy, electron scattering form factors were then calculated. Brown et. al. described a new method of calculating nuclear charge and matter distributions which is complementary to the Hartree-Fock method talking into account shell method configuration mixing. Brown et. al. calculated the rms radii of valence orbits in the tin isotopes using the single-particle potential model. Lojewski et. al.

---

[1] Dr, Lecturer, Department of Physics, Defence Services Academy, Pyin Oo Lwin,

2. Rector (Rtd), emeritous Professor, Department of Physics, University of Mandalay

used realistic single-particle WS potential to evaluate the mean-square charge radii of even-even nuclei. The various parameterizations of the WS potential were examined. Schwierz et. al. established a new parameterization for the WS potential. Its six parameters are fitted to single-particle spectra around doubly magic nuclides and experimental charge radii. In the eigenvalues have been calculated using Numerov method for a Sturm-Liouville problem defined with the boundary values. Recently, Arkan has been calculated the nuclear charge density distributions, elastic charge form factors and rms charge, proton, neutron and matter radii for $^{4}\mathrm{He}$, $^{12}\mathrm{C}$, and $^{16}\mathrm{O}$ nuclei using WS and HO radial waves function using different well potential depths for WS potential for each subshell.

The Harmonic-Oscillator Potential

We know our experience with classical mechanics that a particle of mass m subject to the linear restoring force F(x)= -kx ,where k is the force constant, results in one-dimensional simple harmonic motion with an oscillation frequency $\omega = \sqrt{k/m}$. The potential that the particle moves in is quadratic $V(x) = kx^2/2$, and so in this case the potential has a minimum at position x=0. The idea that a quadratic potential may be used to describe a local minimum in an otherwise more complex potential turns out to be a very useful concept in both classical and quantum mechanics. It is assumed that the nucleons moves in an average harmonic oscillator potential given by

$$V_{HO} = \frac{1}{2} m\omega^2 r^2 \qquad (1)$$

Where m is the mass of the nucleons and ω is the oscillator frequency.

Woods-Saxon Potential

For the local potential, the Woods-Saxon shape is used in the compact form shown below

$$v(r) = v_{cent}(r) + v_{so}(r) + v_c(r) \qquad (2)$$

$$v(r) = \frac{-U_0}{\left(1+e^{\left(\frac{r-R}{a}\right)}\right)} + \left(\frac{\hbar}{m_\pi}\right)^2 \frac{1}{r}\frac{U_{so}}{a_{so}} \frac{e^{\left(\frac{r-R_{SO}}{a_{SO}}\right)}}{\left(1+e^{\left(\frac{r-R_{SO}}{a_{SO}}\right)}\right)} \left\langle \hat{\ell}, \hat{\sigma} \right\rangle + v_c(r) \qquad (3)$$

The Woods-Saxon potential equation contains three parts, they are central potential, spin-orbit potential and coulomb potential.

Central Potential

The central potential equation can be written as

$$v_{cent}(r) = \frac{-U_0}{\left(1+e^{\left(\frac{r-R}{a}\right)}\right)} \qquad (4)$$

Where,

$\nu_{\text{cent}}(\text{r})$ = the central potential

U_0 = the strength or depth of the central potential

a = the diffuseness of central potential

Spin-Orbit Potential

Spin-orbit splitting of nuclei is one of the main factors which determine nuclear structure in nuclei both near and far from the closed shells. Spin and orbit refer to the attributes of a single nucleon moving in an averaged potential well. Spin-Orbit splitting in atoms is due to the magnetic interaction of the magnetic dipole moment of the electron spin and the magnetic field experienced by the electron in its rest frame as it moves through the Coulomb field of the nucleus. A nucleon moving in the central potential of the nucleus with orbital angular momentum ℓ, spin s and total angular momentum j,

$$\vec{\ell}.\vec{\text{s}} = \frac{1}{2}\ell \qquad \text{for } \text{j} = \ell + \frac{1}{2} \tag{5}$$

$$\vec{\ell}.\vec{\text{s}} = -\frac{1}{2}(\ell + 1) \quad \text{for } \text{j} = \ell - \frac{1}{2} \tag{6}$$

The splitting due to the spin-orbit interaction is larger for higher values of orbital angular momentum, and can consequently produce level crossing. For large angular momentum (ℓ), the splitting of any two neighbouring degenerate levels can shift the j= ℓ+1/2 state of the initially lower level to lie above the j= ℓ-1/2 state of the previously higher level.

$$\nu_{so}(r) = -2\left(\frac{\hbar}{m_\pi c}\right)^2 \frac{U_{so}}{r}\frac{d}{dr}\frac{1}{\left(1+e^{\left(\frac{r-R_{SO}}{a_{SO}}\right)}\right)}\left\langle\hat{\ell},\hat{\sigma}\right\rangle = 2\left(\frac{\hbar}{m_\pi c}\right)^2 \frac{U_{so}}{ra}\frac{e^{\left(\frac{r-R_{SO}}{a_{SO}}\right)}}{\left(1+e^{\left(\frac{r-R_{SO}}{a_{SO}}\right)}\right)^2}\left\langle\hat{\ell},\hat{\sigma}\right\rangle \tag{7}$$

Where,

$$\left(\frac{\hbar}{m_{\pi c}}\right)^2 \approx 2.0 \text{ fm}^2$$

U_{so} = the strength or depth of the spin-orbit potential

a_{so} = the diffuseness of central potential

R_{so} = the radius parameter of spin-orbit

$\hat{\ell}$ = angular momentum

$\hat{\sigma}$ = spin operator

Coulomb Potential

The Coulomb potential part of WS potential

$$\nu_c(r) = \begin{cases} (Z-1)\dfrac{e^2}{r} & \text{if} \quad r > R_c \\ \dfrac{(Z-1)e^2}{2R}\left[3 - \dfrac{r^2}{R^2}\right] & \text{if} \quad r < R_c \end{cases} \tag{8}$$

Where $\nu_c(r)$ = 0 for neutrons, with e^2 = 1.44MeV

Configuration for light nuclei (^{4}He, ^{12}C and ^{16}O)

The nuclide contains protons and neutrons. According to shell configuration, the terms of protons and neutrons are represented by the following equation. The configuration of protons is $\left(1s_{\frac{1}{2}}\right)^2$ and the configuration of neutrons is $\left(1s_{\frac{1}{2}}\right)^2$ for ^{2}He. The configuration of protons is $\left(1s_{\frac{1}{2}}\right)^2$ $\left(1p_{\frac{3}{2}}\right)^4$ the configuration of neutrons is $\left(1s_{\frac{1}{2}}\right)^2\left(1p_{\frac{3}{2}}\right)^4$ for ^{12}C. The configuration of protons is $\left(1s_{\frac{1}{2}}\right)^2\left(1p_{\frac{3}{2}}\right)^4\left(1p_{\frac{1}{2}}\right)^2$ The configuration of neutrons is $\left(1s_{\frac{1}{2}}\right)^2\left(1p_{\frac{3}{2}}\right)^4\left(1p_{\frac{1}{2}}\right)^2$ for ^{16}O.

The reduced radial wave function of two body Schrödinger equation

The Schrodinger wave equation can be expressed as the following.

$$\left(\frac{\hbar^2}{2\mu}\frac{d^2}{dr^2} - V(r) - \ell(\ell+1)\frac{\hbar^2}{2\mu r^2} + E_{nlj}\right)R_{nlj}(r) = 0 \tag{9}$$

This equation is the Schrödinger equation for the single-particle radial wave function .Where μ is the reduce mass of the core (A-1) and single nucleon, m is the mass of nucleon, A is the atomic mass, E_{nlj} is the single nucleon separation energy, $R_{nlj}(r)$ is the radial eigenfunction of the system and n, ℓ and j are the principal, orbital angular and total angular quantum numbers. Single particle energy level of a nucleon moving in a potential well is determined by using the Numerov method. The Schrödinger radial equation is given by

Where, $R_{nlj} = \dfrac{U(r)}{r}$ is the radial wave function. (10)

Separation Energies, Density Distributions and Roots-Mean Square Radii of the Light Nuclei

The energy required to remove the last neutron from the nucleus is called the separation energy of the last neutron. If a neutron is removed from a nuclide (Z, N), a nuclide (Z, N-1) is obtained. The energy needed for removal the last neutron is the difference in binding energies between these two nuclides. According to the shell model the last neutron separation energy is the binding energy of the outermost filled level of a nucleus.For light nuclei, the calculated orbitals are in angular momentum states. In $^4_2$He, $1S_{1/2}$ orbit is found. In $^{12}_6$C nuclei, $1s_{1/2}$, $1P_{3/2}$

and in $^{16}_{8}O$, $1s_{1/2}$, $1P_{3/2}$, $1P_{1/2}$ orbits are found. This kind of single particle orbits cannot be seen in ordinary nuclei. There are calculated the parameters for central potential, spin-orbit potential, centrifugal potential and Coulomb's potential term with Woods-Saxon potential. The values are shown in Table (1).

To understand the structure of the nuclei we have determined the root-mean square radius and charge density distribution. The root-mean square radius of the nucleus $\langle r^2 \rangle^{\frac{1}{2}}$ is defined as

$$\langle r^2 \rangle^{\frac{1}{2}}_{n,p,ch,m} = \sqrt{\frac{4\pi}{X} \int U^*(r) U(r) r^2 dr} \qquad (11)$$

The calculated results of physical quantities are shown in table (2). The density distribution of the nuclei is defined as the following equation,

$$\rho(r) = \int |R_{nl}|^2 r^2 dr = \int \left| \frac{U(r)}{r} \right|^2 r^2 dr \qquad (12)$$

Therefore, the point density distribution of neutrons, protons and matter can written respectively as;

$$\rho_{n,p\,or\,m}(r) = \frac{1}{4\pi} \sum_{n\ell j} X^{n\ell j}_{n,p\,or\,m} \left| R_{n\ell j}(r) \right|^2 \qquad (13)$$

Where $X^{n\ell j}_{n,p\,or\,m}$ represented the number of neutrons, protons or nucleons in the $n\ell j$ -subshell.

Results and Discussion

In this research work, the nuclear shell model is used to calculate the charge density distribution and rms radii for ^4He, ^{12}C and ^{16}O nuclei. The harmonic oscillator and Woods-Saxon potentials are used to regenerate the radial wave function and reduced radial wave function. It was calculated the CDD' s by using reduce radial wave function and also rms radii by using reduced radial wave function for ^4He, ^{12}C and ^{16}O nuclei. In the present work, light nuclei have the following configurations, $(1S_{1/2})^2$ state are used for ^4He, $(1S_{1/2})^2$, $(1P_{3/2})^4$ for ^{12}C, $(1S_{1/2})^2$, $(1P_{3/2})4$ and $(1P_{1/2})^2$ for ^{16}O nuclei. The diffuseness parameters chosen for WS potential of light nuclei as shown in Table (1). The results for the calculated single nucleon separation energies for ^4He, ^{12}C and ^{16}O nuclei of different sub-shells are shown in Table (2). The experimental charge rms radii and calculated rms radii for neutron and proton in light nuclei ^4He, ^{12}C and ^{16}O are displayed in Table (3). The calculated charge density distributions are depicted in Fig (1) to Fig (3) for ^4He, ^{12}C and ^{16}O nuclei. Comparison of charge density distributions are illustrated in Fig (4) for investigated nuclei.

Table 1 The WS parameters U_o, $U_{s.o}$, a_o, $a_{s.0}$, r_o, $r_{s.o}$ and R_c for ^{4}He, ^{12}C and ^{16}O nuclei.

Nucleus	**nl$_j$**	**U$_o$(MeV)**	**U$_{s.o}$(MeV)**	**a$_o$(fm)**	**a$_{s.o}$(fm)**	**r$_o$(fm)**	**r$_{s.o}$(fm)**	**R$_c$(fm)**
N	$1s_{1/2}$	56.70	15.0	0.1	0.01	1.350	1.350	0.0
P	$1s_{1/2}$	56.53	15.0	0.01	0.01	1.333	1.333	0.0
^{12}C								
N	$1s_{1/2}$	59.76	15.0	0.527	0.527	1.236	1.236	0.0
	$1p_{3/2}$	59.10	15.0	0.527	0.527	1.236	1.236	0.0
P	$1s_{1/2}$	60.05	15.0	0.518	0.518	1.230	1.230	1.23
	$1p_{3/2}$	59.21	15.0	0.518	0.518	1.230	1.230	1.23
^{16}O								
N	$1s_{1/2}$	51.0827	15.0	0.5	0.5	1.375	1.375	0.0
	$1p_{3/2}$	50.1804	15.0	0.5	0.5	1.375	1.375	0.0
	$1p_{1/2}$	52.4350	15.0	0.5	0.5	1.375	1.375	0.0
P	$1s_{1/2}$	50.6656	15.0	0.5	0.5	1.375	1.375	1.375
	$1p_{3/2}$	50.3532	15.0	0.5	0.5	1.375	1.375	1.375
	$1p_{1/2}$	52.4822	15.0	0.5	0.5	1.375	1.375	1.375

Table 2 Calculated ($E_{calculted}$) and ($E_{experiment}$) single neutron and proton separation energies for nlj subshells for ^{4}He, ^{12}C and ^{16}O.

^{4}He	**nl$_j$**	**E $_{experiment}$(MeV)**	**E $_{calculated}$(MeV)**
n	$1s_{1/2}$	20.5776	20.7538
p	$1s_{1/2}$	19.8139	19.7523
^{12}C			
n	1s1/2	34.03	34.05
	1p3/2	18.72	18.74
p	$1s_{1/2}$	30.9	30.65
	$1p_{3/2}$	15.75	15.70
^{16}O			
n	1s1/2	34.03	34.04
	1p3/2	21.81	21.83
	1p1/2	15.65	15.68
p	1s1/2	29.81	29.66
	$1p_{3/2}$	18.44	18.34
	$1p_{1/2}$	12.11	11.90

Table 3 The value of rms radii in (fm) with corresponding available literature data.

Nucleus	**literature** $\langle r^2\rangle_n^{\frac{1}{2}}$	**Exp.** $\langle r^2\rangle_{ch}^{\frac{1}{2}}$	**Calculated** $\langle r^2\rangle_p^{1/2}$	**Calculated** $\langle r^2\rangle_n^{\frac{1}{2}}$
^{4}He	WS:1.704	1.676	WS:1.714	WS:1.704
	HO:1.659		HO:1.577	HO:1.676
^{12}C	WS:2.316	2.464	WS:2.501	WS:2.399
	HO:2.287		HO:2.390	HO:2.291
^{16}O	WS:2.589	2.737	WS:2.698	WS:2.578
	HO:2.458		HO:2.670	HO:2.412

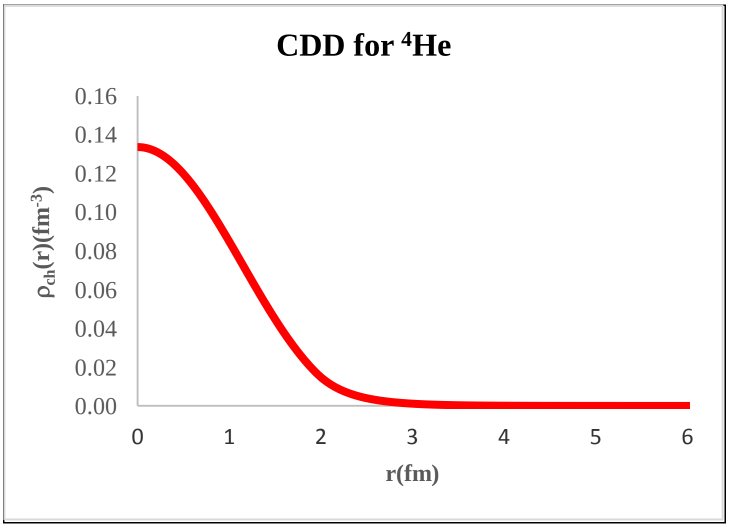

Figure 1 CDD's for nlj state in ^{4}He nucleus.

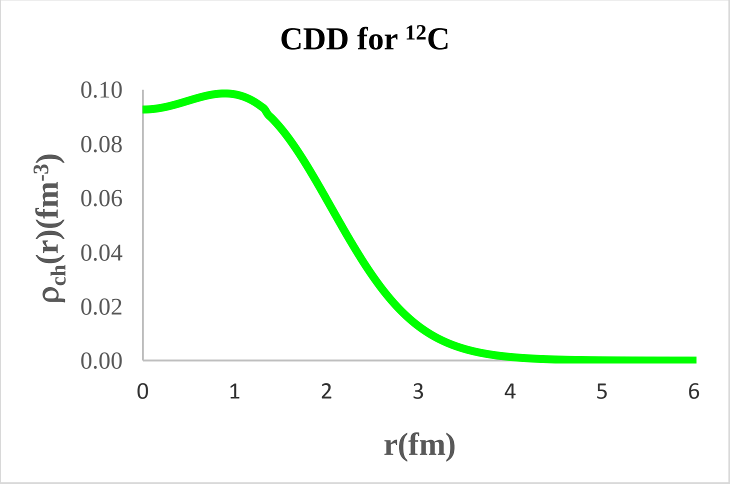

Figure 2 CDD's for nlj state in ^{12}C nucleus with WS potential.

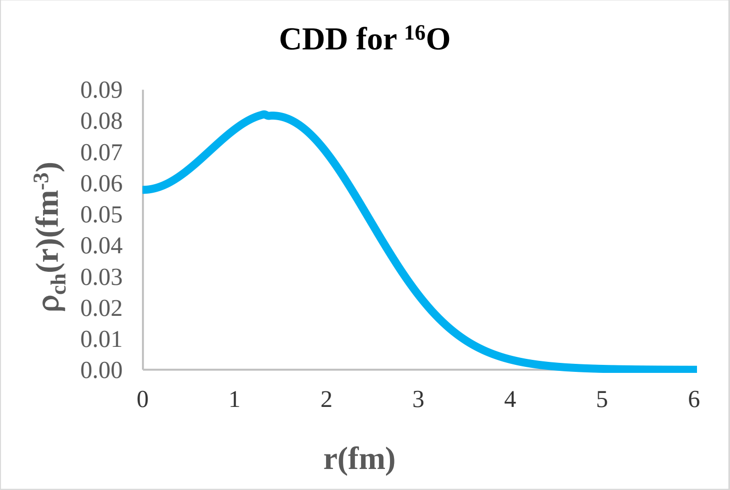

Figure 3 CDD's for nlj state in ^{16}O nucleus with WS potential.

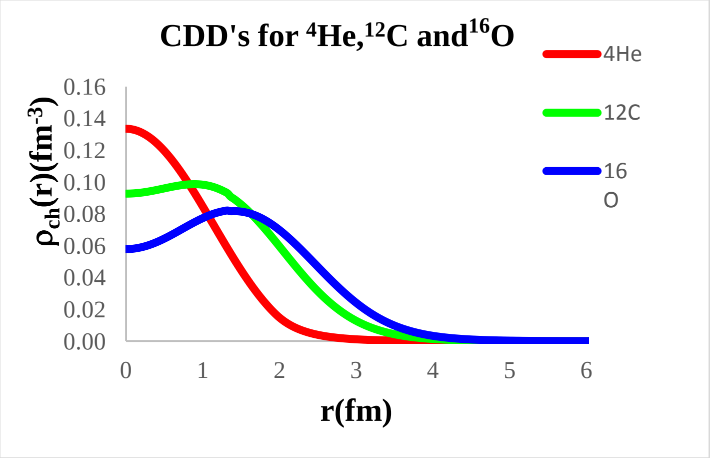

Figure 4 Comparison of CDD's for nlj state in ^{4}He ,^{12}C and^{16}O nucleus with WS potential.

Conclusions

For the calculated CDD's and root mean square radii, the result of Woods-Saxon potential are much better than harmonic oscillator potential in ^{4}He, ^{12}C and ^{16}O nuclei. The calculated results of separation energies for consider nuclei obtained by WS potential are in very good agreement with experimental data. It can be seen that the tightly bound in ^{4}He nucleus and loosely bound at the surface of ^{16}O nucleus

Acknowledgements

I would like special thanks to Rector of Defence Services Academy, Brigadier General Thein Lwin, for his kind permission and encouragement.

The author also wishes to extend his thanks to Lieutenant Colonel Saw Myint Oo, Dean of Faculty of Physics at Defence Services Academy, for his valuable suggestion. I wish to extend my gratitude to person, Lieutenant Colonel Kyaw Htay Naing, Associate Professor, Head of Department of Nuclear Physics, Defence Services Academy for giving comments and suggestions. I am deeply indebted to my Supervisor, Dr Khin Swe Myint, Rector(Rtd), emeritous Professor, Physics Department, Mandalay University for their valuable guidance.

References

Brown B.A, S. E.Massen, and P. E. Hodgson, (1979) "Proton and neutron density distributions for A=16-58 nuclei", Journal of Physics G. 5, 1655-1698.

Elton L. R. B. and A. Swift, (1967) "Single-particle potentials and wave functions in the 1p and 2s-1d shells", Nuclear Physics A. 94, 52-72.

Fatah A. H., (2012) Calculation of the eigenvalues for Wood-Saxon's potential by using Numerov method, Advances in theoretical and applied mechanics, 5, 23-31.

Gibson B. F., A. Goldberg, and M. S.Weiss, (1968) "Single-particle ground-state model of ^{4}He", Nuclear Physics A. 111, 321-330.

Lojewski Z., B. Nerlo-Pomorska, and K. Pomorski, (1995) "Mean square radii of nuclei calculated with the Woods-Saxon potential", Physical Review C. 51(2), 601-605.

Owen A. S., B. A.Brown, and P. E. Hodgson, (1981) "Nucleon orbit radii in tin isotopes", Journal of Physics G: Nuclear Physics, **7**, 1057-1061.

Ridha A. R., (2016) "Study of charge density distributions, elastic charge form factors and root-mean square radii for ^{4}He, ^{12}C and ^{16}O nuclei using Woods-Saxon and harmonic-oscillator potentials", Iraqi Journal of physics, 14, 42-50.

Schwierz N., I. Wiedenhover, and A. Volya, (2007) "Parametrization of the Woods-Saxon potential for shell-model calculations", arxiv: nucl-th/0709.3525v1, 1-19**,** 21 Sep.

Wang, M., G. Audi, A.H. Wapstra, F.G. Kondev, M. MacCormick, X. Xu and B. Pfeiffer,(2012) The AME 2012 Atomic Mass Evalution.

J. Myanmar Acad. Arts Sci. 2020 **Vol. XVIII.No.2C**

KINEMATICAL ANALYSIS OF SINGLE-Λ HYPERNUCLEI WITH NEUTRAL PARTICLE DECAY PRODUCTS IN NUCLEAR EMULSION

Htike Nandar Kyaw[1], Thida Oo[2], Hnin Yee Hlaing[3], Thinzar Myat Oo[4]

Abstract

In this research work, five single-Λ hypernuclei which were detected in nuclear emulsion of KEK-PS E373 experiment are analyzed by applying relativistic kinematics. The analyzed single-Λ hypernuclei decayed into a charged particle and invisible neutral particles. The ranges and position angles of charged particle tracks are firstly measured in nuclear emulsion. To perform kinematical analysis, both mesonic and non-mesonic decay of single-Λ hypernuclei are taken into account. The kinetic energy and momentum of charged particle decay products are extracted by range-energy relation and that of neutral particles are calculated by momentum conservation. Moreover, possible masses of single-Λ hypernuclei are deduced by mass-energy relation equation. Due to contamination of neutral particles, the single-Λ hypernuclei cannot be identified uniquely and the calculated masses are slightly less than known masses within the acceptable limit. According to our analysis, it is found that the possible species of single-Λ hypernuclei are either ${}^{3}_{\Lambda}H$ (or) ${}^{4}_{\Lambda}H$ and their decay products of charged particles are possible to be proton (or) deuteron.

Keywords: Single-Λ hypernuclei, nuclear emulsion, relativistic kinematics, decay, range-energy relation, mass-energy relation

Introduction

Hypernuclei are bound systems of nucleons with one or more hyperons which contain strange quark. Hyperons are unstable particles with a mean lifetime of the order of 10^{-10}s. In the family of hyperons, Λ is the lightest particle and it can stay in contact with nucleons inside nuclei and form hypernuclei. If a nucleus contains one Λ hyperon, it is said to be a single-Λ hypernucleus and a nucleus which made up of two Λ hyperons in addition to nucleons is called a double-Λ hypernucleus. Hypernuclei are considered to be the core of strange matter such as neutron stars that may exist in distant parts of the universe, and could allow physicists to probe the inside of the nucleus. One of the most important purposes of hypernuclear physics is to complete the knowledge of baryon-baryon interactions in a unified way. To do so, it is essential to understand the N-N, Λ-N and Λ-Λ interactions which can be extracted from ordinary nuclei, strangeness -1 hypernuclei and strangeness -2 hypernuclei. At the same time, one of the most important things for the study of strangeness hypernuclei is to identify the nuclear species and measure their masses. Observation of hypernuclei in nuclear emulsion will give significant contribution to strangeness -1 and -2 sectors of nuclear chart. Therefore, the more hypernuclei are expected and hypernuclei searching experiments are well developed.

Nuclear emulsion is a three-dimensional photographic tracking device for charged particles. A hypernucleus having the energy of a few MeV can transverse several micrometers before stopping and decaying. Hypernuclei can be identified in the emulsion by their sequential decay topology. In the year 1998, an experiment, KEK-PS E373 has been performed at High Energy Accelerator Research Organization, Japan to study strangeness hypernuclei by emulsion-

---

[1] Dr, Lecturer, Department of Physics, Defence Services Academy

[2] Dr, Lecturer, Department of Physics, Defence Services Academy

[3] Assistant Lecturer, Captain, Department of Physics, Defence Services Academy

[4] Assistant Lecturer, Captain, Department of Physics, Defence Services Academy

counter hybrid technique. It aim was to search for strangeness hypernuclei such as double-Λ hypernuclei, twin-Λ hypernuclei, single-Λ hypernuclei and H-dibaryon. During the semi-automatic emulsion scanning of KEK-PS E373 experiment, seven events of double-Λ hypernuclei, two events of twin-Λ hypernuclei and 46 events of single-Λ hypernuclei were detected among the 10^3 Ξ^- hyperon captures. Among them, observation of Nagara event is very famous and epoch-making finding because it is uniquely identified as ${}^{6}_{\Lambda\Lambda}\mathrm{He}$. The data analysing is very interesting and important to extend the strangeness nuclear chart and to complete the knowledge of baryon-baryon interaction. In this paper, five events of single-Λ hypernuclei which were detected in the nuclear emulsion of KEK-PS E373 experiment are analyzed kinematically. The analyzed events have one charged particle decay product and one or more neutral particle decay products according to the conservation laws. We will discuss about the differences between the identified mass and known experimental mass of single-Λ hypernuclei due to contamination of neutron.

Methods of Analysis

Kinematical Analysis

Analysis of strangeness hypernuclei events has a great physical interest. Since, hypernuclei consist of elementary particle hyperons, they are so small and very fast when they traverse the emulsion medium. Their velocity is nearly reaching the velocity of light, so we use relativistic kinematics to perform our analysis. Kinematical analysis is quite essential to identify the hypernucleus events which were observed in nuclear emulsion. Kinematical analysis is an analysis which is performed by using physical quantities due to particles’ motion such as range, velocity, momentum and kinetic energy, etc. After detecting the hypernucleus events in nuclear emulsion, we can measure the range and position angles of charged particle tracks only. Using the relativistic kinematics, kinetic energy, velocity, momentum, mass, binding energy and interaction energy can be derived. So many physical quantities will be obtained using the range data only. How beautiful is relativistic kinematics? We reconstructed the hypernucleus events which were observed in nuclear emulsion using the relativistic kinematics.

Characteristics of Analyzed Events

In this section, the characteristics of five single- Λ hypernuclei which observed in nuclear emulsion of KEK-PS E373 experiment are presented with the help of photograph and schematic diagram.

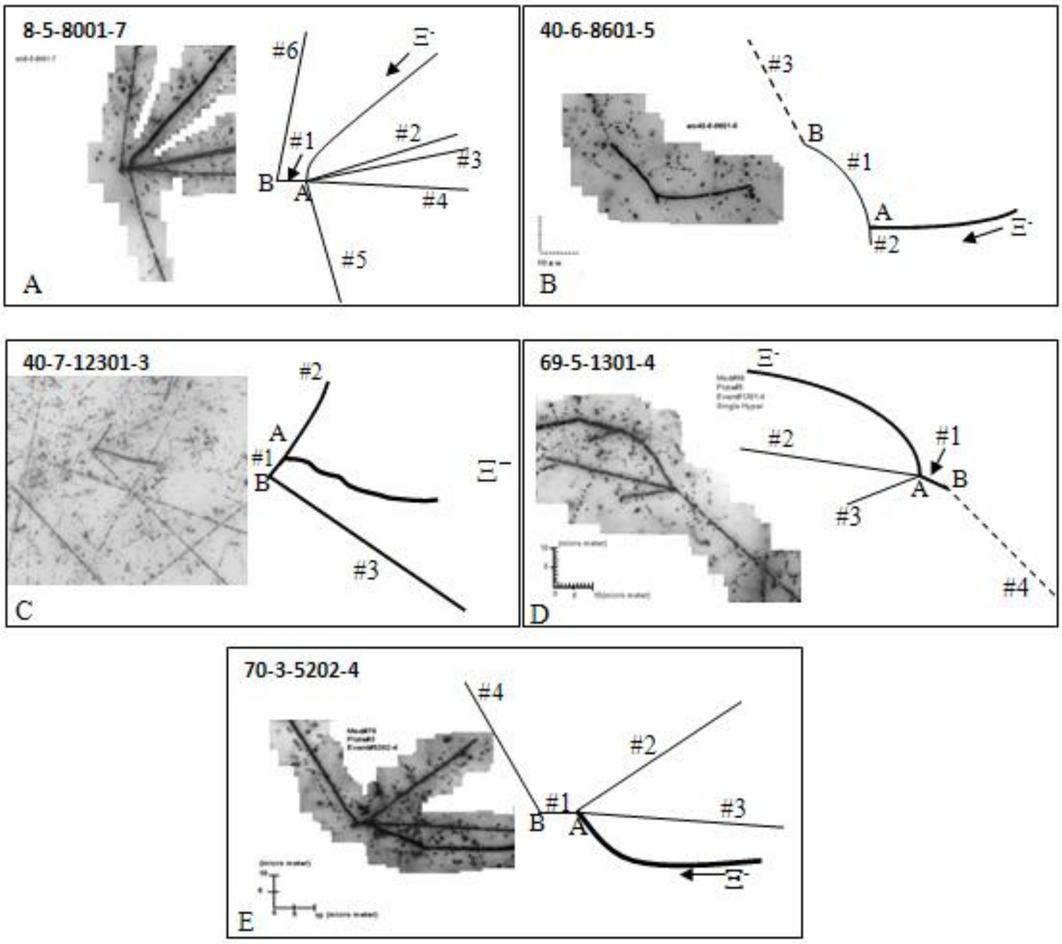

Figure 1 (A-E). Photographs and schematic diagrams of analyzed hypernuclei in nuclear emulsion of KEK-PS E373 experiment

In figure 1(A-E), a Ξ^- hyperon produced in the reaction (K^-,K^+) reaction is captured by an emulsion nucleus at point A, from which charged particles tracks are emitted. Among them, the particle of track #1 shows decay topology at point B, i.e., decays into a charged particle track. In the analyzed events, we found the formation point A and decay point B as the vertices. When the Ξ^- particles comes to rest in emulsion, double-strangeness system will be produced by reaction $\Xi^- p \rightarrow \Lambda\Lambda + 28\text{MeV}$. If one Λ is captured by the nucleus and another one Λ is escaped, the event can be interpreted as a single hypernucleus and this type of events has two decay vertex points in nuclear emulsion. Therefore, we can predict track #1 as a single hypernucleus because of its decay topology. There is no V-topology around the decay vertex. So, another one lambda may decay into neutral particles ($\Lambda \rightarrow n\pi^0$). The measured ranges of single-Λ hypernucleus track #1 and charged particle decay products of analyzed events are shown in the following table1.

Table 1 Measured ranges of hypernucleus track #1 and charged particle decay products

Event	**8-5-8001-7** **A**	**40-6-8601-5** **B**	**40-7-12301-3** **C**	**69-5-1301-4** **D**	**70-3-5202-4** **E**
R(μm) of Tk#1	6.7±0.1	6.2 ± 0.1	5.1±0.1	5±0.1	3.1±1.0
R(μm) of decay products	4292.6±0.9	8140.6±0.8	2023.7±0.7	5878±0.9	61.5±0.7

Possible Decay Modes and Q-value Calculation

The analysis was performed on the decay vertex B of all events. Because of visible structure and decay topology, track #1 can be identified as a single-Λ hypernucleus. If track #1 is a single-Λ hypernucleus, we have to consider the main characteristics of the decay processes such as mesonic decay and non-mesonic decay. For the mesonic decay mode (decay with the emission of π meson), a single-Λ hypernucleus decays via the pionic channels: $\Lambda \rightarrow p\pi^-$ and $\Lambda \rightarrow n\pi^0$. For the non-mesonic decay process (decay without the emission of π meson), the main decay modes are $\Lambda n \rightarrow nn$ and $\Lambda p \rightarrow np$. At the decay vertex B, we observed only a charged particle track #1. Therefore, track #1 should be a proton, deuteron, triton or helium, etc. For the analyzed events of single- Λ hypernuclei, the following decay mode is allowed at point B.

$$\text{rack \#1} \rightarrow \text{charged particle + neutral particles} \qquad (1)$$

In this analysis, we take into account the possible single-Λ hypernuclei from ${}^{3}_{\Lambda}\mathrm{H}$ to ${}^{9}_{\Lambda}\mathrm{Li}$ and twenty possible decay modes are obtained. In order to check the decay modes are allowed or forbidden, the Q-values at point B are calculated by the formula

$$Q(\mathrm{MeV}) = [M(\text{track \#1}) - M(\text{charged particle}) - M(\text{neutral particles})]c^2 \qquad (2)$$

According to our calculation, the calculated Q-values are all positive and all possible decay modes are taken into consideration to perform analysis.

Kinetic Energy of Charged Particle Decay Product

In nuclear emulsion, event reconstruction of hypernuclei is based on the conservation laws of energy and momentum, and the mass of hypernuclei are calculated from the energies of their decay daughters. Since the kinetic energy of a charged particle is obtained by measuring its range. So, the range-energy relation is quite important for emulsion analysis. Range-Energy relation in nuclear emulsion is different from range-energy relation in one element medium. Because nuclear emulsion consists of mixture of eight elements and we have to consider the various factors which depend on these elements. To calculate range-energy relation in nuclear emulsion, we firstly use a traditionally used range-energy formula in nuclear emulsion such as

$$R = R_1 + R_2 = \frac{R_s/F}{Z^2(M_p.M_{mass})} + \frac{M}{R_{ext}} \qquad (3)$$

where, $R_1 = \frac{R_s/F}{Z^2(M_p.M_{mass})}$ is the measured range. In this equation, $\frac{R_s}{F}$ is range straggling of proton, $F = \frac{RR \times D - 1}{RR \times D_0 - 1} + \frac{RR(D_0 - D)}{RR.D_0 - 1}.\frac{R_s}{R_w}$ is range of a proton at velocity β, RR is ratio of the volume increment in cubic centimeters to the weight increment in grams, D is emulsion density, D_0 is density of standard emulsion, R_s is proton range in standard emulsion and R_w is proton range in water. In the second term, $R_2 = \frac{M}{R_{ext}}$ is the range of correction of track end. Here, $R_{ext} = Mz^{2/3}C_z$ is the range of electrons captured by the positive charged ions, C_z is a unique function of $\beta/_Z$, independent of the species of the incident particle and β is the velocity of the incident particle relative to the velocity of light.

Kinetic Energy of Neutral Particles

It is known that the neutral particles cannot be seen in nuclear emulsion because of non-electric property, we assumed that the neutral particle decay products go off together in the opposite direction of charged particle track as shown in figure 2.

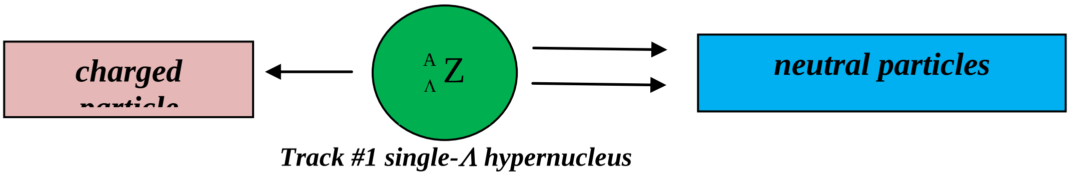

Figure 2 Schematic diagram of decay of analyzed single-Λ hypernuclei events

The kinetic energy of neutral particles are obtained from total energy conservation law such as,

$$E_n = M_n + T_n \tag{4}$$

where, E_n refers to total energy of neutral particles, M_n refers to rest mass energy of neutral particles and T_n refers to kinetic energy of neutral particles. Again, we considered the energy-momentum relation equation and the kinetic energy of neutral particles can be calculated by the formula

$$T_n = -M_n \pm \sqrt{\left(M_n^2 + p_n^2\right)} \tag{5}$$

According to the equations (3) and (5), the kinetic energy of charged particle decay product and neutral particle decay products can be calculated.

Mass of Single-Λ Hypernucleus

The reconstruction of all events was performed at point B by comparing the calculated masses and known masses of single-Λ hypernuclei for all possible decay modes. We assumed that a single-Λ hypernucleus (track #1) at rest decays into a charged particle and invisible particles and the mass of a single-Λ hypernucleus was calculated from kinetic energy value of its decay products by the relativistic total energy equation such as

$$E = T + M \tag{6}$$

$$Mc^2 = T + M \tag{7}$$

$$M\left({}^A_\Lambda Z\right)c^2 = \sum_i \left(M_i + T_i\right) \tag{8}$$

In equation 8, M_i and T_i denotes the mass and kinetic energy of i^{th} particles emitted from the decay of single-Λ hypernucleus and $M\left({}^A_\Lambda Z\right)$ is mass of identified single-Λ hypernucleus.

Identification of Single-Λ Hypernucleus

After calculating the possible masses by extracting the rest mass energy and kinetic energy of decay products, the possible masses of single-Λ hypernuclei track #1 for analyzed events are obtained. In order to identify the hypernuclei species using relativistic kinematics, we have to compare our calculated masses with known experimental masses of single-Λ hypernuclei which are assigned by experimental particle physics group and 15 acceptable modes are obtained. For the decay modes of event E (70-3-5202-4), the calculated masses are very much smaller than the known masses and we rejected those decay modes. The results are summarized in following table 2.

Table 2 Comparison of calculated masses and known masses of analyzed single-Λ hypernuclei

Event	**Decay modes**			**Calculated mass of single-Λ hypernucleus (MeV/c^2)**	**Known mass of single-Λ hypernucleus (MeV/c^2)**	**ΔM (MeV/c^2)**	**ΔM (%)**
	Track #1	**Charged particle**	**Neutral**				
8-5-8001-7 A	${}^{3}_{\Lambda}H$	${}^{1}_{1}H$	nn	2864.90±0.07	2991.12±0.07	126.22±0.14	4.2
	${}^{3}_{\Lambda}H$	${}^{2}_{1}H$	n	2939.79±0.07	2991.12±0.07	51.33±0.14	1.7
	${}^{4}_{\Lambda}H$	${}^{1}_{1}H$	nnn	3799.18±0.06	3922.53±0.06	123.35±0.12	3.1
	${}^{4}_{\Lambda}H$	${}^{2}_{1}H$	nn	3839.60±0.06	3922.53±0.06	82.93±0.12	2.1
40-6-8601-5 B	${}^{3}_{\Lambda}H$	${}^{1}_{1}H$	nn	2886.01±0.07	2991.12±0.07	105.11±0.14	3.5
	${}^{4}_{\Lambda}H$	${}^{1}_{1}H$	nnn	3817.84±0.06	3922.53±0.06	104.69±0.12	2.7
	${}^{4}_{\Lambda}H$	${}^{2}_{1}H$	nn	3878.05±0.06	3922.53±0.06	44.48±0.12	1.1
40-7-12301-3 C	${}^{3}_{\Lambda}H$	${}^{1}_{1}H$	nn	2848.29±0.07	2991.12±0.07	142.83±0.14	4.8
	${}^{3}_{\Lambda}H$	${}^{2}_{1}H$	n	2986.54± 0.07	2991.12±0.07	4.58±0.14	0.2
	${}^{4}_{\Lambda}H$	${}^{1}_{1}H$	nnn	3784.43±0.06	3922.53±0.06	138.10±0.12	3.5
	${}^{4}_{\Lambda}H$	${}^{2}_{1}H$	nn	3809.77±0.06	3922.53±0.06	112.76±0.12	2.8
69-5-1301-4 D	${}^{3}_{\Lambda}H$	${}^{1}_{1}H$	nn	2878.35±0.07	2991.12±0.07	112.77±0.14	3.8
	${}^{3}_{\Lambda}H$	${}^{2}_{1}H$	n	2968.87±0.07	2991.12±0.07	22.25±0.14	0.7
	${}^{4}_{\Lambda}H$	${}^{1}_{1}H$	nnn	3807.51±0.06	3922.53±0.06	115.02±0.14	2.9
	${}^{4}_{\Lambda}H$	${}^{2}_{1}H$	nn	3857.01±0.06	3922.53±0.06	65.52±0.12	1.7
70-3-5202-4 E	Could not identify the hypernuclear mass because the calculated masses are very much smaller than known masses of hypernucleus						

Results and Discussions

We have identified the five single-Λ hypernuclei which were observed in nuclear emulsion of KEK-PS E373 experiment during semi-automatic scanning. A type of analysis based on relativity theory, namely "kinematical analysis" is performed in this research. In the analyzed events, a single-Λ hypernucleus (track #1) decayed into a charged particle and invisible neutral particles at point B. Therefore, our analysis is started from decay point B of all single-Λ hypernuclei. Both mesonic and non-mesonic decay modes of track #1 were taken into considerations for our analysis. The hypernuclei tracks are visible and it is concluded that the Ξ^- hyperon is captured by the light emulsion nucleus. As the first step of analysis, the range and position angles of hypernuclei and their decay products particle are measured. In this analysis, we take into account ${}^{3}_{\Lambda}\mathrm{H}$ to ${}^{9}_{\Lambda}\mathrm{Li}$ single-Λ hypernuclei and twenty possible decay modes are obtained according to the charge and baryon conservation. We considered the decay modes which have one to three neutrons to perform analysis. Then, the Q-values for all possible decay modes are calculated and it is found that all calculated results have positive values. Therefore, the possible decay modes are energetically possible and taken into considerations to perform analysis. In our analysis, it is also assumed that the charged particle track is emitted back-to-back with neutral particle decay products. Accordingly the masses of single-Λ hypernuclei are deduced from the kinematics of the decay products. Kinetic energy of charged particles is calculated by range-energy relation and that of neutral particles are derived by momentum conservation. The possible masses of hypernuclei are calculated by mass-energy relation equation and the results are compared with known experimental masses of hypernuclei as presented in table 2.

According to the table 2, event A (8-5-8001-7) has four acceptable decay modes, event B (40-6-8601-5) has three acceptable decay modes, event C (40-7-12301-3) has four acceptable decay modes, and event D (69-5-1301-4) has also four acceptable decay modes. Unfortunately, event E (70-3-5202-4) has three possible decay modes and they are rejected because the calculated masses are very much smaller than the known mass of single hypernucleus.

If all charged particles are emitted as decay products, the calculated masses of single-Λ hypernucleus should be equal to known mass. If neutral particles exist in decay products, the calculated masses of single-Λ hypernucleus should be less than known mass. In our results, the calculated masses are slightly smaller than known mass because of contamination of neutrons in decay products. According to that assumptions, it is found that the possible species of single-Λ hypernuclei is either ${}^{3}_{\Lambda}\mathrm{H}$ or ${}^{4}_{\Lambda}\mathrm{H}$ and the charged particle decay product is possible to be proton or deuteron.

We observed that the smallest mass difference is 4.58 MeV/c^2 and the largest mass difference is 51.33 MeV/c^2 for the mode ${}^{3}_{\Lambda}\mathrm{H}$ hypernucleus decays into one deuteron and one neutron. In this case the calculated masses are 0.15% to 2% smaller than known masses. In the decay of ${}^{3}_{\Lambda}\mathrm{H}$ with one proton and two neutrons, the smallest mass difference is 105.11 MeV/c^2 and the largest mass difference is 142.83 MeV/c^2. In this decay, the calculated masses are 3.5% to 4.8% smaller than known masses. Moreover, in the decay of ${}^{4}_{\Lambda}\mathrm{H}$ with one deuteron and two neutrons, the smallest mass difference is 44.48 MeV/c^2 and the largest mass difference is 112.76 MeV/c^2 so that the calculated masses are 1.1% to 2.8% smaller than known masses.

Furthermore, in the decay of ${}^{4}_{\Lambda}\mathrm{H}$ with one proton and three neutrons, it is found that the calculated masses are 2.6% to 3.7% smaller than known masses. In this decay mode, the smallest mass difference is 104.69 MeV/c^2 and the largest mass difference is 138.10 MeV/c^2. The summarized results are presented in table 3. According to table 3, it is concluded that the mass difference of hypernucleus is quite small for one neutron emission case. If two or three neutrons are emitted as the decay products, the mass differences are slightly larger than one neutron emission case.

Table 3 Percentage of mass difference for each decay mode

Event	Decay modes			ΔM (MeV/c^2)	ΔM (%)
	Track #1	Charged particle	Neutral		
40-7-12301-3	${}^{3}_{\Lambda}\mathrm{H}$	${}^{2}_{1}\mathrm{H}$	n	4.58±0.14	0.2
69-5-1301-4	${}^{3}_{\Lambda}\mathrm{H}$	${}^{2}_{1}\mathrm{H}$	n	22.25±0.14	0.7
8-5-8001-7	${}^{3}_{\Lambda}\mathrm{H}$	${}^{2}_{1}\mathrm{H}$	n	51.33±0.14	1.7
40-6-8601-5	${}^{3}_{\Lambda}\mathrm{H}$	${}^{1}_{1}\mathrm{H}$	nn	105.11±0.14	3.5
69-5-1301-4	${}^{3}_{\Lambda}\mathrm{H}$	${}^{1}_{1}\mathrm{H}$	nn	112.77±0.14	3.7
8-5-8001-7	${}^{3}_{\Lambda}\mathrm{H}$	${}^{1}_{1}\mathrm{H}$	nn	126.22±0.14	4.2
40-7-12301-3	${}^{3}_{\Lambda}\mathrm{H}$	${}^{1}_{1}\mathrm{H}$	nn	142.83±0.14	4.8
40-6-8601-5	${}^{4}_{\Lambda}\mathrm{H}$	${}^{2}_{1}\mathrm{H}$	nn	44.48±0.12	1.1
69-5-1301-4	${}^{4}_{\Lambda}\mathrm{H}$	${}^{2}_{1}\mathrm{H}$	nn	65.52±0.12	1.7
8-5-8001-7	${}^{4}_{\Lambda}\mathrm{H}$	${}^{2}_{1}\mathrm{H}$	nn	82.93±0.12	2.1
40-7-12301-3	${}^{4}_{\Lambda}\mathrm{H}$	${}^{2}_{1}\mathrm{H}$	nn	112.76±0.14	2.8
40-6-8601-5	${}^{4}_{\Lambda}\mathrm{H}$	${}^{1}_{1}\mathrm{H}$	nnn	104.69±0.14	2.7
69-5-1301-4	${}^{4}_{\Lambda}\mathrm{H}$	${}^{1}_{1}\mathrm{H}$	nnn	115.02±0.14	2.9
8-5-8001-7	${}^{4}_{\Lambda}\mathrm{H}$	${}^{1}_{1}\mathrm{H}$	nnn	123.35±0.14	3.1
40-7-12301-3	${}^{4}_{\Lambda}\mathrm{H}$	${}^{1}_{1}\mathrm{H}$	nnn	138.10±0.14	3.5

Conclusion

In this work, five single-Λ hypernuclei which were detected in nuclear emulsion of KEK-PS E373experiment are analyzed kinematically. The analyzed events have one charged particle decay product and one or more neutral particle decay products. Because of contamination of neutrons in decay products we could not identify uniquely. According to our calculation, it is found that the possible species of single-Λ hypernuclei is either ${}^{3}_{\Lambda}\mathrm{H}$ or ${}^{4}_{\Lambda}\mathrm{H}$ and the charged particle decay product is possible to be proton or deuteron. Moreover, we established the differences between calculated mass and known mass of single-Λ hypernuclei in non-mesonic decay as the first time. It is observed that the calculated masses are 0.15% to 2% smaller than known masses for ${}^{3}_{\Lambda}\mathrm{H}\rightarrow{}^{1}_{1}\mathrm{H}+\mathrm{n}$ decay mode. In the decay of ${}^{3}_{\Lambda}\mathrm{H}\rightarrow{}^{1}_{1}\mathrm{H}+2\mathrm{n}$, the calculated masses are 3.5% to 4.8% smaller than known masses. Moreover, in the decay of ${}^{4}_{\Lambda}\mathrm{H}$ with one deuteron and two neutrons, the calculated masses are 1.1% to 2.8% smaller than known masses.

Furthermore, in the decay of ${}^{4}_{\Lambda}\mathrm{H} \rightarrow {}^{1}_{1}\mathrm{H} + 3\mathrm{n}$, it is found that the calculated masses are 2.6% to 3.7% smaller than known masses.

Acknowledgements

The authors would like to thank Lieutenant Colonel Saw Myint Oo, Dean of Faculty of Physics, Defence Services Academy for his encouragement and permission to complete this work. The authors also would like to thank all collaborators of KEK-PS E373 experiment for their discussions, supports and valuable advices to carry out hypernuclear research.

References

Aoki S., *et al.*,(1998), Nuclear Physics **A644**, 365.

Bando H., *et al*., (1990), International Journal of Modern Physics **A5** and references therein.

Danysz M., and Pniewski J., (1953), Philosophical Magazine **44.**

Ichikawa A., *et al*., (2001), Physical Review Letters **B500**.

Nakazawa K., (2018), Private Communication.

Nakazawa K., et al., (2013), Physical Review Letters **C 88.**

Takahashi H. et al., (2001), Physical Review Letters **87** (212502).

Thida Wint, (2009), *"Ξ^- particle identification with updated automatic scanning system and reconstruction of a single-Λ hyperucleus event"*, PhD Thesis, Physics Department, Mandalay University (Unpublished).

GRAPHENE GROWTH ON COPPER BY CHEMICAL VAPOR DEPOSITION

Myat Shwe Wah[1], Win Tha Htwe[2] and Soe Myint Maung[3]

Abstract

Synthesis methods are needed for its growth on wafer scale to bring graphene to the production level. One of the more promising production techniques to synthesize large area graphene is chemical vapor deposition (CVD) onto transition copper substrates. Recently copper has gained popularity as an important substrate material for graphene growth due to its lower carbon solubility, which allows better control over number of graphene layers. CVD growth has been performed at temperatures ranging from 1000°C to 1050°C using methane as the carbon source with diluted in a suitable mixture of argon (Ar) and hydrogen (H_2). It was found that apart from growth parameters surface texture plays a very important role in graphene growth. The growth mechanism of graphene on copper is surface related and surface morphology was determined by Scanning Electron Microscopy (SEM) and Raman spectroscopy was used to distinguish number of layers on gaphene deposition on copper foil.

Keywords: Graphene, Chemical Vapor Deposition (CVD), Scanning Electron Microscopy (SEM) and Raman Spectroscopy

Introduction

Graphene is one of those materials which are topic of current research interest due to its excellent properties e.g. one atom thick, mobility of the order of 200000 cm^2/Vs, ability to with stand current density of 10^8 A/cm^2, transmittance of about 97% of visible light and high thermal conductivity of the order of 5×10^3 W/mK [Lerf, A., et al.]. It was long believed that two-dimensional materials (2D) were unstable thermodynamically and they only serve as building blocks of complex three dimensional (3D) structures [Gein, A. K., et al.]. Graphene is the name given to arrangement of carbon atoms on hexagonal honeycomb lattice that is exactly one atom thick [Niyogi, S., et al.]. It is this arrangement and symmetry of carbon atoms that gives unique properties to graphene [Nakajima, T., et al.]. Graphene was first obtained in the form of small flakes of the order of several microns through mechanical exfoliation of graphite using scotch tape production scale, fabrication method is needed that can synthesize wafer scale graphene.

Though this method gives the highest quality graphene but to bring graphene to the Chemical vapor deposition (CVD) is one technique that has the ability to synthesize wafer scale graphene [Nima R., et al.]. Two techniques such as Atmospheric Pressure CVD (APCVD) and Low Pressure CVD (LPCVD) are available and LPCVD is implemented in this investigation. The method mainly involves the adsorption, decomposition and segregation of carbon containing precursor on the transition metal surface at elevated temperature either at low or atmospheric pressure which results in graphene synthesis. The aim of this project is to synthesize monolayer graphene through CVD method. In this study, copper had been used as the substrate material for graphene synthesis due to its small carbon solubility at elevated temperatures which allows better control over the number of graphene layers. The deposited graphene on silicons were investigated by Scanning Electron Microscopy (SEM). Raman spectroscopy was used to distinguish number of layers on gaphene deposition on copper foil.

---

[1] Associate Professor, Head of Department of Physics, University of Computer Studies , Kyaing Tong, Myanmar

[2] Professor, Science and Math Department, Spoon River College, Canton, IL 61520, USA

[3] Brigadier General, Defense Academic Service Science and Technical Research Centre, Pyin Oo Lwin

Materials and Methods

Commercially available copper foils have been used for the graphene synthesis for overall cost reduction in fabrication process. However, these foils have some face roughness and strongly inhomogeneous corrugated surface due to pressure in nano level due to cold rolling process during manufacturing and this surface unevenness cause to produce graphene thickness variation on copper [Niyogi, S., et al.]. Since graphene growth on copper is surface limited, so smoothness of copper surface plays very important role in getting monolayer coverage across the entire surface of the substrate. Figure shows SEM image of as grown graphene on copper. From electronic applications point of view, field effect mobility, transmittance and sheet resistance are the important parameters. For CVD grown graphene shows field effect mobilities of the order of $3000 cm^2/Vs$, optical transmittance of the order of 90% and sheet resistance of the order 280 Ω/sq. It must be mentioned that graphene obtained by CVD is inferior to graphene obtained by mechanical exfoliation in terms of above mentioned parameters.

One reason is that graphene obtained by CVD is in the form of continuous sheet which is inherently polycrystalline because graphene domains of different orientations merge together to from graphene sheet and because of the presence of grain boundaries, the overall film shows poor electrical properties. So efforts have begun in this direction to obtain single crystal isolated graphene domains with improved electrical properties.

Chemical Vapor Deposition Method

The essence of this technique is that precursors in the vapor phase adsorb and react at the substrate surface at elevated temperatures under low pressure (of the order of millitorr) or atmospheric pressure that results in the deposition of thin film as a result of chemical reaction. In case of graphene synthesis, precursors are usually carbon containing gas e.g. methane or vapors of any liquid carbon source e.g. alcohols that react on the transition metal surface under the ambient environment (e.g. Ar to avoid deposition of amorphous carbon). Graphene obtained recently is the result of refinement of previous methods to get controllable deposition. The solubility of carbon in transition metal along with CVD conditions play an important role in determining growth mechanism and ultimately controls the number of graphene layers. Recent promising results of graphene growth on copper shows that it may serve as alternate route towards scalable growth of graphene with higher monolayer coverage.

Solvent cleaning

The starting substrate is 25μm thick, 99.999% pure copper foil from Amarica. The as-received copper foil may contain thin layer of grease or organic impurities that may result in the deposition of amorphous carbon at high temperatures, so solvent cleaning step is performed to remove them. The recipe for solvent cleaning step is summarized in Table 1. Acetone is used mainly to remove organic impurities but it also leaves its own residues due to its very fast evaporation rate so methanol is used as solvent to remove left over acetone. Finally foil is placed in De-ionized (DI) water bath to remove remaining organic solvents. After Nitrogen dry step, foil is pressed between two clean quartz slides to keep it as straight as possible. During ozone clean, foil is placed on clean quartz slide that is also used during thermal annealing step.

Table 1 Solvent cleaning recipe

Acetone	**Methanol**	**De-ionized Water (DI) dip**	**Nitrogen dry**	**Ozone Clean**
5 minutes	5 minutes	5 minutes	Gently until foil is dry	2 minutes

Thermal annealing

As received copper foil contains thin layer of native copper oxide, which is highly undesirable for graphene growth. Acetic acid may be used to remove native oxide layer but it leaves the surface too rough which is also not desirable. Thermal annealing of annealing of copper foil is performed in Ar and H_2 at 900°C. The purpose of thermal annealing is two-fold: first, to remove native copper oxide layer by H_2 reduction and second, to increase the grain size of polycrystalline copper foil. As received foil has much smaller grain size with large number of grain boundaries. Graphene tends to grow preferentially on grain boundaries first as compared to flat copper surface, which ultimately leads to multilayer graphene on those regions. Thermal annealing increase copper grain size which reduce the effect of grain boundaries on grapheme growth.

Thermal annealing was performed in our home made CVD system. It essentially consists of Lindberg blue M furnace with 1 in. diameter quartz tube. The tube can be fed by Ar, H_2 and CH_4. The flow rate of CH_4 and H_2 is maintained by single regulated flow meter while Ar flow rate is measured by unregulated flow meter. Typical thermal annealing recipe is summarized in Table 2. Copper foil on quartz slide was loaded into the quartz tube and the temperature was ramped up to 900°C under H_2 (36 sccm*) and Ar (280 sccm) ambient. H_2 was used during the ramp up step to avoid oxidation of copper at elevated temperatures. After reaching the annealing temperature, flow rate of gases were left unchanged and annealing was performed for 2 hours. After the annealing step, temperature was ramped down and furnace was allowed to cool down naturally under H_2 (36 sccm) and Ar (280 sccm) ambient. Copper foil was unloaded from the quartz tube at room temperature.

Table 2 Thermal annealing recipe

Step Number	**Processing Step**	**Temperature**	**Processing gas**	**Duration (minutes)**
1	Ramp up	1000°C	Ar (280 sccm) and H_2 (36 sccm)	20
2	Annealing	1000°C	Ar (280 sccm) and H_2 (36 sccm)	120
3	Ramp down	Room temperature	Ar (280 sccm) and H_2 (36 sccm)	Natural cool down

Synthesis of Graphene by Chemical Vapor Deposition Method (CVD)

Two different types of Cu catalyst deposition were tested for catalyst depositions with E-bean Evaporation system. A mixture of Hydrogen (H_2 99.9995%) and methane (CH_4 99.9995%) was used as a precursor gas for Graphene growth. The CVD reactor is tubular quartz hot-wall, resistivity heated furnace, containing 140 nm inner diameter quartz tubes. In the deposition system, (Ar, 99.999%) was used as carrier gas, H_2(99.999%) was used for soaking and , the substrates were positioned in the CVD furnace as shown in Figure1.The reactor temperature was increased under an argon flow (using 1000 sccm).

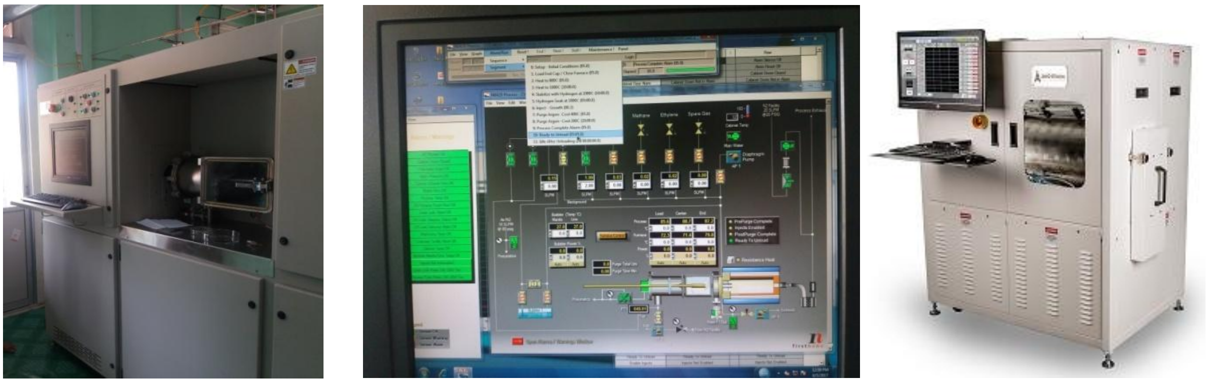

Figure 1 Photo of chemical vapor deposition machine LPCVD AMOD 006 series system manufactured by Angstrom Engineering

Graphene growth on copper

Graphene on copper is in principle straightforward, involving the decomposition of methane gas over a copper substrate typically held at 1000 °C. Growth of predominantly monolayer graphene on copper foil has recently been reported using hexane at 950 °C to explore the possibility of using liquids precursors that could facilitate the doping of graphene during synthesis by using nitrogen and boron containing organic solvents. The specific growth parameters that have been utilized for achieving the best graphene films on Cu. Most of the depositions have been performed on copper foils with thicknesses ranging from 25–50 nm. Recently grapheme deposition on e-beam and thermally evaporated copper thin films has developed and widely used in grapheme film deposition on other substrates.

Results and Discussion

Three objectives of this research is development fabrication of single and many layers graphene grouth on copper foil, secondly, graphene characterization is required to carried out in two-ways: first to identify number of layers in a given sample and second to determine the quality of grown film in terms of defects. Third and ultimate objective is to be able to manufacture the most reliable and highly sensitive biosensors, high efficient solar cells, and rapidly charged high energy density super capacitors in very near future.

The surface morphologies by SEM observation have been characterized using JEOL Scanning Electron Microscope model JSM – 5610 LV. Graphene growth on copper has been successfully prepared by chemical vapor deposition method (CVD) and the shape and size are not well uniformed as shown in Figure 2. Notice that Graphene layer on copper is not homogeneous. The reason could be copper substrate sample preparation, cleaning and handing. Temperature control and gas flow rate may need to be optimized. Copper substrate quality and purification still need to be careful about optimizing the process on CVD method. Photo of copper substrate after graphene growth using chemical vapor deposition was shown in Figure 3.

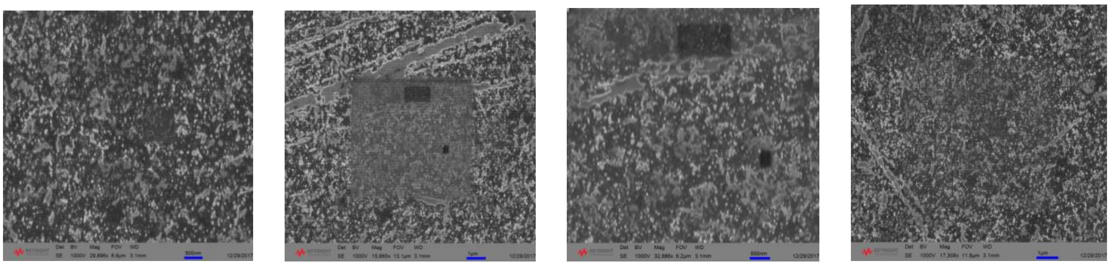

Figure 2 The SEM images of copper substrates after graphene growth on copper

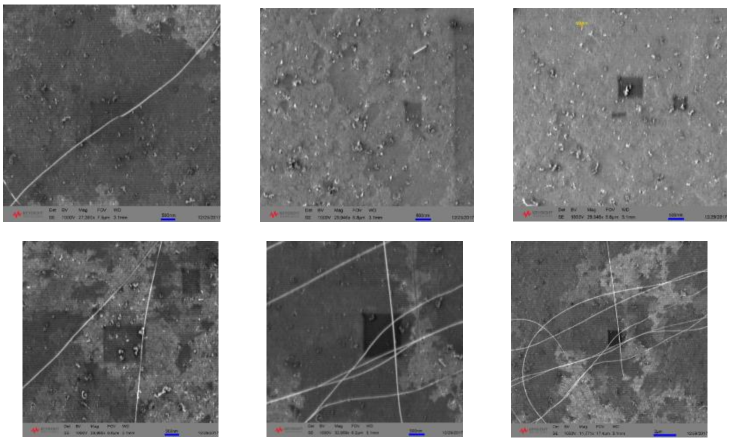

Figure 3 The SEM images of copper substrates after graphene growth on copper (some carbon nano tubes were accindently present during fabrication by CVD on some images in this temperature).

In fact, few layer and bilayer graphene were obtained on the regions where copper surface was not uniform, confirmed by Raman spectroscopy. Raman spectroscopy was used for the graphene characterization because Raman spectrum of graphene contains characteristic bands which can be used to distinguish among number of graphene layers as shown in Figure 4 and also gives information about defects in the sample. Also it is fairly easy to generate spatial Raman area maps of the order of hundreds of microns to study spatial uniformity.

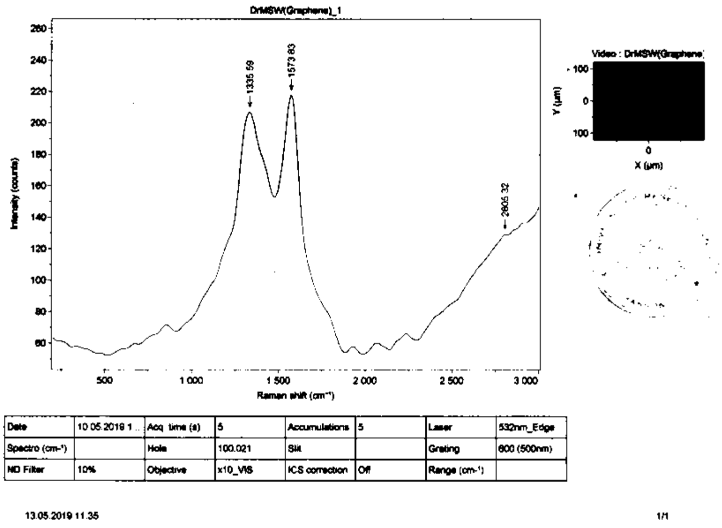

Date	10.05.2019 1 ..	Acq. time (s)	5	Accumulations	5	Laser	532nm_Edge
Spectro (cm-¹)		Hole	100.021	Slit		Grating	600 (500nm)
ND Filter	10%	Objective	x10_VIS	ICS correction	Off	Range (cm-¹)	

13.05.2019 11.35 1/1

Figure 4 Raman spectrum of graphene contains characteristic bands

Conclusion

The main objective of this project was to optimize graphene synthesis and transfer process using CVD was selected as synthesis technique for grapheme growth as it is a simple method for large scale graphene synthesis. Copper foils were chosen as substrate quite promising because of the lower solubility of carbon in copper which is important in controlling number of graphene layers. CH_4 was used was precursor gas while H_2 annealing was used to remove native oxide as well as to grow copper grains. Ar acted as carrier gas during synthesis to dilute the precursor gas. Graphene on copper is in principle straight forward, involving the decomposition of methane gas over a copper substrate typically held at 1000°C.

The specific growth parameters that have been utilized for achieving the best graphene films on Cu. Raman spectroscopy was used as characterization technique as graphene shows characteristic raman spectrum which can be used to distinguish number of layers on a given sample. Recently graphene deposition on copper thin films has developed but it has some defects of SEM images and widely used in graphene film deposition on other substrates. CVD fabrication allows large area graphene of single layer to several layers graphene.

In this work, graphene deposition on copper foil is to be able to manufacture the most reliable and rapidly charged high energy density super capacitors in very near future. The present study provides a proficient approach to synthesize cost effective and to bring graphene to the production level.

Acknowledgements

The authors would like to express their gratitude to Commander in Chief General Soe Myint Maung, Defense Service Science and Technology Research Center, Pyin Oo Lwin for his encouragement to carry out this research and we are profoundly indebted to Dr Win Tha Htwe, Prof., Science and Math Department, Spoon River College, Canton, IL 61520, USA, for all of his invaluable guidance, support, and encouragement.

References

Brodie, B. C., (1859) “On the atomic weight of graphite”. Philos. Trans. R. Soc. London vol.14, pp.249-259.

Boukhvalov, D.W., and Katsnelson, M.I., (2008) “Study of oxygen-containing groups in a series of graphite oxides: Physical and chemical characterization”, J. Am. Chem. Soc., vol.130, pp.10697–10701.

Gein, A. K., (2007) “The rise of graphene”, Nature Mater, vol. 6, pp.183-191.

Hummers, W. S., and Offeman, R. E., (1958) “Preparation of graphite oxide”, vol.80, pp.1339-1339

He, H., Klinowski, J., and Forster, M., (1998) “A new structural model for graphite oxide”, Chem. Phys. Lett vol.287, pp. 53-56.

Higginbotham, A. L., Lomeda, J. R., Morgan, J. M., (2009) “Graphite oxide flame retardant polymer nanocomposites”, Appl. Mater Interfaces, vol.1, pp. 2256-2261.

Hirata, M., Gotou, T., Horiuchi, S., Fufiwara, M., and Ohba, M., (2004) “Thin-film particles of graphite oxide1: High-yield synthesis and flexibility of the particles”, vol.42, 2929-2937.

Lerf, A., He, H., Forster, M., Klinowski J., (1998) “Structure of graphite oxide revisited”, J. Phys. Chem. *B,* vol.102, pp.4477-4482.

Novoselov, K. S., Gein, A. K., Morozov, S. V., Jiang, D., Zhang, Y., Dubonos, S. V., Grigorieva, I. V., and Firsov, A. A., (2004) “Electric field effect in atomically thin carbon films”, Science, vol.306, pp. 666-669.

Niyogi, S., Bekyarova, Itkis, M. E., McWilliams, J. L., Hamon, M. A., and Haddon, R. C., (2006) “Solution properties of graphite and graphene”, J. Am. Chem. *Soc*. vol.128, pp. 7720-21.

Nakajima, T., Mabuchi, A., and Hagiwara, R., (1988) “A new structure model of graphite oxide”, 26 357- 361Philos Trans. R. London, vol. 33, pp. 1585-1592.

Nima R., Dheeraj J., Santiago C., Lluis J., Elliott B., Peter J. B., (2011) “Broadband Conductivity of Graphene from DC to THz”, 11th IEEE International Conference on Nanotechnology

J. Myanmar Acad. Arts Sci. 2020 **Vol. XVIII.No.2C**

THE CHARACTERIZATION OF TiO_2 AND ZnO THIN FILMS BY SPIN COATING TECHNIQUE VIA SOL-GEL METHOD

Nay Myo Tun[1], Hnin Nandar Shwe[2], Thin Thin Naing[3],
Thet Naing[4] and Khin Mya Mya Soe[5]

Abstract

Nowadays, the nano-materials have gained great interest all over the world due to high their surface area to mass or volume ratios. In the present study, Titanium Dioxide (TiO_2) and Zinc Oxide (ZnO) thin films were investigated. Zinc acetate dehydrate , potassium hydroxide, methanol (CH_3OH), Titanium isopropoxide and 2- methoxy ethanol were used as the starting materials for Titanium Dioxide (TiO_2) and Zinc Oxide (ZnO) sol-gel to enhance the thin films. Non-electrolytic glass was also used as the substrate for both thin films. Spin coating technique was mainly applied for fabrication of the TiO_2 and ZnO thin films. X-ray Diffraction (XRD) analysis was used to compare the characterization of the crystal nature and crystallite sizes of those obtained thin films. Scanning Electron Microscopy (SEM) analysis was also mentioned to monitor the morphology of both thin films. LCR meter was finally used to characterize the electrical properties of TiO_2 and ZnO thin films.

Keywords: Sol-gel, Spin coating, X-Ray Diffraction, Scanning Electron Microscopy (SEM), LCR meter

Introduction

Nanotechnology is the branch of engineering which deals with design and manufacture of extremely small electronic circuits and mechanic devices built at the molecular levels of matters. It enables the ability to build a molecular system with atom by atom reproducing multiple variety nanomachines. Recently, nanocrystalline powder with uniform size and shape have been shown interesting properties of them. They are already having a significant commercial impact, which will assuredly increase in the future. Furthermore, ZnO and TiO_2 with its good electrical and optical properties which can be used in many applications such as photoconductors, integrated sensors and transparent conducting oxides electrodes. Here one looks at the photo-degradation of hydrocarbons either in water or in air using suspended small particles or thin films of TiO_2 and ZnO.

In this research, the comparison of the electrical characterization of TiO_2 and ZnO thin films were presented by Sol-gel method. The advantages of using Sol-gel processing methods are low synthesis temperature, high purity, novel materials and low capital costs [Xia and et al]. X-ray diffraction (XRD) was used for the structural nature of TiO_2 and ZnO thin films and scanning electron microscopy (SEM) was also used for the morphology of thin films. LCR meter measurement was performed for their electrical characteristics such as dielectric constant with various frequencies.

Theory Background of TiO2 and ZnO particles and thin films

TiO_2 thin films for photo catalytic application has several naturally occurring modifications, the most common ones being Rutile, Anatase and Brookite. Most research with respect to photocatalysis is performed using Anatase, while in all other aspects Rutile has been much more thoroughly characterized. This is mostly due to the preparation methods: while it is easier to obtain Anatase than Rutile at low temperatures below 600 °C, it is impossible to obtain anything but Rutile at temperatures above 800 °C, the transition temperature to the thermodynamically most stable phase rutile. While TiO_2 powders or films obtained at low temperatures are finely grained (nanocrystalline) because little grain growth can occur, grain growth at temperatures above 800°C can be substantial. Therefore, depending on the preparation method, the nature of the TiO_2 particle or film surface, as well as the active surface area are usually very different for Anatase and Rutile powders and thin films.

Zinc Oxide is an also important, inexpensive, versatile n-type semiconducting material with wide direct energy band gap of 3.37 eV and large exciton binding energy of about 60 MeV at room temperature. ZnO has unique structural, optical and electrical properties. Due to its high trans parent conducting properties, it has many potential applications like light emission display devices, piezoelectric transducers, surface acoustic devices and optoelectronic devices. Various deposition techniques were employed for the preparation of ZnO thin films such as magnetron sputtering, spray pyrolysis, pulsed laser deposition, electron beam evaporation and sol-gel method.

In this work, TiO_2 and ZnO films were prepared by an inexpensive sol-gel spin coating technique and were also studied the effect of electrical characterization as dielectric properties on their structural nature.

Experimental Details for TiO_2 and ZnO thin films

Titanium–isopropoxide (TTIP) and 2-methoxy ethanol with the weight percent of 1:2 were used as the starting chemical materials for TiO_2 sol-gel to perform the TiO_2 thin film. These two materials were mixed together in a closed-beaker by using the magnetic stirrer with vigorous speed at 45 °C to get the homogeneous solution. During the stirring process, some drops of acetic acid were used again to make the transparent solution. In order to control the viscosity of the solution, De-ionized water was used. The obtained sol-gel of TTIP and 2-methoxyethanol was carried on as desired chemical materials to develop the TiO_2 thin film by using spin-coating method. Non-electrolytic-glass was taken as a substrate of the thin film. Before making the spin coating technique, the substrate must be etched with acetone and DI water for releasing the contaminations.

To investigate the ZnO thin films, 15 g of KOH and 45 ml of methanol (1:3) were mixed into the covered-beaker with under constant stirring at the desired temperature of 60 ℃ about 10 min to get the homogeneous solution (1) with transparent colour. Simultaneously 15 g of ZnAc and 45 ml of methanol (1:3) were mixed again into the covered-beaker with under constant stirring at the desired temperature of 60 ℃ about 10 min to get the homogeneous solution (2) with transparent colour. The solution (1) and the solution (2) were mixed together into the next covered-beaker with under stirring at the temperature of 60 ℃. After one day, these ZnO sol-gel composites were obtained. Those obtained ZnO sol-gel were used with the spin coating method to performed ZnO thin films and then both TiO_2 and ZnO thin films were calcined by annealing with the temperature of 300 ℃, 400 ℃ and 700 ℃ about 1 hour to perform TiO_2 and ZnO crystallization on both films. The obtained TiO_2 and ZnO thin films were synthesized by XRD and SEM techniques to examine their structures, morphologies and crystallite sizes. The LCR meter also used as the determination of their electrical characterizations as dielectric properties.

Results and Discussion

The ultra fine TiO_2 and ZnO powders were investigated to know the crystalline state of thin films by calcining the TiP/ 2 Methoxyethanol sol-gel at 400 ºC and 700 ºC and ZnO sol-gel at 300 ºC and 400 ºC. The crystallite diameters 'D' were obtained from XRD peaks according to the Debye- Scherrer equation:

$$D = \frac{0.89\,\lambda}{\Delta W \cos\theta}$$

where 'λ' is the wavelength of the incident X-ray beam (1.5405 Å for Cu / K-α1), 'θ' is the Bragg's reflection angle, 'ΔW' is the width of X- ray pattern line at peak half peak height in radians. According to the XRD results that all particles possessed polycrystalline nature of tetragonal structures from planes: (101), (004), (200), (211), (213) for TiO_2 and hexagonal wurtzite structures from planes: (100), (101), (102), (110), (103) for ZnO. The average particles sizes were 8.42 nm at 400 ^{o}C and 36.20 nm at 700^{o}C for TiO_2 thin films and 27 nm at 300 ºC and 25 nm at 400 ºC for ZnO thin films. The size distribution was not in homogenous and the crystal quality was not in optimum condition because of uncontrolled of the ambient conditions for both films. The average thickness of the TiO_2 thin films for both temperatures was about 595 nm and 714 nm for ZnO thin films as shown in figures (9-12).

In order to realize the electrical characterization such as dielectric properties should be performed on TiO_2 and ZnO thin films. Using Digital impedence Analyzer (insteak: 8110G LCR Meter), the dielectric properties of TiO_2 and ZnO thin films were measured over the frequency range between 100 Hz to 100 kHz. The dielectric constant and dissipation factor were calculated by the following equations as; $\varepsilon_r = \frac{C\,d}{\varepsilon_0\,A}$; $tan\delta = \frac{D}{\varepsilon_r}$ where 'ε_r' is dielectric constant, 'C' is capacitance measured, 'd' is the thickness of the film, 'A' is the area of the top electrode, 'D' is dielectric loss and '$tan\delta$' is dissipation factor. The change in capacitance and dissipation factor with various frequencies at temperatures of 400 ^{o}C and 700 ^{o}C for TiO_2 and 300 ^{o}C and 400 ^{o}C for ZnO thin films were presented in Tables (1, 2, 3, and 4).

As the results, when the low frequency (<100 Hz) was applied to the TiO_2 thin films, the change in capacitance and dielectric loss were not detected in TiO_2 thin films by the Digital impedence Analyzer (insteak: 8110G LCR Meter). This is due to the properties of the highly response of photons in TiO_2 which can't detect in low energy or frequencies. However, when the high frequency (>1 kHz) was applied to the TiO_2 thin films, the change in dielectric constant and capacitance were found to be decreased as shown in Figures (13-16). Moreover, the dissipation factor was also decreased with various frequencies at different temperatures. In contrary, the change in capacitance and dielectric loss were detected in ZnO thin films under 100 Hz frequency range. But, the change in dielectric constant and capacitance were found to be decreased as the same as TiO_2 thin films shown in Figures (17– 20). Especially, the higher dielectric constants were found to be in ZnO thin film compared than in TiO_2 thin films. In addition, when the frequencies ranges >10 kHz were applied to TiO_2 thin films, they would well response and maintain the electrical charges as shown in Tables 1 and 2. However, when the frequencies ranges >10 kHz was applied to ZnO films, they were not response and maintain the electrical charges as TiO_2 thin films. This is because of the optical properties of ZnO particles, most of the molecules cannot retain the charges in high frequencies ranges. Therefore the optimum frequencies ranges for electrical properties for TiO_2 films were about >10 kHz and

<100Hz for ZnO thin films. They can be used as high speed digital, high power gain and low noise performances for the micro and nanoelectronics devices.

Table 1 The values of capacitance, dielectric loss, dielectric constant and dissipation factor with various frequencies for TiO_2 thin film at 400 °C

Frequency (kHz)	**Capacitance ‘C_P’ (pF)**	**Dielectric Loss (D)**	**Dielectric Constant (ε_r)**	**Dissipation factor (tan δ)**
1	125.54	0.09	15.06	6.38×10^{-3}
10	111.85	0.05	13.42	3.84×10^{-3}
20	109.32	0.04	13.11	3.25×10^{-3}
50	107.71	0.03	12.92	2.49×10^{-3}
100	106.27	0.04	12.75	2.75×10^{-3}

Table 2 The values of capacitance, dielectric loss, dielectric constant and dissipation factor with various frequencies for TiO_2 thin film 700 °C

Frequency (kHz)	**Capacitance ‘C_P’ (pF)**	**Dielectric Loss (D)**	**Dielectric Constant (ε_r)**	**Dissipation factor (tan δ)**
1	257.52	0.28	30.89	9.13×10^{-3}
10	158.90	0.21	19.06	11.14×10^{-3}
20	157.88	0.18	18.94	9.47×10^{-3}
50	136.35	0.14	16.36	8.47×10^{-3}
100	134.40	0.12	16.13	7.43×10^{-3}

Table 3 The values of capacitance, dielectric loss, dielectric constant and dissipation factor with various frequencies for ZnO thin film 300°C

Frequency (Hz)	**Capacitance ‘C_P’ (pF)**	**Dielectric Loss (D)**	**Dielectric Constant (ε_r)**	**Dissipation factor (tan δ)**
1	994	10.90	78.25	0.14
100	372	7.03	9.93	0.71
1000	107	4.31	2.84	1.52
10000	0.98	0.49	0.03	18.84
100000	0.69	0.18	0.02	9.44

Table 4 The values of capacitance, dielectric loss, dielectric constant and dissipation factor with various frequencies for ZnO thin film 400 °C

Frequency (Hz)	**Capacitance ‘C_P’ (pF)**	**Dielectric Loss (D)**	**Dielectric Constant (ε_r)**	**Dissipation factor (tan δ)**
1	790	15.12	21.05	0.71
100	535	12.75	14.26	0.89
1000	477	5.23	12.69	0.41
10000	1.78	1.14	0.05	23.97
100000	0.65	0.29	0.02	16.72

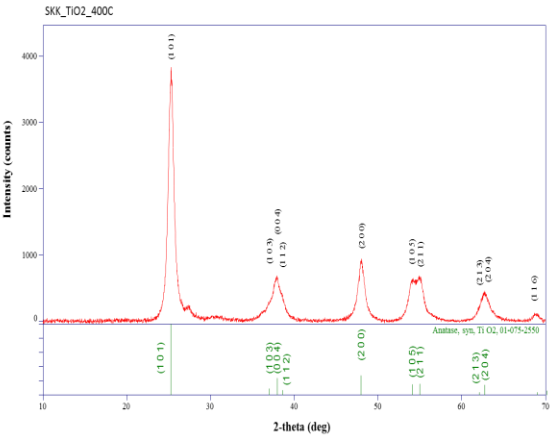

Fig (1)

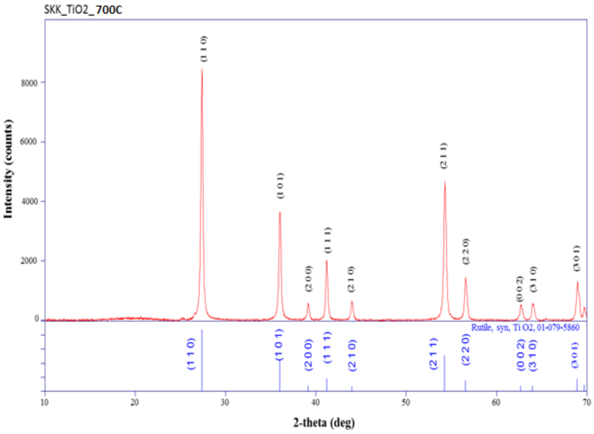

Fig (2)

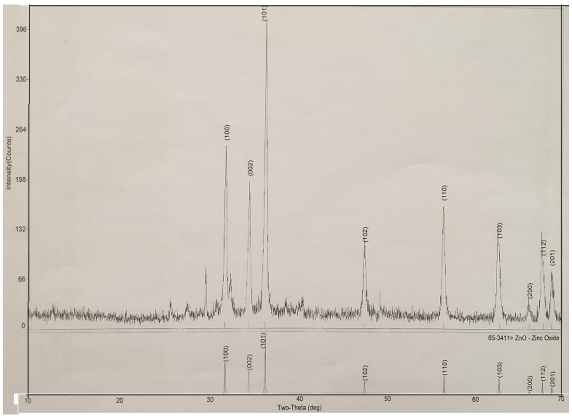

Fig (3)

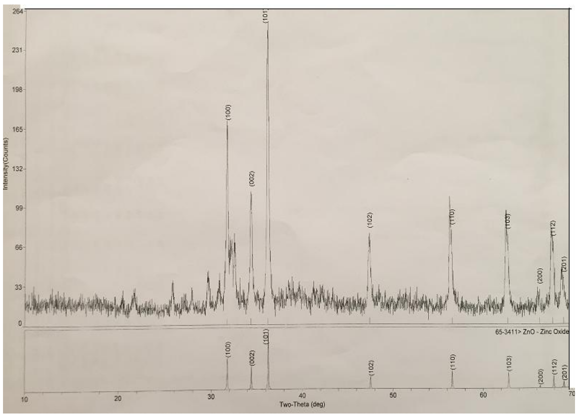

Fig (4)

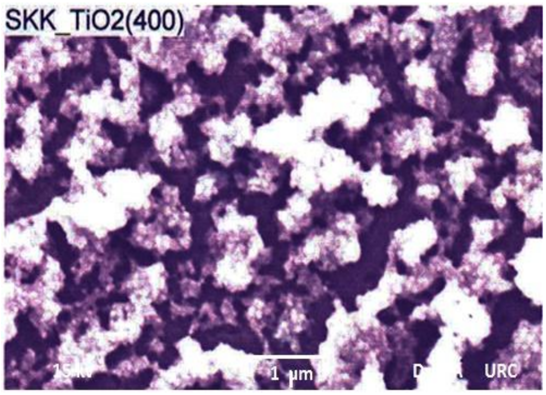

Fig (5)

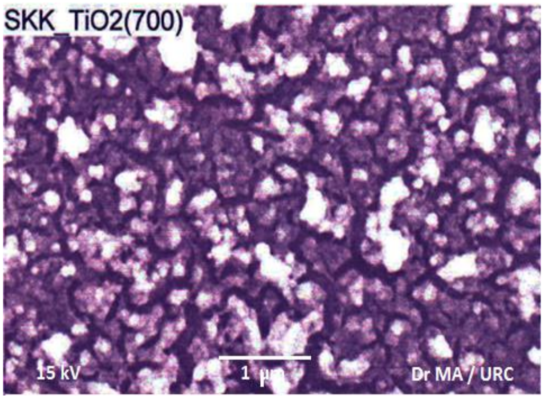

Fig (6)

Figure 1 XRD spectrum of TiO_2 particles at 400 ° C, Figure 2. XRD spectrum of TiO_2 particles at 700 ° C, Figure 3. XRD spectrum of ZnO particles at 300 °C, Figure 4. XRD spectrum of ZnO at 400 °C, Figure 5. The Photograph of SEM for TiO_2 particles on the TiO_2 thin flim at 400 °C, and Figure 6. The Photograph of SEM for TiO_2 particles on the TiO_2 thin flim at 700 °C

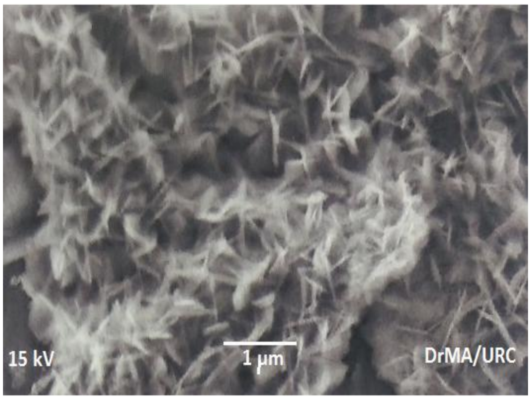

Fig (7)

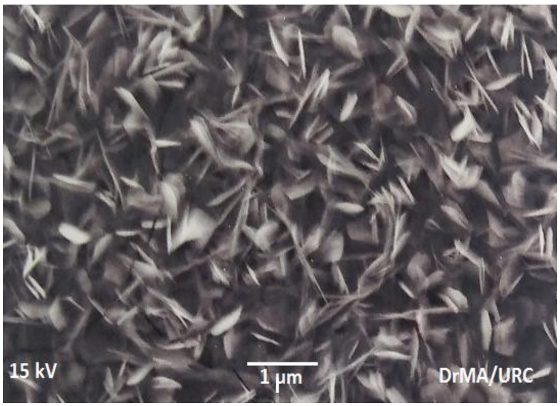

Fig (8)

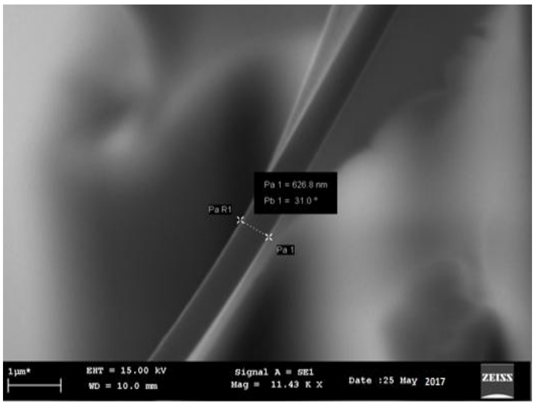

Fig (9)

Fig (10)

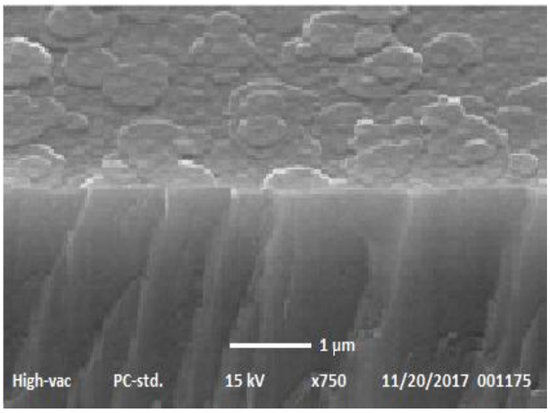

Fig (11)

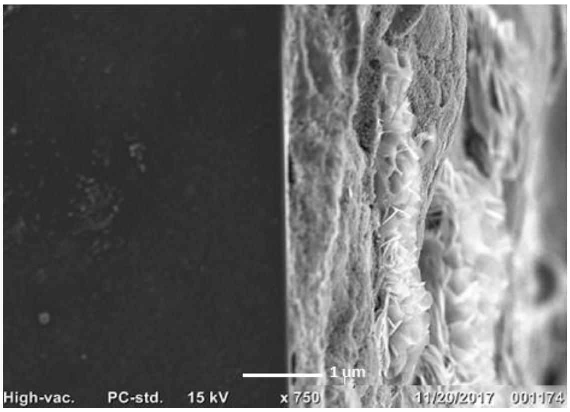

Fig (12)

Figure 7 SEM image of ZnO particles on the ZnO thin flim at 300 ºC, Figure 8. SEM image of ZnO particles on the ZnO thin flim at 400 ºC, Figure 9. SEM image of thickness measurement for TiO_2 thin film at 400 °C, Figure 10. SEM image of thickness measurement for TiO_2 thin film at 700 °C, Figure 11. SEM image of thickness measurement for ZnO thin film at 300 ℃, and Figure 12. SEM image of thickness measurement for ZnO thin film at 400 ℃

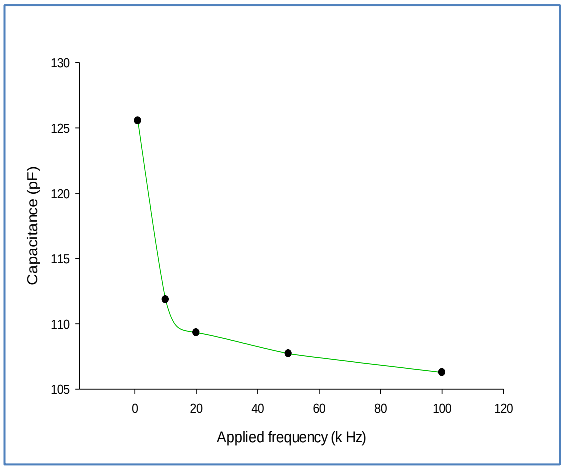

Fig (13)

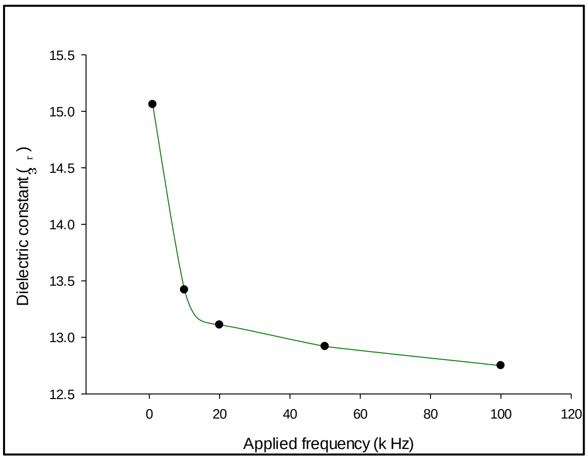

Fig (14)

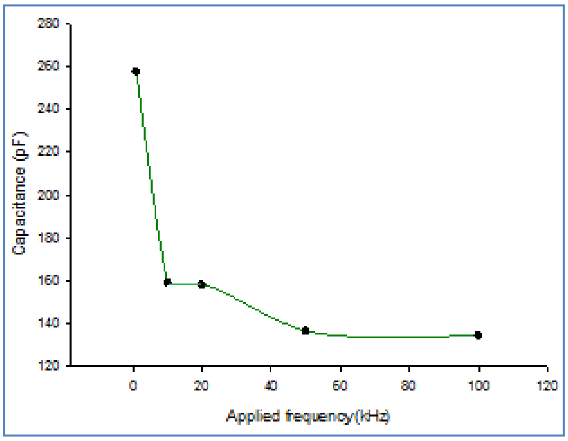

Fig (15)

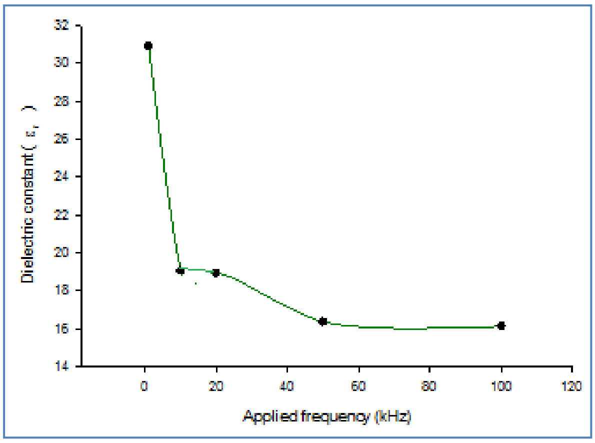

Fig (16)

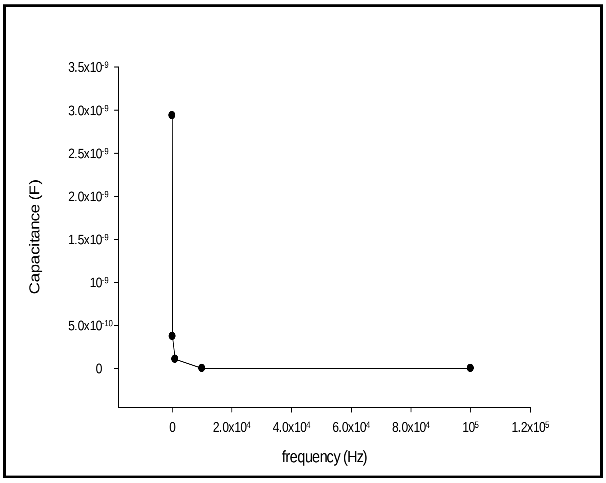

Figure (17)

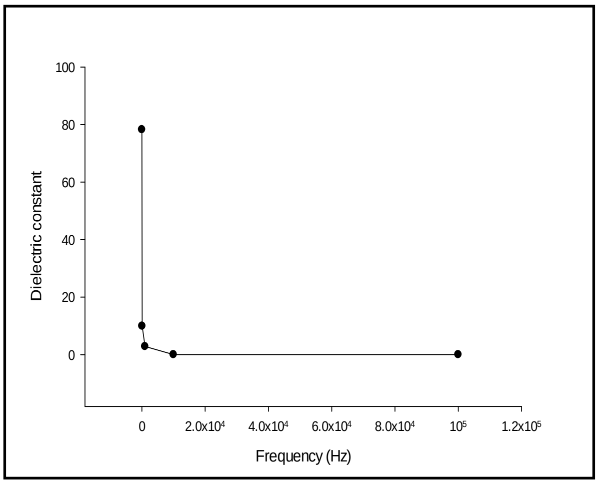

Figure (18)

Figure 13 The variation of Capacitance with applied frequencies at 400 ºC for TiO_2 thin film, Figure 14. The variation of Dielectric constant with applied frequencies at 400 ºC for TiO_2 thin film, Figure 15. The variation of Capacitance with applied frequencies at 700˚C for TiO_2 thin film, Figure 16. The variation of Dielectric constant with applied frequencies at 700 ºC for TiO_2 thin film and Figure 17. The variation of Capacitance with applied frequencies at 300˚C for TiO_2 thin film, Figure 18. The variation of dielectric constant with applied frequencies at 300 ºC for ZnO thin film

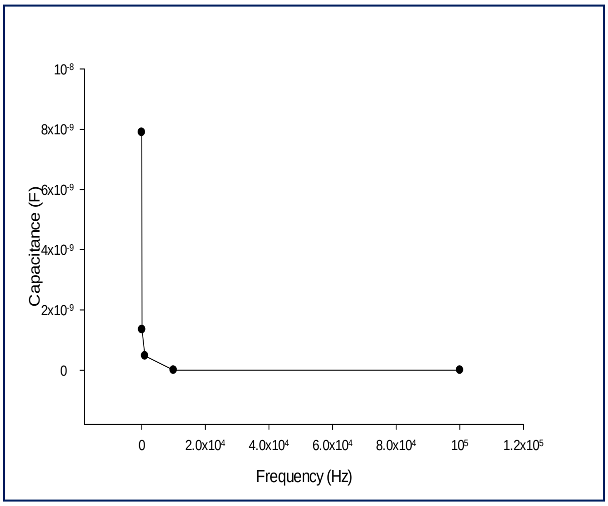

Figure 19 The variation of capacitance with applied frequencies at 400 ºC for ZnO thin film

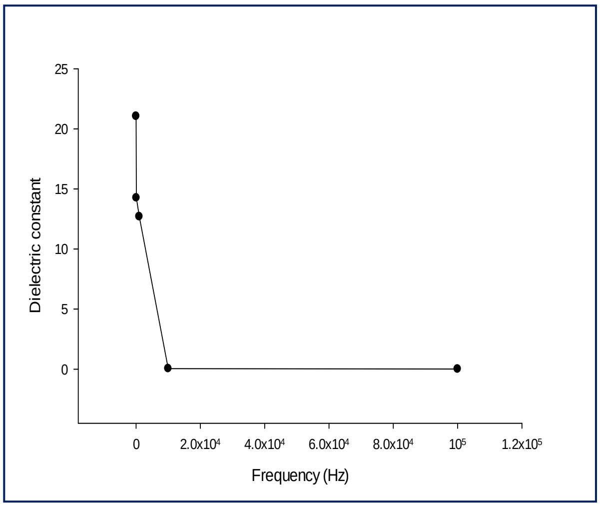

Figure 20 The variation of dielectric constant with applied frequencies at 400 ºC for ZnO thin film

Conclusion

Zinc acetate dehydrate , potassium hydroxide, methanol (CH_3OH), Titanium isopropoxide and 2- methoxy ethanol were used as the starting materials for Titanium Dioxide (TiO_2) and Zinc Oxide (ZnO) sol-gel to enhance the thin films via spin coating method. Non-electrolytic glass was also used as the substrate for both thin films. The average particles sizes were calculated by Debye's Scherrer equation as 8.42 nm at 400 ^{o}C and 36.20 nm at 700 ^{o}C for TiO_2 thin films and 27 nm at 300 ºC and 25 nm at 400 ºC for ZnO thin films. The size distribution was not in homogenous and the crystal quality was not in optimum condition because of un-controlling the ambient conditions for both films. As the SEM results, the average thickness of the TiO_2 thin films for both temperatures was about 595 nm and 714 nm for ZnO thin films.

In order to realize the electrical characterization, the dielectric properties should be performed on TiO_2 and ZnO thin films by using Digital impedence Analyzer (insteak: 8110G LCR Meter). As the results, when the low frequency (<100 Hz) was applied to the TiO_2 thin films, the change in capacitance and dielectric loss were not detected in TiO_2 thin films by the Digital impedence Analyzer. When the high frequency (>1 kHz) was applied to the TiO_2 thin films, the change in dielectric constant and capacitance were found to be decreased. In contrary, the change in capacitance and dielectric loss were detected in ZnO thin films under 100 Hz frequency range. But, the change in dielectric constant and capacitance were found to be decreased as the same as TiO_2 thin films. Especially, the higher dielectric constants were found to be in ZnO thin film compared than in TiO_2 thin films. However, when the frequencies ranges >10 kHz was applied to ZnO films; they were not response and maintain the electrical charges as TiO_2 thin films. Therefore the optimum frequencies ranges for electrical properties for TiO_2 films were about >10 kHz and <100Hz for ZnO thin films. They can be used as high speed digital, high power gain and low noise performances for the micro and nano electronics devices.

Acknowledgements

I would like to thank to Professor Dr Kyaw Lwin Oo, Principle, Technological University (Sittwe) for his kindly permission to carry out this research. I also would like to thank to Professor Dr Khin Mya Mya Soe, Head of Department of Physics, East Yangon University, for her valuable advice to do this research. I also would like to thank to Professor Dr Thet Naing, Department of Physics, East Yangon University, for his warmly discussion to complete this research. Finally, I would like to thank to all of the stuffs in Technological University (Sittwe), Physics Department, East Yangon University and all my family for supporting to complete this research.

References

Kato H, Sano, Michichiro, Miyamato, Kazuhiro, Yao and Takafumi, (2002), "Growth and Characterization of Ga-doped ZnO layers", Journal of Crystal Growth, 237-239

Noboru I, Ozaki Y, Kasu S and James M, (1992), "Chemical Manufacturing processes, Super fine particle technology" Springer Ver Lag, New York

Ohgaki, Takeshi, Ohashi, Naoki, Sugimura, Shigeaki, Royken, Haruki,

Qin Y, Wang X D, and Wang Z L, (2008), "Microfiber – Nanowire Hybrid Structure for Energy Scavenging Nature", 451, 809-813

Sima M, EnculescuI,SimaM,Enache M, Vaslile E, and Ansermet J P, (2007),Phys Status Solid B, 244, 1522

Sun JH, Dong SY, Wang YK, and Sun SP, (2009), J Hazardous Mat, 172 1520

J. Myanmar Acad. Arts Sci. 2020 **Vol. XVIII.No.2C**

SEPARATION OF MICROPARTICLES USING ULTRASONIC STANDING WAVE

Khin Nwe Zin Tun*

Abstract

Acoustic particle separation in millimeter scale channel is becoming a useful technology for microfluidics to control micro sized particles or cells. Particle separation methods have widely used in medical, chemical, biological and life science. In this paper, modern method of particle separation focuses on acoustic method. This technology is based on inducing an ultrasonic standing wave inside a millimeter scale channel. Ultrasonic standing wave is generated across a microfluidic channel by piezoelectric transducer integrated in one of the channel wall. This standing wave enables particles to aggregate its pressure node or anti-node lines due to acoustic radiation force. Acoustic radiation force is a function of the density and compressibility of the particles and fluid. In this study, 10 μm particles will be concentrated in water by using ultrasonic standing wave at 2.2 MHz. The objectives of this study are to obtain the fundamental understanding of particle manipulation in millimetre scale rectangular channel at resonance frequency. And then, two-dimensional theoretical model is developed for particle position calculations. The acoustic field numerical models will be constructed using the finite element methods in COMSOL Multiphysics to estimated number of separation lines and acoustic radiation force. The results of this acoustic based COMSOL simulation approach will be compared with the theoretical results.

Keywords: ultrasonic standing wave, acoustic radiation force, millimeter scale channel, microparticles.

Introduction

In recent decades, precise control of microparticles, biomolecules and cells has become increasingly important inengineering, life sciences and medicine. Following this demand, particle manipulation technologies have been developing actively. Particle trapping, levitation, sorting and separation are the different forms of particle manipulation. Using ultrasonic standing wave is one way of manipulating the particles in microfluidic systems. This ultrasound method is suitable for both biological and non-biological suspended particles. The ultrasonic separation principle is based on the acoustic radiation force acting on microparticles. The acoustic radiation force depends on the ratio of the density and compressibility of the suspended microparticles and the surrounding medium, as well as the frequency and energy density of the imposed ultrasound field. Acoustic radiation forces move the particles to acoustic nodes within the acoustic field. Acoustic forces are utilized to separate particles based on their size and density. Ultrasonic method has many advantages. There are no chemical additives requirement, non-contact and no fouling, continuous operation and no effect on cell viability.

In a basic study, King derived an acoustic radiation pressure equation for incompressible particles in liquid. Yosioka et al. developed King's radiation pressure equation for compressible particles in liquid. They discovered the particles aggregate in the nodes or in the anti-nodes in ultrasonic standing wave. Tolt and Fake demonstrated a separation process based on the acoustic radiation force in a stationary ultrasonic standing wave field. Mandralis and Fake collected submerged polystyrene particles with an ultrasonic standing wave, and then moved the particles by periodically changing the frequency. Hill et al developed a model for the calculation of

---

* Lecturer (Technological University, Thanlyin) , Ph.D Candidate (Yangon Technological University)

particle paths for suspended particles in a fluid for one-dimensional modelling design of resonator for ultrasonic particle manipulation. Most of the models discussed earlier are based on one-dimensional analysis. The two-dimensional modelling of the separation of suspended particle was reported by Francisco J. Trujillo et.al in 2013 by using finite element analysis.

In the present study, a numerical model of an ultrasonic standing wave-based separator is developed. This numerical model performed two dimensional acoustic analysis using COMSOL Multiphysics software. The pressure amplitudes and acoustic radiation force of the ultrasound wave has been determined, the acoustic force acting on particles can be predicted by solving Gor’kov’s equation. All the numerical predictions are compared with the theoretical results.

Background Theory

Ultrasound is sound waves with frequencies higher than the upper audible limit of human hearing. Human can hear sound waves with frequencies between about 20 Hz and 20k Hz. Sound above 20kHz is ultrasound and below 20Hz is infrasound. The characteristics of sound wave are wavelength, amplitude, frequency, velocity and time period.

The number of sound waves produced in unit time is called the frequency of sound waves.

$$f = \frac{1}{T} \tag{1}$$

Thus frequency is the reciprocal of the time period of wave. This means that the frequency is increased with decrease in time and vice versa. Time required to produce one complete wave is called time period or time taken to complete on oscillation is called the time period of the sound wave.[8]

Wavelength is the length between two consecutive peaks. The wavelength of the sound wave in a medium is related to the operating frequency and the sound speed in the medium as follows,

$$\lambda = \frac{c}{f} \tag{2}$$

Where c is the speed of sound in fluid medium and f is the frequency of ultrasonic standing wave.

Ultrasonic Standing Wave

A standing wave is two harmonic waves with equal amplitude, frequency and wavelength that are moving in the opposite direction of each other. Standing wave appears when the medium is confined between two boundaries.

A wave traveling to the right along the x-axis is described by the incident wave equation,

$$y_1 = A\sin(kx - \omega t) \tag{3}$$

An identical wave traveling to the left is described by the reflected wave equation,

$$y_2 = A\sin(kx - \omega t) \tag{4}$$

The standing wave equation is

$$y(x,t) = 2A \sin kx \cos \omega t \qquad (5)$$

This means that the total energy associated with standing wave is twice that of incident or reflected wave. The terms x and t are variables for longitudinal position and time. A is the amplitude of the wave and ω is the angular frequency.

Node and Antinode

A node is a point along a standing wave where the waves amplitude is zero and series of location at equally spaced intervals. Pressure of the wave is zero at node points. The location of the node,

$$x_n = \frac{n\lambda}{2} \ , \quad n=0,1,2,3,\ldots \qquad (6)$$

Anti-node is midway between each pair of nodes and the amplitude is maximum.

$$x_{an} = \left(n + \frac{1}{2}\right)\frac{\lambda}{2} \ , \quad n=0,1,2,3,\ldots \qquad (7)$$

The distance between two nearest node or two nearest antinode is λ/2. The distance between consecutive node and antinode is λ/4.

The number of nodes or separation lines N can be estimated the following formula,

$$N = \frac{W}{\lambda/2} \qquad (8)$$

Two Dimensional Layered Resonator Model

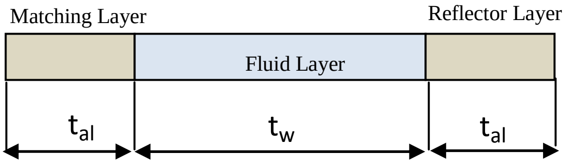

Figure 1 Two-dimensional Layered Resonator Model

Figure 1 shows two dimensional model of layered resonator. There are three layers in the resonator matching, fluid and reflector layers. This resonator is made with aluminium. The piezoelectric transducer and adhesive layer are not considered in this model.

$$t_{al} = n \times \frac{\lambda_{al}}{4} \ , \quad n=1,3,5,7,\ldots \qquad (9)$$

$$t_w = n \times \frac{\lambda_w}{2} \ , \quad n=1,2,3,4,\ldots \qquad (10)$$

Acoustic Radiation Force

King first provided an expression for acoustic radiation force on a small, rigid, incompressible spherical object in an fluid, where the wavelength of the acoustic wave is much larger than the radius of the object. Yosioka and Kawasima expanded King's theory to compressible objects and expressed time-averaged radiation force on a sphere in a plane USW field with acoustic energy density. The acoustic radiation force was calculated using Gor'kov's formulation. The acoustic radiation force is defined as a function of a potential U.

$$F_a = -\nabla U \qquad (11)$$

The force is the negative gradient of the force potential. Where the potential U is defined as,

$$U = 2\pi\rho_w r^3 \left[\frac{f_1}{3\rho_w{}^2 c_w{}^2}\langle p\rangle^2 - \frac{f_2}{2}\langle v\rangle^2\right] \qquad (12)$$

$$f_1 = 1 - \frac{\rho_w c_w{}^2}{\rho_p c_p{}^2} \quad , \quad f_2 = \frac{2\left(\rho_p - \rho_w\right)}{2\rho_p - \rho_w} \qquad (13)$$

So, r is the radius of particles, c is the speed of sound, p is the acoustic pressure and v is the fluid particles velocity. w and p refer to water and particle properties. And the acoustic number k is defined by $2\pi/\lambda$. The notable aspect of the acoustic contrast factor is the possible sign change depending on the densities and compressibility of fluid and particles.

$$\emptyset = \frac{1}{3}\left(\frac{5\,\rho_p - 2\,\rho_w}{2\,\rho_p + \rho_w} - \frac{\rho_w\ c_w^2}{\rho_p\ c_p^2}\right) \qquad (14)$$

Where, ρ_p = densities of particle

ρ_w = densities of water

c_p = sound speed of particle

c_w = sound speed of water

From the equation (14), when ø is positive, particles aggregate at the nodes of the sound pressure profile and other they aggregate at the anti-nodes.

The forces that affect the particle movement are not only acoustic radiation force, but also the drag forces on the particles due to the fluid flow. The stokes drag force F_{drag} can be expressed as:

$$F_{drag} = 6\pi\mu r\left(v_f - v_p\right) \qquad (15)$$

For a spherical particle with radius r, moving at the fluid and particle velocity are v_f and v_p through a liquid with viscosity μ.

Numerical Analysis

This simulation performed with COMSOL Multiphysics software in two dimensional finite element model of fluid layer was constructed using acoustic module. The rectangular model is 6mm width and 50mm length. For this simulation, maximum mesh size of the element is around λ/10. The input parameters for the simulations are density of water ρ_w = 1000 kg/m^3, viscocity μ = 0.9x10^{-3} kg/ms, speed of sound of water c = 1500 m/s, particle diameter = 10μm and density of particle ρ_p= 1050 kg/m^3.

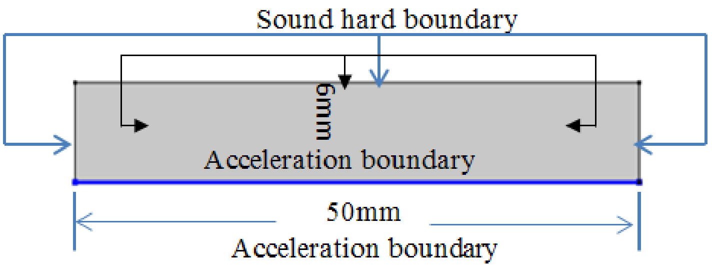

Figure 2 Two Dimensional Channel Geometry

Figure 2 shows the simplified model with boundary conditions. All the rigid walls of the channel were modeled as sound hard boundaries, except the wall where the piezo-actuator was attached. This side of the model was simplified by using an acceleration boundary:

$$-n\left(-\frac{1}{\rho_c}\left(\nabla p_t - q_d\right)\right) = a_n \tag{14}$$

The sound hard boundary was defined by:

$$-n\left(-\frac{1}{\rho_c}\left(\nabla p_t - q_d\right)\right) = 0 \tag{15}$$

Result and Discussion

For the acoustic analysis, a two-dimensional finite element model was constructed using acoustic module in COMSOL. Since the acoustic contrast factor between polystyrene particles and water is approximately 0.78, particles are supposed to be attracted to the pressure nodes. Pressure profiles in the 6 mm width of fluid ch annel can be estimated using finite element model.

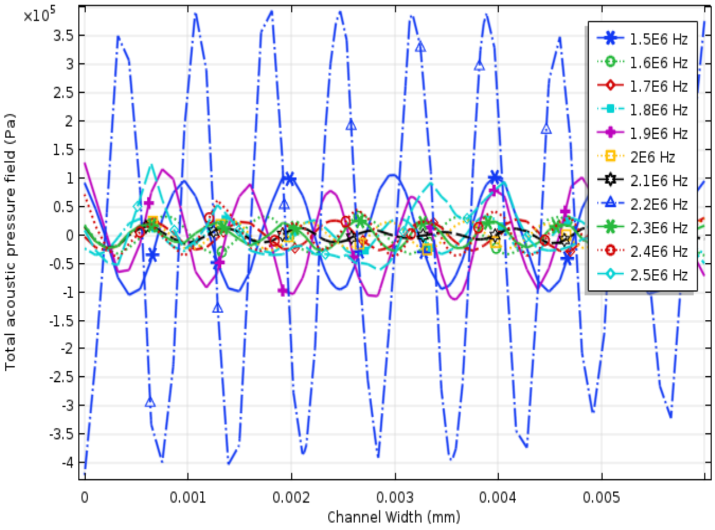

Figure 3 Pressure Profile in Fluid Layer at Frequency 1.5 to 2.5 M Hz

Figure 3 shows the pressure amplitude for frequencies of 1.5 to 2.5 M Hz. The strong changes of the pressure amplitudes at different frequencies are caused by resonance. Operating the system at frequencies close to a resonant frequency will yield higher pressure. The maximum pressure amplitude throughout the process was found at 2.2 MHz.

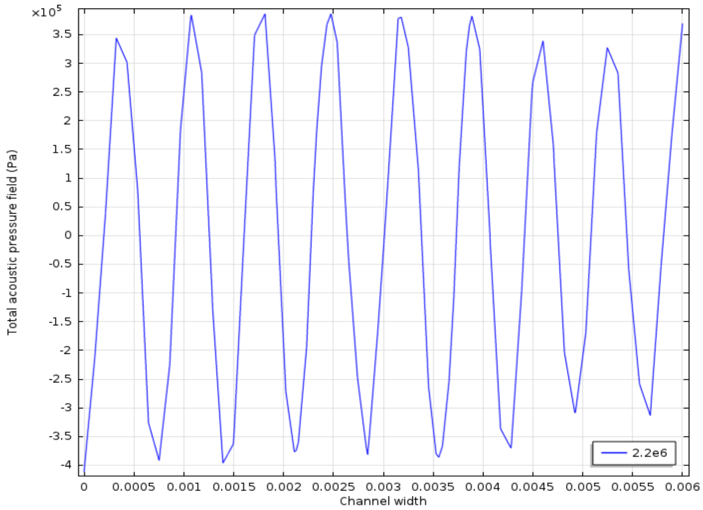

Figure 4 Pressure Profile in Fluid Layer at Frequency 2.2 MHz

As the Figure 4 shows, an ultrasonic standing wave with 8.5λ in the chamber was formed at 2.2 MHz, and the 10μm polystyrene particles aligned on the 17 pressure nodal lines.

Table 1 Theoretical and Simulation of Separation Lines in 6mm Channel

	Theoretical	**Simulation**	**Discrepancy (%)**
λ (mm)	0.6818	0.6729	6
No;of node points	17.6	17	4

As can be seen in the Table I, theoretical and simulation calculated the value of wavelength and node points. The discrepancy of these two is less than 10. So the result is acceptable.

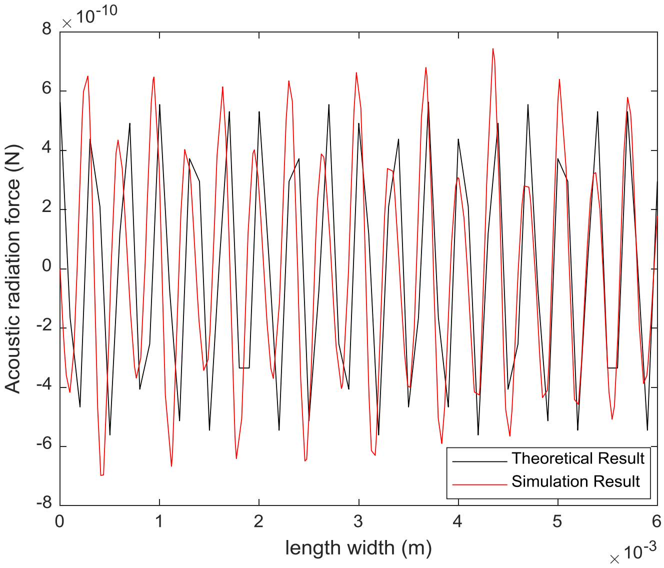

Figure 5 Theoretical and Simulation of Acoustic Radiation Force

Figure 5 shows the theoretical and simulation result of acoustic radiation force for 6mm rectangular channel at frequency 2.2 MHz. As can be seen from the figure, both results are same phase and exactly the same trend.

Conclusion

In this study, basic theory of acoustics in general is first discussed. Next, theory of ultrasonic standing wave is discussed and amount of separation lines in the fluid layer model are estimated. This paper presented theoretical, experimental and numerical model to predict the number of node points and value of wavelength of the ultrasonic standing wave. Theoretical and simulation result of acoustic radiation force are same phase and equal trend in comparison. Two-dimensional acoustic simulation models were built to predict the ultrasound and flow fields inside the fluid layer.

References

Francisco J. Trujillo, Multiphysics modelling of the separation of suspended particles via frequency ramping of ultrasonic standing waves, Ultrasonics Sonochemistry 20,655–666, 2013.

K. Yoshioka, Y. Kawasima. “Acoustic Radiation Pressure on a Compressible 'Sphere.Acoustica,” 1955.

L.V. King. “On the acoustic radiation pressure on spheres. Proc Roy Soc of London,” 1934.

L.P. Gor’kov, “Forces acting on a small particle in an acoustic field within an ideal fluid, Soviet Physics,” Doklady 6, 1962.

Martin Hill and R. J. K. Wood, “Modelling in the design of a flow-through ultrasonic separator,” *Ultrasonics*, vol.38, pp. 662-665, 2000.

Martyn Hill et.al., “Modelling for the robust design of layered resonators for ultrasonic particle manipulation,” Ultrasonics vol.48, pp. 521–528, 2008.

R.J. Townsend et al, Investigation of two-dimensional acoustic resonant modes in aparticle separator, Ultrasonics 44 ,467–471, 2006.

J. Myanmar Acad. Arts Sci. 2020 **Vol. XVIII.No.2C**

IDENTIFICATION OF DYNAMICS CHARACTERISTICS IN A ROTOR BEARING SYSTEM

Mya Thet Hnin[1], Thein Min Htike[2]

Abstract

Vibrations are found almost everywhere in rotating machines. The most common rotating machinery fault is mass unbalance, which is caused by uneven distribution of the mass. In this study, dynamics characteristics of rotor bearing system has been investigated and verified by numerical simulation and experimental measurements. A simple rotor model is considered in the present work. The purposes of this paper are to identify the natural frequencies of rotor bearing system and study the vibration responses due to rotor unbalance. This numerical simulation is done using COMSOL Multiphysics FEM Software Package. The simulation results are verified by rotor bearing test rig for unbalance and residual unbalance conditions.

Keywords: rotor bearing system, dynamics characteristics, vibration responses, FEM, unbalance

Introduction

Rotor unbalance is the most common reason in machine vibrations. Most of the rotating machinery problem can be solved by using the rotor balancing and misalignment. Before detecting the unbalance, the most important fact is to identify the dynamic characteristics of the rotor bearing system. The dynamic characteristics are natural frequency and mode shape (whirling of shaft). A natural frequency is the frequency at which the structure would oscillate if it were disturbed from its rest position and then allowed to vibrate freely. A mode shape is a specific pattern of vibration executed by a mechanical system at a specific frequency. Akash Rajan et al. (2014) investigated dynamic unbalance detection in rotating machinery. These analyses were done without any rotation and with rotation for Jeffcott rotor model. And then, the offset disc and shaft with two rotors were performed for eigenfrequency analysis. Tamrakar and Mittal (2016) discussed about the vibration response of crack rotor with the help of Campbell diagram. Zang et al. (2017) presented the dynamic behaviour of rotor bearing system with bearing inner-race detect and explained the effect of the system stability with the change in speed. A.J.Muminovic et al. (2018) presented numerical and analytical analysis of elastic rotor natural frequency. In previous studies, experimental analysis of dynamic characteristics in rotor bearing system has been rarely investigated.

The main aim of this study is to identify natural frequency and mode shape of system. The results of numerical simulation are validated with the experimental results.

Theory

A rotor dynamics is used to analyse the behaviour of structure ranging from jet engines and steam turbines to auto engines and computer disc storage.

Whirling of Shaft

Whirling of a shaft is its movement in a direction transverse to the axis of rotation. Whirling of shafts occurs due to rotational unbalance of a shaft, even in the absence of external

---

[1] Lecturer, Department of Mechanical Engineering, Yangon Technological University

loads, which causes resonance to occur at certain speeds, known as critical speeds. Whirl plots (mode shape), which plot the mode shapes of a rotor about the rotor axis at discrete rotation intervals.

Free and Forced Vibration

Free vibration occurs when a mechanical system is set in motion with an initial input and allowed to vibrate freely. If a system is subjected to an external force, the resulting vibration is known as forced vibration.

Resonance

Resonance occurs when the applied force or base excitation frequency coincides with a structural natural frequency. During resonant vibration, the response displacement may increase until the structure experiences buckling, fatigue, or some other failure mechanism.

Balancing Methods

The most common balancing methods are as follows.

(1) Static balancing or one plane balancing

(2) Dynamic balancing or two plane balancing

To determine whether a disc is balanced or not, mount the shaft on two low friction bearings. Rotate the disc and permit it to come to rest. Mark the lowest point on the circumference of the disc with chalk. Repeat the process several times, each time marking the lowest point on the disc with chalk. If the disc is balanced, the chalk marks will be scattered randomly all over the circumference. If the disc is unbalanced, all the chalk marks will coincide. The unbalance detected by this procedure is known as *static unbalance.* The static unbalance can be corrected by removing (drilling) metal at the chalk mark or by adding a weight at 180° from the chalk mark. Since the magnitude of unbalance is not known, the amount of material to be removed or added must be determined by trial and error.

Mathematical Modelling

The Jeffcott rotor model is considered for model analysis. It consists of a shaft, at the center of which, a fixed rigid circular disc is mounted, which is supported a pair of bearings. Fig. 1 shows general position of disc in a simple rotor.

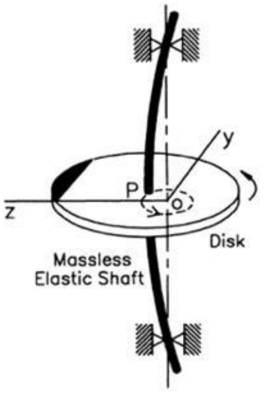

Figure 1 General position of disc in a simple rotor

Equation of Motion

The equations of motion for the rotor may be written, in the coordinates (y,z), as in following equation (3).

$$m\ddot{y}+c\dot{y}+ky=me\omega^2e^{i\omega t} \qquad \text{Eq (1)}$$

$$m\ddot{z}+c\dot{z}+kz=me\omega^2e^{i\omega t} \qquad \text{Eq (2)}$$

$$m\ddot{r}+c\dot{r}+kr=me\omega^2e^{i\omega t} \qquad \text{Eq (3)}$$

Where, e = mass eccentricity, m

ω = shaft rotational speed, rpm

k = shaft lateral stiffness, N/m

y, z = coordinates of the shaft

r = whirl radius, m

$$I_p = m\left(\frac{d^2 - D_0^2}{8}\right) \qquad \text{Eq (4)}$$

$$I_p = m\left(\frac{d^2 + D_0^2}{16} + \frac{h^2}{12}\right) \qquad \text{Eq (5)}$$

Where, I_P = Polar mass moment of inertia, kg-m^2

I_d = Diametral mass moment of inertia, kg-m^2

d = diameter of shaft, m

D_o = diameter of rotor disc, m

h = thickness of disc, m

The natural frequency of the Jeffcott rotor model can be calculated by the following equation.

$$\omega_n = \frac{\pi}{2}\times\left(n+\frac{1}{2}\right)^2 \times\sqrt{\frac{gEI}{ml^4}} \qquad \text{Eq (6)}$$

Simulation Model

In this paper, the numerical simulation is done for simple rotor model with residual unbalance condition. Simple rotor model with residual unbalance, shown in Fig. 2, is simulated for eigenfrequency analysis by using COMSOL Multiphysics software. The rotor geometry is drawn by using Bezier polygon as shown in Fig. 3. From this simulation, the natural frequencies and mode shapes (whirling of shaft) are investigated. And then, the comparison of natural frequencies from numerical simulation and experiment are discussed.

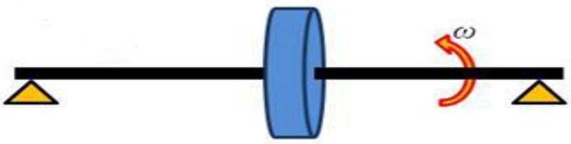

Figure 2 Simple rotor model

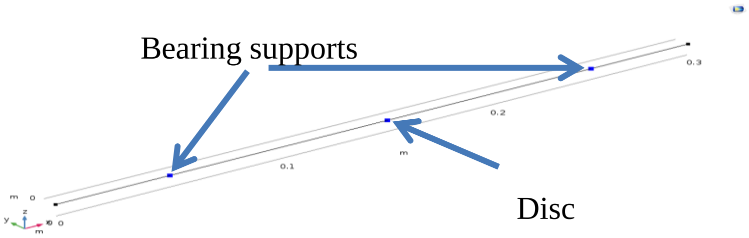

Figure 3 Geometry of rotor model

Table1 Specifications of shaft and disc

Shaft	Disc
Diameter = 8 mm	Diameter = 100 mm
Length = 300 mm	Thickness = 5 mm
ρ = 7850 kg/m3	ρ = 1250 kg/m3
$\nu = 0.3$	$\nu = 0.36$
E = 210 GPa	E = 1280 MPa

Table 1 shows the specifications of shaft and disc. Shaft is made with steel and disc and bearing housing are made with polymer (PLA).

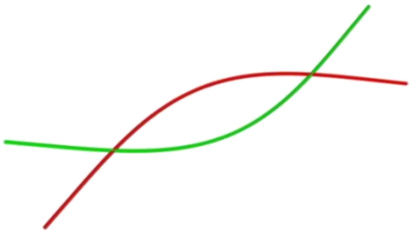

Figure 4 First mode at eigenfrequency 195.79 Hz

Figure 4 Second mode at eigenfrequency 457.85 Hz

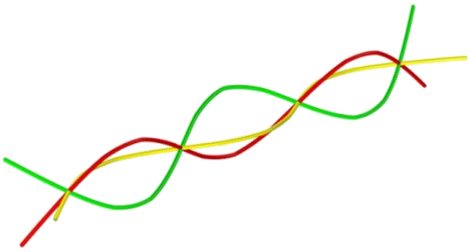

Figure 4 Third mode at eigenfrequency 855 Hz

From numerical simulation, mode shapes and natural frequencies are obtained. First mode occurs at 195.79 Hz as shown in Fig. 4. Second and third mode occurs at 457.85 Hz and 855 Hz.

Experiment

The shaft, 8 mm in diameter and 300 mm in length, is supported by two bearings. A disc, 100 mm in diameter and 5mm in thickness, is mounted at the mid span of the shaft. The accelerometer 1 (Fujikura ARF – 500 A) is placed on right side bearing block to measure the acceleration amplitude in vertical (Z-axis) directions. The accelerometer 2 is placed on left side bearing block to measure the acceleration amplitude in vertical (Z-axis) directions. The data from the sensor is collected by the computer which is connected to the data logger. The natural frequencies are identified from free vibration experiment. Impact hammer (Bruel & Kjaer 8204) is applied to get the initial disturbance in the rotor system. The responses are collected from accelerometer and time domain responses are converted to frequency domain responses by using data logger (Fujikura DC – 7004P).

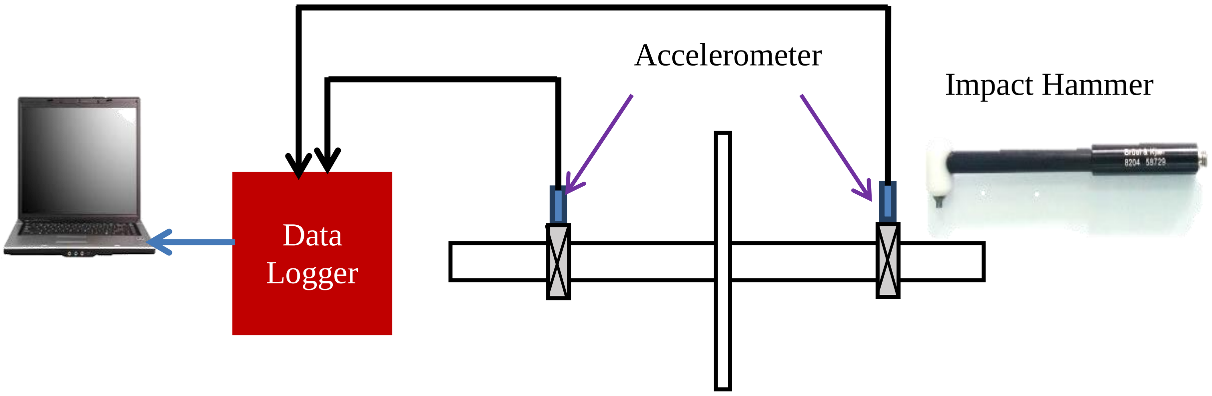

Figure 5 Experimental set up diagram

The experimental set up diagram is shown in Fig. 5. The actual experimental set up figure can be seen in Fig. 6. From free vibration experiment, the natural frequencies are observed as shown in Fig. 7. The results are discussed in next section.

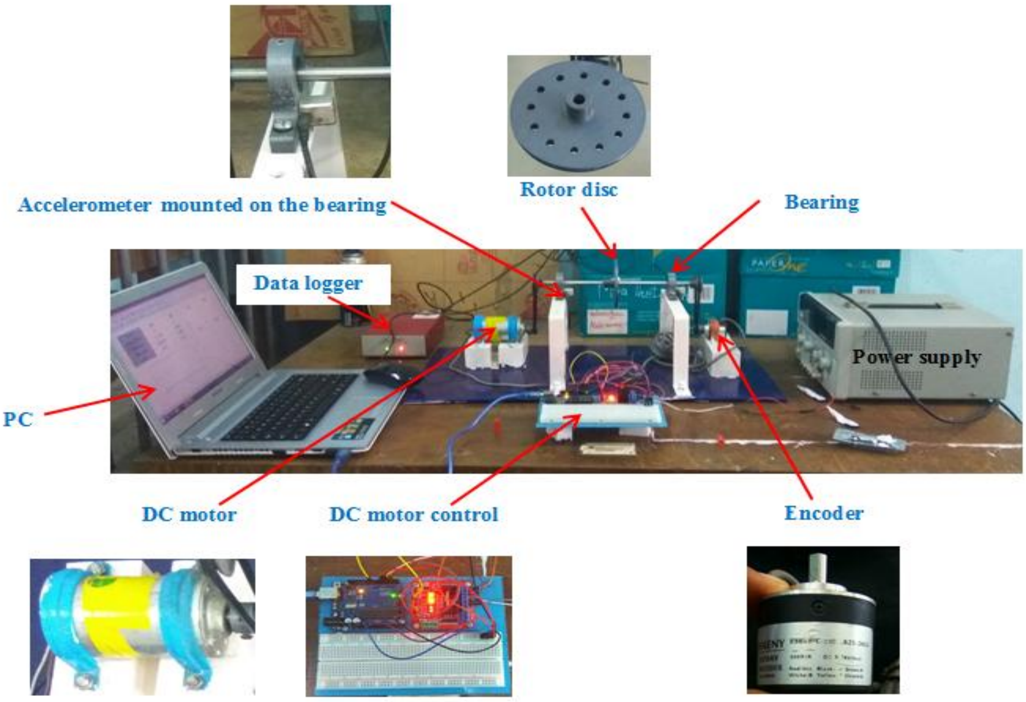

Figure 6 Actual experimental set up figure

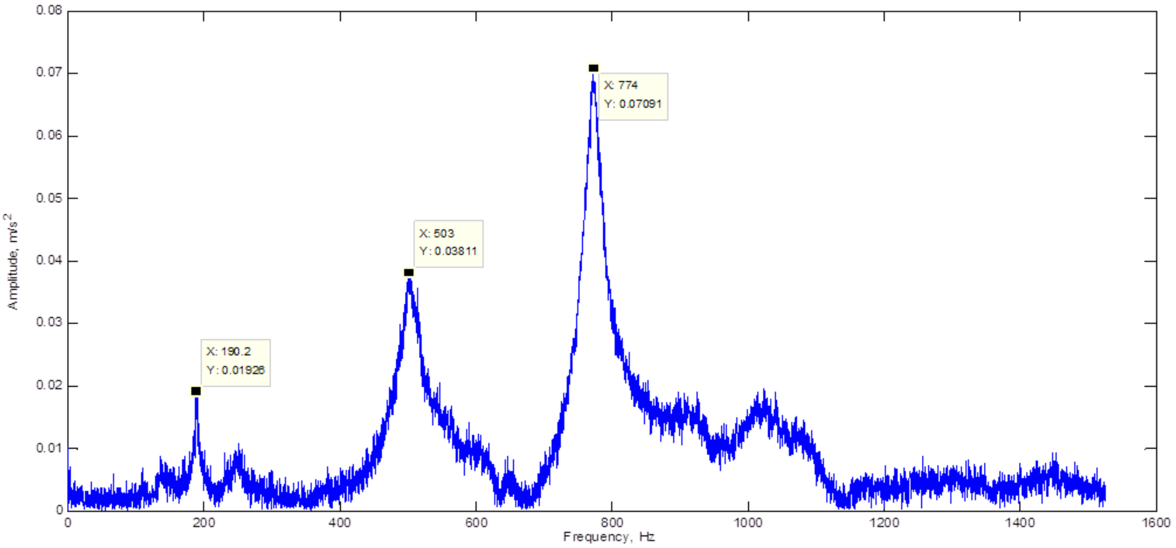

Figure 7 Natural frequency from experiment

Results and Discussions

The comparative results of eigenfrequencies between simulation and experiment for simple rotor system are shown in Table II. It can be seen that the natural frequencies for first three modes are investigated. Although there is a little difference between theoretical and simulation results, these results are nearly the same. The maximum discrepancy is 9.47%which occurs at third mode. There is a good agreement in natural frequencies with maximum difference of less than 10%.

Table 2 Comparison of Natural Frequency

Mode no.	Natural frequency (Hz)		Discrepancy (%)
	Simulation	Experiment	
1	195.79	190.2	2.86
2	457.85	503	8.97
3	855	774	9.47

Conclusion

This paper presented analysis of natural frequencies for simple rotor system. In this study, the dynamic characteristics of a simple rotor system were identified under numerical simulation and experiment. From the simulation and experiment, it can be seen that the comparison of dynamic characteristics was a good agreement although a little discrepancies. It is important to know the natural frequency of the system because of the resonance.

References

Adis J. Muminovic et al., (2018) “Numerical and analytical analysis of elastic rotor natural frequency.” *TEM Journal*, vol. 3.

Akash Rajan et al., (2014)“Dynamic analysis of unbalance in rotating machinery.” *International Journal of Scientific and Engineering Research*, vol. 5, pp.1785-179.

B.K.Kumar et al., (2012) “Determination of Unbalance in Rotating Machine Using Vibration Signature Analysis.” International Journal of Modern Engineering Research, 3415-3421.

Chong Won Lee, (1993) *Vibration analysis of rotor*. Korea Advanced Institute of Science and Technology, Springer Science.

D.J.Ewins, (2000) *Modal testing: theory and practice*. Research Studies Press Ltd.

G.N.D.S. Sudhakar, A.S. Sekhar, (2011) “Identification of unbalance in a rotor bearing system.” *Journal of Sound and Vibration*, pp.2299-2313.

Singiresu S. Rao, (2011) *Mechanical vibration*. 5th ed., Prentice Hall.

Zhang, J., Liu, J., Ma, L. and Wang, J., (2017) “Dynamic analysis of a rotor bearing system with bearing inner-race defect.” *Shock and Vibration*, vol. 4.

J. Myanmar Acad. Arts Sci. 2020 **Vol. XVIII.No.2C**

ANALYSIS OF SINGLE-PARTICLE ENERGY LEVELS OF A NEUTRON IN $^{208}\mathrm{Pb}$ AND LAMBDA IN $^{209}_{\Lambda}\mathrm{Pb}$

Mar Mar Htay[1] and Khin Mar Win[2]

Abstract

We calculated single-particle energy of a neutron in ^{208}Pb and single-particle energy of a lambda in $^{209}_{\Lambda}\mathrm{Pb}$ with harmonic oscillator, Woods-Saxon without spin-orbit and with spin-orbit potentials. In these models, We solved by using Numerove's method to obtain single-particle energy levels in ^{208}Pb and $^{209}_{\Lambda}\mathrm{Pb}$. This model can also be extended to include the more complex configurations that arise for the nuclei with nucleon numbers that are in between the magic numbers. The lambda single-energies for 1s,1p,1d,1f states in $^{209}_{\Lambda}\mathrm{Pb}$ and neutron single-energies for various states in ^{208}Pb are calculated by using Woods-Saxon with spin-orbit potentials. The results of our theoretical calculation for $^{209}_{\Lambda}\mathrm{Pb}$ are compared with experimental data and with the previous theoretical work. It is observed that our results are nearly agreement with experimental results. Therefore, Numerov's method is suitable to search single particle energy levels.

Keyword: single-particle energies, ^{208}Pb, $^{209}_{\Lambda}\mathrm{Pb}$, Numerove method.

Introduction

Single-particle and single-hole neutron states have been previously investigated in the region around the doubly magic ^{208}Pb nucleus [Blomqvist, J., Wahlborn Ark. S]. The interaction of a neutron with the rest of the nucleus referred to as the core has been represented in these studies by a Hamiltonian containing a nuclear Woods-Saxon (WS) potential [Woods . R. D and Saxon. D. S] and a spin-orbit (SO) coupling term. Although the same potential parameterization has been used in [Blomqvist, J., Wahlborn Ark. S] a unique set of parameter values has not been found. They have used the generalized Woods-Saxon (GWS) potential instead of the original WS potential [Woods . R. D and Saxon. D. S] , with the expectation of reproducing the experimental binding energies of single-particle and single-hole neutron orbitals that exist in the neutron shells N = 126 - 184 and 82 - 126, respectively. This potential contains the WS potential plus a term referred to as the surface (SU) potential that maximizes in the nuclear surface and is linearly proportional to the derivative of a WS function. It is a well known fact that the WS potential alone does not reproduce the energies of l= 0 single-particle levels with enough accuracy when applied to a wide nuclide region.

A hypernucleus is a nucleus which contains at least one hyperon in addition to the normal protons and neutrons. The first was discovered by Marian Danysz and Jerzy Pniewski in 1952 using the nuclear emulsion technique.

Protons and neutrons are made of up (u) and down (d) quarks. A Lambda (Λ) hyperon consists of one up, one down, and one strange (s) quark. Like neutrons the Λ-hyperons have no charge, but Λ-s are heavier than neutrons. As a hyperon does not have to obey the Pauli Exclusion principle with the neutrons and protons, it can enter deep inside a nucleus and occupy the same levels already filled with nucleons. This property of hyperons enabled us to view the

---

[1] Dr, Associate Professor, Department of Physics, Myanmar Institute of Information Technology, Mandalay

[2] Dr, Lecturer, Department of Physics, *Sagaing University of Education, Sagaing*

deep-lying shell model structure of nuclei that can not be seen in reactions with nucleons due to the Pauli blocking. The hyperons seem to act as glue inside a nucleus. It was found that if one replaces a neutron with a Λ-hyperon, it makes a bound ${}^{10}_{\Lambda}\mathrm{Li}$ nucleus, while the normal ${}^{10}\mathrm{Li}$ nucleus is known to be unbound [Saha.P.K et al] . This indicates that hypernuclei with large neutron-to-proton ratios could exist in a stable state, even though the corresponding normal neutron-rich nuclei could be unstable.

Although the nucleon-nucleon (NN) interaction is reasonably well known, the ΛN, ΛΛN and ΛΛ interactions are yet to be fully understood. One studies the Λ-hypernucleus to estimate the basic Λ-nucleon interaction. Experimentally about thirty-five hypernuclei with one Λ-hyperon and six hypernuclei with two Λ-hyperons have been found so far [Nakazawa. K et al]. The Λ and ΛΛ- separation energies from hypernuclei provide a window to estimate the ΛN, ΛΛN- interactions properties of Λ and nucleons.

Numerical Calculation

We solved numerically the radial part of Schroedinger's equation by using Numerov's method to obtain neutron single-particle energy. Numerov's method is a numerical method to solve ordinary differential equations of second order in which the first-order term does not appear. It is a fourth-order linear multistep method. The method is implicit, but can be made explicit if the differential equation is linear.

The Numerov method can be used to solve differential equation

$$\frac{d^2u}{dr^2} = -k(r)u(r) + S(r) \qquad (1)$$

Three values of u_{n-1}, u_n, u_{n+1} taken at three equidistant points r_{n-1}, r_n, r_{n+1} are related as follows:

$$u_{n+1}(1+\frac{h^2}{12}k_{n+1}) = 2u_n(1-\frac{5h^2}{12}k_n) - u_{n-1}(1+\frac{h^2}{12}k_{n-1}) + \frac{h^2}{12}(S_{n+1}+10S_n+S_{n-1}) + 0(h^5) \qquad (2)$$

Where $u_n = u(r_n)$, $k_n = k(r_n)$, $S_n = S(r_n)$ and $h = r_{n+1}-r_n$.

For nonlinear equations of the form

$$\frac{d^2u}{dr^2} = f(u,r) \qquad (3)$$

the method gives

$$u_{n+1}-2u_n + u_{n-1} = \frac{h^2}{12}(f_{n+1}+10f_n+f_{n-1}) + 0(h^5) \qquad (4)$$

This is an implicit linear multistep method which reduces to the explicit method given above if f is linear in u by setting $f(u, r) = -k(r)u(r) + S(r)$. It achieves order-4 accuracy.

In numerical physics the method is used to find solutions of the unidimensional Schrodinger equation for arbitrary potentials. It is used to solve the radial equation for a spherically symmetric potential. After separating the variables and analytically solving the angular equation, we get the following equation of the radial function R(r):

$$\frac{d^2u(r)}{dr^2}+\frac{2\mu}{\hbar^2}\left[E-V(r)-\frac{\hbar^2}{2\mu}\frac{\ell(\ell+1)}{r^2}\right]u(r)=0 \tag{5}$$

Where $u(r) = rR_{nl}$ is the reduced radial wave function.

A regular solution near the origin for $u(r): u(r\to 0)\to r^{\ell+1}$

The asymptotic solution at $r\to\infty : u(r\to\infty)\to u(r)=e^{-\alpha r^2}, \alpha$ = constant

The Schrödinger Radial Equation can be written as follow:

$$\frac{d^2u(r)}{dr^2}+k(r)u(r)=0 \tag{6}$$

$$\frac{d^2u(r)}{dr^2}=u_r''=-k(r)u(r) \tag{7}$$

$k(r) = \dfrac{2\mu}{\hbar^2}\left[E-V(r)-\dfrac{\hbar^2}{2\mu}\dfrac{\ell(\ell+1)}{r^2}\right]$ is the kernel equation.

Equation (5) can be solved by Numerov Algorithm as follow:

First we split the r range into N points according to $r_n = r_{n-1} + h$; then we write the wave function $u_n \equiv u(r_n)=u(r_{n-1}+h)$ and $k_n \equiv k(r_n) =k(r_{n-1}+h)$.

Expanding u(r) around r_n:

$$u(r) = u(r_n) + (r-r_n)u'(r_n) + \frac{(r-r_n)^2}{2!}u''(r_n) + \frac{(r-r_n)^3}{3!}u'''(r_n)$$

$$+\frac{(r-r_n)^4}{4!}u^{iv}(r_n)+0(h^5) \tag{8}$$

If we evenly discretize the space, we get a grid of r points, where $h=r_{n+1}-r_n$. By applying the above equations to this discreet space, we get a relation between the u_n and u_{n+1}:

$$u_{n+1} \equiv u(r_n+h) = u(r_n) + hu'(r_n) + \frac{h^2}{2!}u''(r_n) + \frac{h^3}{3!}u'''(r_n) + \frac{h^4}{4!}u^{iv}(r_n) + 0(h^5) \tag{9}$$

Since $u_n \equiv u(r_n)$,

$$u_{n+1} = u_n + hu_n' + \frac{h^2}{2}u_n'' + \frac{h^3}{6}u_n''' + \frac{h^4}{24}u_n^{iv} + 0(h^5) \tag{10}$$

Computationally, this amounts to taking a step forward by an amount h. If we want to take a step backwards, we repleace every h with –h and get the expression for u_{n-1}:

$$u_{n-1} \equiv u(r_n-h) = u(r_n) - hu'(r_n) + \frac{h^2}{2!}u''(r_n) - \frac{h^3}{3!}u'''(r_n) + \frac{h^4}{4!}u^{iv}(r_n) + 0(h^5) \tag{11}$$

$$u_{n-1} = u_n - hu_n^{'} + \frac{h^2}{2}u_n^{''} + \frac{h^3}{6}u_n^{'''} + \frac{h^4}{24}u_n^{iv} + 0(h^5) \qquad (12)$$

By summing the two equation (10) and equation (12),

$$u_{n+1} - 2u_n + u_{n-1} = h^2 u_n^{''} + \frac{h^4}{12}u_n^{iv} + 0(h^5) \qquad (13)$$

To get an expression for the u_n^{iv} factor, we simply have to differentiate $u_n^{''} = -k_n u_n$ twice and approximate it again in the same way we did this above:

$$u_n^{iv} = \frac{d^2}{dx^2}(-k_n u_n) \qquad (14)$$

From equation (13),

$$u_{n+1} - 2u_n + u_{n-1} = h^2 u_n^{''} \qquad (15)$$

$$u_{n+1}^{''} - 2u_n^{''} + u_{n-1}^{''} = h^2 u_n^{iv} \qquad (16)$$

$$-u_{n+1}k_{n+1} + 2u_n k_n - u_{n-1}k_{n-1} = h^2 u_n^{iv} \qquad (17)$$

Substituting equation (17) into equation (13)

$$u_{n+1} - 2u_n + u_{n-1} = -h^2 u_n k_n + \frac{h^2}{12}(-u_{n+1}k_{n+1} + 2u_n k_n - u_{n-1}k_{n-1}) \qquad (18)$$

$$u_{n+1}(1 + \frac{h^2}{12}k_{n+1}) - 2u_n(1 - \frac{5h^2}{r^2}k_n) + u_{n-1}(1 + \frac{h^2}{12}k_{n-1}) = 0 \qquad (19)$$

from equation (19), we obtained the following relations.

For forward recursive relation

$$u_n = \frac{2(1 - \frac{5h^2}{12}k_{n-1})u_{n-1} - (1 + \frac{h^2}{12}k_{n-2})u_{n-2}}{(1 + \frac{h^2}{12}k_n)} \qquad (20)$$

For backward recursive relation

$$u_{n-1} = \frac{2(1 - \frac{5h^2}{12}k_n)u_n - (1 + \frac{h^2}{12}k_{n+1})u_{n+1}}{(1 + \frac{h^2}{12}k_{n-1})} \qquad (21)$$

Therefore when we calculate our wave function using the backward-forward technique, we should note that the recursive formulas imply having knowledge of two initial values for each direction. It is also necessary to know the first derivative at the appropriate order. By subtraction from equation (20) to equation (21)

$$u_{n+1} - u_{n-1} = 2hu_n' + 2\frac{h^3}{6}u_n''' \tag{22}$$

$$u_n' = \frac{1}{2h}\left[(1+\frac{h^2}{6}k_{n+1})u_{n+1} - (1+\frac{h^2}{6}k_{n-1})u_{n-1}\right] \tag{23}$$

We used harmonic-oscillator potential and Woods-Saxon potential in Schrodinger equation to obtain wave functions and energy states. The harmonic-oscillator potential (HO) is given by

$$V(r) = \frac{1}{2}\mu\omega^2 r^2 \tag{24}$$

where μ is reduce mass of nucleon and ω is the parameter. $\hbar\omega \approx 45 \times A^{-1/3}$.

The Woods-Saxon potential is based upon the sum of a spin-independent central potential, a spin-orbit potential, and the Coulomb potential. The spin-orbit potential has the form, $V_{so}(r)\ell.s$, where ℓ is the orbital angular momentum and s is the intrinsic spin angular momentum of the nucleon.

$$V(r) = V_0(r) + V_{so}(r)\vec{\ell}.\vec{s} + V_c(r) \tag{25}$$

V_0(r) is the spin-independent central potential:

$$V_0(r) = \frac{V_0}{1+\exp\left(\frac{r-R}{a}\right)}, \quad R = \text{nuclear radius} \tag{26}$$

$R = r_0 A^{1/3}$. V_{so}(r) is the spin-orbit potential:

$$V_{so}(r) = V_{so}\frac{1}{r}\frac{d}{dr}\frac{1}{1+\exp\left(\frac{r-R}{a}\right)} = -V_{so}\frac{1}{ra}\frac{\exp\left(\frac{r-R}{a}\right)}{\left(1+\exp\left(\frac{r-R}{a}\right)\right)^2} \tag{27}$$

The Woods-Saxon form of potential is assumed for the single-particle potential for the nucleon. The chosen parameters are r_0= 1.25 fm and a= 0.65 fm .

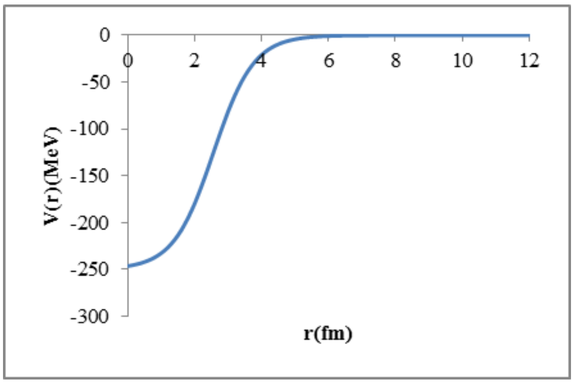

Figure 1 Woods-Saxon potential

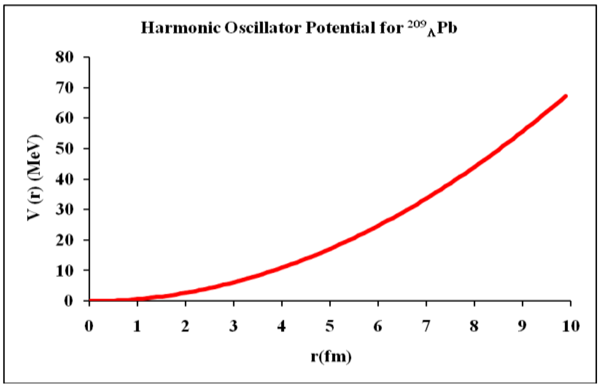

Figure 2 Harmonic-oscillator potential

Calculation of Energy Levels

Since both $u_{out}(r)$ and $u_{in}(r)$ satisfy a homogeneous equation, their normalization can always be chosen so that they are set to be equal at the r_c point. An energy eigen value is then signaled by the equality of derivatives at this point. At the matching point the eigen functions $u_{out}(r)$ and $u_{in}(r)$ and first derivatives $u'_{out}(r)$ and $u'_{in}(r)$ must all satisfy the continuity conditions:

$$(u_{out})_{rc} = (u_{in})_{rc} \qquad (u'_{out})_{rc} = (u'_{in})_{rc} \tag{28}$$

thus, we can write the corresponding condition for the logarithmic derivative at r_c as

$$\left[\frac{u'_{out}}{u_{out}}\right]_{rc} = \left[\frac{u'_{in}}{u_{in}}\right]_{rc} \tag{29}$$

and then we can define a Match (E) function at r_c whose zeros correspond to the energy eigenvalues as

$$\mathrm{Match}(E) = \left[\frac{u'_{out}}{u_{out}}\right]_{rc} - \left[\frac{u'_{in}}{u_{in}}\right]_{rc} \tag{30}$$

Therefore we proceed numerically in the following way: we set a trial energy range splitting this E range into N points, according to $E_n = E_{n-1} + \Delta E$, where ΔE is the energy step. For each E_n we calculate their eigenfunctions u_{out} and u_{in} at the r_c point; and we build the Match(E) function here, looking for a change of sign in it (which implies a zero cross).

When we find the energy eigenvalue, the calculated inwards and outwards eigenfunctions will tend not to match at the r_c point. However we can look for a strategy to solve this problem. Denoting the outwards and inwards functions directly obtained from the recursive formulas as uo(r) and ui (r), respectively.

Results and Discussion

4.1 Single-Particle Energy Levels of a Neutron in ^{208}Pb

We solved numerically the shoredinger equation by using Numerov's method to obtain single particle energy levels of a neutron in ^{208}Pb. It is used the harmonic oscillator potential, central potential and Woods-Saxon potential. The neutron single particle energy levels and sub energy levels are obtained from central potential and Woods-Saxon potential with spin orbit. The results are shown in table(1) and figure (3). It is observed that energy levels are split sub energy levels by using Woods-Saxon potential. The wave functions for various state such as s, p and d states. The results are shown in Fig. (4), (5) and (6). It is seen that wave functions for all bound states are convergent. Figure (7), (8) and (9) are shown various principal number of s, p and d state. These wave functions are shifted to higher state.

Table 1 Single particle energies in ^{208}Pb for various states

Harmonic Oscillator Potential		**Woods-Saxon potential without Spin-orbit**		**Woods-Saxon potential with Spin-orbit**	
Shell	Energy (MeV)	Shell	Energy (MeV)	Shell	Energy (MeV)
1s	-42.6	1s	-42.6	1s	-42.6
1p	-34.76	1p	-38.36	$1p_{3/2}$ $1p_{1/2}$	-38.45 -38.19
1d, 2s	-27.16	1d 2s	-33.41 -31.6	$1d_{5/2}$ $1d_{3/2}$ 2s	-33.68 -33.03 -31.6
1f , 2p	-19.56	1f 2p	-27.72 -24.94	$1f_{7/2}$ $1f_{5/2}$ $2p_{3/2}$ $2p_{1/2}$	-28.26 -27.04 -25.12 -24.59
1g, 2d, 3s	-11.96	1g 2d 3s	-21.37 -17.85 -14.44	$1g_{9/2}$ $1g_{7/2}$ $2d_{5/2}$ $2d_{3/2}$	-22.28 -20.3 -18.28 -17.23
1h, 2f, 3p	-4.36	1h 2f 3p	-11.96 -10.44 -8.66	$1h_{11/2}$ $1h_{9/2}$ $2f_{7/2}$ $2f_{5/2}$	-15.79 -12.9 -11.15 -9.48

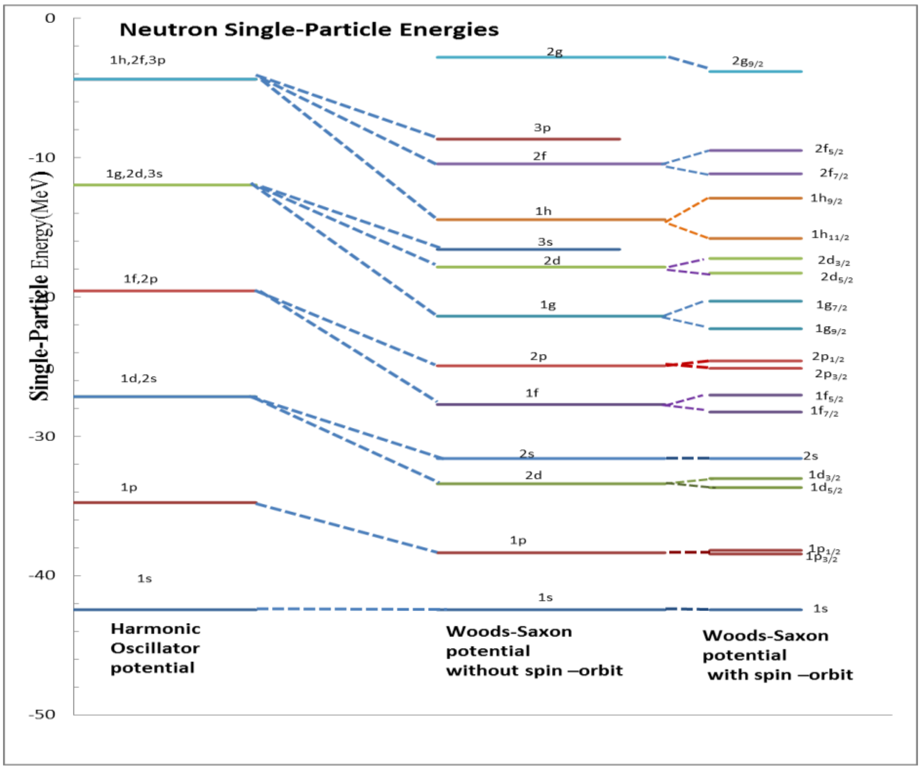

Figure 3 Neutron single-particle states in ^{208}Pb

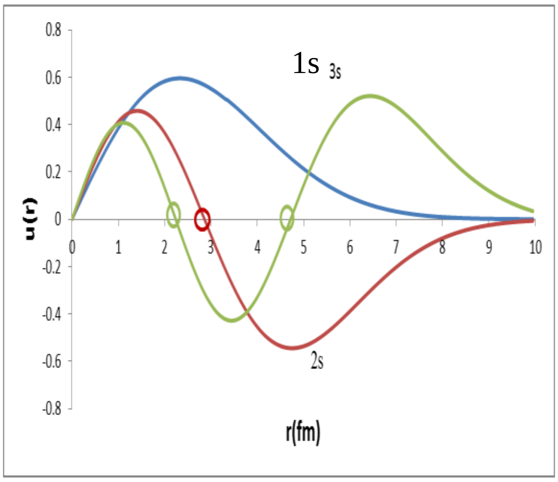

Figure 4 s-states wave functions for ^{208}Pb

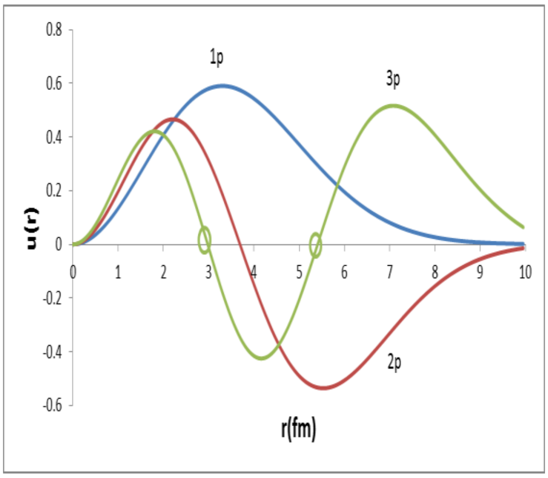

Figure 5 p-states wave functions for ^{208}Pb

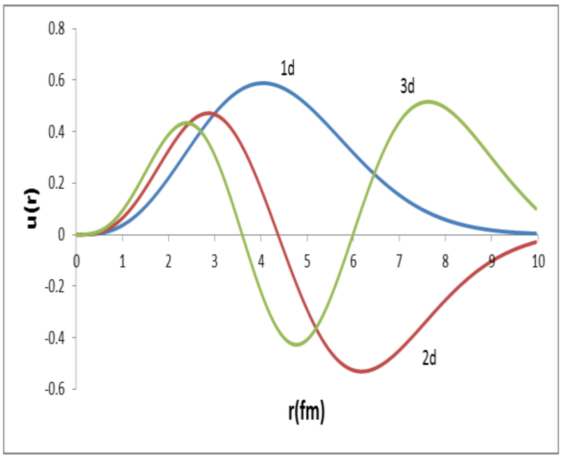

Figure 6 d-states wave functions for ^{208}Pb

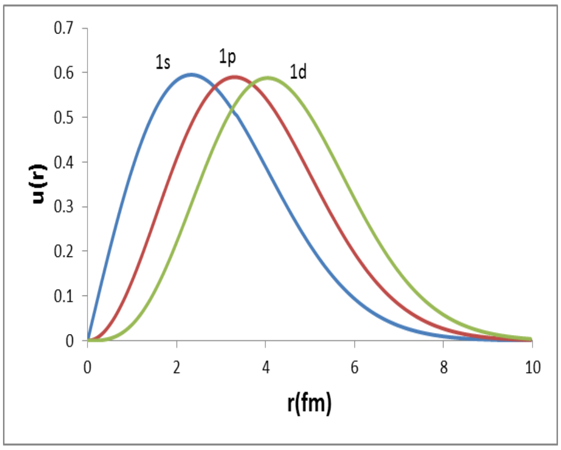

Figure 7 wave functions for 1s,1p and 1d states

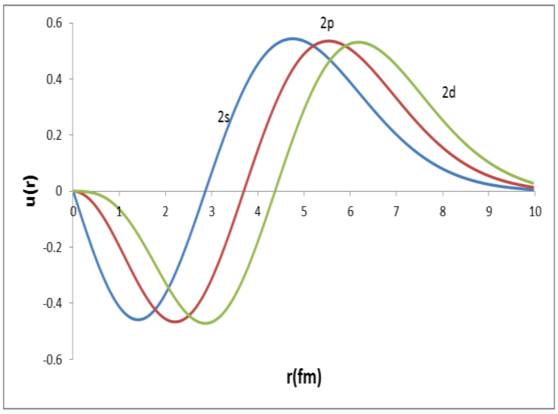

Figure 8 wave functions for 2s, 2p and 2d for ^{208}Pb

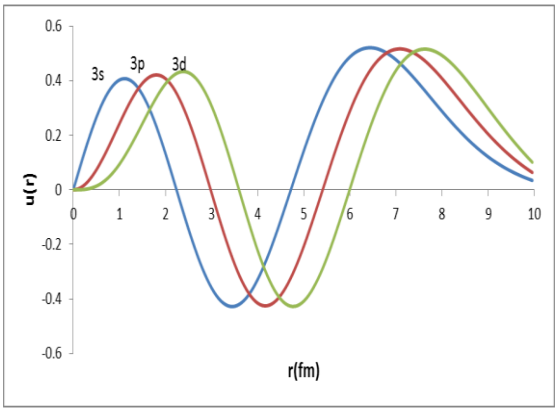

Figure 9 wave functions for 3s,3p and 3d for ^{208}Pb

4.2 Single-Particle Energy Levels of a Lambda in $^{209}_{\Lambda}\text{Pb}$

The number of neutrons are allowed by the Pauli principle to occupy one of these levels. As a hyperon does not have to obey the Pauli Exclusion principle with the neutrons and protons, it can enter deep inside a nucleus and occupy the same levels already filled with nucleons. Lambda single-particle energy in $^{209}_{\Lambda}\text{Pb}$ are calculated by using Numerov's method. The results are shown in the following figures.

Fig.(10) shows lambda s-states wave functions with harmonic oscillator potential for $^{209}_{\Lambda}\text{Pb}$. Fig. (11) and (11) show lambda p and d-states wave functions with harmonic oscillator potential for $^{209}_{\Lambda}\text{Pb}$. It is seen that all wave functions are finite. The lambda single-particle states in $^{209}_{\Lambda}\text{Pb}$ with Woods-Saxon spin orbit potential are obtained by solving Schrödinger equation. The results are shown in Table (1). It is indicated the effect of the spin-orbit potential in splitting the states of a given ℓ value. The overall strength of the spin-orbit potential has been determined empirically. We compare our results with experimental results [Ajimura. S et al] and theoretical results of *Vidana.A et al*.

Table 2 Comparison of theoretical results and experimental results of Lambda single-particle energies in $^{209}_{\Lambda}\text{Pb}$

Sub Shell	**Theoretical results [*Vidana.A et al*] (MeV)**			**Experimental results** [Ajimura.S et al] **(MeV)**	**Our results (MeV)**
	O	**A**	**F**		
1s	-23.1	-29.5	-26.5	-27.0	-25.85
1p	-19.6	-25.7	-22.4	-22.0	-21.89
1d	-14.5	-21.0	-17.5	-17.0	-17.18
1f	-10.5	-15.7	-11.8	-12.0	-11.9
1g	-5.1	-9.7	-5.6	-7.0	-6.0

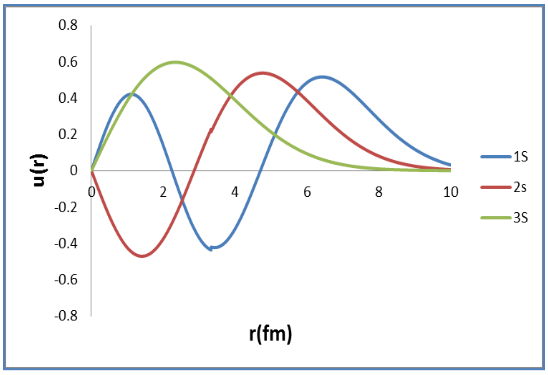

Figure 10 Neutron s-states wave functions for $^{209}_{\Lambda}\text{Pb}$

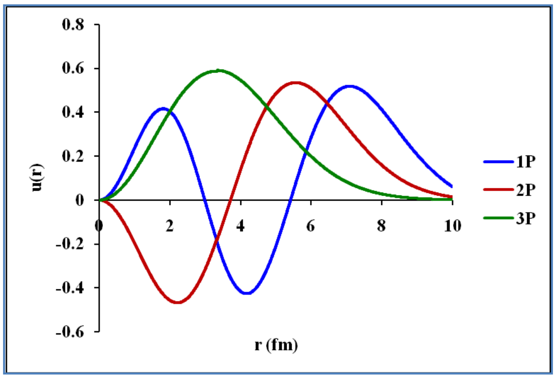

Figure 11 Neutron p-states wave functions for $^{209}_{\Lambda}\text{Pb}$

Conclusion

We calculated neutron single particle energies in ^{208}Pb and lambda single particle energies in ${}^{209}_{\Lambda}\mathrm{Pb}$ by using Numerov's method for harmonic oscillator, central potential and spin-orbit WoodsSaxon potential. It is observed that the energy levels are split in to sub energy levels. Our results for ${}^{209}_{\Lambda}\mathrm{Pb}$ are compared with experimental results [Ajimura.S et al] and other theoretical results by Vidana. A. et al., are calculated Brueckner-Hartree-Fock method for Nijmegen various O, A and F which are divided according to effective mass of lambda $m^*_\Lambda / m_\Lambda = 0.78, 0.67$ and 0.81. Our calculated results for ${}^{209}_{\Lambda}\mathrm{Pb}$ are nearly agreement with the experimental results and theoretical results of Nijmegen potential F.

Acknowledgements

I would like to express sincere thanks to Professor Dr Khin Swe Myint, Rector (Rtd), emeritus Professor, Physics Department, Mandalay University for her valuable advice and discussion. I am very deeply grateful to Theoretical Nuclear Physics Group, Mandalay University for their valuable discussion and advice.

References

Blomqvist, J., and Wahlborn Ark. S. (1959) "Effective nuclear moments in ^{207}Pb" *Journal of Nuclear Physics,*Europ, vol. 86, pp.395-404.

Woods . R. D and Saxon. D. S (1954) "Diffuse Surface Optical Model for Nucleon-Nuclei Scattering" *Physical Review Journal*, American, vol 95. pp.577-578.

Woods . R. D and Saxon. D. S (1954) "Diffuse Surface Optical Model for Nucleon-Nuclei Scattering" *Physical Review Journal*, American, vol 95. pp.577-578.

Saha.P.K et al (2005) ." Production of the Neutron-Rich Hypernucleus $10\Lambda\mathrm{Li}$ in the $(\pi-,K+)$ Double Charge-Exchange Reaction" *Phys. Rev. Lett.* American, vol 94, pp.052502-052505.

Nakazawa. K et al (2015) . "Study of Double-strangeness Nuclear Systems with Nuclear Emulsion" *Phys. Procedia* ,Japan, vol 80, pp. 69-73.

Ajimura. S et al (1995)"The Lambda hypernuclear spectroscopy with the SKS spectrometer at KEK 12-GeV PS" *Nucl.Phys* Japan, A585, pp. 173C-182C.

Vidana.A et al (2001) "Hypernuclei with a Microscopic Lambda-Nucleon Force" *Nuclear Physics A*, Japan, vol 835.pp.19-26.

J. Myanmar Acad. Arts Sci. 2020 **Vol. XVIII.No.2C**

DISTRIBUTION SYSTEM RELIABILITY IN SHWE SAR YAN PRIMARY SUBSTATION

Hlaing Zin Myint[*]

Abstract

This paper is intended to find the most reliable method in distribution by using protective devices because high reliability power system is urgently needed in Myanmar. Approximately 80% load interruptions are due to breakdown in distribution system and insufficient supply. Therefore, it is important to understand the impact of the outages on the customer's outage costs, system adequacy and security. In this research, the impacts of protective devices installation on distribution system reliability were analyzed using analytical method and evaluation techniques. Load data on the feeders were collected from Shwe Sar Yan primary distribution substation from December 2017 to December 2018 and system data were calculated on monthly basis for one year. In this research, fuses were used in every lateral line for lateral protection and it could be seen that the energy not supplied (ENS) in feeder 1 was decreased from 448.92 MWh/yr to 32.91 MWh/yr. By using fuses, total ENS were reduced from 17207.11 MWh/yr to 4451.65 MWh/yr in all feeders besides it was abated from 17207.11 MWh/yr to 4377.14 MWh/yr because of disconnecting switch and also depleted from 17207.11 MWh/yr to 4416.71 MWh/yr by 90% protection failure. In this research, reliability improvement scheme was tested as lateral protection with fuse, feeder protection with disconnecting switches and effect of protection failure rate and then the amount of total ENS were reduced too much during one year. In this research, using disconnecting switches method is the best. By studying this research, it could be chosen the most reliable method in distribution system.

Keywords: protection failure rate, Energy not supplied (ENS), impacts, distribution system, protective devices, disconnecting switch, fuses

Introduction

Electricity is one of the most important forms of energy in the world. The ability of an electric power network to provide an adequate supply of electrical energy is usually designated by the term power system reliability(Brown Richard E,2008). Reliability means the ability of a system to perform required function under state conditions for a given period of time. It is very important for power system to meet the required power demand and to be reliable as possible. This research is intended to analyze the distribution system reliability and describes the hierarchical levels in electrical power system and described reliability indices and calculation of power system reliability is Shwe Sar Yan substation. The system rating is 230/33/11 kV. In this research, the analysis of reliability improvement will be calculated by protection system.

---

[*] Lecturer, Department of Electrical Power Engineering, Technological University (Banmaw)

Analysis of Power System Reliability

Reliability refers to the continuity of power flow when power distribution network is considered. It supplies continuous power to the customers. It provides power in such manner that the system behavior carrying on without interruption. System adequacy and system security are basic concepts of power system reliability. Power system adequacy is the ability of the system to supply all energy demand requirements at all times. System adequacy is associated with system steady-state conditions and offers information on future system behavior that can be used in system planning. Security, on the other hand, is the ability of the system to avoid service interruption under sudden disturbances. System security is associated with the dynamic and transient real-time system operation, such as general and transmission line contingencies and generation uncertainties(Leonel de Megathacs ,2008).

2. 1. Basic Power System Planning

A power system can be divided into the subsystems of generation, transmission, and distribution facilities according to their functions. For the purpose of conduction power system reliability assessment, these systems are combined into different system hierarchical levels or functional zones (Lee Layton, 2004). In this research, only distribution system reliability is calculated. Customer-oriented indices and load-oriented indices are classifications of distribution system reliability. In this research, only customer- oriented indices as SAIFI, SAIDI, CARDI and ENS are calculated by using protection system and used formula e are as follows.

The system average interruption frequency index (SAIFI) is given in Equation (1)

$$\text{SAIFI} = \frac{\text{Total number of customer interruptions}}{\text{Total number of customers served}} \qquad (1)$$

System average interruption duration index (SAIDI) is followed in Equation (2)

$$\text{SAIDI} = \frac{\sum \text{Customer Interruption Durations}}{\text{Total Number of Customers Served}} \qquad (2)$$

Customer Average Interruption Duration Index (CAIDI)is shown in Equation(3)

$$\text{CAIDI} = \frac{\sum \text{Customer Interruption Durations}}{\text{Total Number of Customer Interruptions}}$$

$$\text{CAIDI} = \frac{\sum \gamma_i N_i}{N_T} = \frac{\text{SAIDI}}{\text{SAIFI}} \qquad (3)$$

Total energy not supplied by the system is estimated using Equation (4)

$$\text{ENS}=\sum L_{a(i)} U_i \qquad (4)$$

Where $L_{a(i)}$ and U_i respectively are the average connected load and the average annual outage time at load point i.

Reliability Indices Calculation

3.1 Reliability and Load Data

Shwe Sar Yan primary substation has two transformers, 100MVA and 60MVA transformer, 230 kV/ 132 kV line supplies to Tagontine and Pyin Oo Lwin. In 60MVA transformer (230 kV/ 33 kV), there are four feeders such as Shwelyanbo, Patheingyi, Chan Mya Tharsi and Pyi Kyi Tagon. Shwelyanbo is designated as load point A. Patheingyi is referred to load point B. Chan Mya Tharsi and Pyi Kyi Tagon are assumed as load point C and D. Figure (1) illustrates the load data in Shwe Sar Yan primary substation from December 2017 to December 2018. Figure (2) shows single line diagram of Shwe Sar Yan primary substation.

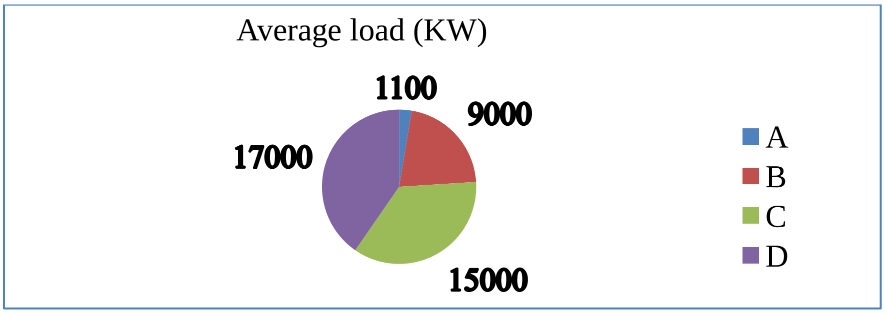

Figure 1 Average Load in Shwe Sar Yan Primary Substation during One Year

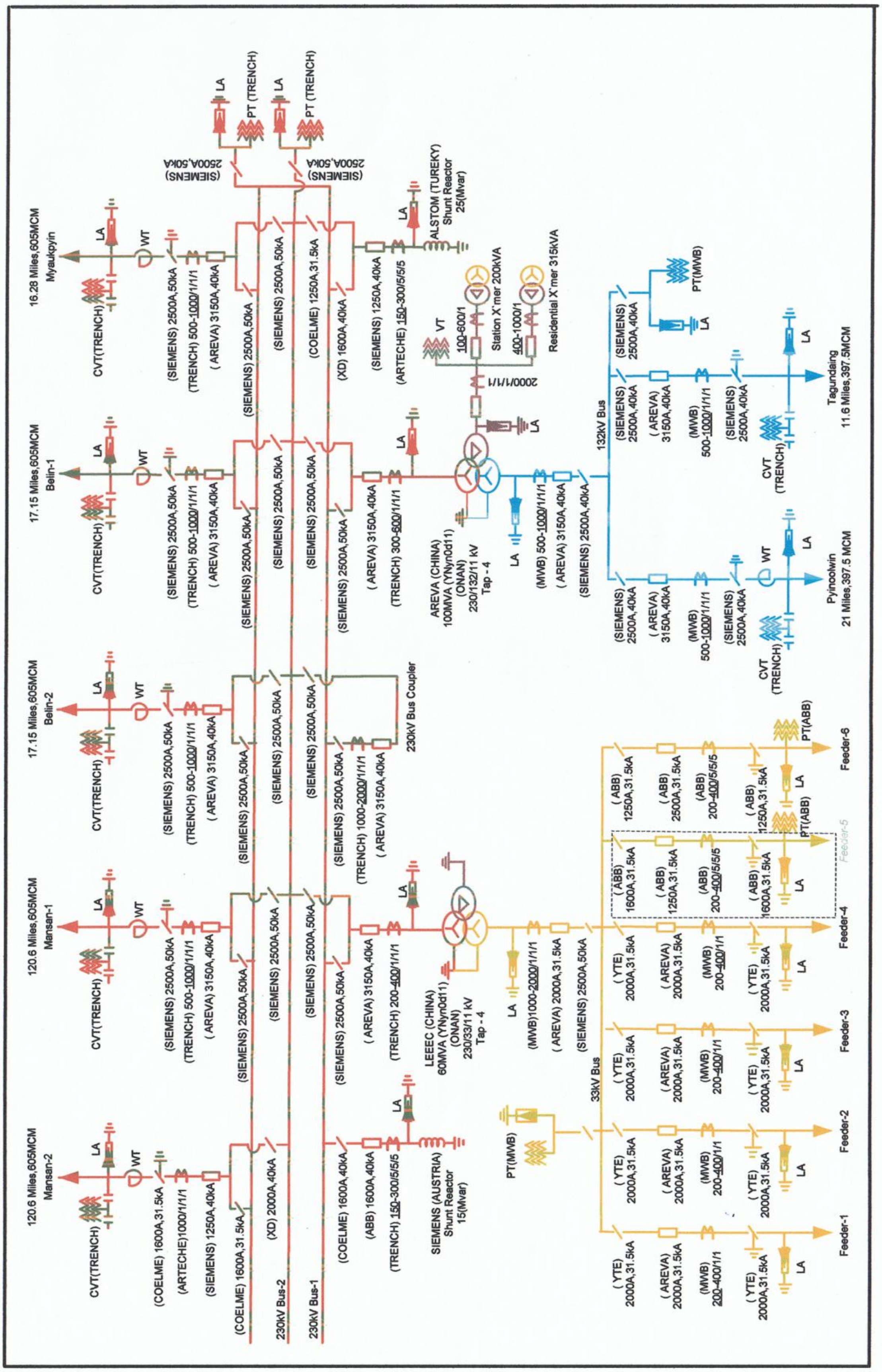

Figure 2 Single Line Diagram of Shwe Sar Yan Primary Substation

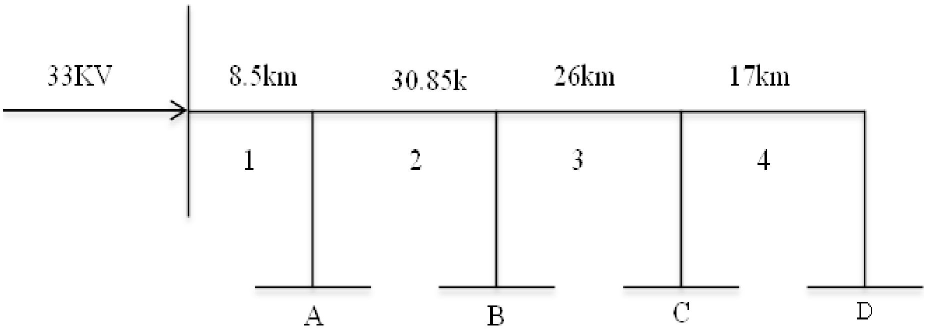

Figure 3 Radial Distribution Network of Shwe Sar Yan Primary Substation

Table 1 Basic System Data of Radial Distribution Network of Shwe Sar Yan Primary Substation

Component	**λ (f/ yr)**	**r (hours)**	**Average load (KW)**
Section			
1	0.13	4	1100
2	0.46	4	
3	0.39	4	9000
4	0.26	4	
Distributor			
A	4.16	6	15000
B	11.17	10	
C	10.75	11	17000
D	11.4	13	

3. 2. Reliability Indices without Protective Device

In this case, no protective device is used in the system. After that using the basic load point indices, system indices and energy-oriented indices can be calculated below:

Table 2 Basic Load Point Indices for Without Protective Device

	Load Point A			Load Point B			Load Point C			Load Point D		
Comp-onent	λ (f/yr)	r (h)	U (hr/yr)	λ (f/yr)	r (h)	U (h/yr)	λ (f/ yr)	r (h)	U (h/yr)	λ (f/yr)	r (h)	U (h/yr)
Section												
1	0.13	4	0.52	0.13	4	0.52	0.13	4	0.52	0.13	4	0.52
2	0.46	4	1.84	0.46	4	1.84	0.46	4	1.84	0.46	4	1.84
3	0.39	4	1.56	0.39	4	1.56	0.39	4	1.56	0.39	4	1.56
4	0.26	4	1.04	0.26	4	1.04	0.26	4	1.04	0.26	4	1.04
Distri-butor												
A	4.16	6	24.96	4.16	6	24.96	4.16	6	24.96	4.16	6	24.96
B	11.17	10	111.7	11.17	10	111.7	11.17	10	111.7	11.17	10	111.7
C	10.75	11	118.25	10.75	11	118.25	10.75	11	118.25	10.75	11	118.25
D	11.4	13	148.2	11.4	13	148.2	11.4	13	148.2	11.4	13	148.2
Total	**38.72**	**10.54**	**408.07**	**38.72**	**10.54**	**408.07**	**38.72**	**10.54**	**408.07**	**38.72**	**10.54**	**408.07**

Basic indices for each load point can be calculated using equation (1), (2), (3) and (4) . The results are shown in Table (3). In this case, no protective device is used in the system. With the obtained the basic load point indices, system indices and energy-oriented indices can be calculated as follow.

From equation (1) ,

$$\text{SAIFI} = \frac{\text{Total number of customer interruptions}}{\text{Total number of customers served}}$$

$$\text{SAIFI} = \frac{38.72+38.72+38.72+38.72}{4}$$

$$= 38.72 \text{ interruption/ customer/ yr}$$

From equation (2),

$$\text{SAIDI} = \frac{408.07+408.07+408.07+408.07}{4}$$

$$= 408.07 \text{ hr/ customer/ yr}$$

From equation (3),

$$\text{CAIDI} = \frac{10.54+10.54+10.54+10.54}{4}$$

$$\text{CAIDI} = 10.54 \text{ hr/ customer interruption / yr}$$

From equation (4),

$$\text{ENS} = 408.07 \times 42.1 \text{ MW}$$

$$= 17207.11 \text{ MWh/ yr}$$

3. 3 Reliability Indices with Protective Devices

Using protective device on radial system has a great effect on reliability of the system. With the obtained the basic load point indices, system indices and energy-oriented indices can be calculated. By using protective devices, reliability improvement scheme is tested as follows :

(1) Lateral protection with fuse
(2) Feeder protection with disconnecting switches
(3) Effect of protection failure rate (Ohn Zin Lin, 2016)

3.3.1. Lateral Protection with Fuse

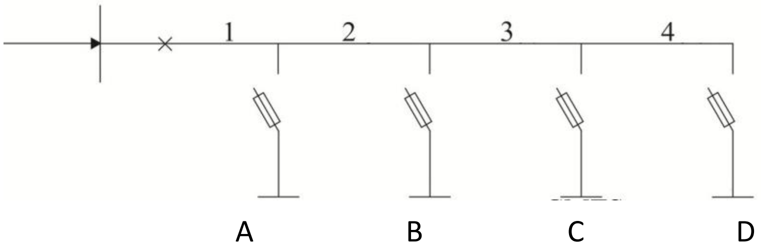

Figure 4 Schematic Diagram of Shwe Sar Yan Primary Substation by using Fuse

Table 3 Impact of Fuse on System Reliability Indices

Component	Load Point A			Load Point B			Load Point C			Load Point D		
	λ (f/yr)	**r (hr)**	**U (hr/yr)**	**λ (f/yr)**	**r (hr)**	**U (hr/yr)**	**λ (f/yr)**	**r (hr)**	**U (hr/yr)**	**λ (f/yr)**	**r (hr)**	**U (hr/yr)**
Section	0.13	4	0.52	0.13	4	0.52	0.13	4	0.52	0.13	4	0.52
1	0.46	4	1.84	0.46	4	1.84	0.46	4	1.84	0.46	4	1.84
2	0.39	4	1.56	0.39	4	1.56	0.39	4	1.56	0.39	4	1.56
3	0.26	4	1.04	0.26	4	1.04	0.26	4	1.04	0.26	4	1.04
4												
Distri-butor												
A	4.16	6	24.96									
B				11.17	10	111.7						
C							10.75	11	118.25			
D										11.4	13	148.2
Total	**5.4**	**5.54**	**29.92**	**12.41**	**9.40**	**116.66**	**11.99**	**10.28**	**123.21**	**12.64**	**12.12**	**153.16**

The most unreliable load point is D because of the domain effect of the failures on its lateral distributor 11.4 f/yr compared with 4.16, 11.17 and 10.75 f/yr on other laterals. By using equations (1), (2), (3) and (4) . The calculated values of SAIFI is 10.61 interruption / customer / yr, SAIDI is 105.74 h /customer/ yr, CAIDI is 9.97 h /customer interruption / yr and ENS is 4451.65 MWh/yr.

3. 3. 2. Feeder Protection with Disconnecting Switches

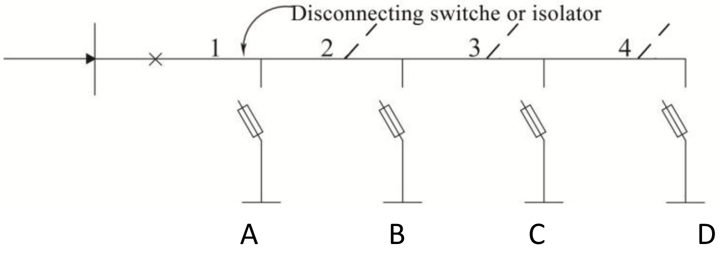

Figure 5 Schematic Diagram of Shwe Sar Yan Primary Substation by using Disconnecting Switches

Table 4 Impact of Disconnecting Switches on System Reliability Indices

	Load Point A			**Load Point B**			**Load Point C**			**Load Point D**		
Component	**λ (f/yr)**	**r (hr)**	**U (hr/yr)**	**λ (f/yr)**	**r (hr)**	**U (hr/yr)**	**λ (f/yr)**	**r (hr)**	**U (hr/yr)**	**λ (f/yr)**	**r (hr)**	**U (hr/yr)**
Section												
1	0.13	4	0.52	0.13	4	0.52	0.13	4	0.52	0.13	4	0.52
2	0.46	0.5	0.23	0.46	4	1.84	0.46	4	1.84	0.46	4	1.84
3	0.39	0.5	0.2	0.39	0.5	0.2	0.39	4	1.56	0.39	4	1.56
4	0.26	0.5	0.13	0.26	0.5	0.13	0.26	0.5	0.13	0.26	4	1.04
Distri-butor												
A	4.16	6	24.96									
B				11.17	10	111.7						
C							10.75	11	118.25			
D										11.4	13	148.2
Total	**5.4**	**4.82**	**26.04**	**12.41**	**9.22**	**114.39**	**11.99**	**10.2**	**122.3**	**12.64**	**12.12**	**153.16**

By using equation (1), (2), (3) and (4) , the values of SAIFI, SAIDI, CAIDI and ENS are 10.61 interruption/customer/yr, 103.97 h/customer/yr, 9.79 h/customer interruption/yr and 4377.14 MWh/yr.

3 . 3. 2 Effect of Protection Failure Rate

Failure rate = (failure rate/fuse operates) x P (fuse operates) + (failure rate/ fuse fails) x P (fuse fails) (5)

Table 5 Impacts of 90% Protection Failure Rate

	Load Point A			**Load Point B**			**Load Point C**			**Load Point D**		
Component	λ **(f/yr)**	r **(hr)**	U **(hr/yr)**	λ **(f/yr)**	r **(hr)**	U **(hr/yr)**	λ **(f/yr)**	r **(hr)**	U **(hr/yr)**	λ **(f/yr)**	r **(hr)**	U **(hr/yr)**
Section												
1	0.13	4	0.52	0.13	4	0.52	0.13	4	0.52	0.13	4	0.52
2	0.46	0.5	0.23	0.46	4	1.84	0.46	4	1.84	0.46	4	1.84
3	0.39	0.5	0.2	0.39	0.5	0.2	0.39	4	1.56	0.39	4	1.56
4	0.26	0.5	0.13	0.26	0.5	0.13	0.26	0.5	0.13	0.26	4	1.04
Distributor												
A	4.16	6	24.96	0.42	0.5	0.21	0.42	0.5	0.21	0.42	0.5	0.21
B	1.12	0.5	0.56	11.17	10	111.7	1.12	0.5	0.56	1.12	0.5	0.56
C	1.08	0.5	0.54	1.08	0.5	0.54	10.75	11	118.25	1.08	0.5	0.54
D	1.14	0.5	0.57	1.14	0.5	0.57	1.14	0.5	0.57	11.4	13	148.2
Total	**8.74**	**3.17**	**27.71**	**15.05**	**7.69**	**115.71**	**14.67**	**8.43**	**123.64**	**15.26**	**9.99**	**152.56**

The values of SAIFI,SAIDI, CAIDI, and ENS are calculated by using equation (1) (2), (3) and (4). And result are 13.43 interruption/customer/yr, 104.91 h/customer/ yr, 7.81 h/customer interruption/ yr and 4416.71 MWh/yr.

Comparison of Energy Not Supply (Ens) Value for Without Protective Devices and Fuse

Table 6 Energy Not Supply (ENS) for Normal State

Feeder	**Failure Rate (f/ yr)**	**Outage Time (hr/ yr)**	**ENS (MWhr/ yr)**
1	38.72	10.54	448.92
2	38.72	10.54	3672.98
3	38.72	10.54	6121.63
4	38.72	10.54	6937.85

Table 7 Energy Not Supply (ENS) Improvement with Fuse

Feeder	**Failure Rate (f/ yr)**	**Outage Time (h/ yr)**	**ENS (MWh/ yr)**
1	5.4	5.54	32.91
2	12.41	9.4	1049.89
3	11.99	10.28	1848.86
4	12.64	12.12	2604.35

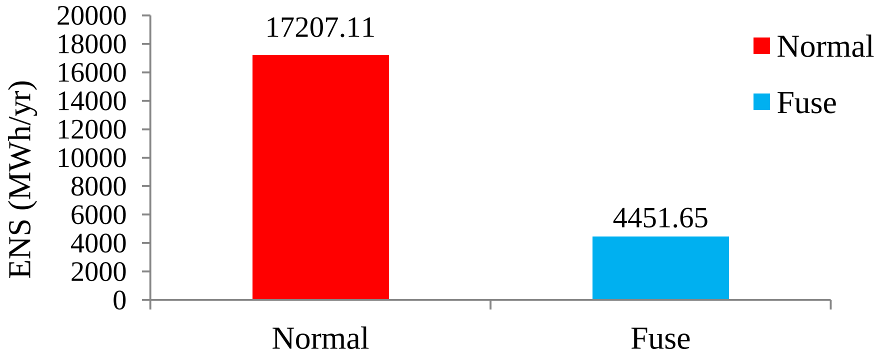

Figure 6 Comparison of ENS between Normal and Fuse

Comparison of Ens Value For Without Protective Devices and Disconnecting Switches

Table 8 Energy Not Supply (ENS) Improvement with Disconnecting Switches

Feeder	**Failure Rate (f/ yr)**	**Outage Time (h/ yr)**	**ENS (MWh/ yr)**
1	5.4	4.82	28.63
2	12.41	9.22	1029.78
3	11.99	10.2	1834.47
4	12.64	12.12	2609.35

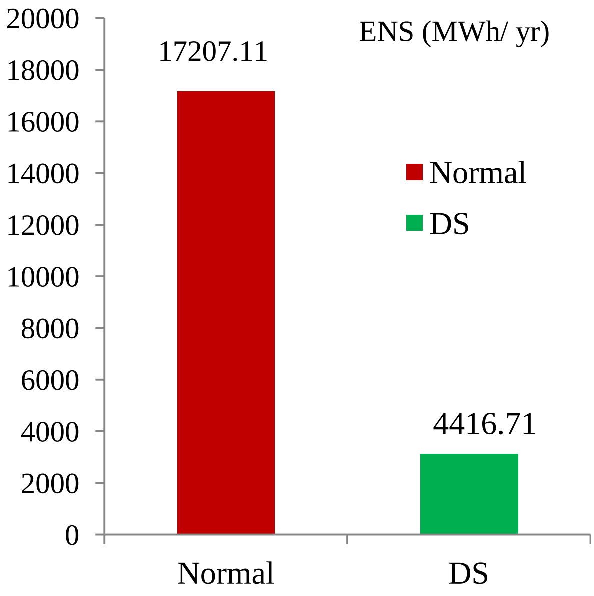

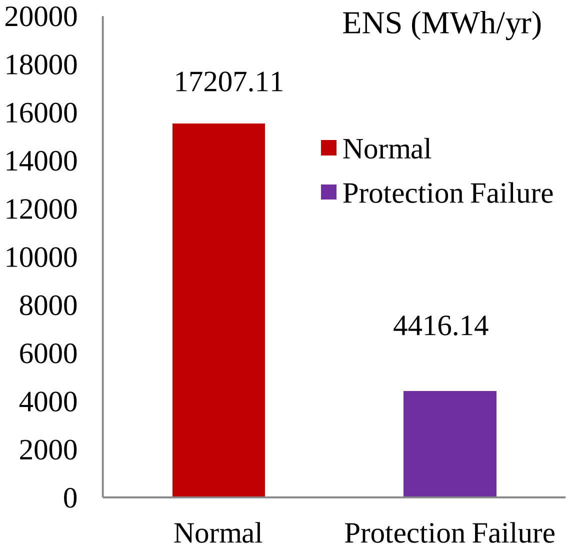

Figure 7 Comparison of ENS between Normal and Disconnecting Switches

Figure 8 Comparison of ENS between Normal and Protection Failure

Comparison of Ens Value For Without Protective Devices and 90% Protection Failure Rate

Table 9 Energy Not Supply (ENS) Improvement with 90% Protection Failure Rate

Feeder	Failure Rate (f / yr)	Outage Time (h / yr)	ENS (MWh / yr)
1	8.74	3.17	30.48
2	15.05	7.69	1041.61
3	14.67	8.43	1855.02
4	15.26	9.99	2591.61

As above calculation, using protective devices, e.g. disconnecting switches and fuse decrease ENS (Energy not supplied) than calculation without using protective devices

Result Data for Reliability Indices

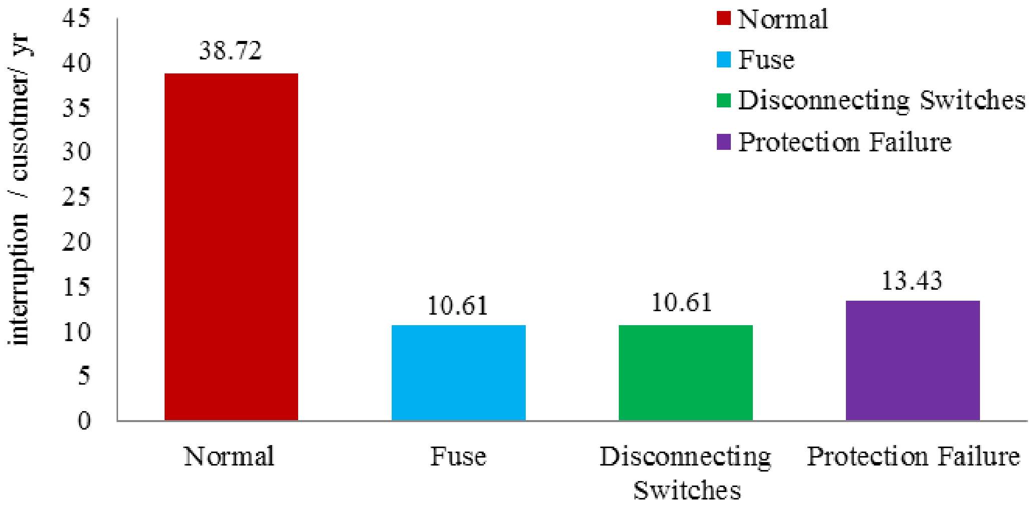

Figure 9 Result Comparisons for SAIFI

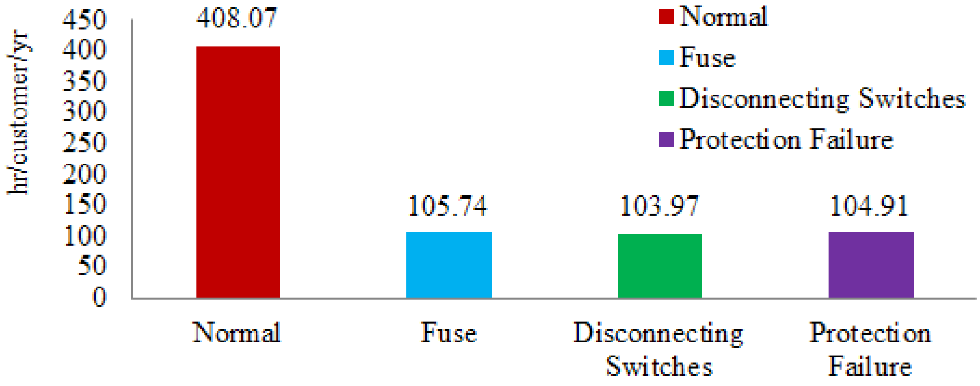

Figure 10 Result Comparisons for SAIDI

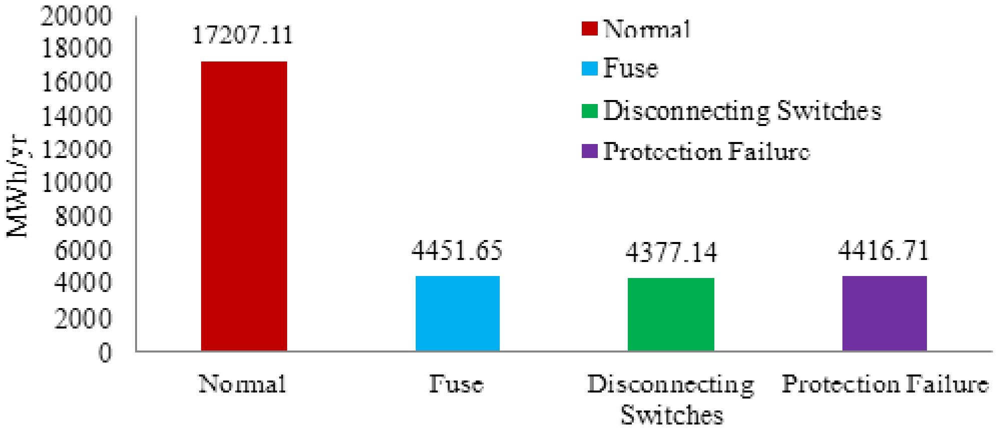

Figure 11 Result Comparisons for ENS

Discussion

In this research, the impact of protective devices installation, e.g, disconnecting switch and fuse on distribution system reliability is analyzed using hand calculations and hence fully understand reliability models and evaluation techniques. The reliability index of ENS, energy not supply is mainly evaluated and shown the comparison of ENS values with and without protective device. And then, the method that is the least value of ENS is chosen to improve the distribution using analytical method.

Conclusion

The reliability level of the system is computed after analyzing the real condition of the Shwe Sar Yan primary substation from December 2017 to December 2018. According to results, the values of ENS are as different as the protective devices which are used for reliability improvement and it is focused to check the condition of system reliability. Therefore, it can be found to get the most reliable method in distribution system. Shwe Sar Yan substation supplies the electricity to Tagontine, Pyin Oo Lwin, Shwelyanbo, Patheingyi, Chan Mya Tharsi and Pyi Kyi Tagon which are the large regions of Mandalay. There are many industrial zones and customers in it. So, the more outage, much indirect costs the customers impose. If the distribution networks will not be fully protected, interruptions will be occurred frequently.

Acknowledgement

The author would like to express her profound gratitude to the Department of Higher Education , Ministry of Education, Myanmar , for provision of opportunity to do this research and Myanmar Academy of Arts and Science for allowing to present this paper.

References

Brown Richard E. (2008) "Electric Power Distribution Reliability", Second Edition.

Le e Layton, (2004) "Reliability Indices for Utilities".

Leonel de Magalhães Carvalho, (2008) "Using Evolutionary Swarms (EPSO) In Power System Reliability Indices Calculation".

Ohn Zin Lin, (2016) "Distribution System Reliability Improvement in Dry Zone Area of Myanmar".

Rahamathulla Mohammad, "New Methods for Reliability Evaluation and Enhancement of Power Systems.

Shwe Sa Yan Primary Substation, (2017-2018) "Documents of System Data and Load Data", Mandalay Regional Division, Myanmar.

Wang and Peng, (1999) "Reliability Cost and Worth Consideration in Distribution System Evaluation".

J. Myanmar Acad. Arts Sci. 2020 **Vol. XVIII.No.2C**

STRUCTURAL ANALYSIS AND PHASE FORMATION OF PbO - MnO_2 SOLID SOLUTIONS (Pb_2MnO_4 STRUCTURE)

Pwint Hlaing Ni[1], Win Win Yee[2], Zin Oo Hlaing[3],
May Aye Khine[4] and Pwint Yi Thein[5]

Abstract

PbO - MnO_2 solid solutions (Pb_2MnO_4 structure) are prepared by using starting materials, PbO and MnO_2 with equal molar ratio and solid state reaction method. The mixed samples are heat treated at 600 °C, 650 °C, 700 °C, 750 °C and 800 °C for 3 hrs, respectively.

After heat treatment schedule, structural properties and phase formation of the samples are characterized by using XRD. From the XRD investigation, structural properties, such as, lattice parameters, lattice micro strain and crystallite size are evaluated. Furthermore, variation of sintering temperature with structural properties are also examined.

Keywords : XRD, solid solutions, structural properties.

Introduction

The A_2BO_4 spinel oxides forms a family of ~120 compounds spanning a significant range of properties including ferro ~ and antiferromagnetism, coexistance of transparency and conductivity, superconductivity and ferroelectricity. In spinels, A and B can be divalent, trivalent, or tetravalent cations. In the normal atom pattern, the oxygen forms a cubic closed packed (face centered) array A(II) and B (III) in the tetrahedral (1/8 occupied) and octahedral (1/2 occupied) sites in the lattice. Few works are reported concerning antiferromagnetic Pb_2MnO_4 structures.

In this study, PbO - MnO_2 solid solutions (Pb_2MnO_4 structure) is investigated by using solid state reaction method and conventional funance annealing process. Structural properties and phase formation of the samples are characterized by using XRD. From the XRD investigation, variation of sintering temperature with structural properties are examined.

Experimental

PbO - MnO_2 solid solutions (Pb_2MnO_4 structures) were prepared solid state reaction method. Locally available, analar grade starting materials PbO and MnO_2 were weighted in equal molar ratio using digital balance. The two oxides powder were mixed in agate mortar for 2 hrs.

After mixing the powders, the mixture was pre heat treated at 500°C (the melting point of MnO_2 is 535°C) for 3 hrs. After that, the mixture was grinded with ball milling for 6 hrs to get the homogeneous mixture. Then, the mixture was heat treated again at 600°C, 650°C, 700°C, 750°C and 800°C for 3 hrs respectively. X - rays diffraction studies were carried to determine the structural properties and phase formation of the samples by means of Rigaku Multiflux 2000 using Cu/K_α monochromatic radiation. The wavelength, voltage and current were respectively,

---

[1] Lecturer, Department of Physics, University of Information Technology, Yangon.

[2] Department of Physics, University of Computer Science, Yangon.

[3] Department of Physics, University of Maubin.

[4] Department of Physics, University of Kyaing Ton.

[5] Department of Physics, Nationality Youth Resources Development Degree College Yangon.

1.5418 Å, 40 kV and 50 mA. From the XRD spectra, structural properties were evaluated. Furthermore, variations of sintering temperature with structural properties were examined.

Results and Discussion

Specimen were scanned from 10^o to 70^o in diffraction angle, 2ϴ, with a step size of 0.01 ^{o}/sec, as depicted in figure (1). Peak search algorithm, known as Jade software was used to identify the peaks in this study. It was obvious that, at sintering temperature at 600^oC, only PbO structure was found. Both PbO and Pb_2MnO_4 structures were coexisted together at sintering temperature 650^oC.At the sintering temperatures 700^oC, 750^oC and 800^oC, single phase spinel Pb_2MnO_4 polycrystalline structures were obtained and (131) peak was peak maximum, known as Bragg peak in those temperatures. Lattice parameters “a” and “c” were evaluated and listed in table (1). Crystallite size and micro strain were examined by using Debye - Sherrer equations and also listed in table (1).

According to the table (1), it is noted that, structural properties, especially, lattice parameters "a " and " c " values are nearly the same as standard values (a = 12.7854 Ȧ and c = 5.1228 Ȧ).It is found that, there are very small variations of lattice parameters with sintering temperature. It may be due to, solid- state- reaction mixtures become more crystalline on heating process. During the sintering temperature range from 650^oC to 750^oC, crystallite size decreases with increasing full width at half maximum of (131) peak, it is possible due to lower crystal quality. At sintering temperature 800^oC, crystallite size abruptly increases and the better crystal quality is obtained. This result leads to the sintering temperature 800^oC is the optimum condition for preparation of Pb_2MnO_4 structure in this study.

Figure (2) shows the variation of lattice parameters "a" and "c" with process temperature. Effect of process temperature on lattice distortion is depicted in figure(3). The minimum lattice distortion is occurred at temperature 800^oC, as seen in figure (3). Influence of process temperature on (tetragonal type) cell volume is illustrated in figure (4). The minimum cell volume is found at temperature 800^oC, as seen in figure (3).These results indicate, variation of process temperature with lattice distortion (c/a) and cell volume of the Pb_2MnO_4 ceramics are nearly the same, in the range of temperature 700^oC - 800^oC.

Louis Neel literally defined antiferromagnetic materials as" interesting but useless " during his Nobel lecture in 1970.Antiferromagnetic materials concentrate numerous features that encourage the research on its integration in devices for both information processing and storage. Works based on spintronic device applications on antiferromagnets have grown exponentially during the last decad.

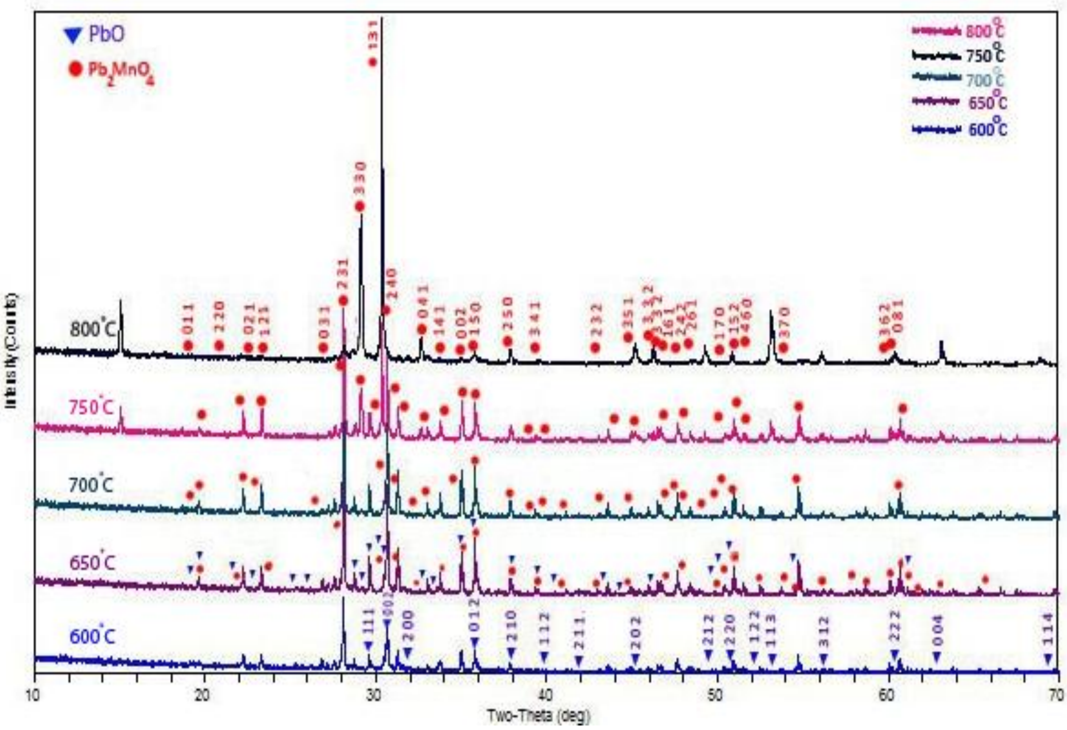

Figure 1 XRD spectra of Pb_2MnO_4 ceramics at different sintering temperatures.

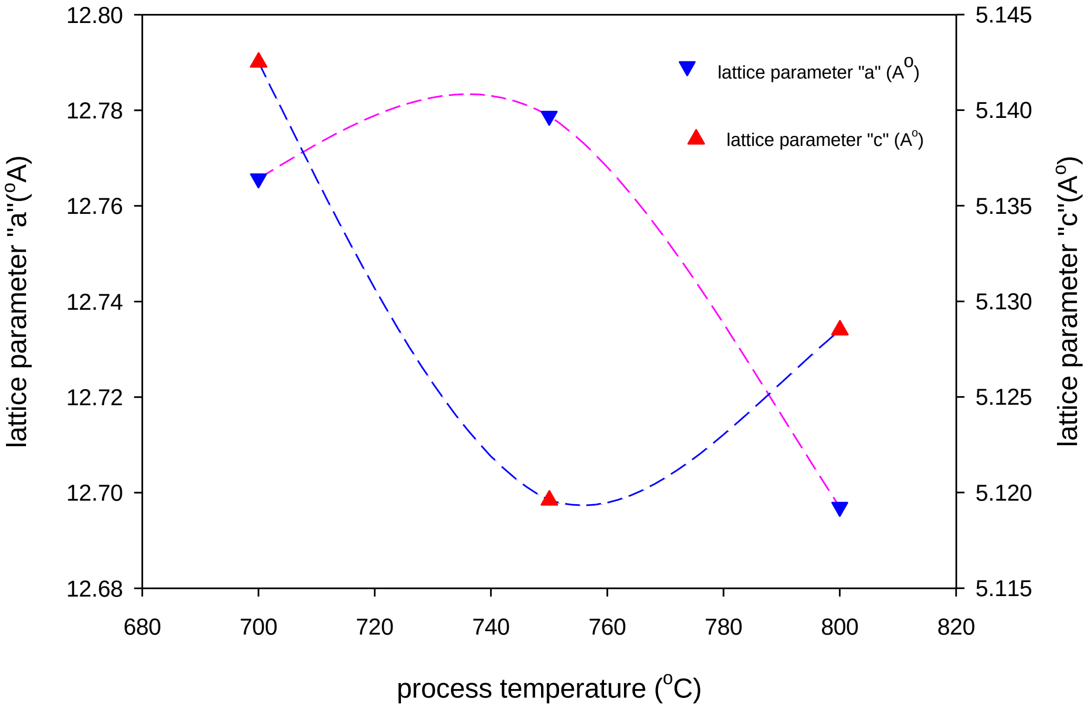

Figure 2 The variation of lattice parameters " a " and " c " with process temperature of the Pb_2MnO_4 ceramics

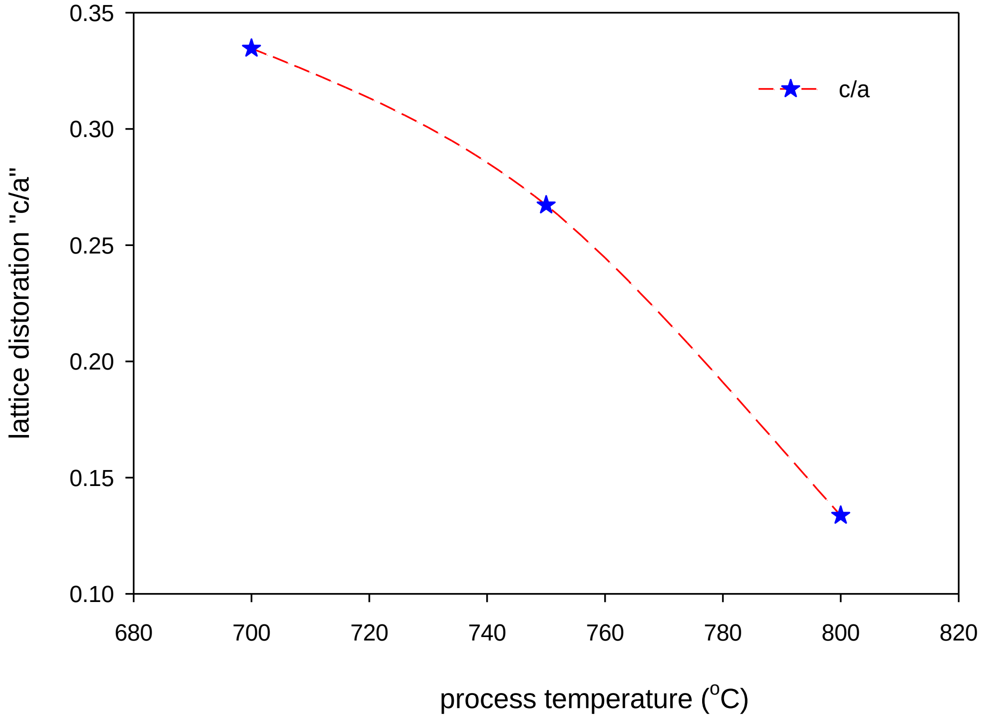

Figure 3 The variation of process temperature with lattice distortion (c/a) of the Pb_2MnO_4 ceramics

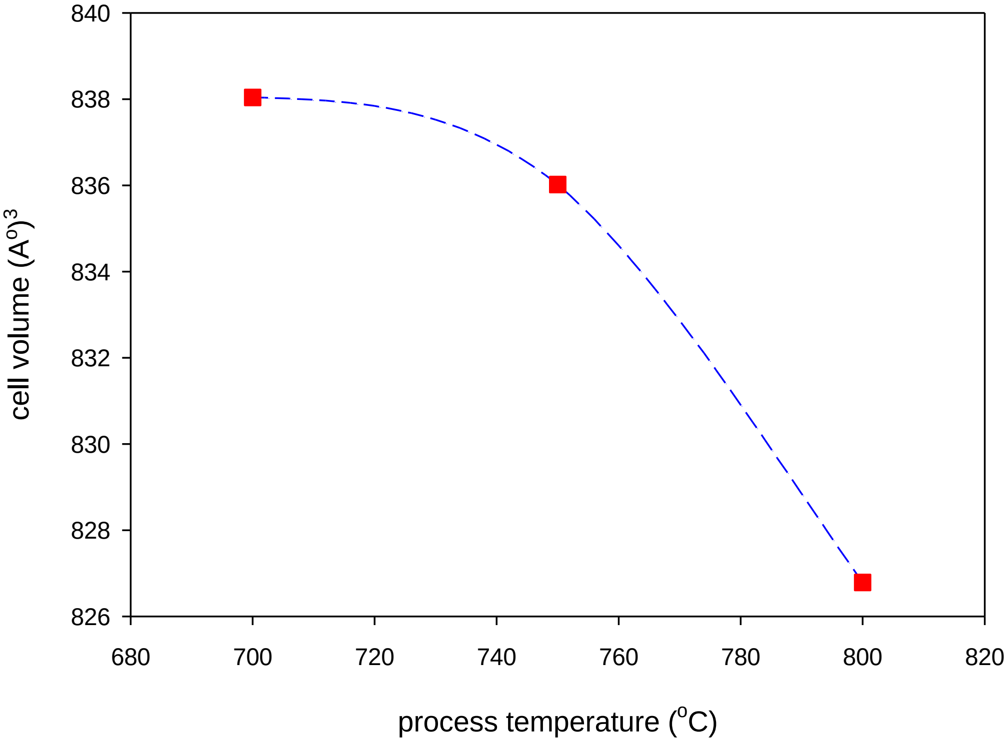

Figure 4 The variation of process temperature with cell volume of the Pb_2MnO_4 ceramics

Table1 Structural properties of Pb_2MnO_4 ceramics.

temperature ^oC	lattice parameter "a(A^o)"	lattice parameter "c(A^o)"	lattice distortion	crystallize size (nm)	micro strain	FWHM of (131) peak(^{o})
650^oC	12.8978	5.1162	0.2648	77.26	1.845×10^{-3}	0.3973
700^oC	12.7657	5.1425	0.3346	59.77	2.387×10^{-3}	0.4015
750^oC	12.7788	5.1196	0.2672	56.87	2.511×10^{-3}	0.4008
800^oC	12.6970	5.1285	0.3371	75.82	1.884×10^{-3}	0.4045

Conclusion

In this study, spinel Pb_2MnO_4 structure is examined by using conventional solid state sintering method. Experimental data, especially, lattice parameters are nearly the same as standard data.

Solid state sintering method is eco - friendly, requires less times and easy to workup. Solid state reaction mixtures becomes more crystalline on sintering process. Nowadays, research based on spintronic devices are concerned with antiferromagnets. Antiferromagnetic Pb_2MnO_4 structure is one of the possible candidates for spintronic device applications. This work may provide the new direction to the researcher into the development of Pb_2MnO_4 ceramics in short time with eco - friendly and cost effectiveness.

Acknowledgments

The authors would like to acknowledge the Universities Research Centre (URC), University of Yangon, for XRD measurements. The authors would like to express her appreciation to University of Information Technology (UIT), Yangon. The authors would like to express her heart and soul thanks to Dr. Pwint Yi Thein, who gave kind help and advice for the accomplishment of this paper.

References

Kimber S A and Attfield J P (2007) : " Magnetic Order in Acentric Pb_2MnO_4 ", J. Mat. Chem., 17, 4885 - 4888.

Helene Serier - Brault and Martin Jackson (2011) : " Properties and High - Pressure Behavior of a Ternary lead oxide Pb_2MnO_4 ", Solid.State. Sci.,13, 326 -330.

Vladen Stevanovic, Mayeul d` Avezac and Alex Zunger (2011) : " Universal Electrostatic Origin of Cation Ordering in A_2BO_4 Spinal Oxides " ,J.Am Ceram. Soc.,133, 11649 - 11654.

Razmara Z (2018) : " Synthesis, Characterization and Magnetic Properties of Nanocomposite Pb_2MnO_4 and PbO. A New Metal - Organic Complex " , Asian. J.Chem., 10, 2171 - 2174.

Du S F, Tian Y J, Liu H D, Liu J and Chen Y F (2006) : " Calcination Effect on the Properties of Gallium Doped Zinc Oxide Powders " ' J.Am.Cer.Soc., 89, 2440 - 2443.

Zelezny J, Wadley P, Olejnik K, Hoffmann A and Ohno H (2018) : " Spin - Transport, Spin - Torque and Memory in Antiferromagnetic Devices " , Nat.Phy., 14, 220 - 228 .

Jungwrith T, Sinova J, Manchon A, Marti X, Wuderlich C and Felser C (2018) : " The Multiple Directions of Antiferromagnetic Spintronics " , Nat.Phy., 14, 200 -203 .

Matthias B Jungfleish and Axel Hoffmann (2018) : " Prospectives of Antiferromagnetic Spintronics " ,Phy.Lett.A., 382 (13) , 865 - 871 .